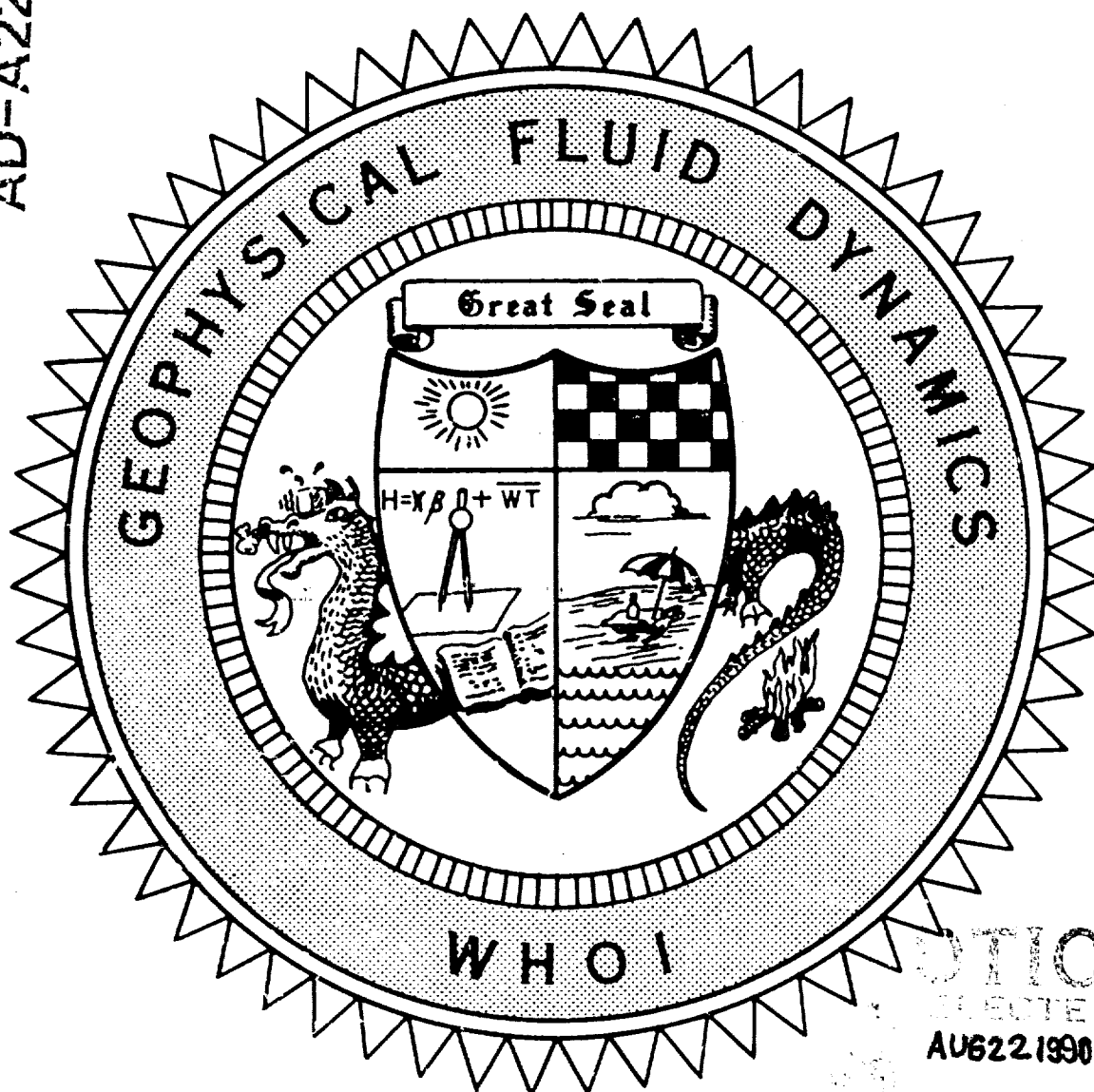


AD-A225 571

WHOI-89-54  
1989

DTIC FILE COPY



DTIC  
ELECTE  
AUG 22 1990

Course Lectures  
Abstracts of Participants  
Fellows Project Reports

90 08 21 083

DTIC  
AUG 22 1990

# GEOPHYSICAL FLUID DYNAMICS PROGRAM

Summer of 1989  
Staff and Visitors

NAME	AFFILIATION
Anderson, James	Stevens Institute of Technology
Badan-Dangon, Antoine	CICESE
Cessi, Paola	Scripps Institution of Oceanography
Cushman-Roisin, Benoit	Florida State University
Dewar, William	Florida State University
Fauve, Stephen	Ecole Normal Supérieure
Flierl, Glenn	Massachusetts Institute of Technology
Fowler, Andrew C.	Oxford University
Gibson, Carl H.	University of California, San Diego
Hendershott, Myrl C.	Scripps Institution of Oceanography
Huppert, Herbert E.	D.A.M.P.T., University of Cambridge
Ierly, Glenn	Michigan Technical University
Malkus, Willem V.R.	Massachusetts Institute of Technology
Ledwell, James	Florida State University
Rhines, Peter B.	University of Washington
Rooth, Claes	University of Miami, Rosenstiel School
Rosby, Thomas	University of Rhode Island
Salmon, Rick	Scripps Institution of Oceanography
Spiegel, Edward	Columbia University
Stern, Melvin	Florida State University
Stommel, Henry	Woods Hole Oceanographic Institution
Thieberger, Rubin	Ben Gurion University
Veronis, George	Yale University
Woods, Andrew	Cambridge University
Yano, Jun-Ichi	Massachusetts Institute of Technology
Young, William	Scripps Institution of Oceanography

## Fellows

Chassignet, Eric	University of Miami, Rosenstiel School
Chen, Liang Gui	Florida State University
Condie, R. Vance	Columbia University
Ghosal, Sandip	Columbia University
Jarvis, Richard	Cambridge University
Jones, Scott	University of California
Mallier, Roland	Brown University
Sutyrin, George	Shirshov Institute of Oceanography
Thompson, LuAnne	MIT/WHOI Joint Program
Yushina, Irene	Shirshov Institute of Oceanography

## PREFACE

The success of this summer's Geophysical Fluid Dynamics Program owes much to Myrl Hendershott's excellent and engaging survey of the Oceans' General Circulation, including recent developments in the Theory of Recirculation Gyres and Thermocline Ventilation. Hendershott's lecture notes are included in the first part of this volume.

The diverse fluid dynamical subjects discussed in this summer's program are summarized in the abstracts of lectures by the staff and visitors. But the main thrust of this summer is, as always, revealed in the reports of the individual research by the Fellows.

We thank the Office of Naval Research and The National Science Foundation for their continuing support.

The GFD Steering Committee.



**Myrl Hendershott**





Row 1: J. Hart, B. Frazel, J. Whitehead, S. Ghosal, W. Young, J. Ledwell, P. Cessi, L. Thompson, J. Anderson, W. Malkus, C. Rooth,  
G. Sutyryn, R. Jarvis, R. Mallier, A. Woods, H. Huppert

Row 2: E. Spiegel, S. Jones, I. Yushina, E. Chassignet, W. Dewar, M. Stern, G. Veronis, L. Chen, V. Condie, G. Jerley, B. Cushman-  
Roisin, M. Hendershott, A. Badan-Dangon

**LECTURES**

<b>1</b>	<b>The General Circulation of The Oceans: The Basic Equations</b>	<b>7</b>
1.1	Introduction	
1.2	Approximations	
1.3	Scaling	
1.4	Simple models	
1.5	References	
1.6	Suggested reading	
<b>2</b>	<b>Observations</b>	<b>14</b>
2.1	A Description of the Surface Circulation	
2.2	A Description of the Interior Circulation	
2.3	Formation Sites and Circulation of Deepwater Masses	
2.4	Mode Waters	
2.5	Western Boundary Current and Interior Circulation in the Upper Kilometer of the Atlantic	
2.6	References	
<b>3</b>	<b>Fundamental Large Scale Circulation Theories</b>	<b>38</b>
3.1	Ekman Flow	
3.2	The Sverdrup Transport	
3.3	Combining Sverdrup and Ekman Ideas	
3.4	Abyssal Circulation	
3.5	References	
<b>4</b>	<b>Barotropic Vorticity Equation</b>	<b>55</b>
4.1	Barotropic Vorticity Equation	
4.2	Canonical Sverdrup Problem	
4.3	Stommel Problem (1948)	
4.4	Extended Stommel Problem	
4.5	Basin of Arbitrary Shape - Stommel Problem	
4.6	Munk Problem (1950)	
4.7	References	
<b>5</b>	<b>The Effect of Inertia</b>	<b>67</b>
5.1	Non-linear Perturbation of the Stommel Problem	
5.2	Fofonof Free Non-linear Solutions	
5.3	Bottom Friction and Inertial Boundary Layers	
5.4	Lateral Diffusion and Inertial Boundary Layers	
5.5	References	

# CONTENTS

<b>6</b>	<b>Initiation of Sverdrup Flow</b>	<b>83</b>
6.1	Introduction	
6.2	Linear Wave Solutions	
6.3	Mid-latitude Rossby Waves in Rectangular Basins	
6.4	Waves in the Tropics	
6.5	Establishment of Deep Water Circulation	
6.6	References	
<b>7</b>	<b>The General Circulation of the Oceans: Statistical One-layer Problems</b>	<b>100</b>
7.1	Introduction	
7.2	Fofonoff Flows	
7.3	The Statistical Mechanics of the Problem	
7.4	Numerical Results	
7.5	References	
<b>8</b>	<b>Multi-layer and Continuously Stratified Quasi-geostrophic Wind Driven Flows</b>	<b>117</b>
8.1	Mid-ocean Gyre	
8.2	Interior of the Subtropical Gyre	
8.3	The Western Boundary Layer	
8.4	Parsons' Model of Subtropical Gyre	
8.5	References	
<b>9</b>	<b>Parsons' Model applied to the Subpolar Gyre</b>	<b>136</b>
9.1	Thermocline Theories	
9.2	References	
<b>10</b>	<b>The Theory of the Ventilated Thermocline</b>	<b>146</b>
10.1	Part I	
10.2	Part II	

# **CONTENTS**

## **ABSTRACTS OF PARTICIPANTS**

<b>The Flow Over San Lorenzo Sill .....</b>	<b>164</b>
Antoine Badan-Dangon	
<b>The Agulhas Retroflection and Ring Formation .....</b>	<b>171</b>
Eric P. Chassignet	
<b>The Propagation of Isolated Nonlinear Eddies in a Two-layer Ocean .....</b>	<b>173</b>
Eric P. Chassignet	
<b>Kinematics of Ocean Subduction .....</b>	<b>176</b>
Benoit Cushman-Roisin	
<b>Connected Thermal and Transport Anomalies in the General Circulation .....</b>	<b>180</b>
William Dewar	
<b>Localized Structures Generated by Subcritical Instabilities .....</b>	<b>181</b>
Stephan Fauve and Olivier Thual	
<b>Arnold's Theorem and the Instability of Elliptical Vortices .....</b>	<b>182</b>
Glenn R. Flierl	
<b>Frost Heave .....</b>	<b>184</b>
Andrew C. Fowler	
<b>Critical Tests of Fossil Turbulence in the Ocean .....</b>	<b>186</b>
Carl H. Gibson	
<b>Oscillatory Flow Over Topography in a Rapidly Rotating Fluid .....</b>	<b>187</b>
John E. Hart	
<b>The Modulated Complex Lorenz Equations: Baroclinic Instability with Seasonal Forcing on the <math>\beta</math>-plane .....</b>	<b>191</b>
John E. Hart	
<b>The Fluid Mechanics of Solidification .....</b>	<b>199</b>
Herbert E. Huppert	
<b>A Biased Sample of Numerical Models of the Large Scale Circulation, I &amp; II .....</b>	<b>200</b>
Glenn Ierley	

## **CONTENTS**

<b>Diapycnal Mixing and the Circulation of the Mid-depth Ocean .....</b>	<b>204</b>
James R. Ledwell	
<b>The "Collapse" of Three Dimensional Instabilities in Elliptical Flow .....</b>	<b>209</b>
W.V.R. Malkus and F.A. Waleffe	
<b>The Equatorial Undercurrent .....</b>	<b>210</b>
Joseph Pedlosky	
<b>Ocean Dynamics from a Climate Perspective .....</b>	<b>212</b>
Claes G.H. Rooth	
<b>Bounds on Spatial and Temporal Variability of the Gulf Stream .....</b>	<b>216</b>
Thomas Rossby	
<b>Dynamics of Interacting Solitary Structures .....</b>	<b>217</b>
Edward A. Spiegel	
<b>Entrainment Into a Large Reynolds Jet .....</b>	<b>219</b>
Melvin E. Stern	
<b>The Dimensions of Cosmic Fractals .....</b>	<b>220</b>
R. Thieberger, E.A. Spiegel and L.A. Smith	
<b>A Possible Simplicity in global M2 Tidal Currents .....</b>	<b>221</b>
Henry Stommel	
<b>Evolution of Long-lived Vortices .....</b>	<b>226</b>
George G. Sutyrin	
<b>An Inverse Analysis of CSalt Data .....</b>	<b>229</b>
George Veronis	
<b>Boundary Driven Mixing .....</b>	<b>231</b>
Andrew W. Woods	
<b>An Estimate of the Dimensions of the Attractor of a Quasi-geostrophic System .....</b>	<b>233</b>
Jun-Ichi Yano	
<b>Statistics of Agglomeration .....</b>	<b>234</b>
William Young, Y. Pomeau and G. Carnevale	

# CONTENTS

## FELLOWS PROJECT REPORTS

<b>On the Meridional Propagation of Isolated Eddies .....</b>	<b>236</b>
Eric P. Chassignet	
<b>Finite Amplitudes Long Wave Baroclinic Instability .....</b>	<b>260</b>
Liang Gui Chen	
<b>Barotropic Boundary Layer Separation Regimes .....</b>	<b>289</b>
R. Vance Condie	
<b>Convection with Heat Sources .....</b>	<b>311</b>
Sandip Ghosal	
<b>A Two-layer Wind-Driven Ocean With Recirculation .....</b>	<b>367</b>
Richard A. Jarvis	
<b>Multiple Resonant Topographic Waves in a Barotropic Flow .....</b>	<b>392</b>
Scott W. Jones	
<b>The Parametric Model of Western Boundary Outflow .....</b>	<b>408</b>
Roland Mallier	
<b>A Coupled Thermocline-abyssal General Geostrophic Model .....</b>	<b>434</b>
George G. Sutyrin	
<b>Can Potential Vorticity Homogenize in Closed Gyres? .....</b>	<b>448</b>
LuAnne Thompson	
<b>Evolution of the Near-wall Jet.....</b>	<b>470</b>
Irene G. Yushina	

1989 Summer Study Study Program

in

Geophysical Fluid Dynamics

THE GENERAL CIRCULATION OF THE OCEANS

LECTURES

Myrl C. Hendershott

Scripps Institution of Oceanography

## LECTURE 1

THE GENERAL CIRCULATION OF THE OCEANS: THE BASIC EQUATIONS

## 1.1 Introduction

In order to study the dynamics of the ocean and atmosphere, we have to follow basic laws of physics which lead us to try to solve a series of conservation equations,

$$\text{Mass: } \frac{D\rho^*}{Dt} + \rho^* \nabla \cdot \underline{u} = 0 \quad (1)$$

$$\text{Momentum: } \rho^* \frac{Du_i}{Dt} = - \frac{\partial p^*}{\partial x_i} - \rho^* \frac{\partial P'}{\partial x_i} + \frac{\partial \tau_{ij}}{\partial x_j} \quad (2)$$

$$\text{Heat: } \rho^* \left[ C_{ps} \frac{DT}{Dt} - \rho^{*-1} B T \frac{Dp}{Dt} \right] = - \nabla \cdot \underline{q} + \tau_{ij} \frac{\partial u_i}{\partial x_j} - \underline{i} \cdot \nabla \left( \mu - T \frac{\partial \mu}{\partial T} \Big|_{ps} \right) \quad (3)$$

$$\text{Salt: } \rho^* \left[ \frac{DS}{Dt} \right] = - \nabla \cdot \underline{i} \quad (4)$$

$$\text{State: } \rho^* = \rho^*(p^*, T, S) \quad (5)$$

with the appropriate boundary conditions at the solid earth and sea surface. The most critical is that at sea surface, requiring a good knowledge of the dynamics of the atmosphere and its interaction with the ocean.

Note:  $P'$  = potential of body forces,  $\rho^*$  = density,  $\underline{u}$  = velocities,  $T$  = temperature,  $S$  = salinity,  $p^*$  = pressure,  $\tau_{ij}$  = stress tensor,  $\mu$  = chemical potential for  $S$ ,  $\underline{q}$  = heat flux,  $\underline{i}$  = salt flux and  $B = \alpha \frac{\partial \rho^*}{\partial T}$ .

One can try to solve all the above equations together numerically, but because of the wide range of scales present, insight must be gained from approximations which help to focus on a certain parameter range and transform the system into a solvable one.



## 1.2 Approximations

Approximations are of two kinds: (1) Neglect of small terms relative to large ones; (2) Parameterization of the effects of averaged scales.

The most common approximations are summarized below:

### a. Incompressibility of the ocean

Equation (1) becomes  $\nabla \cdot \underline{u} = 0$  as long as equations (3), (4) and (5) imply  $\frac{\partial \rho^*}{\partial t} \ll \rho^* \nabla \cdot \underline{u}$

### b. Boussinesq

Assumes that the spatial and temporal variations of  $\rho^*$  are small, hence the density can be treated as  $\rho_0$ , except in the hydrostatic equation. Thus (2) becomes

$$\rho_0 \frac{\partial u_i}{\partial t} = - \frac{\partial p}{\partial x_i} - \rho \frac{\partial p'}{\partial x_i} + \frac{\partial \tau_{ij}}{\partial x_j}$$

where  $\rho$  and  $p$  are now the departure of  $\rho^*$  and  $p^*$  from the hydrostatic state and  $\rho_0$ , the spatial and temporal average of  $\rho^*$ .

### c. Eddy diffusivity parameterization

(4) becomes  $\overline{S_t} + \nabla \cdot \underline{\overline{u}} \overline{S} = K \nabla^2 \overline{S}$

where  $K$  is the eddy diffusivity for the salinity,...

### d. Equation of State

(5) is conventionally approximated by  $\rho \sim a(T - \overline{T}) + b(S - \overline{S})$  where  $a$  and  $b$  are constants. As a consequence, the perturbation density  $\rho$  is usually assumed to obey

$$\rho_t + u \rho_x + v \rho_y + w \rho_z = K_v \rho_{zz} + K_H \nabla_H^2 \rho \quad (6)$$

in which  $K_v, K_H$  are eddy diffusivities of both salt and heat.

Since the earth rotates, the set of equations has to be written in rotating coordinates. The result of the traditional approximations, setting  $r \approx a$  (earth radius),  $v/r$  small ( $|v| \ll 2\Omega a$ ), the introduction of the  $\beta$ -plane coordinates and neglect of the metric terms (see Pedlosky, (1979, page 327 for discussion) leads to

$$u_t + uu_x + vu_y + wu_z - fv = -p_x/\rho_0 + (A_V u_z)_z + A_H \nabla_H^2 u \quad (7)$$

$$v_t + uv_x + vv_y + wv_z + fu = -p_y/\rho_0 + (A_V v_z)_z + A_H \nabla_H^2 v \quad (8)$$

$$w_t + uw_x + vw_y + ww_z = -p_z/\rho_0 - \partial \rho / \partial z + (A_V w_z)_z + A_H \nabla_H^2 w \quad (9)$$

$$u_x + v_y + w_z = 0, \quad (10)$$

in which  $f = f_0 + \beta y$ ,  $f_0 = 2\Omega \sin \theta_0$ ,  $\beta = \frac{2\Omega}{a} \cos \theta_0$

In addition to a simplified set of equations, to solve a specific problem, one needs some knowledge about the boundary conditions at the surface and bottom. At the boundaries, the stresses (wind friction and bottom drag, respectively) influence the interior flow through the Ekman vertical velocities associated with the divergence of the Ekman transports,  $w_E = (\tau_x^s - \tau_x^b) / (\rho_0 f_0)$  at the surface and  $w_E = D_E (v_x - u_y)$  at the bottom where  $D_E$  is the Ekman layer depth  $D_E = (2A_V / f)^{1/2}$ . The Ekman vertical velocities are significant because they are the means by which surface and bottom stresses communicate with the flow outside the Ekman layers, where vertical diffusion of momentum has ceased to be important. For details on the derivation, the reader is referred to Ekman (1905) and Pedlosky (1979).

### 1.3 Scaling

One can now try to estimate the relative size of each term in the above equations (6) - (10) in order to assess their importance.

Scales:

$$\begin{array}{ll} x, y \rightarrow L(x, y) & z \rightarrow H(z) \\ u, v \rightarrow U(u, v) & t \rightarrow (L/U)(t) \\ w \rightarrow W(w) & \rho \rightarrow \rho(\rho) \\ & p \rightarrow P(p) \end{array}$$

We introduce  $R_o = \frac{U}{f_0 L}$  (Rossby number),  $\beta_o = \frac{\beta L}{f_0}$  and  $\delta = \frac{H}{L}$ .

Equation (9) leads to  $\frac{W}{U} \leq \frac{H}{L}$ . If we consider the vertical velocities to be extremely small, then  $\frac{W}{U} \ll \frac{H}{L}$  and we can introduce  $\gamma$  such that  $\frac{W}{U} = \gamma \frac{H}{L}$  and  $W = \gamma \delta U$  ( $\gamma$  becomes of order 1 if  $W$  not so small).

With small vertical velocities and a small  $R_o$  number (valid for most places in the ocean), the leading terms in equations (7), (8) and (9) are

$$\left. \begin{array}{l} -f_0 v \sim -p_x / f_0 \\ +f_0 u \sim -p_y / f_0 \end{array} \right\} \text{Geostrophic balance}$$

and

$$0 = p_z - g\rho$$

This leads to  $P = \rho_0 f_0 UL$  and  $D = \rho_0 f_0 UL / gH$ . (7), (8), (9), and (10) then become

$$\begin{aligned} R_o (u_t + u u_x + v u_y) + R_o \gamma W u_z - v - \beta_o y v = \\ -p_x + E_v u_{zz} + E_H \nabla_H^2 u \end{aligned} \quad (11)$$

$$\begin{aligned} R_o (v_t + u v_x + v v_y) + R_o \gamma W v_z + u + \beta_o y u = \\ -p_y + E_v v_{zz} + E_H \nabla_H^2 v \end{aligned} \quad (12)$$

$$\begin{aligned} R_o \delta^2 \gamma (w_t + u w_x + v w_y) + R_o \gamma^2 \delta^2 w w_z = \\ -p_z - \rho + \gamma \delta^2 (E_v w_{zz} + E_H \nabla_H^2 w) \end{aligned} \quad (13)$$

$$u_x + v_y + \gamma w_z = 0 \quad (14)$$

where  $E_H = A_H / f_0 L^2$  and  $E_v = A_v / f_0 H^2 = \text{Ekman number}$ .

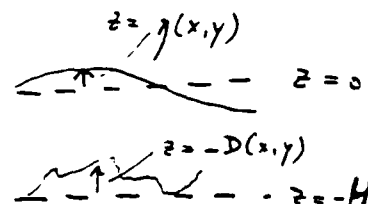
#### 1.4 Simple models

From the set of equations (11) - (14), we can look at a series of models, each resulting from certain approximations.

##### a. Shallow water model

Assumptions: { Homogeneous  
No vertical friction  
 $u_x + v_y \leq w_z$   
 $\delta$  small

$$W \leq UH/L = U\delta \quad (\text{and therefore } \gamma = 1)$$



As  $\delta \rightarrow 0$ ,  $W \rightarrow 0$  and  $0 = -\rho_z^*$  which gives  $\rho^* = g\rho(\eta(x, y) - z)$ . The horizontal pressure gradient is independent of  $z$ , implying that the horizontal velocities remain independent of  $z$  if they are so initially ( $u_z = v_z = 0$ ). As a result, the fluid moves in column. This is valid even if  $Ro \gg 1$  as long as the fluid is homogeneous and  $\delta \ll 1$ . The momentum equations are

$$u_t + uu_x + vv_y - fv = -g\eta_x \quad (15)$$

$$v_t + uv_x + vv_y + fv = -g\eta_y \quad (16)$$

$$\eta_t + ((\eta + D)u)_x + ((\eta + D)v)_y = 0 \quad (17)$$

Horizontal momentum diffusion can be added without violating  $u_z = v_z = 0$ . The above result can also be extended to several layers. This procedure retains the simplicity of the shallow water dynamics, but with stratification. The inviscible layer flow over/under one another. A particular case is the 1 1/2 layer model where the lower layer is asserted to be at rest, but where deformation of the interface remains possible.

##### b. Quasi - geostrophic Shallow Water Model

Assumptions:

$$\left\{ \begin{array}{l} \text{No vertical diffusion} \\ \text{Homogeneous} \\ R_o \ll 1, \beta_o \ll 1, f \ll 1 \\ \Delta \text{ relief} / \text{relief} \ll 1 \end{array} \right.$$

Between the Ekman layers, using equations (15) and (16), we can derive the vorticity equation,

$$\frac{D_H (\beta + f)}{Dt} + (\beta + f) (u_x + v_y) = A_H \nabla_H^2 \beta \quad (18)$$

where  $\beta = \text{vorticity} = v_x - u_y$

Vertically integrated mass conservation gives

$$\eta_t + \frac{w_E(0) - w_E(-H)}{\rho_o f_o} + \nabla_H ((\eta + D) \underline{u}) = 0$$

$$= \frac{(z_y^* - z_x^*)}{\rho_o f_o} = D_E (u_x - v_y)$$

which leads to

$$\frac{D_H}{Dt} \left( \frac{\beta + f}{\eta + D} \right) = \frac{A_H \nabla_H^2 \beta}{(\eta + D)} + \frac{\beta + f}{(\eta + D)^2} \left( \frac{z_y^* - z_x^*}{\rho_o f_o} - D_E \beta \right) \quad (19)$$

Using the fact that  $R_o, \beta_o, f \ll 1$ , the lowest order of (11), (12) and (13) give

$$\left. \begin{array}{l} -f_o v = -g \eta_x \\ f_o u = -g \eta_y \end{array} \right\} \text{ and } u_x + v_y = 0$$

which imply that  $f_o \psi = g \eta$  where  $\psi = \text{streamfunction}$ .

To first order,  $\frac{\beta + f}{\eta + D}$  can then be approximated by

$$\frac{1}{H} \left( \nabla^2 \psi + \beta_o y - f_o^2 \frac{\psi}{g H} + f_o \frac{h}{H} \right)$$

with  $D = H - h(x, y)$ .

which, substituted in (19), gives the quasi-geostrophic equation.

$$\left[ \partial_t + \mathcal{J}(\psi, \cdot) \right] \left[ \nabla^2 \psi + \beta y - \frac{\psi}{R^2} + \frac{f_0 h}{H} \right] = \nabla^4 \psi + \frac{c_T^2 - c_T^*}{\rho_0 H} - \frac{f_0 D_E}{H} \nabla^2 \psi \quad (20)$$

This can be extended to n-layers (Pedlosky, 1979). When the fluid is continuously stratified, then we can no longer integrate the vorticity equation vertically. Instead the vorticity and mass conservation equations must be cross-differentiated to eliminate the vertical velocities. In the absence of external forcing and lateral diffusion, the quasi-geostrophic equation becomes

$$\left( \partial_t + \mathcal{J}(\psi, \cdot) \right) \left[ \nabla^2 \psi + \beta y + \left( \frac{f_0^2}{N^2(z)} \psi_z \right)_z \right] = 0 \quad (21)$$

where  $N(z)$  is the Brünt-Väisälä frequency.

### 1.5 References

- Ekman, V.W. 1905: On the influence of the earth rotation rotation on ocean currents. Arkiv.  
 Natem, Astr. Fysik, Stockholm 2 (11).  
 Pedlosky, J. 1979: Geophysical Fluid Dynamics.  
 Springer-Verlag, Berlin and New York.

### 1.6 Suggested reading

- Evolution of Physical Oceanography (1981). Edited by  
 B. A. Warren and C. Wunsch, The MIT Press, 623 pp.

Notes submitted by: Eric Chassignet, University of Miami

## LECTURE 2

### 2. OBSERVATIONS

This talk provides basic observational background and acts as a guide for the upcoming discussion of the various general circulation theories.

#### 2.1 A DESCRIPTION OF THE SURFACE CIRCULATION

The first figure we will look at is the ocean surface wind pattern. Surface wind stress plays an important role in theories of ocean circulation by inducing an Ekman vertical velocity at the top of the ocean.

Fig. 2.1. 2.2. are of the global surface wind distribution in summer (2.1) and winter (2.2). One feature we should note is the dependence of the wind direction with latitude. In both north mid-latitudes and south mid-latitudes, the wind is generally eastward. In the tropics, the wind is westward. Both mid-latitude and tropical winds are strong; the mid-latitude winds are quite variable. Another aspect of the global wind is its "seasonality". This is most obvious in the Indian Ocean, where the wind field actually reverses direction between winter and summer; the "monsoon".

The next figure (Fig 2.3) is of global surface currents, which broadly resemble the surface wind structure. Principle features on this map are the great circulation "gyres" in each ocean. The so-called subtropical gyres are found in the mid-latitudes. They have counter-clockwise circulation in the southern hemisphere and clockwise circulation in northern hemisphere. There are counter-clockwise subpolar gyres in the higher northern hemisphere latitudes also.

The subtropical gyres have intense western boundary currents. The two most obvious western boundary currents are the "Gulf Stream" in the north Atlantic Ocean and "Kuroshio" in the north Pacific Ocean. There are western boundary currents in the south oceans also, but they are less obvious and weaker than the Gulf Stream. It should be noted that Somali Current, which is a western boundary current of the Indian Ocean, reverse direction seasonally in accordance with the local winds.

The equatorial currents between two mid-latitude gyres flow westward as do the westward trade winds, but an eastward north equatorial counter current is visible in the Pacific and Atlantic.

Also shown on the map is the Southern Ocean or Antarctic Circumpolar Current (ACC). This current goes around the world without being blocked by land masses. It is deep and its volume transport is estimated as up to hundreds of Sverdrups ( $1 \text{ Sv} = 10^6 \text{ m}^3/\text{s}$ ). In comparison, the Gulf Stream Volume transport is  $0(100) \text{ Sv}$ . Thus the ACC is one of the strongest currents in the oceans.

Variability in global surface circulation can be observed from satellites. Fig 2.4 is the global meoscale sea height variability measured by the SEASAT altimeter (Cheney, 1982). The contours reveal features in the variability pattern, some of which correspond to features of the large scale current system. Variability in the North Atlantic and North Pacific is dominated by the highly energetic and variable Gulf Stream, and Kurshio system.

In the southern hemisphere, the Agulbas Current below Africa and the Falkland/Brazil current confluence off South America are clearly apparent (Although the later may be an artifact of imperfect filtering of Patagonian tides). High sea level variability in the Antarctic Circumpolar Current extends in a nearly continuous band around the polar oceans. Also, the north equatorial current systems in both the Atlantic and Pacific can be seen as zonal bands of much higher variability.

## 2.2 A DESCRIPTION OF THE INTERIOR CIRCULATION

Fig 2.5 shows vertical profiles in the three major oceans of temperature from the top of the ocean to the bottom. The lower 2500-3500m of water are close to  $0^\circ \text{C}$  and exhibit very little temperature variation relative to water near the surface. These cold deep temperature suggests that such water comes from the surface at high latitude. Note also the transition region from the vertically homogeneous deep water to more heterogeneous surface water. This transition region is identified as the main thermocline. Understanding its structure is a main research target of general circulation theories.

Lynn and Reid (1968) published vertical sections of potential temperature, density and salinity in Atlantic, Pacific and Indian Oceans. Fig-2.6 comes from the Atlantic Ocean. Note the apparent connection between the deep waters



and the surface at high latitudes. The passage of Norwegian Sea and Greenland sea water can be tracked by its low temperature and especially by its relatively high salinity ( $5 \sim 54.7\%$ ). This is broadly called North Atlantic Deep Water (NADW). Another source of deep water is in the Antarctic whence very cool (below  $0^{\circ}\text{C}$ ) and less salty (than NADW) water penetrate northward. This water is broadly called Antarctic Bottom Water, (AABW). Note also that on this section, the upper 2000 m of the ocean is much more complex than the deep water, suggesting great variability in the processes that set water properties near the surface. Note that very warm, salty, and light near surface water is seen at the center of the subtropical gyres. Large latitudinal variations of the thermocline are also present here. The thermocline is much shallower and sharper in the tropics (above 200m) and deepest at mid-latitudes ( $800 \sim 1000 \text{ m}$ ); at higher latitudes it tilts upward.

On the Pacific Ocean Fig 2.7 and Indian Ocean Fig 2.8, there is no deep water source to the north comparable to that of North Atlantic Deep Water (NADW). The deep water is mixing of the North Atlantic Deep Water which comes around Antarctic and the Antarctic Bottom Water. Again we can see the location of the subtropical gyres and a thermocline pattern very similar in the tropics and mid-latitudes to that of Atlantic Ocean. There is high salinity water from the Red Sea in the Indian Ocean; the mediterranean salt tongue in the Atlantic is not obvious at the western section. No such high salinity source occurs in the Pacific Ocean.

### 2.3 FORMATION SITES AND CIRCULATION OF DEEP WATER MASSES

The previous pictures show that the deep water have sources from high latitudes. Fig 2.9 a.b shows the overflow current from the Norwegian Sea as proposed by Worthington. Dense water passes through the Denmark Strait and the Iceland, Scotland passage, through the Labrador Sea and finally becomes the North Atlantic Deep Water.

Fig 2.10 shows the distribution of bottom water potential temperature in the Weddell Sea. This picture suggests flow of heavy water off the ice shelf to form the deep bottom water which finally contributes to Antarctic Bottom Water.

The deep water circulation is very different from that of the surface. Fig 2.11 shows some aspects of the global deep water movement, observed by direct measurement as inferred from property distribution. North Atlantic Deep

Water moves along the west Atlantic, moving southward under the Gulf Stream and further into the South Atlantic. The Antarctic bottom Water also goes along the western boundary in the South Atlantic but northward, under the southward flowing (NADW). In both Pacific and Indian Ocean, deep water goes northward along the western boundaries. At great depths, abyssal basins are bounded by mid-ocean ridge systems as well as continents; narrow passes in the ridges are probably important paths for the flow of abyssal water.

Stommel (1957) proposed a deep circulation scheme, which is based on simple global dynamics in a flat bottom ocean. This is shown in Fig 2.12. The deep water, with its sources at both the north and south high latitudes, moves equatorward in western boundary current. Poleward flow (which is toward the sources in the model) occurs in the interior, and forms a counter-clockwise flow in the north hemisphere and clockwise flow in the south hemisphere. The strong boundary currents in this picture are in rough agreement with observations and inferences about the deep circulation; the interior pattern has not been thoroughly studied but must be strongly influenced by bottom relief.

## 2.4 MODE WATERS

Fig 2.13, 2.14 show the vertical distribution of potential temperature and salinity across the North Atlantic Ocean at 36 N. A major feature at shallow depth in these pictures is the presence of a region of vertically homogeneous potential temperature and salinity just east of the Gulf Stream.. This water mass, with its temperature just above 18 C, is called eighteen degree water. It is found on the western side of the subtropical gyre and is believed to be formed by winter convection in the upper ocean.

Modification of water properties at the surface in winter time is followed by subduction and the modified water below lighter water is an important feature of upper ocean circulation. Thus on Fig 2.13, a mass of subducted, nearly isothermal water is visible at ~~600~~ ~ 800 m depth in the east Atlantic. Note that it overrides the tongue of salty water emerging from the Meditterrean at roughly 1000-1200 m.

## 2.5 WESTERN BOUNDARY CURRENT AND INTERIOR CIRCULATION IN THE UPPER KILOMETER OF THE ATLANTIC

The Gulf Stream is a major feature of the North Atlantic general circulation. It is perhaps the best studied western boundary current in the world oceans and its

observation provide major testing grounds for comparison with theories.

An important aspect of the Gulf Stream is that its path is highly time dependent. As an extreme example Fig 2.15 (Fuglister, 1951) shows, over a period of several days, the detachment of a piece of the Gulf Stream. The detached portion forms an individual eddy while the main current closes behind it. Such newly formed eddies or "rings" subsequently generally drift westward. Some may rejoin the Gulf Stream at some upstream location. It is hypothesized that the Gulf Stream ring formation provides an important mechanism for cross-stream transport of materials and water property.

Fig 2.16 shows a plot of the vertical structure of Gulf Stream flow at about 55 W due to Richardson. This plot is based on calculation from floats, drifters, and current meters. This picture clearly shows the main eastward surface intensified Gulf Stream jet (into the paper) and two counter-flows on either side. It is not fair from this picture to say that Gulf Stream flow is depth independent, but is fair to say that the Gulf Stream does reach the bottom in this region.

Fig 2.17 shows the variation of volume transport of the Gulf Stream as a function of downstream path (Knauss 1969). These transports are larger than those simple wind-driven theories can account for, suggesting the presence of recirculation in the vicinity of the western boundary current. Worthington (1976) hypothesized the North Atlantic Circulation given in Fig 2.18, which shows a highly confined gyre in the north western corner of the North Atlantic subtropical gyre. This recirculation pattern has a Gulf Stream Volume transport of 147 Sv, which is consistent with Knauss's picture (Fig 2.17) and well above the expected wind driven transport.

Also shown in Fig 2.18 are average east-west flow velocities  $\langle u \rangle$  and meridional eddy fluxes  $\langle u'v' \rangle$  of zonal momentum at 4000 m along 70 W and 55 W (Schmitz, 1977); note the eddy convergence of eastward momentum in the vicinity of the deep mean flows in both cases. Hogg (1980) suggests that the eddy "thickness flux"  $-\frac{f}{N} \langle u'\eta' \rangle$  similarly contributes to the maintenance of deep recirculation near the Gulf Stream. There is no general agreement about the spatial structure of the deep recirculation.

Fig 2.19 is the Ivers (1975) interpretation of the circulation pattern for the northern North Atlantic. Panel A

is the upper water and panel B is the deep water. The circulation was based on the geostrophic calculation and the distribution of properties. Note that Ivers also suggests a strong recirculation of the Gulf Stream.

He shows a bifurcation of Gulf Stream into northward and southward flowing branches at about 50 W. The southward branch feeds back to the subtropical gyre. The northward branch eventually reaches the Labrador Sea, a site of North Atlantic Intermediate and deep water formation.

The flow associated with that part of the Gulf Stream that is believed to return to the subtropical gyre has not been well mapped. On the basis of limited number of drifter paths, it appears quite variable. The mode water visible at depth of 600-800 m in the east Atlantic in Fig 2.13, 2.14 above the Mediterranean salt tongue is evidence of this return flow.

The flow beneath the ocean subtropical gyre is very different. Reid (1979) has suggested that some salty water from the Mediterranean overflow makes its way northward along the eastern boundary to the Norwegian Greenland Sea.

Water which follows the northward branch eventually enters the Labrador Sea, in Ivers' circulation, it is there much denser than when it left the Gulf Stream. There it may overturn to such great depth in the winter that the Labrador Sea is believed to be a significant source of deep water in the North Atlantic.

## 2.6 References

- Cheney, R.E., J.G. Marsh and B.K. Beckley, 1982: Global mesoscale variability from colinear tracks of SEASAT altimeter data. J. Geophys. Res., 88, 4343-4354.
- Fuglister, F. C., and L. V. Worthington, 1951. Some results of a multiple ship survey of the Gulf Stream. Tellus 3:1-14, (212).
- Hogg, N.G., 1983: A note on the deep circulation of the western North Atlantic: Its nature and causes. Deep-Sea Res., 30, 945-961.
- Ivers, W.D., 1975. The deep circulation in the northern North Atlantic, with especial reference to the Labrador Sea. Ph.D. Thesis, University of California at San Diego, 179 pp.

- Knauss, J.A., 1969. A note on the transport of the Gulf Stream. Frederick C. Fuglister Sixtieth Anniversary Volume, Deep-Sea Research 16 (Supplement):117-123.
- Lynn, R. J., and J.L. Reid, 1968. Characteristics and circulation of deep and abyssal waters. Deep-Sea Research 15:577-598.
- Reid, J. L., 1979. On the contribution of the Mediterranean Sea outflow to the Norwegian-Greenland Sea. Deep-Sea Research 26:1199-1223. (111).
- Richardson, P.L., 1983:Eddy kinetic energy in the North Atlantic form surface drifters. J. Geophys. Res., 88(C7), 4355-4367.
- Schmitz, W.J., Jr., 1977. On the deep general circulation in the Western North Atlantic. Journal of Marine Research 35:21-28.
- Stommel, H. 1958. The abyssal circulation. Deep-Sea Research 5:80-82.
- Worthington, L.V., 1976. On the North Atlantic circulation. The Johns Hopkins Oceanographic Studies 6: 110 pp.
- Notes Submitted by: Liang gui Chen, Florida State University, Tallahassee, Florida

## Figures

- Fig. 2.1      Global surface wind distribution in summer.
- Fig. 2.2      Global surface wind distribution in winter.
- Fig. 2.3      Global surface ocean current.
- Fig. 2.4      Global meoscale sea height variability measured  
by the SEASAT altimeter.
- Fig. 2.5      Vertical profiles in the three major oceans of  
temperature from the top of the ocean to the  
bottom.
- Fig. 2.6      Vertical section of potential temperature,  
density and salinity in the Atlantic Ocean.
- Fig. 2.7      Vertical section of potential temperature,  
density and salinity in the Pacific Ocean.
- Fig. 2.8      Vertical section of potential temperature,  
density and salinity in the Indian Ocean.
- Fig. 2.9 a.b   a:overflow current from the Norwegian Sea.  
b:Dense water passes through the Denmark Strait  
and the Iceland, Scotland Passage.
- Fig. 2.10     Distribution of bottom water potential  
temperature in the Weddell Sea.
- Fig. 2.11     Global deep water movement.
- Fig. 2.12     Deep circulation scheme proposed by Stommel  
(1957).
- Fig. 2.13     Vertical distribution of potential temperature  
across the North Atlantic Ocean at 36 N.
- Fig. 2.14     Vertical distribution of salinity across the  
North Atlantic Ocean at 36 N.
- Fig. 2.15     Gulf Stream detachment Fuglister (1951).
- Fig. 2.16     Vertical structures of Gulf Stream flow at 55  
W.
- Fig. 2.17     Variation of volume transport of the Gulf  
Stream as a function of down stream path,  
(Knauss 1968).

Fig. 2.18      Average east-west flow velocities  $\langle u \rangle$  and meridional eddy fluxed  $\langle u'v' \rangle$  of zonal momentum at 4000 m along 75 W and 55 W.

Fig. 2.19 a.b   Interpretation of the circulation pattern for the northern North Atlantic, Ivers (1975).

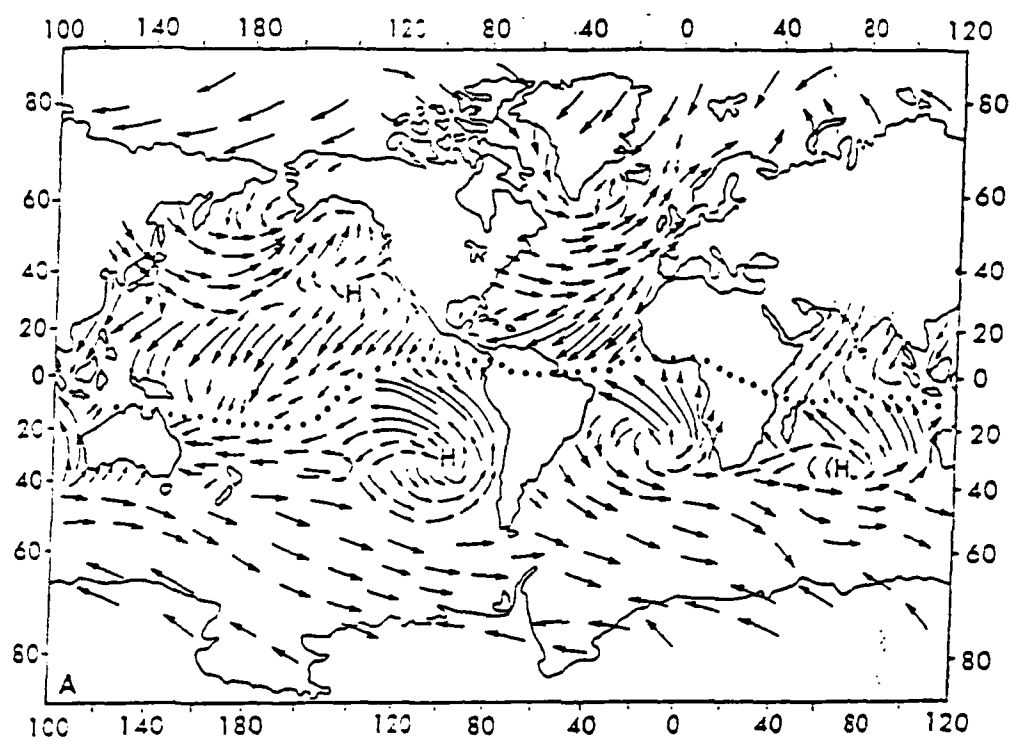


Fig 1

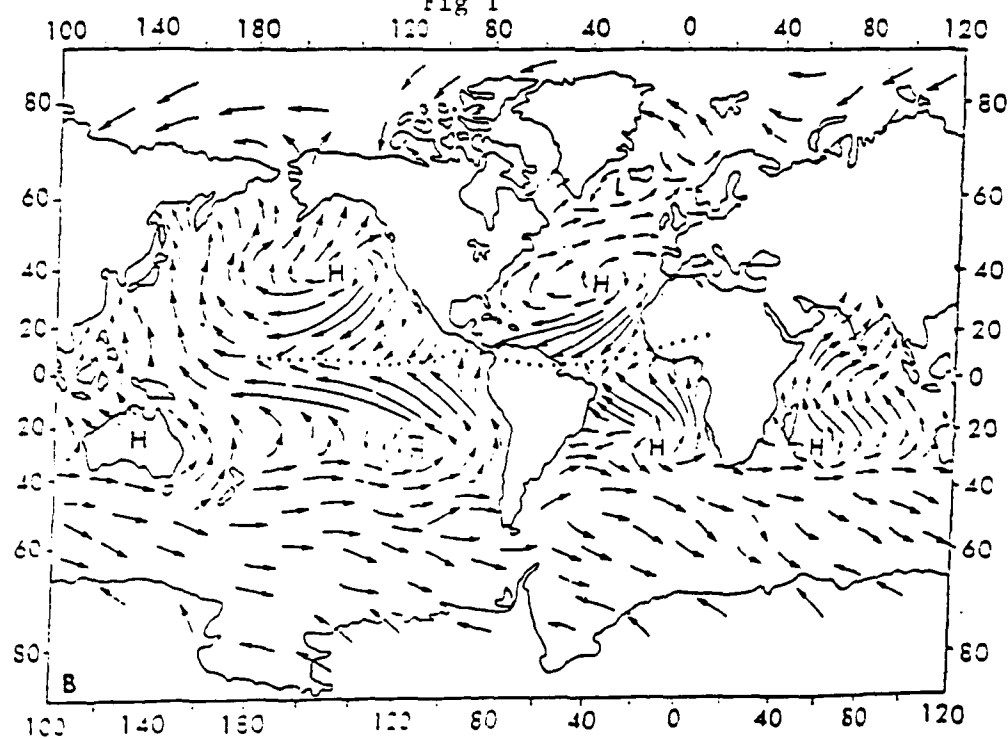


Fig 2



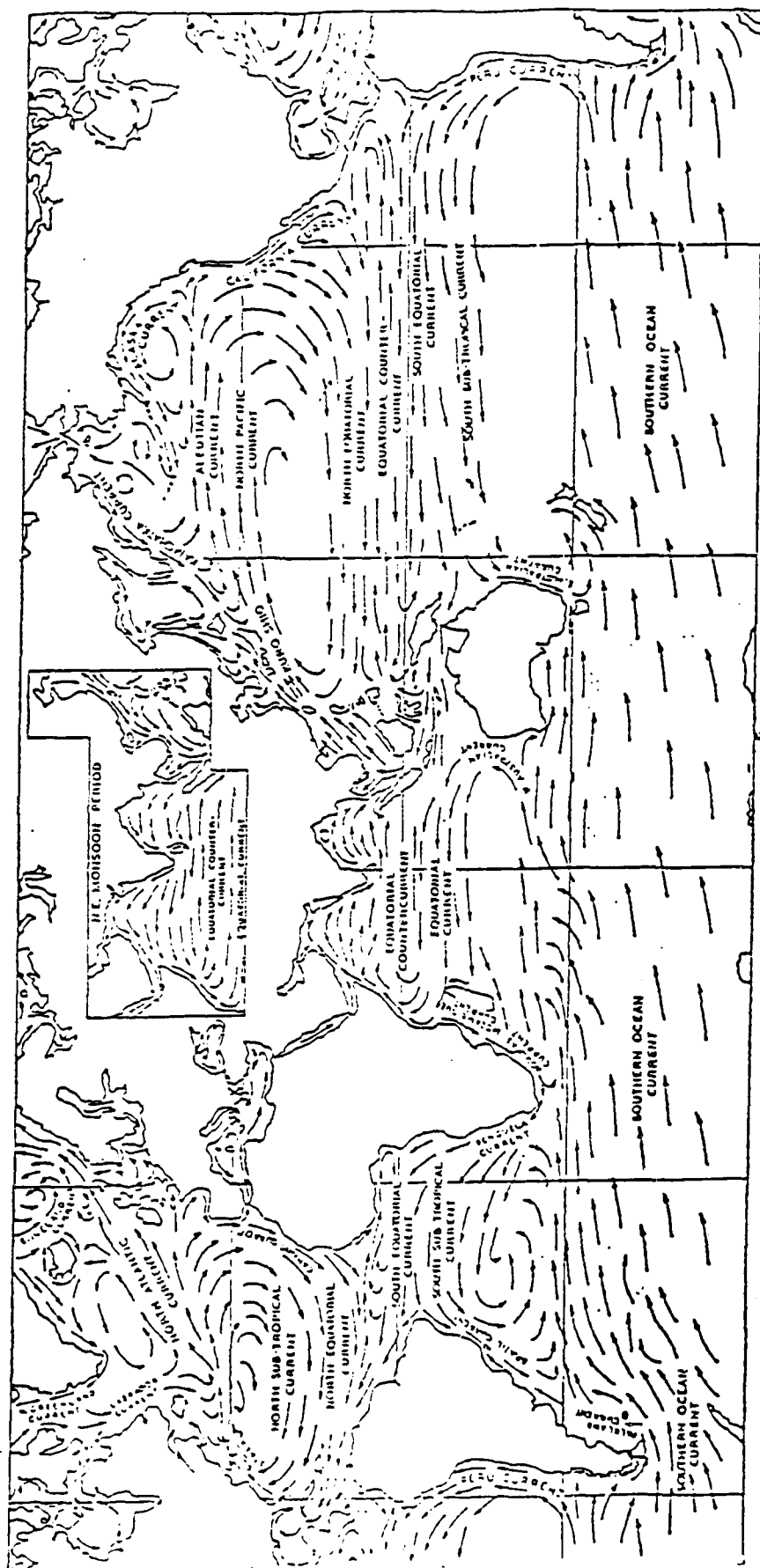
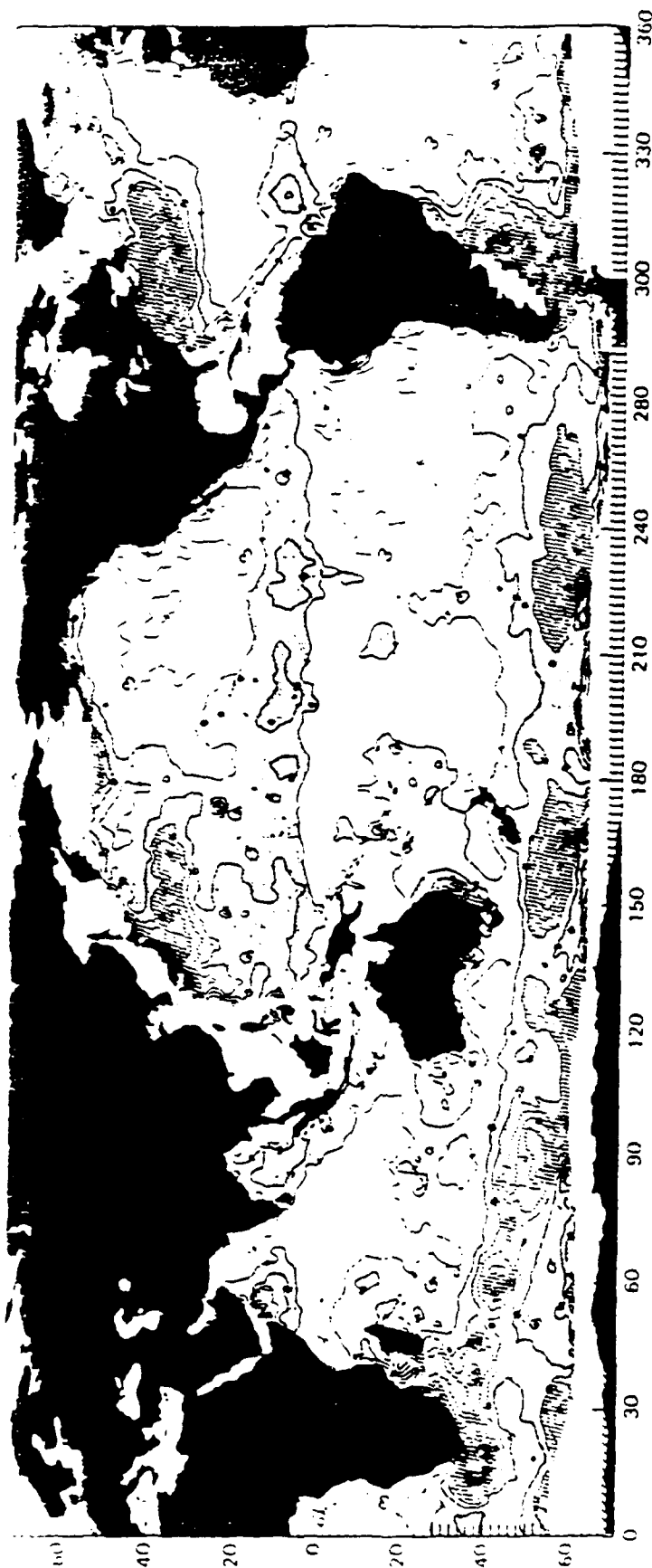


FIG 3

## SEASAT ALTIMETER MESOSCALE VARIABILITY



Global mesoscale sea height variability measured by the SEASAT altimeter, September 15 to October 10, 1978. This map was constructed from 110,000 globally distributed variability values determined every 7 km along the tracks shown in Figure 1. A gridding routine was then used to obtain smoothed values at regular 2° intervals of latitude and longitude (see appendix A). These were contoured to reveal large-scale variability patterns due to current systems. The North Atlantic and North Pacific are dominated by the highly energetic Gulf Stream and Kuroshio systems that extend seaward nearly 4000 km. In the southern hemisphere the Agulhas Current below Africa and the Falkland/Brazil Current confluence off South America are clearly apparent. High variability due to the Antarctic Circumpolar Current extends in a nearly continuous band around the polar oceans, with isolated maxima coinciding with major topographic ridges and plateaus. Owing to the predominance of values less than 4 cm in mid-ocean, the north equatorial current systems in both the Atlantic and Pacific can be seen as zonal bands of higher variability.

Fig 4

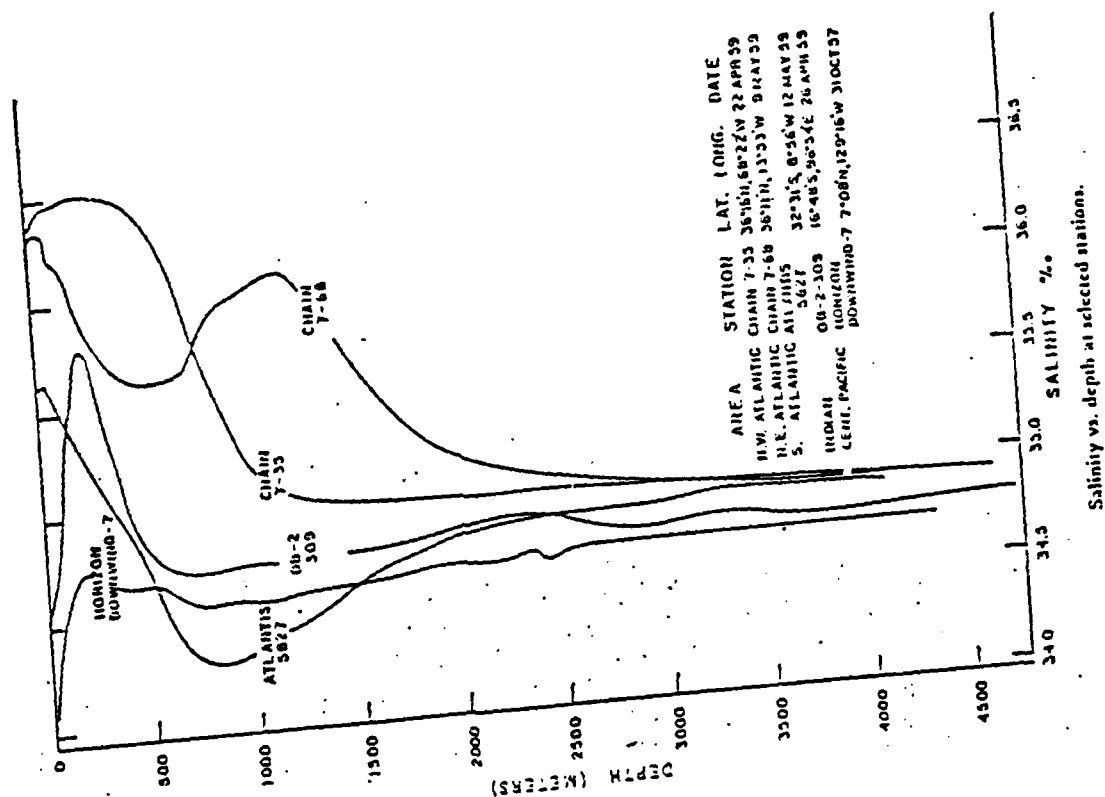
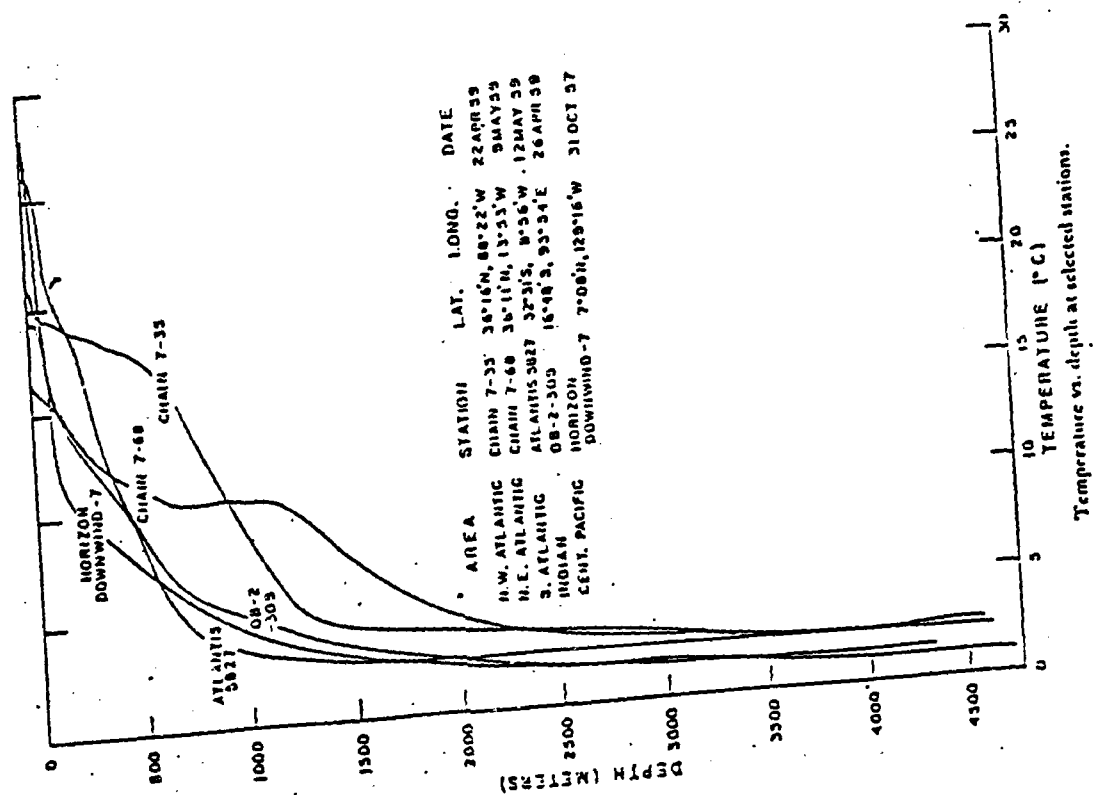
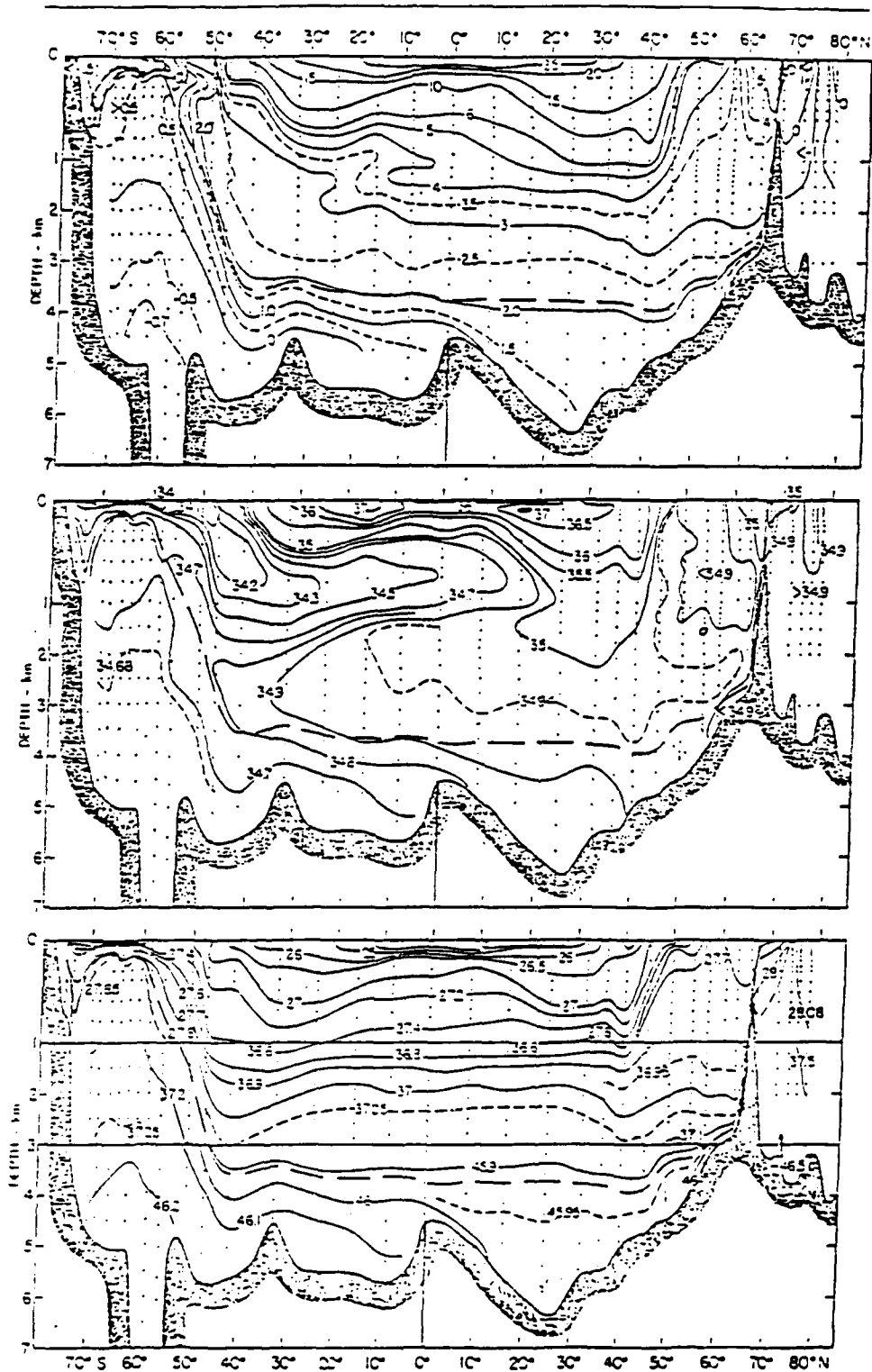


Fig 5



Potential temperature, salinity, and  $\sigma_t$  (0-1000 m),  $\sigma_t$  (1000-3000 m), and  $\sigma_t$  (> 3000 m) on a meridional vertical section in the western Atlantic Ocean. On Figs. 3a, 3b, 3c and 11 the vertical exaggeration is  $2.22 \times 10^2$  above 1000 m depth and  $1.11 \times 10^2$  below. The heavy dashed line indicates the stratum defined in the text. Stations are identified in the Appendix.

Fig 6

Copy . . . . . does not  
permit fully legible reproduction

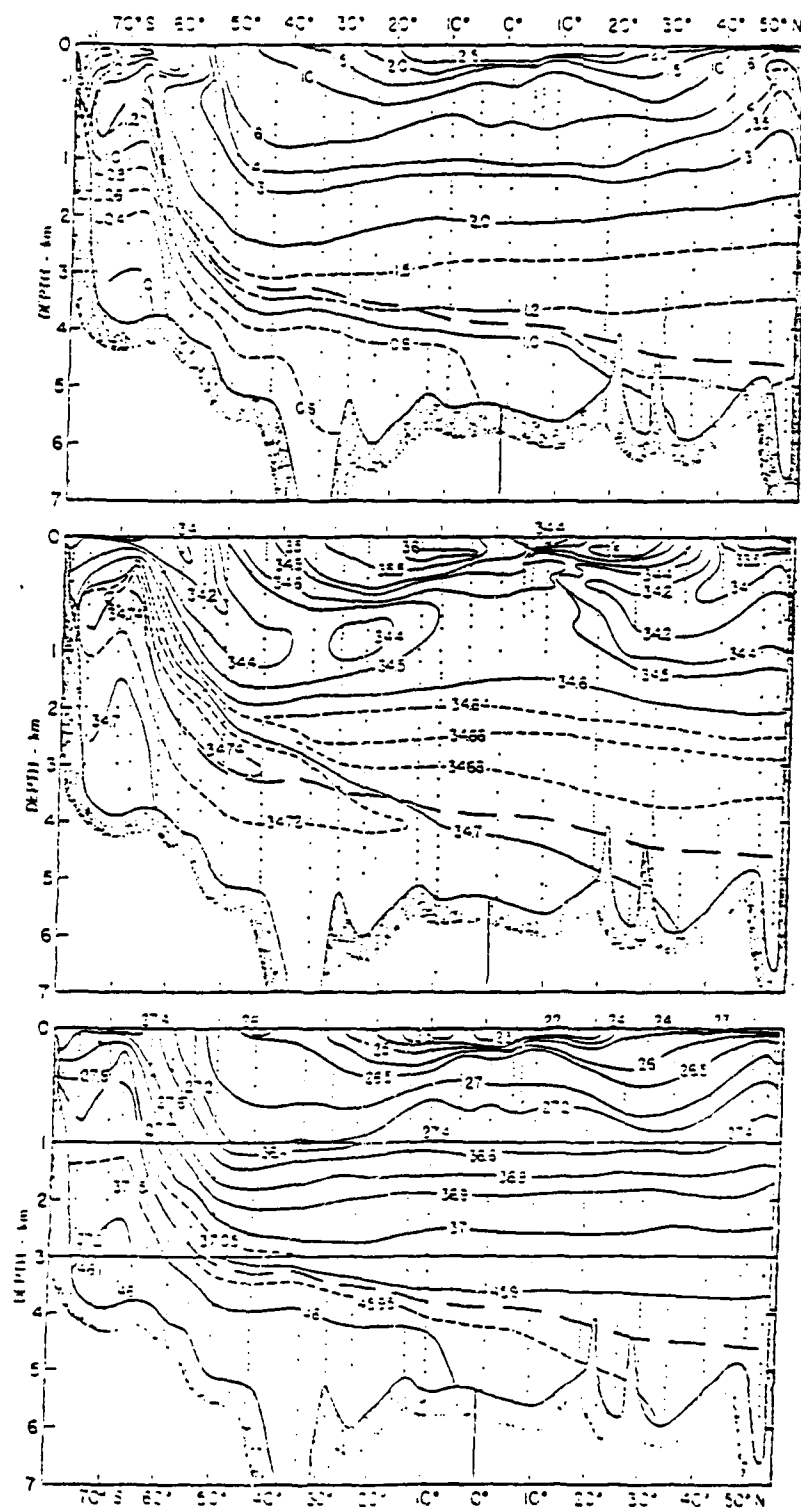


Fig. 6. Potential temperature, salinity, and  $\sigma_t$  (0–1000 m),  $\sigma_t$  (1000–3000 m), and  $\sigma_t$  (> 3000 m) on a meridional vertical section in the western South Pacific and central North Pacific Ocean. The heavy dashed line indicates the stratification depth defined in the text. Stations are identified in the Appendix.

Fig 7

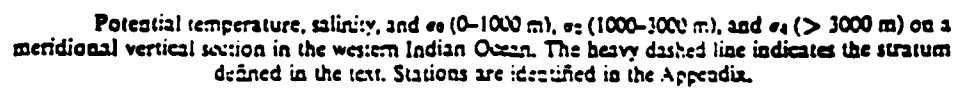


Fig 8

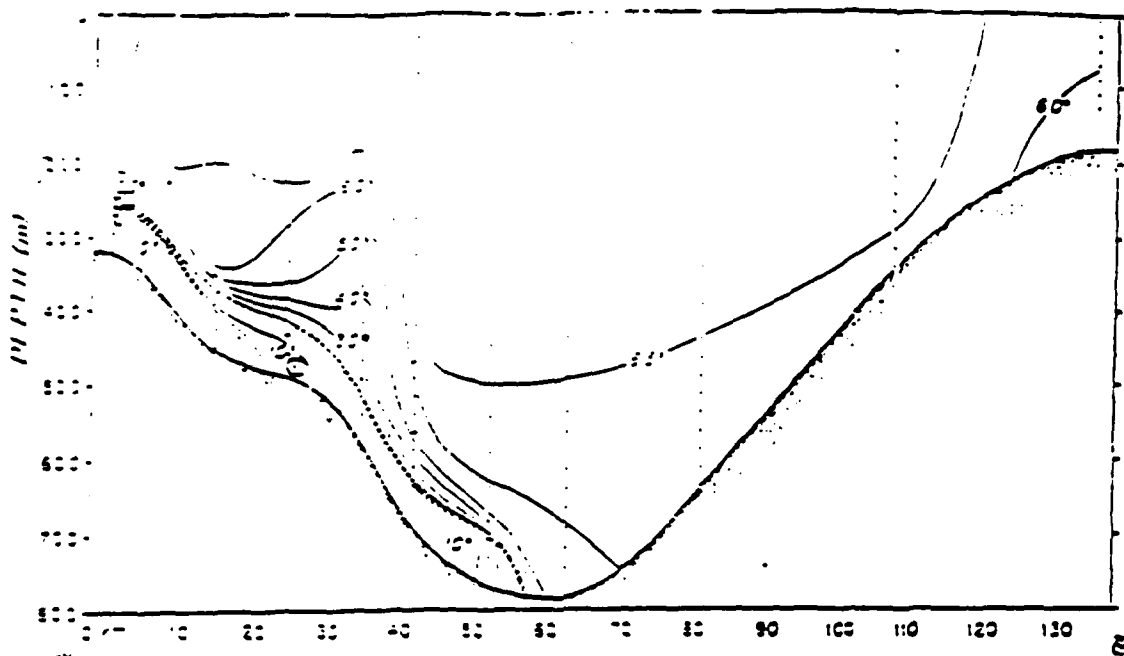


Figure 1.8 Temperature ( $^{\circ}\text{C}$ ) section across the Denmark Straits in lats.  $65-66^{\circ}\text{N}$  (left, west; see figure 1.7, illustrating the southward flow of cold water from the Norwegian Sea. C.S.S. Hudson cruise B1 0267, stations 3-13, 28-29 January 1967. (Worthington 1969.)

Fig 9a

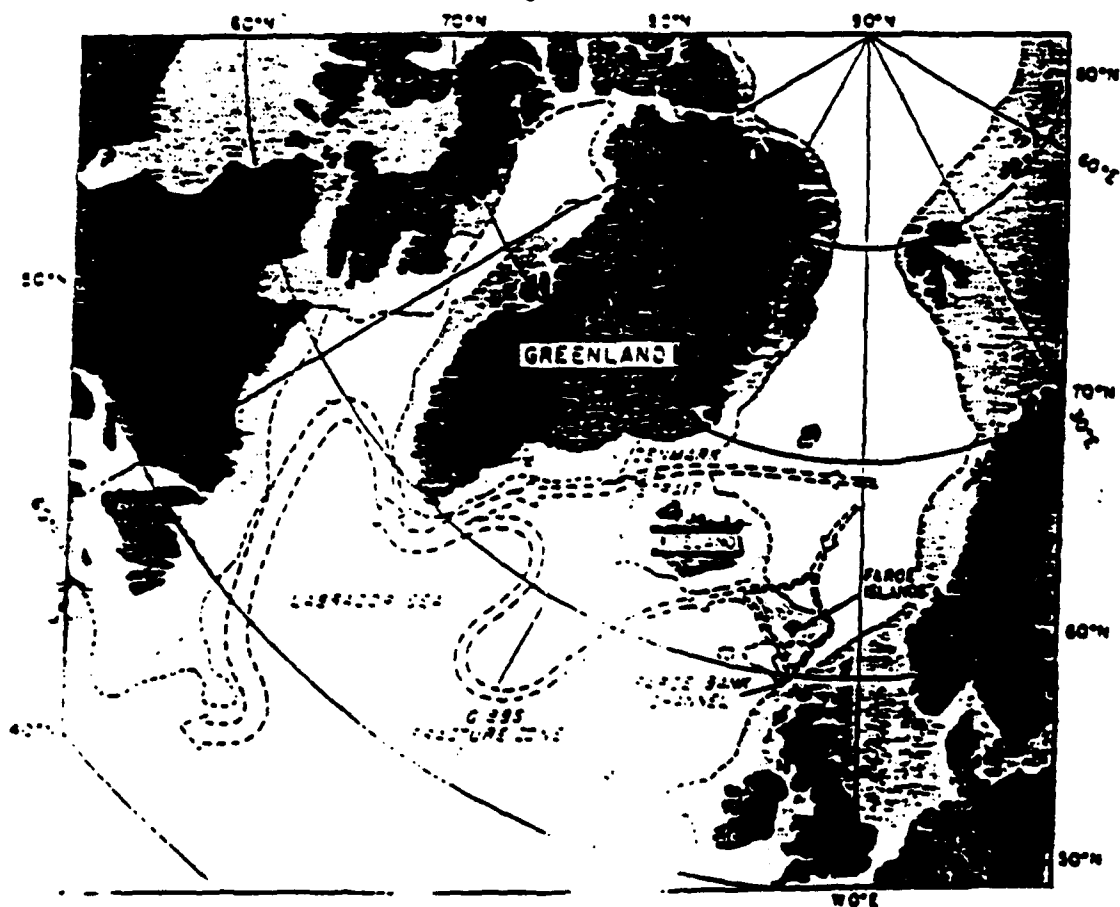
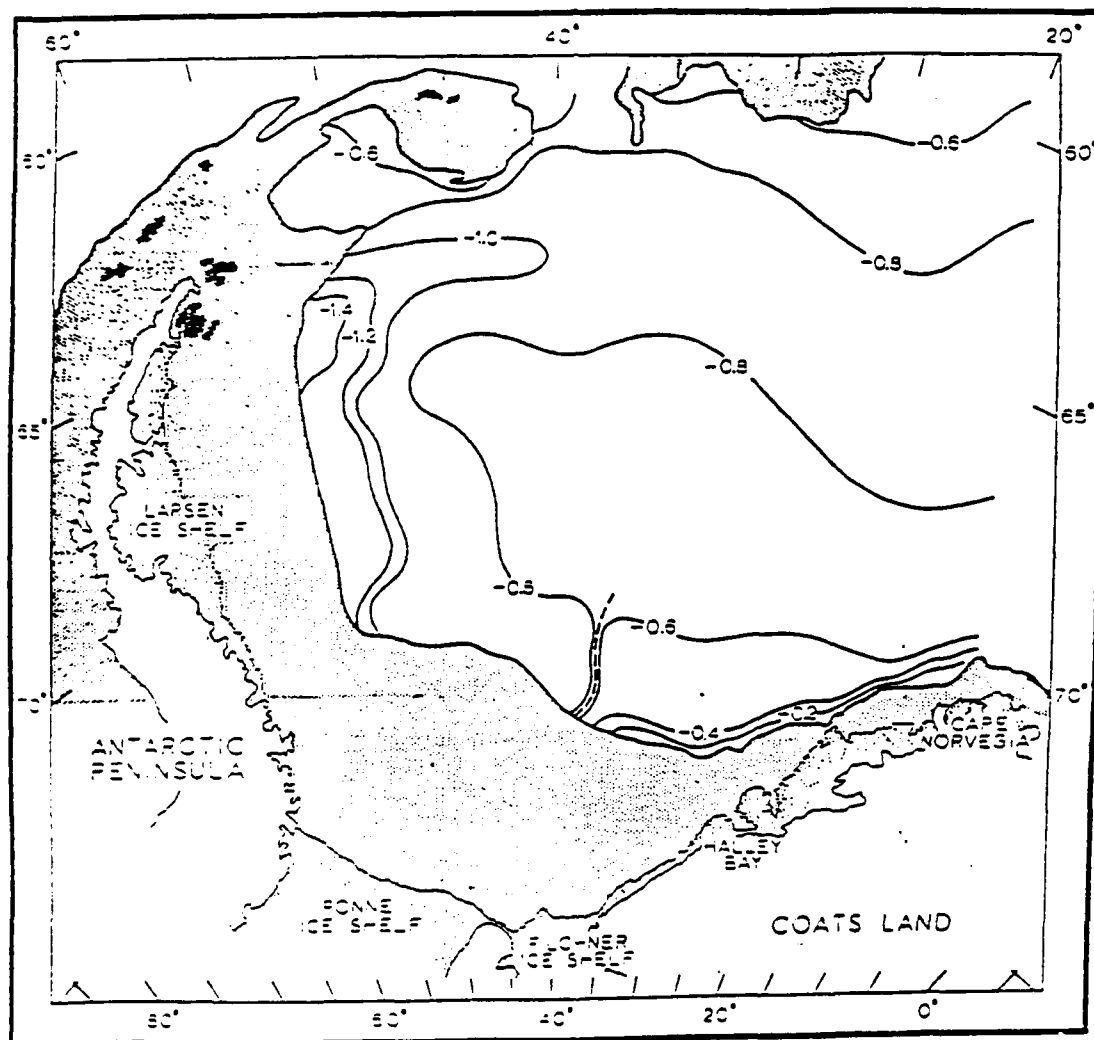


Fig 9b



Distribution of bottom potential temperatures in the Weddell Sea, illustrating the eastward spreading of newly formed bottom water from the northern tip of the Antarctic Peninsula. (Foster and Carmack, 1976a.)

Fig 10



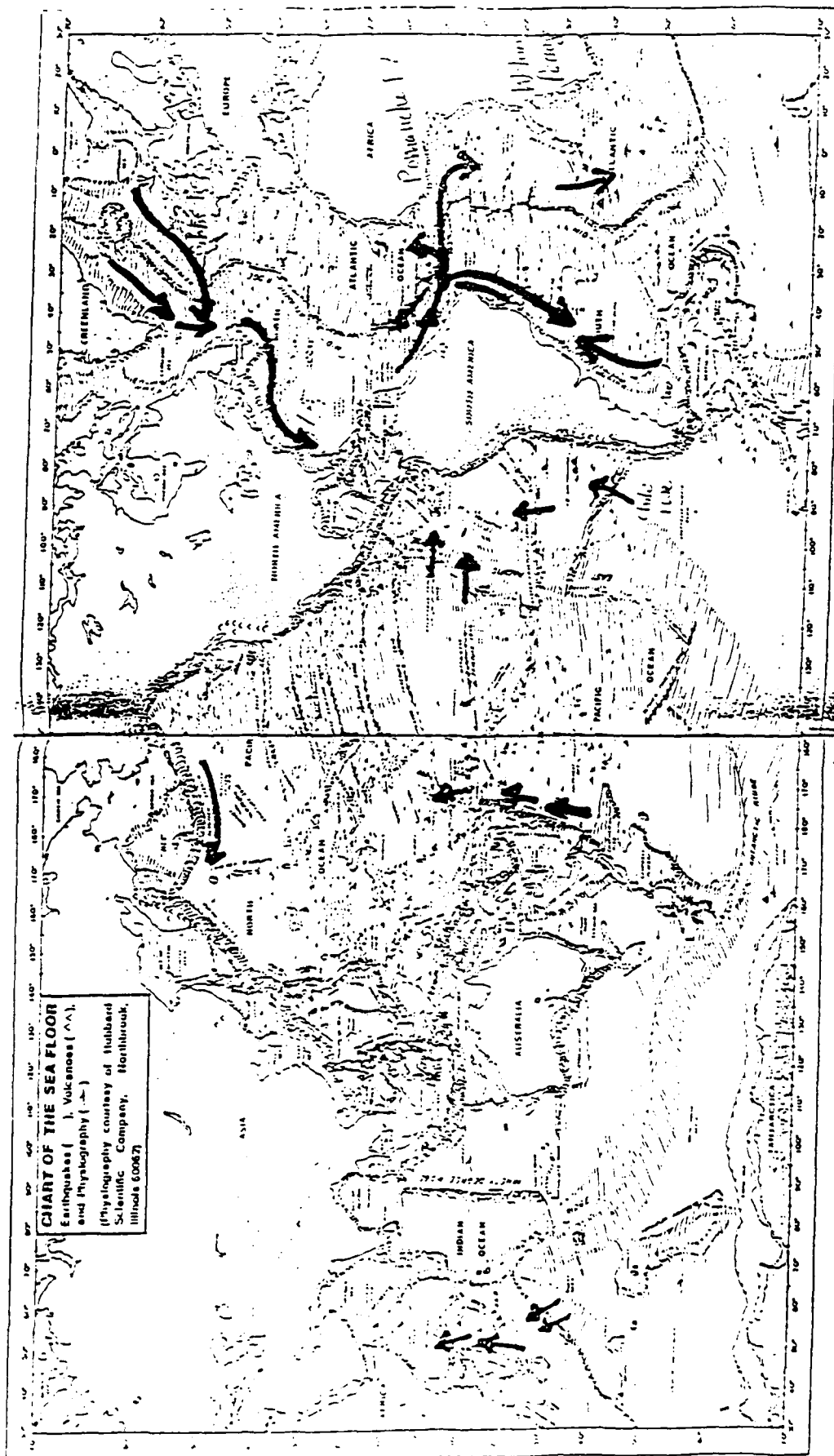
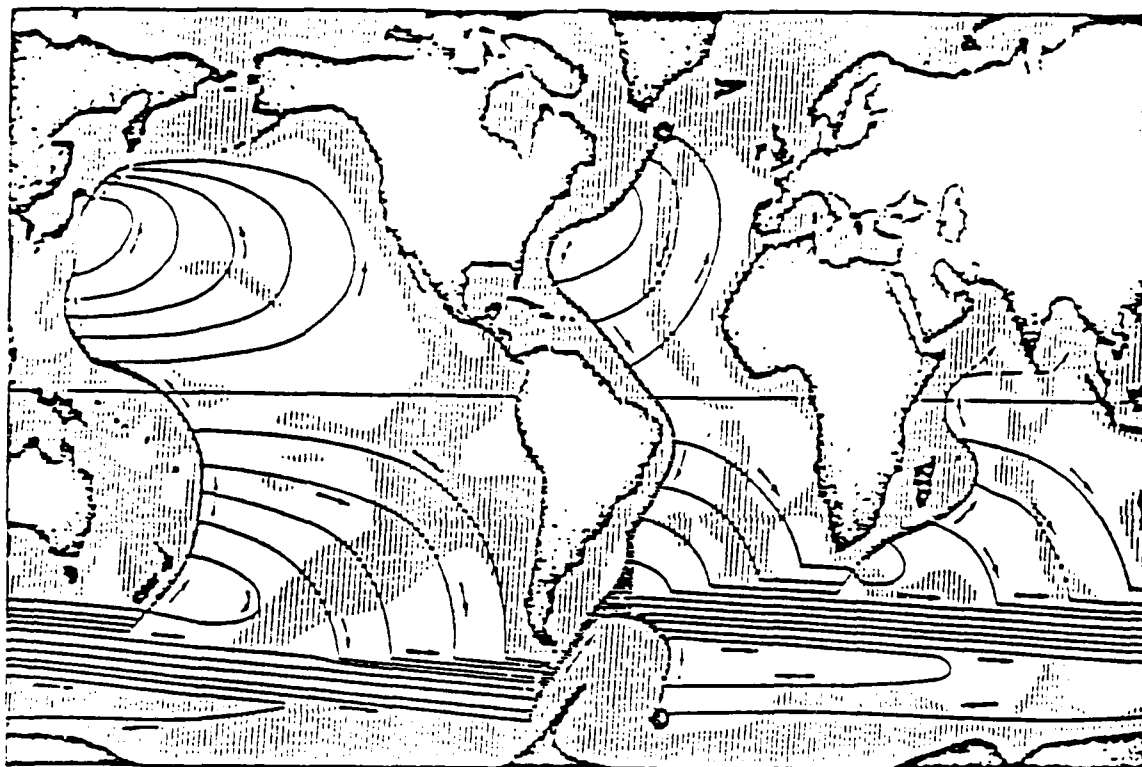


Fig 11



The deep circulation of the world ocean according to Stommel.  
[From H. Stommel, 1957, *Deep-Sea Res.*, 4.]

Fig 12

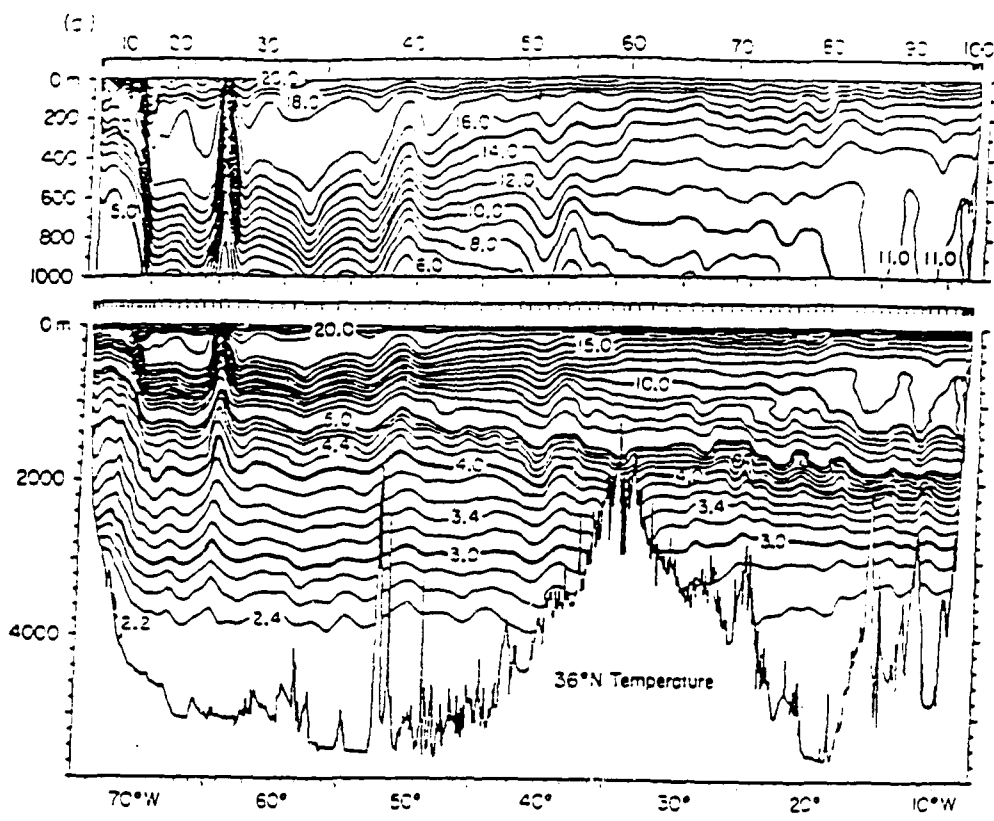


Fig 13

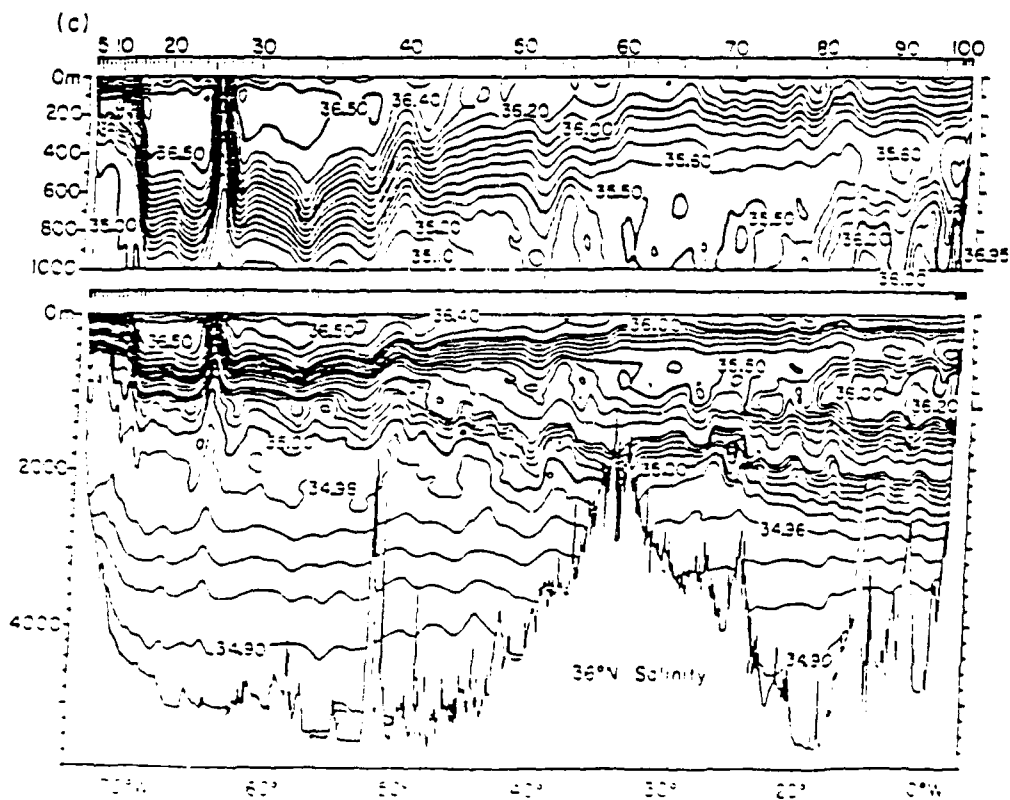
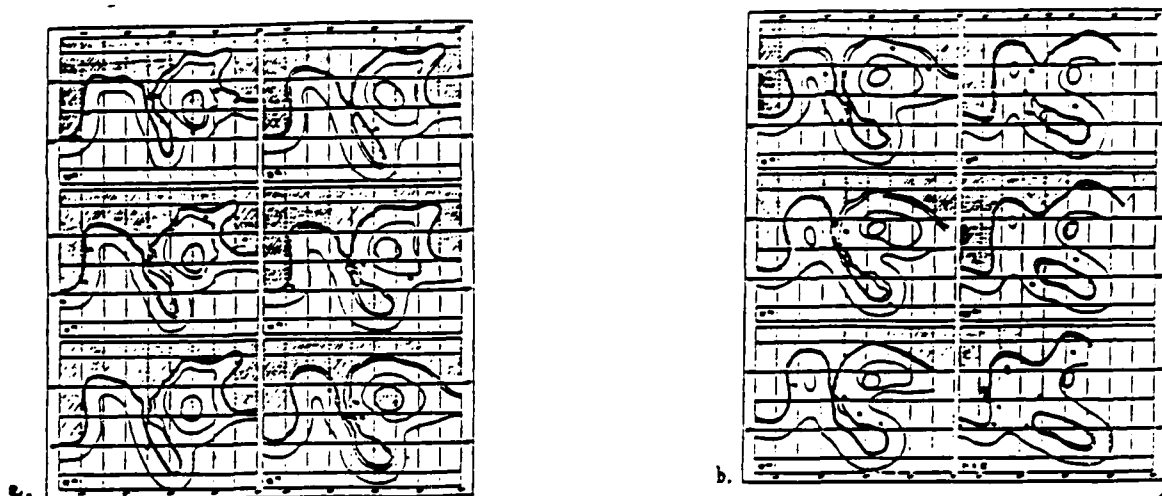


Fig 14



a. Positions of the Gulf Stream, 10th to 15th June. Shaded areas denote a mean temperature in the upper 200 meter layer of less than 65°F. Thin line is 68°F. isotherm. Small numbers indicate the maximum observed values of the warm core.

b. Positions of the Gulf Stream, 16th to 20th June. Shaded areas denote a mean temperature in the upper 200 meter layer of less than 65°F. Thin line is 68°F. isotherm. Small numbers indicate the maximum.

Fig 15

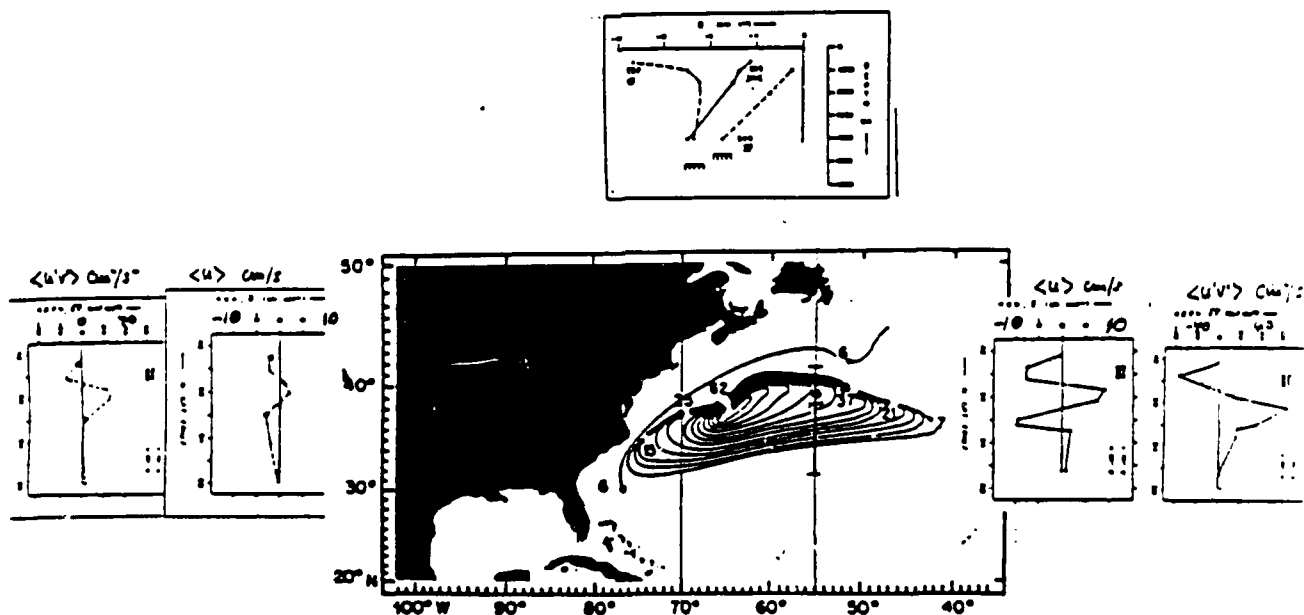
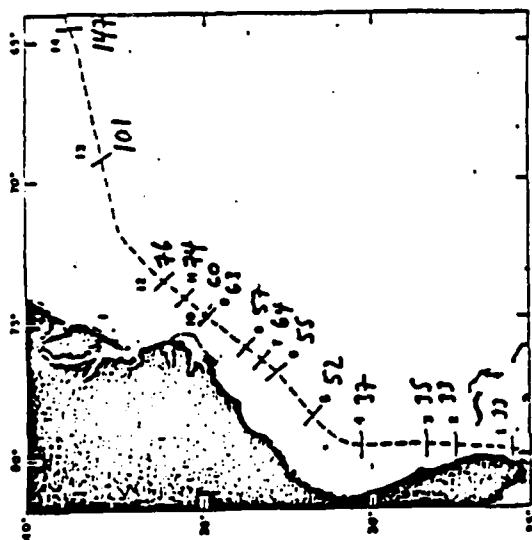
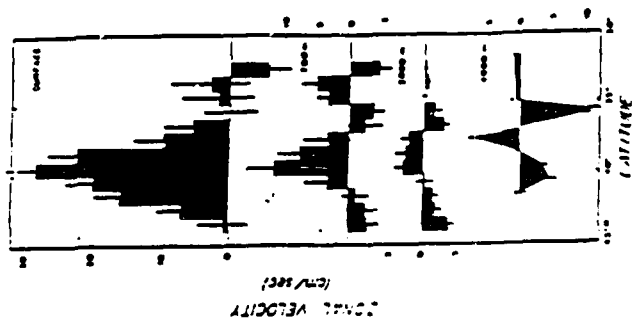


Fig 16

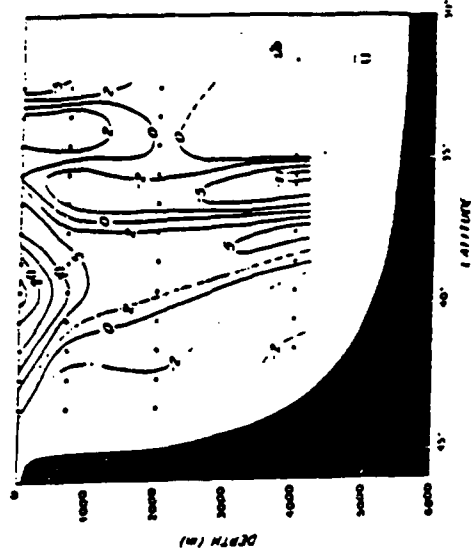


The location of the fourteen sets of volume transport measurements given in Table 1.  
 KNOWN DSR 1968 15 (Appendix) 117-23



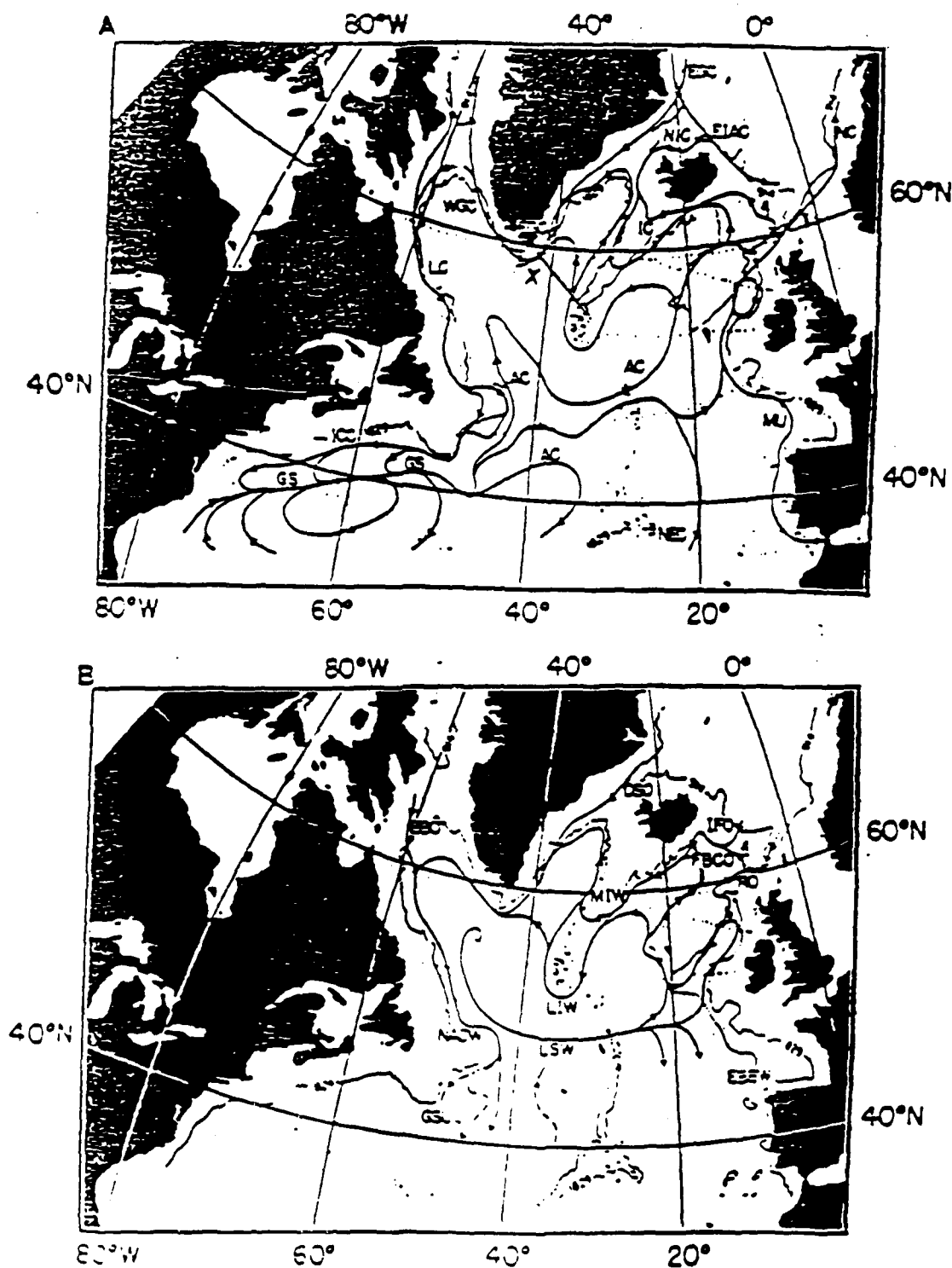
Mean zonal velocity across 55W from surface drifters, SOIAR floats at 700 m, and current meters at 4000 m. Mean velocity was calculated from drifter and current meter measurements into bins one degree in latitude by ten degree longitude. Error bars represent estimates of the standard error of the mean.

FIG 17



Contoured zonal velocity section ( $\text{cm s}^{-1}$ ) along 55W and through the Gulf Stream from drifters, floats, and current meters. Eastward velocity is shaded. Dots indicate centers of boxes used in calculating velocity except at 4000 m, where they show current meter locations. The bottom profile is from 55W; the average bottom profile between 50-60W is shifted southward from this by about one degree in latitude (see Fig 1a).

Fig 18



The Ivers (1975) interpretation of the circulation pattern for the northern North Atlantic. Panel A in the upper water. Panel B the deep water. The isobath values, in meters, represent conversions from round numbers of fathoms.

Fig 19

## LECTURE 3

## FUNDAMENTAL LARGE SCALE CIRCULATION THEORIES

Stommel's review article on the large scale ocean circulation (1957) discusses the evolution of ocean circulation theories. Beginning with Hough (1897) and Goldsborough's (1933) models in which precipitation and evaporation were driving mechanisms for the oceans' circulation, Stommel comments: "Indeed, one needs merely to introduce two additional physical ideas:

- 1 . Ekman's (1905) notion that the direct frictional stress of the wind is confined to a thin surface 'boundary layer', and that viscous shearing stresses are unimportant dynamically in the deeper body of the ocean, excepting perhaps, at the bottom.
- 2 . The concept of a narrow western boundary current of a highly frictional and/or inertial character."

Dr. Hendershott discussed the first of these ideas in this lecture, including the effect of the resultant Ekman pumping as an upper boundary condition for Sverdrup's interior solution. The final part of this lecture is a discussion of abyssal circulation theories.

## 3.1 Ekman Flow

The fundamental circulation theories all hinge upon the ability to incorporate boundary forcing into a model. Ekman's theory incorporates the wind or bottom stress as the driving mechanism in a thin boundary layer.

Consider an incompressible, homogeneous, rotating ( $2\Omega = f_o$ ) fluid with infinite depth. At the surface boundary we may impose the following boundary conditions:

$$w(0) = 0$$

$$\underline{\tau} = (\tau^x, \tau^y)$$

and as  $z \rightarrow \infty$ ,  $u, v = 0$ . The primitive equations then reduce to:

$$-f_o v = \nu u_{zz} = \frac{1}{\rho} \frac{\partial}{\partial z}(\tau^x) \quad (1)$$

$$+f_o u = \nu v_{zz} = \frac{1}{\rho} \frac{\partial}{\partial z}(\tau^y) \quad (2)$$

$$u_x + v_y = 0. \quad (3)$$

It is a simple matter to solve these equations and the resultant velocity fields are:

$$u = \frac{1}{(\rho_0 f_0 \nu)^{1/2}} e^{-z/D} [\tau^x \cos(2z/D - \pi/4) - \tau^y \sin(2z/D - \pi/4)] \quad (4)$$

$$v = \frac{1}{(\rho_0 f_0 \nu)^{1/2}} e^{-z/D} [\tau^x \sin(2z/D - \pi/4) + \tau^y \cos(2z/D - \pi/4)] \quad (5)$$

$$w = 0 \quad \text{where} \quad D = (\nu/2f_0)^{1/2} \quad (6)$$

The solutions are the familiar Ekman spiral, and of notable interest are the decay scale, clockwise rotation of the velocity vector with depth, and integrated transport which is perpendicular to the surface wind stress. These features may be seen in figure 1 below.

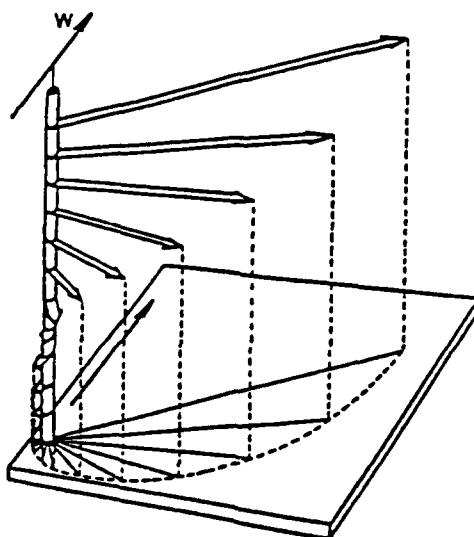


Figure 1

A typical value for the decay depth above is computed from different sets of observations, and according to measurements done by Gonella (1968) is of the order 20 m. Sverdrup took this idea a step further by allowing horizontal variations in the wind stress, and arrived at a consistent formulation of a driving mechanism for the large scale wind driven circulation.

Horizontal variations in the wind stress may be considered as a direct extension of the Ekman spiral result provided the variations are small compared to variations in the vertical. This is equivalent to having the Rossby and Ekman numbers small with respect to one. If we define the Ekman transports  $U_E, V_E$  as

$$U_E, V_E = \int_{-\infty}^0 (u, v) dz, \quad (7)$$



then the vertical Ekman velocity, pumping or suction, is obtained from mass conservation as

$$W_E = U_{Ez} + V_{Ey}. \quad (8)$$

For a given surface stress this expression may be rewritten

$$W_E = \frac{1}{\rho_0 f} \left[ \frac{\partial}{\partial x} \int_{-\infty}^0 \tau^y_z dz + \frac{\partial}{\partial y} \int_{-\infty}^0 \tau^x_z dz \right] \quad (9)$$

$$= \frac{1}{\rho_0 f} \underline{k} \cdot \nabla \times \underline{\tau} \quad (10)$$

where  $\tau$  is the surface wind stress.

The ideas of Ekman flows and their associated Sverdrup transport are so simple that people have been moved to ask if they are visible in the observations. These concepts set the foundation for more involved theories in latter lectures and hence both a thorough understanding and careful sense of confidence in them is requisite to understanding and developing more complicated theories of the general circulation.

One of the prettiest sets of evidence for Ekman flows are measurements done by Gonella (1968). Figure 2 is a progressive vector diagram compiled by making current measurements simultaneously at 10, 25, and 75 m at one mooring for several days. (The scallop shaped cusps are inertial oscillations with a period of  $\approx 14$  hours). Figure 3 is their interpretation of the data in which the mean currents at each depth are subtracted from the total. We can see the characteristic clockwise turning of the velocity with depth, as well as a decay in strength of the current. The spiral shaped dashed line is a theoretical fit to the data using a constant vertical eddy-viscosity of  $A_v = 125 \text{ cm}^2/\text{s}$ . This set of observations as well as others (see for example Hunkins (1967)), lend support to the existence of the Ekman flow. There is however a large disparity in necessary values of the vertical eddy-viscosity  $A_v$ , and its vertical dependence, ranging from 60–540  $\text{cm}^2/\text{s}$  necessary to fit the data. There was much discussion on the ease of observing the Ekman flow, and it was pointed out that the effects of inertial motions and heating and cooling may completely overwhelm the Ekman signature in observational data. The supportive evidence may still be used to help justify that part of the circulation theory attributed to the wind.

### 3.2 The Sverdrup Transport

The original Sverdrup paper (1947) is independent of Ekman's work in that Sverdrup doesn't divide the ocean into an Ekman layer and a Sverdrup interior. The following section will discuss Sverdrup's original ideas, while section 3.3 combines the two original ideas.

Consider an incompressible fluid in geostrophic balance, possibly perturbed by vertical momentum diffusion.

$$-fv = \frac{-p_z}{\rho_o} + A_v u_{zz} \quad (11)$$

$$+fu = \frac{-p_y}{\rho_o} + A_v v_{zz} \quad (12)$$

$$u_x + v_y + w_z = 0 \quad (13)$$

At the surface,  $z = 0$ , we impose a rigid lid, and wind stress as:

$$w = 0, \quad \rho_o A_v u_z = \tau \quad (13)$$

If we now integrate equations (11-12) from the surface to some constant depth  $-D$ , then

$$-f\bar{v} = -P_z + \frac{\tau^x}{\rho_o} \quad (14)$$

$$+f\bar{u} = -P_y + \frac{\tau^y}{\rho_o} \quad (15)$$

$$\text{where } \bar{a} = \int_{-D}^0 a dz \quad \text{and} \quad P = \int_{-D}^0 \frac{p}{\rho_o} dz.$$

Cross-differentiating 14 and 15, and further assuming the surface at  $z = -D$  is impermeable we obtain Sverdrup's relation:

$$\beta\bar{v} = \nabla \times \frac{\tau}{\rho_o}. \quad (16)$$

Sverdrup compares north-south transports predicted by this relation using observed winds with independent transports calculated from hydrographic density measurements. Figures 4a,b show a quite remarkable quantitative agreement between the two methods, including a counter-current in the east-west transports.

### 3.3 Combining Sverdrup and Ekman Ideas

The next logical step in formulating a model for the circulation is to couple Ekman's surface layer with a Sverdrup interior. This is easily understood by considering the interior flow, below the Ekman layer, to be in geostrophic balance. Integrating from a depth  $D$  up to the base of the Ekman layer we may define geostrophic transports as:

$$\oint \bar{u}' = \int_{-D}^{-D_E} \frac{\hat{k} \times \nabla P}{\rho_0} dz \quad (16)$$

then taking  $\nabla \cdot$  of this equation we obtain

$$\oint (\bar{u}'_x + \bar{v}'_y) + \beta \bar{v}' = 0 \quad (17)$$

At this point, through mass conservation, we make the connection with the adjacent Ekman layer.

$$\bar{u}'_x + \bar{v}'_y = -\omega = \omega_E. \quad (18)$$

That is we allow the Ekman layer to pump into, or suck fluid out of the interior, and hence the relation

$$\beta \bar{v}' = \oint \omega_E = \frac{f}{\rho_0} \left[ \left( \frac{\tau_y}{f} \right)_x - \left( \frac{\tau_x}{f} \right)_y \right]. \quad (19)$$

The total transport now becomes the sum of a Sverdrupian interior and an Ekman surface layer transport.

$$\bar{V} = \bar{V}_E + \bar{V}' \quad (20)$$

We now relate these ideas in terms of the approximate equations derived in Lecture 1. Consider the mean flow equations involving only vertically integrated quantities. The single layer, non-dimensional, vorticity equation becomes:

$$R_o(\partial_t - \psi_y \partial_x + \psi_x \partial_y) \nabla^2 \psi + \psi_x = (\tau_x^y - \tau_y^x) - \epsilon_s \nabla^2 \psi + \epsilon_m \nabla^4 \psi. \quad (21)$$

For  $R_o$ ,  $\epsilon_s$ , and  $\epsilon_m$  all much less than 1, we can solve

$$\psi_x = (\tau_x^y - \tau_y^x) \quad (22)$$

for various schematic wind fields to get an idea of what the general circulation 'looks' like. Note that we have dropped higher order derivatives, and hence must supply a reduced set of boundary conditions. The point was made in the lecture that one of the triumphs of this theory was how well its solutions compared with large scale observations.

Consider the rectangular basin Figure 5.

Recalling  $\bar{v} = \psi_x$ ,  $\bar{u} = \psi_y$ , and rewriting (22) in dimensional form:

$$\beta\psi_x = \frac{1}{\rho_0}(\tau_x^y - \tau_y^x) \quad (23)$$

$$\text{or} \quad \beta\psi_x = \frac{2\tau_0\pi}{\rho_0 b} \sin \frac{2\pi y}{b}. \quad (24)$$

To complete the problem we must pose boundary conditions. The no normal flow condition,  $\psi = \text{constant}$ , may be imposed at either the eastern or western boundary. Fortuitously we have chosen a wind stress whose curl vanishes on the northern and southern boundaries. Thus, setting the constant to zero,  $\psi = 0$ , the two main solutions are shown below.

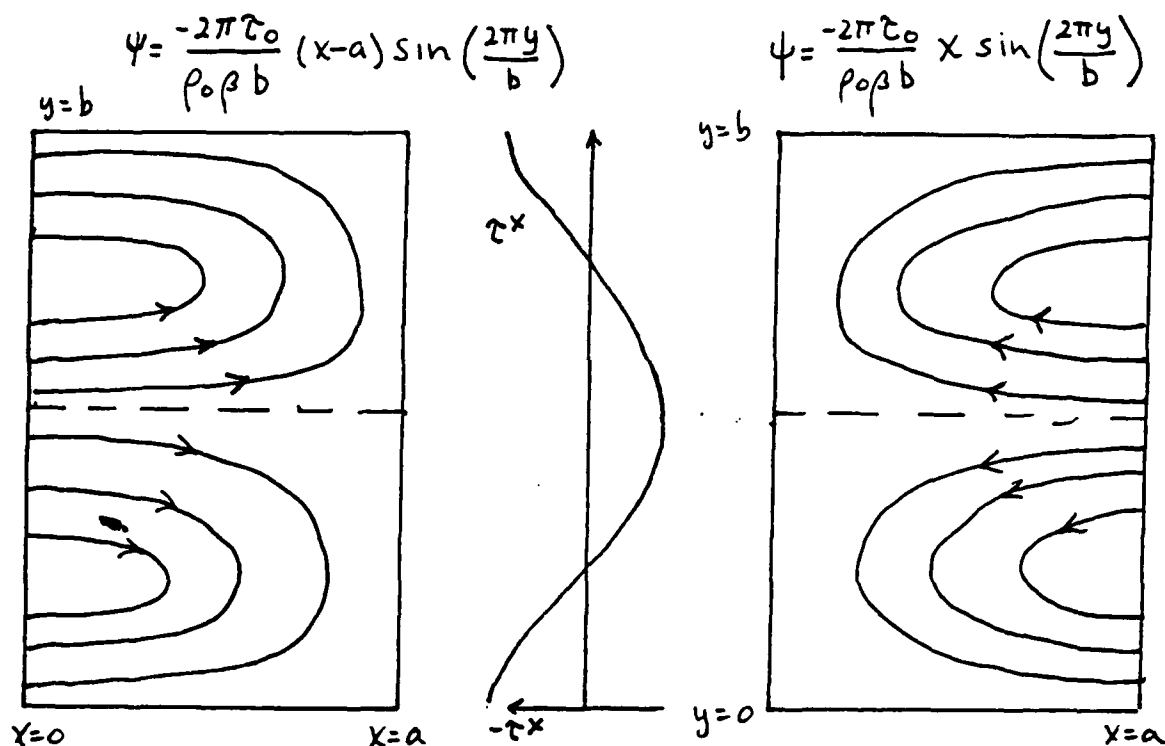


Figure 6

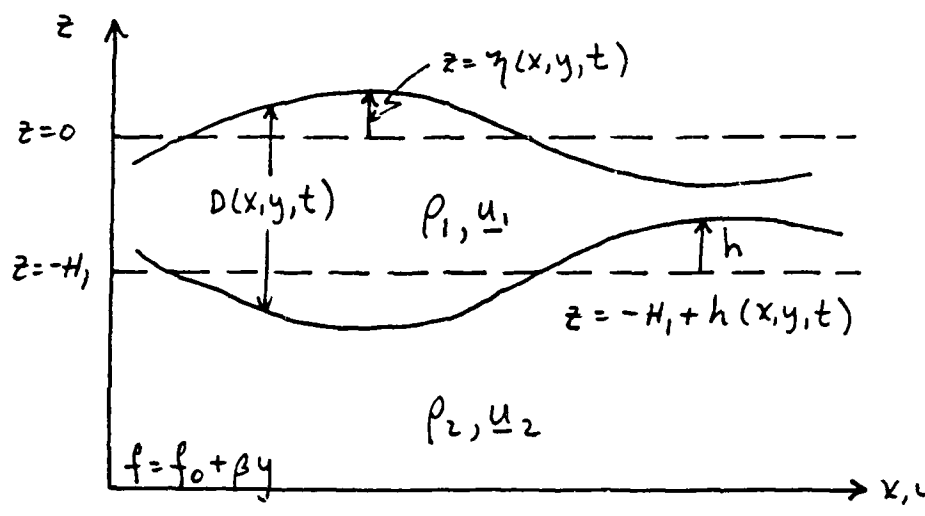
The solutions correspond to either setting  $\psi = 0$  on the eastern (fig. 6a.) or western (fig. 6b.) boundaries.

If we consider the wind as representative of that over the sub-polar and sub-tropical basins, we could conject that the solution in figure. 6a. was the more physical. One member of the staff argued that this solution was the only one in which the vorticity was consistent with that of the imposed wind stress. Analytically, it is not until we append boundary layers that we find the circulation must

be closed by a western boundary layer. Using observed mean wind stresses this relation produces mass transport streamlines which show considerable resemblance to the observed surface circulation (figure 7.).

We can extend the concept of combining Sverdrup and Ekman ideas by considering a layered model of the interior circulation. Although layered models will be discussed more extensively in latter lectures, we begin the frame work here in order to compare the theory with observations as well as to introduce the abyssal circulation.

Consider the two layer system in figure 7. below:



The 1.5 layer model is defined such that the lower layer is at rest. The steady, geostrophic equations integrated over the upper layer are:

$$-f D v_1 = -g' D D_z + \frac{\tau^x}{\rho_1} - \epsilon u_1 \quad (25)$$

$$+f D u_1 = -g' D D_y + \frac{\tau^y}{\rho_1} - \epsilon v_1 \quad (26)$$

$$(u_1 D)_z + (v_1 D)_y = 0 \quad (27)$$

The interfacial friction terms proportional to  $\epsilon$  will only become important in the boundary layer and will thus be neglected in this analysis. Defining a mass transport stream function  $\psi$  such that

$$v_1 D = \psi_x \quad u_1 D = -\psi_y,$$

and cross-differentiating the momentum equations (25-26) we obtain Sverdrups relation in the upper layer:

$$\beta \psi_z = \underline{k} \cdot \nabla \times \frac{\tau}{\rho_1} \quad (28)$$

Integrating this equation out from the eastern boundary we have the following relations (see Lecture 9. for steps in derivation):

$$\psi(x, y) = \psi(x_E, y) + (x_E - x) \frac{\tau_y^x}{\beta \rho_1} \quad (29)$$

$$D^2(x, y) = D^2(x_E, y) + \frac{(x_E - x)}{\rho_1 g'} \left( \frac{f \tau_y^x}{\beta} - \tau^x \right) \quad (30)$$

The effects of including vortex stretching due to a spatially variable thermocline depth ( $D$ ) are seen in the schematic representation of the solution in figure 8 below.

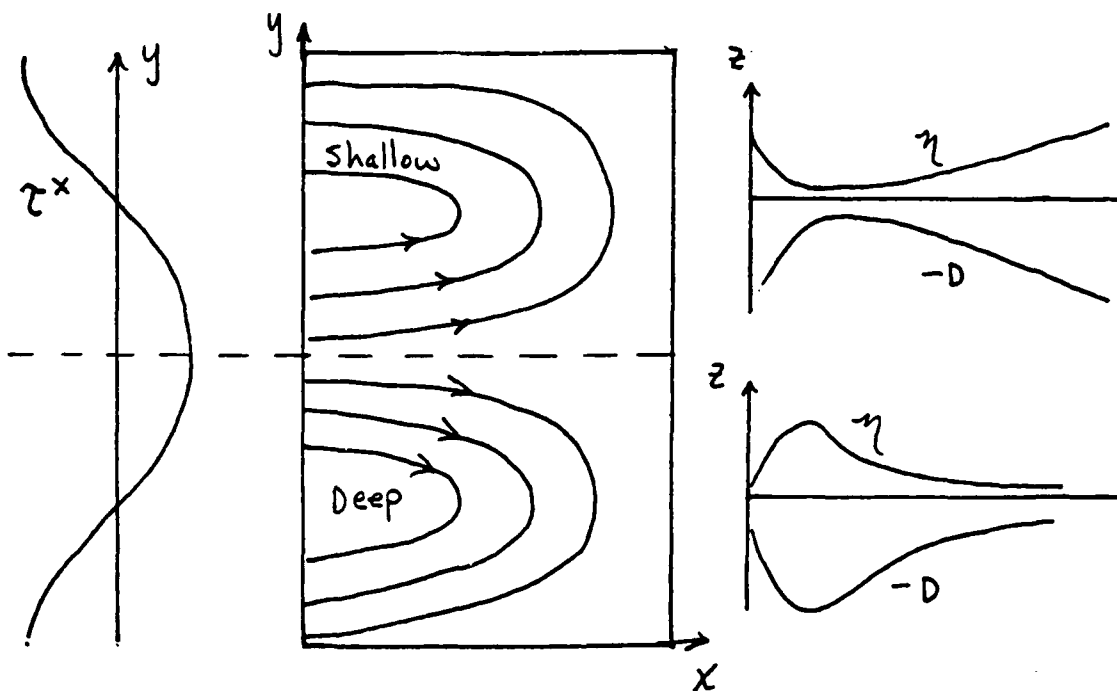


Figure 8

The solutions are intuitively clear with the notions of Ekman pumping and suction, a deepening of the thermocline towards the center of the subtropical gyre due to Ekman convergence, and shallowing in the sub-polar gyre.

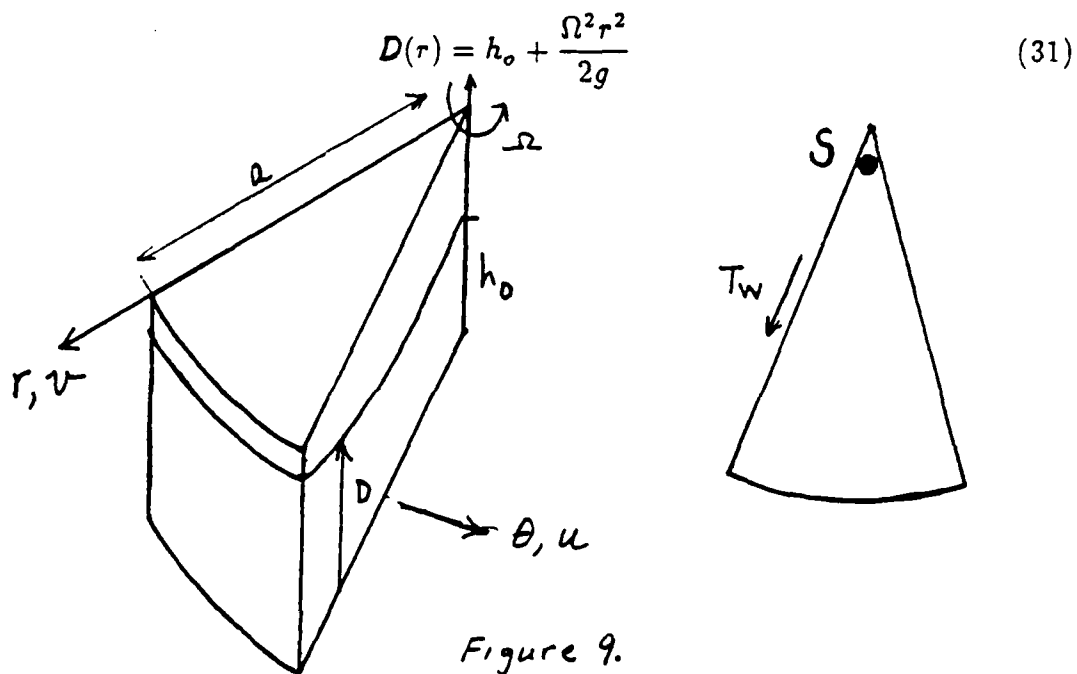
Verifying the Sverdrup balance relation away from boundary layers in the ocean may, as in the case of the Ekman flow, be an over-simplification. From hydrographic measurements, investigators must choose a 'level of no motion', and then using the thermal wind relations calculate transports. Leetma and Bunker (1978), and Leetma, Niiler and Stommel (1977) support a Sverdrup balance in much of the interior ocean to within possible errors in the data, e.g. these measurements do not take into account fluctuations in the dynamics. Wunsch and Roemmich (1985) argue however that in order to balance the heat budget for the ocean-atmosphere system the interior transport must be greater than that predicted by the Sverdrup relation. The Sverdrup balance has also been tested in primitive equation numerical models. Holland and Rhines (1980) find that over large regions in the interior the Sverdrup balance holds.

We have attempted to summarize the evolution of early wind-driven ocean circulation theories. The 1.5 layer framework now enables us to go a step further and consider an abyssal circulation, somewhat independent of the upper wind driven circulation.

### 3.4 Abyssal Circulation

Much of what is known about the abyssal circulation comes from observations of the fluid properties rather than direct current measurements. We may obtain insight into the distribution of these properties by studying a simple model/experiment discussed in a series of papers by Stommel and Arons (1960a,b) and Stommel, Arons and Faller (1958).

We start with the basic notion that fluid at the poles loses heat and possibly becomes more saline (if there is freezing taking place). These processes cause the fluid to become more dense and consequently 'sink' to lower depths, acting as a source of deep water. Next consider, a rotating pie shaped region (see figure 9 below) with a free surface described by:



We now draw the analogy between sinking regions at the poles with a source, ( $S$ ), at the apex of the pie shaped region.

$$S = h_0 \frac{a^2 \theta_0}{2} \cdot [cm^3/s] \quad (32)$$

Considering geostrophic dynamics, we write the momentum equations in polar coordinates.

$$-2\Omega v = \frac{-P_\theta}{\rho r} \quad 2\Omega u = \frac{-P_r}{\rho} \quad (33)$$



$$h_t + \frac{1}{r} [(uD)_\theta + (vDr)_r] = 0 \quad (34)$$

$$\text{or using (33)} \quad h_t + \frac{1}{r} \left[ \left( \frac{-DP_r}{2\Omega\rho} \right)_\theta + \left( \frac{dP_\theta}{2\Omega\rho} \right)_r \right] = 0. \quad (35)$$

Cross-differentiating (32) and using (34) we have

$$h_t + vDr = 0 \quad u_\theta + (rv)_r = 0 \quad (36)$$

and with (31) and (32) the result:

$$v = \frac{-2gS}{a^2\Omega^2 r\theta_o} \quad u_\theta = 0 \quad (37).$$

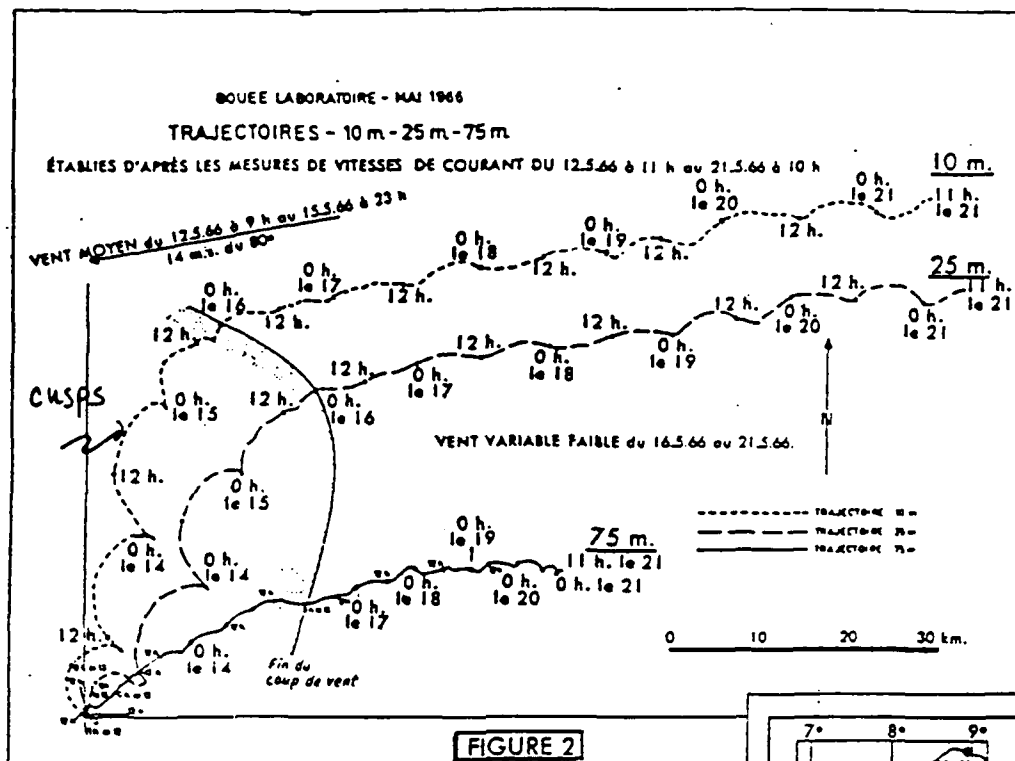
Note: For  $S > 0$ ,  $v < 0$  and we have flow towards the source! We develop the analogy further by considering the transport of fluid in the pie shaped region (basin). For  $S > 0$  at the apex we have:

$$\text{Water in} = S_o v(r) D(r) r \theta_o = S \left( 1 + \frac{2gh_o}{\Omega^2 a^2} + \frac{r^2}{a^2} \right)$$

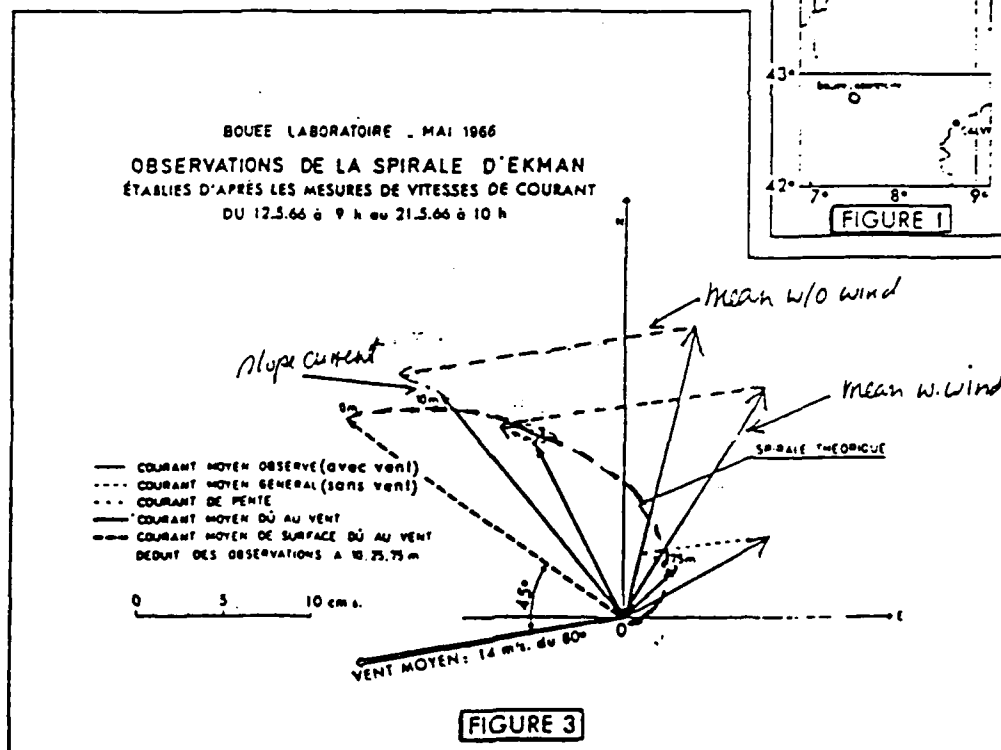
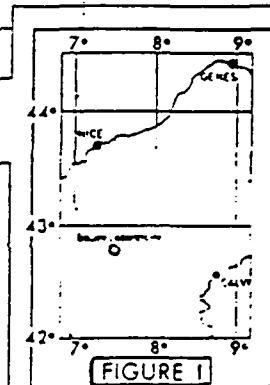
$$\text{Water out} = S \frac{r^2}{a^2}, \text{ surface is rising}$$

$$\text{Difference} = \text{Western Boundary Current} = T_w(r) S \left( 1 + \frac{2gh_o}{\Omega^2 a^2} \right) \quad (38)$$

From (38) we notice that the transport in the western boundary layer is greater than the source and we therefore conclude that the fluid is recirculating into the boundary layer. An interesting way to predict the behavior of these flows was pointed out by one of the staff during the lecture. In the geostrophic approximation, the Taylor-Proudman theorem is valid and we may think of the flow as a bundle of columns which as the surface rises move towards the source in order to minimize the vortex stretching effect due to the variable surface height. Analogues like these may be considered for many combinations of sources and sinks placed around the periphery of the region. The model is also easily extended to a spherical coordinate system. Strong implications may be made concerning the abyssal circulation in the oceans. Kuo and Veronis (1971) sketch a possible circulation pattern for two point sources, one in the southern ocean and the other in the north atlantic, see figure 10.



MUSEUM NATIONAL D'HISTOIRE NATURELLE  
LABORATOIRE D'OCEANOGRAPHIE PHYSIQUE



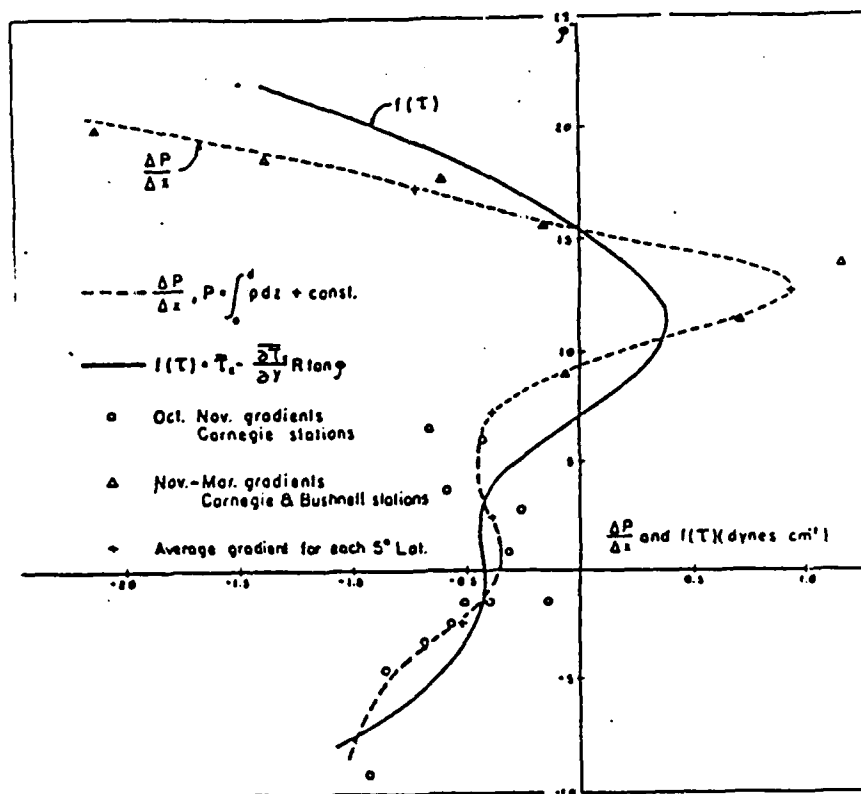


Figure 4a

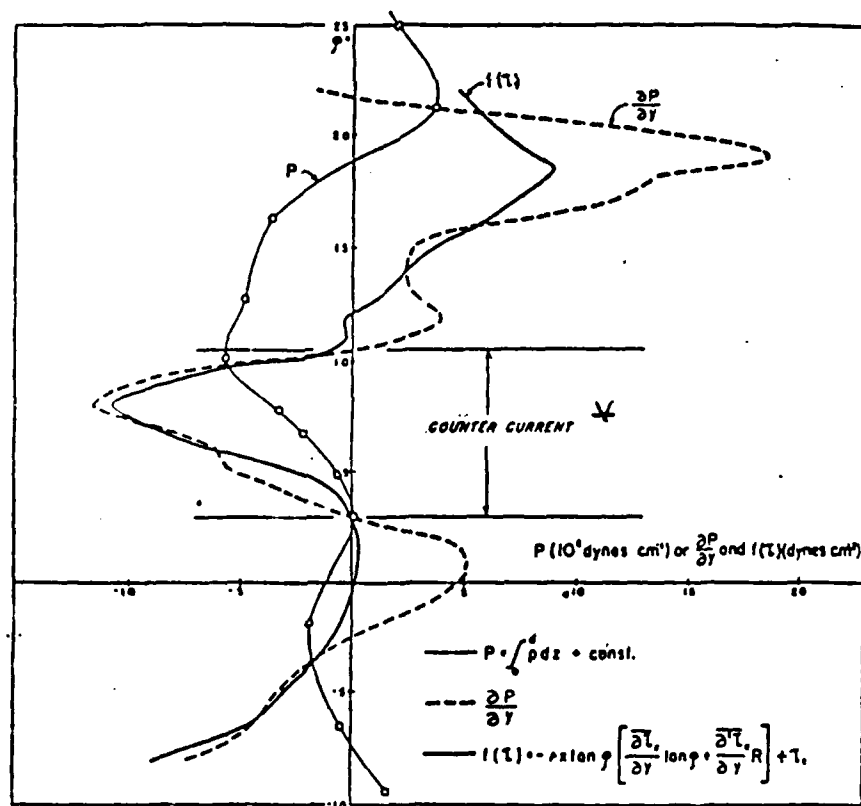


Figure 4b

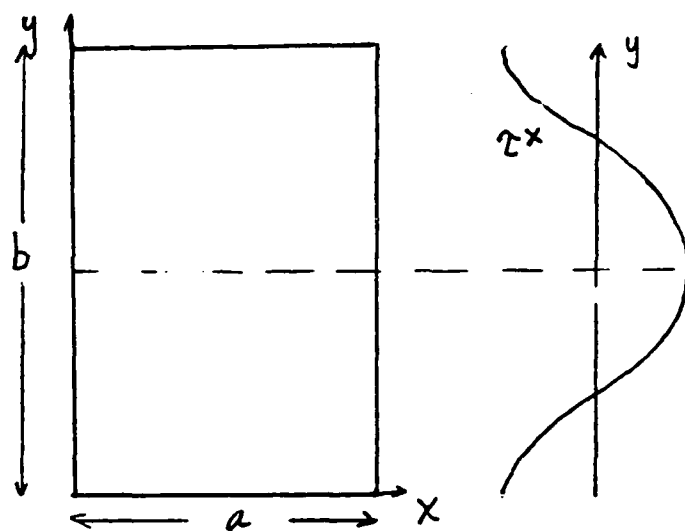


Figure 5.

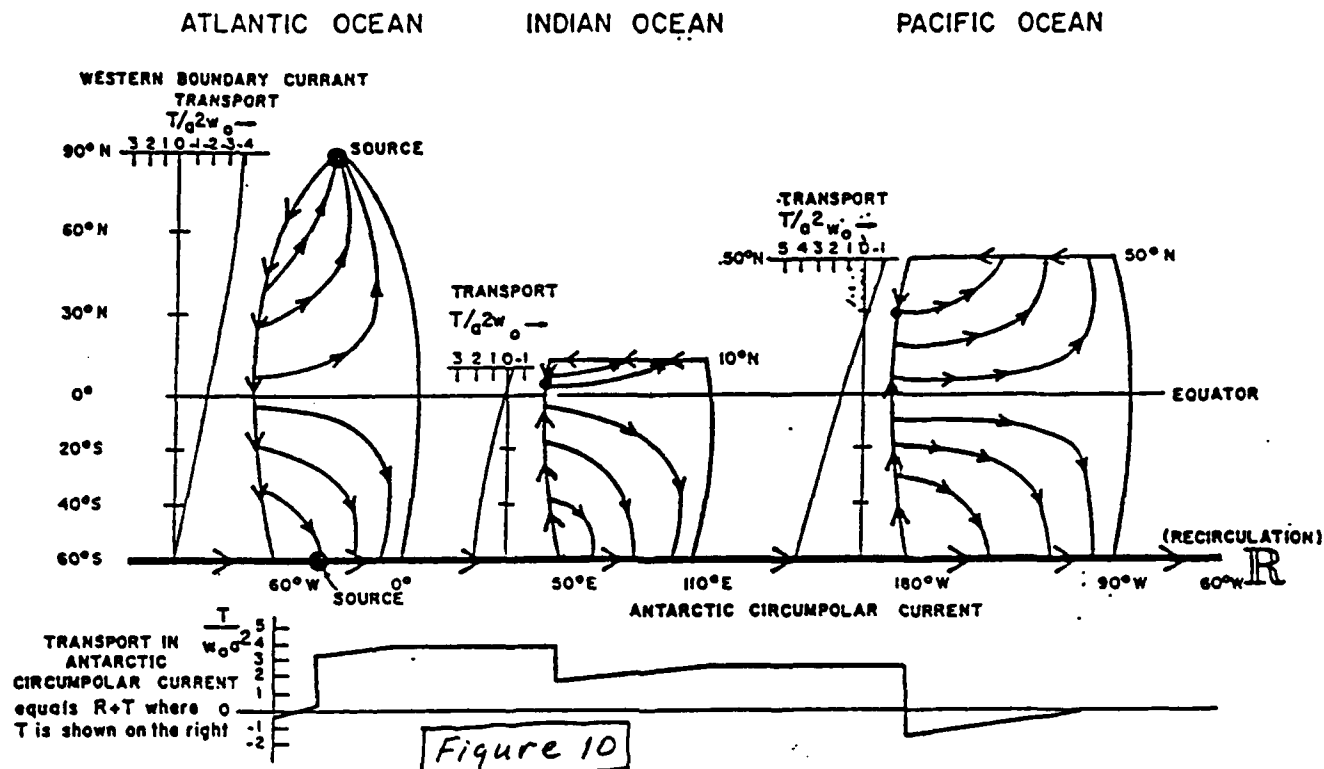


Fig. 2. The model for the abyssal circulation of the world ocean and the transport in the boundary currents. ( $w_0 \sim$  upwelling velocity;  $a \sim$  radius of earth).

### 3.5 References

- Ekman, V.W. 1905: On the influence of the earth's rotation on ocean currents. Akkiv. Matem., Astr. Fysik Stockholm, 2 (11).
- Goldsborough, G. 1933: Ocean currents produced by evaporation and precipitation. Proc. Roy. Soc. London. A., 141, 201-257.
- Holland, W. and P. Rhines, 1980: An example of eddy induced ocean circulation. J. Phys. Oceanogr.
- Hough, S.S. 1897: On the application of harmonic analysis to the dynamical theory of the tides.-Part I. On Laplace's "Oscillations of the first species, and on the dynamics of ocean currents". Phil. Trans. Roy. Soc. London. A., 189, 201-257.
- Hunkins, K. 1966: Ekman drift currents in the Arctic Ocean. Deep-Sea Res. 13, 607-620.
- Kuo, H.H. and G. Veronis, 1971: The source-sink flow in a rotating system and its oceanic analogy. J. Fluid Mech. 45, 441-466.
- Leetma, A. and A. Bunker, 1978: Updated charts of the mean annual wind stress, convergences in Ekman layers, and the Sverdrup transports in the North Atlantic. J. Mar. Res., 36, 311-322.
- Leetma, A., P. Niiler and H. Stommel, 1977: Does the Sverdrup relation account for the mid-Atlantic circulation? J. Mar. Res., 35, 1-9.
- Stommel, H., A.B. Arons and A.J. Faller, 1958: Some examples of stationary flow patterns in bounded basins. Tellus, 10, 179-187.
- Stommel, H. and A.B. Arons, 1960a: On the abyssal circulation of the world ocean-I. Stationary planetary flow patterns on a sphere. Deep-Sea Res., 6, 140-154.
- Stommel, H. and A.B. Arons, 1960b: On the abyssal circulation of the world ocean-II. An idealized model of the circulation pattern and amplitude in oceanic basins, Deep Sea Res., 6, 217-233.

Sverdrup, H., 1947: Wind driven currents in a baroclinic ocean; with application to the equatorial currents of the eastern Pacific. Proc. Nat. Acad. Sci. Wash., 33, 318-326.

Notes submitted by: R. Vance Condie, Columbia University

## LECTURE 4

## 4.1 BAROTROPIC VORTICITY EQUATION

The midlatitude barotropic vorticity equation is

$$(\partial_t - \psi_y \partial_x + \psi_x \partial_y) \nabla^2 \psi + \beta \psi_x = \frac{\tau_x^y - \tau_y^x}{\rho_0 D_0} - r \nabla^2 \psi + A_H \nabla^4 \psi$$

Here  $\psi$  is a stream function for the vertically averaged flow, in the  $x, y$  direction in an ocean of constant depth and density:

$$v = \psi_x, \quad u = -\psi_y$$

$$f = f_0 + \beta y$$

$\tau_x^y, \tau_y^x$  are components of wind stress,  $A_H$  is the horizontal eddy coefficient and  $r$  is the inverse time scale characterizing damping by bottom friction.

With the scaling

$$x, y \rightarrow lx, ly$$

$$t \rightarrow (l/u)t$$

$$\tau \rightarrow \tau_0 \tau$$

$$\psi \rightarrow (\tau_0 / \rho_0 D_0 \beta) \Psi$$

we have

$$R_0 (\partial_t - \Psi_y \partial_x + \Psi_x \partial_y) \nabla^2 \Psi + \Psi_x$$

$$= (\tau_x^y - \tau_y^x) - \epsilon_s \nabla^2 \Psi + \epsilon_H \nabla^4 \Psi$$

$$R_0 = \frac{u}{(\beta l) l}, \quad \epsilon_s = \frac{r}{\beta l}, \quad \epsilon_H = \frac{A_H}{\beta l^3}$$



If  $R_0, E_s, E_M \ll 1$

we have

$$\Psi_z = \tau_z^y - \tau_y^x$$

or, in dimensional form,

$$\beta \psi = (\tau_z^y - \tau_y^x) / \rho_0 D_0$$

This is Sverdrup balance.

Total transport:

$$\beta \bar{v} = (\tau_z^y - \tau_y^x) / \rho_0$$

Ekman transport:

$$\bar{v}_E = -\tau^x / \rho_0 f$$

Geostrophic transport:

$$\beta \bar{v}' = \frac{f}{\rho_0} \left[ \left( \frac{\tau^y}{f} \right)_x - \left( \frac{\tau^x}{f} \right)_y \right]$$

#### 4.2 Canonical Sverdrup Problem

$$\beta \Psi_x = (\tau_z^y - \tau_y^x) / \rho_0 D_0, \quad (a \geq x \geq 0, \quad b \geq y \geq 0)$$

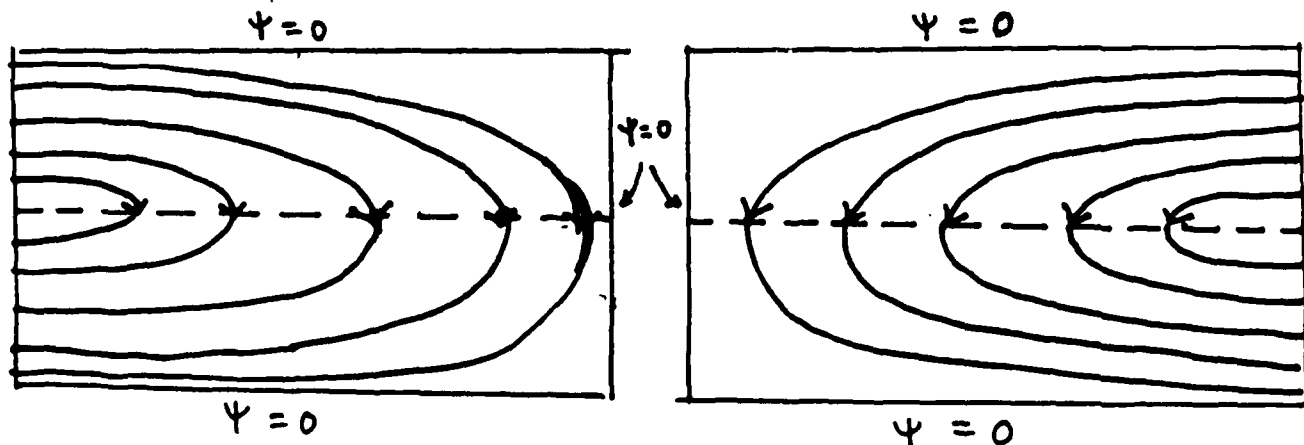
$$\tau^y = 0 \quad ; \quad \tau^x = -\tau_0 \cos(\pi y / b)$$

$$\Psi = 0 \quad \text{on boundary}$$

Two equally possible solutions  
(cannot satisfy  $\Psi = 0$  on one boundary)

$$(1) \quad \Psi = -\frac{\tau_0 \pi}{\rho_0 D_0 b} (x-a) \sin\left(\frac{\pi y}{b}\right) \quad (2) \quad \Psi = -\frac{\tau_0 \pi}{\rho_0 D_0 b} x \sin\left(\frac{\pi y}{b}\right)$$

(Sverdrup's Choice)



Choice of correct solution requires consideration of frictional effects. Physical consideration suggests Sverdrup's choice.

- Case (1) Wind inputs clockwise vorticity,  
Western boundary friction inputs counterclockwise vorticity.
- Case (2) Wind inputs clockwise vorticity Eastern boundary friction inputs clockwise vorticity.

#### 4.3 Stommel Problem (1948)

Assume bottom friction plays dominant role in boundary layer.

$$r \nabla^2 \psi + \beta \psi_x = \frac{\tau_x^y - \tau_y^x}{\rho_0 D_0} \quad (a \geq x \geq 0, b \geq y \geq 0)$$

$$\psi = 0 \quad \text{at boundaries}$$

$$\tau^y = 0$$

$$\tau^x = -\tau_0 \cos(\pi y/b)$$

Use scaling:

$$x \rightarrow ax$$

$$y \rightarrow by$$

$$\psi \rightarrow (\tau_0 / \rho_0 D_0 \beta) \psi$$

$$\& \quad O(a) = O(b)$$

Then

$$\epsilon_s \nabla^2 \psi + \psi_x = -\pi \sin(\pi y)$$

$$\epsilon_s = r / \beta a \ll 1$$

$$\psi = 0 \quad \text{at} \quad x=0,1 \quad \& \quad y=0,1$$

Interior solution (Sverdrup):

$$\psi_I = (c-x) \pi \sin \pi y$$

Boundary layer solution:

Western  $x = \xi \epsilon^\alpha$

Eastern  $x-1 = \xi \epsilon^\alpha$

$$\epsilon^{1-2\alpha} \Psi_{\xi\xi} + \epsilon \Psi_{yy} + \epsilon^{-\alpha} \Psi_\xi = -\pi \sin(\pi y)$$

With  $\alpha=1$ ,

$$\Psi_{\xi\xi} + \Psi_\xi = O(\epsilon)$$

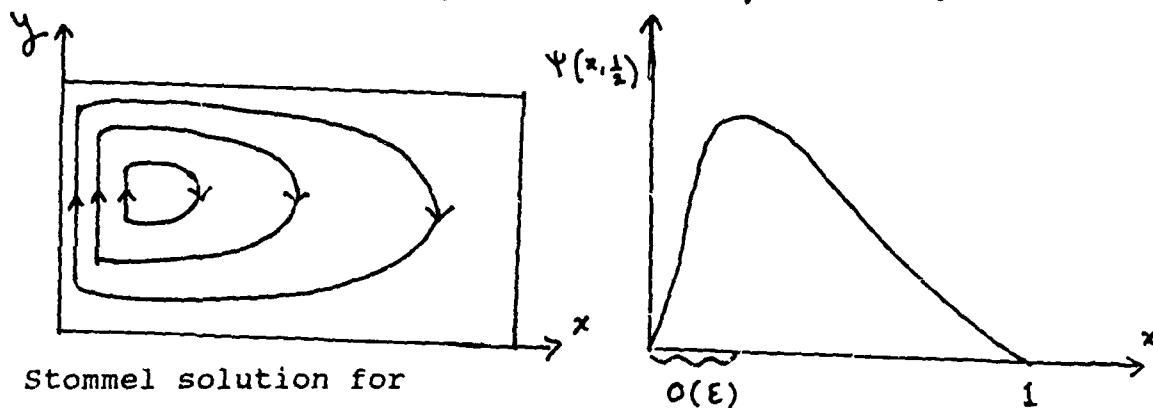
$$\Rightarrow \Psi = A + B e^{-\xi}$$

Match solutions:

$$\Psi = \begin{cases} (1-x) \pi \sin \pi y, & x \gg O(\epsilon) \\ (1 - e^{-x/\epsilon}) \pi \sin \pi y, & x \leq O(\epsilon) \end{cases}$$

(Note: W. Boundary layer  $\Rightarrow c=1$ .)

$$\Psi = (1 - e^{-x/\epsilon} - x) \pi \sin(\pi y)$$



Stommel solution for

$$\tau^x = -\tau_0 (y - l/2)/l$$

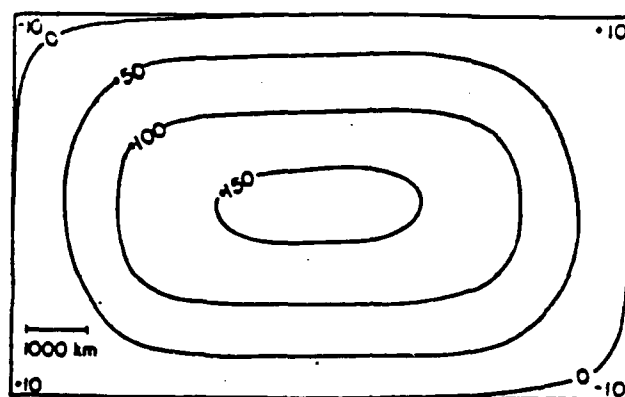


Fig. 4. Surface height contours for the uniformly rotating ocean in cm referred to an arbitrary level

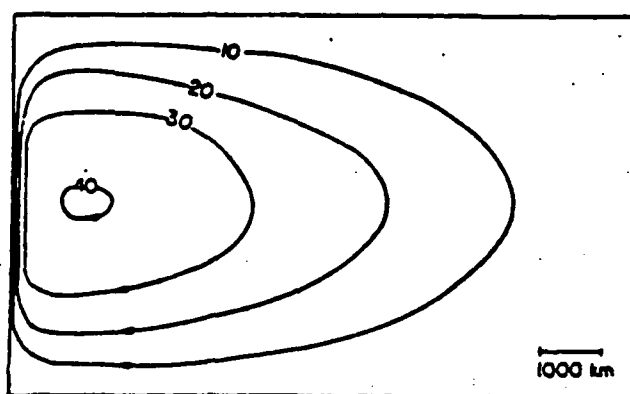
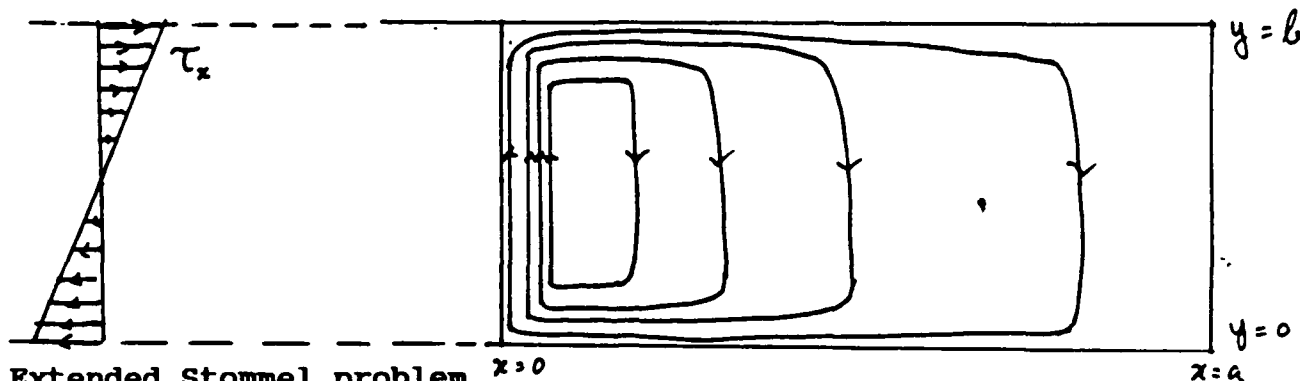


Fig. 5. Streamlines for the case where the Coriolis force is a linear function of latitude

is shown below; note that in this case northern/southern boundary layers are also needed.



#### 4.4 Extended Stommel problem

Consider a rectangular basin with  $a \gg b$

$$\tau (\Psi_{xx} + \Psi_{yy}) + \beta \Psi_x = - \frac{\tau_0 \pi}{\rho_0 D_0 b} \sin\left(\frac{\pi y}{b}\right)$$

We look for solutions in the form

$$\Psi = \sin\left(\frac{\pi y}{b}\right) \left\{ \phi(x) + \frac{\tau_0}{\rho_0 D_0} \frac{b}{r\pi} \right\}$$

Then

$$\phi_{xx} + \left(\frac{\beta}{r}\right) \phi_x - \left(\frac{\pi}{b}\right)^2 \phi = 0$$

or

$$\phi_{xx} + \frac{1}{L_B} \phi_x - \frac{\pi^2}{b^2} \phi = 0$$

where  $L_B = r/\beta$

General solution is

$$\phi = A e^{\ell_1 x} + B e^{\ell_2 x}$$

where  $l_1, l_2 = \frac{1}{2} \left[ -\frac{1}{L_B} \pm \sqrt{\left(\frac{1}{L_B}\right)^2 + \frac{4\pi^2}{b^2}} \right]$

A and B are determined from the boundary conditions

$$\Psi = 0$$

for  $x = 0, a$

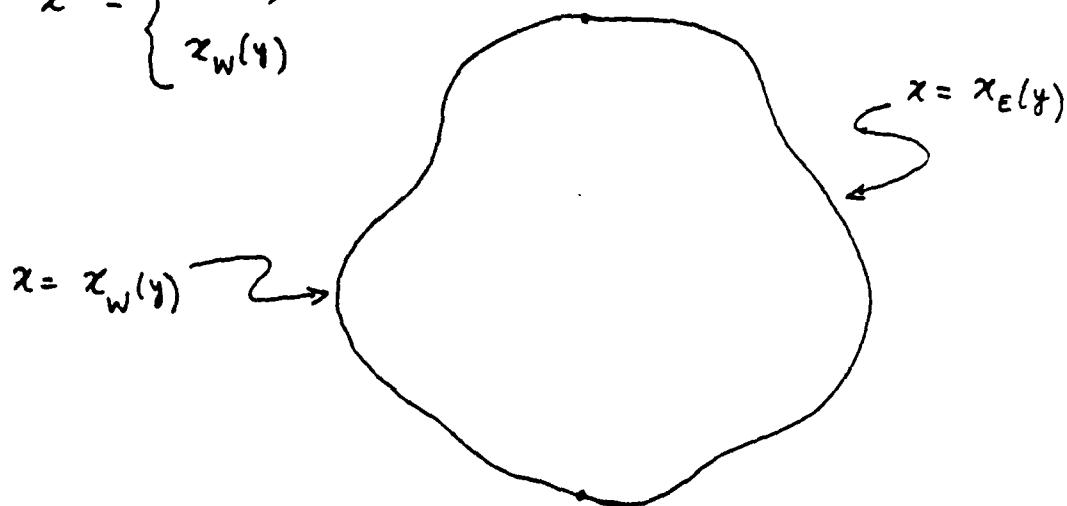
Limiting case: For  $L_B \ll b$

$$l_1 \cong -1/L_B, \quad l_2 \cong \pi^2 b^{-1} (L_B/b)$$

#### 4.5 Basin of arbitrary shape - Stommel problem.

$$\varepsilon \nabla^2 \Psi + \Psi_x = \tau_x^y - \tau_y^x$$

$$\Psi = 0 \text{ at } x = \begin{cases} x_E(y) \\ x_W(y) \end{cases}$$



Interior solution:

$$\Psi_I = \int_{x_E(y)}^x (\tau_{x'}^y - \tau_y^{x'}) dx'$$

Boundary layer: We anticipate a western boundary layer.  
Therefore set

$$\begin{aligned}
 x - x_w(y) &= \xi \varepsilon^a \\
 \Rightarrow \quad \varepsilon^{1-2a} \Psi_{\xi\xi} [1 + (\partial_y x_w)^2] - \varepsilon^{1-a} \frac{1}{2} (\partial_y x_w) \Psi_{\xi y} \\
 &+ \varepsilon^{1-a} \Psi_{\xi} (\partial_{yy} x_w) + \varepsilon \Psi_{yy} + \varepsilon^{-a} \Psi_{\xi} \\
 &= \tau_x^y - \tau_y^x
 \end{aligned}$$

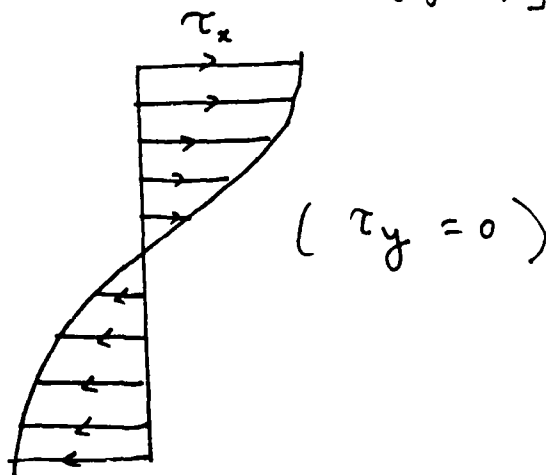
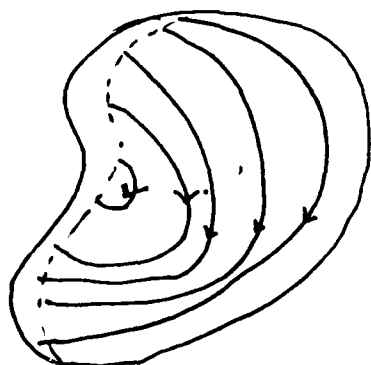
Put  $a = 1$

$$[1 + (\partial_y x_w)^2] \Psi_{\xi\xi} + \Psi_{\xi} = 0$$

$$\Psi = A(y) + B(y) \exp[-\xi / (1 + (\partial_y x_w)^2)]$$

Matching interior to boundary layer gives

$$\begin{aligned}
 \Psi &= \int_{x_E(y)}^x (\tau_{x'}^y - \tau_y^x) dx' \\
 &- \left[ \int_{x_E(y)}^{x_w(y)} (\tau_{x'}^y - \tau_y^x) dx' \right] \exp \left\{ - \frac{x \varepsilon^{-1}}{1 + (\partial_y x_w)^2} \right\}
 \end{aligned}$$



#### 4.6 Munk problem (1950)

We assume lateral friction plays the dominant role in the boundary layer to close the Sverdrup flow. This is the Munk problem. We take the wind stress as

$$\tau^y = 0$$

$$\tau^x = -\tau_0 \cos\left(\frac{\pi y}{b}\right)$$

Then the Munk problem can be formulated as

$$-A_H \nabla^4 \Psi + \beta \Psi_x = (\tau_x^y - \tau_y^x) / \rho_0 D_0$$

$$\Psi = \Psi_x = 0 \quad \text{at } x = 0, a \quad \dots\dots\dots (i)$$

$$\Psi = \Psi_{yy} = 0 \quad \text{at } y = 0, b \quad \dots\dots\dots (ii)$$

Boundary conditions ( ) correspond to no tangential stress at northern and southern boundaries ("slip boundaries"). This has been chosen for analytical convenience since in this case no northern and southern boundary layers would be necessary.

We adopt the scaling

$$x \rightarrow ax \quad (\text{assume } a \sim b)$$

$$y \rightarrow by$$

$$\Psi \rightarrow \frac{\tau_0}{\rho_0 D_0 \beta} \Psi$$

Then

$$\epsilon_M \nabla^4 \Psi - \Psi_x = \pi \sin(\pi y)$$

where

$$\epsilon_M = (A_H / \beta b^3) \ll 1$$

Boundary conditions

$$\Psi = \Psi_x = 0 \quad \text{at } x = 0, 1$$

$$\Psi = \Psi_{yy} = 0 \quad \text{at } y = 0, 1$$



Boundary layer solution techniques give

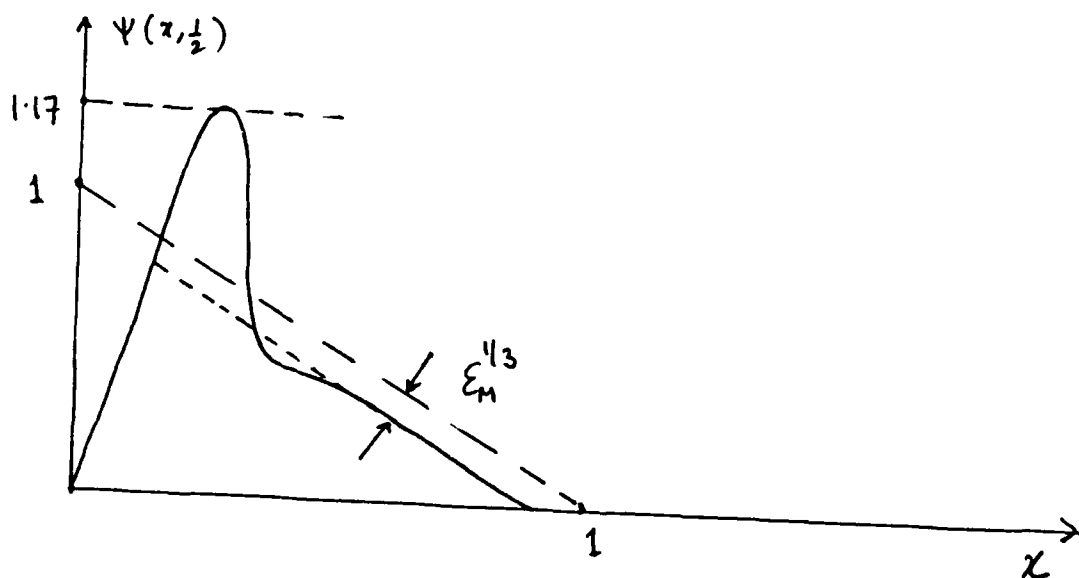
$$\Psi = \pi \sin(\pi \Psi) \{ \Psi_{WBL} + \Psi_I + \Psi_{EBL} \}$$

where  $\Psi_{WBL}$ ,  $\Psi_I$  and  $\Psi_{EBL}$  correspond to the western boundary, interior and eastern boundary respectively and are given by

$$\begin{aligned} \Psi_{WBL} = & -\frac{2}{3} (1 - \varepsilon_M^{1/3}) e^{-x/(2\varepsilon_M^{1/3})} \cos\left(\frac{x\sqrt{3}}{2\varepsilon_M^{1/3}} - \frac{\pi}{6}\right) \\ & + \frac{2}{\sqrt{3}} e^{-x/(2\varepsilon_M^{1/3})} \sin\left(\frac{x\sqrt{3}}{2\varepsilon_M^{1/3}}\right) \end{aligned}$$

$$\Psi_I = 1 - \varepsilon_M^{1/3} - x$$

$$\Psi_{EBL} = \varepsilon_M^{1/3} e^{(x-1)/\varepsilon_M^{1/3}}$$



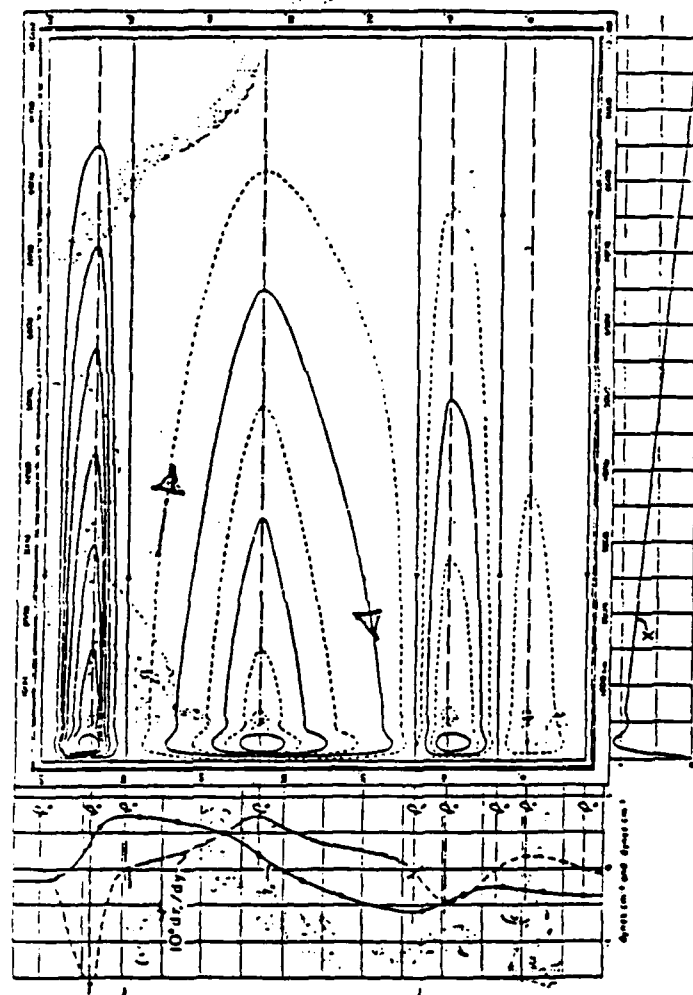


Fig. 2. The mean annual zonal wind stress  $\tau_x(y)$  over the Pacific and its curl  $dr_x/dy$  are plotted on the left, the function  $\Delta(\tau)$  on the lower part. These functions have been combined graphically according to equation (22) to give mass transport streamlines  $\psi(x,y)$ . The transport between adjacent solid lines is  $10 \times 10^{13}$  g sec $^{-1}$ , or 10 million metric tons sec $^{-1}$ . The total transport between the coast and any point  $x, y$  is  $\psi(x,y)$ . The chart of the Pacific has a uniform distance scale throughout. In the relatively narrow northern portion, the transport is greatly exaggerated.

#### 4.7 References

- [1] Munk, W. H., 1950. On the wind driven ocean circulation. J. Meteor., 7, 79-93.
- [2] Munk, W. H., G. W. Groves and G. F. Carrier, 1950. Note on the dynamics of the Gulf Stream. J. Mar. Res., 9, 218-238.
- [3] Stommel, H., 1948. The Westward intensification of wind-driven ocean currents. Trans. Am. Geophys. Union, 29, 2, 202-206.
- [4] Stommel, H., 1957a. A survey of ocean current theory. Deep-Sea Res., 4, 149-184.
- [5] Hendershott, M. C., 1986. Single layer models of the general circulation. General circulation of the ocean, Springer-verlag, Ed. Henry D. I. Abarbanel and W. R. Young.

Notes submitted by: Sandip Ghosal, Columbia University

## LECTURE 5

## THE EFFECT OF INERTIA

## 5.1 Nonlinear perturbation of the Stommel problem

Recall the scaled barotropic vorticity equation

$$Ro [\partial_t - \psi_y \partial_x + \psi_x \partial_y] \nabla^2 \psi + \psi_x = (\tau_y^x - \tau_x^y) - \epsilon_s \nabla^2 \psi + \epsilon_m \nabla^4 \psi \quad (5.1)$$

where

$$Ro = U/b^2\beta, \quad \epsilon_s = \tau/b\beta \quad \text{and} \quad \epsilon_m = A_H/b^3\beta$$

are the magnitudes of the inertial, bottom friction and lateral diffusion terms respectively. In the limit of zero Rossby number  $Ro$ , Stommel (1948) closed the problem by introducing bottom friction in the case of the canonical dimensionless wind stress  $\underline{\tau} = (-\cos \pi y, 0)$ . The steady solution obtained to  $O(Ro^0)$  for the equation

$$Ro [-\psi_y \partial_x + \psi_x \partial_y] \nabla^2 \psi + \psi_x = \pi \sin \pi y - \epsilon \nabla^2 \psi \quad (5.2)$$

was

$$\psi_s = (1-x - e^{-x/\epsilon}) \pi \sin \pi y \quad (5.3)$$

which describes the usual Sverdrup interior flow closed by a boundary layer at the western boundary. Let us now write, for  $Ro \ll E \ll 1$ ,

$$\psi = \psi_s + Ro \psi'$$

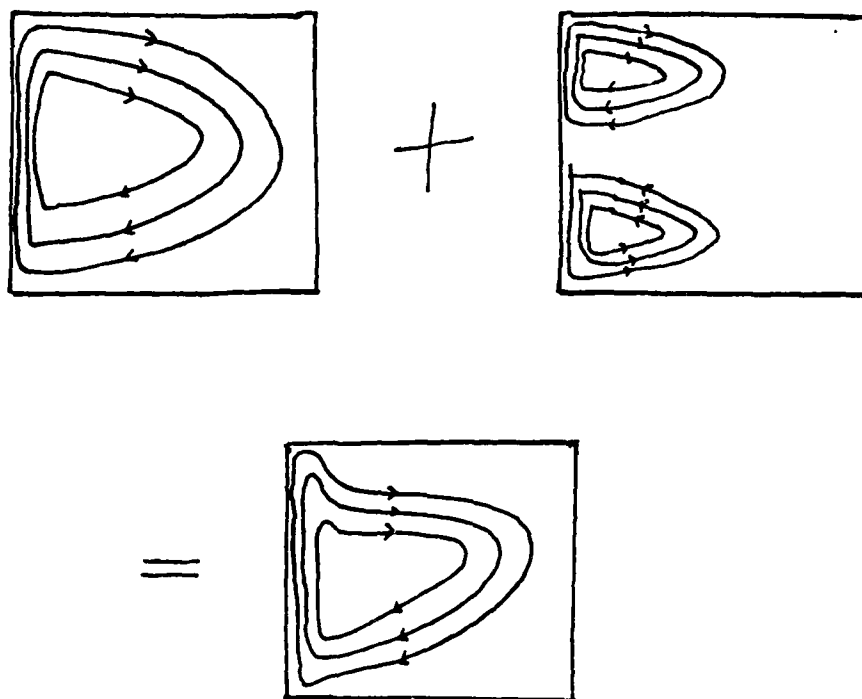


Figure 1. Perturbation to the Stommel solution for  $Ro \ll 1$ .

where  $\psi'$  satisfies the  $O(Ro')$  equation

$$\epsilon \nabla^2 \psi' + \psi'_x = -[-\psi_{sy} \nabla^2 \psi_{sx} + \psi_{sx} \nabla^2 \psi_{sy}] \quad (5.4)$$

and  $\psi' = 0$  on the boundaries. Substituting for  $\psi_s$  gives

$$\epsilon \nabla^2 \psi' + \psi'_x = \frac{\pi^2}{2\epsilon^3} (1-x) e^{-x/\epsilon} \sin 2\pi y + O(\epsilon^{-2}) \quad (5.5)$$

which has a solution in the western boundary layer approximation

$$\psi' = \frac{\pi^3}{2\epsilon^3} (-x) \sin 2\pi y e^{-x/\epsilon}. \quad (5.6)$$

Note that  $\psi'$  is antisymmetric about  $y = 1/2$  and so the symmetry of the Stommel solution is broken by the perturbation, as shown by Figure 1.

The boundary layer north of  $y = 1/2$  is sharpened and the boundary layer transport increased, while it is broadened south of  $y = 1/2$  and the transport decreased. This is because negative relative vorticity is being advected from the southern half-basin into the northern half-basin; before rejoining the Sverdrup interior flow, fluid parcels travelling northwards through the western boundary layer must lose their excess negative relative vorticity through dissipation in the region at the northwest corner of the basin.

## 5.2 Fofonoff Free Nonlinear Solutions

Fofonoff (1954) considered the alternative limit of high  $Ro$  -steady pure inertial flow with negligible forcing and dissipation, i.e. he solved the equation

$$Ro [-\psi_y \nabla^2 \psi_x + \psi_x \nabla^2 \psi_y] + \psi_x = 0 \quad (5.7)$$

with  $\psi = 0$  specified on the boundaries. This can be rewritten

$$\frac{D}{Dt} [Ro \nabla^2 \psi + y] = 0 \quad (5.8)$$

which says that potential vorticity is conserved along streamlines, so we may write

$$R_0 \nabla^2 \psi + y = F(\psi) \quad (5.9)$$

Fofonoff considered the simplest choice for the functional  $F$  by assuming linearity

$$R_0 \nabla^2 \psi + y = y_0 + \psi \quad (5.10)$$

which admits an interior solution for  $R_0 \ll 1$ , viz.

$$\psi_i = y - y_0 \quad (5.11)$$

corresponding to entirely westward zonal flow. The alternative choice of eastward flow could have been made, but we shall see below that it is physically inconsistent.

The boundary condition  $\psi = 0$  can only be satisfied at one of  $y=0,1$  at most, and so boundary layers are required to satisfy  $\psi = 0$  at the other boundaries.

Consider first the western boundary  $x=0$ . Setting  $\psi = \psi_i + \psi_w$ , we obtain

$$R_0 \psi_{wxx} = \psi_w \quad (5.12)$$

which, upon matching with the interior solution  $\psi_i$ , gives

$$\psi_w = -(y - y_0) e^{-x/R_0^{1/2}} \quad (5.13)$$

Doing the same for the other boundaries, we obtain for arbitrary  $y_0$ .

$$\psi = (y - y_0) \left[ 1 - e^{-x/R_0^{1/2}} - e^{-(1-x)/R_0^{1/2}} \right] - (1 - y_0) e^{-(1-y)/R_0^{1/2}} + y_0 e^{-y/R_0^{1/2}} \quad (5.14)$$

The solutions for the choices  $y_0=0,1$  are shown below in Figure 2. Potential vorticity  $\psi_x + f$  must be conserved along streamlines within the boundary layers, and comparison of values of  $\psi_x + f$  at a point within the western boundary layer with its value just outside the boundary layer on the same streamline for either configuration in Figure 2 shows westward interior flow to be consistent with this constraint. Reversing the flow, which corresponds to posing an eastward interior flow, leads to inconsistency with conservation of potential vorticity  $\psi_x + f$  along streamlines. The eight possible constructions are checked for consistency

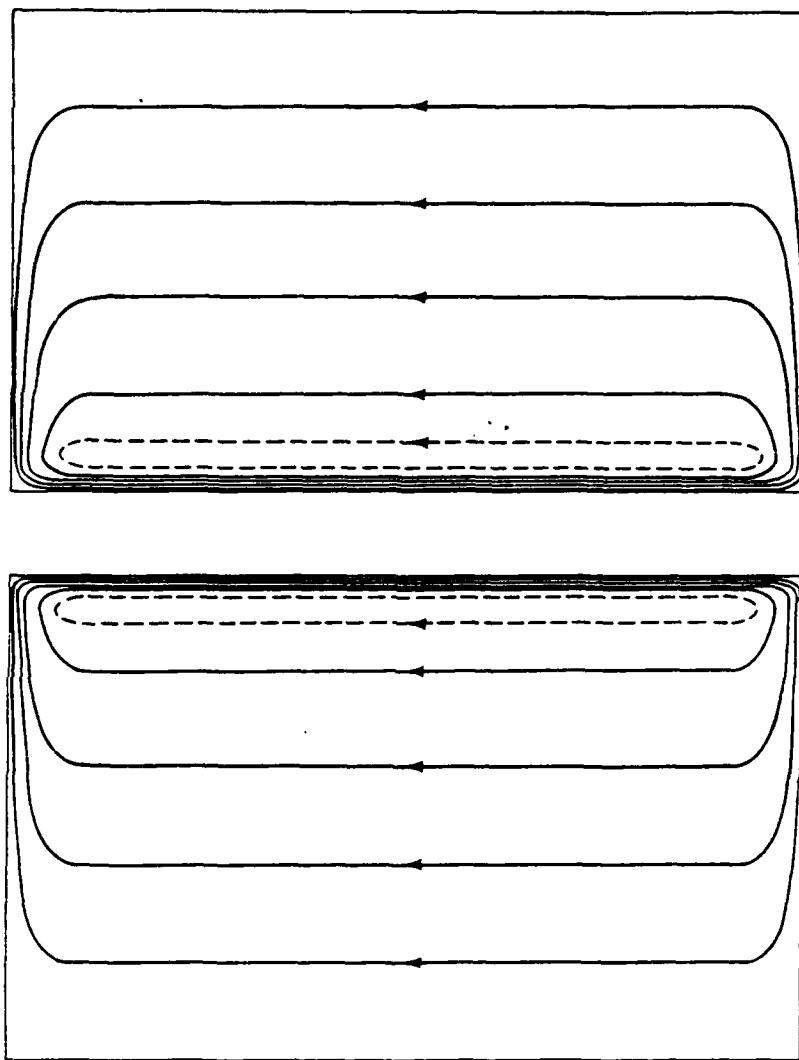


Figure 2. The Fofonoff solution with  $y_0 = 0, 1$ , due to Fofonoff (1954)



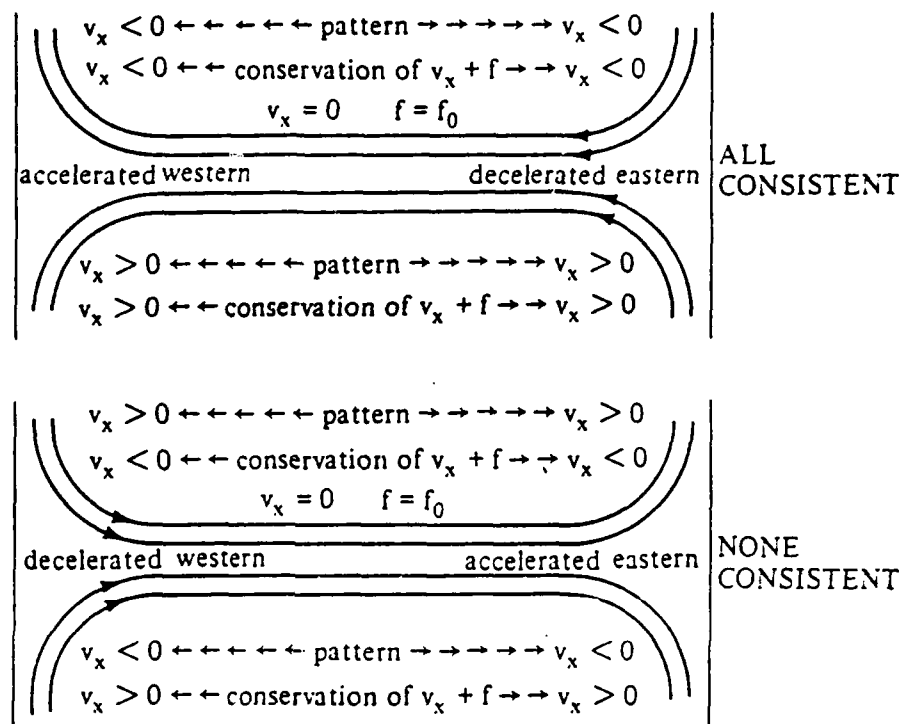


Figure 3. Consistency of the eight possible boundary layer flow patterns with the conservation of  $v_x + f$  along streamlines.

in Figure 3, confirming that in all consistent cases, the western boundary layer is accelerated as it is fed by the westward interior flow and the eastern boundary layer correspondingly decelerated.

### 5.3 Bottom Friction and Inertial Boundary Layers

We now consider perturbing the free inertial solutions with bottom friction and wind stress, i.e.

$$\mathcal{J}(\psi, R_0 \nabla^2 \psi + y) = \text{curl } \underline{\tau} - \epsilon \nabla^2 \psi. \quad (5.15)$$

Suppose the Fofonoff solution to be not significantly altered by the perturbation. Then integrating over the region enclosed by a closed streamline of the Fofonoff flow, we obtain

$$\oint_S \mathcal{J}(\psi, R_0 \nabla^2 \psi + y) da = \oint_S \text{curl } \underline{\tau} da - \epsilon \oint_S \nabla^2 \psi da$$

The left hand side of this is trivially zero and so, by application of the divergence theorem, the following integral constraint is derived,

$$\oint_S \text{curl } \underline{\tau} da = \epsilon \oint_C \underline{u} \cdot d\underline{\ell}. \quad (5.16)$$

Imagine a wind with westerlies in high latitudes and trades in low latitudes. We then have  $\text{curl } \underline{\tau} < 0$  and  $\underline{u} \cdot d\underline{\ell} > 0$  for the flow given by the choice  $y_0 = 0$  (with a northern boundary layer) as the flow is clockwise and the line integral taken counterclockwise. Hence a slightly perturbed Fofonoff flow is not inconsistent with the integral constraint (5.16). The selection of a northern inertial boundary layer is also physically consistent because the self advection of fluid up the western boundary layer will lead to "piling-up" of the streamlines at the northern end of the boundary layer.

Niiler (1966) proceeded to obtain a velocity scale for the Fofonoff flow, noting that the major contribution to  $\oint \underline{u} \cdot d\underline{\ell}$  comes from the northern boundary layer. Applying dimensional analysis to the constraint (5.16) and noting that the boundary layer flow has magnitude  $U_I b / \delta_I$ , we obtain

$$\left[ \frac{\tau_0 b}{\rho_0 D_0} \right] = \pi \left[ \frac{U_I b}{\delta_I} \right] b.$$

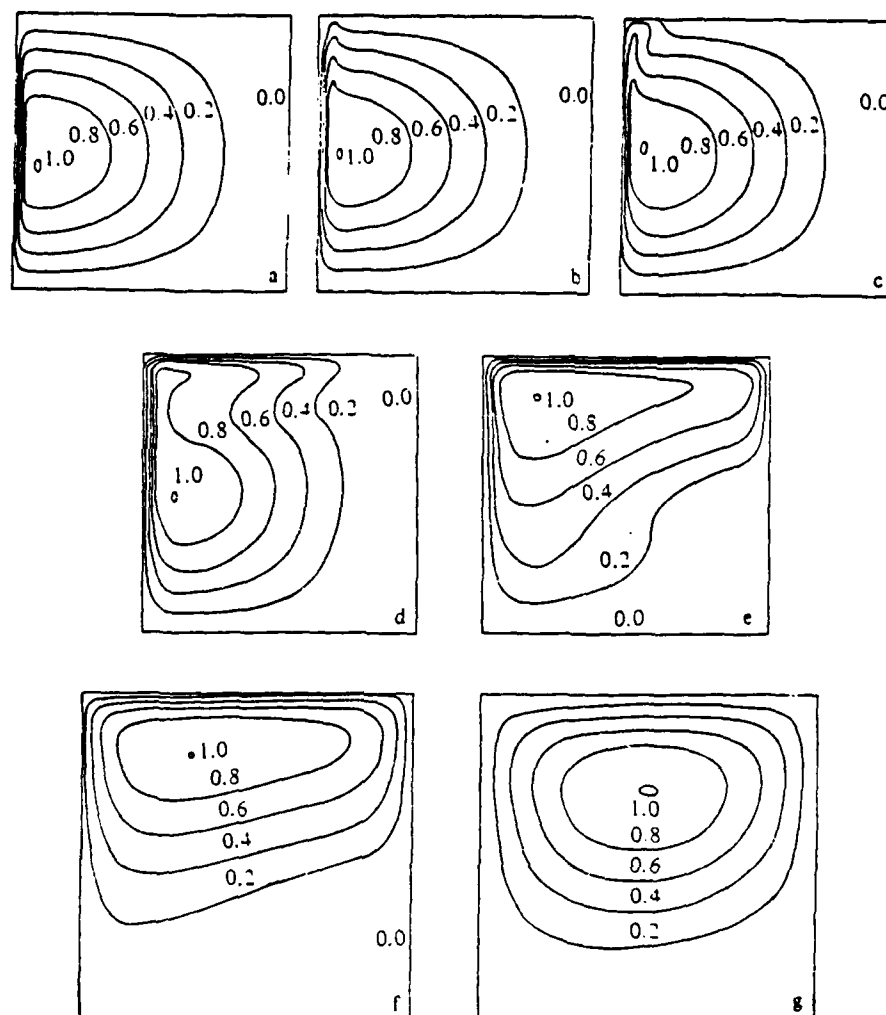


Figure 4. Numerical solution of the bottom friction (Stommel) model due to Veronis (1966) for  $Ro \ll 1$  to  $Ro \gg 1$ .

We know, however, that the inertial boundary layer thickness  $\delta_I$  and the Sverdrup velocity  $U_s$  have magnitudes

$$\begin{aligned}\delta_I &\sim b R_o^{1/2} = (U_I/\beta)^{1/2} \\ U_s &\sim \tau_o / (\rho_o D_o b \beta)\end{aligned}\quad (5.17)$$

Defining  $Ro = U_s / b \beta^2$ , we obtain

$$\frac{U_I}{U_s} \sim \frac{Ro}{\epsilon^2} \quad (5.18)$$

Veronis (1966) solved (5.15) numerically for various values of  $Ro/\epsilon^2$ , showing a smooth transition between the forced dissipative Stommel solution ( $Ro/\epsilon^2 \rightarrow 0$ ) and the free Fofonoff solution ( $Ro/\epsilon^2 \rightarrow \infty$ ). For large  $Ro/\epsilon^2$ , Veronis found that  $U_I/U_s \sim (0.107 - 0.109) Ro/\epsilon^2$ , in agreement with the dimensional analysis above.

The main effect of the nonlinearity is to advect negative relative vorticity up the western boundary, across the northern boundary, and down the eastern boundary.

#### 5.4 Lateral Diffusion and Inertial Boundary Layers

We first wish to apply the same analysis to the Munk problem as we have to the Stommel problem. Munk, Groves and Carrier (1950) solved

$$Ro [-\psi_y \partial_x + \psi_x \partial_y] \nabla^2 \psi + \psi_x = \pi \sin \pi y + \epsilon_m \nabla^4 \psi \quad (5.19)$$

for  $Ro \ll 1$  by setting  $\psi = \psi_m + Ro \psi'$  as before. The results are qualitatively similar to the nonlinear Stommel solution, as shown by Bryan's (1963) no-slip numerical calculations in Figure 5. Increasing  $Ro$  did not, however, lead to the Fofonoff inertial solution. Indeed it was not possible to calculate solutions at all for  $Re \geq 100$ . Let us therefore consider perturbing the Fofonoff solution by the addition of some wind stress and lateral diffusivity, i.e. solve (5.19) in the limit of large  $Ro$ .

As in § 5.3, we can obtain a simple integral constraint on the solution by considering the area enclosed by a streamline of the unperturbed Fofonoff flow (away from any

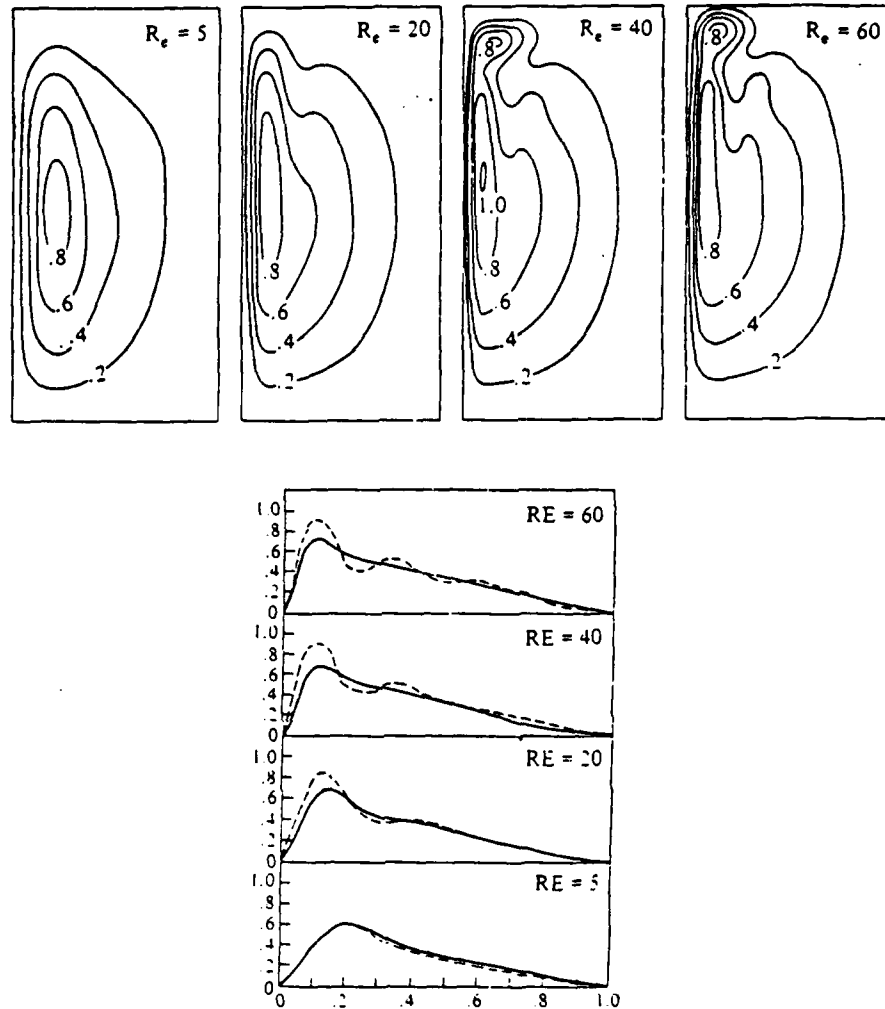


Fig. 10. Numerical solutions of the barotropic vorticity equation (2.1.1) with only lateral diffusivity and with a wind stress curl of the form  $-\sin(\pi y/b)$  (adapted from Bryan, 1963).

Figure 5. Numerical solution of the lateral diffusivity (Munk) model due to Bryan (1963), with Reynolds number  $Re = Ro/\epsilon_m$  ranging from  $Re=5$  to  $Re=60$ , with no-slip at the boundaries.

boundary layers) and by assuming the perturbation to the flow to be small. This yields the requirement

$$-\epsilon_m \oint \nabla(\nabla^2 \psi) \cdot \hat{n} \, dl = \oint \omega l \tau \, da \quad (5.20)$$

which, upon noting that  $\omega l \tau < 0$ , reduces to

$$\oint \nabla \tau \cdot \hat{n} \, dl > 0 \quad (5.21)$$

where  $\tau$  is the relative vorticity ( $=\nabla^2 \psi$ ) and  $\hat{n}$  is normal to the streamline and directed outwards. However, in the interior of the Fofonoff flow  $\tau \sim 0$ , while just outside the boundary layers  $\tau < 0$  and so  $\nabla \tau \cdot \hat{n} < 0$  on the enclosing streamline. The constraint (5.21) is therefore violated, which means that the flow cannot simply be a slight perturbation to the steady Fofonoff solution.

Let us continue, however, to attempt to construct a frictional sublayer under the inertial boundary layer. At the western and eastern boundaries, the boundary layer equation is

$$Ro [-\psi_y^F \psi_{xxx}^F + \psi_x^F \psi_{yxx}^F] + \psi_x^F = \epsilon_m \psi_{xxxx}^F \quad (5.22)$$

with internal inertial boundary layer solutions ( $\epsilon_m \ll 1$ )

$$\begin{aligned} \psi_{IW} &= (y-y_0)(1-e^{-x/Ro^{1/2}}) \\ \psi_{IE} &= (y-y_0)(1-e^{-(1-x)/Ro^{1/2}}) \end{aligned} \quad (5.23)$$

We are now able to deduce the thickness  $\delta$  of the frictional sublayer, given that the streamfunction within the frictional sublayer will scale as the streamfunction within the inertial boundary layer:  $\psi^f = \psi \Psi$ .

Matching nonlinear and frictional terms in (5.22) gives

$$\frac{Ro \Psi^2}{\delta^3} \sim \frac{\epsilon_m \Psi}{\delta^4}.$$

But

$$\Psi \sim \psi_I \sim \delta / R_0^{1/2}$$

and so

$$\delta^2 \sim \frac{\epsilon_m}{R_0^{1/2}} \sim \delta_m^2 \left( \frac{\delta_m}{\delta_I} \right) \ll \delta_m^2 \quad (5.24)$$

which implies that the nonlinearity actually reduces the thickness of the frictional boundary layer, if it exists. Integrating (5.22) with respect to  $x$ , and matching to the internal solution (5.23) we obtain, for the western boundary layer

$$R_0 [-\psi_y^F \psi_{xx}^F + \psi_x^F \psi_{yx}^F] + \psi^F = \epsilon_m \psi_{xxx}^F + (y - y_0) \quad (5.25)$$

scaling  $x = \delta \xi$  and  $\psi^F = \psi \Psi$  gives

$$-\psi_y \psi_{\xi\xi} + \psi_\xi \psi_{y\xi} = (y - y_0) + \psi_{\xi\xi\xi} \quad (5.26)$$

with  $\psi = \psi_\xi = 0$  at  $\xi = 0$

and  $\psi \rightarrow 1$  as  $\xi \rightarrow \infty$ . (5.27)

Writing  $u = -\psi_y$ ,  $v = \psi_\xi$  and  $ky/\rho_0 = -(y - y_0)$

(5.26) and (5.27) become (5.28)

$$u v_\xi + v v_y = -ky/\rho_0 + v_{\xi\xi}$$

and

$$u = v = 0 \quad \text{at } \xi = 0$$

$$v \rightarrow 1 \quad \text{as } \xi \rightarrow \infty.$$

which describes the classical problem of uniform flow in the  $+y$  direction past a flat plate, with a negative downstream pressure gradient. This admits a boundary layer solution. However, the eastern boundary layer equation transforms to

flow past a flat plate with an opposing pressure gradient, which does not allow a boundary layer solution, but instead results in separation.

We have therefore been able to construct a frictional sublayer at the western boundary, but not at the eastern boundary.

Ierley and Ruehr (1986) solved the boundary layer equation (5.25) at the western boundary by writing

$$\psi \equiv \varphi(x) (1 \pm y) \quad (5.30)$$

and rescaling  $x = X\epsilon^{1/3}$  to give the ordinary differential equation

$$\varphi''' = \varphi + \lambda (\varphi'^2 - \varphi \varphi'') - 1 \quad (5.31)$$

where

$$\lambda = \pm R_0 \epsilon^{-2/3}$$

The plus sign is appropriate for the southern half subtropical gyre (interior feeding boundary layer), the minus for the northern half (boundary layer feeding interior).

The boundary conditions are

$$\varphi(\infty) = 1, \quad \begin{cases} \varphi(0) = \varphi'(0) = 0 & \text{no slip at WB} \\ \varphi(0) = \varphi''(0) = 0 & \text{slip at WB} \end{cases} \quad (5.32)$$

The unknown boundary condition on  $\varphi$  at  $x=0$ , obtained by shooting so that  $\varphi(\infty)=1$ , corresponds to the wall stress for the no-slip case and to the  $y$  velocity at  $x=0$  for the stress free case. Let this unknown condition be  $\beta(\lambda)$ , as its value depends on the degree of nonlinearity  $\lambda$ . In Figure 6 we see solutions for  $\beta(\lambda)$ , the solid line being obtained numerically and the dotted line by continued fractions. Ierley (1987) studied the stability of each of the multiple solutions. In both cases a stable solution exists for all  $\lambda < 0$ , and in both cases there is a critical value of  $\lambda > 0$  beyond which no solutions exist. He conjectured that the failure of the boundary layer model was related to the onset



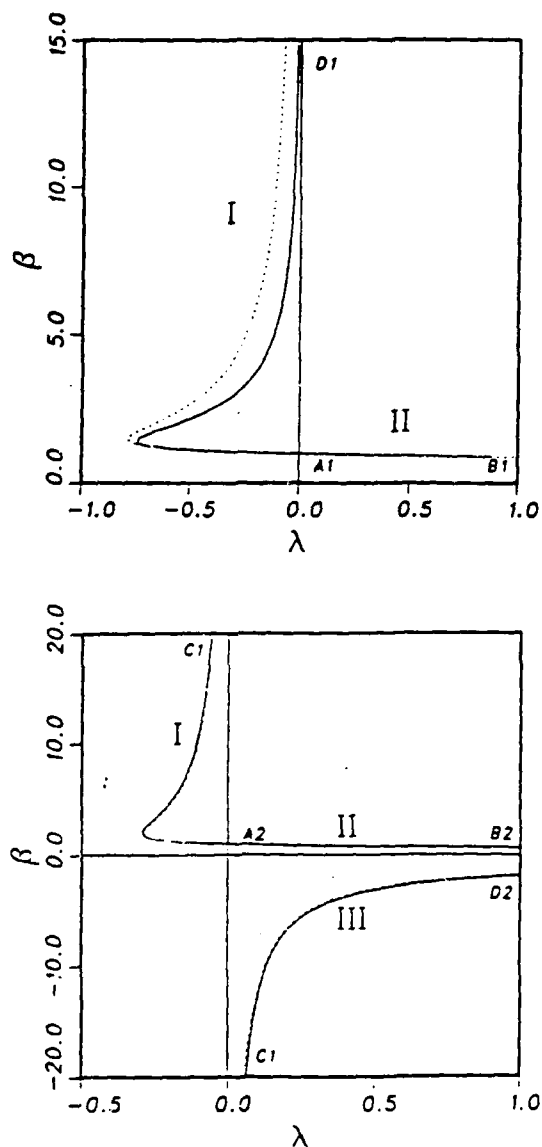


Figure 6. Unknown boundary conditions  $\beta(\lambda)$  for (a) no-slip boundaries,  $\beta(\lambda) = \varphi''(0; \lambda)$ , and (b) no-stress boundaries,  $\beta(\lambda) = \varphi'(0; \lambda)$  (from Ierley and Ruehr, 1986).

of recirculation in solutions of the full partial differential equations.

Böning (1986) also conducted numerical experiments with lateral friction, allowing slip at the boundaries. The major points of comparison with the bottom friction model are:

- \*Small nonlinearity advects negative relative vorticity  $\bar{\zeta}$  up the western boundary in both cases.

- \*Dimensionfull transport initially decreases as  $Ro$  is increased in both cases.

- \*With bottom friction, transport begins to rise with  $Ro$  when the northern boundary layer current reaches the eastern boundary.

- \*With lateral friction and slip, transport begins to rise with  $Ro$  when  $\lambda = Ro/\epsilon_m^{1/2}$  has exceeded the critical value  $\lambda_c \sim 0.29657$  such that for  $\lambda > \lambda_c$ , no boundary layer solution feeding the interior exists.

- \*With lateral friction and slip, the region of enhanced transport in the northwest corner (recirculation region) tends to stay in the north-west corner.

Note that the slip boundary condition (no stress) leads to no vorticity generation at the boundary and so parcels at the wall cannot change their potential vorticity.

## 5.5 References

Böning, C. W. 1986, On the influence of frictional parametrization in wind-driven circulation models. Dyn. Atmos. Oceans 10, 63-92.

Bryan, K. 1963. A numerical investigation of a nonlinear model of a wind-driven ocean. J. Atmos. Sci. 20, 594-606.

Fofonoff, N. P. 1954. Steady flow in a frictionless homogeneous ocean. J. Mar. Res. 13, 254-262.

Munk, W. H. 1950. On the wind-driven circulation. J. Meteor. 7, 79-93.

Munk, W. H., Groves, G. W. & Carrier, G. F. 1950. Note on the dynamics of the Gulf Stream. J. Mar. Res. 9 218-238.

Ierley, G. R. 1987. On the onset of inertial recirculation in barotropic general circulation models. J. Phys. Oceanogr. 17, 2366-2374.

Ierley, G. R. & Ruehr, O. G. 1986. Analytical and numerical solutions of a nonlinear boundary-layer problem. Stud. Appl. Math. 75, 1-36.

Stommel, H. 1948. The westward intensification of wind-driven ocean currents. Trans. Am. Geophys. Union, 29(2), 202-206.

Veronis, G. 1966. Wind-driven ocean circulation - Part 2. Numerical solutions of the nonlinear problem. Deep Sea Res. 13, 31-55.

Notes submitted by: Richard Jarvis, St. John's College,  
Cambridge, England

## LECTURE 6

### INITIATION OF SVERDRUP FLOW

#### 6.1 Introduction

In this lecture we introduce time dependence and examine the initiation of large-scale flow from a state of rest. Thus the steady solutions examined in the preceding lectures are augmented by transient solutions. The time-dependent equations admit a variety of wave solutions. As a consequence this lecture begins with a review of the linear wave solutions of the shallow water equations. We then investigate the transient modifications to the Stommel-type solutions discussed in Lecture 4. These modifications are succinctly demonstrated in the numerical solutions of the linear problem by Anderson & Gill (1975). We also examine the nonlinear problem that is forced by unsteady winds (Veronis, 1970). The lecture concludes with a discussion of the study by Kawase (1987) on the initiation of deep ocean circulation.

#### 6.2 Linear Wave Solutions

The starting point for our review are the linearized shallow water equations

$$\begin{aligned} U_t - fV &= -g\eta_x \\ V_t + fU &= -g\eta_y \\ \eta_t + D(U_x - V_y) &= 0 \end{aligned} \quad (6.1)$$

where  $f = f_0 + \beta y$  and  $\eta(x, y, t)$  describes the free surface. By cross differentiation these equations can be condensed into a single equation for  $v$ :

$$V_{xx} + V_{yy} + \beta V_x + \left( \frac{-\partial_{ttt} - f^2 \partial_t}{gD} \right) V = 0 \quad (6.2)$$

Inserting the plane wave ansatz

$$V = e^{i(lx + ky - \sigma t)} \quad (6.3)$$

in (6.2) yields the dispersion relation

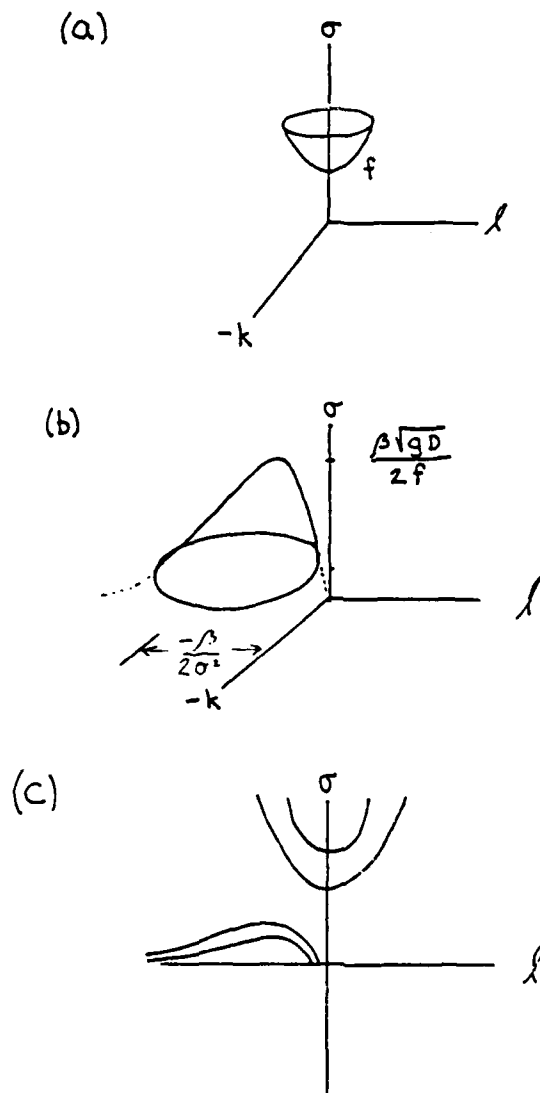


Figure 1. Graphical illustration of the dispersion relation (6.4). (a) The high frequency limit (6.5) (inertia-gravity waves). (b) The low frequency limit (6.6) (Rossby waves). (c) Projection of (a) and (b) on the  $\sigma$ - $l$  plane ( $k \neq 0$ ).

$$l^2 + k^2 + \frac{\beta l}{\sigma} = (\sigma^2 - f^2)/c^2 \quad (6.4)$$

where  $c^2 \equiv gD$ . Note that  $f=f(y)$  so that the plane wave solution can be viewed as the leading term of a WKB approximation.

The high frequency (large  $\sigma$ ) limit of (6.4) reduces to

$$\sigma^2 = f^2 + c^2(l^2 + k^2) \quad (6.5)$$

which is the dispersion relation for inertia-gravity waves. This relation is shown graphically in figure 1(a). Similarly the low frequency limit of (6.4) can be written as

$$\left(l + \frac{\beta}{2\sigma^2}\right)^2 + k^2 = \left(\frac{\beta}{2\sigma}\right)^2 - \frac{f^2}{c^2}. \quad (6.6)$$

This is the dispersion relation for Rossby waves and is illustrated in figure 1(b). In figure 1(c), this information is shown projected onto the  $\sigma$ - $l$  plane.

Another solution is obtained if we assume  $u = 0$  in the interior of the fluid as well as on the solid boundary  $x = 0$ . Then (6.1) becomes

$$\begin{aligned} -fv &= -g\eta_x \\ fu &= -g\eta_y \\ \eta_t + DV_y &= 0. \end{aligned} \quad (6.7)$$

Manipulation of (6.7b,c) yields the wave equation

$$V_{tt} - gDV_{yy} = 0 \quad (6.8)$$

Again we assume plane waves, viz.

$$V = h(x) e^{i(ky - \sigma t)} \quad (6.9)$$

where the amplitude now depends on  $x$ . Inserting (6.9) in (6.8) results in the linear dispersion relation

$$\sigma = \pm ck \quad (6.10)$$

An expression for  $\eta$  can be obtained by using (6.9) in (6.7c) and integrating. The result is

$$\eta = \frac{k D v}{\sigma} . \quad (6.11)$$

Finally we use (6.11) in (6.7a) to get an expression for  $h(x)$

$$h = h_0 e^{\frac{f}{c} x} \quad (6.12)$$

for  $x < 0$ . These non-dispersive waves, whose amplitude and velocity decay exponentially into the interior of the fluid, are known as Kelvin waves.

### 6.3 Mid-latitude Rossby Waves in Rectangular Basins

In mid-latitudes the vorticity equation can be written as

$$\nabla^2 \psi_t - R^2 \psi_t + \beta \psi_x = \hat{k} \cdot (\nabla \times \underline{\tau}) - \varepsilon \nabla^2 \psi \quad (6.13)$$

where  $R = (gD/f_0)$ ,  $\underline{\tau}$  is the wind stress,  $\hat{k}$  is a unit vector parallel to the  $z$ -axis and  $\varepsilon$  is a damping coefficient. It is convenient to first consider free wave solutions; that is solutions of

$$\nabla^2 \psi_t - R^2 \psi_t + \beta \psi_x = 0 \quad (6.14)$$

Assuming plane waves of the form  $\psi = \exp(i(lx + ky - \sigma t))$  we recover the dispersion relation (6.6). The group velocity vector

$$\underline{C}_g = \left( \frac{\partial \sigma}{\partial l}, \frac{\partial \sigma}{\partial k} \right) = \frac{2\sigma}{l^2 + k^2 + R^2} \vec{WC} \quad (6.15)$$

is shown in figure 2(a). The construction for reflected waves, due to Longuet-Higgins (1964), is shown in figure 2(b). From this figure it is apparent that long Rossby waves, that carry energy westward, are reflected at a western boundary as short Rossby waves that carry energy to the east.

The normal modes of a basin are found by assuming time-dependence of the form  $\exp(-i\sigma t)$  so (6.14) becomes

$$\nabla^2 \psi - R^2 \psi + \frac{i\beta}{\sigma} \psi_x = 0 \quad (6.16)$$

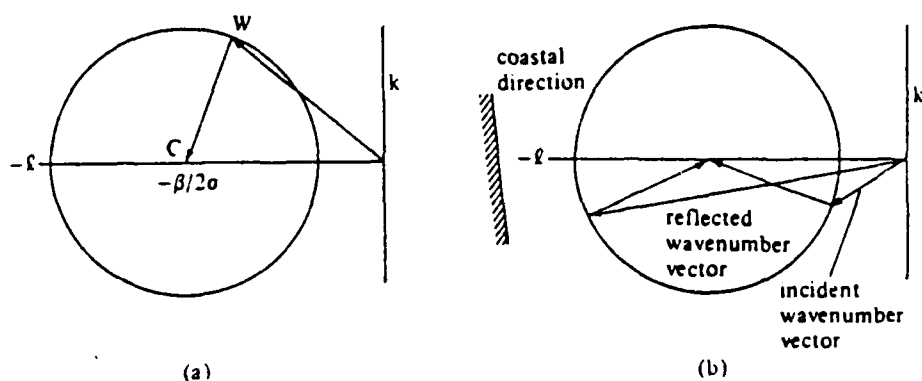


Figure 2. The dispersion relation (6.6) in the  $l$ - $k$  plane. (a) The group velocity vector is proportional to  $WC$ . (b) The incident and reflected wavenumber vectors (labeled) and the group velocity vectors (directed towards the center).

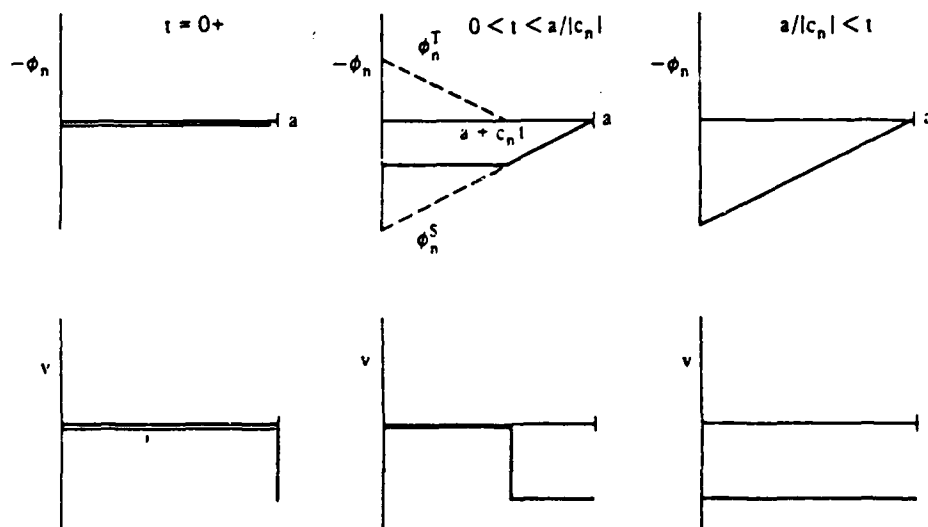


Figure 3. The solution  $\phi$  and  $v$  as functions of time.



subject to the condition of no normal flow through the boundary.

The substitution

$$\psi(x, y) = \phi(x, y) e^{i \frac{\beta}{2\sigma} x} \quad (6.17)$$

generates the Helmholtz equation

$$\nabla^2 \phi_n + k_n^2 \phi_n = 0 \quad (6.18)$$

where is specialized to discrete values and the eigenvalue  $k_n^2$  is

$$k_n^2 = \frac{\beta}{4\sigma^2} - \frac{1}{R^2}. \quad (6.19)$$

We must now discuss boundary conditions. For quasi-geostrophic flows  $\psi = g\eta/f_0$ . This imposes  $\eta=0$  on the boundary. This may violate mass conservation and we generalize to  $\eta = \text{constant}$ . The constant must be determined by requiring  $\int \psi_c dA = 0$ .

Before focusing on the initiation of Sverdrup flow in a closed basin it is instructive to consider Rossby modes in the infinite channel between  $y=0$  and  $y=b$  with  $\psi=0$  along these boundaries. We seek solutions of the form

$$\psi = \sin\left(\frac{n\pi y}{b}\right) \phi_n(x, t). \quad (6.20)$$

Insertion of (6.20) in (6.16) gives an equation for  $\phi_n$

$$\phi_{n, xxt} - (L^2 + R^2) \phi_{n, t} + \beta \phi_{n, x} = 0 \quad (6.21)$$

where

$$L^2 = \frac{n^2 \pi^2}{b^2}$$

and for which we assume

$$\phi_n = e^{i(lx - \sigma_n t)} \quad (6.22)$$

The resulting dispersion relation is

$$\sigma_n = - \frac{\beta l}{L^2 + R^2 + l^2}. \quad (6.23)$$

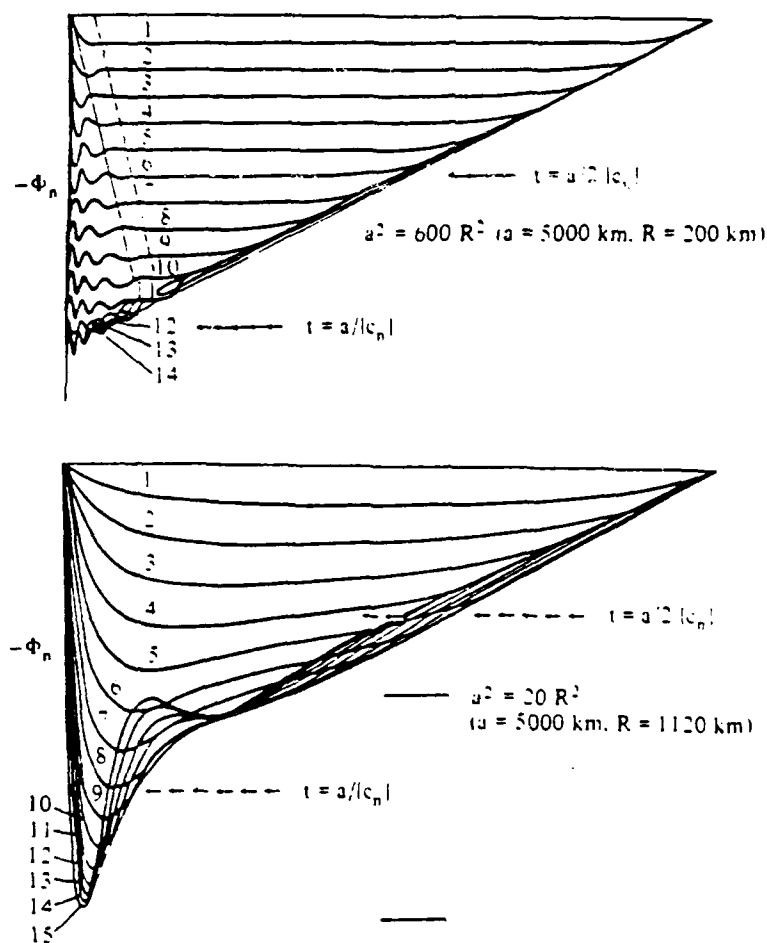


Figure 4. The numerical solutions of Anderson and Gill (1975). The upper panel is the baroclinic case. In this case fast internal modes are generated. The lower panel is the barotropic case in which surface gravity modes are formed.

The limiting cases  $l \rightarrow 0$  and  $l \rightarrow \infty$  display quite different types of behavior. For long waves ( $l \rightarrow 0$ ) The phase speed,  $C_{\text{phase}} = \frac{\omega}{k}$  is

$$C_{\text{PHASE}} = - \frac{\beta}{L^2 + R^{-2} + l^2}. \quad (6.24)$$

These waves are dispersionless and propagate phases westward. The group speed,  $C_g = \frac{\partial \omega}{\partial l}$ , is westward for

$$l^2 < L^2 + R^{-2} \quad (6.25)$$

Thus energy is also propagated westward by long waves. In contrast to the long waves the short waves are dispersive and carry energy to the east. Their maximum group speed is

$$C_g^{\text{MAX}} = \frac{\beta}{8(L^2 + R^{-2})} \quad (6.26)$$

and occurs at a wavenumber

$$l = \sqrt{3(L^2 + R^{-2})} \quad (6.27)$$

We now consider initiation of flow in a mid-latitude basin,  $x=0, a$ ;  $y=0, b$  by switching on the wind stress at  $t=0$ . We use the wind stress

$$\tau^x = -\tau_{0n} \cos(Ly) \quad (6.28)$$

so the vorticity equation is

$$\nabla^2 \psi_t - R^{-2} \psi_t + \beta \psi_x = - \frac{L}{\rho_0 D_0} \tau_{0n} \sin(Ly) \quad (6.29)$$

subject to  $\psi=0$  on the boundaries. As in the infinite channel we seek separated solutions of the form

$$\psi = \frac{L}{\rho_0 D_0} \sin(Ly) \phi_n(x, t) \quad (6.30)$$

The resulting equation for  $\phi_n$  is

$$\phi_{n, xxt} - [L^2 + R^{-2}] \phi_{n, t} + \beta \phi_{n, x} = -\tau_{0n} \quad (6.31)$$

with the conditions

$$\phi_n(x, 0) = 0 \quad (6.32)$$

$$\phi_n(a, t) = 0.$$

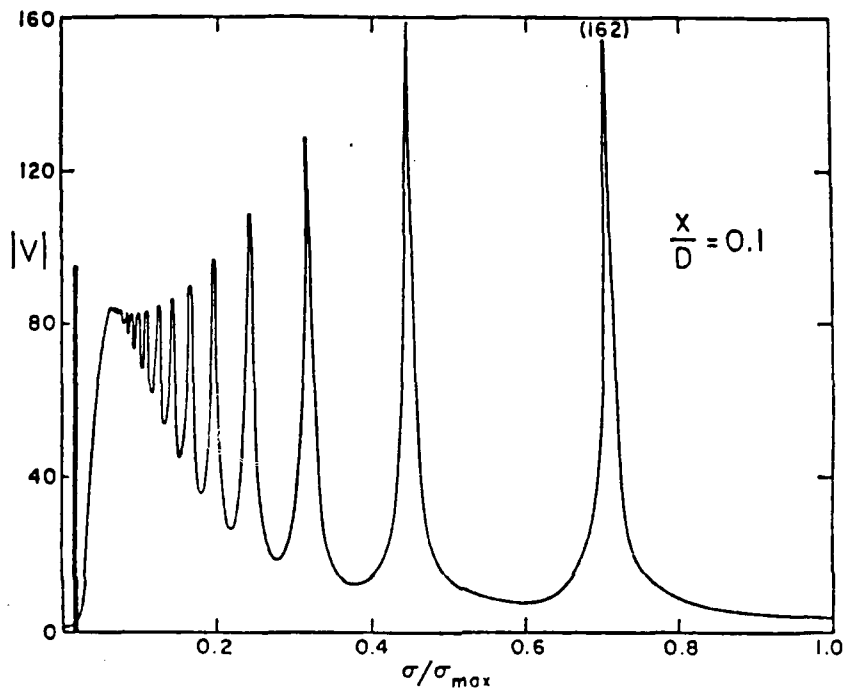


Figure 5. The amplitude of the meridional velocity  $|v|$  plotted versus the forcing frequency normalized by the maximal forcing frequency.

We divide  $\phi_n(x,t)$  into two parts: a transient part  $\phi_n^T(x,t)$  and a steady part  $\phi_n^S(x)$  such that

$$\phi_n(x,t) = \phi_n^T(x,t) + \phi_n^S(x). \quad (6.33)$$

The steady Sverdrup balance is

$$\beta \phi_{n,x}^S = -\tau_{0n} \quad (6.34)$$

which upon integration gives

$$\phi_n^S = -\tau_{0n} \left( \frac{x-a}{\beta} \right) \quad (6.35)$$

The dynamical balance for the transient is

$$-[L^2 + R^{-2}] \phi_{n,t}^T + \beta \phi_{n,x}^T = 0. \quad (6.36)$$

The characteristic solution of (6.36) is

$$\phi_n^T(x,t) = G_n(x - c_n t) \quad (6.37)$$

where

$$c_n = -\beta / (L^2 + R^{-2})$$

from (6.32), (6.33) and (6.35) we see that (6.32) must be

$$\phi_n^T(x,t) = -\phi_n^S(x - c_n t) H(x - c_n t). \quad (6.38)$$

The function  $H(x)$  is the Heaviside function;  $H(x < 0) = 0$ ,  $H(x > 0) = 1$ . The form of  $\phi_n^T$ ,  $\phi_n^S$  and  $\psi$  are shown in figure 3. Finally, to satisfy the condition  $\psi = 0$  at  $x=0$  we must add a reflected field of short dispersive Rossby waves  $\phi_n^R$  that satisfy

$$\phi_{n,xt}^R - R^{-2} \phi_{n,t}^R + \beta \phi_{n,x}^R = 0 \quad (6.39)$$

The full problem was investigated numerically by Anderson and Gill (1975). Figure 4 shows the results of their calculations. The upper panel shows the baroclinic case in which slowly moving short waves penetrate the interior from the west. The addition of weak bottom friction will kill these east-moving waves and the steady solution will be approximately recovered. The lower panel corresponds to the

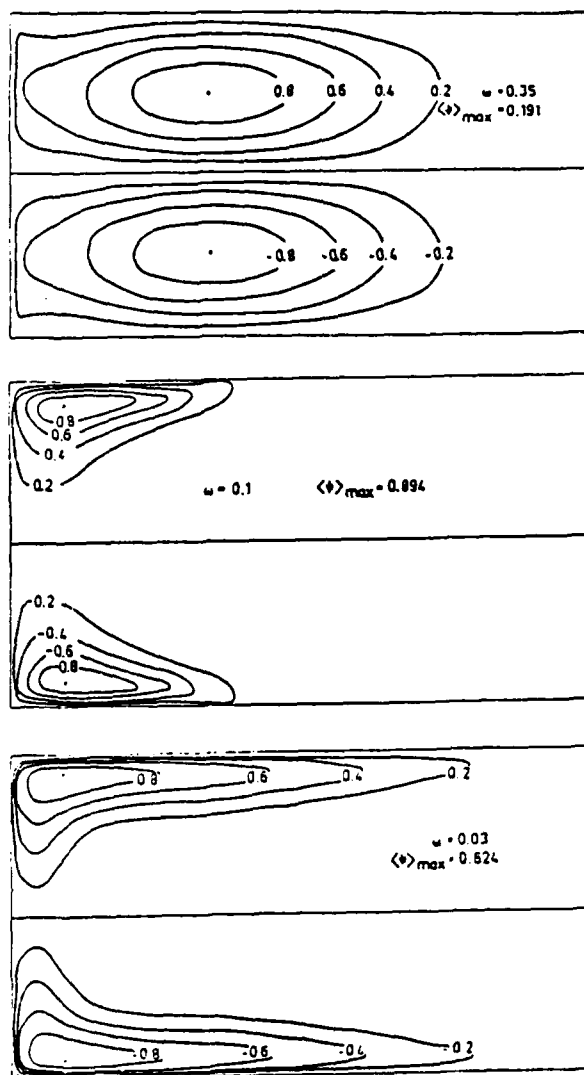


Figure 6. Contours of the time-averaged stream function normalized by the maximum value of the stream function. The forcing frequency decreases from top to bottom.

barotropic case. For typical values of  $a$  and  $r$  the basin traversal time is only a few days.

The effects of fluctuating winds on the mean and transient circulation were investigated by Veronis (1970). In this case the nonlinear vorticity equation

$$\nabla^2 \psi_t + R J(\psi, \nabla^2 \psi) + \beta \psi_x = \hat{k} \cdot (\nabla \times \underline{\tau}) - \varepsilon \nabla^2 \psi \quad (6.40)$$

is integrated numerically. With oscillatory wind forcing there can be resonance between the forcing frequency and the normal modes of the basin. This effect is illustrated in figure 5 where the amplitude of the meridional velocity is plotted versus the forcing frequency. At much lower frequencies than those at which sharp resonances occur the instantaneous solution is the steady solution driven by  $\tau(t)$ , i.e. time only appears parametrically. The nonlinear perturbative treatment of the steady solution (lecture 5) thus implies rectification of the flow in a manner qualitatively similar to that shown in figure 6. Note that care must be taken to distinguish between eulerian and lagrangian means if calculations such as these are invoked in discussion of the distribution of properties.

#### 6.4 Waves in the Tropics

In the tropics  $f = \beta y$  so the shallow water equations become

$$\begin{aligned} U_t - \beta y V &= -g \eta_x \\ V_t + \beta y U &= -g \eta_y \\ \eta_t + D(U_x + V_y) &= 0 \end{aligned} \quad (6.41)$$

Now solutions are of the form

$$v = V(y) e^{i(lx - \sigma t)} \quad (6.42)$$

The function  $V(y)$  is given by

$$V(y) = H_m(\eta) e^{-\frac{1}{2}\eta^2} \quad (6.43)$$

where  $\eta = y \sqrt{\beta/C}$  and  $H_m(\eta)$  are Hermite polynomials. The dispersion relation is

$$l^2 + (2m+1) \frac{\beta}{C} + \frac{\beta l}{\sigma} = \frac{\sigma^2}{C} \quad m = -1, 0, 1, \dots \quad (6.44)$$

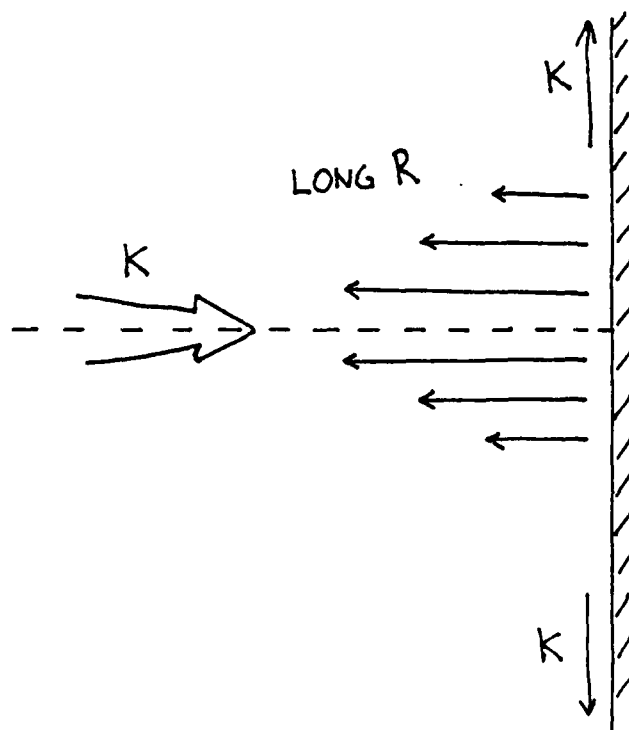


Figure 7. Schematic illustration of the scattering of an equatorial Kelvin wave at an eastern boundary energy is scattered into two coastal Kelvin waves and into long Rossby waves whose group velocity decreases with latitude.



For  $m = -1$   $V(y) = 0$ , but  $u \neq 0, \eta \neq 0$ .

At sufficiently low frequencies the dispersion relation has two limits. For short waves ( $l \rightarrow \infty$ )

$$\sigma = -\frac{\beta}{l} \quad (6.45)$$

For long waves ( $l \rightarrow 0$ )

$$\sigma = -\frac{c l}{2m+1} \quad m=1,2,3 \quad (6.46)$$

The former are dispersive Rossby waves that carry energy to the east. The latter are non-dispersive Rossby waves that transport energy westward. As shown previously we can find Kelvin wave solutions ( $m = -1$ ), however this time we let  $v=0$  and these Kelvin waves travel eastward along the equator.

In anticipation of the results of Kawase (1987), to be presented in the next section, we consider the scattering of an equatorial Kelvin wave when it reaches an eastern boundary. At the boundary this energy is scattered into two coastal Kelvin modes that travel along an eastern boundary, one in the northern hemisphere moving northward and one in the southern hemisphere moving southward. In addition there is a long Rossby mode that is reflected back to the west. This scattering is sketched in figure 7.

## 6.5 Establishment of Deep Water Circulation

We conclude this lecture by considering the initiation of deep-water circulation. This discussion follows the paper of Kawase (1987). Kawase's model consists of two layers; a thermocline layer and a deep layer. The governing equations are

$$\begin{aligned} U_t^v - fV^v &= -\frac{1}{\rho_0} P_x^v \\ V_t^v + fU^v &= -\frac{1}{\rho_0} P_y^v \\ -h_t + H^v(U_x^v + V_y^v) &= w \end{aligned}$$

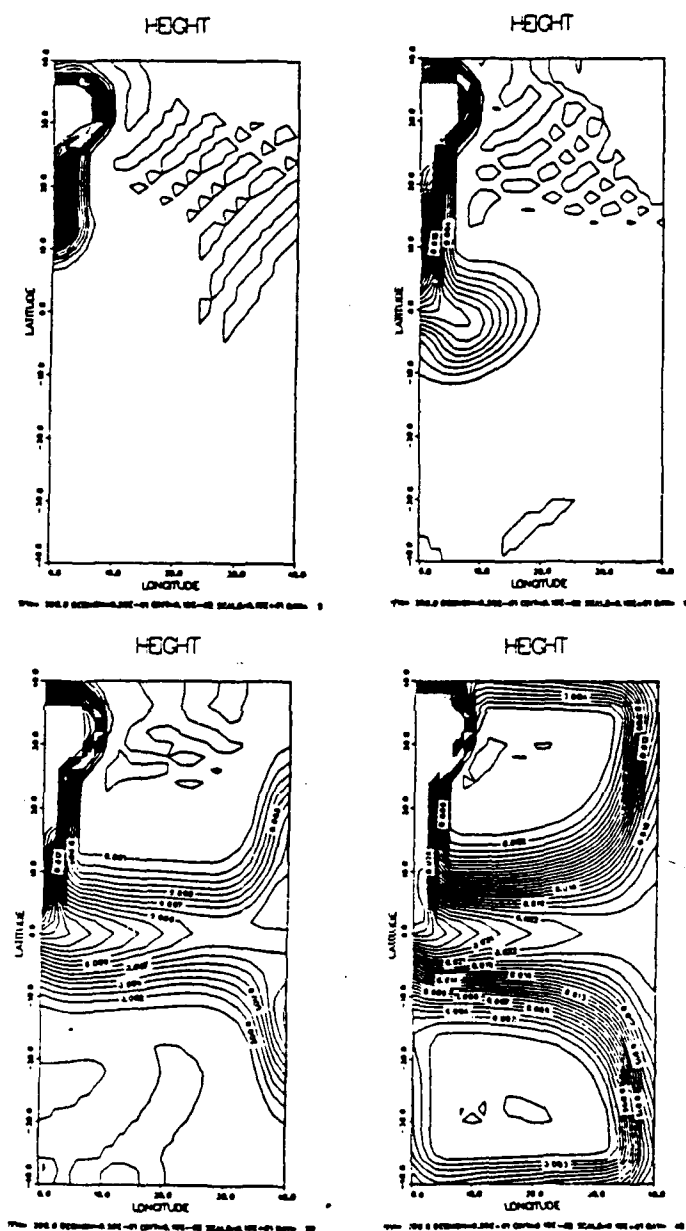


Figure 8. A numerical simulation of Kawase (1987), showing the development of flow at (a) 5, (b) 10, (c) 20, and (d) 40 days. The contours are of layer height.

$$\begin{aligned}
 U_t^l - f v^l &= -\frac{1}{\rho_0} p_x^u - g' h_x \\
 V_t^l + f u^l &= -\frac{1}{\rho_0} p_y^u - g' h_y \\
 h_t + H^l (U_x^l + V_y^l) &= -w
 \end{aligned}
 \tag{6.47}$$

Where  $g' = \frac{\Delta \rho}{\rho} g$  and the u and l superscripts denote the upper and lower layers respectively. Neglecting the barotropic mode permits formulation of the baroclinic mode in terms of lower layer variables.

$$\begin{aligned}
 U_t - f v &= -g'' h_x - r u \\
 V_t + f u &= -g'' h_y - r v \\
 h_t + H^l (U_x + V_y) &= Q - w
 \end{aligned}
 \tag{6.48}$$

where  $Q$  is a localized source of deep water in the northwest corner of the basin. Kawase closes his model by specifying  $w$  to be

$$w = -\lambda h \tag{6.49}$$

where  $\lambda = \text{constant}$ . Here we note, without further discussion, that this parameterization of  $w$  is controversial (see Kawase (1987) §2 for his justification of this choice). figure 8 (b) shows his results. This figure shows contours of layer height. In this sequence one sees a southward traveling Kelvin wave along the western boundary moving away from the mass source in the northwest corner. This wave turns eastward Fig 8(b) with little energy loss. Figures 8(c) & (d) show the evolution sketched in figure 7. The westward propagating Rossby waves result in an equatorward thickening of the eastern boundary layer.

## 6.6 References

- Anderson, D.L.T. & Gill, A.E. 1975 Spin-up of a stratified ocean, with application to upwelling. Deep-Sea Res. 22, 583-596.
- Kawase, M. 1987 Establishment of deep ocean circulation driven by deep-water production. J. Phys. Oceanogr. 17, 2294-2317.
- Longuet-Higgins, M. S. 1964 On group velocity and energy flux in planetary wave notions. Deep-Sea Res. 11, 35-43.
- Veronis, G. 1970 Effect of fluctuating winds on ocean circulation. Deep-Sea Res. 17, 421-434.

Notes submitted by: Scott Jones, University of California,  
San Diego

## LECTURE 7

## THE GENERAL CIRCULATION OF THE OCEANS: STATISTICAL ONE-LAYER PROBLEMS

## 7.1 Introduction

In today's lecture we will discuss statistical one-layer problems, with the material drawn primarily from a set of numerical experiments by Griffa and Salmon (1989) [henceforth referred to as G&S] and also the statistical mechanical theory necessary to understand these experiments, principally the result that for a large number of realizations of a system, with constraints only on the averages of the energy, potential enstrophy and potential vorticity, if we choose the most probable distribution of the ensemble in phase space (in a sense to be defined later) we recover the Fofonoff equation. Some of the material presented in this session, in particular the Fofonoff flows, has already been covered in earlier lectures but will be presented again for the completeness of this lecture.

## 7.2 Fofonoff Flows

We considered earlier the equation

$$J(\psi, \nabla^2 \psi + \beta y) = -\varepsilon \nabla^2 \psi + \text{curl} \tau. \quad (7.1)$$

In the case where there is neither forcing nor wind stress this reduces to

$$J(\psi, \nabla^2 \psi + \beta y) = 0 \quad (7.2)$$

and we get the Fofonoff flows for which

$$\nabla^2 \psi + \beta y = \beta y_0 + \beta \psi / U \quad (7.3)$$

where  $U$  is the interior velocity. This of course is just a special case and we could have written

$$\nabla^2 \psi + \beta y = F(\psi)$$

where  $F$  is any function; however, we chose the linear case because of its tractability.

As we mentioned earlier, Veronis (1970) pointed out that if we solve (7.1) with some Ekman drag and a wind stress that is favorable to the Fofonoff flows in the sense that the integral of the right-hand side of (7.1) over an area bounded by a streamline vanishes, that is

$$\oint \tau \cdot dl = \epsilon \oint u \cdot dl,$$

then it would be possible to have a solution where

$$\nabla^2 \psi + \beta y = \mathcal{F}(\psi)$$

where  $\mathcal{F}$  is a functional and thus the left-hand side of (7.1) is zero and the integrals of the two terms on the right-hand side of (7.1) around every streamline cancel. Thus we concluded that as one increased the size of the wind stress, this set of problems went quite smoothly from the Stommel problem to a class of solutions which we will term the Fofonoff-Veronis solutions, namely the Fofonoff flows but with small amounts of drag and wind stress.

In this lecture, we will see these Fofonoff flows emerge in two very different situations. Firstly if we solve the time-dependent version of the conservation equation (7.2)

$$\nabla^2 \psi_t + \mathcal{J}(\psi, \nabla^2 \psi + \beta y) = 0$$

in a box with  $\nabla^2 \psi = 0$  on the boundaries, starting from random initial conditions, and run the numerical experiment for a long time and then average the stream function over a long time we will show, both from the results of G&S and from theoretical insight, that the average solution  $\langle \psi \rangle$  will satisfy the same equation as (7.3)

$$\nabla^2 \langle \psi \rangle + \beta y = \beta y_0 + \gamma \langle \psi \rangle. \quad (7.4)$$

From the theory we will learn how the constants in (7.4) turn back on the initial conditions.

Secondly, as G&S pointed out, if we consider the same problem again starting from random initial conditions but with small amounts of wind stress and bottom drag added, that is

$$\nabla^2 \psi_t + \mathcal{J}(\psi, \nabla^2 \psi + \beta y) = -\epsilon \nabla^2 \psi + c \omega \tau, \quad (7.5)$$

then if the wind stress is favorable to the Fofonoff flows in the sense mentioned earlier then we will again recover a solution that essentially obeys (7.4). If however the wind

stress is unfavorable to the Fofonoff circulation then, not surprisingly, the solution is very different and very noisy because the Reynolds' stress terms will be large.

### 7.3 The Statistical Mechanics of the Problem

Before reviewing the numerical work of G&S, we will first make a detour into theory and look at the statistical mechanics of a truncated set of equations. Firstly, we will rewrite (7.5) in terms of  $q$ , the potential vorticity,

$$q_t + J(\psi, q) = -\varepsilon q + \text{curl} \tau$$

and average this over a very long time

$$\langle J(\psi, q) \rangle = -\varepsilon \langle q \rangle + \langle \text{curl} \tau \rangle$$

so that

$$J(\langle \psi \rangle, \langle q \rangle) + \langle J(\psi', q') \rangle = -\varepsilon \langle q \rangle + \langle \text{curl} \tau \rangle \quad (7.6)$$

where we have used the usual Reynolds' decomposition and  $'$  denotes the fluctuation from the mean. If the two terms on the right-hand side of (7.6) balance, as they did in the case we considered earlier where we recovered (7.3), then we expect the Reynolds' stresses, that is  $\langle J(\psi', q') \rangle$ , to be small and we expect to see solutions like the Fofonoff circulation. If, on the other hand, the terms on the right-hand side of (7.6) do not balance, we expect the deviations from the average to be of the same order of magnitude as the average and just as energetic as the steady solution arising in the case where the forcing balances the wind stress.

We will now consider the initial value problem. The first case we will deal with is the one considered earlier with no forcing or wind stress

$$\nabla^2 \psi_t + J(\psi, \nabla^2 \psi + h) = 0 \quad (7.7)$$

with  $\psi = 0$  on the boundaries. Initially we will deal with a general  $h \equiv h(x, y)$ , but will later revert to  $h \equiv \beta y$ , and choose some random initial condition for  $\psi$ . One method of attacking this problem is to expand the solution in terms of those eigenfunctions  $\phi_i$  (with associated eigenvalues  $k_i$ ) of the Laplacian  $\nabla^2$  appropriate to the geometry of our basin, with

$$\nabla^2 \phi_i + k_i^2 \phi_i = 0$$

and the eigenfunctions ordered so that  $k_i^2$  are an ascending sequence of numbers. We can then write the stream function as

$$\psi(x, y, t) = \sum_i \left( \frac{y_i(t)}{k_i} \right) \phi_i(x, y) \quad (7.8)$$

The orthogonality of the eigenfunctions means that, with an appropriate normalization,

$$\overline{\phi_i \phi_j} = \iint dx dy \phi_i \phi_j = \delta_{ij}$$

where  $\overline{\quad}$  denotes the integral over the basin. If we substitute the expansion for  $\psi$  (7.8) into the equation which it obeys, (7.7) and also expand the topography  $h$  in terms of the  $\phi_i$ ,  $h = \sum_i h_i \phi_i$  where the  $h_i$  are coefficients of the topography, then we will get a set of coupled equations for  $y_i(t)$  of the form

$$\dot{y}_i(t) + \sum_{j,l} A_{ijl} y_j y_l + \sum_{j,l} B_{ijl} y_j h_l = 0$$

where  $A_{ijl} = \frac{k_j}{k_i k_l} \overline{\phi_i \mathcal{T}(\phi_j, \phi_l)}$  and  $B_{ijl} = \frac{1}{k_i k_l} \overline{\phi_i \mathcal{T}(\phi_j, \phi_l) h}$ .

If we truncate the expansion (7.8) at some level, say  $i, j, l \leq N$ , then we have a spectral model.

The equation (7.7) which  $\psi$  obeys has a number of simple conservation quantities, amongst which are the kinetic energy  $E = \frac{1}{2} \overline{(\nabla \psi)^2}$  and also  $\overline{F(\psi)}$  where  $F$  is any function. In particular  $\mathcal{N} = \overline{\psi^2}$ , the average potential enstrophy, and  $\mathcal{Z} = \overline{\psi}$ , the average potential vorticity, are integral invariants, and all of these quantities may be expressed in terms of the  $y_i$ 's. The simplest example is the energy

$$E = \iint_{\text{basin}} \nabla \psi \cdot \nabla \psi dx dy = - \iint_{\text{basin}} \psi \nabla^2 \psi dx dy$$

ie.

$$E = \sum_i y_i^2 \quad (7.9)$$

Similarly we find

$$\mathcal{N} = \sum_i (k_i^2 y_i^2 - 2 k_i y_i h_i) \quad (7.10)$$

$$\mathcal{Z} = - \sum_i k_i y_i \quad (7.11)$$

We will now consider a large number of systems (7.7), (7.8), all of which started with initial conditions which were different for each system but were such that when we average over the initial conditions we get an average energy  $E$ , an average potential enstrophy  $\mathcal{N}$  and an average



potential vorticity  $\zeta$ . Thus we have an ensemble of realizations of this system. In the many-dimensional space whose coordinates are the  $y$ 's the evolution of one point (that is one realization), with time will define a path. If we think of a large number of realizations with initial conditions that are in some sense close together we will initially have a "cloud" of points. If we imagine that we have such a large ensemble that we can think of this as a "fluid" of system points in the same sense that we apply the continuum approximation in fluid mechanics then, since none of these realizations will cease to exist, the ensemble will satisfy a conservation equation of the form

$$\rho_t + \sum_i \frac{\partial}{\partial y_i} (\dot{y}_i \rho) = 0 \quad (7.12)$$

where  $\rho \equiv \rho(y_1, \dots, y_n, t) \equiv \rho(y, t)$  corresponds to the density of the realizations in phase space. This equation looks exactly like the standard mass conservation equation

$$\rho_t + \nabla \cdot (\rho \mathbf{u}) = 0.$$

From the definition of the  $A_{ij}$ , if any of the indices are equal then  $A_{ij} = 0$ . Together with the  $B_{ij}$  this tells us that the velocity field  $\dot{y}_i$  is divergence free, i.e.

$$\sum_i \frac{\partial \dot{y}_i}{\partial y_i} = 0.$$

This is the analog of  $\nabla \cdot \mathbf{u} = 0$  and (7.12) reduces to

$$\rho_t + \sum_i \dot{y}_i \frac{\partial \rho}{\partial y_i} = 0$$

which is analogous to  $\rho_t + (\mathbf{u} \cdot \nabla) \rho = 0$ . Thus the volume of this "cloud" of points is conserved, although the region occupied by this cloud might be tremendously contorted as the phase flow develops. The function  $\rho$  is important because it enables us to calculate averages of quantities in this flow, for example

$$\langle F(y) \rangle = \frac{\int F(y) \rho(y, t) dy}{\int \rho(y, t) dy}$$

where  $\langle \rangle$  now denotes an average over the ensemble and

$$\int F(y) dy = \int \dots \int F(y_1, \dots, y_n) dy_1 \dots dy_n.$$

Here  $\int \rho(y, t) dy$  is simply the volume of the phase space. Normally we set  $\int \rho(y, t) dy = 1$ .

$P$  is at this stage unknown. The essence of the statistical mechanics used here is to average over the ensemble using the most probable  $P$  subject to the constraints applied to the system. In this case if initially all of the realizations have the same  $E, \mathcal{N}$  and  $Z$  then we know, since in phase space  $E$  defines a sphere,  $\mathcal{N}$  an ellipse and  $Z$  a plane, that at later times all of the realizations will lie on a subspace determined by the intersection of these surfaces. Instead we will choose for simplicity the most probable distribution of  $P$ , which we label  $\bar{P}$ , subject to the constraints not on each system but on the averages of  $E, \mathcal{N}$  and  $Z$

$$\begin{aligned} E_0 &= \int \sum_i y_i^2 P(y_i) dy_i \\ \mathcal{N}_0 &= \int \sum_i (k_i^2 y_i^2 - 2k_i y_i h_i) P(y_i) dy_i \\ Z_0 &= \int \sum_i (-k_i y_i) P(y_i) dy_i. \end{aligned}$$

In this sense "most probable" means that  $P$  which maximizes the quantity  $-\int P(y_i) \log P(y_i) dy_i$ . This differs in principle from, and is more tractable than, the situation where all of the realizations had the same values of  $E, \mathcal{N}$  and  $Z$ . If we have a large number of realizations and if  $N$ , the number of  $y_i$ , is large so that we have large systems, then these two situations produce virtually identical results.

We will now motivate this choice of  $-\int P(y_i) \log P(y_i) dy_i$  as the quantity which is to be maximized. Suppose we have a large number of realizations of this evolving model, where  $y_j$  are in state  $j$ . For a system where the  $y_i$ 's are discrete the definition of being in state  $j$  is obvious, that is the  $y_i$ 's take specified values. For the case where the  $y_i$ 's are continuous a realization lies in state  $j$  if it lies within a specified volume in phase space. We will suppose that we can define the states uniquely in this way. The number of ways  $\mathcal{N}_v$  that we can divide  $v$  systems such that we have  $v_1$  in state 1,  $v_2$  in state 2 and so on is given by  $\mathcal{N}_v = \frac{v!}{v_1! v_2! \dots}$ .

Clearly  $\sum_i v_i = v$ . Taking the natural logarithm of  $\mathcal{N}_v$  we define Boltzmann's entropy function  $S_v$  as

$$S_v = k \log \mathcal{N}_v = k [\log v! - \sum_i \log v_i!]. \quad (7.13)$$

We now define  $p_j$  as  $p_j = v_j/v$ ; this is the probability that a realization is in state  $j$ . Using Sterling's formula that  $\log n! \approx n \log n$  for large  $n$ , we can rewrite the entropy (7.13) as

$$\begin{aligned} S_v &= k [v \log v - \sum_i v_i \log v_i] \\ &= k [v \log v - \sum_i v_i (\log p_i + \log v)] \\ &= -k \sum_i v_i \log p_i \\ &= -k v \sum_i p_i \log p_i. \end{aligned} \quad (7.14)$$

Thus maximizing  $-\sum_i p_i \log p_i$  means maximizing  $S_v$  and thus finding the configuration of the ensemble, with  $v_j$  realizations in state  $j$  and so on, that is most probable in the sense that there are more ways  $\Omega_v$  to divide the system into this configuration than any other configuration.

Hence our aim is to maximize  $-\int p(y) \log p(y) dy$  subject to the constraints  $E, \Omega_0$  and  $Z_0$ . This is a calculus of variations problem which we will tackle by introducing Lagrange multipliers and denoting

$$\Lambda = \lambda_E (\sum_i y_i^2 - E_0) + \lambda_\Omega (\sum_i k_i^2 y_i^2 - 2k_i y_i h_i - \Omega_0) + \lambda_Z (-\sum_i k_i y_i - Z_0)$$

we must now maximize

$$\int -p(y) [\log p(y) + \Lambda] dy \quad (7.15)$$

with respect to variations in the  $\lambda$ 's and in  $P$ . When we set the variations in the  $\lambda$ 's,  $\delta \lambda$ 's, equal to zero we simply recover the constraints  $E, \Omega_0$  and  $Z_0$ . We now vary the  $P$ 's by writing  $P = P + \epsilon_P$  and hence we require

$$\frac{\partial}{\partial \epsilon} (7.15) |_{\epsilon=0} = 0$$

and so

$$\begin{aligned} 0 &= \frac{\partial}{\partial \epsilon} \int - (P + \epsilon_P) [\log (P + \epsilon_P) + \Lambda] dy |_{\epsilon=0} \\ &= \int p [1 + (\log P + \Lambda)] dy \\ &= \int -p [\log P + \Lambda] dy \end{aligned}$$

if we choose  $p$  such that  $\int p(y) dy = 0$ . We find that

$$P = C \exp [-\lambda_E \sum_i y_i^2 - \lambda_n \sum_i (k_i^2 y_i^2 - 2k_i y_i h_i) - \lambda_z \sum_i k_i y_i] \quad (7.16)$$

where  $C$  is some constant which we determine from the fact that  $\int P(y) dy = 1$ . This is known as the Boltzmann distribution.

Once we have found  $P$ , the most probable distribution of  $P$ , we are able to calculate averages over the ensemble. For example, the average of one of the Fourier components  $y_j$  is

$$\begin{aligned} \langle y_j \rangle &= \frac{\int P(y) y_j dy}{\int P(y) dy} = \frac{\int y_j dy_j [\int \dots \int P(y) \prod_i dy_i]}{\int dy_j [\int \dots \int P(y) \prod_i dy_i]} \\ &= \frac{\int y_j \exp [-\lambda_E y_j^2 - \lambda_n (k_j^2 y_j^2 - 2k_j y_j h_j) - \lambda_z k_j y_j] dy_j}{\int \exp [-\lambda_E y_j^2 - \lambda_n (k_j^2 y_j^2 - 2k_j y_j h_j) - \lambda_z k_j y_j] dy_j} \end{aligned}$$

since  $P$  is of the form (7.16), that is it is separable in the  $y_i$  so that the contributions from the  $y_i$  other than  $y_j$  cancel in the numerator and denominator. Using the standard Gaussian integrals

$$\int_{-\infty}^{\infty} e^{-(ax^2+b)} dx = e^{b^2/4a} / \sqrt{a/\pi}$$

$$\int_{-\infty}^{\infty} x e^{-(ax^2+b)} dx = -\frac{b}{2a} e^{b^2/4a} / \sqrt{a/\pi}$$

we find that

$$\langle y_j \rangle = \frac{\lambda_n k_j h_j - \frac{1}{2} \lambda_z k_j}{\lambda_E + \lambda_n k_j^2}.$$

We can now rewrite this in a more familiar form

$$\sum_i \langle y_i \rangle (\lambda_E + \lambda_n k_i^2) \frac{\phi_i}{k_i} = \sum_i (\lambda_n h_i - \frac{1}{2} \lambda_z) \phi_i \quad (7.17)$$

where the  $\phi_i$ 's are the spatial basis scc of (7.8) for the stream function  $\psi$ . Averaging over the ensemble, (7.8) becomes

$$\sum_i \frac{\langle y_i \rangle}{k_i} \phi_i = \langle \psi \rangle$$

so that we can write (7.17) as

$$\lambda_E \langle \psi \rangle - \lambda_n \nabla^2 \langle \psi \rangle = \lambda_n h - \frac{1}{2} \lambda_z$$

or

$$\nabla^2 \langle \psi \rangle + h = \frac{\lambda_E}{\lambda_\eta} \langle \psi \rangle + \frac{\lambda_z}{2\lambda_\eta}.$$

Thus starting out with the three simple invariants  $E, \Omega_0$  and  $Z_0$  and choosing the most probable  $P$  we have recovered the Fofonoff equation. In this equation  $\lambda_E/\lambda_\eta$  is related to the energy, and is determined by the initial energy, since in the original Fofonoff problem (7.3) the corresponding coefficient was  $\beta/U$ .  $\lambda_z/2\lambda_\eta$  is analogous to the  $\beta y_0$  term and thus specifying the average vorticity in the basin tells us where the streamline  $\psi = 0$  lies.

#### 7.4 Numerical Results

We will now review some of the numerical results obtained by G&S. Their work consisted of four different cases, the first two of which (referred to as QG1 and QG2) are run-down experiments with no forcing but with a scale selective damping given by

$$\nabla^2 \psi_t + \mathcal{J}(\psi, \nabla^2 \psi + h) = -\nu \mathcal{J}(\psi, \nabla^2 \mathcal{J}(\psi, \mathcal{J}))$$

where  $\mathcal{J}$  is the relative vorticity. This model conserves both energy and the mean vorticity in the basin, but both momentum and enstrophy are dissipated. QG1 and QG2 had random initial conditions with QG1 being about fifteen times as energetic as QG2. This model was devised in such a way that when one reaches the final flow, the boundary layer structure in the Fofonoff flow is well resolved. The initial evolution of QG1 is shown in figure 7.1 (all of the diagrams in this lecture are reproduced from G&S); times in these figures are scaled in a basin turnover time which depends on the initial rms velocity. Clearly the flow has developed rather rapidly to something which to a certain extent resembles the Fofonoff flow after only 5 time units [fig 1(e)]. We can follow this development by looking at  $c(t) = -\int \mathcal{J} \beta_y dy$ . If we are dissipating  $\mathcal{J}^2$  then  $c(t)$  will go strongly positive and in figure 7.2, where we plot  $c(t)$  for QG1, we can see that it rises quite rapidly initially followed by strong oscillation which appears to be associated with a persistent Rossby wave which only very slowly decays even when we get to the end of the evolution of the system. In figure 7.3, where we show  $c(t)$  for QG2, the less energetic system, we see a similar rapid growth

initially, but do not get the oscillation that occurred for QG1. In figure 7.4 we see the final state of QG1 at times which are four tenths of a turnover time apart. This is the one-two Rossby mode in the basin. We have virtually reached the Fofonoff circulation except that we still have the fairly energetic Rossby wave superimposed upon it; when we average over the Rossby wave we get figure 7.5. The final state of QG2, which was essentially QG1 but with much less energy, is shown in figure 7.6, and clearly QG2 has not progressed as far towards being a Fofonoff-like flow as QG1. A more sensitive way to look at this experiment is to plot  $\langle q \rangle$  against  $\langle \psi \rangle$ , which we do in figure 7.7 for QG1. We see that the two gyres are different and not completely equilibrated. As the experiment has progressed the two slopes in figure 7.7 have become more and more equal but are not yet exactly equal. The regions between the two lines come from points along the boundary and the central latitude.

The other two experiments by G&S were forcing experiments, one of which (QGa) had a wind stress favorable to the Fofonoff circulation and the other (QGb) had an unfavorable wind stress, calculated by changing the sign of the wind from QGa. The wind was of the form  $\sin y$ . The final flow from QGa is shown in figure 7.8 and that from QGb is figure 7.9. Clearly these two cases are very different and there is nothing in the final state of QGb which resembles the Fofonoff flow to any significant extent. In figures 7.10 and 7.11 we plot  $\langle q \rangle$  versus  $\langle \psi \rangle$  for QGa and QGb respectively. The QGa plot looks similar to that for QG1 [figure 7.7] with the simple linear dependence of the two gyres again quite well-developed and a small cluster of points in the center associated with the boundary and the centre-line. By contrast, the plot for QGb is totally different. The horizontal line of points in this case comes from the two recirculating gyres. As in figure 7.9 which showed the final state of QGb, there is no evidence in figure 7.11 that the Fofonoff mode has emerged, and the fluctuations in QGb are much stronger relative to the mean than in QGa.

### 7.5 References

1. Griffa, A. and Salmon, R. 1989. (in press).
2. Salmon, R. 1982. Hamilton's principle and Ertel's theorem. In "Mathematical Methods in Hydrodynamics and Integrability in Dynamical Systems"; ed. M. Tabor & M. Treve, Am. Inst. Phys. Proc., 88, 127-135.
3. Salmon R., Holloway, G. & Hendershott, M.C. 1970. The equilibrium statistical mechanics of simple quasi-geostrophic models. J. Fluid Mech., 75 691-703.
4. Veronis, George 1970. Effect of Fluctuating Winds on Ocean Circulation. Deep-Sea Res., 17 (13) 421-434.

Notes submitted by: Roland Mallier, Brown University,  
Providence, RI

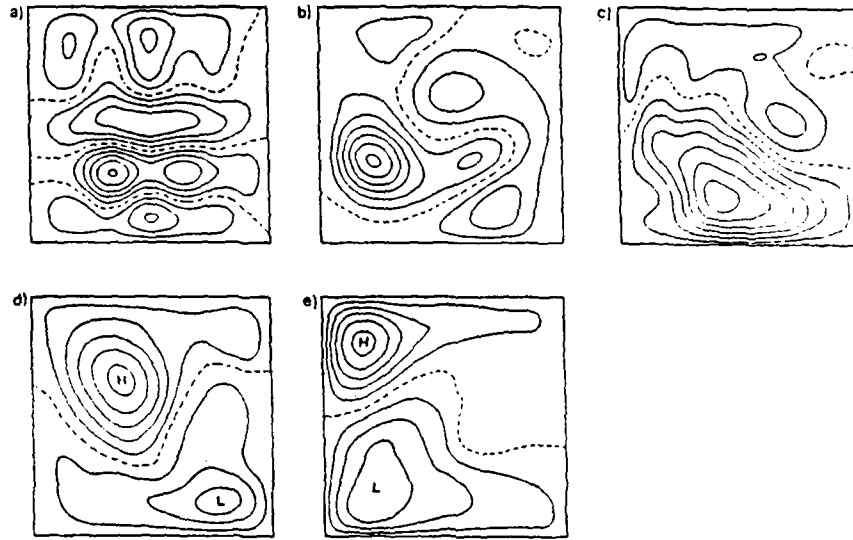


Figure 7.1 Initial evolution of QG1 at times 1 to 5.

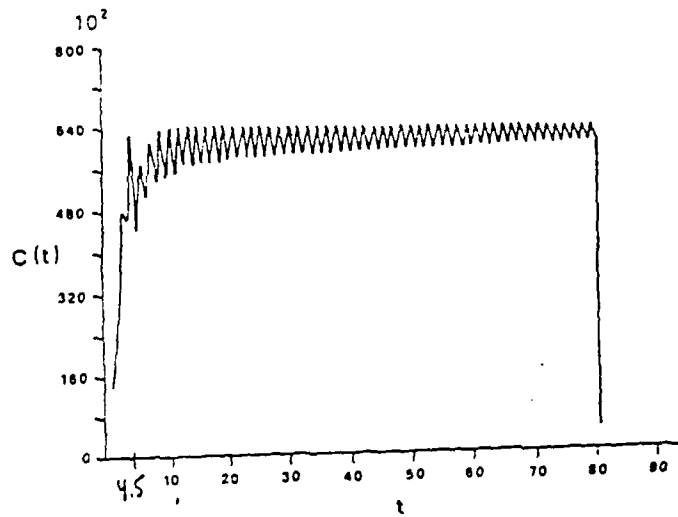


Figure 7.2  $c(t)$  for QG1.



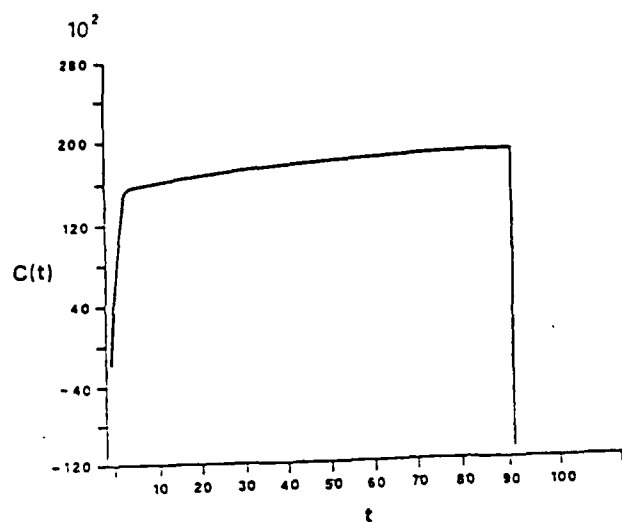


Figure 7.3  $c(t)$  for QG2.

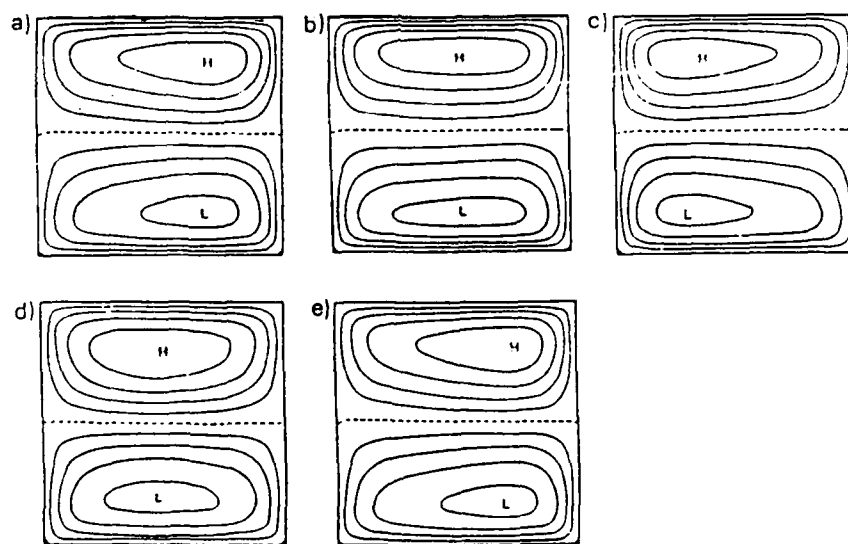


Figure 7.4 Final state of QC1 at time  $\approx 78$ . Frames are 0.4 time units apart.

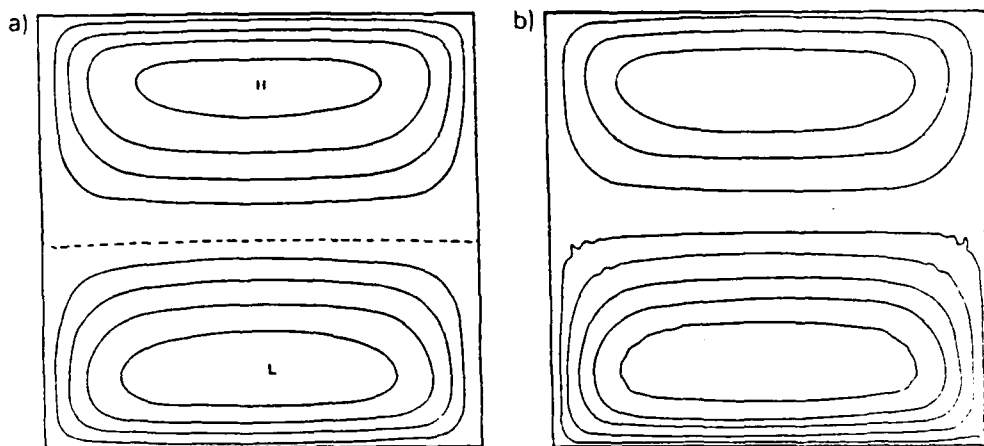


Figure 7.5 Final state of QC1 averaged over the Rossby wave.

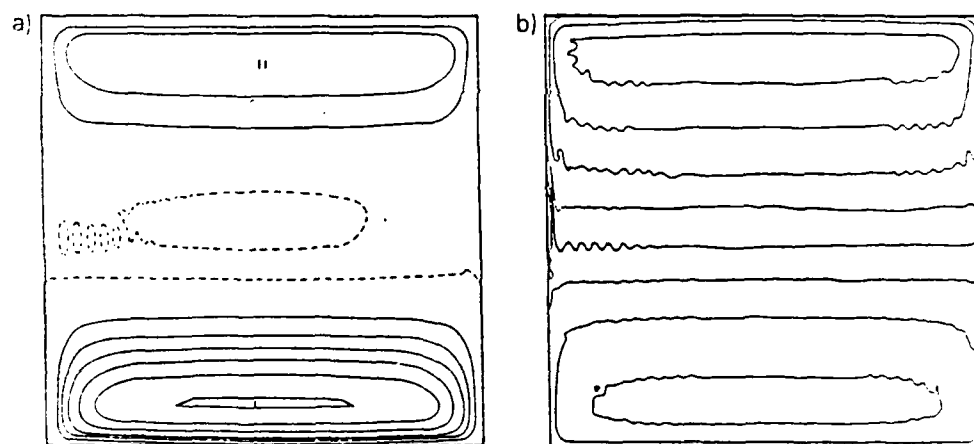


Figure 7.6 Final state of QC2 at time  $\approx 91.2$ .

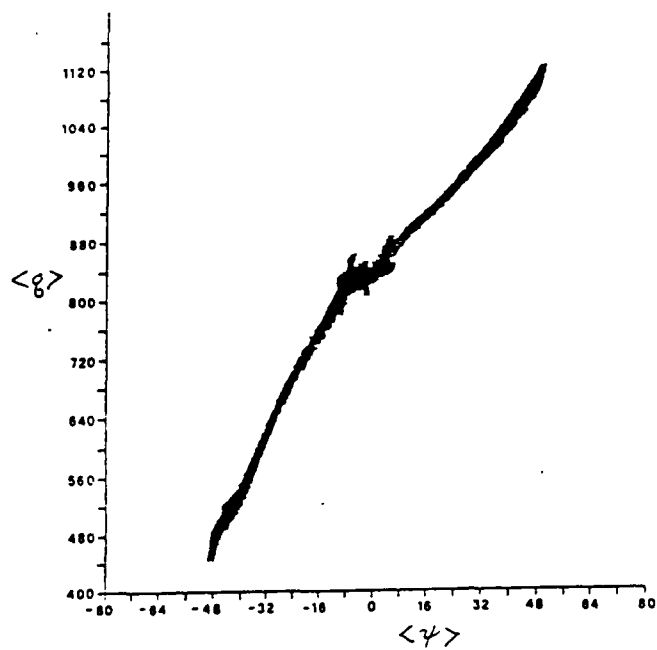


Figure 7.7  $\langle q \rangle$  versus  $\langle \psi \rangle$  for QG1.

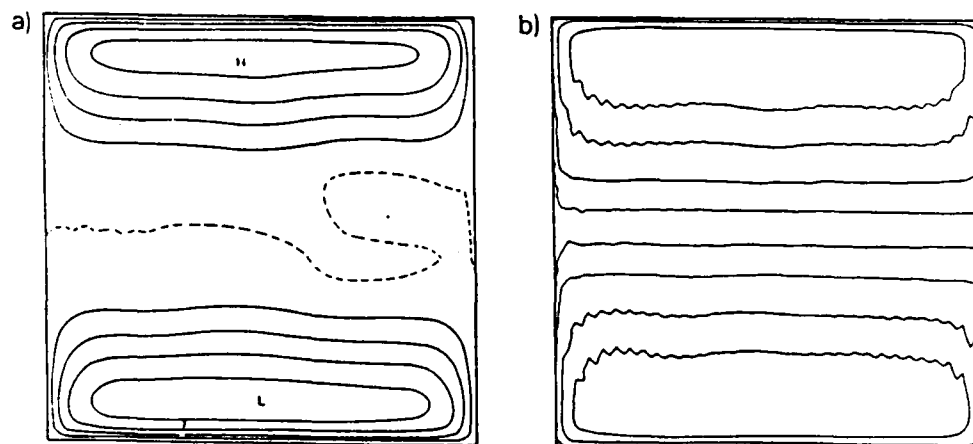


Figure 7.8 Final state of QGa.

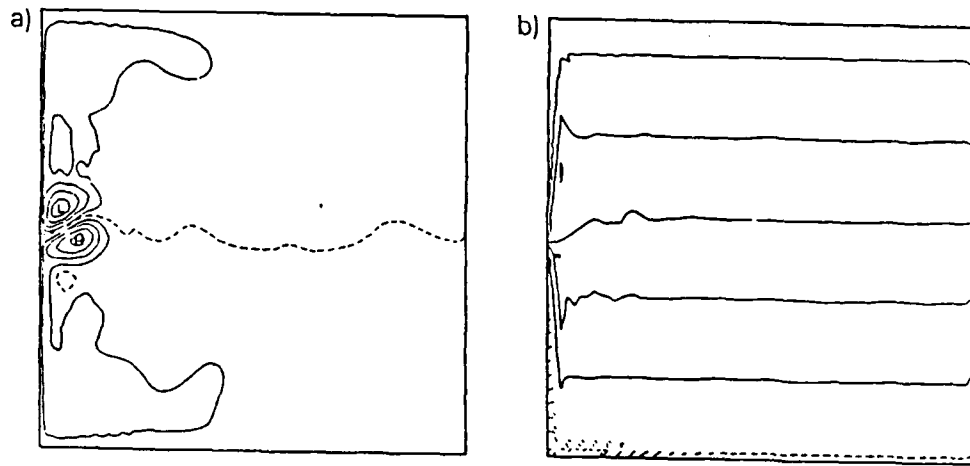


Figure 7.9 Final state of QGb.

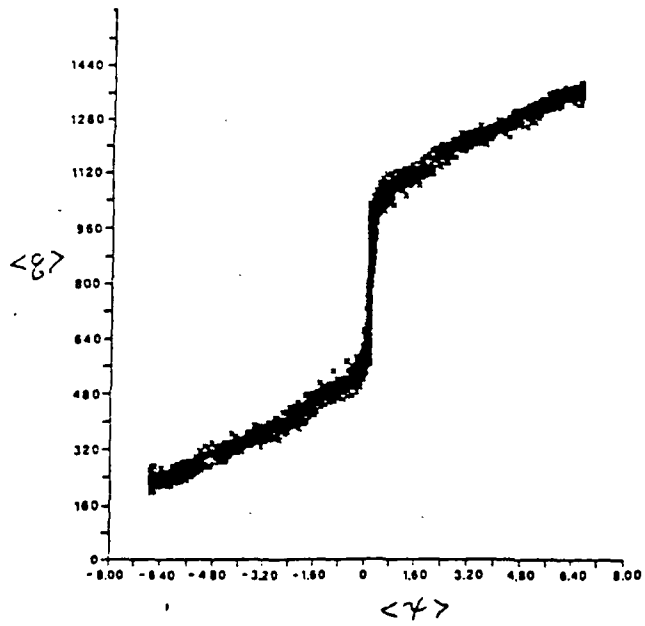


Figure 7.10  $\langle q \rangle$  versus  $\langle \psi \rangle$  for QGa.

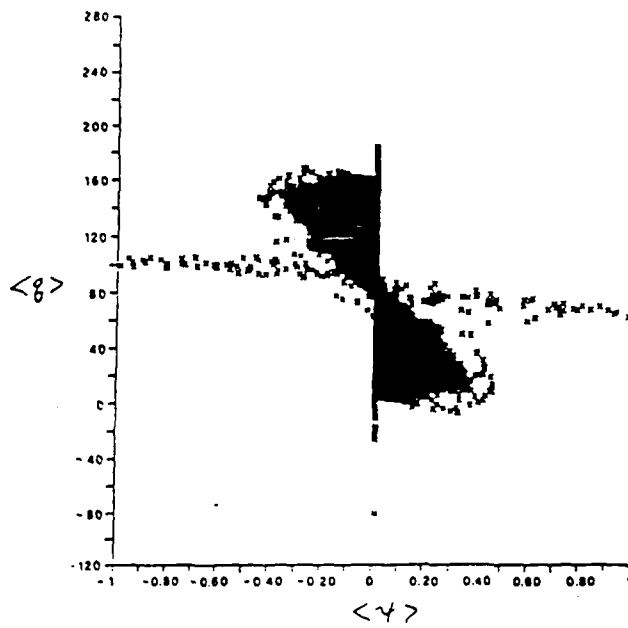


Figure 7.11  $\langle q \rangle$  versus  $\langle \psi \rangle$  for QGb.

## LECTURE 8

## MULTI-LAYER AND CONTINUOUSLY STRATIFIED QUASIGEOSTROPHIC WIND DRIVEN FLOWS

Here the new effect that we introduce is vortex stretching. We neglect the relative vorticity *ab initio*. In the quasigeostrophic approximation layers don't surface, but don't give up!

We specify the wind stress through the Sverdrup relation..

$$\mathcal{J}(\bar{\psi}, \beta y) = f_0 w_e \quad (8.1)$$

## 8.1 Mid-ocean gyre

Initially we consider  $\bar{\psi}$  such that streamlines are closed. Thus we need not consider the western boundary layer (Rhines & Young, 1982a).

The three-layer quasigeostrophic equations are:

$$H_1 \mathcal{J}(\psi_1, q_1) = f_0 w_e - R H_1 \nabla^2 (\psi_1 - \psi_2), \quad q_1 = \beta y + F_1 (\psi_2 + \psi_1) \quad (8.2)$$

$$H_2 \mathcal{J}(\psi_2, q_2) = -R H_2 \nabla^2 (2\psi_2 - \psi_1 - \psi_3), \quad q_2 = \beta y + F_2 (\psi_1 + \psi_3 - 2\psi_2) \quad (8.3)$$

$$H_3 \mathcal{J}(\psi_3, q_3) = -R H_3 \nabla^2 (\psi_3 - \psi_2) - E H_3 \nabla^2 \psi_3, \quad q_3 = \beta y + F_3 (\psi_2 - \psi_3) \quad (8.4)$$

Here  $F_i = f_0^2 / g' H_i$  (assume equal density jumps),  $R$  is interfacial friction,  $E$  is bottom drag. For simplicity we assume further that the ocean layer depths are equal:  $H_i = H$  and  $F_i = F$ .

We can calculate the barotropic flow immediately by summing (8.2) - (8.4) and neglecting the bottom drag (the nonlinear and inter-facial friction terms cancel):

$$H(\psi_1 + \psi_2 + \psi_3) = \bar{\psi} \quad (8.5)$$

When (8.5) is inserted in (8.3) a linear equation

$$\mathcal{I}(\psi_2, \beta y + F\bar{\psi}/H) = 0 \quad (8.6)$$

is obtained. We write the general solution

$$\psi_2 = \mathcal{A}_2(\hat{q}_2), \quad \hat{q}_2 = \beta y + F\bar{\psi}/H \quad (8.7)$$

For calculating  $\mathcal{A}_2$  one has in the middle layer, by integrating (8.3) along a closed contour:

$$\oint \mathcal{I}(\psi_2, q_2) d\ell = -HR \oint \nabla(2\psi_2 - \psi_1 - \psi_3) \cdot \hat{n} d\ell = 0 \quad (8.8)$$

On application of (8.5) we obtain

$$3 \oint \nabla \psi_2 \cdot \hat{n} d\ell = H^{-1} \oint \nabla \bar{\psi} \cdot \hat{n} d\ell = 3 \mathcal{A}_2' \oint \nabla(\beta y + F\bar{\psi}/H) \cdot \hat{n} d\ell \quad (8.9)$$

Thus  $\mathcal{A}_2' = 1/3F$  and

$$\psi_2 = \frac{1}{3} (\beta y/F + \bar{\psi}/H) + C_2 \quad (8.10)$$

Using (8.10) we have for the lowest layer

$$\mathcal{I}(\psi_3, \beta y + F(\psi_2 - \psi_3)) = \mathcal{I}(\psi_3, \frac{2}{3}\beta y + F\bar{\psi}/3H) = 0 \quad (8.11)$$

The general solution is

$$\psi_3 = \mathcal{A}_3(\frac{2}{3}\beta y + F\bar{\psi}/3H) \quad (8.12)$$

In a similar way we obtain  $\mathcal{A}_3' = R/F(R+E)$  or

$$\psi_3 = \frac{R}{3(R+E)} \left( \frac{2\beta y}{F} + \frac{\bar{\psi}}{H} \right) + C_3 \quad (8.13)$$

Finally

$$\psi_1 = \bar{\psi}/H - \psi_2 - \psi_3 \quad (8.14)$$

Now

$$q_2 = \beta y + F(\bar{\psi}/H - 3\psi_2) = \text{const} \quad (8.15)$$

i.e.  $q_2$  is homogeneous inside the closed contours. After this

$$q_3 = \beta y + F(\psi_2 - \psi_3) = \frac{4E}{3(R+E)} (\beta y + F\bar{\psi}/3H) + \text{const} \quad (8.16)$$

I.e.  $q_3$  is homogeneous too if there is no bottom friction. Also  $\psi_3 = \text{const}$  if  $R \rightarrow 0$  or  $E \gg R$ .

All the above assumes the existence of closed  $\hat{q}_2, \hat{q}_3$  isolines but this must be checked for a given  $\bar{\psi}$ . If  $\bar{\psi}$  is weak no closed contours of  $\hat{q}_3$  or even  $\hat{q}_2$  may exist. The flow in this case is not shielded from the eastern no-flux boundary condition which switches off the flow in the open contour region.

The region of closed  $\hat{q}_3$  is smaller than, and properly contained in, the region of closed  $\hat{q}_2$  contours (see fig. 8.1). The complete  $O(1)$  solution (8.10), (8.13), and (8.14) is independent of friction providing the ratio  $E/R = \text{const}$  and obeys a simple "Couette" numerology, in which the average circulation in the  $j$ -th layer of the velocity about  $\hat{q}_j$  is the average of that above and below (Fig. 8.2).

The flow patterns are plotted in Fig. 8.3 using the simple pattern, corresponding to a dipole of vertical velocity forcing  $W_0 = -\alpha x$  inside a circle of radius  $r_1$ . The center of the gyre in layer 2 is a distance  $y_0 = \beta^2/\alpha F$  poleward of the center of  $\bar{\psi}$ , the barotropic gyre, while the deepest, smallest gyre (layer) is displaced a distance  $y_0$  poleward of the center of  $\bar{\psi}$  regardless of the choice of parameters (for equal mean layer depths,  $H$ ).

Now we will extend the above results to a continuously stratified model providing all contours of  $\bar{\psi}$  are closed. The Boussinesq potential vorticity equation is

$$\mathcal{J}(\psi, q) = -\nu \cdot \text{diss} \quad , \quad q = \beta y + \frac{f_0^2}{N^2} \psi_{zz} \quad (8.17)$$



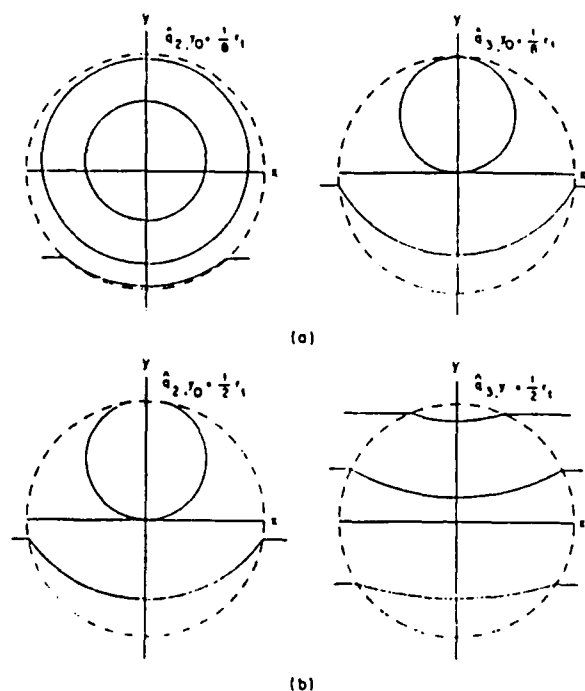


Figure 8.1. Contours of  $\bar{q}_2$  from (8.15) and  $\bar{q}_1$  from (8.16). (a) Strong forcing. The forcing is strong enough to produce both closed  $\bar{q}_2$  and closed  $\bar{q}_1$  contours. The subsurface flow is confined to the region of closed contours. (b) Weaker forcing. The  $\bar{q}_2$  contours are closed but all the  $\bar{q}_1$  contours are open. Consequently there is no flow in the deepest layer.

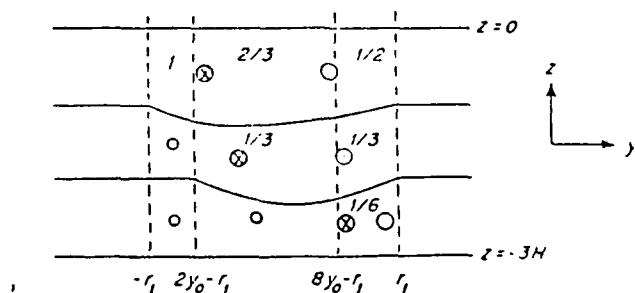


Figure 8.2. A schematic meridional section through the three-layer gyre. The numbers indicated the fraction of the Sverdrup transport carried by each layer. Note that each nonzero number is the average of those above and below.

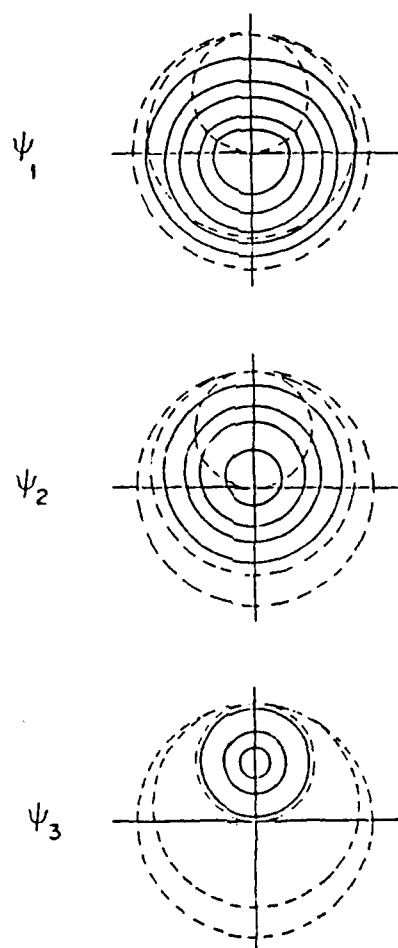


Figure 8.3. The streamfunctions  $\psi_1$ ,  $\psi_2$  and  $\psi_3$  with  $y_0 = 1/8$ . Note the poleward shift of the gyre center as one moves downward. The outer dashed circle is  $x^2 + y^2 = r_1^2$ . The inner dashed circles are the outermost closed  $\hat{q}_1$  and  $\hat{q}_2$  contours.

while we neglect the relative vorticity as before.  
The boundary conditions are

$$w = -f_0 N^2 \gamma(\psi, \psi_z) = w_e(x, y) \quad \text{at } z = 0 \quad (8.18)$$

and

$$\psi, \psi_z \rightarrow 0 \quad \text{as } z \rightarrow -\infty \quad (8.19)$$

Actually circulation penetrates to the depth  $D(x, y)$ , below which fluid is at rest and the conditions (8.19) are satisfied. The total transport is Sverdrup transport.

$$\int_{-\infty}^0 \psi dz = \bar{\psi} \quad (8.20)$$

Assume  $q$  is homogeneous if  $z > -D(x, y)$  so that

$$\psi_{zz} + \frac{N^2}{f_0^2} \beta(y - y^*) = 0 \quad (8.21)$$

Using the conditions (8.19) at  $z = -D(x, y)$  we obtain

$$\psi = \frac{1}{2} (z + D(x, y))^2 \frac{\beta N^2}{f_0^2} (y^* - y) \quad (8.22)$$

Applying (8.20) we have

$$D^3(x, y) = \frac{6 f_0^2 \bar{\psi}}{\beta N^2 (y^* - y)} \quad (8.23)$$

The full solution (8.22), (8.23), may be combined to give

$$\psi = \frac{\beta N^2}{2 f_0^2} \left[ z (y^* - y)^{1/2} + \left( \frac{6 f_0^2 \bar{\psi}}{\beta N^2} \right)^{1/3} (y^* - y)^{1/6} \right]^2 \quad (8.24)$$

Where  $y^*$  is determined by the curve  $\bar{\psi}=0$ ;  $y^*$  is the poleward-most value of  $y$  on this curve if  $\bar{\psi}>0$ , and the equatorward most value if  $\bar{\psi}<0$ . We have assumed that  $\bar{\psi}>0$  so  $y^*>y$ .

The displacement of an isopycnal surface in this solution is proportional to  $\psi_2$ . This is shown in Fig. 8.4 for the same barotropic streamfunction  $\bar{\psi}$  as before. The gyre is deepest at  $(x=0, y=y_N)$  where  $D=D_{\max}$ .

## 8.2 Interior of the Subtropical Gyre

Now consider the basin-bounded circulation with the condition

$$\int w_e dx \neq 0 \quad (8.25)$$

We shall use the three layer quasigeostrophic model in which the thickness of the lowest layer is much greater than that of the other two. Thus a negligible fraction of the Sverdrup transport is in the lowest layer and

$$\bar{\psi} = H_1 \psi_1 + H_2 \psi_2 \quad (8.26)$$

This case is called the two and a half layer model (Yound & Rhines, 1982).

If  $R=0$  from (8.3) we obtain by assuming  $\psi_3=0$

$$\mathcal{I}(\psi_2, q_2) = \mathcal{I}(\psi_2, \beta y + F_2 \bar{\psi}/H_1) = 0 \quad (8.27)$$

$$q_2 = \beta y + F_2 (\bar{\psi}/H_1 - (2 + H_3/H_1) \psi_2) \quad (8.28)$$

A little thought shows that (8.27) and (8.28) imply that  $\psi_2$  and  $q_2$  are functions of the known quantity

$$\hat{q}_2 = \beta y + F_2 \bar{\psi}/H_1 \quad (8.29)$$

Notice that if  $H_2$  is large,  $F_2$  is small and  $\hat{q}_2 \approx \beta y$ , i.e. all deep  $\hat{q}_2$  contours are blocked. Thus  $\psi_2$  is very small.

We shall use meridionally variable wind stress for the subtropical gyre with the following form of

$$w_e = -w_0 \sin(\pi y/2\ell) \quad (8.30)$$

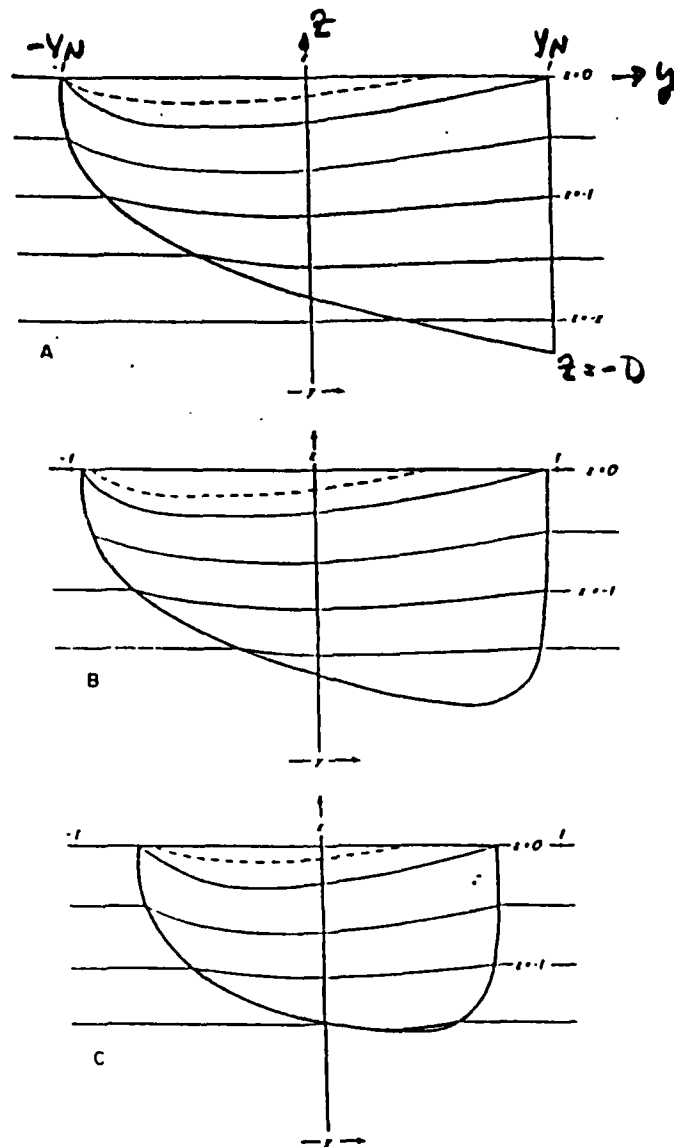


Figure 8.4. Three meridional sections through the gyre at  $x = 0, \frac{y_N}{3}, \frac{2y_N}{3}$  showing the density field  $z + \left(\frac{\beta L_y}{f_0}\right) \psi$ , computed from (5.12) with  $(\beta L_y / f_0) = \frac{1}{4}$ . The isopycnal slope is discontinuous at  $z = -D(x, y)$  (shown as a heavy line in the figure). An additional contour (dashed) has been included near the surface to show the isopycnal intersections with  $z = 0$ .

$$\Phi \sim y_N^2 - (x^2 + y^2)$$

The barotropic streamfunction calculated from (8.1) will be written as

$$\bar{\psi} = \psi_0 \left(1 - \frac{x}{a}\right) \sin \frac{\pi y}{2b}, \quad \psi_0 = a f_0 w_0 / \beta \quad (8.31)$$

where  $x=a$  is the eastern boundary where  $\bar{\psi} = 0$ . The corresponding pattern of  $\bar{\psi}$  is shown in Fig. 8.5. The function  $\bar{\psi}$  corresponding to (8.31) is contoured for various values of  $\psi_0 F_2 / \beta H_1$  in Fig. 8.6. The contours are closed in the northwest of the basin; the extent of this region increases as  $\psi_0 F_2 / \beta H_1$  increases. If the forcing is weak then all of the geostrophic contours may be blocked. For instance using (8.31) it is easy to show that closed contours exist only if

$$\gamma \equiv \frac{\psi_0 F_2}{\beta b H_1} > 1 \quad (8.32)$$

In the shielded region of closed contours there can be substantial lower layer flows which pass through the western boundary layer. In the absence of dissipation one is free to choose an arbitrary functional relationship between  $q_2$  and  $\hat{q}_2$ . This difficulty is overcome using the generalized Batchelor-Prandtl theorem given by Rhines & Young, (1982) which shows that if the dominant dissipative process is lateral diffusion of  $q_2$ , then the potential vorticity is homogeneous in the closed region.

The outside closed contour emanates from the northern boundary where  $y=b$  and  $\bar{\psi}=0$ ; it is thus  $\hat{q}_2 = \beta b$ . It is also the streamline  $\psi_2 = 0$ , hence from (8.28) we obtain inside closed contours

$$\psi_2 = (\beta y - \beta b + F_2 \bar{\psi} / H_1) / F_2 (2 + H_2 / H_1) \quad (8.33)$$

and  $\psi_2 = 0$  elsewhere. Note that  $\psi_2$  is known from (8.35), and  $\psi_1$  is calculated from (8.26). The streamline pattern calculated from (8.26), (8.31) and (8.33) is sketched in Fig. 8.7. Note the north-south asymmetry of the flow and the poleward shift of the gyre center with depth.

Now we can extend the above results to a continuously stratified model (8.17) - (8.20). As before we have the solution (8.23) - (8.24) where  $y^* = b$  now. The surface  $z = -D(x, y)$  bounds the region containing the wind-driven circulation from which the potential vorticity gradients have been expelled. This is shown in Fig. 8.8 for the simple forcing function

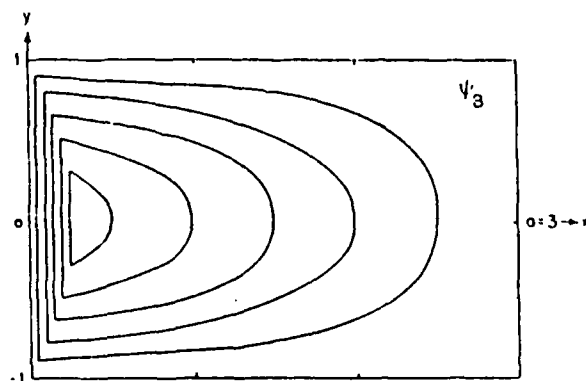


Figure 8.5. The barotropic streamfunction given by (8.31). The western boundary layer is shown schematically.

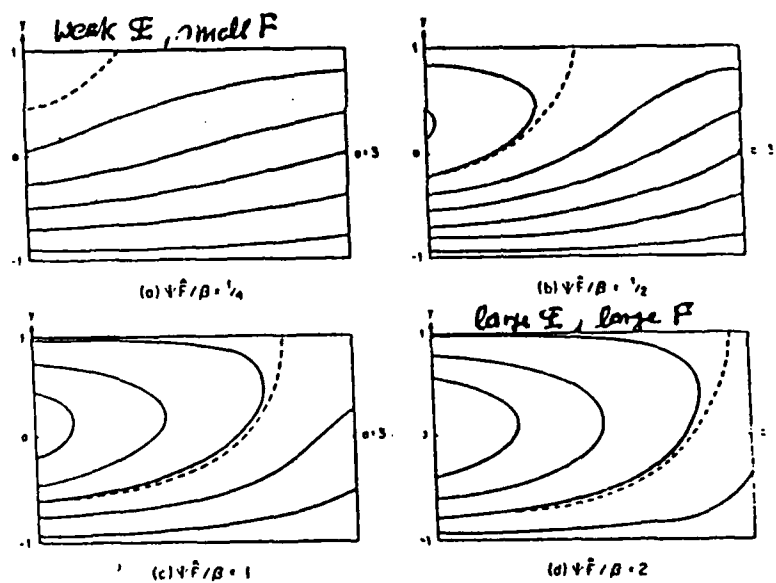


Figure 8.6 The function  $\hat{q}_y = y + (\Psi F / \beta)(a - x) \cos\left(\frac{\pi y}{b}\right)$  for various values of  $\Psi F / \beta$ . The outermost closed contour is dashed. As the strength of the forcing increases the closed contour region expands southward and eastward.

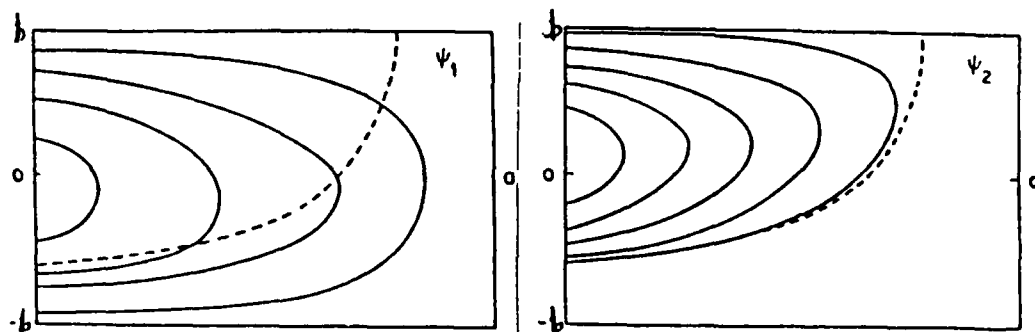


Figure 8.7. The streamline pattern corresponding to (8.33). The dashed curve is the outermost closed  $\psi_1$  contour inside of which the potential vorticity is uniform in the lower layer. Outside this region,  $\psi_1 = 0$ .

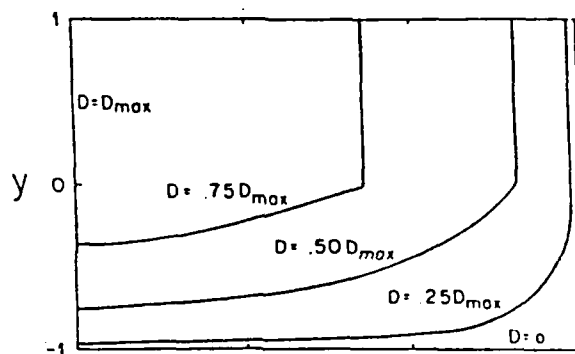


Figure 8.8. The depth of the wind-driven circulation as a function of position from (8.23) and (8.34). The bowl is deepest at the line segment  $x = 0$ ,  $0 < y < \frac{1}{2}$ . The circulation becomes shallower as one moves south and east.

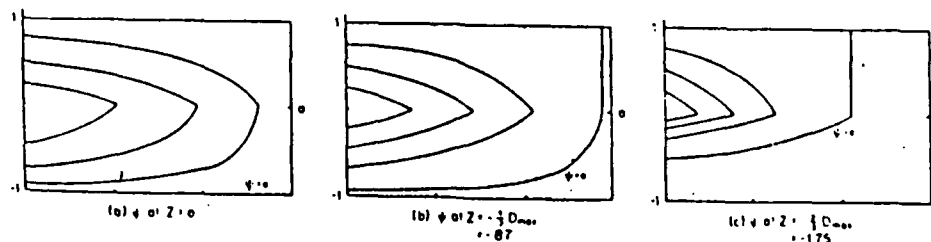


Figure 8.9. The streamlines from (8.24) at various depths in the wind-driven gyre. This is no motion in the stippled regions outside the surface  $z + D = 0$ . The flow is confined to the region of uniform potential vorticity.



$$w_e = -w_0(1 - |y|/b) \quad (8.34)$$

The region is deepest in the northwest corner of the basin and shoals as one moves south and east. The streamlines corresponding to (8.24) are sketched in Fig. 8.9. This sequence clearly shows how the wind-driven flow is compressed into the northwest corner of the basin as one moves downward.

The maximum depth of the circulation from (8.23) and (8.34) is

$$D_m = \left[ \frac{6f_0^3 w_0 a}{N^2 \beta^2 b} \right]^{1/3} \quad (8.35)$$

For  $f_0 = 7 \cdot 10^{-5} \text{ s}^{-1}$ ,  $\beta = 2 \cdot 10^{-11} \text{ m}^{-1} \text{ s}^{-1}$ ,  $N = 5 \cdot 10^{-3} \text{ s}^{-1}$ ,  $w_0 = 2 \cdot 10^{-6} \text{ m s}^{-1}$  and  $a = 2b$  (i.e., a square basin) it follows that  $D_m \approx 1 \text{ km}$ .  $D_m$  increases as the aspect ratio,  $a/b$ , of the gyre increases.

### 8.3 The western boundary layer

The interior circulation patterns shown in Figures 8.7 and 8.9, must be closed by appending western boundary layers. This problem has been solved numerically for the quasigeostrophic two layer model by Ierley & Young (1983).

Assuming  $\psi_3 = 0$  we can write (8.2) and (8.3) in the form

$$J(\psi_1, q_1) = f_0 w_e / H_1 - R \nabla^2 (\psi_1 - \psi_2), \quad q_1 = \beta y + F_1 (\psi_2 - \psi_1) \quad (8.36)$$

$$J(\psi_2, q_2) = -R \nabla^2 (\psi_2 - \psi_1) - E \nabla^2 \psi_2, \quad q_2 = \beta y + F_2 (\psi_1 - \psi_2) \quad (8.37)$$

Now the boundary conditions are

$$\psi_1 = \psi_2 = 0 \quad \text{at } x = 0, a; \quad y = -b, b \quad (8.38)$$

In (8.37)  $R$  is an interfacial drag which transfers momentum vertically between the layers, and  $E$  is bottom drag. Adding (8.36) and (8.37) we obtain

$$\beta \bar{\psi}_x = f_0 w_e - E H_2 \nabla^2 \psi_2, \quad \bar{\psi} = H_1 \psi_1 + H_2 \psi_2 \quad (8.39)$$

In the Sverdrup interior the last term in (8.39) is small and barotropic streamfunction is defined by (8.31) for  $w_e$  of the form (8.30). Using (8.26) one can eliminate  $\psi_1$  from (8.37) to obtain

$$\mathcal{Y}(\psi_2, \beta y + F_2 \bar{\psi}/H_1) = R \nabla^2 \bar{\psi}/H_1 - (E + R + RH_2/H_1) \nabla^2 \psi_2 \quad (8.40)$$

It is clear that since  $\bar{\psi}=0$  on the boundary, a contour of  $q = \beta y + F_2 \bar{\psi}/H_1$ , which starts at  $y^*$  in the eastern boundary must also hit the western boundary at  $y^*$  (Fig. 8.10). Away from the western boundary layer  $\psi_2=0$ ,  $\psi_1 = \bar{\psi}/H_1$ , outside the closed contour of  $q$  and inside.

$$\psi_2 = G(q) \quad (8.41)$$

where  $G$  is determined by conditions at the outer edge of the northern boundary layer where fluid enters the interior. For a general  $w_e$  thus northern exit region is the region in which  $\partial q / \partial y > 0$ . Let us suppose that

$$H_2 \psi_2 = \lambda \bar{\psi} \quad (8.42)$$

where  $\lambda$  is a constant to be determined. Substituting (8.42) into (8.39) gives

$$\beta \bar{\psi}_x = -\lambda E \bar{\psi}_{xx} \quad (8.43)$$

Substituting (8.42) into (8.40) gives also

$$\beta \bar{\psi}_x = - (E + R + RH_1/H_2 - RH_2/\lambda H_1) \bar{\psi}_{xx} \quad (8.45)$$

i.e.

$$\lambda^2 - (1 + 2\alpha) \lambda + \alpha = 0$$

where  $\alpha = R/E$  if  $H_1 = H_2$ . This quadratic has two solutions but only

$$\lambda = [1 + 2\alpha - (1 + 4\alpha^2)^{1/2}] / 2 \quad (8.46)$$

gives a physically acceptable solution.

The behavior of  $\lambda$  as  $\alpha$  is varied is interesting. If  $\alpha \rightarrow \infty$  so that interfacial friction overpowers drag on the lowest layer,  $\lambda \rightarrow 1/2$ . From (8.42) this means that the boundary flow is

barotropic. If  $\lambda \rightarrow 0$ , so the interfacial friction is weak,  $\lambda \rightarrow \lambda \ll 1$ . This means that the second layer flow is weak.

We now calculate  $G$  in (8.41) by requiring that the boundary layer solutions obtained from (8.42) and (8.43)

$$\psi_2^{BL} = -\lambda a [1 - \exp(-\beta x / \lambda E)] f_0 w_e(y) / \beta H, \quad (8.47)$$

and the interior solution

$$\psi_2^I = G(\beta y + F f_0 w_e(y)(x-a) / \beta H) \quad (8.48)$$

match in the intermediate region

$$\psi_2^{BL}(x \rightarrow \infty) = \psi_2^I(x \rightarrow 0) \quad (8.49)$$

Thus  $G$  is calculated by the elimination of  $y$  between (8.47) and (8.48) using (8.49).

Full solution of the problem including the region where flow is out of the interior needs the careful numerical calculations. The result is shown in Fig. 8.11a. One can compare it with (8.33) obtained by asserting that  $\psi$  is homogeneous inside closed isolines (Fig. 8.11b). The striking contrast of these figures makes it quite evident that the functional relation between  $\psi_2$  and  $\eta$  is appreciably altered in the passage of streamlines through the western boundary layer.

This consideration is intended to emphasize the possibility of a strong affect of the western boundary layer on the potential vorticity distribution in the interior of a wind gyre. This failure of the Prandtl-Batchelor theorem is due to the passage of every streamline through a frictional boundary layer.

#### 8.4 Parsons' model of subtropical gyre

A particular difficulty in constructing closed models of the ocean circulation is providing an adequate description of the path of the separated western boundary current, a separation which seems essential to a realistic model of the gyre circulation. A surprisingly simple model of the wind-driven circulation for a two-layer ocean which predicts both the point of separation and the path of the separated current was

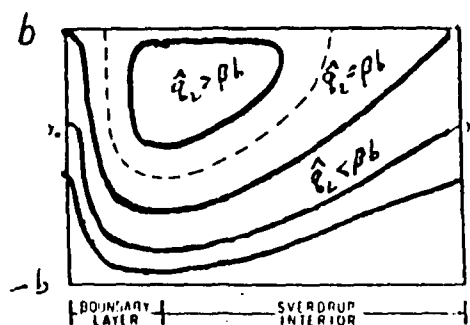


Fig. 8.10. A schematic illustration of the way the contours in Fig. must close in the western boundary layer. Because  $\psi_n$  is zero on the boundary, a blocked contour which starts at  $y_n$  on the eastern boundary must also intersect the western boundary at  $y_n$ .

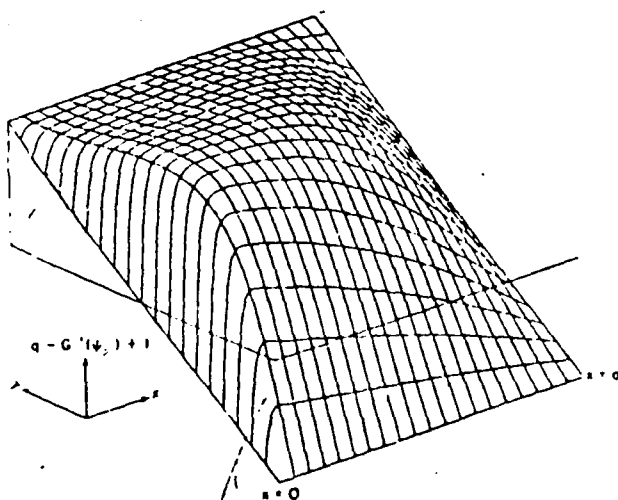


Fig. 8.11a.  $q - G^{-1}(\psi_2) + 1$  with  $G$  calculated using the boundary layer matching argument; see (3.21). The agreement between theory and numerical calculation is indicated by the plateau in the northwest corner of the basin which coincides with the closed  $q$  contours.

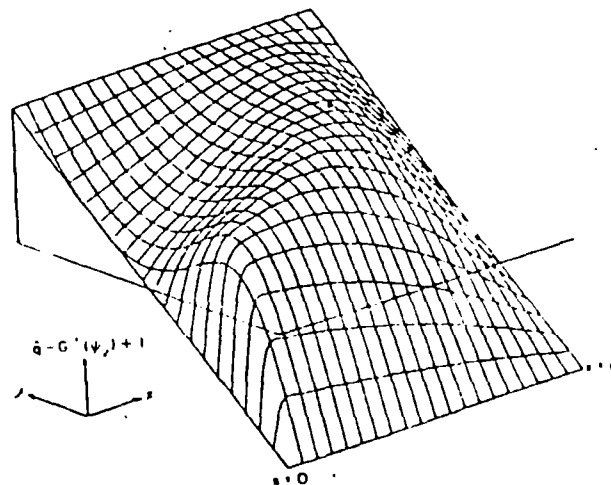


Fig. 8.11b.  $q - G^{-1}(\psi_2) + 1$  with  $G$  calculated by the incorrect application of the Prandtl-Batchelor theorem [see (3.9)]. If  $\psi_2$  were correctly given in terms of  $q$  by (3.9), then the function in this figure would be flat in the northwest corner where the  $q$  contours close (cf., Fig. 8.11a).

introduced by Parsons (1969) in a model of a subtropical gyre (negative wind stress curl as before).

Consider only an upper layer of depth  $D$  to be moved by wind stress of the form (8.30):

$$-f\bar{v} = -g'\partial\partial x + \tau^x(y)/\rho \quad (8.50)$$

Here  $\bar{v}$  is the meridional velocity in the upper layer. Let the lower layer outcrop, i.e. intersects the free surface at  $x = x_s(y)$ . From the conditions

$$\int_{x_s}^{x_E} \bar{v} dx = 0, \quad \partial(x_s) = 0 \quad (8.51)$$

we obtain

$$x_s(y) = x_E - (\rho g' \partial_E^2) / 2 \tau^x(y) \quad (8.52)$$

The depth at the eastern boundary  $D_E$  is obtained for a given by fixing the volume of the upper layer

$$\int_{\partial > 0} \partial dx dy = 2 \partial_0 b x_E \quad (8.53)$$

The values of  $h = D_E/D$  and  $D_{min}/D_0$  are shown in Figures 8.12a and 8.12b as functions of  $\lambda = x_E \tau_{max} / \rho_0 g' \partial_0^2$ . The upper-layer depth first surfaces in the north-west corner of the basin when  $\lambda = \lambda_c$  where  $\lambda_c$  is the smallest root of (8.52) at  $x_s = 0$  that can be represented in nondimensional form

$$h^2(\lambda) = 2\lambda \quad (8.54)$$

For the wind stress  $\tau = -\tau_{max} \cos(\pi y / 2b)$  the calculation gives  $\lambda_c = 0.26$ . Position of surfacing line for different values of  $\lambda > \lambda_c$  is shown in Figure 8.13. Full solution including frictional western boundary layer is shown in Figure 8.14 for  $\lambda = 0.15$ .

A comparison of this figure with charts of the observed north Atlantic circulation shows good qualitative agreement, particularly in the circulation of the separated current and in the gross features of the return flow.

For  $\lambda > \lambda_c$  deep layer is exposed to wind but we assumed the deep layer to be motionless. This problem will be considered in the next lectures.

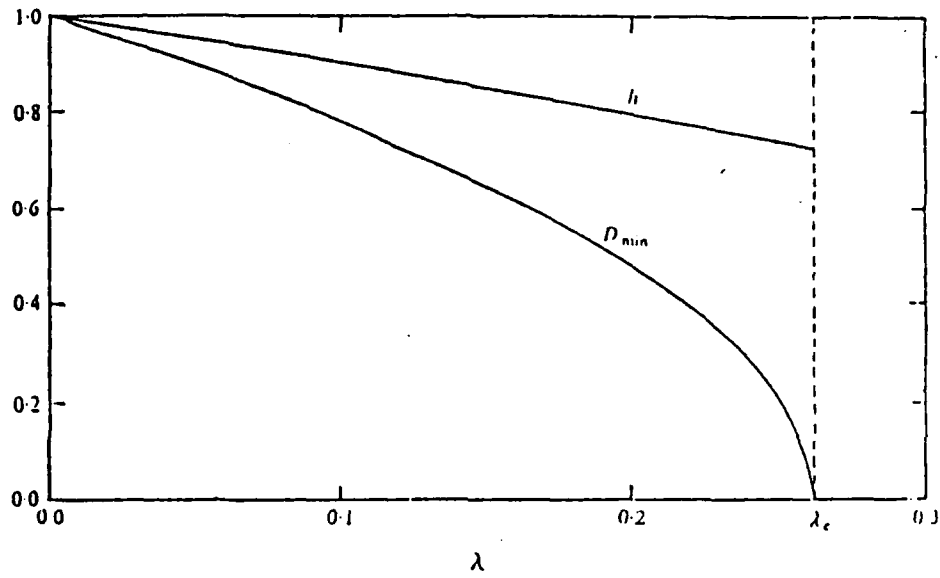


Fig. 8.12a. Layer depth at eastern coast and minimum layer depth as functions of amplitude. Surfacing occurs at critical amplitude  $\lambda_c$ .

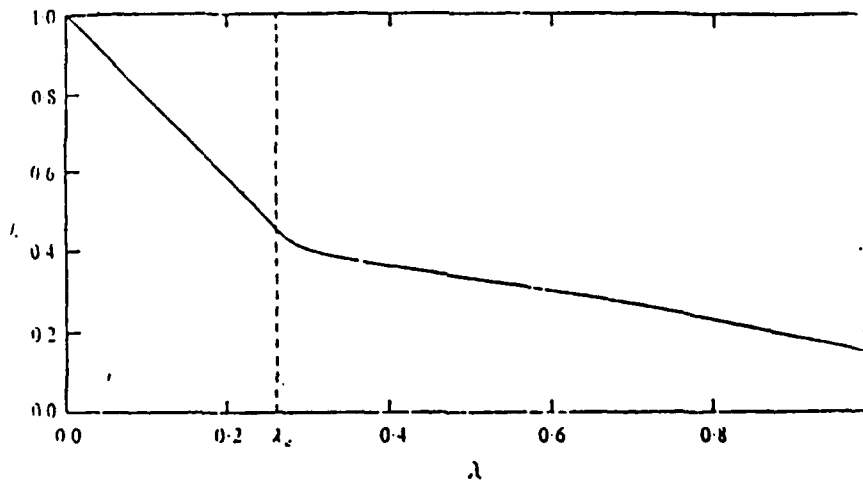


Fig. 8.12b. Layer depth at eastern coast against amplitude. Dependence extended beyond critical amplitude  $\lambda_c$ .

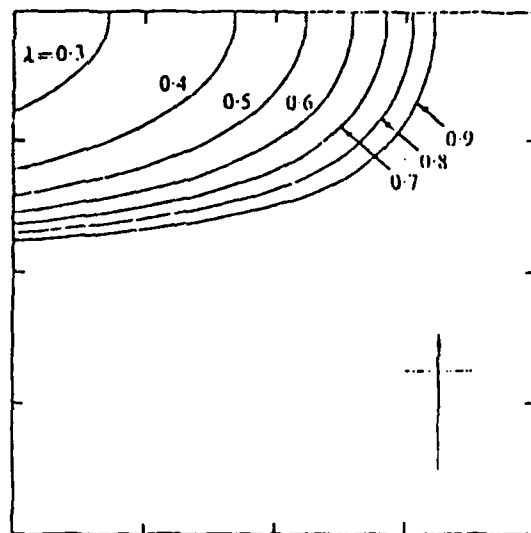


Fig. 8.13. Position of surfacing line for different values of amplitude.

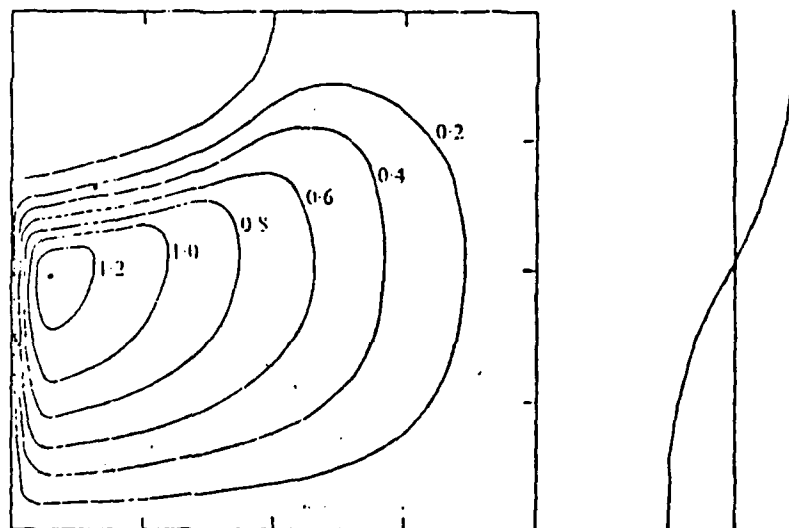


Fig. 8.14 Contour lines of stream function for upper-layer transport when  $c \approx 0.03$ ,  $\lambda \approx 0.45$ .

## 8.5 References

- Rhines P. B., Young W. R. 1982a. A theory of wind-driven circulation. I. Mid-ocean gyres. Mar. Res., V. 40 Suppl., 559-596.
- Rhines P. B., Young W. R. 1982b. Homogenization of the potential vorticity in planetary gyres. G. Fluid Mech., V. 122, 347-367.
- Young W. R., Rhines P. B. 1982. A theory of the wind-driven circulation II. Gyres with western boundary layers. Mar. Res., V. 40, N3, 849-872.
- Ierley G. R., Young W. R. 1983. Can the western boundary layer affect the potential vorticity distribution in the Sverdrup interior of a wind gyre? Phys. Oceanogr., V. 13. N10. 1753-1763.
- Parsons A. T. 1969. A two-layer model of Gulf Stream Separation. Fluid Mech., V. 39, pt. 3, 511-528.
- Notes submitted by: George Sutyrin, P.P. Shirshov' Institute of Oceanology Acad. Sci., U.S.S.R.



## LECTURE 9

## 9 PARSON'S MODEL APPLIED TO THE SUBPOLAR GYRE

Huang and Flierl (1987) extended Parson's model to include an outcropping subpolar gyre. The lower layer first outcrops in the subpolar gyre at the point where If the outcrop region becomes larger, it can expand into the subpolar gyre (Fig.1). In contrast to the isolated subtropical gyre the outcropped region is not bounded by the western boundary. For there to be mass transport between the eastern boundary and the outcrop line, where it crosses the zero wind stress line ( $\tau_y^x = 0$ ) there must be transport along the western boundary, and the bounding streamline of the outcrop has a stream function value of  $\psi_m \neq 0$ .

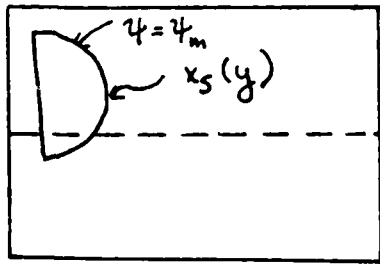


Fig. 1. Schematic of outcrop line

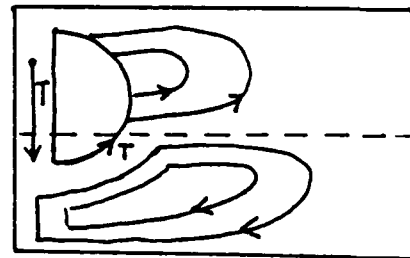
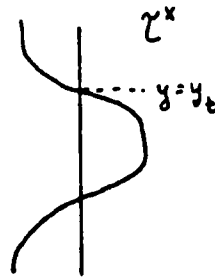


Fig. 2. Schematic of the flow

The resulting flow has transport  $T$  on the western boundary of the subtropical gyre. The interior of both gyres is in Sverdrup balance, and the Gulf Stream leaves the coast and carries the subtropical Sverdrup transport plus  $T$ . It crosses the line where  $\tau_y^x = 0$ ; there the western boundary transport is exactly zero.

At  $y = y_t$ ,  $\tau_y^x = 0$  so that

$$\psi_m + \int_{x_s}^{x_E} v dx = 0.$$

As in the previous section, we can find the outcrop line

$$x_s(y) = x_E - \left( \frac{g' D_E^2}{2} + \beta \psi_m \right) / \lambda \tau_y^x(y). \quad (1)$$

To find  $\psi_m$ , we look at  $x_s(y_t)$  from (1) above, and use L'Hopital's rule to find

$$\frac{g' D_E^2}{2} + \beta \psi_m = 0, \quad \text{so that} \quad \psi_m = -\frac{g' D_E^2}{2\beta}, \quad \text{and}$$

thus

$$x_s(y_t) = x_E - \frac{\beta \psi_m}{\lambda \tau_y^x(y_t)}.$$

In summary, the amount of warm water in the basin is given by  $V_m$ . The circulation is completed by frictional boundary layers on the western boundary and along  $x, (y)$ . The western boundary transport and the frictional boundary layer at  $x$ , are the same magnitude, in opposite directions. At  $y_t$ , the Sverdrup interior returns all of the transport,  $V_m$  northward and there is no separated western boundary transport north of  $y_t$ . The circulation is summarized in fig.2.

Pedlosky (1987) modified Parson's model so that Ekman flow is allowed to cross the outcrops, and there is no geostrophic flow across the outcrops. This changes the mass balance and thus the flow pattern. In Parson's model we had the sum of the western boundary current, frictional boundary current, geostrophic, and Ekman transport is zero. It allows leakage of water to the south, since the Ekman velocities are to the south. Parson's model is fairly sensitive to changes such as this one.

### 9.1 Thermocline Theories

In principle, thermocline theories explain the thermocline between the abyssal waters of high latitude origin and surface waters that are strongly influenced by the wind. These models are inviscid and steady and the relative vorticity is neglected, and they ignore the sources of the deep water. The equations that govern the flow are momentum conservation (geostrophy)

$$-f\rho v = -p_x \quad f\rho u = -p_y. \quad (2)$$

The hydrostatic balance

$$0 = -p_z - g\rho. \quad (3)$$

The continuity equation

$$\nabla \cdot \underline{u} = 0, \quad (4)$$

and density conservation

$$\underline{u} \cdot \nabla \rho = 0. \quad (5)$$

From these equations the conservation of Bernoulli function  $B = p + \rho g z$

$$\underline{u} \cdot \nabla B = 0 \quad (6)$$

and potential vorticity  $Q = f\rho_z$

$$\underline{u} \cdot \nabla Q = 0 \quad (7)$$

can be derived. Therefore there are 3 conserved quantities on streamlines,  $\rho$ ,  $B$ , and  $Q$ .

If surfaces of constant  $\rho$  and  $B$  intersect, then the solution is the lines of intersection.  $Q$  is constant on this line. Therefore, there is a rule which associated values of  $\rho$ ,  $B$  with  $Q$  i.e.  $Q=F(\rho, B)$ , and only two tracers are independent.

Welander (1971) solved this problem by choosing  $f\rho_z = F(\rho)$ . Then we have

$$\frac{d\rho}{F(\rho)} = \frac{dz}{f} \quad (8)$$

and

$$I(\rho) - I(\rho_0) = \frac{z-z_0}{f} \quad \text{where} \quad I(\rho) = \int^\rho F(\rho) d\rho$$

or

$$\rho = I^{-1} \left( \frac{z-z_0}{f} \right) + I(\rho_0).$$

As an example Welander let

$$f\rho_z = a\rho + b$$

to get

$$\rho = \rho_{\text{surface}}(x, y) e^{az/f} + \rho_\infty.$$

From the general solution to (8) we can show that

$$\frac{\rho_y}{\rho_z} = \frac{\rho_y}{\rho_z} \Big|_{z=z_0} - \frac{(z-z_0)}{f} \beta.$$

At the surface  $\rho_y > 0$ ,  $\rho_z < 0$  and  $\rho_y/\rho_z < 0$ ;

likewise at depth

$$\rho_y/\rho_z \text{ depth} > 0.$$

The center of the gyre moves northward in Fig. 3.

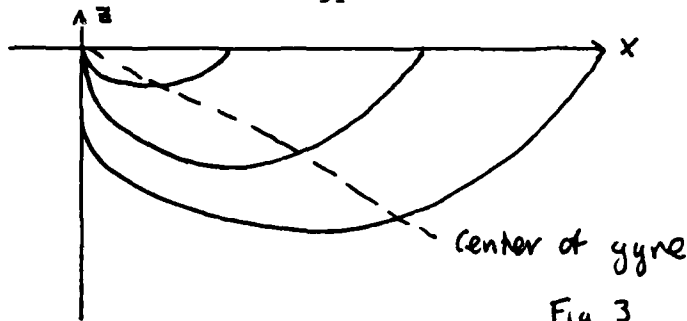


Fig 3 cross section of gyre

Another possible solution is

$$f\rho_z = a\rho + b(P + \rho g z)$$

To obtain a second order equation for  $\rho$ , making use of 2-3;

$$f\rho_{zz} + a\rho_z + b\rho_z g z = 0$$

To solve this, we set  $\rho_0(x, y)$  at the surface and  $\rho_{\infty}(x, y)$  at depth. However, the solution determines

$$w = \frac{u\rho_x + v\rho_y}{\rho_z} \Big|_{z=0} \quad \text{at the surface and we are}$$

not free to specify the Ekman pumping. If on the other hand we specify  $\rho_0$  and  $w_e$ , we may find that  $\rho$  is discontinuous where the fluid meets the stagnant deep water.

To solve the more general problem, we try to specify both  $\rho$  at the surface.

$$\rho(x, y, 0) = \rho_s(x, y)$$

and  $w$  at the surface, using (2-7),

$$J(\rho_s, \rho_s) + \rho_0 w_e F(\rho_s, \rho_s) = 0.$$

We use these boundary conditions to solve

$$f\rho_z = F(\rho, P + \rho g z).$$

If  $\rho_s(x, y)$  and  $P_s$  are specified along a coast, then we know  $P_s(x, y)$  everywhere, and from that the solution can be found everywhere. However, this leads us to Killworth's theorem. We would like to specify  $u=0$  at  $x=x_e$ . Using density conservation there we see that

$$v\rho_y + w\rho_z = 0$$

But  $u_z = 0$  so  $-f u_z = g \rho_y = 0$  which leaves us with  $w\rho_z = 0$ . In carrying this argument out, we find that as long as all the fields are infinitely

differentiable, and the solution obeys  $u=0$  on the eastern boundary then  $\rho = \text{constant}$  there. If  $\rho_s(x_e, y, z) \neq 0$  then the interior must be stagnant. Note that if we are considering a layered model, then some of the derivatives will be discontinuous and Killworth's theorem will not apply.

These considerations motivate a class of problems where a circulation is driven by the wind at the surface and overlies a deep resting fluid of density  $\rho_a(z)$ . (Fig. 4)

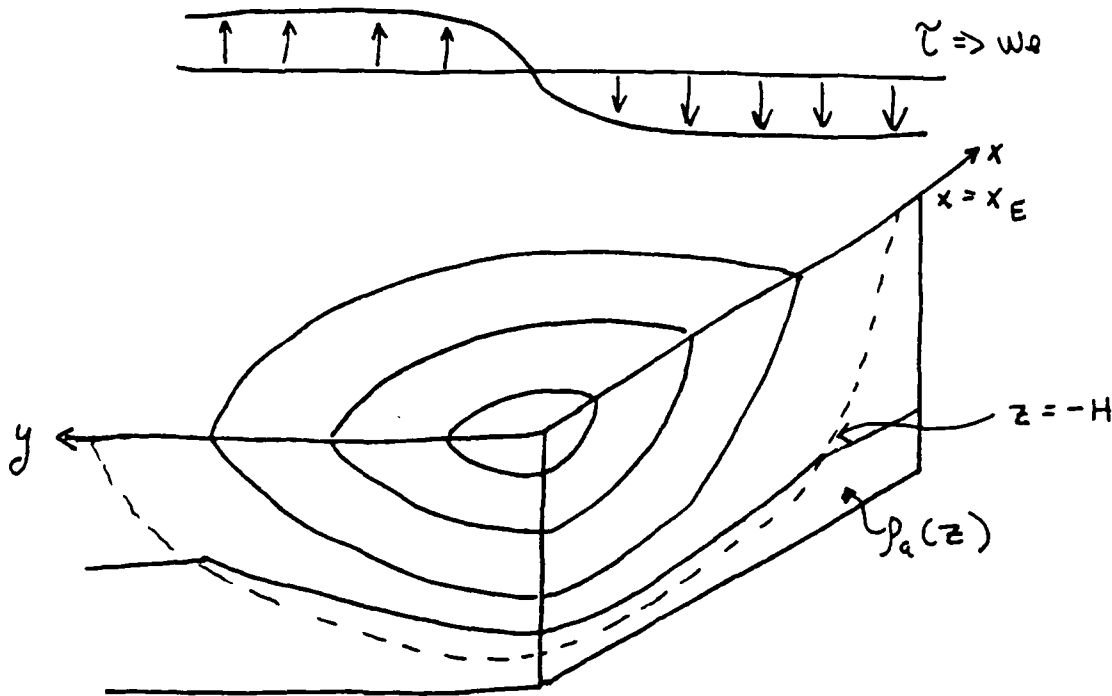


Figure 4. Schematic of gyre

We can formulate the problem as follows. We seek solutions subject to imposed surface density  $\rho(x, y, 0) = \rho_s(x, y)$  where the Ekman velocity  $w_e(x, y)$  is less than zero. Also, the water is quiescent below  $z = -H$ , and there is no density jump there. The problem is reduced to solving

$$z = -H \quad \rho(x, y, -H(x, y)) = \rho^* (-H(x, y))$$

$$p_x = p_y = w = 0$$

$$0 > z > -H \quad f \rho_z = F(\rho, p + \rho g z)$$

$$z=0 \quad \rho(x,y,0) = \rho_s(x,y) \\ w(x,y,0) = w_e$$

The surface conditions will determine the function  $F$ , and  $H(x,y)$  will be determined in the course of solving the problem.

To solve for the problem in a general way, we transform the equations to density coordinates. For example, consider

$$B(x,y,z) = B(x,y,z(x,y,p))$$

then

$$B_x|_p = B_x|_z + B_z|_{x,y} z_x|_p = P_x|_z + P_z|_{x,y} z_x|_p + g(pz)_x|_p \\ = P_x|_z + P_z|_{x,y} + pg z_x|_p = P_x|_z \quad \text{if} \quad 0 = P_z - pg$$

Thus in density coordinates equations 2 - 7 become

$$-\rho_0 f v = -B_x \quad \rho_0 f u = -B_y$$

$$0 = B_p - g z$$

$$u z_x + v z_y - w = 0$$

$$(u z_p)_x + (v z_p)_y = 0$$

$$\frac{f g}{B_p p} = Q(p, B)$$

for the governing equations.

The boundary conditions can then be derived. Requiring no jump in density across  $z = -H$  gives

$$\rho_b(x,y) = \rho_a(-H(x,y))$$

in  $(x,y,z)$  coordinates. Given  $\rho^a(z)$  we can find

$$B^a(z) = \text{constant} - \int_0^z g \rho^a(z') dz' + g \rho^a(z) z \quad (9)$$

We then invert  $\rho^a(z)$  to get  $z = z^a(p)$ , and insert into (9). From this, we see that if we know  $\rho^a(z)$  then we know  $B^a(p)$  to a constant. Thus continuity of  $\rho$  requires

$$B_p(\rho_b) = B_p^a(\rho_b)$$

Likewise, if we want  $P_x = P_y = 0$  at  $\rho_b$ , we require

$$B(\rho_b) = B^a(\rho_b)$$

Generally, we must find  $\rho_b(x,y)$  in the course of the solution.

Notice that if the resting fluid is homogeneous,  $\rho^*(z) = \rho^\infty$ , then  $\rho_b(x, y) = \rho^\infty$ ,  $B^* = C - g\rho^\infty z + g\rho^\infty z = C$  and  $B_p^* = 0$ . Therefore we have

$B_x|_p = 0$  and  $u=v=0$  at  $p = p_\infty$ , but although  $\rho$  is continuous across  $z = -H$ ,  $\rho_x, \rho_z$  may be discontinuous and Killworth's theorem will not hold.

Since we specify  $w_e$  at the surface and  $u=v=w=0$  at  $z = -D$  the fluid in between must carry the Sverdrup transport. We can express this as

$$J(p_s, p_s) + \rho_0 w_e F(p_s, p_s) = 0 \text{ at } z = 0.$$

This fixes the variation of  $w$  along specified outcrops in terms of  $w$  and  $F$ . More directly,

$$\partial_x \int_{-H}^0 \rho dz + \rho(-H) H_x = \rho_0 f^2 w_e / \rho$$

which is equivalent to the Sverdrup relation,  $\beta V = f w_e$ .

In density coordinates we have

$$J(B^s, B_o^s) + g\rho_0 f w_e(x, y) = 0, \rho = p_s$$

At the surface ( $z=0$ )  $B_p = 0$  but  $B_{p_x}|_{p=p_s} \neq 0$  since  $\partial_x|_p \neq \partial_x|_z$ . If we move along the surface

$$dB_p(x, y, p)|_{p_s} = 0 = B_{p_x}|_p dx + B_{p p} p_{s,x} dx$$

Thus we have

$$J(B^s, p_s) - \rho_0 w_e g(p^s, B^s) = 0, \rho = p_s$$

To derive the Sverdrup relation in density coordinates, we combine

$$\beta V = f w_p / z_p \quad \text{and} \quad -\rho_0 f V = -B_x$$

to get

$$B_x z_p = \rho_0 f^2 w_p / \beta$$

Integrating with respect to  $p$  we find

$$\begin{aligned} \frac{\rho_0 f^2 w_e}{\beta} &= \int_{p_b}^{p_s} B_x (z_p = B_{p p} / g) dp = \frac{1}{g} \int_{p_b}^{p_s} [(B_x, B_p)_p - \left(\frac{B_p^2}{2}\right)_x] dp \\ &= -\frac{1}{g} \int \left(\frac{B_p^2}{2}\right)_x = -\frac{1}{g} \partial_x \int \left(\frac{B_p^2}{2}\right)_x - \frac{1}{g} \frac{B_p^2}{2}(p_b) p_{b,x} \end{aligned}$$

to finally get

$$-\partial_x \int_{p_b}^{p_s} \left(\frac{B_p^2}{2}\right) dp - \left(\frac{B_p^2}{2}\right) \Big|_{p_b} p_{b,x} = \frac{\rho_0 f^2 g}{\beta} w_e$$

To summarize, the  $x, y, z$  and  $x, y, \rho$  formulations can be displayed side by side

$$x, y, z$$

$$x, y, \rho$$

$$z=0 \quad P_z^s = -g\rho_s(x, y)$$

$$\rho = \rho_s(x, y) \quad B_p^s = 0$$

$$J(P^s, \rho_s) + \rho_0 w_e F(P^s, \rho_s) = 0 \quad J(B^s, B_p^s) + g\rho_0 f w_e = 0$$

$$0 > z > -H \quad \frac{f P_{zz}}{g} = -F\left(\frac{-P_z}{g}, \rho - z P_z\right) \quad \rho_\infty > \rho > \rho_s \quad B_{pp} = \frac{g f}{\rho} (P, B)$$

$$z = -H \quad P_z = -g\rho_\infty$$

$$\rho = \rho_\infty \quad B = \text{constant}$$

$$P_x = P_y = 0$$

$$P(x, y, -H) = \rho_\infty g H + \text{constant}$$

In density coordinates, the bottom boundary condition is applied at a known density, however, in  $(x, y, z)$  coordinates, the bottom boundary condition is more complex and is applied at the unknown  $z = -H$ . Also  $B$  is discontinuous at  $z = -H$  because  $z$  is not defined in a homogeneous fluid.  $H$  can be calculated afterwards by

$$B_p(\rho \rightarrow \rho_\infty^-) = gH$$

If the deep fluid is uniformly stratified,  $\rho = \rho_0$  is the deepest outcropping isopycnal,  $\rho = \rho_b(x, y)$  at the base of the moving layer, and  $\rho^a(z)$  is the abyssal stratification, then the model is formulated as follows:

$$\rho = \rho^s(x, y) \quad B_p = 0$$

$$\partial_x \int_{\rho_b}^{\rho_s} \left( \frac{B_p^2}{2} \right) d\rho = \frac{\rho_0 f^2 g w_e}{\rho} + \left. \frac{B_p^2}{2} \right|_{\rho_b} \rho_{bx}$$

$$B_{pp} = \frac{f g}{\rho(B, \rho)}$$



and to match to the abyssal layers

$$\rho = \rho^b(x, y) \quad \text{and} \quad B = B^a(\rho_b)$$

$$B_\rho = B_{\rho^a}(\rho_b)$$

where now  $\rho_b(x, y)$  is unknown.

Huang (1986) solved the problem by starting in the north west corner and solving the above equations point by point in  $x$  and  $y$ . The integration progresses from the northwest to the west and the north to the south. This progression comes from the need to determine  $q(B, \rho)$  first on density outcrops and because  $\rho^s$  along the outcrop is fixed at the east coast.

At any point in  $x, y$  the procedure is as follows:

1. Guess  $\rho_b$  and compute  $B$  and  $B_\rho$  at  $\rho_b$ .
2. Integrate  $B_\rho = \frac{\partial q}{\partial \rho}$  to the surface. To do this,  $q(B, \rho)$  is needed on all the deeper isopycnals which was developed earlier in the solution. At the surface  $q(B^s, \rho^s) = q^s$  is arrived at.
3. Adjust  $q^s$  in order to make  $B_\rho = 0$  at  $\rho = \rho^s$ .
4. Repeat 1-3 varying  $\rho_b$  until the Sverdrop relation is satisfied.

## 9.2 References

Huang, R.X. and G.R. Flierl, 1987: Two-layer models for the thermocline and current structure in subtropical subpolar gyres. J. Phys. Oceanogr., 17, 872-884.

Huang, R. X., 1986: Solutions of the ideal fluid thermocline with continuous stratification. J. Phys. Oceanogr., 16, 39-59.

Pedlosky, J., 1987: On Parsons' Model of the Ocean Circulation. J. Phys. Oceanogr., 17, 1571-1582.

Welander, P., 1971: Some exact solutions to the equations describing an ideal-fluid thermocline. J. Mar. Res., 29, 60-68.

Notes submitted by: LuAnne Thompson, MIT/Woods Hole  
Oceanographic Institution

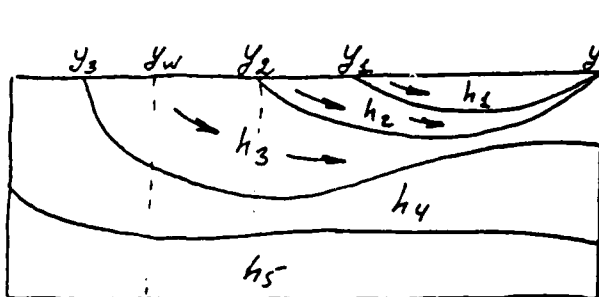
## LECTURE 10

THE THEORY OF THE VENTILATED THERMOCLINE

## Lecture 10 Part I

This theory was developed by J.R. Luyten, J. Pedlosky and H. Stommel (J.P.O., 1983, 13, pp 292-309).

Let us consider N-layers model with thickness  $h_1, h_2, \dots, h_N$  which intersect the sea surface at latitudes  $y_i$  ( $y_i = y_i(x)$ , (i.e. the outcrop lines are a function of longitude). The density of each layer is a constant  $\rho_i$ ,  $i = 1, 2, \dots, N$ , they are immiscible and there is no frictional coupling between the layers. There is a model for the region immediately below the surface mixed layer, so that vertical velocity on  $z = \eta(x, y)$  is  $w = w_e(x, y)$  (Ekman pumping velocity),  $\eta$  is the elevation of the air-sea surface. Let  $w_e$  be positive north of the line  $y = y_w(x)$  and negative between  $y_w$  and  $y = 0$ . The motions within each layer are geostrophic and hydrostatic.



$$\rho_n \oint u_n = - \frac{\partial \rho_n}{\partial y} \quad (1)$$

$$\rho_n \oint v_n = \frac{\partial \rho_n}{\partial x} \quad (2)$$

$$\rho_n g = - \frac{\partial \rho_n}{\partial z} \quad (3)$$

$$\frac{\partial u_n}{\partial x} + \frac{\partial v_n}{\partial y} + \frac{\partial w_n}{\partial z} = 0 \quad (4)$$

Here  $n=1, 2, \dots, N$ . The Sverdrup vorticity equation is (from (1, 2, 4))

$$\beta v_n = \oint \frac{\partial w_n}{\partial z} \quad (5)$$

When (5) is integrated over each layer and we sum over all moving layers we get:

$$\beta \sum_n h_n v_n = f w_e(x, y) \quad (6)$$

Now we begin from the situation, when the only third layer moves, and the region is restricted by  $y_2 \leq y \leq y_w$ . Integration of the equation (3) coupled with the requirement that layer 4 remain at rest yields:

$$- f v_3 = -g' \frac{\partial h_3}{\partial x} \quad (7)$$

$$f u_3 = -g' \frac{\partial h_3}{\partial y} \quad (8)$$

where  $g' = g \Delta \rho / \rho$  and  $\Delta \rho \ll \rho$ . Let us assume, that  $\Delta \rho_1 = \Delta \rho_2 = \dots = \Delta \rho_N$ . From (6) and (7) one can obtain

$$\frac{\partial}{\partial x} (h_3^2) = \frac{-2 f^2}{\beta g'} w_e(x, y) \quad (9)$$

If we define the function  $D_0^2(x, y) = \frac{-2 f^2}{\beta g'} \int_x^{x_e} w_e(x', y) dx'$  (Sverdrup function), which is positive for  $y < y_w$  and some constant  $H_0$ :  $H_0 = h_3|_{x=x_e}$  so, that there is no zonal flow on  $x = x_e$ , we can get

$$h_3^2 = D_0^2(x, y) + H_0^2 \quad (10)$$

Between  $y_2$  and  $y_w$

$$\beta h_3 v_3 = f w_e < 0 \quad (11)$$

so that fluid columns are directly driven downward and southward. As they cross the line  $y = y_2$  they are subducted and in the region south of  $y_2$  layers 2 and 3 are in motion, i.e.

$$- f v_3 = -g' \frac{\partial (h_2 + h_3)}{\partial x} \quad (12)$$

$$\phi u_3 = -g' \frac{\partial(h_2 + h_3)}{\partial y} \quad (13)$$

Then, if  $H = h_2 + h_3$  is the thickness of the fluid in motion,

$$-\phi v_3 = -g' \frac{\partial H}{\partial x} \quad (12')$$

$$\phi u_3 = -g' \frac{\partial H}{\partial y} \quad (13')$$

and  $u_3 \frac{\partial}{\partial x}(\phi/h_3) + v_3 \frac{\partial}{\partial y}(\phi/h_3) = 0$ , i.e.  $\mathcal{V}(H, \phi/h_3) = 0$   
 The last equation gives  $\phi/h_3 = G_3(H)$  where  $G_3$  is some arbitrary function, i.e. the potential vorticity trajectories coincide with the isobars in layer 3.

Within layer 2 the hydrostatic equation gives:

$$\phi v_2 = g' \frac{\partial}{\partial x}(H + h_2) \quad (14)$$

$$\phi u_2 = -g' \frac{\partial}{\partial y}(H + h_2) \quad (15)$$

$$\frac{\partial}{\partial x}(u_2 h_2) + \frac{\partial}{\partial y}(v_2 h_2) = 0 \quad (16)$$

eq. (6) yields  $\frac{\partial}{\partial x}(H^2 + h_2^2) = \frac{2\phi^2}{\beta g'} W_e(x, y)$

whose integral is  $H^2 + h_2^2 = D_0^2(x, y) + \text{Const}$  (17)

The constant of integration must, by continuity of  $h_2$ , be  $H_0^2$  so that on  $x=x_2$  at  $y=y_2$ ,  $H = h_3 = H_0$ .

Now we can determine function  $G_3$ , so that on  $y=y_2$   $h_3=H$ , thus, noting that  $f = f(y)$ :

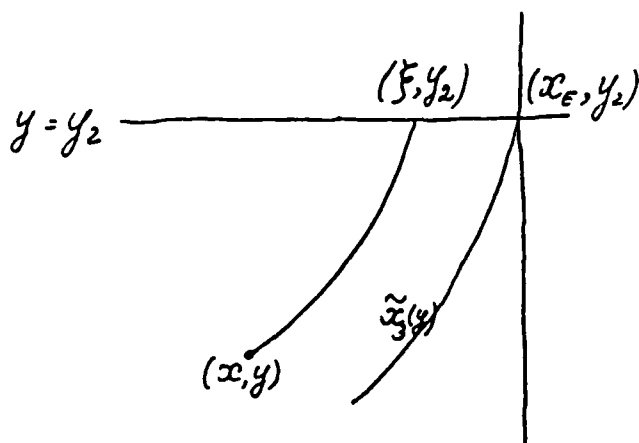
$$\frac{\phi(y_2)}{H} = G_3(H), \quad y = y_2, \quad \text{i.e. } G_3(H) = \frac{\phi_2}{H}$$

where  $\phi_2 = \phi(y_2)$ . Thus in  $y_1 \leq y \leq y_2$   $h_3 = \frac{\phi}{\phi_2} H$ . (18)

Remember that  $H = h_3 + h_2$  then (18) yields:

$$h_2 = \left(\frac{\phi_2}{\phi} - 1\right) h_3 = \left(\frac{\phi_2}{\phi} - 1\right) \frac{\phi}{\phi_2} H = \left(1 - \frac{\phi}{\phi_2}\right) H \quad (19)$$

So, from (9) and (19):  $H^2(x, y) = \frac{D_0^2(x, y) + H_0^2}{1 + (1 - \phi/\phi_2)^2}$  (20)



In layer 3 the point  $(x, y)$  on a geostrophic trajectory is connected by the indicated contour to its origin at the point of subduction  $(\xi, y_2)$ .

The trajectory of a fluid column in layer 3, that is subducted at the point  $(\xi, y_2)$ , traverses a path of constant  $\ell/h_3$  which is also a path of constant  $H$  (eq.18). The resulting path is given implicitly by the relation  $H(x, y) = H(\xi, y_2)$

or  $D_0^2(x, y) = D_0^2(\xi, y_2) [1 + (1 - \ell/\ell_2)^2] + H_0^2 (1 - \ell/\ell_2)^2$ . The trajectory  $\tilde{x}_3(y)$  emanating from this point is given by  $H(\tilde{x}_3, y) = H(x_e, y_2) = H_0$  or  $D_0^2(\tilde{x}_3) = H_0^2 (1 - \ell/\ell_2)^2$ . If  $H_0 = 0$ ,  $\tilde{x}_3(y) = x_e$  ( $y < y_2$ ) and the trajectory will hug the eastern boundary, otherwise, for all  $H_0 \neq 0$  the trajectory emanating from  $(x_e, y_2)$  must swerve westward. So along the eastern boundary all layer thicknesses must be constant to avoid a zonal thermal wind current at  $x = x_e$ , but in this case a column of fluid flowing southward along the boundary would be continuously reducing its potential vorticity whereas in fact its potential vorticity must be conserved. The resulting trajectory then enters the fluid interior searching out a potential vorticity isopleth. If  $H_0 = 0$ ,  $h_3$  vanishes on  $x_e$  and columns on the eastern boundary possess an infinite store of potential vorticity, in that case alone can they flow parallel to the eastern boundary at  $x = x_e$  and conserve potential vorticity.

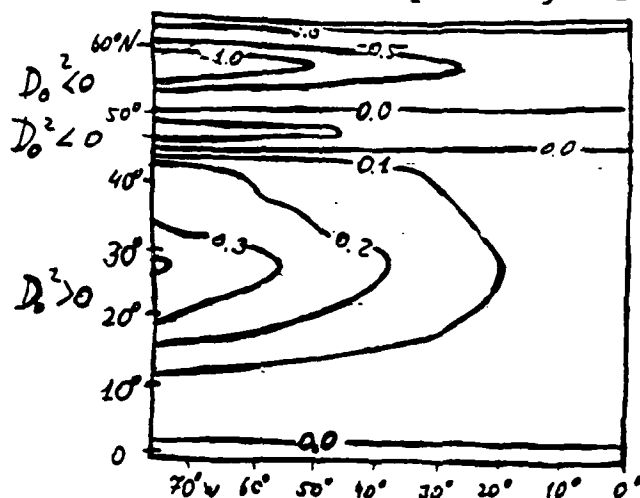
Thus for  $H_0 \neq 0$ ,  $x_e - \tilde{x}_3(y) > 0$  for all  $y < y_2$ . The trajectory emanating from  $x_e, y_2$  separates the gyre into (at least) two regions. To the west of  $\tilde{x}_3(y)$  both layers are in motion and this motion is determined by the memory of the potential vorticity, each column of layer 3 has as it slips under the blanket of layer 2 at  $y = y_2$ . East of  $\tilde{x}_3(y)$  no potential vorticity trajectory from  $y = y_2$  can ventilate layer 3. The shadow region carved out by  $\tilde{x}_3(y)$  in layer 3 is bounded on the east by eastern wall through which no fluid penetrates and on the west by the streamline  $\tilde{x}_3(y)$ . The depth of

layer 3 is  $H_0$  on both these boundaries. Since this shadow region within layer 3 is not driven by either surface Ekman pumping or inflow across  $\tilde{x}_3(y)$  or  $x_e$ , i.e.  $u_3 = v_3 = 0$ .

In the unventilated, stagnant shadow region east of  $\tilde{x}_3(y)$  the solution is  $h_2^2 = D_0^2(x, y)$ ,  $h_3 = H_0 - D_0$ .

Luyten, Pedlosky and Stommel showed that the model predicts an unventilated region sweeping across the entire lowlatitude North Atlantic from the eastern boundary at the depth of the 27.40 isopycnal surface.

The total amount of fluid pumped down from the Ekman layer was determined by the annual mean Ekman flux. There have been used the zonally averaged Ekman flux.

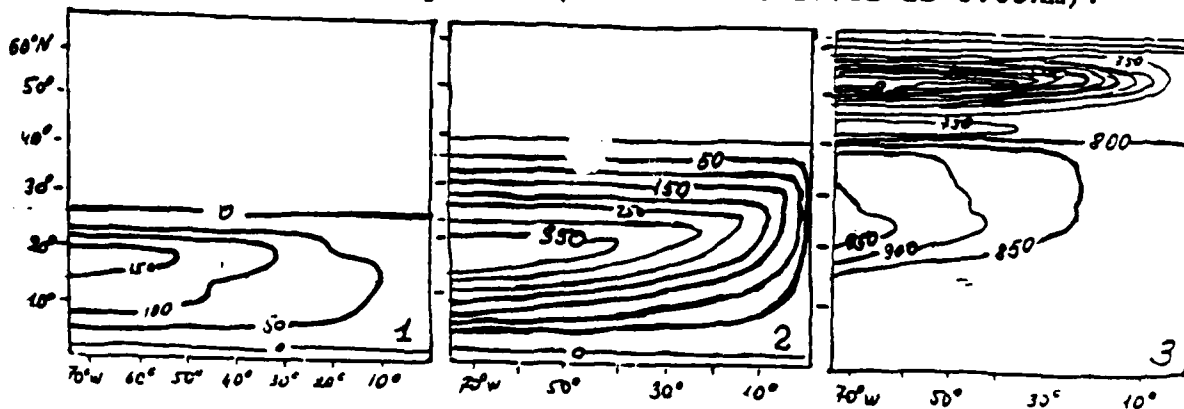


This is the distribution of Sverdrup function  $D_0^2$  (in  $10^3 m$ )

$$D_0^2 = -\frac{2f^2}{\beta \delta_3} \int_{x_e}^{\tilde{x}_e} w_e(x', y) dx'$$

Here  $\delta^3 = g(\rho_1 - \rho_3)/\rho_2$  which is equivalent to  $g' = g \Delta \rho / \rho$  in the beginning of the lecture.

The layer depths for each of the three active layers are presented as contour plots. (the contour level is 0.05km).



The feature which is most clear from these plots is the large region of uniform depth in layer 3 sweeping across from the subduction point on the eastern wall to the western boundary of the circulation in which there is no motion.

## Lecture 10 Part II

**SIMILARITY SOLUTION. A RESTRICTIVE FORM BUT DON'T NEED POTENTIAL VORTICITY CONSERVATION.** (W. R. Young and G.R. Ierley, T.P.O., 1986, 16, pp. 1884-1900.

The thermocline equations on  $\beta$ -plane are: ( $f = \beta y$ )

$$fu = -\frac{\partial p}{\partial y} \cdot \frac{1}{\rho_0}$$

$$fv = \frac{\partial p}{\partial x} \cdot \frac{1}{\rho_0} \quad (1)$$

$$\rho g = \frac{\partial p}{\partial z}$$

$$\frac{\partial u}{\partial x} + \frac{\partial v}{\partial y} + \frac{\partial w}{\partial z} = 0$$

$$u \frac{\partial \rho}{\partial x} + v \frac{\partial \rho}{\partial y} + w \frac{\partial \rho}{\partial z} = k \frac{\partial^2 \rho}{\partial z^2}$$

The use of spherical coordinates introduces only some changes

$$\beta v = f \frac{\partial w}{\partial z}$$

$$f \frac{\partial u}{\partial z} = \frac{g}{\rho_0} \frac{\partial p}{\partial y}$$



$$f \frac{\partial v}{\partial z} = -\frac{g}{\rho_0} \frac{\partial \rho}{\partial x} \quad (2)$$

$$u \frac{\partial q}{\partial x} + v \frac{\partial q}{\partial y} + w \frac{\partial q}{\partial z} = k \frac{\partial^2 q}{\partial z^2}$$

where

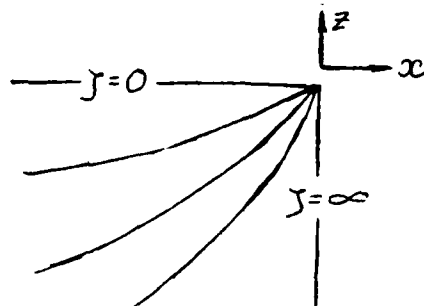
$$q = f \frac{\partial \rho}{\partial z}$$

is the potential vorticity.

The general family of solutions of (1) has the form

$$\rho = -\rho_0 g z + \rho_0 g \varepsilon D^{m+1} e^{-m} M_{\zeta}(\zeta, y), \quad \zeta = -\frac{z}{D(x, y)} \quad (3)$$

Where  $D$  is  $D(x, y)$  with dimensions of length,  $\varepsilon$  is dimensionless,  $L$  is a length scale.



Some curves of  $\zeta$  constant in the  $(x, z)$  plane. Note that  $D \rightarrow 0$  as  $x \rightarrow 0$  so that

both the eastern boundary and the abyss are at  $\zeta \rightarrow \infty$ . This collapse of two conditions in the three-dimensional  $(x, y, z)$  space into one condition in the  $(y, \zeta)$  space is typical of similarity solutions.

At the eastern boundary the density is of the form:

$$\rho = \rho_0 (1 + \varepsilon (-z/\ell)^m), \quad m \geq 0 \quad (4)$$

Here  $\varepsilon$  and  $\ell$  are introduced separately so that in the special case  $m=0$  the density at great depth, and at the eastern boundary, is  $\rho_0(1+\varepsilon)$ . The density field in (4) will be referred to as the "resting stratification".

From (3) and the hydrostatic relation one can get the density:

$$\rho = \rho_0 (1 + \varepsilon (D/\ell)^m M_{\zeta \zeta}) \quad (5)$$

And if (5) is to satisfy the eastern boundary conditions (4),

$$M_{\zeta\zeta} \rightarrow +\zeta^m \text{ as } \zeta \rightarrow \infty$$

More precisely the requirement is the difference between  $M_{\zeta\zeta}$  and  $\zeta^m$  must vanish as  $\zeta \rightarrow \infty$  as some algebraic power of  $\zeta$  (e.g.  $\zeta^{-3}$ ). In special cases ( $m=0,1$ ) it is exponentially small.

$$\text{From (2) } w = -(\beta \epsilon g / f^2) (D/e)^m D D_x [(m+2)M - \zeta M_\zeta] \quad (5)$$

From (1), (4), (5) and the horizontal velocities given by the geostrophic balance

$$\begin{aligned} fu &= -\epsilon g D_y (D/e)^m [(m+1)M_\zeta - \zeta M_{\zeta\zeta}] - \epsilon g D^{m+1/2} e^{-m} M_{\zeta y} \\ fv &= \epsilon g D_x (D/e)^m [(m+1)M_\zeta - \zeta M_{\zeta\zeta}] \end{aligned} \quad (5')$$

we can get the equation for M:

$$\begin{aligned} & y \zeta [M_{\zeta\zeta\zeta} M_{\zeta y} - M_{\zeta\zeta} M_{\zeta\zeta y}] + y [(m+1) M_\zeta M_{\zeta\zeta y} - \\ & - m M_{\zeta y} M_{\zeta\zeta}] + [(m+2)M - \zeta M_\zeta] M_{\zeta\zeta\zeta} = - \{ f^2 k e^m / \beta \epsilon g D^{m+2} \} M_{\zeta\zeta\zeta\zeta} \end{aligned} \quad (6)$$

Because M does not depend on  $x$ , the first term in curly brackets on the right-hand side must be a function of  $y$  alone:

$$D^{m+3} = (m+3) \{ f^2 k e^m A(y) / \beta \epsilon g \} (-x) \quad (6')$$

where  $A(y)$  is any function of  $y$ .

If  $M_y = 0$  then the horizontal advective terms vanish identically.

$A(y)$  must be constant, say 1 and

$$((m+2)M - \zeta M_\zeta) M_{\zeta\zeta\zeta} = -M_{\zeta\zeta\zeta\zeta} \quad (7)$$

Hence, the vertical balance

$$w \rho_z = k \rho_{zz} \quad (8)$$

It is convenient to rewrite (7) by putting M in the form

$$M(\zeta) = [\zeta^{m+2}/(m+1)(m+2)] + N(\zeta) \quad (9)$$

For  $N$  one finds

$$[(m+2)N - \zeta N_{\zeta}][m\zeta^{m-1} + N_{\zeta\zeta\zeta}] = -m(m-1)\zeta^{m-2} - N_{\zeta\zeta\zeta\zeta} \quad (10)$$

and the boundary conditions on  $N(\zeta)$  are:

$$\begin{aligned} N(0) &= N_0 \\ N'(0) &= 0, \text{ if } m \neq 0 \\ N'(0) &= -1, \text{ if } m = 0 \\ N'(\infty) &= 0 \end{aligned} \quad (11)$$

$$\text{Then } w(x, y, 0) = \frac{\kappa(m+2)}{D(x, y)} N(0) \quad (12)$$

The first of (11) specifies the strength of the Ekman pumping at  $z=0$ . Eq. (12) was gotten from (5) and (6'). As  $N_0 \rightarrow -\infty$  with all other external boundaries fixed, one can anticipate recovering the ideal fluid limit.

The second boundary condition in (11) is that the surface density is  $\rho_0$ , in terms of  $N$  density is

$$\rho = \rho_0(1 + \varepsilon(-z/e)^m + \varepsilon(D/e)^m N_{\zeta\zeta}) \quad (13)$$

so that if the surface density is to be  $\rho_0$ , the case  $m=0$  must be distinguished. The third condition in (11) is that deep density field and the density on the eastern boundary, is given by the resting stratification (see eq.4). This condition also implies that the horizontal velocities in (5') also vanish at great depth. If we take a special case, when  $m=0$  in addition to  $A=1$  and  $M=0$ , we can get from (5), (6'), (8), (13):

$$w\rho_z = k\rho_{zz}, \rho = \rho_0(1 + \varepsilon + \varepsilon N_{\zeta\zeta}), w = -\frac{\beta \varepsilon g}{\rho^2} D D_x [2N - \zeta N_{\zeta}], D^3 = \frac{\beta^2 k}{\beta \varepsilon g} (-x) \quad (14)$$

From (5) it follows that the deep upwelling velocity is not a function of  $z$ :

$$w_{\infty} = \frac{2\kappa N(\infty)}{D(x, y)}$$

The vertical velocity at the surface is  $w(x, y, 0) = w_e(x, y) = \frac{2\kappa N(0)}{D(x, y)}$

In this case the N equation is

$$(2N - \zeta N_\zeta) N_{\zeta\zeta\zeta} = -N_{\zeta\zeta\zeta\zeta} \quad (15)$$

the boundary conditions are: (Numerical solutions Fig. 1, 2, 3)

$$\begin{aligned} \text{a) } N(0) &= N_0 \Rightarrow w_e(x, y) = 2kN_0/D \\ \text{b) } N_\zeta(0) &= -1 \Rightarrow \rho(x, y, 0) = \rho_0 \\ \text{c) } N_{\zeta\zeta}(\infty) &= 0 \Rightarrow \rho(x, y, -\infty) = \rho_0(1+\varepsilon), \rho(0, y, z) = \rho_0(1+\varepsilon) \quad (16) \\ \text{d) } N_\zeta(\infty) &= 0 \Rightarrow u(x, y, -\infty) = v(x, y, -\infty) = 0 \end{aligned}$$

It follows from d) that  $N(\infty) = \text{const}$ , that is  $w_\infty$  independent from  $\zeta$ , so  $\rho = \text{const}$  at depth.

In numerical solution as  $N_0 \rightarrow \infty$ , i.e. Ekman pumping is very strong, the solution develops an internal boundary layer at some position  $\zeta^*$ , so the right-hand side of (15) is very small everywhere outside this boundary layer.

$$N_{\zeta\zeta\zeta} = 0 \quad (\zeta < \zeta^*) \Rightarrow N = -(\zeta - \zeta^*)^2/2$$

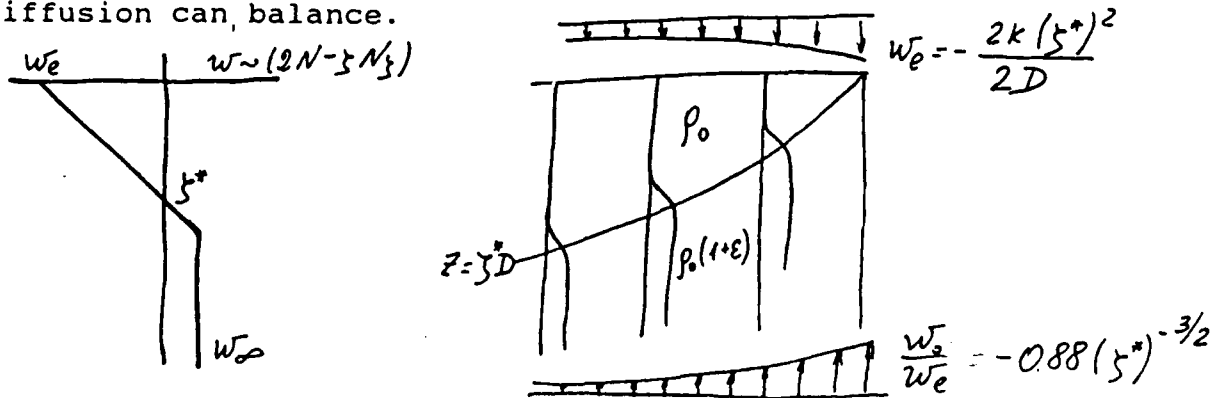
$$2N - \zeta N_\zeta = 0 \quad (\zeta > \zeta^*) \Rightarrow N = 0$$

where  $\zeta^*$  is defined by  $\zeta^* = (-2N_0)^{1/2}$ . (17)

The asymptotic  $\zeta^* \rightarrow \infty$  estimation of  $N_\infty$ :

$$N_\infty = 0.44(\zeta^*)^{3/2} + \frac{1}{2\zeta^*} + O((\zeta^*)^{-3/2}) \quad (18)$$

Heat diffuses out of the bowl through the boundary layer and into the abyssal region. This diffusive flux is balanced by a vertical upwelling which is related to the surface Ekman pumping by  $W_\infty = -0.88(d/a)^{1/2} w_e$ , where  $d$  is "diffusive depth",  $d = D/\zeta^*$  and  $a$  is an "advective depth"  $a = \zeta^* \cdot D$  and  $D = a^{2/3} d^{1/3}$  is the vertical scale on which advection and diffusion can balance.



In the case  $m=1$  the density at the eastern boundary increases linearly of depth (5). This is also the stratification in the abyss, below the influence of surface conditions

$$\begin{aligned}\rho &= \rho_0 [1 + \varepsilon(z/e) + \varepsilon(D/e)N_{zz}] \\ w &= -(\beta \varepsilon g / 4^2)(D/e) D D_x (3N - 5N_z) \\ D^4 &= [4\phi^2 k e / (\beta \varepsilon g)] (-\infty) \\ w_e &= 3k N_0 / D\end{aligned}\quad (19)$$

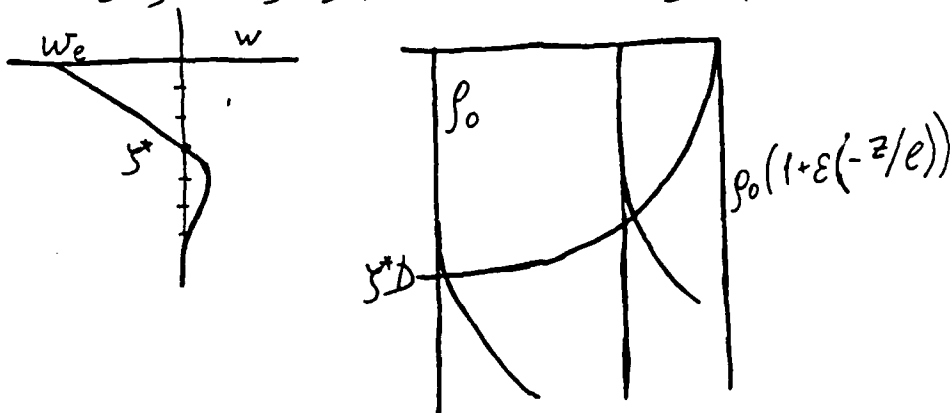
The equation for  $N$  and the associated boundary conditions are:

$$\begin{aligned}(3N - 5N_z)(1 + N_{zz}) &= -N_{zz} \\ N(0) &= N_0 \\ N_{zz}(0) &= 0 \Rightarrow \rho(x, y, 0) = \rho_0 \\ N(\infty) &= 0 \Rightarrow \rho(x, y, z \rightarrow -\infty) = \rho_0 [1 + \varepsilon(-z/e)] = \rho_0(0, y, z)\end{aligned}\quad (20)$$

(Numerical Solutions Fig 4 and 5)

A simple analysis of (20) shows that if  $zN_z \rightarrow 0$  as  $z \rightarrow \infty$ , then  $N$  must vanish. Consequently the vertical velocity vanishes at great depth and this implies that the advective flux of heat also vanishes in abyss. So,  $w_\infty = 0$ ;  $u=v=0$ ,  $N_z=0$ . If  $(N_0) \gg 1$ , then  $N_{zz}$  is small so

$$\begin{aligned}1 + N_{zz} &= 0 \quad (z < z^*) \Rightarrow N = -(z - z^*)^2 (z + 2z^*) / 6 \\ 3N - 5N_z &= 0 \quad (z > z^*) \Rightarrow N = 0, \quad z^* = (-3N_0)^{1/3}\end{aligned}\quad (21)$$



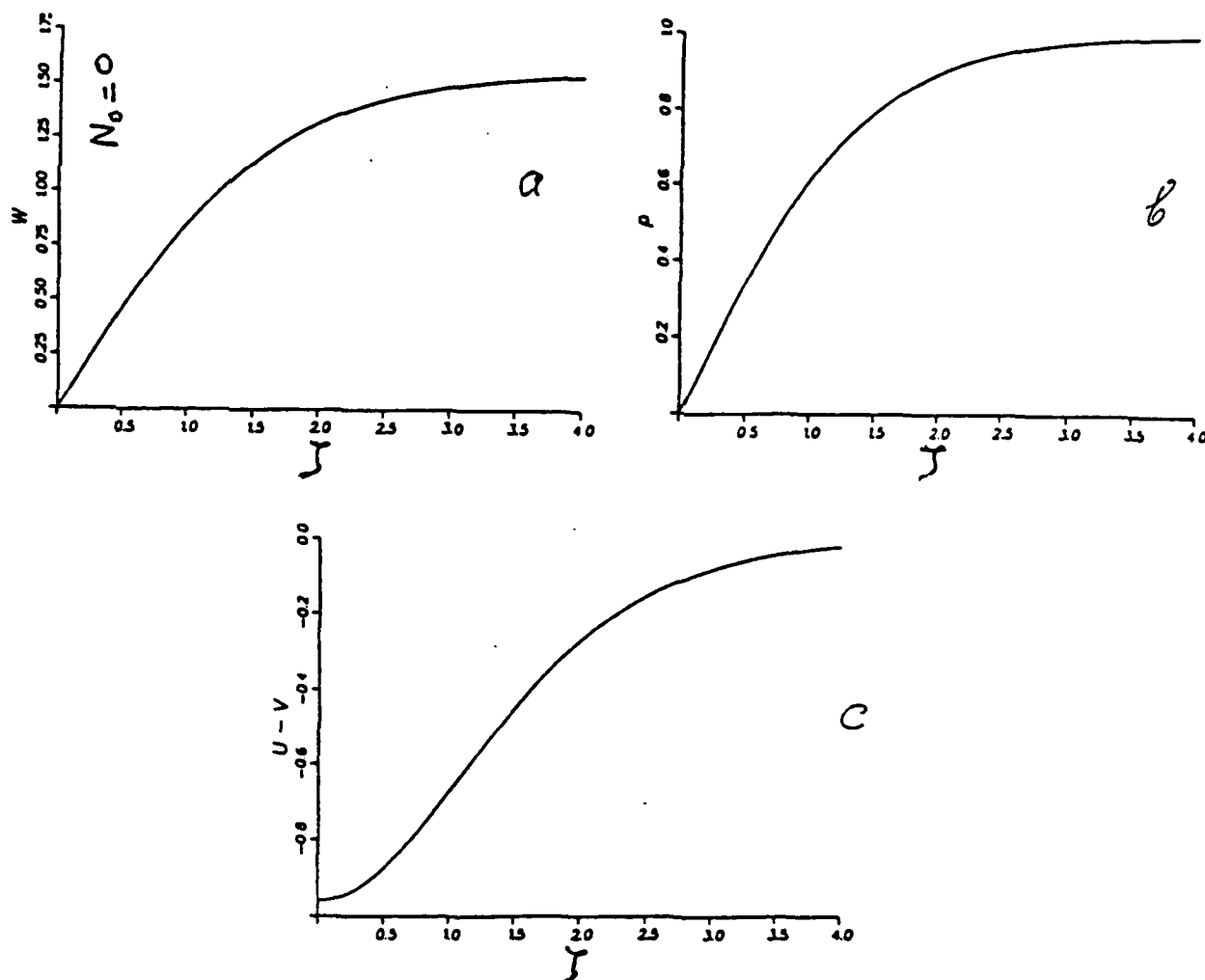


Fig 1. Solution of (15), when  $N_0 = 0$ . (a)-In this case the vertical velocity is zero at the surface and approaches a constant positive value at great depth. The density field (more precisely  $\varepsilon^{-1}[\rho - \rho_0(1 + \varepsilon)]$ ) (b)-There is a smooth transition from  $\rho_0$  (surface density) to the abyssal density  $\rho_0(1 + \varepsilon)$ . (c)-The horizontal velocity difference  $u - v$ .

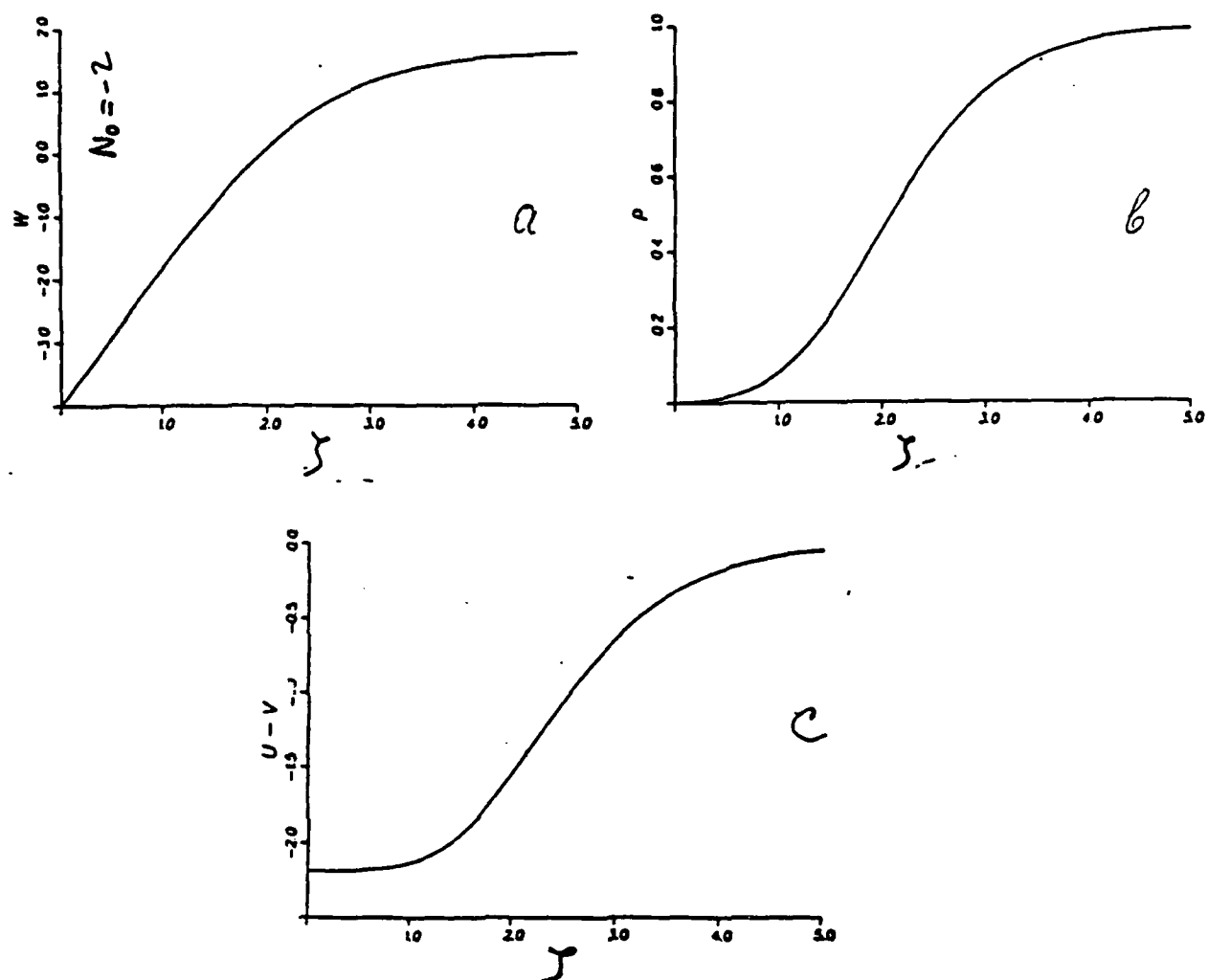


Fig 2. Solution of (15), when  $N_0 = -2$ . Here the vertical velocity is large enough to produce a "pycnostad".

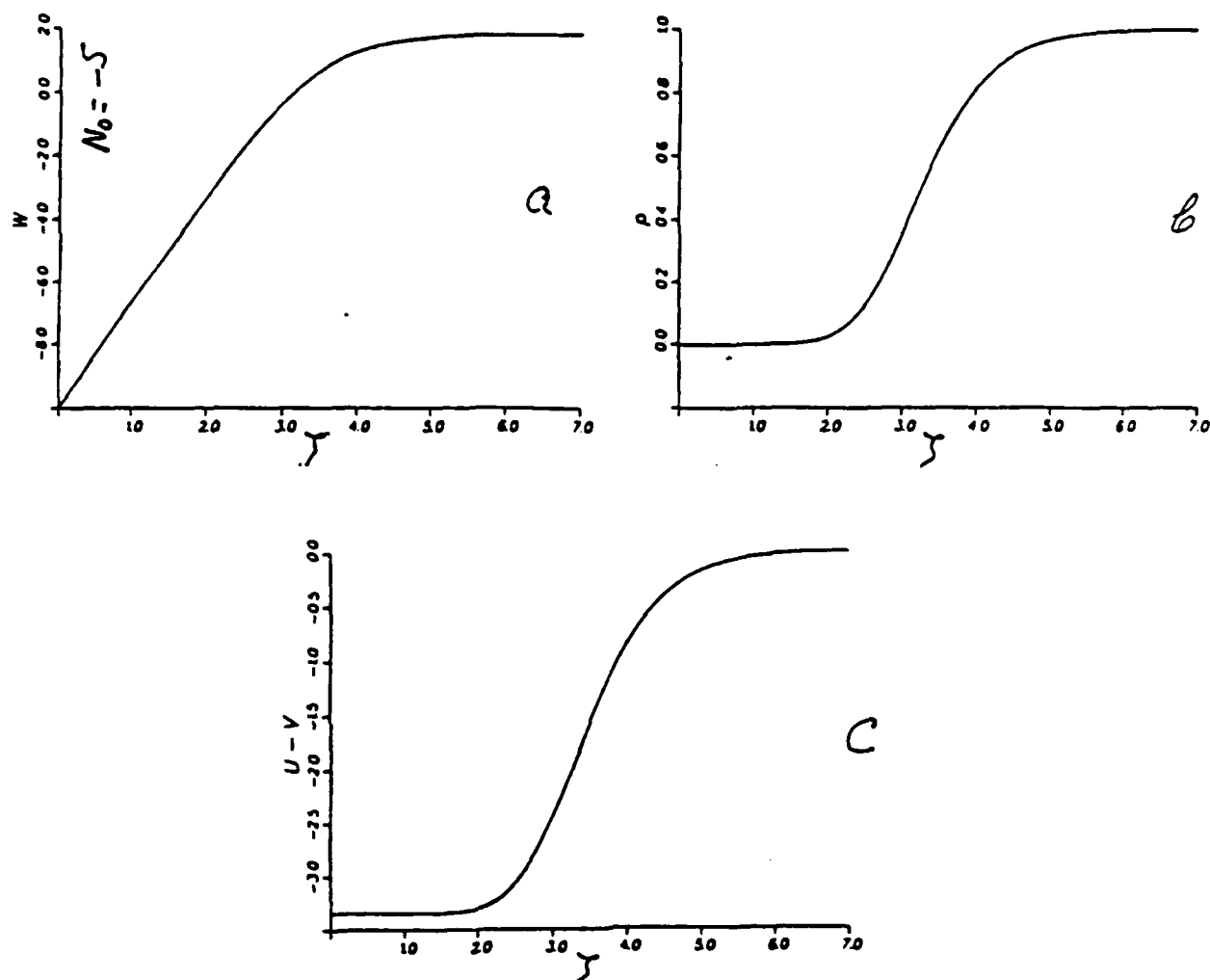


Fig 3. Solution of (15) when  $N_0 = -5$ . There is a region of uniform density extending down to about  $y = 2$ . There is an internal boundary layer at about  $y = 3.5$  ( $y^* = (-2N_0)^{1/2}$  from (17),  $N_0 = -5$ ,  $y^* = \sqrt{10}$ ). Below the internal boundary layer there is the uniform upwelling regime, when an advective heat flux balances the diffusive flux from the bowl of warm fluid above  $y = y^*$ .



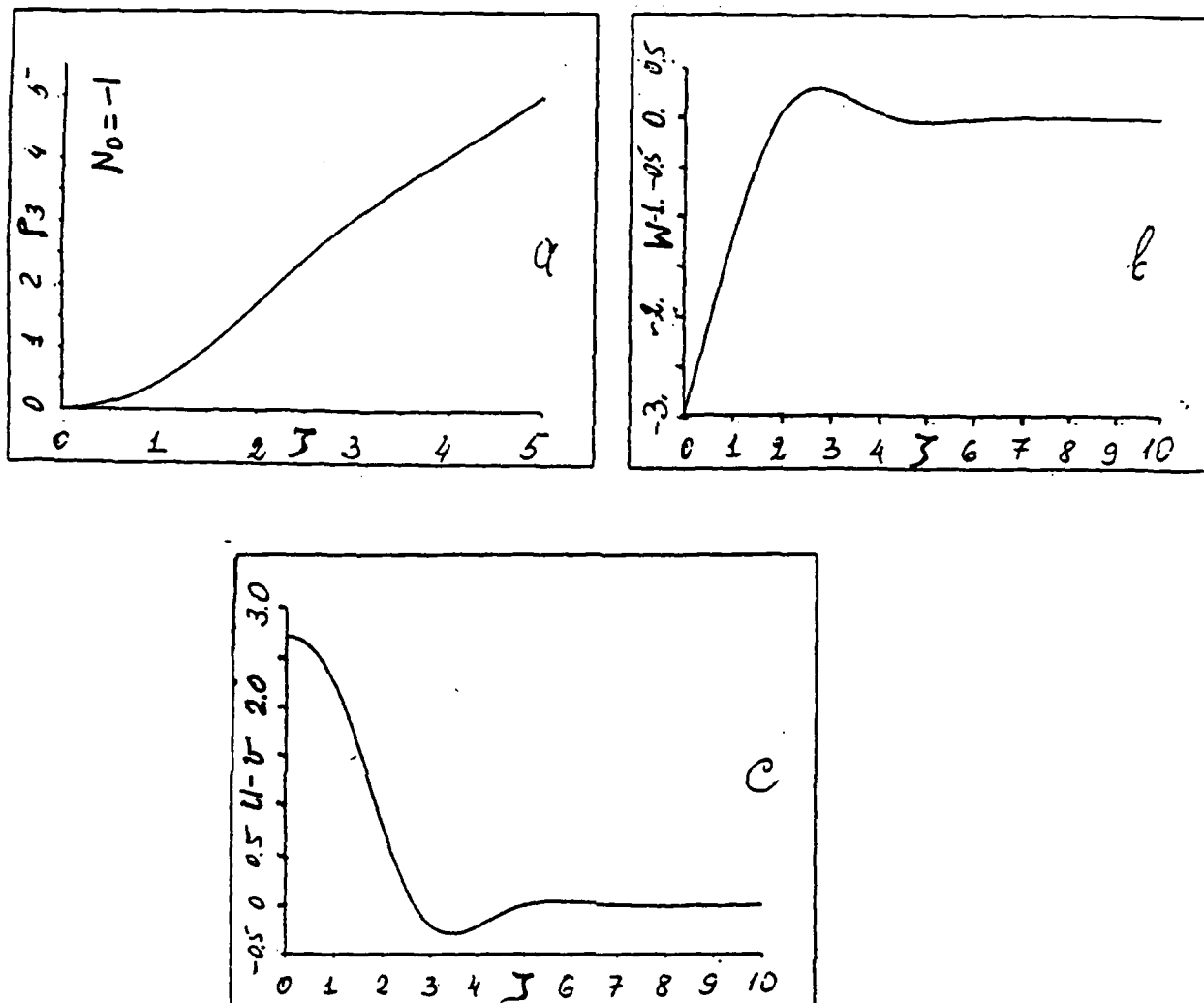


Fig 4. Solution (20) with  $N_0 = -1$ . There is no density inversion in this full nonlinear solution. Also in contrast to the  $m=0$  solution in Fig 1-3 the vertical velocity vanishes in the abyssal region.

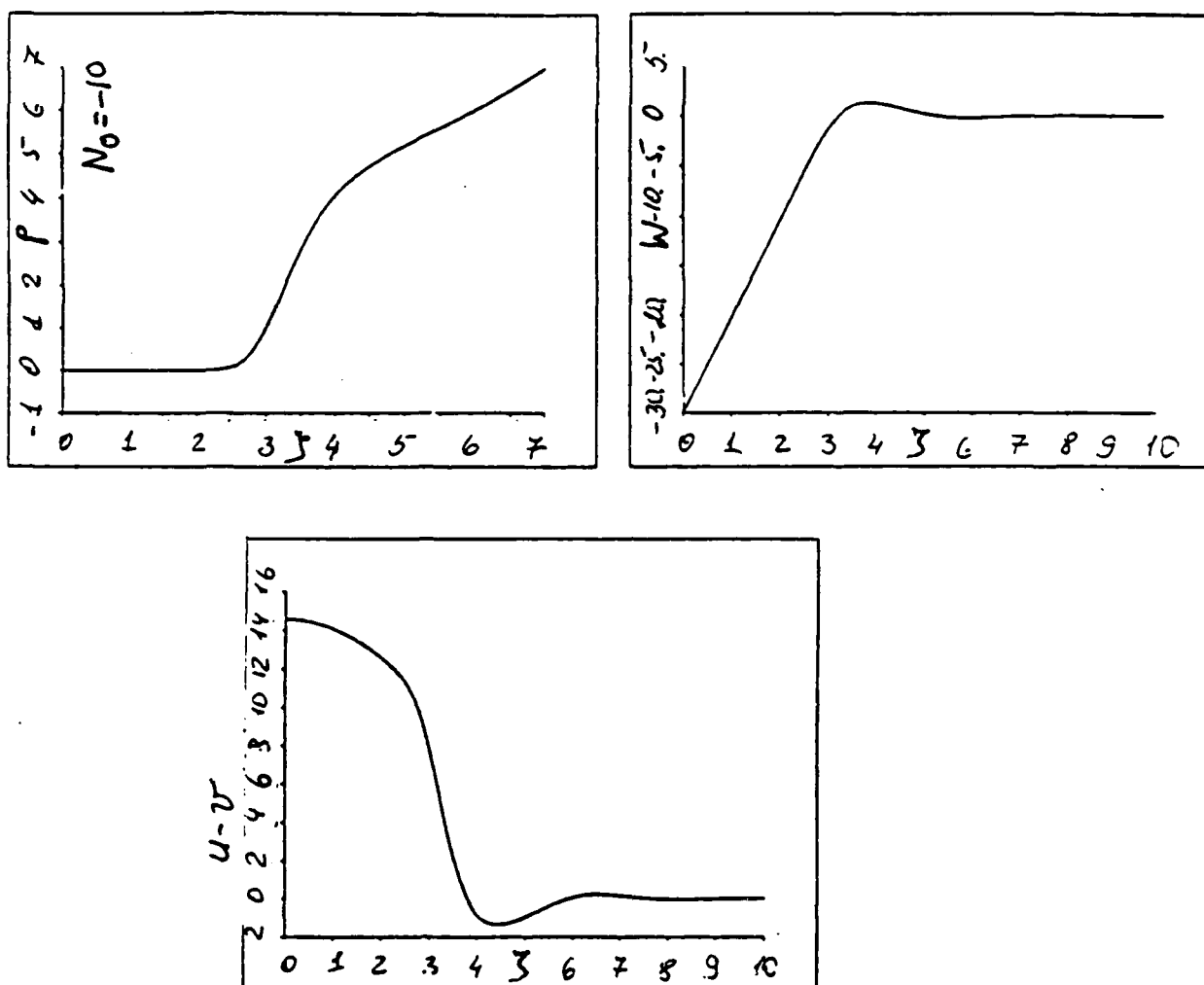


Fig 5. Solution (20) when  $N_0 = -10$ . In this case the vertical velocity is large enough to create a "pycnostad" of density  $\rho_0$  which extends down to about  $z = 2.7$ . The vertical velocity is a linear function of depth in this region. The pycnostad is bounded below by an internal boundary layer at about  $z = 3.6$  (compare with  $z = \sqrt[3]{30}$  from (21)). At still greater depth there is linearly stratified motionless fluid.

**References:**

J.R. Luyten, J. Pedlosky and H. Stommel. 1983. J.P.O., 13, pp. 292-309.

W.R. Young and G.R. Ierley, 1986. J.P.O., 16, pp. 1887-1900.

Notes prepared by: Irene G. Yushina, P. P. Shirshov  
Institute of Oceanology, Moscow

**1989 Summer Study Program**

**in**

**Geophysical Fluid Dynamics**

**ABSTRACTS OF PARTICIPANTS**

*Summer Geophysical Fluid Dynamics volume, 1989.*

## The flow over San Lorenzo sill

ANTOINE BADAN-DANGON

CICESE

At the southern end of Ballenas Channel, in the Gulf of California, the ridge that supports San Lorenzo island extends southward for about 25 km and then bends towards the peninsula of Baja California, forming a sill at 435 m depth, which divides the southern end of the 1600m deep Ballenas channel from the Guaymas Basin, itself over 2500 m deep. Current observations in the lower half of the water column over the sill indicate a mean inflow that varies from zero at middepth to about  $0.5\text{ms}^{-1}$  near the bottom. Tidally induced velocity fluctuations close to  $0.5\text{ms}^{-1}$  are independent of depth, and superimposed on the mean velocity profile so the flow reverses direction regularly at middepth, but seldom does so near the bottom. This configuration of the flow suggests that the concepts of the hydraulics of two layer exchange over an oceanic sill are useful in assessing the consequences of this inflow into Ballenas channel.

### Two layer exchange

The essence of the exchange between two basins of different water characteristics is that it usually takes place in two layers separated by an interface which extends asymmetrically through the straits from one basin to the other, and conforms to the requirements of continuity of the flow and conservation of the energy difference between the two layers (Gill, 1977, 1982; Armi, 1986). When this is the case, there exists at least one section of *hydraulic control* of the flow, where the flow is transitory through a condition of criticality, expressed by the composite Froude number, which for two layer exchange is

$$G^2 = F_1^2 + F_2^2 - (1 - r)F_1^2 F_2^2 = 1, \quad (1)$$

where  $F_i^2 = u_i^2/g'y_i$  is the internal densimetric Froude number,  $u_i$  is the fluid velocity, and  $y_i$  is the thickness of each layer,  $i = 1, 2$ . The reduced gravity is  $g' = (1 - r)g$ , with  $r = \rho_1/\rho_2$ . In oceanic applications it is usual that  $(1 - r) \ll 1$ , whence the statement of hydraulic control is simply

$$G^2 = F_1^2 + F_2^2 = 1. \quad (2)$$

The geometry of the straits connecting the two basins is defined by its breadth  $b(x)$ , and by the configuration of the bottom  $-h(x)$ , usually referred to the crest of the sill  $h_0 = 0$ . The height of the free surface of the ocean above the bottom is then the sum of the layers thicknesses  $y_1 + y_2$ . In nondimensional terms,

$$b' = b/b_0, \quad (3)$$

$$h' = h/(y_1 + y_2)_0, \quad (4)$$

$$y'_i = y_i/(y_1 + y_2)_0, \quad (5)$$

where  $b_0$  is a reference breadth, and  $(y_1 + y_2)_0$  is the total water depth at the sill; since the external Froude number is small, the free surface of the ocean can be approximated as a rigid lid

$$y'_1 + y'_2 + h' = 1. \quad (6)$$

The volumetric flow rate in each layer,  $q_i = u_i y_i b$ , is fixed along  $x$  since the flow is steady and the two layers are immiscible within the straits. Then,  $q_r = q_1/q_2$  is the ratio of the flow rates and  $q_r = 1$  expresses the absence of a net barotropic flow. The velocities and the flow rates are expressed in nondimensional form as

$$u'_i = \frac{u_i}{[g'(y_1 + y_2)_0]^{\frac{1}{2}}}, \quad (6)$$

$$q'_i = \frac{q_i}{g'^{\frac{1}{2}} b_0 (y_1 + y_2)_0^{\frac{3}{2}}}. \quad (7)$$

The Bernoulli function of each layer can be expressed as

$$H_1 = \frac{1}{2} u_1^2 + \rho_1 g (y_1 + y_2 + h), \quad (8)$$

$$H_2 = \frac{1}{2} u_2^2 + \rho_1 g y_1 + \rho_2 g (y_2 + h). \quad (9)$$

The energy difference between the two layers, nondimensionalized by  $g' \rho_2 (y_1 + y_2)_0$ , is then

$$2\Delta H' = u_1'^2 - u_2'^2 + 2y'_1 - 2, \quad (10)$$

which is a conserved quantity in the straits, in the absence of hydraulic jumps or other dissipative processes.

The internal Froude numbers are the essential expression of the nonlinearity of the flow, and crucial indicators of hydraulic control in the straits. It is useful

then to express the behavior of the flow in Froude number space  $F_1^2, F_2^2$  (Armi, 1986). The layer thicknesses can be written as

$$y'_i = \left( \frac{q'_i}{b'} \right)^{2/3} F_i^{-2/3}, \quad (11)$$

the rigid lid approximation (6) becomes

$$q_r^{2/3} F_1^{-2/3} + F_2^{-2/3} = \left[ \frac{q'_2}{b'(1-h')^{3/2}} \right]^{-2/3}, \quad (12)$$

and the energy difference equation (10) can be written

$$F_2^2 = q_r \left[ 2F_1^{-2/3} + F_1^{4/3} - 2\Delta H' q_1'^{-2/3} \right]^{3/2}. \quad (13)$$

The solutions to this set of equations have been discussed in detail by Armi (1986), with particular emphasis on the differences between narrows, where the geometry controls both layers of the flow directly, and sills, where only the lower layer is influenced by the topography and the upper layer responds indirectly through hydraulic requirements. In both cases, there exists a particular solution, which requires that two control sections bound a central portion of the straits in which the flow is subcritical; away from these sections the flow is supercritical into each basin, the supercriticality being attributable to a different layer in each basin. This solution is named the *maximal exchange solution*, since it identifies the optimal rate of exchange for the conditions prescribed in the straits and in the adjacent basins. The maximal exchange solution for a simple contraction ( $h(x) = 0$ ) results in a nondimensional transport  $q'_i = 0.25$  and equal layer thicknesses  $y'_1 = y'_2 = 0.5$  at the sill (Armi and Farmer, 1986). The maximal exchange solution for a sill and the combination of a sill and a contraction are examined in detail by Farmer and Armi (1986); they obtain  $q'_i = 0.208$  and a ratio of the layer thicknesses  $y'_1/y'_2 = 5/8$ , and thus, for a given set of conditions, the flow rate over a sill is somewhat less than through a contraction. The maximal exchange solution is unique for each geometry, and any other flow configuration is therefore submaximal, as has been emphasised by Armi and Farmer (1987).

The maximal exchange problem can be posed in a simplified manner once the requirement of the two control sections is established (Farmer and Armi, 1986; Bryden and Kinder, 1989). The first control usually takes place at the crest of the

sill ( $h_0 = 0$ ); the second control section could be at a neighboring contraction, at the exit of the straits, or at any other section  $e$ , say, sufficiently removed from the first one for the upper layer to become thin enough to make  $F_{1e}^2 = 1$ . Then the control statements are

$$\frac{u'_{10}{}^2}{y'_{10}} + \frac{u'_{20}{}^2}{y'_{20}} = 1 ; \quad \frac{u'_{1e}{}^2}{y'_{1e}} = 1. \quad (14)$$

Continuity now requires

$$u'_{10}y'_{10} = u'_{1e}y'_{1e}B, \quad (15)$$

where  $B = b_e/b_0$  is the ratio of the widths of the two control sections. The Bernoulli energy difference (10) is conserved between the two sections:

$$u'_{20}{}^2 - u'_{10}{}^2 - 2y'_{10} = -u'_{1e}{}^2 - y'_{1e}, \quad (16)$$

and, if  $q_r = 1$ ,

$$u'_{1e}y'_{1e} = -u'_{20}y'_{20}. \quad (17)$$

Bryden and Kinder (1989) inscribe the problem in the geometry of a triangular cross-section, in the fashion of Bormans and Garrett (1989), neglect  $u'_{10}{}^2$  in favor of  $u'_{20}{}^2$ , and obtain two approximate expressions that relate  $y'_{10}$  and  $y'_{1e}$ :

$$5y'_{10} - 1 = 6y'_{1e}, \quad (18)$$

$$B^{2/3}(1 - y'_{10})^{5/3} = 2y'_{1e}, \quad (19)$$

which they solve iteratively to get  $y'_{10} \approx .479$  and  $q'_i = 0.069$ , for the case of the straits of Gibraltar. For the sill at San Lorenzo, the cross-sectional area can be taken to be triangular for the lower layer, but rectangular for the upper layer. Equation (19) now becomes simply

$$(1 - y'_{10}) = 2By'_{1e}, \quad (20)$$

and together with (17), assuming  $B = 1$ , provides  $y'_{10} = 1/2$ ,  $y'_{1e} \approx 1/4$ , and  $q'_i = 1/8$ . With this particular geometry we have recovered, over a sill, the layer configuration first proposed by Stommel and Farmer (1953) and by Bryden and Stommel (1984), which otherwise should correspond to the maximal exchange solution through a contraction (Armi and Farmer, 1986). The transport, however, is halved because it is now confined to a lower layer of triangular cross-section.



### Application

Ballenas channel is bounded at its southern end by the sill at San Lorenzo, which concerns us here, and by a contraction near the northern end of Angel de la Guarda island, 130 km to the north, where it connects with the shallow northern Gulf of California. There is ample evidence of intense mixing within the channel. Satellite images indicate the permanent presence of cool water at the surface, particularly near the sills; plumes of cool water spread away from the channel, and a well defined front often forms to the south of the sill at San Lorenzo (Badan-Dangon, Koblinsky, and Baumgartner, 1985). Tidal flows are prominent in the channel, and Filloux (1973) has calculated considerable tidal dissipation around the islands. Often, hydrographic sections suggest the presence of hydraulic jumps in the lee of the sill, and strong boils appear at the surface of the channel in their vicinity. Fu and Holt (1984) have reported packets of internal solitons that propagate away from the sills as the flow reverses with each tidal cycle. Such strong mixing acts to decouple the sill from the contraction, since any net flow through one of them should appear as a barotropic flow of Ballenas channel water to the other.

These observations also support the idea that the flow must be supercritical at least during part of the tidal cycle. The current meter observations made over the sill at San Lorenzo support a mean inflow of  $1.36 \times 10^5 \text{ m}^3 \text{ s}^{-1}$  into the channel, flowing through a layer which can be estimated to occupy somewhat less than the lower half the water column. From the theory of two layer exchange, we expect an equivalent outflow through the upper layer, which removes water warmed at the surface of the channel. A typical temperature difference between the inflow and the outflow is about  $3^\circ \text{C}$ . An approximate reduced gravity results

$$g' \sim \rho^{-1}(\Delta\rho)g \sim \alpha(\Delta T)g \sim 5 \times 10^{-3} \text{ ms}^{-2}, \quad (21)$$

where  $\alpha = 2 \times 10^{-4}$  is the coefficient of thermal expansion. By eq. (7), the nondimensional exchange flow is  $q'_i \sim 0.04$ . Clearly, the exchange over the sill is submaximal in the mean. Indeed, the speed of long internal waves on a (virtual) interface of  $3^\circ \text{C}$  is about

$$c = \left[ g' \frac{(y_1 y_2)}{(y_1 + y_2)} \right]^{1/2} \sim 0.4 \text{ ms}^{-1}, \quad (21)$$

much above the average speed of the inflow,  $0.2 \text{ ms}^{-1}$  over the sill. The flow must then be supercritical only during those portions of the tidal cycle when the

velocity of the flow surpasses that of the waves. The exchange flow would probably be better represented by taking into account the strong time dependent variations in the criticality of the flow.

Nonetheless, the measured inflow has considerable consequences. The channel operates in reverse fashion to the Mediterranean, and requires the upper layer to remove the heat (buoyancy) gained at the surface of the channel (Badan-Dangon and Hendershott, 1985). Of course, it is the powerful stirring by the tides that mixes the water column inside the channel and provides the energy to drive the two layer exchange over the sill; the heat gain inside the channel is incidental to this process. Calculations of the baroclinic pressure from hydrographic observations across the sill indicate a gradient directed southward in the upper layer, of about 0.02 m per 10 km of equivalent pressure head, reversing to an equal but opposite value in the lower 200 m of the water column. These values are quite comparable with the tidal sea surface slopes proposed by Filloux (1973). Given that distribution of the currents, the channel exports heat at a rate equal to  $1.35 \times 10^5 \text{ }^\circ\text{C m}^3\text{s}^{-1}$ , or about  $5.69 \times 10^{11} \text{ W}$  of heat flow for every degree of temperature difference between the upper and lower layers. This represents, for the  $3 \text{ }^\circ\text{C}$  difference between inflow and outflow, about  $7.2 \times 10^6 \text{ W.m}^{-2}$  of heat deficit through the section of the lower layer over the sill. If this heat loss were to be replaced entirely by gains from the atmosphere, it would require close to  $525 \text{ W.m}^{-2}$  of net heat gain through the total surface,  $3.25 \times 10^9 \text{ m}^2$ , of Ballenas channel. This is considerably larger than the heat gain of about  $50 \text{ W.m}^{-2}$  that has been reported for the northern gulf (Lavin and Organista, 1988). Translated in terms of vertical eddy heat diffusivities inside the channel, such that

$$w \frac{\delta T}{\delta z} = \kappa \frac{\delta^2 T}{\delta z^2} \quad (23)$$

holds, suggests values of  $\kappa$  of about  $20 \text{ cm}^2\text{s}^{-1}$  for the entire surface of the channel, or about  $10^4 \text{ cm}^2\text{s}^{-1}$  if all the heat were mixed upwards in the region of the hydraulic jumps. These are very large values compared to those usually reported in the open ocean ( $\sim 1 \text{ cm}^2\text{s}^{-1}$ ). Ballenas channel is a portion of the gulf of California, where very large exchanges with the atmosphere take place.

*Acknowledgements.*- I am most grateful to M.C. Hendershott for his hospitality on Crooked Pond, and to Prof. George Veronis for many helpful comments. This research was supported by the Secretaría de Programación y Presupuesto of Mexico.

### References

- Armi, L. (1986). *J. Fluid Mech.* **163**: 27.
- Armi, L. & D. Farmer (1986). *J. Fluid Mech.* **164**: 27.
- Armi, L. & D. Farmer (1987). *J. Geoph. Res.* **92**: 14,679.
- Badan-Dangon & M.C. Hendershott (1985). *Proc. IAPSO meeting, Honolulu*.
- Badan-Dangon, A., C.J. Koblinsky, & T. Baumgartner (1985). *Oc. Acta.* **8**: 13.
- Bryden, H.L. & T.H. Kinder (1989). *Deep-Sea Res.* in the press.
- Bryden, H.L. & H.M. Stommel (1984). *Oc. Acta.* **7**: 289.
- Bormans, M. & C. Garrett (1989). *J. Phys. Oc.* in the press.
- Filloux, J. (1973). *Nature.* **243**: 217.
- Fu, & Holt (1984). *J. Geoph. Res.* **89**: 2053.
- Gill, A.E. (1977). *J. Fluid Mech.* **80**: 641.
- Gill, A.E. (1982). *Atmosphere-Ocean Dynamics*. Academic Press.
- Lavin, M. & S. Organista (1988). *J. Geoph. Res.* **93**: 14,033.
- Stommel, H.M. & H.G. Farmer (1953). *J. Mar. Res.* **12**: 13.

## THE AGULHAS RETROFLECTION AND RING FORMATION

Eric P. Chassignet

The physical mechanisms of the Agulhas retroflection and associated ring formation are analysed in detail in a wind-driven numerical model configured in an idealized South Atlantic-Indian Ocean basin. First, the model retroflection is discussed through illustration of the Agulhas' vorticity balance among various experiments. Then, the ring formation process is described in terms of its vertical structure and the associated energy conversions.

A one-layer model demonstration shows that both inertia and internal friction may account for a partial retroflection where a linear, weakly viscous system has none. When stratification is introduced and baroclinicity increased, the stretching term exerts an increasing influence. With 40 km resolution, terms included so that the numerical model conserves potential vorticity become important as well. When grid resolution is halved, the importance of the extra conserving terms diminishes and the stretching term exerts an even greater influence. The importance of a substantial viscous stress curl along the coast of Africa, as provided by the no-slip condition, is illustrated through comparison with a slippery Africa experiment. Finally, an experiment with a more realistic South African coastal geometry, giving a more realistic order of importance to  $\beta v$  in the separating Agulhas is described. The planetary vorticity advection term plays a smaller role along the coast. Viscous effects on the coastal side of the current are still strong, however, and are balanced primarily by stretching and relative vorticity advection.

Whether rings form in the model and their frequency depend on two primary factors: the shape of Africa and southward inertia/baroclinicity in the overshooting Agulhas. The boundary condition on Africa (no-slip/free-slip) and horizontal resolution are also important. Experiments in which rings form exhibit considerably larger values of KM to KE transfer than those in which no rings form. In three of the experiments, ring formation is studied in detail with the help of instantaneous top and bottom layer flow patterns and time series energetics. In a low Rossby number experiment with a rectangular Africa, rings are formed almost continuously, and basin mode resonance plays a significant role in ring formation. Whether a form of instability (barotropic or baroclinic) plays an important role as well is unclear. In two high Rossby number experiments, one with rectangular and the other with triangular African geometry, basin mode resonance is not a factor, and, it is suggested that ring formation is associated with release of mixed barotropic-baroclinic

instability.

For more details on the experiments, the reader is referred to Boudra and Chassignet (1988), Chassignet and Boudra (1988) and Boudra *et al.* (1989).

#### REFERENCES:

- Boudra, D.B. and E.P. Chassignet, 1988: Dynamics of Agulhas retroflection and ring formation in a numerical model. Part I. The vorticity balance. *J. Phys. Oceanogr.*, 18, 280-303.
- Boudra, D.B., K.A. Maillet and E.P. Chassignet, 1989: Numerical modeling of Agulhas retroflection and retroflection with isopycnal outcropping. In *Mesoscale Synoptic Coherent Structures in Geophysical Turbulence*. B.M. Jamart and J.C.J. Nihoul, Eds. Elsevier, Amsterdam, 319-336.
- Chassignet, E.P. and D.B. Boudra, 1988: Dynamics of Agulhas retroflection and ring formation in a numerical model. Part II. Energetics and ring formation. *J. Phys. Oceanogr.*, 18, 304-319.

# THE PROPAGATION OF ISOLATED NONLINEAR EDDIES IN A TWO-LAYER OCEAN

Eric P. Chassignet

In most previous works, the temporal evolution of isolated rings in numerical models has been described in the framework of a particular approximation such as quasi-geostrophic or reduced-gravity ( $1\frac{1}{2}$  layer) dynamics (Flierl, 1977, 1984; McWilliams and Flierl, 1979; Nof, 1981, 1983). For a review, the reader is referred to Flierl (1987). The departure from quasi-geostrophic dynamics in the ring behavior has been explored in some details by McWilliams *et al.* (1986) using a balance equations model (Norton *et al.*, 1986). The standard was the more general and more complex primitive equations.

Here, we seek to investigate the validity of the second approximation widely used to study the evolution of isolated vortices, the reduced gravity model (one active layer over an infinite one). We concentrate our attention on the following question: How deep does the lower layer of a two-layer system have to be to have a negligible influence on the dynamics of the upper layer? In order to study the transition regime between a finite depth system and the reduced gravity system (infinitely deep second layer), a series of experiments are performed with a primitive equation, isopycnal coordinate, two-layer numerical model whose upper-lower layer depth ratio is varied from 1/5 to 1/1000. We shall then be able to isolate the influence of the lower layer on the dynamics of the upper one. This type of model (Bleck and Boudra, 1986) allows the specification of desired initial conditions through the positioning of the isopycnal surfaces and, in particular, can reproduce the initial conditions of lens-like eddies; *i.e.* ones where isopycnals surface. This model is also free of artificial deterioration of the eddies due to cross-isopycnal numerical diffusion.

The trajectories for both cyclones and anticyclones are presented in Figure 1 as the ratio  $R = H_1/(H_1 + H_2)$  is varied from 1/5 (realistic oceanic ratio) to 1/1000. All rings move westward in analogy to a circular Rossby wave (Cushman-Roisin *et al.*, 1989). They also have a meridional motion (poleward for cyclones and equatorward for anticyclones) due to a form drag on the lower layer (Flierl, 1984) and interactions with the Rossby wave wake in the upper layer. As the thickness of the lower layer increases, the meridional displacement of the ring decreases due to a smaller form drag of the lower layer on the upper layer ring. The only factor remaining important for the meridional displacement is the interaction with the

Rossby wave wake. If this effect is suppressed, the ring should move purely westward. This is effectively the case with a lens. With initial conditions for the ring being Gaussian with a maximum interface displacement of 500 meters and with a radius of maximum velocities equal to 60 kilometers, the influence of the lower layer began to be negligible when equal to 50 kilometers (upper layer thickness for this particular case is equal to 1000 meters).

A scaling analysis of the two-layer system (Cushman-Roisin, 1989, personal communication) provides a criterion specifying how deep the lower layer has to be to justify using the one-layer, reduced gravity model:

$$H \gg \max \left( H_1, \min \left( H_1 \frac{L^4}{L_R^4}, h_o \frac{L_\beta}{L} \right) \right)$$

where  $L_R$  and  $L_\beta$  are the radius of deformation and planetary scale defined as  $\frac{\sqrt{g'H_1}}{f_o}$  and  $\frac{L_o}{\beta_o}$ , respectively. This criterion agrees with the numerical results for the above set of parameters. Further analysis will be performed to confirm the robustness of the criterion. For more details on the derivation and a discussion of the above results, the reader is referred to Chassignet *et al.* (1989).

#### REFERENCES:

- Bleck R. and Boudra D.B. (1986): Wind-driven spin up in eddy-resolving ocean models formulated in isopycnic and isobaric coordinates. *J. Geophys. Res.*, 91, 7611-7621.
- Chassignet, E.P., D. Nof and B. Cushman-Roisin (1989): The propagation of isolated nonlinear eddies in a two-layer ocean. To be submitted.
- Cushman-Roisin, B., E.P. Chassignet and Benyang Tang (1989): On the westward motion of mesoscale eddies. To be submitted.
- Flierl, G. (1977): The application of linear quasi-geostrophic dynamics to Gulf Stream rings. *J. Phys. Oceanogr.*, 7: 365-379.
- Flierl, G. (1984): Rossby wave radiation from a strongly nonlinear warm eddy. *J. Phys. Oceanogr.*, 14: 47-58.
- Flierl, G. (1987): Isolated eddy models in geophysics. *Ann. Rev. Fluid Mech.*, 19: 493-530.

- McWilliams, J. and G. Flierl (1979): On the evolution of isolated non-linear vortices, with application to Gulf Stream rings. *J. Phys. Oceanogr.*, 9, 9, 1155-1182.
- McWilliams, J., P. Gent, and N. Norton (1986): The evolution of balanced, low-mode vortices on the b-plane. *J. Phys. Oceanogr.*, 16: 838-855.
- Nof, D. (1981): On the  $\beta$ -induced movement of isolated baroclinic eddies. *J. Phys. Oceanogr.*, 11: 1662-1672.
- Nof, D. (1983): On the migration of isolated eddies with application to Gulf Stream rings. *J. Mar. Res.*, 41: 399-425.
- Norton, N. J., J. C. McWilliams, P. R. Gent (1986): A numerical model of the Balance Equations in a periodic domain and an example of balanced turbulence. *J. Comp. Phys.*, 67, 439-471.

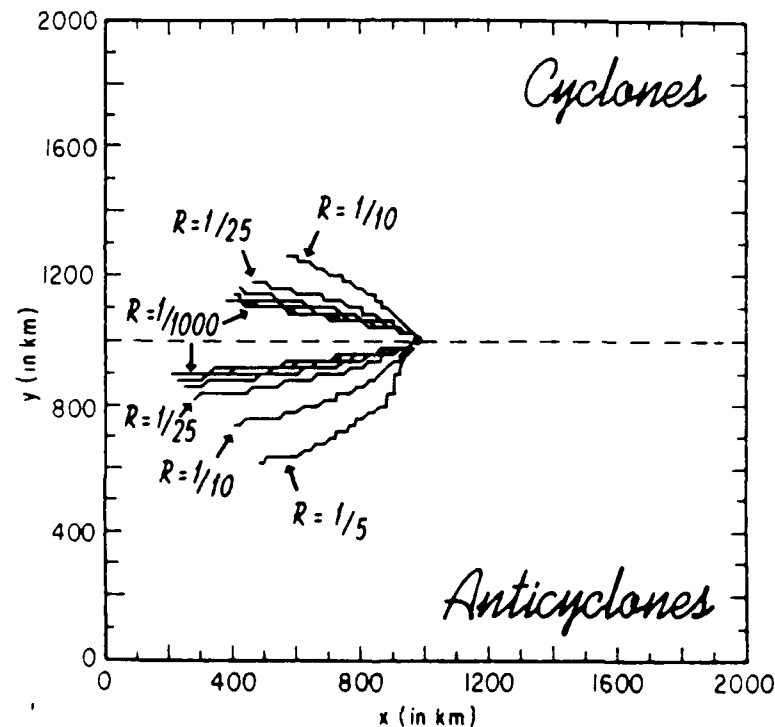


Figure 1: Trajectories of the cyclones (upper half) and anticyclones (lower half) as the depth ratio  $R$  is varied



## KINEMATICS OF OCEANIC SUBDUCTION

Benoit Cushman-Roisin  
Florida State University

### Introduction

Subduction, or the escape of mixed-layer fluid into the deeper circulation, and its twin process, entrainment of underlying stratum in the mixed layer, are mechanisms that couple mixed-layer dynamics with that of the general circulation. While mixed-layer modelers usually take the state of the ocean interior as specified, it is customary for large-scale circulation theorists to represent the mixed layer as a mere converter of surface wind stress into vertical pumping. However, recent theories for the large-scale ocean circulation (Luyten et al., 1983, and sequels) point to the crucial role played by subduction in maintaining the permanent thermocline and its associated circulation. As theories become increasingly refined, the process of subduction deserves thorough consideration.

The purpose of the present lecture is to elucidate the kinematics of subduction (and of its counterpart, entrainment) by inductive reasoning through a series of increasingly more complex models. Yet, prior to the development of these models, it is useful first to define the word subduction and second to clarify the various vertical velocities and volume fluxes that naturally enter the formalism. Some thoughts and results were discussed by Stommel (1979), on whose work the present study is largely based, and a more complete text on the following considerations can be found in Cushman-Roisin (1987).

### Definition of subduction and subduction rate

A definition is hereby proposed: Subduction is the process by which mixed-layer convergence and/or retreat leave formerly turbulent fluid to become part of the underlying stratum. To quantify subduction, one can state: The subduction rate is the volume of subducted fluid per unit time and per unit horizontal area. Subduction rate is thus expressed in meters per second, and entrainment can be considered as negative subduction.

### Vertical velocities and volume fluxes

Four vertical-velocity-like variables naturally appear in the study of subduction:  $\partial h / \partial t$  (the mixed-layer deepening rate),  $w$  (the vertical velocity of a water parcel at the mixed-layer base),  $Su$  (the subduction rate, positive for entrainment, negative for subduction), and  $Ek$  (the Ekman pumping velocity, positive upward). Of course, these quantities are not independent. Continuity of volume, after neglect of evaporation and precipitation fluxes, requires:

$$\frac{\partial h}{\partial t} + \frac{\partial}{\partial x}(hu) + \frac{\partial}{\partial y}(hv) = Su, \quad (1)$$

while a kinematic condition at the mixed-layer base imposes:

$$\frac{\partial h}{\partial t} + u \frac{\partial h}{\partial x} + v \frac{\partial h}{\partial y} + w = Su. \quad (2)$$

Now, if one assumes that the flow in the mixed layer is but the Ekman drift, the first equation becomes:

$$Su = \frac{\partial h}{\partial t} + Ek, \quad (3)$$

which implies that the subduction rate ( $Su$ ) is equal to the Ekman pumping ( $Ek$ ) only if (i) precipitation and evaporation are neglected, (ii) the mixed-layer motion is but the Ekman drift, and (iii) a time-average is performed over a mixed-layer cycle.

Retention of likely geostrophic currents in the mixed layer shows that two additional mechanisms can contribute to subduction. First, since the isobars along which the geostrophic currents flow do not necessarily parallel the isopleths of  $h$ , convergence (divergence) results, and fluid is passed to (entrained from) the interior circulation. Second, the beta-effect induces a divergence of the geostrophic current when it has a meridional component. Orders of magnitude for these different processes show that they are expected to be as large as the Ekman pumping rate, casting doubts on the validity of (3).

### Hierarchy of models

The lecture then continued with the presentation of a series of models analyzing the intermittency of subduction and the properties of waters subducted at different locations and at different times.

Using Beta-Triangle data ( $25^{\circ}\text{N} - 35^{\circ}\text{W}$ ; Stommel, 1979), the first, depth-time model shows that the seasonal cycle is divided into three regimes: effective subduction from late winter until early spring, temporary subduction until complete mixed-layer retreat, and recapture of temporarily subducted fluid during subsequent mixed-layer deepening. Efficiencies in time and in volume can be defined and are estimated to be about 34% and 26%, respectively, i.e. neither small nor large.

The second, latitude-depth-time model illustrates the effect of meridional advection. It is found that even if the mixed-layer depth variability is more temporal than lateral, large spatial variations may occur in the properties of subducted waters. The third, longitude-latitude-depth-time model only stresses the previous conclusion.

### Steady interior

As a year goes by, water parcels passing at the same point in the permanent thermocline will have different latitudes and times of origin, some parcels may have originated in winter further north while some others, six months later or so, may have originated in the spring further south. Hence, it is not guaranteed that the interior stratification will be steady under variable subduction. Requiring that steadiness be the case implies a relation between variables of the mixed-layer (depth  $h$ , density  $\rho$ ) and of the interior (velocity components  $u, v$  and  $w$ ), namely

$$\left(u \frac{\partial h}{\partial x} + v \frac{\partial h}{\partial y} + w\right) \frac{\partial \rho}{\partial t} = \left(u \frac{\partial \rho}{\partial x} + v \frac{\partial \rho}{\partial y}\right) \frac{\partial h}{\partial t}. \quad (4)$$

After retention of only the largest terms, the requirement simplifies to

$$w \frac{\partial \rho}{\partial t} \approx v \frac{\partial \rho}{\partial y} \frac{\partial h}{\partial t}. \quad (5)$$

Data from the North Atlantic show that the latter relation is close to being satisfied, leading us to believe that the spatial and temporal variability of subduction tend to cancel each other to feed a steady interior. Physically, a parcel subducted in

late winter when the mixed layer is deep originates further south than a parcel subducted in the spring when the mixed layer retreats. Since mixed-layer temperature is lowest in the winter but increases southward, both parcels may have identical temperatures.

### Potential-vorticity input

The recent thermocline models (Luyten et al., 1983; and subsequent articles) point to the importance of potential vorticity at the time of subduction in determining the large-scale interior circulation. Here, kinematics considerations are developed to construct the expression of potential vorticity (PV) of particles being subducted. The result is:

$$PV = f \frac{\rho_t + u\rho_x + v\rho_y}{h_t + uh_x + vh_y + w}, \quad (5)$$

which combine variables of the mixed layer ( $h, \rho$ ) and of the interior ( $u, v, w$ ) at the base of the mixed layer. If and only if the oceanic interior is steady, this expression combined with (4) can be reduced to:

$$PV = f \frac{\rho_t}{h_t}. \quad (6)$$

### References

Cushman-Roisin, B., 1987: Subduction. Dynamics of the Oceanic Surface Mixed Layer, Hawaiian Winter Workshop, Inst. of Geophysics, U. of Hawaii at Manoa, 181-196.

Luyten, J.R., J. Pedlosky, and H. Stommel, 1983: The ventilated thermocline. J. Phys. Oceanogr., 13, 292 - 309.

Stommel, H., 1979: Determination of water mass properties of water pumped down from the Ekman layer to the geostrophic flow below. Proc. Natl. Acad. Sci. USA, 76, 3051-3055.

**Connected Thermal and Transport Anomalies  
in the General Circulation**

by  
William Dewar  
Florida State University

**Abstract**

Two models of the oceanic response to cooling are discussed. Both are motivated by a desire to understand the effects of variable diabatic forcing on the general circulation. The first model considers an initial value problem in which an initially resting warm ocean is "slowly" cooled on "broad" scales. The lower layer in this model is fully active and it is further argued that the slow and broad scales are relevant to 18°C water formation. The purpose of this model is to illustrate the short term barotropic and baroclinic response to variability in thermal forcing.

The second problem addresses the longer-term evolution of finite amplitude thermocline anomalies (which are assumed to have been formed by diabatic effects). A "one and three-quarter" layer model is used, i.e., the lower layer is assumed to be deep, but not stagnant, and care is taken to compute its evolution.

Based on these models, it is argued that diabatic forcing can result in local modifications of the Sverdrup constraint and that mass transport evolves through at least three distinct phases. The first short-term ocean response to cooling is the radiation of eastward moving barotropic planetary waves which leave the Sverdrup transport and the planetary geostrophic wave equation (PGWE) in its wake. Local Sverdrup dynamics and the PGWE dominate the second phase of evolution. The last phase occurs as the fronts obtain deformation radius length scales, and the tendency for the system to produce coherent structures results in persistent, spreading regions of anomalous transport. Global measures of the mass transport, however, collapse back to the classic Sverdrup constraint. Implications for the generation of barotropic and baroclinic variability are discussed.

## LOCALIZED STRUCTURES GENERATED BY SUBCRITICAL INSTABILITIES

Stephan Fauve and Olivier Thual  
Ecole Normal Supérieure

Localized structures are widely observed in fluid flows. Well known examples are the local regions of turbulent motion surrounded by laminar flow, which develop in many open-flow experiments (pipe-flow, channel-flow, boundary layers) [1]. More recently, spatially localized standing waves have been observed on a horizontal layer of fluid submitted to vertical vibrations [2], and convection in binary fluid mixtures displayed localized travelling waves [3]. In all cases the possible origin of localized structures lies in the existence of a subcritical instability, which implies that two stable homogeneous states coexist in an interval range of the control parameter. The localized structure then consists of a small region in the bifurcated state surrounded by the basic state. When the amplitude equation that describes the bifurcation, admits a Lyapunov functional, i.e. when there exists a free energy to minimize, a localized structure is not stable; it shrinks or expands. We have shown numerically in the case of a subcritical Hopf bifurcation that the stability of the localized structure is a non-variational effect that traces back to the coupling between the amplitude and the phase of the wave complex amplitude [4]. In slightly dissipative systems, we have shown that these localized structures can be computed perturbatively; the leading order effect of dissipative terms is just to select the size of the structure among a family of scale invariant solitons [5].

### References

1. D.J. Tritton, Physical Fluid Dynamics (chap. 19), Van Nostrand Reinhold Company (1977).
2. J. Wu, R. Keolian and I. Rudnick, Phys. Rev. Letters 52, 1421-1424 (1984).
3. P. Kolodner, D. Bensimon and C.M. Surko, Phys. Rev. Letters 60, 1723-1726 (1988).
4. O. Thual and S. Fauve, J. Physique (France) 43, 1829-1833 (1988).
5. S. Fauve and O. Thual, Solitary waves generated by subcritical instabilities in dissipative systems, (preprint 1989).

## ARNOLD'S THEOREM AND THE INSTABILITY OF ELLIPTICAL VORTICES

Glenn R. Flierl

Center for Meteorology and Physical Oceanography  
MIT

### Arnold's Theorem

When a conserved quantity has a local extremum for an equilibrium state of the system, the system is stable to perturbations. If the gradients with respect to variations in the system state vanish, but the second variations are not definite in sign, the system may be unstable. Frequently, however, the gradient of the energy with respect to deviations from the equilibrium are not zero, and, in order to apply similar arguments, we must construct a different conserved quantity which does have vanishing gradients. This invariant,  $\mathcal{A}$ , is then useful in determining the stability: the state is stable if the second variations are definite in sign. For fluids, the invariant is some combination of the energy and enstrophy and perhaps other conserved quantities. Treating the vorticity as piecewise constant permits us to define systematically the possible isovortical perturbations to the system. Thus we can attempt to determine if  $\mathcal{A}$  is positive for all possible weak perturbations or is negative definite. In either case, the flow is then stable.

Consider the linearized analog to  $\mathcal{A}$ . If we linearize the dynamics, we find that the perturbation energy is no longer conserved (in the case when the gradient of energy did not vanish.) and thus it cannot serve as a suitable quadratic invariant. But the analog to the Arnold invariant is still conserved under the linearized dynamics, so that we can still use the approach above to explore stability to linearized displacements. For quasi-geostrophic motions, we have  $\mathcal{A} = |\nabla\psi|^2 + (f^2/N^2)|\psi_z|^2 + q^2/(d\bar{q}/d\bar{\psi})$ .

For flows with piecewise constant potential vorticity, we can rewrite the dynamics to give equations for the evolution of the boundaries between various regions. There are a number of equilibrium states known for different dynamics and symmetries. We can write the perturbation equations in a fairly simple form if we introduce as coordinates  $\bar{\psi}$  and a tangential coordinate  $s$  proportional to the travel time along the boundary. We can then naturally define the displacement of a contour  $\eta(s, t)$ . We can ensure that the perturbed flow has the same area within contours and thus conserves potential vorticity; we can also define a complete set of functions to represent the  $\eta$  field. The stability problem reduces to a set of ODE's relating the changes in the amplitudes. We can also show there is a quadratic form (in the amplitude variables) corresponding to  $\mathcal{A}$ .

### Sufficiency

When the basic state is sufficiently symmetric, the sine and cosine modes in the expansion of  $\eta$  are decoupled. We then have two equations

$$\begin{aligned} A_t &= -JSB \\ B_t &= JCA \end{aligned}$$

where the  $J$  matrix is diagonal and the  $S$  and  $C$  matrices are symmetric. The invariant is

$$A = A^T C A + B^T S B$$

We can show that when both of the  $S$  and  $C$  matrices are positive definite (meaning all eigenvalues of each are positive), the system is stable. Likewise, if both are negative definite, the invariant is elliptical and perturbations cannot grow; also, we can prove directly that the eigenfrequencies are real. We have furthermore proved that if one matrix is positive definite (or negative definite) and the other is indefinite, then the flow is unstable. This represents an extension of Arnold's theorem to show that the possibility of instability can be realized for some configurations — the necessary condition is sufficient. However, this is not always true, since we have not proved the flow is unstable when both matrices are indefinite. In fact, the elliptical case seems to be a counter example.

### Stability of the Kirchhoff Vortex

For a barotropic elliptical vortex with uniform vorticity inside, rotating at a constant rate, the stability depends on the aspect ratio (unstable for a value  $< 1/3$ ) when the motions are barotropic. Baroclinic (but quasi-geostrophic) perturbations have not been studied previously. We have calculated the matrices as functions of the aspect ratio and the baroclinicity of the perturbation. We have used three cases : (a) azimuthal mode 1 only, (b) azimuthal mode 3 only, and (c) azimuthal modes 1 and 3 together. The results are essentially the same: the vortex is unstable to mode 3 when the aspect ratio is less than a number depending on the vertical wavenumber  $m$  but which is always less than  $1/3$  and decreases as  $m$  increases. Mode 1 perturbations, which cause the axis of the vortex to tilt with height, can be unstable even when the vortex is almost circular if the vertical wavenumber is appropriately chosen. Thus we find an instability to baroclinic perturbations in regions where the vortex is stable to barotropic modes.

When we truncate to only one mode, the Arnold condition becomes both necessary and sufficient. But when we consider a two mode truncation, the condition is necessary and sufficient on the large vertical wavenumber side of the stability boundary, but not on the small wavenumber side.



**FROST HEAVE**  
 Andrew C. Fowler  
 Oxford University

In secondary frost heave, a frozen soil surface 'heaves' upwards due to the suction of groundwater towards the freezing front. The phenomenon can cause spectacular damage to roads and buildings, and is of immense economic importance as a result. Frost heave is not primarily due to expansion of water on freezing, but arises through a capillary suction effect at the freezing front, whereby groundwater is sucked upwards towards it. In secondary frost heave, a thin frozen fringe exists at the freezing front, consisting of a region (mush) of co-existing ice, water and soil, analogous to dendritic mushes in alloy solidification (see GFD 1984). Within this fringe, the overburden pressure is partitioned between the effective pressure  $\phi_e$  (that transmitted through the soil skeleton) and the pore pressure, which itself is partitioned between the water pressure  $\phi_w$  and the ice pressure  $\phi_i$ . In Miller's theory (1980), a capillary/adsorption relation exists between  $\phi_i$  and  $\phi_w$ , i.e.,  $\phi_i - \phi_w = f(W)$ , where  $W$  is water fraction. At the top of the fringe, ice lenses exist parallel to the freezing front. At the base of a lens,  $\phi_i = P$  (overburden), so that  $\phi_w = -f(W)$  there, whereas  $\phi_w \rightarrow \phi_0$  below the fringe, where  $\phi_0$  is the ambient groundwater pore pressure. The resultant pressure difference drives water through the fringe towards the lowest lens. Since  $W$  will vary through the fringe, so will  $\phi_i$ , as well as  $\phi_w$ , and it can occur that the effective pressure  $\phi_e \rightarrow 0$  at some point within the fringe. If this happens, then there is no pressure to keep the soil coherent, and upwelling water can force the soil apart, more or less as a (transverse) fracture; in this way, a new lens is formed within the fringe, and as freezing progresses, a sequence of such lenses is formed.

A realistic model to describe and predict the phenomenon is complicated. The fringe model, for example, is that for a two-phase reactive continuum in a porous medium, and involves four partial differential equations and five algebraic constitutive relations. Such a model is presented by O'Neill and Miller (1985). It is possible to simplify dramatically this model, based on four realistic and major approximations:

- (i) gravity is small;

- (ii) heat advection is small (small Peclet numbers);
- (iii) the fringe is thin;
- (iv) the permeability  $k$  within the fringe is a function of  $W$ ,  $k \propto W^\gamma$ , and the exponent  $\gamma$  is large (e.g.  $\gamma=9$ ). With these simplifications, the model collapses to one of steady heat conduction with two free boundary conditions each of which is determined by a generalized Stefan condition.

The one-dimensional heave problem can in fact be reduced to two linear first order differential equations!! Future work will compare these analytic results in detail with O'Neill and Miller's computed results, and with experimental tests. In conjunction with W. B. Krantz at Boulder, we aim to use a two-dimensional instability theory to explain the formation of patterned ground in permafrost regions. Some of the work reported here is published by Fowler (1989), and there is also a preprint by Fowler and Krantz.

#### References

- Fowler, A. C. 1989, Secondary frost heave in freezing soils. SIAM. J. Appl. Math., in press (August 1989).
- Miller, R. D. 1980 Freezing phenomena in soils. In: Applications of soil physics, by D. Hillel, Academic Press, New York, pp. 254-299.
- O'Neill, K. and R. D. Miller 1985 Exploration of a rigid ice model of frost heave. Water Resour. Res. 21, 281-296.

## Critical Tests of Fossil Turbulence in the Ocean

by

Carl H. Gibson

University of California at San Diego

San Diego, CA 92093

(619) 534-3184

### ABSTRACT

Critical field experiments are needed to distinguish between two quite different categories of physical models for the evolution of stratified ocean turbulence and mixing; that is, fossil turbulence models where active turbulence exists for only the initial stages and a small portion of the lifetime of the scrambled fossil microstructure it produces, and non-fossil turbulence models with no fossil turbulence regime where microstructure is created and decays in continuous equilibrium with the turbulence. Turbulence is defined as a random, eddy-like state of fluid motion where the Reynolds, Froude and Rossby numbers of the eddies exceed critical values. For a flow to be turbulent the inertial-vortex forces of the eddies must exceed the constraining forces of viscosity, buoyancy and rotation. All other motions are by definition nonturbulent. Fossil turbulence is a fluctuation in any flow or physical field produced by turbulence that persists after the flow ceases to be turbulent at the scale of the fluctuation. Fossil turbulence is easy to observe in the laboratory where patches of stratified turbulence always leave fossil turbulence patches (or relics, or footprints, or remnants) of scrambled microstructure that persist long after the flow becomes nonturbulent, or in the atmosphere where persistent contrails of jet aircraft may be seen. The first critical experiment is to establish whether turbulence ever leaves such fossil turbulence remnants in the ocean. If one oceanic fossil of turbulence is observed, the hypothesis (presently accepted by many oceanographers) fails that oceanic turbulence does not leave fossils. Further critical experiments would then be needed to establish whether typical sources, or perhaps all sources, of oceanic turbulence leave fossils, and whether the evolution of stratified, rotating oceanic turbulence and fossil turbulence is qualitatively and quantitatively the same as fossil turbulence in the laboratory, as predicted by fossil turbulence theory. A fossil turbulence interpretation of present ocean microstructure data suggests that turbulence and mixing in many oceanic layers has been vastly undersampled and that large undersampling errors (underestimates) of mean dissipation rates and diffusivities have resulted from taking a non-fossil turbulence interpretation. Present ocean microstructure (and mesostructure for 2D fossil turbulence) sampling and data analysis techniques should be modified to avoid such errors and to take full advantage of the information preserved by fossil turbulence. Towed body rather than dropsonde sampling should be used to increase microstructure data sets to more appropriate sizes and to sample the horizontal mesostructure which may be producing it. More efficient techniques of statistical inference should be developed ("hydropaleontology") that take full advantage of the information preserved by the fossil turbulence.

# OSCILLATORY FLOW OVER TOPOGRAPHY IN A RAPIDLY ROTATING FLUID

J. E. Hart

Department of Astrophysical, Planetary and Atmospheric Sciences  
University of Colorado  
Boulder, CO 80309

June 28, 1989

Quasi-geostrophic flow in a cylinder with both a polar  $\beta$ -effect and zonally varying topography is considered. The rotation rate of the tank is modulated about its mean value  $\Omega_0$  in an amount  $\delta'$  with frequency  $\omega$ . This modulation produces a solid body rotation that sinusoidally sloshes back and forth over the mountains. Linear and nonlinear theories are presented and compared with laboratory experiments. The main features of the theoretical problem are that a very substantial retrograde mean zonal current is generated in the interaction between the sloshing flow and the topography on the  $\beta$ -plane. This mean flow is largest when the external parameters are sub-resonant so that the effective  $\beta$ -parameter is lower than that required for a frequency resonance between the sinusoidal forcing and the frequency of a linear free Rossby wave with a spatial structure equal to that of the topography. The predicted nonlinear Eulerian flows are periodic, not chaotic, although multiple equilibria can occur for realistic laboratory parameter values. However, the Lagrangian particle paths for fluid columns in this barotropic flow are chaotic near the nonlinear resonance. The theoretical results are shown to be in agreement with laboratory experiments.

The bottom topography is taken to be that of a free mode of the linear wave problem,

$$H_b^* = H_b J_n(\alpha_n r) \cos(n\theta), \quad (1)$$

where  $J_n$  is a Bessel function of index  $n$ ,  $r$  is the non-dimensional radius (with scale  $L$ ),  $\theta$  the azimuthal (zonal) angle, and  $\alpha_n$  is the total wavenumber of the topography. It is assumed that  $J_n(\alpha_n) = 0$  so that the topography vanishes at the outer sidewall.

When the tank rotates at an almost constant value of  $\Omega$  the free surface deforms into a parabola given by

$$H_T^* = \frac{\Omega_0^2 r^2 L^2}{2g}. \quad (2)$$

This parabolic distribution of height gives us an equivalent topographic  $\beta$ -effect. In view of the sloshing induced by the modulation of the basic rotation of the tank, the geostrophic pressure is written as,

$$188 \quad p = \frac{\delta' r^2}{4\epsilon} \sin(t) + \phi(r, \theta, t) . \quad (3)$$

With (1)-(3) the governing quasi-geostrophic vorticity equation including an Ekman layer at the bottom becomes,

$$\begin{aligned} \frac{\partial \nabla^2 \phi}{\partial t} + \beta' \left( \frac{\partial \phi}{\partial \theta} + \eta' \sin(t) \frac{\partial \nabla^2 \phi}{\partial \theta} \right) + Q \nabla^2 \phi + S' \sin(t) \frac{\partial h_b}{\partial \theta} \\ + J(\phi, \nabla^2 \phi + \Gamma' h_b) = 0 . \end{aligned} \quad (4)$$

The parameters in this equation are:

$$\beta' = \frac{H_T}{\epsilon D} , \text{ where } H_T = \frac{\Omega_0^2 L^2}{g} , \quad (5a)$$

$$S' = \frac{\delta' H_b}{2\epsilon^2} , \quad (5b)$$

$$\eta' = \frac{\delta'}{2\epsilon \beta'} , \quad (5c)$$

$$\Gamma' = \frac{H_b}{\epsilon D} , \quad (5d)$$

$$h_b = J_n(\alpha_n r) \cos(n\theta) . \quad (5e)$$

$Q$  is the bottom damping parameter and  $\epsilon = \omega/2\Omega_0$  is the Rossby number based on the forcing frequency  $\omega$ . The important parameters are  $S'$ , which reflects the magnitude of the mountain forcing, and  $\beta'$ , which is the nondimensional (w.r.t. frequency)  $\beta$ -effect.

The linear problem for topographic wave excitation leads to a first order equation for the complex amplitude  $F$  which can be written as

$$\frac{dF}{dt} + QF - i\beta F(1 - \eta' \sin(t)) = i S \sin(t), \quad (6)$$

where

$$S \equiv \frac{n S'}{\alpha_n^2} , \quad (7a)$$

$$\beta \equiv \frac{n \beta'}{\alpha_n^2} . \quad (7b)$$

The two important features of the linear solution are that 1) the solution is resonant for all integer values of  $\beta$ , and 2) that  $F$  has a non-zero

average for almost all parameter settings. The fact that the linear solution  $X_s$  has an average means that there is a topographic vortex, in the time-mean, which is not in phase with the topography. This phase shifted mountain vortex is responsible for generating a mean zonal retrograde (westward) jet.

The linear theory predicts large amplitudes near the  $\beta=j=1,2,3,4\dots$  resonances. However, the resonances can be moved when nonlinear effects are included. This problem can be analyzed by studying a weakly nonlinear expansion that focuses on the competition between nonlinearity, friction, and off-resonance in determining the slow-time evolution of the amplitude of a free resonant solution to (6) with  $Q=0$ .

The amplitude equations for the long-time evolution of the near-resonant mode have the form:

$$\left(\frac{d}{d\tau'} + \mu\right) U(\tau') = X_s, \quad (8)$$

$$\left(\frac{d}{d\tau'} + \mu\right) X_c(\tau') = (\delta - U) X_s, \quad (9)$$

$$\left(\frac{d}{d\tau'} + \mu\right) X_s(\tau') = -(\delta - U) X_c - 1, \quad (10)$$

where  $U$  is the amplitude of the zonal jet, and  $X_c$  and  $X_s$  are the amplitudes of the in phase and out-of-phase components of the wave.

Here,  $\beta = j + \Delta$  and

$$\mu = \frac{Q}{S^{2/3}(b_n \text{abs}(I_j)^2)^{1/3}}, \quad (11)$$

$$\delta = \frac{\Delta}{S^{2/3}(b_n \text{abs}(I_j)^2)^{1/3}}. \quad (12)$$

$I_j$  just depends on the resonance index  $j$ . The values of the wave-mean interaction integrals are evaluated numerically. The important result is that  $b_n$  is negative for  $n=1$  topography, but are positive for all  $n>1$ .

The steady solutions for the amplitudes of the mean jet and the periodic waves are given by

$$\mu^2 U + (\delta - U)^2 U + 1 = 0. \quad (13)$$

From (13) it is seen that the maximum amplitude of the retrograde mean current is obtained when  $\delta = -\mu^{-2}$ , and has a value  $U = -\mu^{-2}$ . This relationship giving the biggest mean zonal velocity translates into

$$\Delta_{\max} = - \frac{b_n J_j (j\eta')^2 S^2}{\eta^2 Q^2}, \quad (14)$$

suggesting that large mean Eulerian currents would be obtained on the subresonant side of the  $j$ 'th resonances for  $n>1$ .

Two experimental tests of this theory, and an improved version which contains an additional quenching term  $-cU$  on the RHS of (10) that reflects the generation of Rossby waves by the cross-isobath flow of the wave-excited zonal jet, are given. The appearance of chaotic parcel trajectories in the theory when  $\beta=0.65$  as well as a maximum in the Eulerian retrograde jet at this nonlinear resonance value are both reproduced in an experiment with a water depth of 10cm, radius 22cm, topography amplitude 1cm (peak to valley),  $n=2$ ,  $\Omega_0=3$ , and a modulation amplitude of one percent.

**The Modulated Complex Lorenz Equations:  
Baroclinic Instability with Seasonal Forcing on the  $\beta$ -plane**

J. E. Hart

Dept. of Astrophysical, Planetary, and Atmospheric Sciences  
University of Colorado  
Boulder, CO 80309

We consider the simplest model which can address the question of the effect of seasonally variable zonal winds (or currents) on finite-amplitude baroclinic instabilities. How do nonlinear wave-interactions and direct oscillatory zonal flow forcing compete to determine the finite-amplitude dynamics?

The standard two-layer quasi-geostrophic potential vorticity equations, which include Ekman-layer damping at rigid top and bottom surfaces and along the immiscible interface, can be written as

$$\left(\frac{\partial}{\partial t} + J(P_j, \cdot)\right)(\nabla^2 P_j + F(-1)^j(P_1 - P_2) + \beta r^2) = -q(\nabla^2 P_j) - 0.5q(\nabla^2 P_2 - \nabla^2 P_1)(-1)^j, \quad (1)$$

where  $P_j$ , with  $j=1$  or  $2$ , are the geostrophic stream-functions in the two layers and  $J$  is the Jacobian advection operator. The parameters are the rotational Froude number

$$F = \frac{2\Omega^2 L^2 (\rho_1 + \rho_2)}{gD(\rho_2 - \rho_1)}, \quad (2)$$

a friction parameter

$$q = \frac{\sqrt{\nu\Omega}}{D\omega}, \quad (3)$$

and a dimensionless planetary vorticity gradient parameter  $\beta$ .

The flow is imagined to take place in a cylinder of radius  $L$  that is rotating at a basic rate  $\Omega$ . For simplicity we consider that the layer depths  $D$  and the viscosities  $\nu$  are same in each layer. The specific driving mechanism is not detailed here, but could consist of a lid, differentially rotating at rate  $\omega$ , as is commonly used in laboratory experiments (e.g. Hart, 1972). The timescale is  $\omega^{-1}$ , the horizontal length scale is  $L$  and the velocity scale is  $L\omega$ . The lid-forcing terms are not explicitly included in (1) but would, for the laboratory case, appear on the right-hand-sides of (1) as Ekman suction velocities driven by the lid vorticity.

A basic flow consisting of solid rotation in both the upper and lower layers, but with a vertical shear in the azimuthal velocity  $v$  of magnitude  $2\omega r$  across the two layers, is set up. We analyze the finite-amplitude instability process by making a Galerkin expansion of the two  $P$  fields using the eigenfunctions of the linear stability problem. This procedure yields amplitude equations which are similar to those derived by a more formal weakly-nonlinear analysis.



Split the pressure fields up into their barotropic and baroclinic parts. Then expand them in terms of the linear eigenfunctions (i.e. Bessel functions) and the lowest meanflow-correction that is generated by both the wave self-interaction and the externally imposed seasonal forcing. Write

$$P_1 + P_2 = Q_b \frac{X(t')}{h} J_n(ar) e^{in\theta} \quad (4)$$

and

$$P_2 - P_1 = r^2 + iQ_b^2 \frac{Y(t')}{h} J_n(ar) e^{in\theta} - \frac{Q_b^2 Z(t') J_0(a_1 r)}{n^2 e} \quad (5)$$

with

$$t' = \frac{(Q_b + Q') \alpha^2 t}{2F + \alpha^2} \quad (6)$$

$X(t')$  represents the barotropic part of the unstable wave. The baroclinic part is  $Y(t')$ , and the correction to the mean flow has amplitude  $Z(t')$ . The frictional terms are divided into rigid boundary damping  $Q_b = q$  and interfacial damping  $Q' = q$ . The scaling factors  $h$  and  $e$  are easily determined (Hart, 1986), and do not appear in the amplitude equations describing the state of the wave-mean system (although they do appear in the dimensional amplitudes of the various components of the flow).

When the expansions are substituted into the vorticity equations, a projection onto the expansion set itself leads to a set of five nonlinear amplitude equations. These are:

$$\frac{dX}{dt'} = \sigma (Y - X) + \frac{2i\beta}{1-\Delta} X, \quad (7)$$

$$\frac{dY}{dt'} = (R - Z - \epsilon R \sin(\gamma t')) X - Y + i\beta Y, \quad (8)$$

$$\frac{dZ}{dt'} = \text{Re}(X^* Y) - b Z. \quad (9)$$

The parameters occurring in these equations are a "Prandtl number"

$$\sigma \equiv \frac{Q_b}{Q_b + Q'} \frac{2F + \alpha^2}{\alpha^2} \quad (10)$$

a "Rayleigh number"

$$R \equiv \frac{\sigma \Delta n^2}{Q_b^2}, \quad (11)$$

and an aspect ratio

$$b \equiv \frac{\alpha_1^2}{\alpha^2} \frac{2F + \alpha^2}{2F + \alpha_1^2} \quad (12)$$

$$\Delta \equiv \frac{2F - \alpha^2}{2F + \alpha^2} \quad (13)$$

is the inviscid supercriticality. If  $Q$  is small, the critical neutral

curve is approximately  $F_c = \alpha^2/2$ . Thus  $\Delta$  measures the degree of instability. The amplitude of the external seasonal forcing is  $\epsilon$  and its dimensionless frequency is  $\gamma$ . The dimensional values scale with  $\Delta\omega L$  and the (small) viscous spinup frequency, respectively (Hart, 1989).

Equations (7)-(9) reduce to the classical "Lorenz Equations" (Lorenz, 1963) when  $\beta$  and  $\epsilon$  are zero, and to a form of the "Complex Lorenz Equations" (Gibbon and McGuinness, 1982) when  $\epsilon = 0$ . When  $\sigma$  is near one and  $\epsilon = 0$ , both tend to be non-chaotic. Eqn. (10) shows that small  $\sigma$ 's are the rule for near-critical flows, especially if interfacial friction is included (see (10)).

If  $\beta$  is  $O(1)$ , then as  $R$  is increased (with  $\epsilon=0$  and keeping  $\Delta$  and  $Q$  small) the flow first becomes unstable to a travelling baroclinic wave which equilibrates to a constant amplitude. The phase trajectory of  $X_r$  and  $Y_r$  is a limit cycle (Fig 1a) that reflects the phase propagation. The amplitude of the wave and of the mean flow correction  $Z$  are constant in time. At larger  $R$  a bifurcation to periodic motion in  $Z$  occurs. The oscillation in  $Z$  represents an amplitude vacillation, while the associated quasi-periodic behavior in  $X$  and  $Y$  reflects a combination of the amplitude vacillation and the unrelated phase propagation frequency. Although the baroclinic time series looks complicated (Fig. 1b) it is just quasi-periodic, while that of the mean flow correction (Fig. 1c) is periodic (with period-2 for the parameters illustrated).

As  $\epsilon$  is raised above zero, the two-looped limit cycle corresponding to Fig. 1c becomes a two-looped torus. A cross-section through this torus yields a Poincare section as shown in Fig. 2a. This is constructed in the manner used by Lorenz (1963) where successive maxima of  $Z$  are plotted against the previous maxima. As  $\epsilon$  is increased this torus folds and ultimately fractures. Two stages of this process are illustrated in Figs. 2b and 2c. At larger  $\epsilon$ , corresponding to about a 6 percent fluctuation in the applied zonal shear, the motion becomes highly chaotic but with irregular winters as illustrated in Fig. 3. Weak seasonality can have a profound effect on the nonlinear dynamics of baroclinic waves, leading to chaos where none exists with steady forcing, and with intermittent behavior that is reflected in interseasonal variability. In this numerical example,  $\gamma$  is much smaller than the internal dynamical frequency  $\sqrt{R}$ .

In spite of these disparate timescales, a small amount of seasonal forcing is strongly destabilizing.

In the  $f$ -plane case a similar scenario is found. There, the large- $R$  behavior of the amplitude equations consists of almost-adiabatic (stable) symmetric and (unstable) asymmetric limit cycles. The seasonal forcing causes the adiabatic invariants to drift on the slow timescale towards a homoclinic orbit which divides the two types of inviscid cycle. When this happens, the flow near the origin leads to sensitive dependence on initial conditions (Hart, 1989). On the  $\beta$ -plane we speculate that seasonal effect similarly cause a breakdown of the adiabatic tori that occur in the  $\epsilon=0$  complex Lorenz equations (Fowler, et. al., 1984).

## References

- Fowler, A.C., J.D. Gibbon, and M.J. McGuinness, "The complex Lorenz equations." *Physica*, **4d**, 139-163 (1982).  
 Fowler, A.C., and M.J. McGuinness, "On the nature of the torus in the complex Lorenz equations." *SIAM J. Appl. Math.*, **44**, 681-700 (1984).

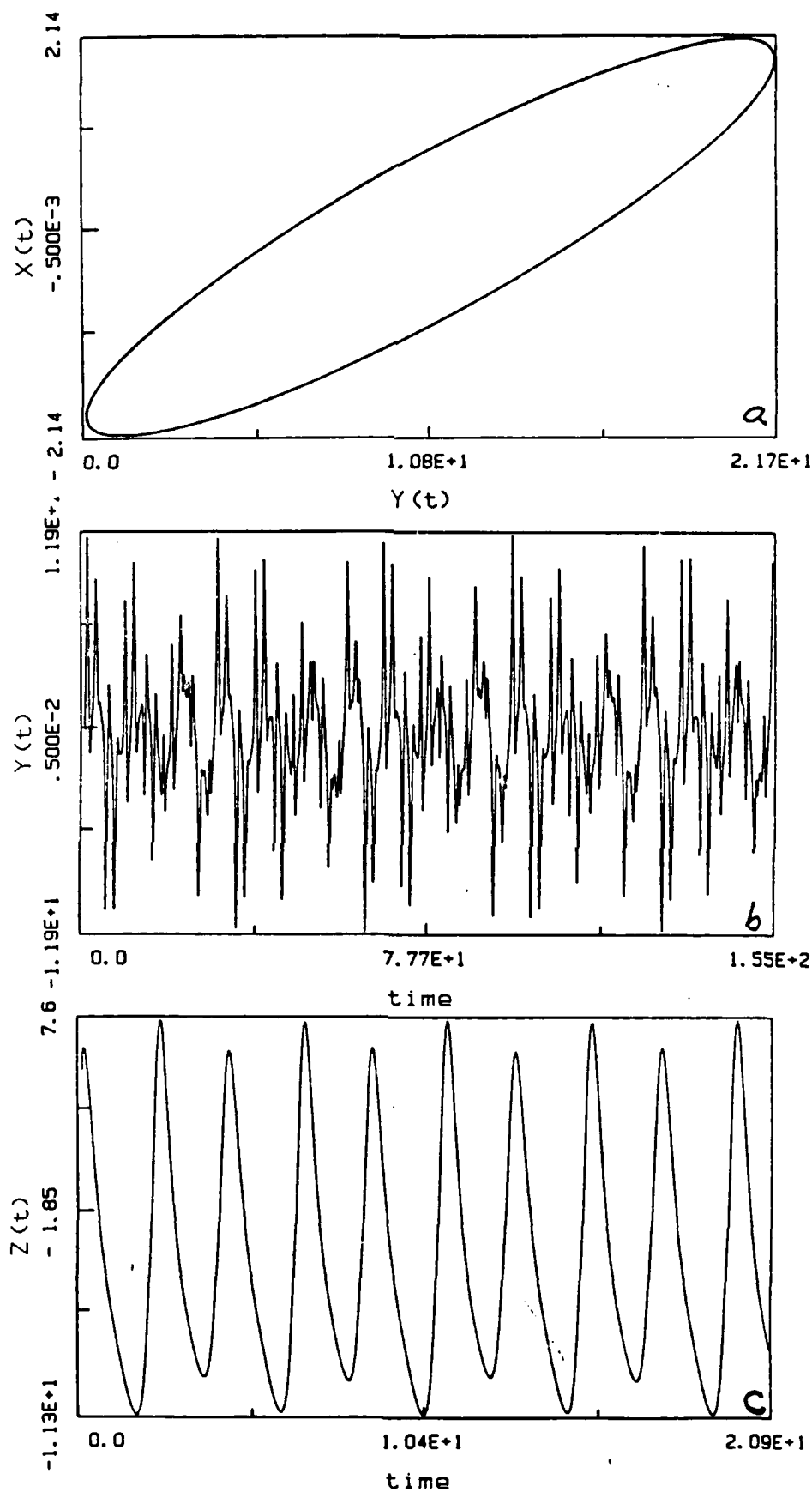


Fig. 1. Numerical results for  $\sigma=1.5$ ,  $b=.34$ ,  $\beta=1$ ,  $\Delta=0.1$ ,  $\epsilon=0$   
 (a)  $R=14.7$  (b)  $R=35.2$  (c)  $R=35.3$

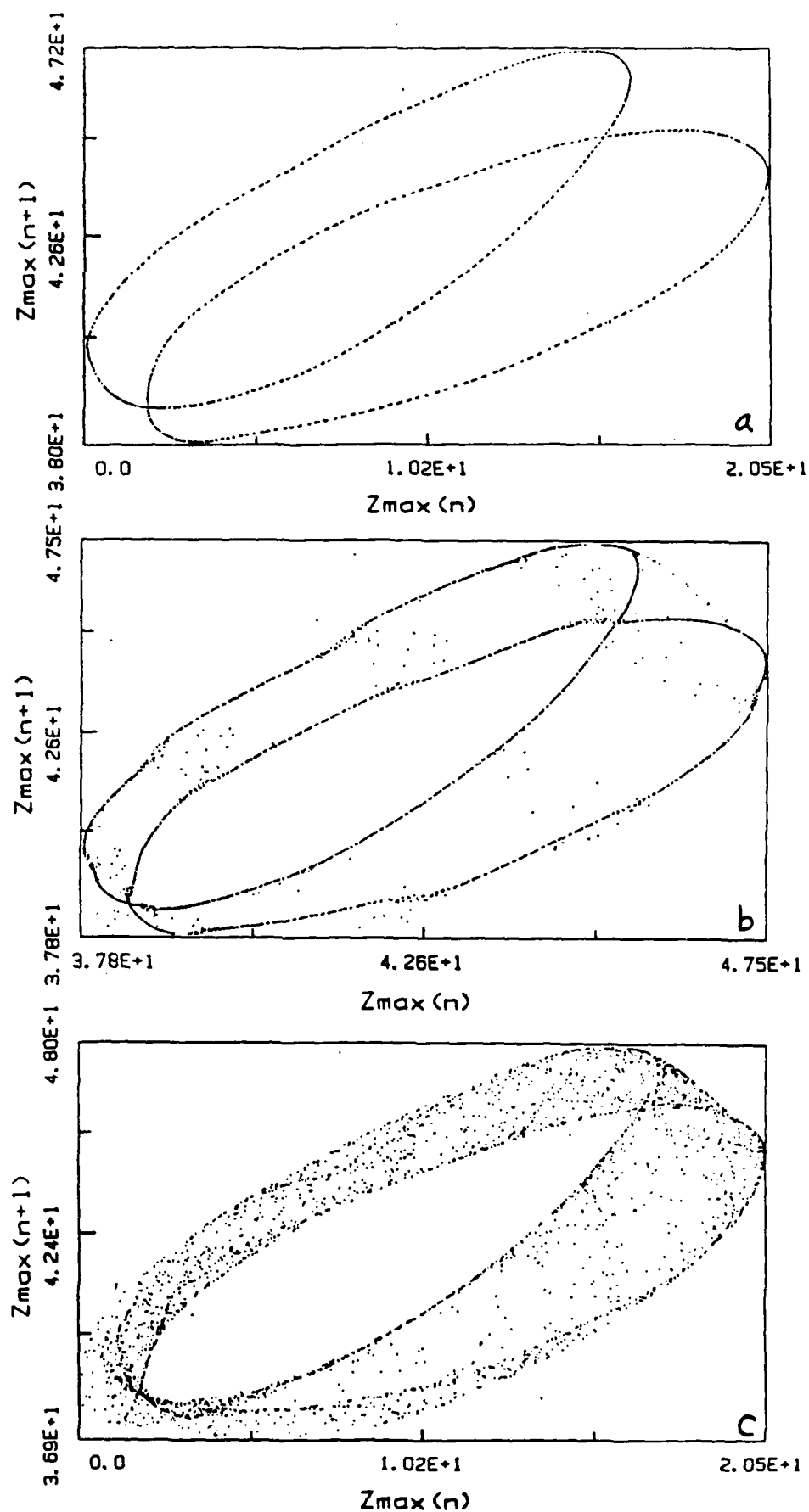


Fig. 2. Poincaré section for parameters as in Fig. 1b except:  
 (a)  $\epsilon=0.09$ ,  $\gamma=0.33$  (b)  $\epsilon=0.097656$ ,  $\gamma=0.33$  (c)  $\epsilon=0.11$ ,  $\gamma=0.33$

- Gibbon, J.D., and McGuinness, M.J., "The real and complex Lorenz equations in rotating fluids and lasers." *Physica*, 5D, 108-117 (1982)
- Hart, J.E., "A laboratory study of baroclinic instability." *Geophys. Fluid Dyn.*, 3, 181-209 (1972).
- Hart, J.E., "A model for the transition to baroclinic chaos." *Physica*, 20D, 350-362 (1986).
- Hart, J.E., "Finite amplitude baroclinic instability with periodic forcing." *Physica D*, in press (1989).
- Lorenz, E.N., "Deterministic nonperiodic flow." *J. Atmos. Sci.*, 20, 130-141 (1963).

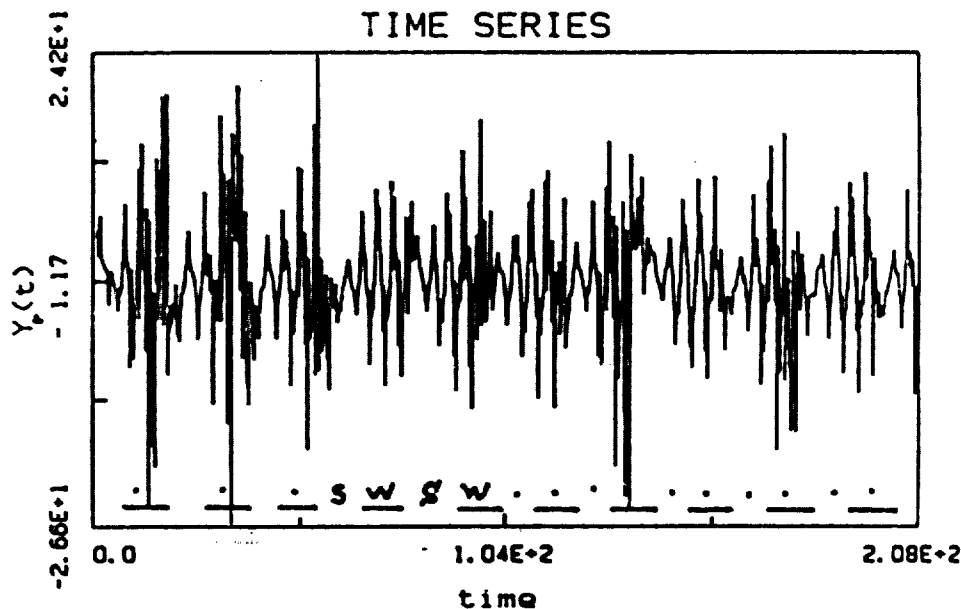


Fig. 3. Baroclinic wave amplitude for  $R=68$ ,  $\epsilon=.64$ ,  $\gamma=.25$ ,  $\sigma=1.6$ ,  $b=.34$ ,  $\beta=.8$ ,  $\Delta=.1$ .

## THE FLUID MECHANICS OF SOLIDIFICATION

Herbert E. Huppert  
D.A.M.T.P.  
University of Cambridge  
Silver Street, Cambridge CB3 9EW

Fluid mechanics can play a fundamental role in the phase transitions that accompany solidification. This is because when a liquid of two or more components solidifies, the composition of the solid product generally differs from that of the original liquid. For example, salty water in the polar oceans freezes to form almost pure ice. The difference in composition between liquid and solid implies that the composition of the liquid in the neighbourhood of the solidification front can be different from that further away. This difference in composition is generally associated with a difference in density, which can drive fluid motions, transport both heat and mass convectively and alter the rate and maybe even the mode of the solidification processes. The aim of the lecture was to systematically review some of the fundamental concepts in this subject.

My investigations in this field commenced with the consideration of the principles involved in cooling an initially homogeneous two-component melt at a single horizontal boundary (Huppert & Worster 1985). We identified six different flow regimes dependent upon whether the cooling takes place at an upper or lower boundary to the melt and whether the density of the fluid released on solidification is the same, greater or less than that of the melt. This differentiation between the flow regimes is one of the major concepts upon which the talk was based.

Consider initially the cooling from below of a liquid whose solidified product is compositionally identical. This is a classical Stefan problem (Hill 1987), a problem which has no fluid mechanical ingredient. The influence of an unstable thermal field that results from cooling such a fluid from above has been extensively studied by Turner, Huppert & Sparks (1986). Compositional effects can be incorporated by considering the cooling and crystallizing from below of a liquid that releases fluid of greater density when solidifying. The moving interface between fluid and solid is generally unstable, which leads to the formation of a mushy layer. Huppert & Worster (1985) describe a simple theoretical model for this mushy layer,

which we derived in Walsh Cottage in 1984, and we then demonstrated that predictions of the model agree well with data from our laboratory experiments.

This theoretical model was extended by Kerr, Woods, Worster & Huppert (1989) in a study of the solidification by cooling from above a liquid which releases less dense fluid. Assuming first that solidification occurs at thermodynamic equilibrium and that the cooling temperature exceeds the eutectic temperature, we determined the rate of growth of the mushy layer that forms on the roof. The agreement between the theoretical predictions and the laboratory data was good, but not perfect. The agreement was improved by incorporating non-equilibrium effects into the model by specifying a relationship between the rate of growth of the mushy layer and the non-equilibrium undercooling at the interface between mush and liquid.

Lowering the cooling temperature below the eutectic temperature can lead to compositional stratification in the solid (Woods & Huppert 1989). In addition, cooling at the top of a container can lead to solidification at the base - a result relevant to the cooling of a large magma chamber, or storage chamber of liquid rock, from above. Global two-dimensional effects, which result from cooling at either a vertical or a sloping wall (Huppert, Sparks, Wilson & Hallworth 1986) were also discussed.

The talk was very loosely based on the material presented in Huppert (1990), which was written in honour of George Batchelor's seventieth birthday.

## References

- Hill, J.M. 1987 One-dimensional Stefan Problems: An Introduction. Longman.
- Huppert, H.E., Sparks, R.S.J., Wilson, J.R. & Hallworth, M.A. 1986 Cooling and crystallization at an inclined plane. *Earth and Planet. Sci. Lett.* **79**, 319-328.
- Huppert, H.E. & Worster, M.G. 1985 Dynamic solidification of a binary melt. *Nature* **314**, 703-707.
- Kerr, R.C., Woods, A.W., Worster, M.G. & Huppert, H.E. 1989 Disequilibrium and macrosegregation during solidification of a binary melt. *Nature* **340**, 357-362.

- Turner, J.S., Huppert, H.E. & Sparks, R.S.J. 1986 Komatiites II: Experimental and theoretical investigations of post-emplacement cooling and crystallization. J. Petrol, 27, 397-437.
- Woods, A.W. & Huppert, H.E. 1989 The growth of compositionally stratified solid above a horizontal boundary. J. Fluid Mech. 199, 29-53.



WHOI - GFD 1989. 31:000-000

## A BIASED SAMPLE OF NUMERICAL MODELS OF THE LARGE SCALE CIRCULATION, I & II

*Glenn R. Ierley*

Fluids Research Oriented Group, Department of Mathematical Sciences,  
Michigan Technological University, Houghton, Michigan 49931

### PART I

Numerical models of the large scale circulation seems usefully divided into two categories: "gedanken" experiments and engineering computations. The former can serve as a testing ground for hypothesized mechanism, complementing the role of laboratory experiment, and suggesting new conjectures while the latter attempt to fit the large scale circulation as well as can be done with our present incomplete knowledge subject always to computational limits imposed by the current technology. Representative of the "gedanken" experiments are the early computations in quasigeostrophic models by Bryan (1963) and Veronis (1966) which played a significant role in developing our understanding of and intuition about the role of nonlinearity in modifying the earlier (analytic) linear theories of the circulation.

One hypothesis which we (Bill Young, Joe Pedlosky and I) are examining by numerical means is the suggestion that quasigeostrophic dynamics can provide a reasonable zeroth order description of the large scale circulation in the limit of vanishing viscosity. The answer is not yet clear, but at present I believe it to be no. The large scale circulation of the ocean is very nearly inviscid. What determines its structure and amplitude as we require more than an austausch coefficient description of the physics seems to depend quite sensitively upon the precise paths by which vorticity is ultimately dissipated. Quasigeostrophic models seem to rely upon a recirculation region spun up to an implausible degree. Perhaps ageostrophic instability provides a far more potent mechanism

for transferring potential vorticity through the system where it may ultimately be dissipated at the sidewall boundaries.

A multilayer QG model has been run at NCAR using Laplacian friction with a coefficient as small as  $10 \text{ m}^2/\text{sec}$ . As seen in a movie shown in the lecture, premature boundary layer separation is a characteristic feature of the turbulent state. An interesting comparison is the barotropic model computation by Panteleev (1985) which appears similar in character but with even more intense recirculation. The dynamics of this separation is the subject of current work. Variability in the latitude of separation appears to be induced by the collision of a westward moving cyclonic eddy with the boundary layer. Curiously, Boland and Church (1981) see evidence for a similar event in maps of dynamic topography for the East Australia Current.

When run with slippery boundary conditions (rather than the no-slip EW conditions in the runs described above), a double gyre run with no forcing in the northern gyre produces a result entirely reminiscent of Harrison and Stalos (1982) tempting one to believe that stress-free boundary conditions favor an asymptotic state substantially similar to that for models with only bottom drag. No-slip boundaries produce a more complex result which, however, retains a substantially linear relation between potential vorticity and streamfunction even instantaneously.

Following the main part of the lecture some brief remarks on spectral (Chebyshev) methods, their advantages and disadvantages, were delivered to those of a distinctly numerical bent.

## PART II

The paper by Schmitz & Holland (1986) provides one of the most serious points of comparison between observation and quasigeostrophic numerical model results. An eight layer model with 20 km grid resolution in a 3600 km (EW) by 2800 km (NS) rectangular basin was used. Bottom (second order) and biharmonic (sixth order) frictional terms provided damping. As the wind stress was varied, two statistically steady equilibrium states of 20 Sverdrups and 30 Sverdrups of wind-driven transport in a single gyre were found to provide a reasonable fit to the zonal distribution of abyssal kinetic energy under the jet axes of the Kuroshio and Gulf Stream respectively. Tested then were other statistics about the spatial and temporal structure in the vicinity of the jets. Surprisingly for a model lacking any ageostrophic instability mechanisms, the vertical distribution of kinetic energy agreed fairly well with observation even when decomposed into short, mesoscale, and secular frequency bands. The mean vertical shear was also in accord with observation, but the absolute zonal velocity was overestimated in

the numerical model by approximately 12 cm/sec. The second major discrepancy was the zonal distribution of eddy kinetic energy in the upper layer in the North Atlantic which peaks several hundred kilometers closer to the point of separation than at depth. The numerical model showed no such progression. The absence of topography in the latter may account for this discrepancy.

The Semtner & Chervin (1988) paper describes a global eddy-resolving model which traces its ancestry back to the Bryan Cox 1969 model. The present version is highly vectorized and permits 1/2 degree resolution with 20 layers in the vertical to be evolved at a cost of about 50 CPU hours per model year. Mainframe improvements are expected to permit 1/8 degree resolution with 40 layers in the vertical to be run for about the same cost sometime in the mid-1990's. An efficient spinup of the model constraining all levels to relax to interpolated (T,S) values from the Levitus data set was followed by two experiments in which the thermocline was free to evolve constrained by steady surface forcing and the abyssal layer relaxed to the Levitus data with a three year time constant. The principle distinction between the two experiments was to dramatize the difference between Laplacian (fourth order) and biharmonic (sixth order) friction. The latter induces substantial eddy activity which doubles the mean kinetic energy.

While at some level the results may be said to be "realistic" in resembling oceanic patterns of circulation, a central issue is what can be learned from such "engineering" models by way of advancing our deductive understanding of the large scale circulation? Goodness of fit is as yet ill-defined and rarely discussed in evaluating the utility of primitive equation models in this capacity. More obvious is their plausible applicability as a strictly interpolatory tool in conjunction with sophisticated methods of data assimilation. The Semtner & Chervin model has a Gulf Stream which separates north of Hatteras, about halfway to Long Island. Is this a significant error? They suggest the remedy may lie in the crude model treatment of the Greenland-Norwegian Sea. This may well be, but equally, it seems to me, some dynamic aspects of the large scale circulation in such numerical models must ultimately fail to give satisfactory agreement with observation even at much finer resolution and much lower viscosities as long as basic issues such as the asymptotic behavior of various parameterizations of vorticity dissipation remain unclear. For this reason, in my view, complementary studies of process models in simplified settings, such as quasigeostrophic dynamics will continue to be a crucial adjunct in assessing the validity of the more complex global model results. I believe progress in oceanography now is at least as much limited by our inadequate understanding of processes which are easily resolved by present computers as it is by inadequate

computational resources for even more highly resolved global climate models.

The second half of this lecture was given over to two numerical topics. A discussion of the method of cyclic reduction for rapid solution of elliptic problems (for which see the discussion in Press, et. al 1988.) was followed by an outline of work by Pares-Sierra & Vallis (1989). The latter describes a fast solver for nonseparable elliptic problems in irregular domains using an iterative capacitance matrix method. Timing tests of two algorithms presented show substantial gains in performance (a factor of 3-5 times faster) over optimal SOR algorithms. For a restricted class of nonseparable problems, a preconditioner leads to yet another factor of two in performance, however for problems with strong spatial variation in the diffusion coefficient, the method fails to converge.

#### Literature Cited

- Boland, F. M., Church, J. A., 1981. The East Australia current 1978. *Deep-Sea Res.* 28A:937-57
- Bryan, K. 1963. A numerical investigation of a nonlinear model of a wind-driven ocean. *J. Atm. Sci.* 20:594-606
- Haidvogel, D. B., Wilkin, J. L., Young, R., 1988. A semi-spectral primitive equation ocean circulation model using vertical sigma and orthogonal curvilinear coordinates. submitted to *J. Comput. Phys.*
- Harrison, D. E., Stalos, S., 1982. On the wind-driven ocean circulation. *J. Mar. Res.* 40:773-91
- Panteleev, M. C. 1985. The influence of friction on the character of the barotropic wind-driven wind circulation. (in Russian) *Izvestia POLY-MODE* 15:34-9
- Pares-Sierra, A., Vallis, G. K., 1988. Numerical experiments on a fast semi-direct method for the solution of non-separable elliptic equations in irregular domains. submitted to *J. Comput. Phys.*
- Press, W. H., Flannery, B. P., Teukolsky, S. A., Vetterling, W. T., 1986. *Numerical Recipes: The Art of Scientific Computing*. New York: Cambridge University Press. 818 pp.
- Schmitz, W. J., Jr., Holland, W. R., Jr. 1986. Observed and modeled mesoscale variability near the Gulf Stream and Kuroshio extension. *J. Geophys. Res.* 91:9624-38
- Semtner, A. J., Jr., Chervin, R., 1988. A simulation of the global ocean circulation with resolved eddies. *J. Geophys. Res.* 93:15502-22
- Veronis, G. 1966. Wind-driven ocean circulation - Part 2. Numerical solution of the non-linear problem. *Deep Sea Res.* 13:30-5

## Diapycnal Mixing and the Circulation of the Mid-Depth Ocean

James R. Ledwell

Lamont-Doherty Geological Observatory of Columbia University

Stommel (1958) and Munk (1966) have provided two sketches of the circulation of the deep interior ocean which have come to permeate current thinking. In Stommel's picture for the interior of all the oceans a uniform upwelling velocity in the deep water,  $w$ , which is increasing upward on average, drives a net poleward mass flux everywhere in the interior through the linearized, steady equation for the planetary vorticity balance:

$$v = (f/\beta) w_z \quad (1)$$

where  $v$  is the meridional velocity,  $f$  is the Coriolis parameter,  $\beta$  is its meridional derivative, and a subscript denotes differentiation. Although for isopycnal surfaces diverging toward the poles this relation can refer at least partially to purely isopycnal flow, the vertical velocity here is often viewed as largely across isopycnals (diapycnal) and must in that case be driven by diapycnal mixing.

In Munk's picture for the interior of the mid-depth Pacific Ocean (between 1000 m and 4000 m depth), both  $w$  and the diapycnal diffusivity,  $\kappa$  (roughly the same for heat and salt), are hypothesized to be constant with depth, and a simple one-dimensional balance obtains for potential temperature,  $\theta$  (this should be defined with respect to local reference levels rather than the surface), and salinity,  $S$ , throughout the interior of the basin:

$$w \theta_z = \kappa \theta_{zz} \quad (2)$$

and:

$$w S_z = \kappa S_{zz} \quad (3)$$

This is the simplest interpretation one can make of the apparently exponential potential temperature and salinity profiles observed in the mid-depth Pacific.

Because Munk's picture has a constant  $w$ , it implies that the poleward flow in (1) would be confined to an abyssal layer below 4000 m depth, if it exists anywhere. In the abyss, though, bottom topography and bottom friction might perturb the simple balance represented by (1). Thus the two pictures may be fundamentally inconsistent. There is strong circumstantial evidence for the Stommel picture in the existence of deep western boundary currents (although not so much for the North Pacific; see, e.g., Warren, 1981), but on the other hand, the exponential  $\theta$  and  $S$  profiles in the mid-depth Pacific seem to be still on rather firm observational ground. Furthermore, we shall suggest below that diapycnal mixing in the mid-depth North Pacific drives neither poleward flow suggested by the Stommel picture, nor the absence of meridional flow suggested by the Munk picture, but equatorward flow.

An exercise that seems worth while is to rediagnose the  $\theta$ ,  $S$  and density fields in the Pacific using modern data for information on  $w$  and  $K$ . Recent studies suggest that in doing so we should allow for the possibility that  $K$  as well as  $w$  may vary with  $z$ . Gargett (1984) reviewed the situation, and suggested that, in parts of the ocean where the energy for diapycnal mixing is to be drawn from the internal wave field, such as the mid-depth North Pacific,  $K$  varies inversely with the buoyancy frequency,  $N$ :

$$K = a_1 N^{-1} \quad (4)$$

where  $a_1 = 10^{-3} \text{ cm}^2/\text{s}^2$ . She based this suggestion on a large body of data from lakes and fjords, and the scanty evidence from oceanic measurements.

My coworkers and I (Ledwell et al., 1986; Ledwell and Watson, 1989) have measured  $K$  in a basin off Southern California by releasing tracer on an isopycnal surface and measuring its subsequent dispersion, finding a value of around  $0.25 \text{ cm}^2/\text{s}$  at  $N = 1.1 \text{ cph}$ . A second experiment presently underway appears to be yielding a value of  $K$  about 5 times larger at a value of  $N$  about 5 times smaller, consistent with the power law dependence in (4). Both basin results are a factor of 2 or so lower in magnitude than implied by (4), however, as are the fjord results reviewed by Gargett (1984). The basins, although around 50 km across, are clearly not large enough to be considered the open ocean, so the evidence from them are perhaps best considered as extending the fjord and lake data to buoyancy frequencies characteristic of the deep ocean. The next experimental step is to use our technique in the open ocean, and we have indeed proposed an experiment for the pycnocline of the eastern subtropical North Atlantic as part of the World Ocean Circulation Experiment.

Inferences of diapycnal mixing from microstructure measurements are in some cases consistent with (4) (e.g., Gargett, 1984; Moum and Osborn, 1986), but a recent synopsis of data by Gregg (1989) argues for the very low value  $K = 0.025 \text{ cm}^2/\text{s}$ , in the presence of a background internal wave field, independent of  $N$ . It is not clear yet what the microstructure measurements are telling us, or whether they can give us accurate estimates of diapycnal diffusivities for large enough space and time scales to be useful for modelling the general circulation of the ocean. We hope to make progress on this front by including microstructure studies in future tracer release experiments so the two techniques can be compared directly.

Some of the observations, then, suggest that  $K$  varies with  $N$ , while others suggest a small constant  $K$ . Of course,  $K$  is most often taken to be constant, or negligible, in theoretical and numerical studies. I might mention that Sarmiento et al. (1976) argued from radiotracer data in the abyss that  $K$  varies with  $1/N^2$ . It seems worth while to explore the consequences of a general power law dependence of  $K$  on  $N$ , which would encompass all of these scenarios:

$$K = a_p N^{-p} \quad (5)$$

If  $K$  is the same for heat and salt, and if we ignore the depth dependencies of the thermal expansion coefficient and of the derivative of density with respect to salinity, then (2) and (3) may be combined into:

$$w N^2 = (\kappa N^2)_z \quad (6)$$

We are assuming flat isopycnal surfaces here. We are also neglecting any contribution to  $w$  from lateral mixing operating on isopycnal T/S gradients through the nonlinear equation of state (see McDougall, 1987). From (1), (5), and (6), we find:

$$v = -(2 - p) \kappa (f/\beta) [(1 + p) (N_z/N)^2 - (N_{zz}/N)] \quad (7)$$

Note that this implies in general a vertical shear in  $v$ , and therefore, through geostrophy, a violation of the assumption of flat isopycnal surfaces. Nevertheless, (7) may be viewed as a diagnostic equation for that part of the local meridional flow driven by diapycnal mixing, given the observed vertical  $N$  profile. If  $p = 2$ , then  $v$  vanishes. In fact, from (5) and (6),  $w$  vanishes because the  $z$  dependence of  $N$  and  $\kappa$  cancel. The interesting point is that if  $0 < p < 2$ , which is suggested by the admittedly weak evidence, then  $v$  is toward the equator rather than the poles as long as  $(N_z/N)^2 > (N_{zz}/N)$ . So we have yet another scenario for  $v$  in addition to those of Stommel (poleward  $v$ ) and Munk (no  $v$ ). Gargett (1984) pointed this out for a particular  $N$ -profile and value of  $p$ .

In particular, if  $N$  varies exponentially at mid-depth in the Pacific, as suggested by Munk's (1966) picture:

$$N = N_0 e^{z/h} \quad (8)$$

then (7) becomes:

$$v = -p (2 - p) \kappa f / (\beta h^2) \quad (9)$$

i.e., equatorward flow for  $0 < p < 2$ . Munk's picture has  $p = 0$ , so  $v = 0$ , as noted earlier. The variation of  $N$  with depth is probably close enough to exponential in the mid-depth Pacific (see Fig. 1), for (9) to be qualitatively correct. Furthermore, Fiadeiro (1982), in modelling the radiocarbon and salinity data in the North Pacific, found evidence for equatorward flow at mid depth. C. Rooth (personal communication) has found a similar result.

Care must be taken, however, to insure that the data support sufficiently accurate higher order derivatives of  $N$  to draw such inferences. Figure 1a shows  $\ln N$  versus  $z$  for the mid-depth Pacific based on a modest sampling and smoothing of data from the eastern part of a recent section at  $24^\circ\text{N}$  across the Pacific. It looks convincingly linear, with a scale height of 1900 m, and thus implies equatorward flow everywhere for  $0 < p < 2$ . The value of  $v$  at  $\kappa = 1 \text{ cm}^2/\text{s}$  and  $p = 1$  is  $-0.008 \text{ cm/s}$ . However, if  $N$  itself is plotted versus  $z$ , an excellent fit can be made with a second order polynomial (Fig. 1b). The polynomial fit, and  $p = 1$ , gives  $w_z < 0$  from (7) only for depths less than 3500 m; at greater depths  $w_z > 0$  is implied. The corresponding crossing point for  $p = 0$  is about 2700 m. In spite of this sensitivity to uncertainties in  $N_{zz}$ , the data may be good enough, especially above 3000 m, to infer the value of  $w_z$  for various scenarios for the  $N$ -dependence of  $\kappa$ . However, I should confess that my attempts to infer the meridional shear,  $v_z$ , and thus the zonal slopes of isopycnals have been defeated at depths less than 3000 m or so by the very small slopes implied, and at greater depths by uncertainty in  $N_{zz}$  and  $N_{zzz}$ .

**Acknowledgements.** Thanks to C. Rooth for lengthy discussions and for comments on a draft of this abstract, and to J. Pedlosky and G. Veronis for comments on my talk. H. Bryden supplied listings of T and S from the TPS 24 section, and J. Toole kindly provided me with a contour plot of Sigma-4 from that section.

#### References

- Fiadeiro, M. E., 1982: Three-dimensional modelling of tracers in the deep Pacific Ocean II. Radiocarbon and the circulation. *J. Mar. Res.*, **40**, 537-550.
- Gargett, A. E., 1984, Vertical eddy diffusivity in the ocean interior, *J. Mar. Res.*, **42**, 359-393.
- Gregg, M. C., 1989: Scaling  $\epsilon$  in the thermocline, submitted to *J. Geophys. Res.*
- Ledwell, J.R., A.W. Watson., and W.S. Broecker, 1986, A deliberate tracer experiment in Santa Monica Basin. *Nature*, **323**, 322-324.
- Ledwell, J. R., and A. J. Watson, 1989: The Santa Monica Basin Tracer Experiment: A study of diapycnal and isopycnal mixing. submitted to *J. Geophys. Res.*
- McDougall, T. J., 1987: Thermobaricity, cabbeling, and water mass conversion. *J. Geophys. Res.*, **92**, 5448-5464.
- Moum, J. N. and T. R. Osborn, 1986: Mixing in the main thermocline. *J. Phys. Oceanogr.*, **16**, 1250-1259.
- Munk, W. H., 1966: Abyssal recipes. *Deep-Sea Res.*, **13**, 707-730.
- Munk, W. H., 1981: Internal waves and small-scale processes, in *Evolution of Physical Oceanography*, B. A. Warren and C. Wunsch, Eds., MIT Press, Cambridge, Mass., USA, pp. 264-291.
- Osborn, T. R., 1980: Estimates of the local rate of vertical diffusion from dissipation measurements. *J. Phys. Oceanogr.*, **10**, 83-89.
- Reid, J. L., 1981: On the mid-depth circulation of the world ocean, in *Evolution of Physical Oceanography*, B. A. Warren and C. Wunsch, Eds., MIT Press, Cambridge, Mass., USA, pp. 70-111.
- Sarmiento, J. L., H. W. Feely, W. S. Moore, A. E. Bainbridge and W. S. Broecker, 1976: The relationship between vertical eddy diffusion and buoyancy gradient in the deep sea. *Earth Planet. Sci. Lett.*, **32**, 357-370.
- Stommel, H., 1958: The abyssal circulation. *Deep Sea Res.*, **5**, 80-82.
- Warren, B. A., 1981: Deep circulation of the world ocean, in *Evolution of Physical Oceanography*, B. A. Warren and C. Wunsch, Eds., MIT Press, Cambridge, Mass., USA, pp. 6-41.



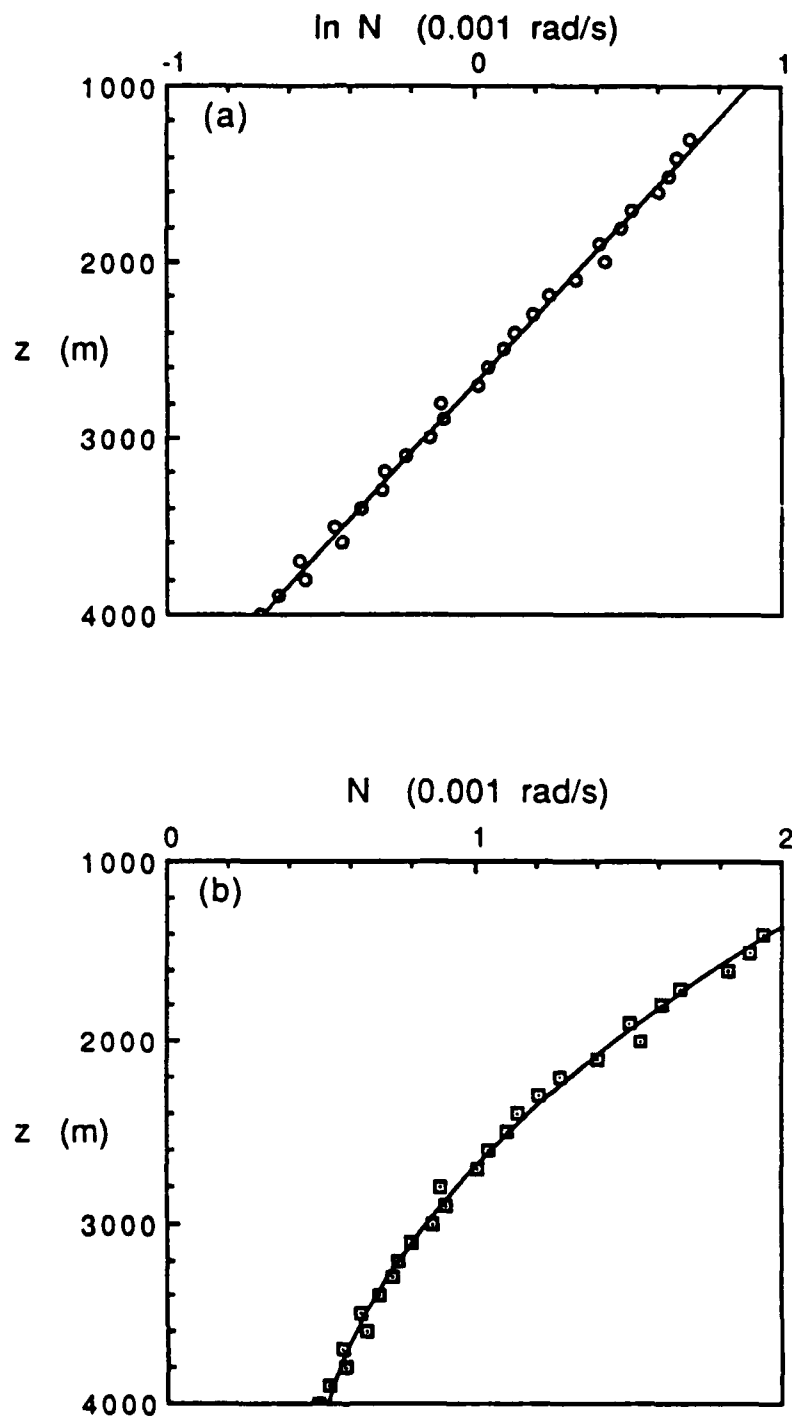


Fig 1. Mid-depth profile of buoyancy frequency,  $N$ , from the TPS24 Section at  $24^\circ\text{N}$  in the Pacific. Temperature and salinity were averaged at 100 m depth intervals over 8 station pairs spaced every  $5^\circ$  longitude from  $135^\circ\text{W}$  to  $170^\circ\text{W}$ .  $N^2$  was then calculated over the 100 m intervals by differencing of the appropriate densities. Panel (a) shows  $\ln N$  versus  $z$ , with a linear fit, while panel (b) shows  $N$  versus  $z$ , with a second order polynomial fit.

# THE "COLLAPSE" OF THREE DIMENSIONAL INSTABILITIES IN ELLIPTICAL FLOW

W.V.R. Malkus and F.A. Waleffe  
Dept. of Math., Mass. Inst. of Technology

Experiments on the instability of fluid in a rotating tidally distorted elastic cylinder reveal that the origin of the observed broadband disordered flow is the "collapse" of the principal three dimensional mode at a critical point in its growth. It is proposed here that the process responsible for this violent passage from completely ordered to disordered flow is a ubiquitous source of shear flow turbulence which by-passes lesser chaotic phases. Here we explore the possibility that the transition is from the hyperbolic behavior of the growing Poincare wave mode, to an elliptic behavior suddenly induced by a critical condition in the changing vortical flow. We show that such a condition for the principal modes is that  $3\Omega + 2\gamma\Omega' < 0$ , where  $\Omega = \Omega(r)$  is the mean angular velocity about the overall axis of rotation. From the amplitude equations describing the growth of a mode and concomittent evolution of the mean field, we estimate the times and radii at which the critical condition is first reached. Current observations of collapse are in qualitative agreement with the proposed transition from hyperbolic to elliptic behavior. However, quantitative discrepancies suggest that the criterion for collapse would be more successful if applied to the local finite-amplitude vortex, and not just the component parallel to the axis of rotation. Further laboratory study is planned, as is a more complete numerical experiment; to define the parameter range in which collapse of the first mode occurs. Outside this range one observes sequences of chaotic modal interaction leading gradually to broadband disorder.

## References

McEwan, A.D., J. Fluid Mech. **40**, 603 (1970)

## THE EQUATORIAL UNDERCURRENT

By

Joseph Pedlosky

Woods Hole Oceanographic Institution

### Abstract

A review of a recent theory for the Equatorial Undercurrent (EUC) was given. The theory builds on the diagnostic picture of the circulation of the equatorial Pacific described by Bryden and Brady (1985). In that picture the observed upwelling along the equatorial takes place on isopycnals which rise upwards to the east, along which the eastward flowing EUC is observed. Except for the upper strata of the EUC, cross-isopycnal flow is weak.

Thus an adiabatic model of the EUC is considered in which density, potential vorticity  $q$ , and Bernoulli function,  $B$ , are conserved. A simple two-layer model is used in which the EUC is represented in the lower layer over a resting abyss. Since the EUC is thin in the meridional direction, the zonal velocity but not the meridional velocity is geostrophic.

The key dynamical question is the determination of the potential vorticity on the streamlines. Or, since streamlines coincide with isolines of the Bernoulli function, the issue is the determination of the potential vorticity as a function of  $B$ , i.e.,  $Q(B)$ . It is shown that  $Q(B)$  can be determined by requiring that the equatorial solution match smoothly to the thermocline solution of Luyten et al., (1983). Thus the undercurrent can be considered as the natural continuation of the ventilated thermocline to the equator. This matching determines both the meridional and zonal structure of the undercurrent as well as definite scales for its width, depth, and velocity.

A completely adiabatic theory leads to a (spatially) continuously accelerating EUC. It was shown that the inclusion of entrainment can produce a termination of the EUC. Whereas in the ocean the entrainment is localized in the uppermost strata of the EUC which sequentially surface as the current flows eastward, the limited vertical resolution of the model required a similar spatial localization in a narrow domain around the equator. This was shown to relate the decrease of  $B$  along the equator ( $B$  is

constant at the equator in the adiabatic theory) to the entrainment. A theory was presented which related the entrainment to the stress-driven dynamics of the upper layer which was at the same time coupled to the lower layer. This coupled model produces a largely adiabatic EUC which terminates at the ocean's eastern boundary on which the Bernoulli function is brought to zero.

**References:**

Bryden, H. L. and E. C. Brady, 1985. Journal of Physical Oceanography, 15, 1255-1273.

Pedlosky, J., 1987. Journal of Physical Oceanography, 17, 1978-1985.

Pedlosky J., 1988. Journal of Physical Oceanography, 18, 880-886.

Pedlosky, J. and R. Samelson, 1989. Journal of Physical Oceanography, to appear.

That ocean and atmosphere dynamics in interaction can lead to "new" phenomena is well established in the context of the "El Nino", but the significance of the oceanic heat transport processes in decadal and longer time scale climate dynamics still elicits divergent opinions based on diagnostic and model studies. It has been questioned, based on atmospheric model results (Covey, 1988), but supported by dramatic examples of multiple equilibria in coupled ocean-atmosphere systems (Manabe and Stouffer, 1988).

Catastrophic state switching effects are characteristic of systems with mixed buoyancy forcing by an essentially flux controlled property (salinity) and one subject to relaxation control at the boundaries (temperature) (Rooth, 1982). F. Bryan (1987) produced the first evidence in a comprehensive numerical model of what he termed the halocline catastrophe. Halocline switching has been invoked to explain the Allerød/Younger Dryas climatic transient (Broecker & al, 1985) and used as an example of the uncertainties associated with prediction of anthropogenic climate trends (Broecker, 1987). I suggest that the underlying physics is credible, whatever the specific shortcomings may be of the models used in these studies, and that only mode changes in ocean dynamics are likely to cause major impacts on the the atmosphere.

The first order climate control, and implicitly the tropospheric density scale height, are imposed by the average vertical flux balances due to visible and infrared radiation (including albedo effects), and convective adjustment in the atmosphere (Manabe and Weatherald, 1975). With the vertical stability fixed, the atmosphere tends to develop a meridional temperature gradient in proportion to the square root of the meridional heat flux demand. Thus, a fractional change in the 20-25% oceanic heat flux contribution to this demand should cause a relative change in the atmospheric temperature range by about one eighth of the relative oceanic heat flux change. It is thus likely that direct effects of changes in wind forcing are linearizeable perturbations, and that major ocean induced climate changes depend on thermohaline regime transitions.

In contrast to surface temperature anomalies, those in salinity can grow until limited by transport processes. Since surface haloclines suppress convection, catastrophic halocline development leading to bimodal system attractors are possible when deep water formation regions are also regions of net fresh water input. This happens in the Manabe & Stouffer model which has two distinct equilibria, one with a climate like our present one, and one where the meridional heat transport in the North Atlantic is cut down by about 80%, resulting in a cooling of the entire high latitude northern hemisphere, with a maximum amplitude in the subpolar Atlantic of 5-6°C. However, a coupled system experiment

by Washington and Meehl (1989) exhibits only quasi-linear adjustments in the functioning of the oceans, which implies that a perturbation analysis might suffice for them. Bryan & al (1984) found that the heat storage lag effects in a fifteen layer ocean model are like those of a parallel set of capacitances with serial impedances which are much larger for the high heat capacity deep layers. Thus, the heat flux amplitudes associated with the long lasting deep water lag effects is fairly small, and of negligible climatic impact compared to those of the surface and thermocline layers. This may not apply in the case of thermohaline regime shifts, which could involve extended periods of anomalous circulation during the salinity field adjustments in the deep waters. Such effects may also have a significant impact on nutrient exchanges between the deep waters and the surface, and thus on the biological control of the atmospheric CO<sub>2</sub> concentration (e.g. Sarmiento and Toggweiler, 1985).

The global thermohaline mode can explain the observed interbasin salinity contrasts without invocation of atmospheric water vapor transfer across basin boundaries, and its equilibrium amplitude is sensitive primarily to the net heat and fresh water balances in the deep water formation regions. Substantial low salinity transients, have been observed in the sub-polar Atlantic at least twice in this century (Dickson & al, 1988). Although the injection depth and intensity for the Labrador Sea (sub-polar) water mode has thus been modified on decadal time scales, the present thermohaline circulation state has not been switched off. As in the model cases, the global thermohaline mode is apparently quite robust.

In contrast to the thermohaline mode characteristics, the gyre scale heat transport effects due to the wind driven lateral circulation can be reasonably estimated based on the trade wind related surface stress. The latter controls the equatorial upwelling intensity, and the upwelling water is thermally conditioned during the winter time convective ventilation events in the eastern gyre sections. This suggests that the meridional heat flux by the gyre circulation should be proportional to the wind stress amplitude times the subtropical temperature range (or in a low order climate model proportional to the cube of the latter).

Further theory development regarding the interplay between wind driven circulation and dense water production in high latitudes (or in other terms the capacity of the system to remove some of the high latitude fresh water input from the sub-polar oceans by wind induced surface currents) appears crucial to prediction of the thermohaline mode intensity. Another key question is the relative significance of heat (buoyancy) transfer between gyres by cross boundary eddy transfers versus mean transport overturning, and how these processes respond to the diabatic forcing effects within the gyre domains.

A better understanding of how deep basin recirculation domains and boundary current patterns modify the transmission of transient water mass characteristics to different portions of the

deep water realm would be important for diagnostic studies of current climate stability as well as for the interpretation of paleoclimatic information preserved in deep-sea sediments. At present we do not know very well how to interpret gradients in abyssal ocean conditions in terms of steady or transient climatic forcing of the oceans. This severely limits our capacity to expand the empirical basis for climate dynamics scenarios based on oceanic data.

#### Selected readings:

- Broecker, W.S.: Unpleasant Surprises in the greenhouse? *Nature* 328 (1987), 123-126.
- Broecker, W. S., D. M. Peteet and D. Rind: Does the ocean-atmosphere system have more than one stable mode of operation? *Nature* 315 (1985), 21-26.
- Bryan, F.: High latitude salinity effects and interhemispheric thermohaline circulations. *Nature* 323 (1986), 301-304.
- Carissimo, B. C., A. H. Oort and T. H. VonderHaar: Estimating the Meridional Energy Transports in the Atmosphere and Ocean. *J. Phys. Oceanography* 15 (1985), 82-91.
- Covey, C.: Atmospheric and oceanic heat transport: Simulations versus observations. *Climatic Change* 13 (1988), 149-159.
- Covey, C. and E. Barron: The Role of Ocean Heat Transport in Climatic Change. *Earth Sci. Rev.* 24 (1988), 429-445.
- Dickson, R. R., J. Meincke, S.-A. Malmberg and A. J. Lee: The "Great Salinity Anomaly" in the Northern North Atlantic 1968-1982. *Prog. Oceanog.* 20 (1988), 103-151.
- Ghil, M., A. Mulhaupt and P. Pestiaux: Deep-water formation and quaternary glaciations. *Climate Dyn.* 2 (1987), 1-10.
- Gordon, A. L.: Interocean exchange of thermocline water. *J. Geophys. Res.* 91 (1986), 5037-5046.
- Manabe, S., and R. J. Stouffer: Two Stable Equilibria of a Coupled Ocean-Atmosphere Model. *J. Climate* 1 (1988) 841-866.
- Manabe, S. and R. T. Wetherald: The effect of doubling the CO<sub>2</sub> concentration on the climate of a general circulation model. *J. Atmos. Science* 32 (1975), 3-15.
- Rooth, C.: Hydrology and Ocean Circulation. *Prog. Oceanog.* 11 (1982), 131-149.
- Ruddiman, W. F. and A. McIntyre: The North Atlantic Ocean during the last glaciation. *Paleogeogr. Paleoclimatol. Paleoecol.* 35 145-214.
- Sarmiento, J., and R. Toggweiler: Oceanic sequestration of CO<sub>2</sub>. In "The Carbon Cycle and Atmospheric CO<sub>2</sub>, Natural Variations, Archaean to Present", E. T. Sundquist and W. S. Broecker, Editors. *Geophysical Monograph* #32 (1985). American Geophysical Union, Wash. D.C. 796 pp.
- Stommel, H. M.: Thermohaline convection with two stable regimes of flow. *Tellus* 13 (1961) 224-230.

## Bounds on Spatial and Temporal Variability of the Gulf Stream.

T. Rossby

Since early summer 1988 we have been launching isopycnal RAFOS floats on the 15 C isotherm in the center of the Gulf Stream off Cape Hatteras. By releasing the floats in the upper main thermocline we take advantage of the strong cross-stream potential vorticity gradient to keep the floats from scattering from the current. Through repeated seeding we can use the float tracks to determine the path of the current and its change with time. Also, pathways of ejection from the current can be used to detect departures from simple dynamics, i.e. geostrophy and gradient wind balances. These subsurface records can be used together with IR views of sea surface temperature to examine the vertical structure of the current.

The strong PV gradient has a striking effect on the downstream spread of floats. Compared to earlier studies with isopycnal floats only 100 to 200 meters deeper (12 C and 9 C), these floats stay in the current at least 2 to 3 times farther over the same period of time whereas the maximum velocity increases from 80 cm/s to 120 cm/s between the 9 and 15 C surfaces. Thus, speed alone cannot explain the greater retention.

Lateral motions within the current are beginning to be the focus of attention. A striking characteristic of the float tracks is the up- and downwelling that occurs along the meandering current. But superimposed on this 'deterministic' behavior (the vertical motions correlate very strongly with path curvature, Bower, 1989) we have several times observed a striking tendency for floats to 'slide' out of the current. We are now experimenting with techniques to isolate this signal more clearly from the float records. From all of the float data to date (> 80 float tracks) there is no evidence for a preferred direction of lateral motion, i.e. there has been a comparable loss of floats to the Sargasso Sea and the Slope Waters (but this question has yet to be addressed thoroughly).

An issue that is beginning to catch our attention is the breakdown of the Gulf Stream as a filamentary feature. The evidence at present is sketchy, but the float tracks seem to have a wider range of expression east of the New England Seamounts than to the west. The picture that emerges, however speculative at this point, is a downstream transition to a field of energetic eddies which can attach to each other to make an 'instantaneous' yet well-defined path of the current. There is much research to be done here.



The availability of Geosat altimeter data has led to an explosive growth in studies of sea level variability. Since the cross-stream structure of the Gulf Stream seems to be so stable, as indicated by the stability of the peak axial velocity in the current, we thought it would be instructive to use the float data together with a model of cross-stream sea level, constructed from the 1980-1983 Pegasus study (Halkin and Rossby, 1985), to infer what the sea level might look like. Using about 50 float tracks in the current, we find the region of eddy activity, as defined by a 0.3 m rms sea level standard deviation, to be very narrow (< 100 km) west of 69 W each of which it rapidly broadens to > 300 km by 66 W. The mean sea level difference was estimated from the Pegasus program to be about 1.1 m.

-----

#### References:

Bower, A., 1989. Potential Vorticity Balances and Horizontal Divergence and Particle Trajectories in Gulf Stream Meanders East of Cape Hatteras. J. Phys. Oceano., 19, Oct. issue.

Halkin, D. and T. Rossby, 1985. The Structure and Transport of the Gulf Stream at 73 W. J. Phys. Oceano., 15, 1439-1452

## DYNAMICS OF INTERACTING SOLITARY STRUCTURES

*E. A. Spiegel*Department of Astronomy  
Columbia University

In this talk, I return to a topic that was already discussed in the three lectures that Christian Elphick and I gave last year and are outlined in those proceedings (GFD, 88; edited by G. Flierl). At issue is the solution of partial differential equations in the style of field theories such as those of particle physics. The idea is that when the original equations admit localized solutions in the form of traveling waves, more general and complicated solutions can be constructed from superpositions of such individual solutions. The result is the replacement of the original PDE by ODEs in some sort of sort of N-body systems. This kind of reduction is known for integrable systems but, when the structures are far apart, this effective particle description may be used on nonintegrable systems with dissipation and instability. (For a bit of history and references to early work see the 1988 Proceedings.)

Elphick, Meron and I have worked out the asymptotics for PDEs with translational invariance (SIAM J. Appl. Math., in press), leading to equations of motion for the localized structures. The paradigm for that case is the reaction-diffusion system without advection. However, the problem is trickier when there is also Galilean invariance, but Elphick, Ierley, Regev and I know how to do such cases now. We get equations of motion for the structures, but now the effective particles have inertia, which they did not in the previous instances. At present, we are checking the agreement with numerical simulation on the original ODE.

Elphick, Qian and I have also been trying to study the interaction of two-d vortices in this way. I am not able to report glowing success, but the problem does seem to be yielding. In all these problems, the fun is that we can give generic descriptions, independently of details, for a given set of invariances of the original problem. This kind of approach is therefore useful for a first look at complicated situations.

## ENTRAINMENT INTO A LARGE REYNOLDS NUMBER JET

Melvin E. Stern  
Florida State University  
Tallahassee, Florida

An eddy with maximum circulation  $D$  (and typical vorticity  $C$ ) located near the outer edge of a jet having typical vorticity  $H$  (less than  $c$ ) will be drawn further inside the jet and eventually surrounded by that fluid. Ambient irrotational fluid is also entrained, and an average entrainment velocity  $(0.11 \pm 0.02) (DC)^{1/2}$  is computed using an inviscid, two dimensional, and piecewise uniform vorticity model. An order of magnitude comparison with observed entrainment rates in a turbulent flow suggests that the model qualitatively describes a phase in the short lifetime of a mature eddy stochastically aligned with the mean flow direction.

## THE DIMENSIONS OF COSMIC FRACTALS

R.Thieberger\*, E.A. Spiegel and L.A. Smith\*  
 Department of Astronomy  
 Columbia University  
 New York, NY 10027, USA

### Abstract

This study is part of an effort to understand the large scale distribution of matter in the universe.

Self similar structures have a long history in Astronomy<sup>1</sup>. The classical approach uses the two body correlation function<sup>2</sup>. For calculating the fractal dimensions we should expect to obtain more precise results using the conditional density function<sup>3</sup>.

We considered model fractals<sup>4</sup>, in addition to a set of galaxy positions measured at the Observatory of Nice<sup>5</sup>, to illustrate the method. We find that the data suggest a rather larger fractal dimension for the distribution of galaxies than is generally accepted.

### References

- [1.] B.B. Mandelbrot (1977) Fractals: Form, Chance and Dimension, (Freeman).
- [2.] P.J.E. Peebles (1980) The Large Scale Structure of the Universe, (Princeton University Press).
- [3.] L. Pietronero (1987) Physica, **144A**, 257.
- [4.] M. Barnsley (1988) Fractals Everywhere (Academic Press).
- [5.] E. Slezak, G. Mars, A. Bijaoui, C. Balkowski and P. Fontanelli (1988) Astron. Astrophys. Suppl. Ser., **74**, 83.

---

\*Normal address: Physics Department, Ben Gurion University, Beer Sheva, Israel.

\*Present address: Research Centre, King's College, Cambridge, UK

A possible simplicity in global M2  
tidal currents.

Henry Stommel  
W.H.O.I.

By comparing M2 tidal ellipses observed at several hundred locations around the world at deep moored current meters (deeper than 1000 meters) Luyten and Stommel (1989) suggested that the Schwiderski (1979) black-box gridded numerical model probably gives a reliable representation of the actual distribution of tidal ellipses globally.

Although the response of sealevel to the M2 force is rather irregular [the phase lines interpolated from data (Villain, 1951) are shown in Figure 1] and bear no obvious cause-effect relation to the phase lines of the disturbing force [whose phase lines are simply meridians, with two cycles around the world], the M2 current ellipses unexpectedly seem simpler. Figure 2 shows [three=quarters of] tidal ellipses from the Schwiderski black box. The radius is drawn at 0 hours Greenwich lunar time, and the hodograph is continued for three quarters of a tidal cycle. This enables the viewer to see the direction of rotation.

In Figure 3 we have drawn, on the same velocity scale, the tidal ellipses calculated from Laplace's theory of the semidiurnal tide in an ocean of uniform depth [4000 meters] covering the entire globe. Comparison of this Figure with Figure 2 suggests that the Laplace unbounded ocean models the Schwiderski black-box [and by implication the real natural] M2 tidal ellipses rather well, both in phase and latitudinal distribution of amplitude. If the Laplace model is refined by putting zonal boundaries at 60N, the high latitude zones of counterclockwise rotation can be reproduced.

We are therefore led to enquire why a simple model like Laplace's - which knows nothing about the coastal boundaries or the irregularity of bottom topography - can give results that even approximately resemble the real ocean tidal ellipses.

What kind of physics is involved? Are the reflected waves from irregular boundaries confined somehow to coastal regions [as Kelvin waves] or do they interfere sufficiently to cancel in the

interior, leaving only the Laplace solution? Or is dissipation of reflected wave energy responsible?

Luyten and I have not been able to explain this strange apparent [we must use the word "apparent" because the correspondence of the two charts 2 & 3 is not perfect ] simplicity of relation between driving force and system response in what has hitherto been considered a very complicated physical phenomenon indeed.

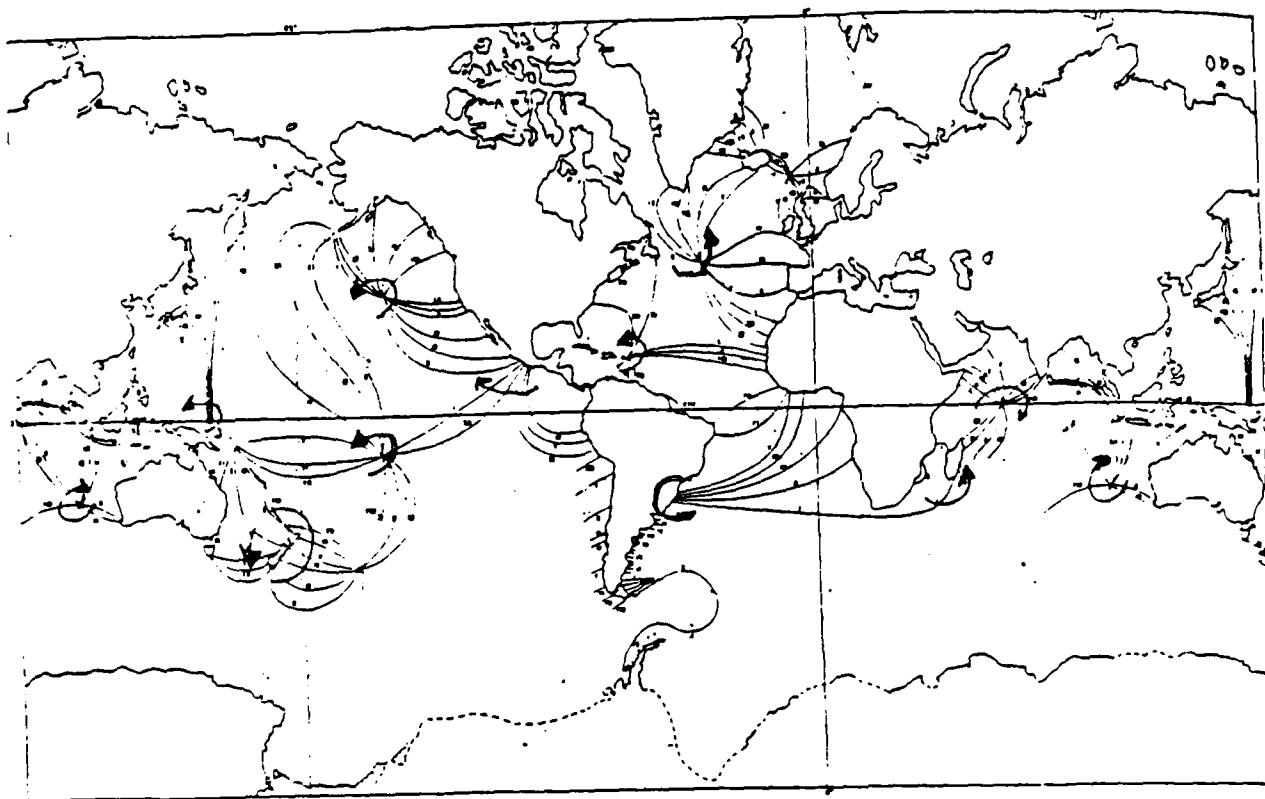


Figure 1 Lines of constant phase of the M2 sea-level, a subjective analysis of observed sea-level data.



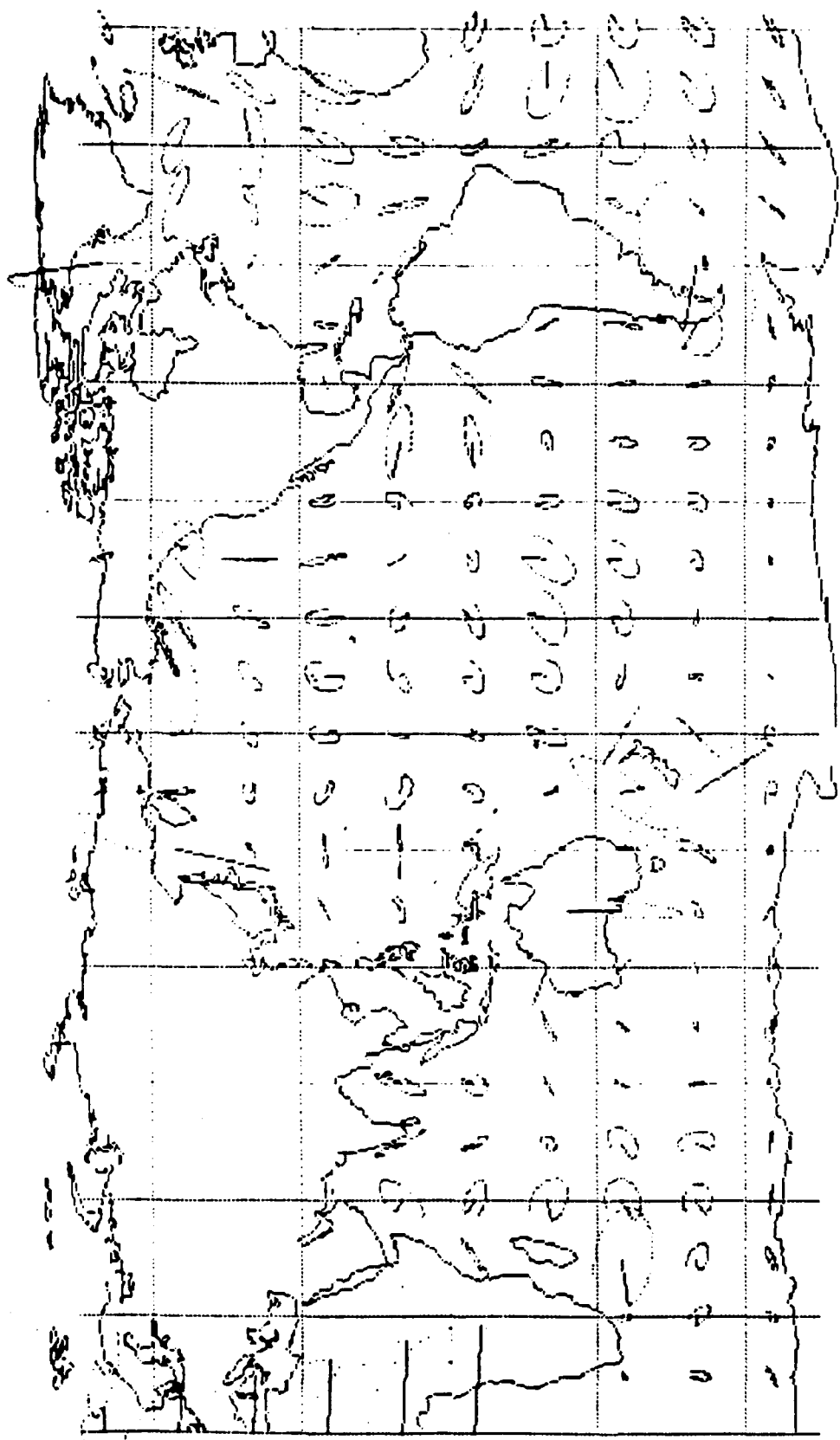


Figure 2     $3/4$  M2 tidal ellipses from Schwiderski's black box.

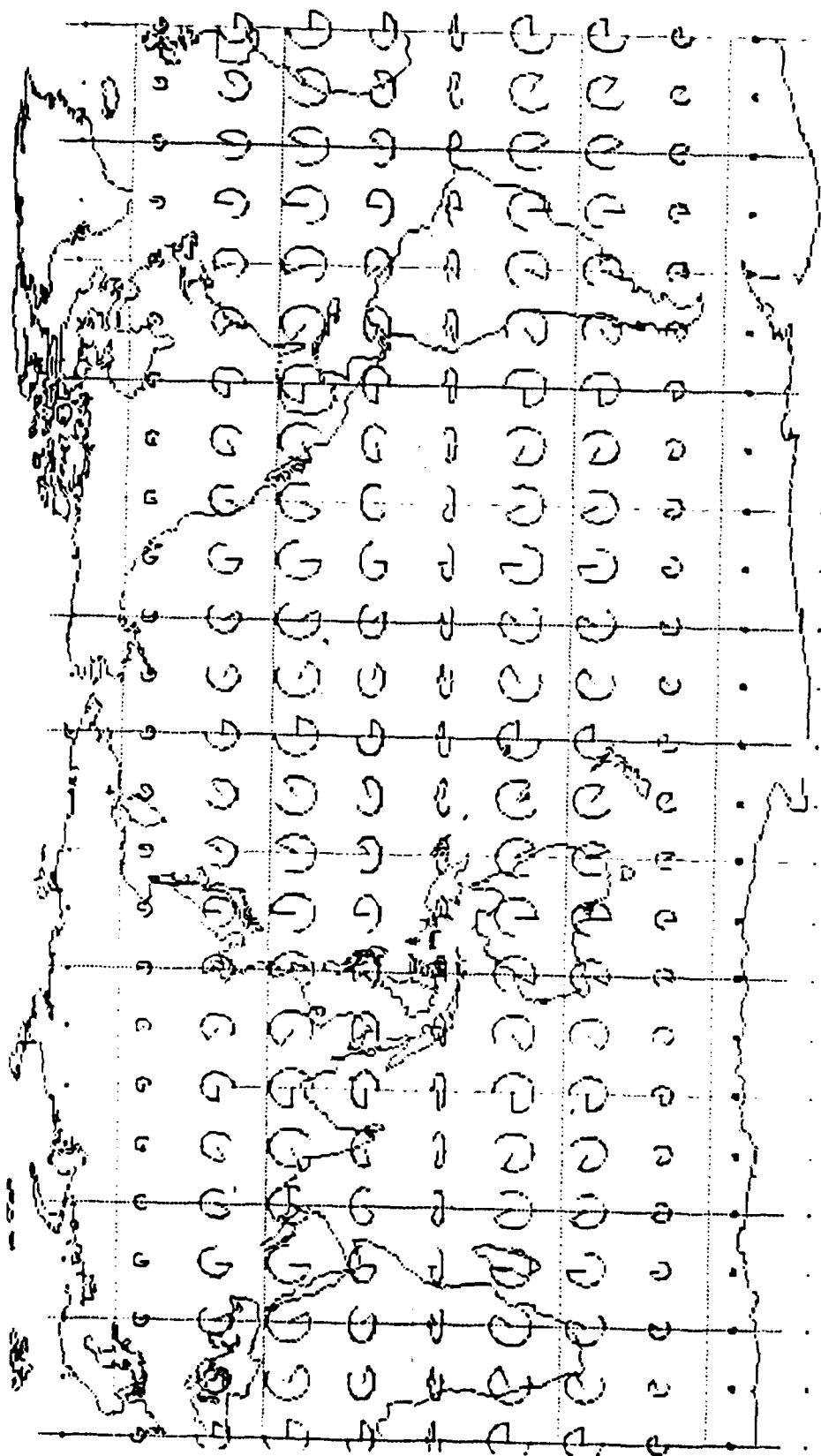


Figure 3  $3/4$  M2 tidal ellipses from Laplace's theory of a uniformly deep (4000m) ocean covering the rotating globe.

## EVOLUTION OF LONG-LIVED VORTICES

George G. Sutyrin  
P.P. Shirshov' Institute  
of Oceanology Acad. Sci  
Moscow, U.S.S.R.

### Part 1.

Isolated intense vortices, such as rings and lens in the ocean, hurricanes and polar vortex in the atmosphere, Jovian and Saturnian Spots and Ovals, seem to be the most long-lived ordered geophysical fluid structures. Their lifetimes are much larger not only compared to a recirculation or advective time but compared to a synoptic variability time. Owing to their high energy and transport properties long-lived vortices play an important role in the general circulation of the ocean.

Geophysical eddies are known to be predominantly in a geostrophic balance (McWilliams, 1988). For understanding of main features of vortex dynamics a reduced-gravity quasigeostrophic approximation can be used. In this case on the beta-plane all stationary translating localized structures must have zero net angular momentum (Flierl, 1987). Let us consider a nonstationary behaviour of a monopolar vortex on the different time scales.

### Part 2

For an intense vortex a recirculation time scale is much smaller than a synoptic time. Analysis of an evolution of small perturbations of a circular vortex shows that in the case of monotonic-continuous radial profile of the potential vorticity azimuthal disturbances decay in time due to shear-dispersion effects (Sutyrin, 1989). For a step-like distribution of the potential vorticity there exist nondecaying azimuthal waves rotating slower than the fluid particles (Polvani, 1988). These conclusions are in qualitative agreement with numerical investigation of an axisymmetrization of an elliptic vortex (Melander et al., 1987).

### Part 3

At the synoptic time scale the beta-effect becomes essential. It leads to an azimuthal deviation and motion of the vortex center. Analysis of development of this

azimuthal deviation shows that it has a dipolar structure that coase the nonstationary translation in addition to westward Rossby wave drift (Sutyrin, 1988). Vortex moves predominantly westward of its radius is larger than the deformation radius that is characteristic for oceanic rings. Predominantly meridional displacement due to the beta-effect is characteristic for a vortex of a hurricane type with the scale which is much smaller than the deformation radius. Nonfrictional decay of an intense vortex is small at the synoptic time scale owing to quick fluid rotation in the core. These results agree well with numerical simulations (McWilliams and Flierl, 1979).

#### Part 4

At the larger time the radiation of Rossby waves reduces the intensity of a vortex. Numerical study shows that central core of a vortex with closed isolines of the potential vorticity remains near circular during many synoptic periods (Sutyrin and Yushina, 1989). Thus the evolution of axisymmetric part of a vortex can be easy calculated by its meridional displacement. When a vortex approaches to a latitude of rest is impossible because of the enstrophy could not increase in agreement with results of Larichev (1983). Some kind of stationary translating vortex was pointed out by Flierl (1984). Though this sollution is not localized and has an infinite potential energy it might be considered as one of the possible limits of evolution of a strong monopolar vortex on the quasigeostrophic beta-plane.

#### References

- Flierl G.R., 1984. Rossby wave radiation from a strongly nonlinear warm eddy. J. Phys. Oceanogr. V. 14, N 1. P. 47-58.
- Flierl G.R., 1987. Isolated eddy models in geophysics. Ann. Rev. Fluid Mech. V. 19, P. 493-530.
- Larichev V.D., 1983. General features of nonlinear synoptic dynamics within a simplest model of the barotropic ocean, Okeanologia. V. 23. N4. P. 551-558.
- McWilliams J.C., 1988. Geostrophic vortices. Lectures notes for the International School of Physics "Enrico Fermi" NCAR, Boulder, Colorado.

McWilliams J.C., Flierl G.R., 1979. On the evolution of isolated, nonlinear vortices. J. Phys. Oceanogr. V. 9. N 6. P. 1155-1182.

Melander M.V., McWilliams J. C., Zabusky N.J., 1987. Axisymmetrization and vorticity-gradient intensification of an isolated two-dimensional vortex through filamentation. J. Fluid Mech. V.178. P. 137-159.

Polvani L.M. 1988. Geostrophic vortex dynamics. Ph. D. Thesis. MIT/WHOI, WHOI-88-48.

Sutyrin G.G., 1988. Motion of an intense vortex on a rotating sphere. Fluid Dyn. Sov. Res. P. 215-223.

Sutyrin G.G., 1989. Azimuthal waves and symmetrization of an intense vortex. Dokl. Akad. Nauk SSSR, Physics, V. 304, N5, P. 1086-1091.

Sutyrin G.G., Yushina I.G., 1989. Numerical modeling of the formation, evolution, interaction and decay of isolated vortices. In "Mesoscale/synoptic coherent structures in geophysical turbulence". J.C.J. Nihoul and B.M.Jamart, Eds. Elsevier. P. 721-736.

## AN INVERSE ANALYSIS OF CSALT DATA

George Veronis  
Kline Geology Laboratory  
Yale University  
New Haven, CT

Jae Hak Lee, a graduate student at Yale University, and I have been analyzing the CSALT data gathered in Spring 1985 to determine diffusion coefficients and velocities in the region of observation. The data are particularly well suited for such a study because vertical soundings were made on a square grid array with 55 km between stations.

R. Schmitt (1987) has summarized many of the observed features. A region with a strong staircase-structure in T and S shows ten layers that are vertically homogeneous locally and separated from each other by what appear to be salt-finger interfaces. Temperature soundings taken at horizontal intervals of 1.5 km show that some of the homogeneous layers are coherent over a horizontal distance of 33 km. A plot of all other data from identifiable layers indicates that the data all fall into one of ten straight-line segments on the T S diagram. Individual line segments connect points as far apart as 400 km; T, S and all vary within a line segment but these properties suffice to identify an observed data point with a specific layer.

It is clear from the observations that the property distributions are conducive to salt fingers. Therefore, vertical eddy diffusion coefficients for salt and heat should be positive if the fluxes are dominated by salt fingers. Mass conservation and advective diffusive equations for T, S and O have been used together with the observed distributions of these properties to determine the velocities and diffusion coefficients. The analysis was restricted to the region with strong staircases where the primary transport mechanism (salt fingering) is understood and can serve as a control on the procedures that were adopted. Because of the restricted amount of available data it is not possible to determine a general distribution of the unknowns. Hence, as a first approximation, horizontal diffusion has been omitted and both vertical diffusion coefficients and vertical velocities have been assumed horizontally uniform; the system is then overdetermined.

The preliminary calculations were meant to test the foregoing simplifications and also to determine the

stability of the solution procedure. Least squares yielded results that were overly sensitive to small perturbations. The method of total least squares provided an improvement in the solution. Constraints on the expected errors may help make the procedure more stable. So far the principal physical result that we have derived is the ratio of vertical heat to salt flux which achieves an average value of about 0.9, in reasonable agreement with the ratio obtained in laboratory salt finger experiments. The associated vertical velocity field is downward, as one might expect from the mean wind-stress curl for that area. The vertical diffusion coefficient for salt is about three times that for heat. The derived horizontal velocity field has a great deal of eddy structure.

#### References

Schmitt, R W (1988). Mixing in a Thermohaline staircase in Small Scale Turbulence and Mixing in the Ocean, eds J.C.J. Nihoul and B.M. Jamart. Elsevier Oceanography Ser.

## BOUNDARY DRIVEN MIXING

Andrew W. Woods  
Cambridge University

We consider two mechanisms of generating a boundary flow in a stratified fluid and show how these can drive mixing of the interior fluid.

The first mechanism arises when a stratified fluid is contained in a vessel with insulated sloping side walls. The isopycnals are thus non-horizontal near the walls of the vessel. This generates a boundary current (Phillips, 1970, Wunsch, 1970) which, in a closed vessel, forces a weak return flow in the fluid interior. It was shown that this return flow is exactly such as to mix the fluid according to the advection-diffusion equation

$$\frac{\partial \rho}{\partial t} = \frac{\kappa}{L} \frac{\partial}{\partial z} \left( L \frac{\partial \rho}{\partial z} \right) \quad (1)$$

where  $L$  is the width of the container,  $\rho$  the fluid density and  $\kappa$  the molecular diffusivity.

The second mechanism of mixing arises when there is a turbulent boundary layer at the walls of the container. The relatively large eddy diffusion coefficients decrease with distance from the wall towards their molecular counterparts in the interior of the fluid. Such variation in the diffusion coefficients may generate horizontal density gradients near sloping or vertical walls. These drive a flow along the wall, which drives a return flow in the interior of the container. A model of this process predicts that the interior fluid mixes according to the advection-diffusion equation

$$\frac{\partial \rho}{\partial t} = \frac{\kappa_b}{L} \frac{\partial}{\partial z} \left( \delta \frac{\partial \rho}{\partial z} \right) + \frac{\kappa_i}{L} \frac{\partial}{\partial z} \left( L \frac{\partial \rho}{\partial z} \right) \quad (2)$$

Where  $\kappa_b$  is the turbulent diffusivity in the boundary layer,  $\kappa_i$  the diffusivity in the interior and  $\delta$  the boundary layer thickness.

This equation was shown to be consistent with some experimental results of Ivey & Corcos, 1982, Thorpe, 1982, Phillips et al. 1986 and Ivey, 1987.

Such enhanced diffusion (2) may have a significant effect in mixing in deep ocean basins (Munk, 1966).



Simple solutions for the mixing of both a pynocline and a point source at the bottom of a basin were described.

### References

Ivey G.N. and Nokes, R.I., 1989, Vertical mixing due to the breaking of critical internal waves on sloping boundaries, J.F.M., 204, 479-500.

Ivey G.N. and Corcos G.M., 1982, Boundary Mixing in a stratified fluid. J.F.M., 121, 1-26.

Ivey G.N., 1987, Boundary Mixing in a rotating stratified fluid, J.F.M., 123, 25-44.

Munk, W.H., 1966, Abyssal Recipes, Deep Sea Res., 13, 707-730.

Phillips, O.M., 1970, On flows induced by diffusion in a stably stratified fluid, Deep Sea Res., 17, 435.

Thorpe, S.A., 1982, On layers produced by rapidly oscillating a vertical grid in a uniformly stratified fluid, J.F.M., 124, 391-410.

Wunsch, C., 1970, On Oceanic Boundary Mixing, Deep Sea Res., 17, 293-301.

Woods, A.W., 1989, Boundary Driven Mixing. I. Molecular Diffusion. II. Turbulent Diffusion, in preparation.

## An Estimate of the Dimension of the Attractor of a Quasi-Geostrophic System

Jun-Ichi Yano

M. I. T.

Recently, the various model studies (e. g. Curry, *et al.*, 1984; Marcus, 1981; Yoden, 1985; Cehesky and Tung, 1987) have pointed out that the model with enough number of modes retained tends to behave in less "chaotic" manner than the model that number of modes is severely limited, implying that the chaotic behavior of severely truncated case is "spurious". The present study is to comment on this point.

I and H. Mukougawa have taken as such an example the quasi-geostrophic two-layer model with topograophic forcing, studied by Cehesky and Tung. With an increase in the number of modes included in the Fourier expansion, the change of the attractor-dimension (Kaplan-Yorke dimension), which is considered as a good measure of the extent of the chaotic behavior of the system, is investigated. No convergence of the dimension is found by increasing the total number of Fourier modes up to 210. The Kolmogorov entropy, that is another measure of chaos, also increases with an increase in number of modes.

The result shows that, even if the solution of the system is less "chaotic", in the sense that the attractor projected on the phase plane spanned by the longest-wave components apparently converges to a solution of the severest-truncation with the higher number of modes included as in the present setting, this does not necessarily mean that the system is really less "chaotic" in the sense defined by the dimension of the attractor or the Kolmogorov entropy.

# STATISTICS OF AGGLOMERATION

W. Young, Y. Pomeau and G. Carnevale  
Scripps Institution of Oceanography  
San Diego, California

As a simple model of agglomeration and inelastic interaction of coherent structures we have studied "ballistic agglomeration". This is an infinite ensemble of particles moving on a straight line. Collisions are perfectly inelastic (i.e. particles stick together) and conserve mass and momentum. The result is ever more massive particles moving ever more slowly and separated increasing gaps.

A simple scaling argument shows that the average mass of a particle increases as  $t^{2/3}$ , the average gap length as  $t^{2/3}$  and the velocity decreases as  $t^{-1/3}$ . These analytic results are confirmed by direct numerical simulation.

It is easy to extend the scaling argument to higher dimension. One finds that the mass of a particle increases as  $t^{2D/(D+1)}$  where  $D$  is the dimension of the space.

**1989 Summer Study Program**

**in**

**Geophysical Fluid Dynamics**

**REPORTS OF FELLOWS**

## ON THE MERIDIONAL PROPAGATION OF ISOLATED EDDIES

Eric P. Chassignet

## ABSTRACT

The meridional motion of isolated eddies is investigated in detail in several numerical experiments. It is found that a distinction has to be made between the center of mass and the eddy center, the latter being defined from either the interface displacement or potential vorticity field. The center of mass is observed to move westward at approximately the same speed as the eddy center. On the other hand, its meridional motion is almost zero and does not coincide with the eddy center which moves significantly. Different mechanisms for the motion are investigated and it is shown that the presence of a dipole in the perturbation field can induce a meridional displacement.

## 1 INTRODUCTION

Little is still known at the present time on the propagation of eddies. Numerical simulations on a  $\beta$ -plane (McWilliams and Flierl, 1989; Mied and Lindemann, 1979; Davey and Killworth, 1984; Chassignet *et al.*, 1989) have shown that an isolated eddy will move westward at approximately the long Rossby wave speed (calculated from the fluid at rest outside the eddy) and will leave behind a Rossby wave wake (Figure 1). A distinction appears between cyclones and anticyclones which move slower and faster, respectively, than the long Rossby wave speed (Nof, 1983; Chassignet *et al.*, 1989). In addition, anticyclones move meridionally equatorward while cyclones move poleward.

Expressions for the westward propagation of the center of mass of the eddy were derived by several authors (Flierl, 1977; Nof, 1981, 1983; Cushman-Roisin *et al.*, 1989). In these studies, the location of the center of mass was assumed to be a fair representation of the position of the eddy. As it will be shown, this is quite a good approximation for the westward component of the drift, but is not for the meridional one.

In this note, with the help of a few numerical simulations, the drift of an isolated eddy is studied in detail. In particular, distinctions between the center of mass and eddy center (defined as an extremum either in interface displacement or potential vorticity) will be made. Emphasis will be on the meridional displacement, but the zonal component will also be discussed, the two being linked.

The following investigation follows mostly the approach taken by the author during

## INTERFACE DISPLACEMENT ANOMALY

Contour Interval = 20 m

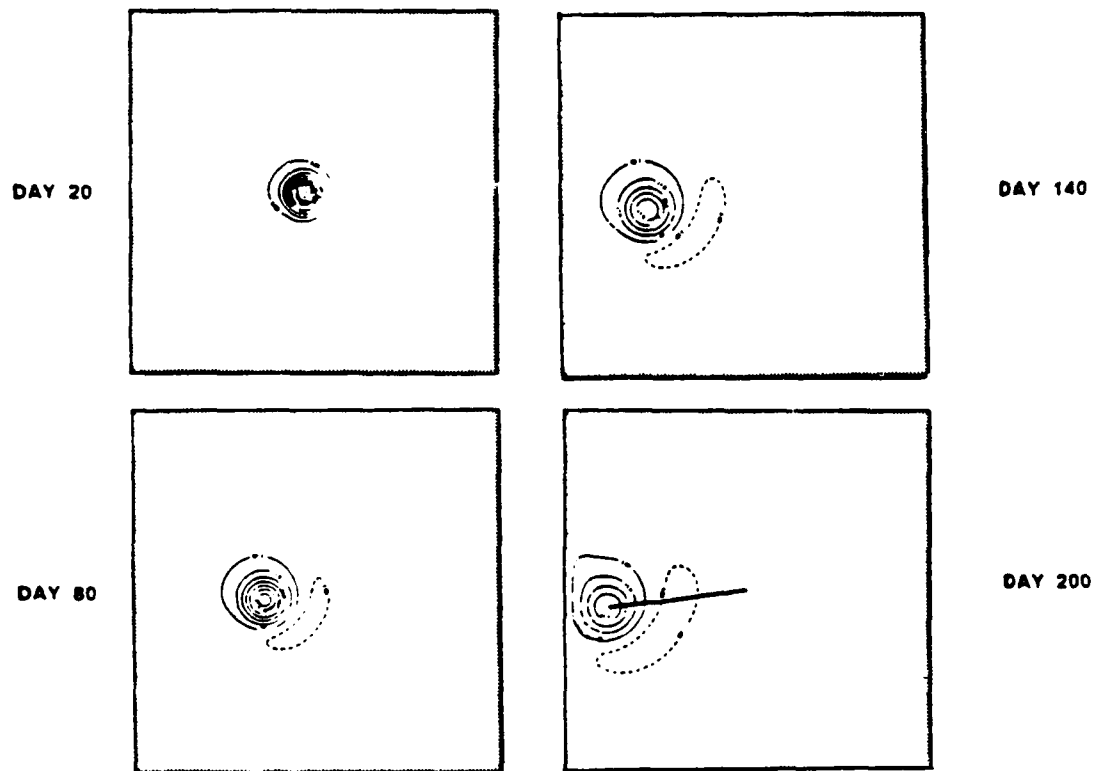


Figure 1: Evolution of an anticyclone for a period of 200 days

the summer. In section 2, the model and experiments are presented. Section 3 discuss the drift of the center of mass versus the one of the eddy center. Section 4 investigate the probable mechanisms for the meridional motion. In section 5, the induced motion by a dipole on a vortex is discussed and related to the mechanisms described in section 4. The results are then summarized in section 6.

## 2 THE MODEL AND EXPERIMENTS

The model used is the primitive equation, isopycnic coordinate model of Bleck and Boudra (1986). This type of model allows the specification of desired initial conditions, through the positioning of the isopycnal surfaces and, in particular, can reproduce the initial conditions of lens-like eddies; i.e. ones where isopycnals surfaces.

The model is configured in a two-layer  $2000\text{ km} \times 2000\text{ km}$  square domain on a  $\beta$ -plane with a grid spacing of either 20 or 10 km (anticyclone or lens, respectively). Lateral boundary conditions are free-slip everywhere. A rigid lid is used for the upper boundary and a flat bottom with no drag for the lower one. The model is initialized with a Gaussian interface displacement  $h = h_0 e^{-r^2/2L^2}$  where  $r$  is the radius from the center,  $L$ , the radius of maximum velocity and  $h_0$ , the center depth of the eddy. The chosen values for  $L$  and  $h_0$  are fixed to 60 km and 500 m, respectively. This is not necessarily the most realistic parameterization of an oceanic eddy (Olson, 1980), but does permit comparisons with other studies (McWilliams and Flierl, 1979; Mied and Lindeman, 1979; McWilliams *et al.*, 1986). The velocities are initially in geostrophic balance in the upper layer and at rest in the lower. The reduced gravity  $g'$  is fixed and equal to  $0.0196\text{ m s}^{-2}$ . The lower layer is chosen to be very deep (ratio 1:1000) to approximate a reduced gravity model. Motion in the lower layer modifies significantly the motion of the upper layer eddy (Chassignet *et al.*, 1989). In this note, we concentrate on the mechanisms driving the eddy propagation in the upper layer.

Four experiments are described in the following sections. L1 is a lens (the upper layer thickness outside the eddy is equal to zero and the isopycnals outcrop) and A1, A2 and A3 are anticyclones with an upper layer thickness of  $H = 1000\text{ m}$  and lateral eddy viscosity of 330, 50 and  $0\text{ m}^2\text{ s}^{-1}$ , respectively ( $330\text{ m}^2\text{ s}^{-1}$  for L1).

## 3 DRIFT OF THE CENTER OF MASS VERSUS THE EDDY CENTER

The westward propagation of an eddy has been traditionally expressed as the evolution in time of the location of its center of mass. The center of mass ( $X, Y$ ) is

defined by

$$X = \langle x\eta \rangle$$

$$Y = \langle y\eta \rangle$$

where  $\langle \dots \rangle = \frac{\int \int \dots dx dy}{\int \int \eta dx dy}$  and  $\eta$  is the interface displacement.

In the context of quasi-geostrophic dynamics, McWilliams and Flierl (1979) showed that the center of mass motion is exactly the long Rossby wave speed in the westward direction and exactly zero meridionally. However, in their numerical experiment, the center of the vortex was observed to not always coincide with the center of mass. In particular, a meridional drift of a quarter of the long Rossby wave speed was observed.

In the reduced gravity case, assuming the eddy to have a small Rossby number (reasonable for most observed oceanic eddies), Cushman-Roisin *et al.* (1989) showed that, to the first order, the drift of the center of mass can be expressed as

$$\dot{X} = -\frac{\beta g' \int \int (H\eta + \frac{1}{2}\eta^2) dx dy}{f_o^2 \int \int \eta dx dy} \quad (1)$$

$$\dot{Y} = 0. \quad (2)$$

where  $\dot{X}$  and  $\dot{Y}$  are the zonal and meridional drift, respectively. The other symbols are conventional. The error on these estimates for a typical eddy is of the order of 10% of the long Rossby wave speed. Cushman-Roisin *et al.* (1989) showed that (1) describes accurately the westward propagation of the eddy with the center of mass moving slightly faster than the vortex itself. On the other hand, the error on the meridional drift is approximately of the same magnitude as of the observed one. Therefore, the derivation of  $\dot{X}$  and  $\dot{Y}$  is performed to the second order in subsection 3.1. The results are then compared to the numerical simulations in subsection 3.2.

### 3.1 Derivation of the center of mass propagation speed

The equation of motion for the inviscid reduced gravity model (infinite lower layer) are

$$u_t + uv_x + vu_y - fv = -g'h_x \quad (3)$$

$$v_t + uv_x + vv_y + fu = -g'h_y \quad (4)$$

$$h_t + \nabla \cdot (\underline{u}h) = 0. \quad (5)$$

The propagation speed of the center of mass is defined by  $\dot{X}$  and  $\dot{Y}$  which are equal



to

$$\begin{aligned}\dot{X} &= \langle x\eta \rangle_t = \langle x\eta_t \rangle = \langle xh_t \rangle = - \langle x\nabla \cdot (\underline{u}h) \rangle \\ &= - \langle \nabla \cdot (x\underline{u}h) \rangle + \langle \underline{u}h \cdot \nabla x \rangle \\ &= \langle hu \rangle\end{aligned}$$

$$\dot{Y} = \langle hv \rangle.$$

If we define  $f = f_0 + \beta y$ , then equation (3) becomes when multiplied by  $h$

$$\begin{aligned}hu_t + h_t u + (uh)_x u + (vh)_y u + hu u_x + hv u_y \\ - f_0 hv - \beta y hv = -g' \left( \frac{h^2}{2} \right)_x.\end{aligned}$$

Taking the average over the whole basin and integrating by parts leads to

$$\langle hu_t \rangle + \langle h_t u \rangle - f_0 \langle hv \rangle - \beta \langle y hv \rangle = 0.$$

We can perform the same for equation (4) and, defining  $\ddot{X}$  and  $\ddot{Y}$  as  $\langle hu \rangle_t$  and  $\langle hv \rangle_t$ , respectively, we have

$$\ddot{X} - f_0 \dot{Y} = \beta \langle y hv \rangle \quad (6)$$

$$\ddot{Y} + f_0 \dot{X} = -\beta \langle y hu \rangle \quad (7)$$

A scaling analysis (Cushman-Roisin *et al.*, 1989) shows that, to the first order, the terms in  $(\ddot{\phantom{x}})$  can be neglected. By replacing  $u$  and  $v$  by their geostrophic values, (6) and (7) provide  $\dot{X}$  and  $\dot{Y}$  as in equations (1) and (2). To obtain the second order expression, we replace  $\dot{Y}$  in equation (7) by its expression from equation (6) and vice-versa for  $\dot{X}$ . This leads to

$$\ddot{Y} + f_0^2 \dot{Y} = -\beta \langle y hu \rangle_t - \beta f_0 \langle y hv \rangle \quad (8)$$

$$\ddot{X} + f_0^2 \dot{X} = \beta \langle y hv \rangle_t - f_0 \beta \langle y hu \rangle \quad (9)$$

Using the fact that  $\langle y hu \rangle_t = \langle y(hu)_t \rangle$  and  $\langle y hv \rangle_t = \langle y(hv)_t \rangle$ , we can rewrite equations (8) and (9) as

$$\ddot{Y} + f_0^2 \dot{Y} = -\beta \langle hvu \rangle - 2\beta f_0 \langle y hv \rangle - \beta^2 \langle y^2 hv \rangle \quad (10)$$

$$\ddot{X} + f_0^2 \dot{X} = -\beta \langle hv^2 \rangle - 2f_0 \beta \langle y hu \rangle + \beta g' \left\langle \frac{1}{2} \eta^2 + H\eta \right\rangle - \beta^2 \langle y^2 hu \rangle \quad (11)$$

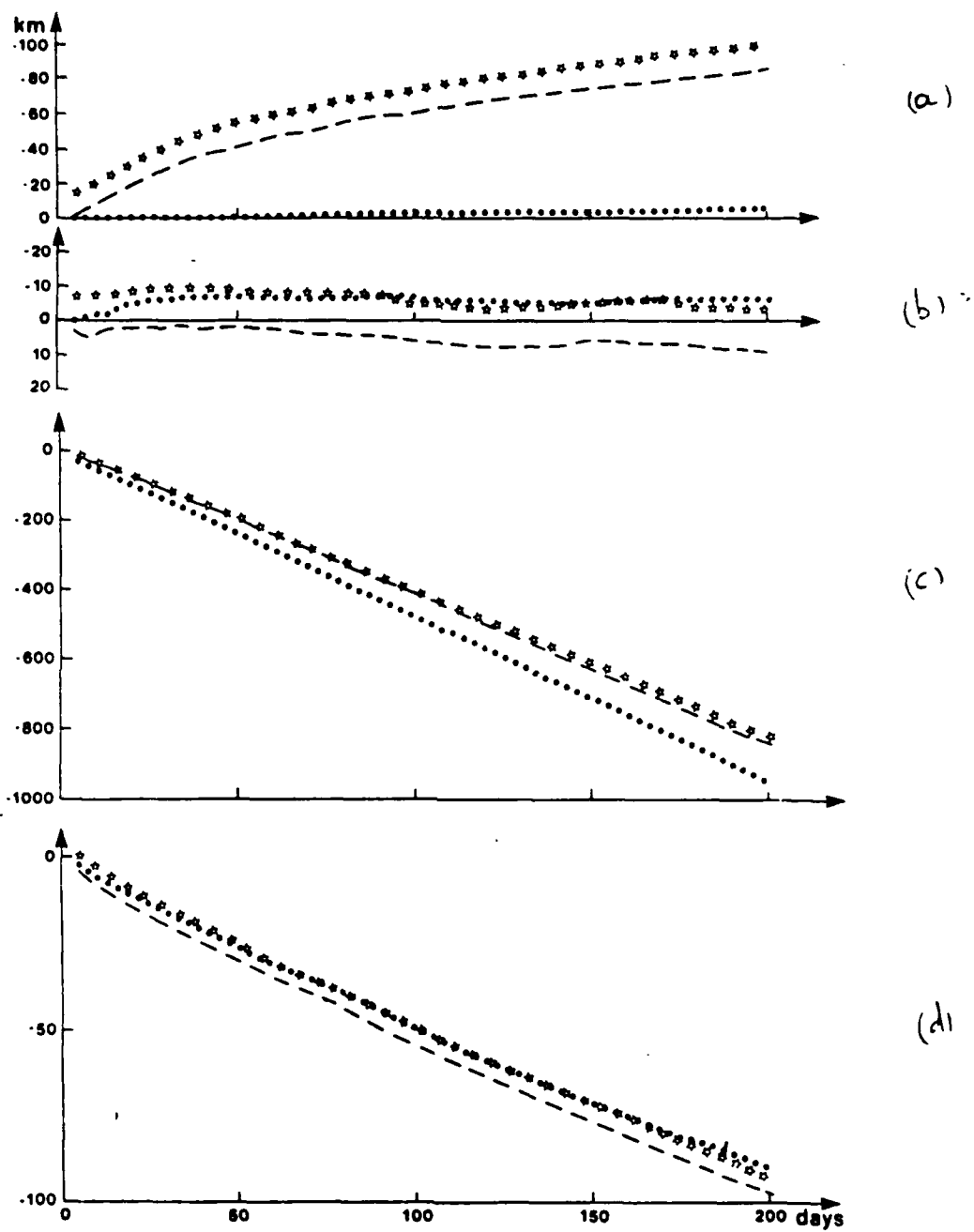


Figure 2: Meridional displacement of the center of mass (dotted),  $C_n$  (dashed) and  $C_q$  (stars) for (a) the anticyclone A2 and (b) the lens L1. Same for westward in (c) A2 and (d) L1.

Again, a similar scaling analysis as the one performed by Cushman-Roisin *et al.* (1989) shows that we can neglect the terms in  $(\ddot{\cdot})$  and therefore

$$\dot{Y} = -\frac{\beta}{f_o^2} \langle h v u \rangle - 2\frac{\beta}{f_o} \langle y h v \rangle - \frac{\beta^2}{f_o^2} \langle y^2 h v \rangle \quad (12)$$

$$\dot{X} = -\frac{\beta}{f_o^2} \langle h v^2 \rangle - 2\frac{\beta}{f_o} \langle y h u \rangle + \frac{\beta g'}{f_o^2} \langle \frac{1}{2} \eta^2 + H \eta \rangle - \frac{\beta^2}{f_o^2} \langle y^2 h u \rangle \quad (13)$$

If the vortex is axisymmetric ( $h$  function of  $r$  only), then (12) is identically zero. The center of mass then coincide with the eddy center and both move only westward.

At this point, we can replace  $u$  and  $v$  by their geostrophic values in (12) and obtain an expression like equation (2) to the second order for  $\dot{Y}$ . We then have

$$\dot{Y} = \frac{\beta g'^2}{f_o^4} \langle h h_x h_y \rangle \quad (14)$$

The meridional motion of the center of mass is therefore not exactly zero. We now compare the above results to the numerical calculations.

### 3.2 Comparisons with the numerical experiments

In order to compare the eddy propagation to the one of the center of mass, one need first to define the eddy center. Traditionally, it is defined as being the extremum of either the interface displacement or the potential vorticity. The location of these three centers (center of mass,  $C_\eta$  and  $C_q$ , respectively) are presented in Figure 2 for A2 and L1. For the anticyclone A2, the center of mass is always located in front of the eddy center defined from either the interface displacement or potential vorticity, but has almost a non zero meridional displacement. On the other hand, the eddy center (defined from either  $C_\eta$  or  $C_q$ ) has a significant displacement equatorward. In this experiment,  $C_q$  follows closely  $C_\eta$ . On the contrary, for the lens L1, the center of mass is located eastward and moves also only westward.  $C_q$  is observed to follow closely the center of mass. On the other hand,  $C_\eta$  moved slightly poleward.

The zonal and meridional velocities of the center of mass and eddy center for A1 and L1 are presented in Figure 3 as well as the estimate of the center of mass westward drift calculated from Cushman-Roisin *et al.* (1989) (equation (1)). For both A1 and L1, the estimate represents accurately the westward drift (center of mass or eddy center since they move at approximately the same speed) (Figure 3). As expected from Figure 2, in the anticyclone A2, the center of mass has almost a zero meridional

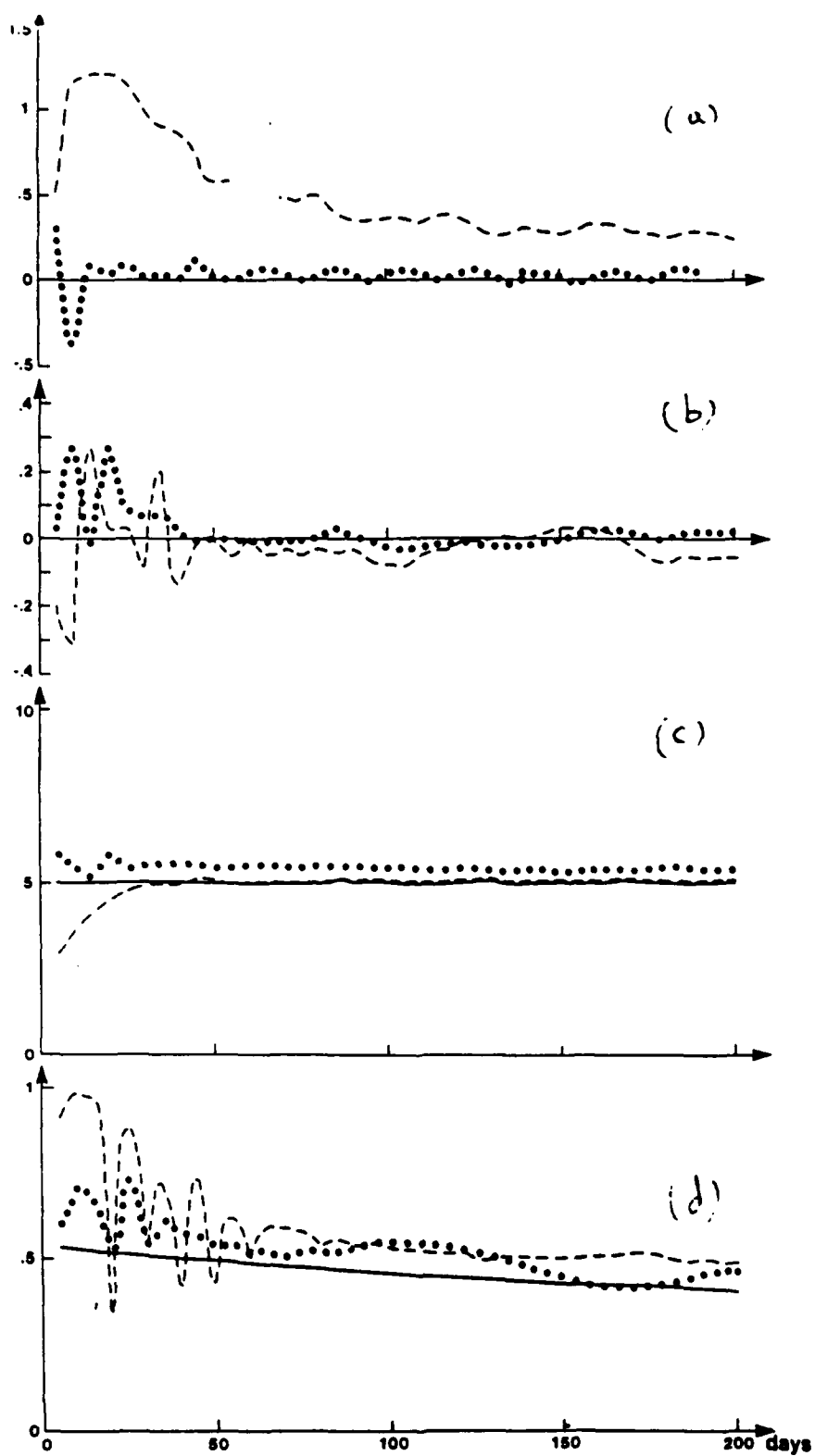


Figure 3: As in Figure 2 for the velocities. Only for the center of mass and  $C_\eta$ .

motion, while the meridional drift of the eddy center is significant. The meridional drift of the center of mass therefore does not describe the meridional drift of the eddy.

In order to check more fully the accuracy of the center of mass drift calculated in equations (6) and (7) (first order estimate) and in equations (12) and (13) (second order estimate), these estimates are computed for A1 and L1 and then compared to the actual translation of the center of mass. The differences are presented in Figure 4. for A1 and L1, respectively. Not to surprisingly, the error decreases when the second order terms are taken in account. The calculated drifts approximate closely the observed ones. The inviscid reduced gravity equations therefore gives a good representation of the vortex behavior in a model with strong lateral eddy viscosity.

#### 4 DRIFT OF THE EDDY CENTER

At this point, we therefore have to make a distinction between center of mass and eddy center, at least for the meridional component of the drift. In subsection 4.1, we first consider a particle located at the center (defined as an extrema in potential vorticity) and study its behavior. In subsection 4.2, we then consider the contribution of the different integrals derived in section 3.1 when integrated over the eddy itself. Finally, subsection 4.3 investigates the flow field which contributes to the eddy propagation.

##### 4.1 Lagrangian approach

If the center of the vortex is defined as the extrema in potential vorticity, then the particle located at the center should remain at the center as it has to conserve its potential vorticity. Based on this consideration, we can express the potential vorticity  $q$  of the particle at the center as

$$q_{\text{center}} = \frac{f_0 + \beta y_{\text{center}} + \xi_{\text{center}}}{h_{\text{center}}} \quad (15)$$

where  $\xi$  is the vorticity of the particle. Since the particle conserves its potential vorticity, at a certain time  $\Delta t$  later, the change in  $y_{\text{center}}$  will be given by

$$\dot{y}_{\text{center}} = \frac{q_{\text{center}}}{\beta} \frac{\Delta h_{\text{center}}}{\Delta t} - \frac{1}{\beta} \frac{\Delta \xi_{\text{center}}}{\Delta t}. \quad (16)$$

$\dot{y}_{\text{center}}$  can be decomposed in two parts, namely  $\dot{y}_1$  and  $\dot{y}_2$ , which correspond to the contribution due to the change in depth and to the change in vorticity at the center, respectively.

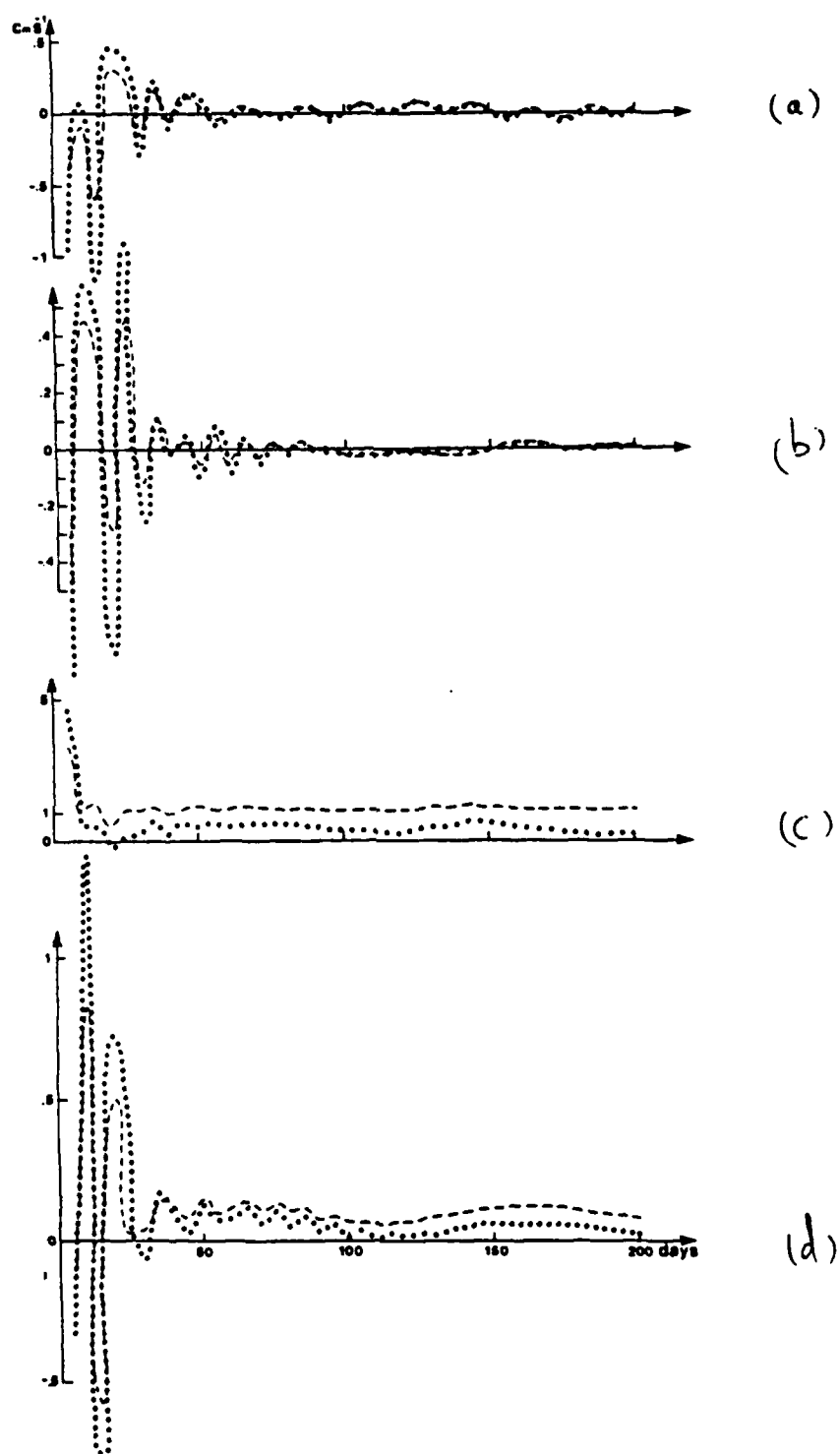


Figure 4: Differences between observed velocities and first (dashed) and second order estimates (dotted) for meridional in (a) A2 and (b) L1 and zonal in (c) A2 and (d) L1.

Lateral viscosity ( $m^2 s^{-1}$ )	$\dot{y}_1$ ( $cm s^{-1}$ )	$\dot{y}_2$ ( $cm s^{-1}$ )	$\dot{y}$ ( $cm s^{-1}$ )	$\dot{y}_{observed}$ ( $cm s^{-1}$ )
330	-2.4	-3.6	-5.0	-0.49
50	-1.0	-5.6	-6.6	-0.3
0	-0.1	-2.5	-2.6	-0.24

Table 1:  $\dot{y}_1$ ,  $\dot{y}_2$ ,  $\dot{y}$ ,  $\dot{y}_{observed}$  averaged over the last 100 days of A1, A2 and A3.

This simple definition of  $\dot{y}_{center}$  illustrates nicely why the cyclones move poleward and anticyclones equatorward. The fact that energy is radiated away in the Rossby wave wake field implies a decrease in interface displacement and in the magnitude of the vorticity within the eddy. In the northern hemisphere, for an anticyclone,  $\Delta h$  is negative and  $\Delta \xi$  positive (since  $\xi$  is negative) which therefore implies from (16) a southward motion. On the contrary, for a cyclone,  $\Delta h$  will be positive and  $\Delta \xi$  negative, therefore implying a northward motion.

The values of  $\dot{y}_1$  and  $\dot{y}_2$  for a period of 100 days are presented in Table 1 for the three anticyclones A1, A2 and A3 (eddy lateral viscosity of 330, 50 and  $0 m^2 s^{-1}$ , respectively) and compared to the observed velocities. One can notice the increase in observed meridional speed as the viscosity increases. This is better illustrated in Figure 5 where the meridional velocities for A1, A2 and A3 are represented as a function of time.

It is of interest to relate the strength of the Rossby wave wake to the meridional propagation rate. The extrema in the interface displacement of the wake as a function of time is presented in Figure 6. One can notice that the wake is stronger for A1 (high viscosity case) where  $\dot{y}_{center}$  observed is the fastest. The wake in A2 and A3 have a similar strength which correspond to a similar meridional displacement. In both A2 and A3, after approximately 70 days, the intensity of the wake starts to decay along with the eddy. This is not the case for A1 where the strong lateral eddy dissipation does not allow for a full development of the wake, therefore accelerating the decay of the eddy and inducing a faster meridional propagation.

In neither A1, A2 or A3, the potential vorticity at the center of the eddy is conserved and, as shown in Table 1, dissipation (explicit lateral eddy viscosity or implicit numerical) produces considerable changes in  $\dot{y}_1$  and  $\dot{y}_2$ . In all cases, one needs only a

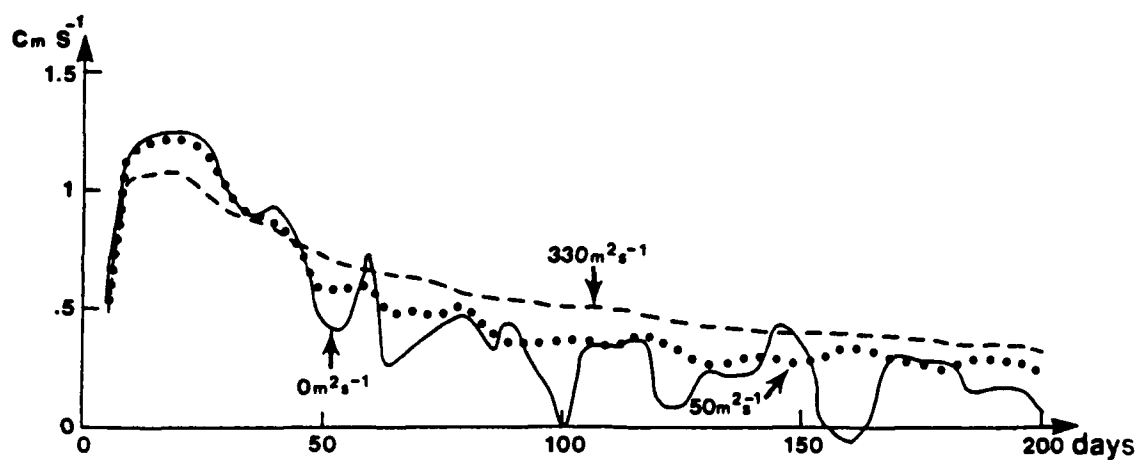


Figure 5: Meridional velocities for A1, A2 and A3 as the eddy lateral viscosity is varied from 330 to  $0 \text{ m}^2 \text{ s}^{-1}$ .

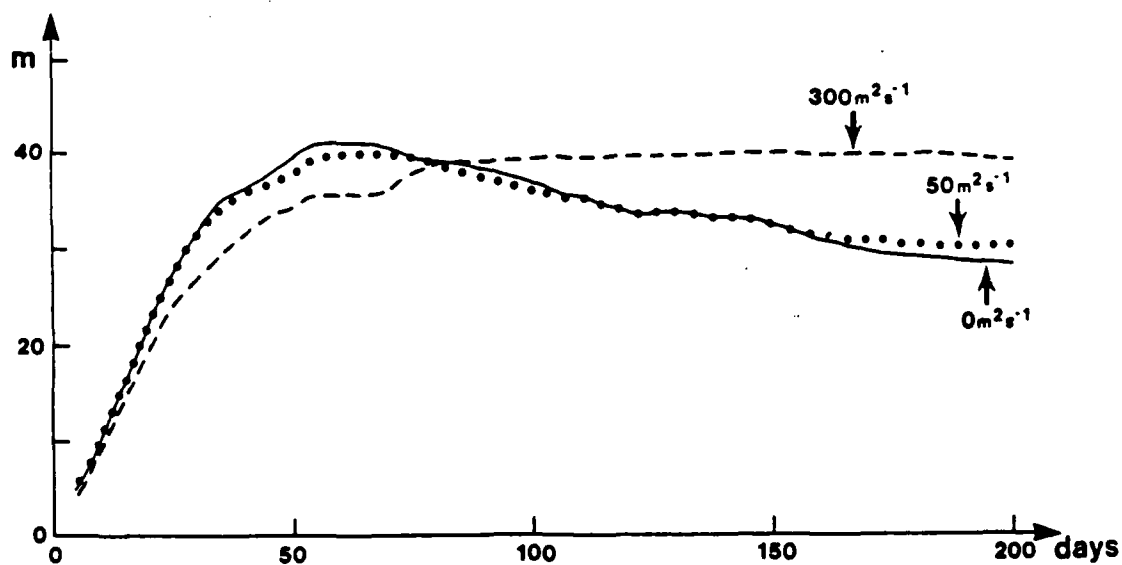


Figure 6: Maximum interface displacement in the wake for A1, A2 and A3.



very small change in the center depth (for example, only a few meters over 100 days for the inviscid case) or in vorticity to obtain a good agreement with the observed drift. On the contrary of section 3 where inviscid dynamics accurately described the center of mass motion, in this case, the dissipation present in the model (explicit or implicit) does not permit conservation of potential vorticity and overcomes any additional insights that one could extract from such an approach.

## 4.2 Eulerian approach

The calculations presented in section 3 were integrated over an infinite area (the whole basin in the case of the numerical experiments) and one can ask about the contributions of each integrals when integrated over the eddy only. In addition, several of the terms that were equal to zero (like divergence) when integrated over the whole domain are now going to contribute to the expression of  $\dot{y}_c$ . The expression of  $\dot{y}_c$  from equation (6) to the first order is then

$$\dot{y}_c = -\frac{\beta}{f_0} \langle y h v \rangle - \frac{g'}{f_0} \langle h h_x \rangle - \frac{1}{f_0} \langle \nabla \cdot (\underline{u} h u) \rangle + \langle \nabla \cdot (\underline{u} y h) \rangle \quad (17)$$

where  $\langle \dots \rangle$  is now an average over a finite surface.

Figure 7 represent the contributions of each of the terms of equation (17) (T1, T2, T3 and T4, respectively) at day 100 for experiment A2 when integrated over a circle of radius  $R$  (x-axis in Figure 7) centered on the eddy center with  $R$  varying from 20 km to " $\infty$ ". One can see that within the core of the eddy ( $R < 150$  km), most of the terms are quite small, but the sum does not agree with the observed drift. As  $R$  increases, the integrals start to take into account the Rossby wave wake and each of the terms become important. When the integral is performed over a large portion of the domain, then all the terms as well as the sum vanish. The only conclusion that one can extract from this simple exercise is that one has to take into account the perturbation field around the eddy. If we define the field as being the sum of an axisymmetric vortex and a perturbation, then the contribution to  $\dot{y}_c$  of the axisymmetric field is zero (equation (17)). The perturbation field is the only one contributing.

## 4.3 Perturbation field

In this subsection, the perturbation field is obtained by subtracting an axisymmetric vortex to the total field. In our numerical experiments, it is assumed that the eddy remain somewhat like a Gaussian and therefore, the subtracted axisymmetric vortex is defined as  $h' = h'_0 \exp^{-\frac{r^2}{2L^2}}$  where  $h'_0$  is the maximum interface displacemt at the

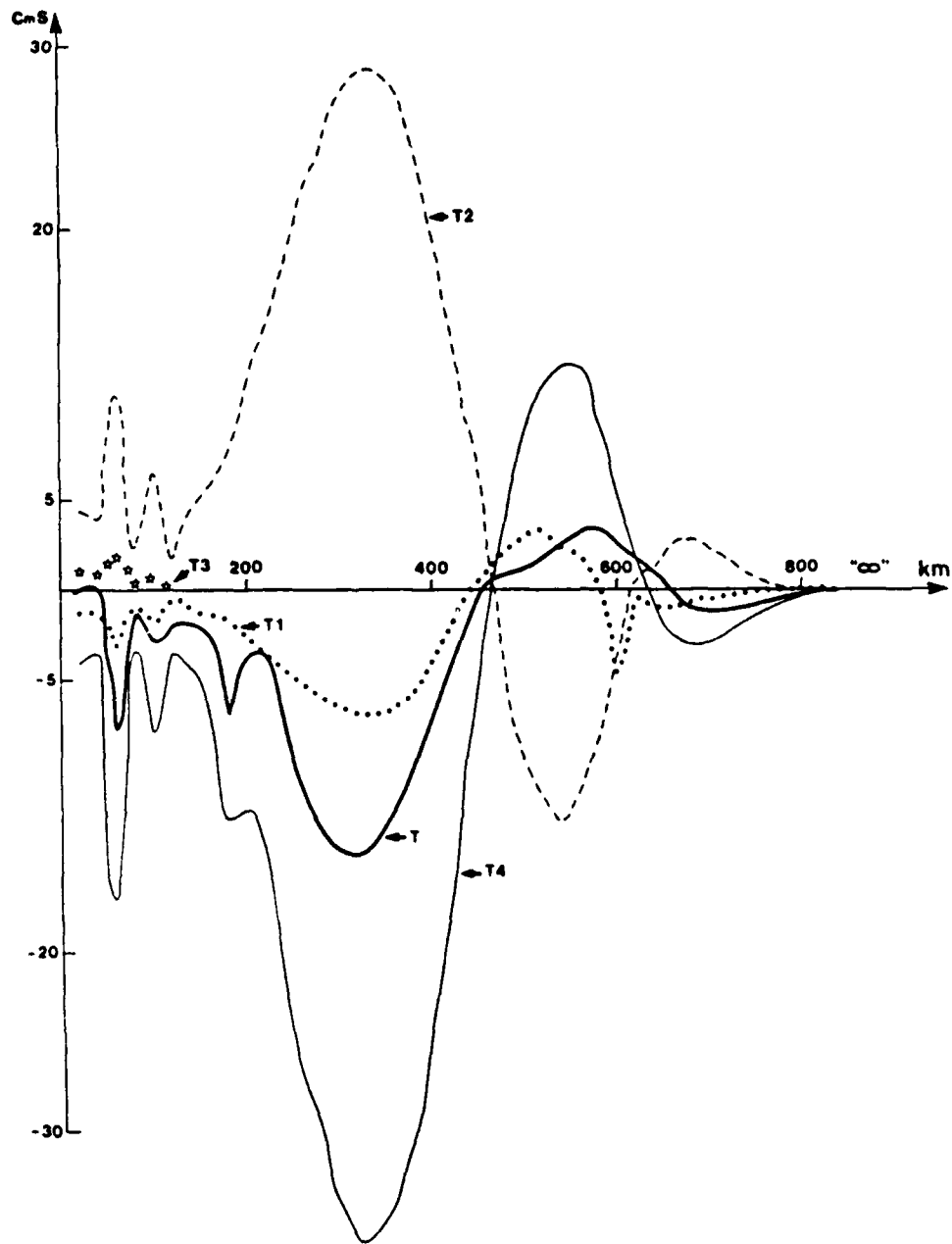


Figure 7: Representation of  $T_1$ ,  $T_2$ ,  $T_3$ ,  $T_4$  and the sum  $T$  ( $y_c$  in the text) as  $R$  is varied from 20 km to  $\infty$ .

center of the eddy and  $L'$ , the radius of maximum velocities. Both fields (total eddy and perturbation) are presented in Figure 8 for day 5 and 100 of experiment A2. One can notice the presence of dipoles in the perturbation fields. At day 5, the dipole is oriented in the east-west direction and is quite weak in amplitude. After a few days (until day 50), the dipole gains in strength and starts to tilt toward a north-south axis. At day 100, the dipole is quite strong and oriented southwest-northeast. The strength of the dipole as time varies can be deduced from the strength of the Rossby wave wake as shown in Figure 6. One can notice that at day 5, the dipole is weak and such is the meridional speed of the eddy (Figure 5). The meridional propagation increases as the dipole grows in strength. The emergence of a dipole in the perturbation field is consistent with Flierl (1984) who showed that a radially symmetric structure propagating on a  $\beta$ -plane will generate a perturbation field of the shape of a dipole. Application to a constant potential vorticity profile of the same size as the present case at day 100 gives for the maximum interface displacement of the dipole a value of 35 m (Flierl, personal communication) versus 25 m observed in Figure 8d.

## 5 INDUCED MOTION ON A VORTEX BY A DIPOLE

The natural question that emerge from subsection 4.3 is: Is the dipole able to induce a meridional motion? In this section, we first investigate this question numerically in 5.1 and then analytically in 5.2.

### 5.1 Numerical approach

The first three experiments that are presented in this subsection investigate the behavior of a dipole when isolated. The fourth one discuss the effect of dipole when superimposed on a symmetric vortex. In all experiments, the dipole is defined from the one at day 100 of A2 in Figure 8, namely a maximum interface displacement of 25 m located at  $L_0 = 170$  km from the center. Experiment D1 is a dipole oriented in the north-south direction and the interface displacement field is given by  $h_1 = Cy \exp^{-\frac{r^2}{2L^2}}$  with  $C = 2.4 \cdot 10^{-4}$ . After 100 days (Figure 9), the dipole is located westward of its initial position and traveled at a speed  $c_x \sim 3.6 \text{ cm s}^{-1}$ . This is less than the long Rossby wave speed ( $4 \text{ cm s}^{-1}$ ). No meridional displacement was observed as well as almost no decay in the amplitude.

The dipole self-advection is investigated in experiment D2 where the same experi-

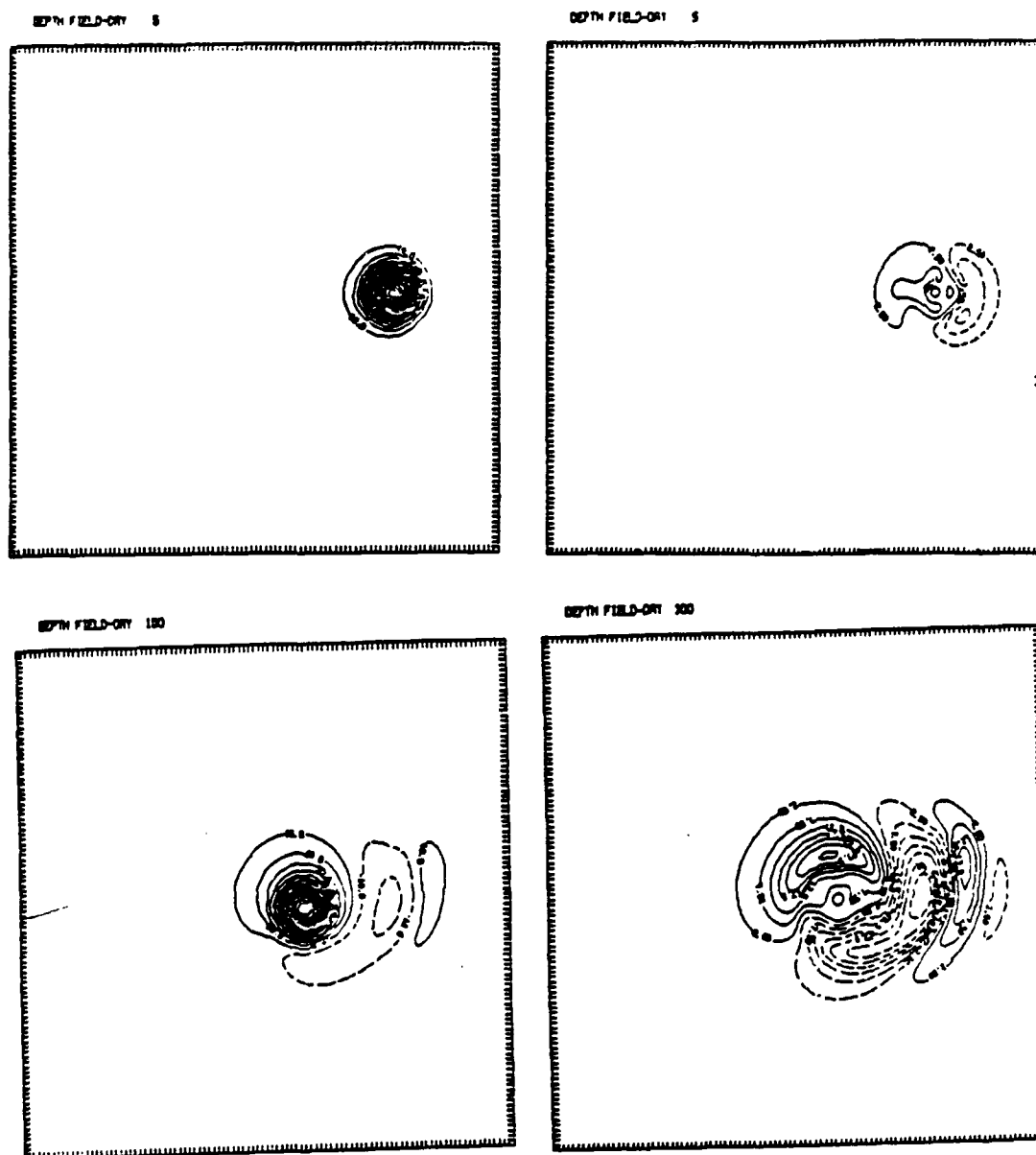


Figure 8: Representation of A2 and its perturbation field at day 5 and 100

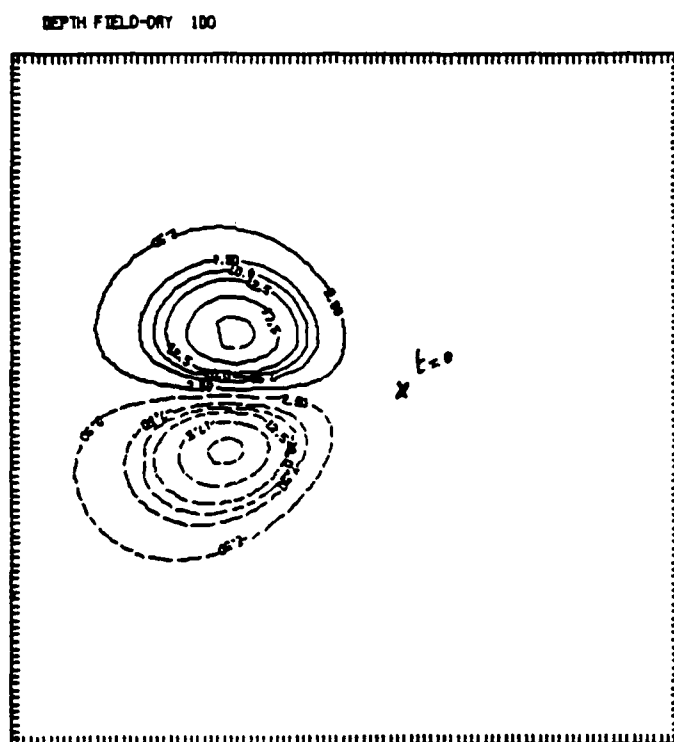


Figure 9: Dipole D1 at day 100.

ment as above is performed on an  $f$ -plane. In this experiment, the dipole moved very slowly at a speed  $c \sim 0.3 \text{ cm s}^{-1}$ .

Finally, the same experiment as D1, but tilted  $45^\circ$ , experiment D3, was performed in order to investigate the influence of the dipole self-advection of the meridional motion (Figure 10). The interface displacement is given by  $h_1 = C(y - x) \exp^{-\frac{x^2}{2L^2}}$  with  $C = 1.7 \cdot 10^{-4}$ . In this case, the dipole moves westward at a speed  $c_x \sim 3.9 \text{ cm s}^{-1}$  and southward at  $c_y \sim 0.2 \text{ cm s}^{-1}$ . One can therefore conclude that the dipole self-advection is enough to induce some meridional displacement when tilted and on a  $\beta$ -plane.

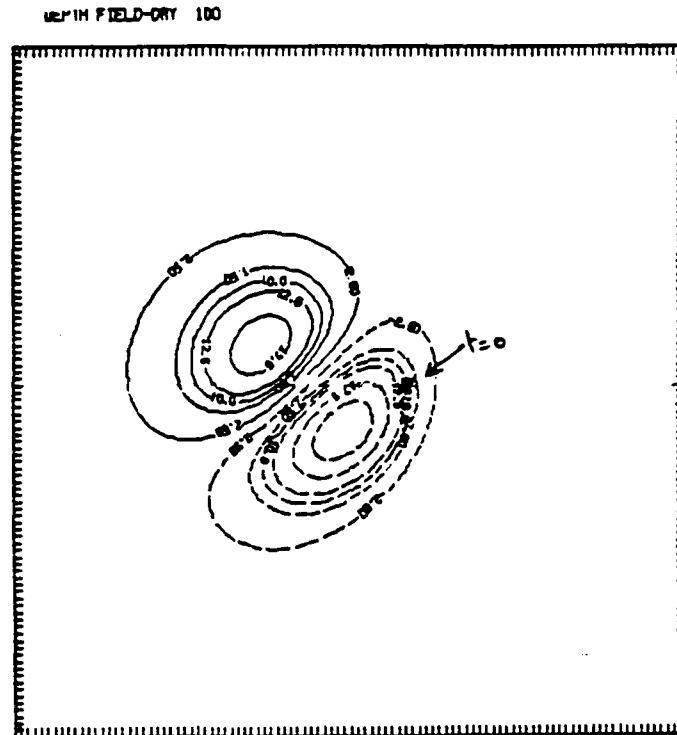


Figure 10: Dipole D3 at day 100.

Experiment D4 is an attempt to understand the effect of such a dipole when superimposed on an axisymmetric vortex. The evolution on an  $f$ -plane of a field  $h = h_0 + h_1$ , where  $h_0$  is a Gaussian vortex as in A2 at day 100 and  $h_1$ , the dipole described above, is presented at day 5 and 100 in Figure 11. The trajectory of the center of  $h$  is

presented in Figure 12. From Figure 11b and d, we can see that the dipole loses its strength rapidly and that the eddy has the tendency to axisymetrize. As shown in Figure 12, this induces a westward motion as well as a northward displacement (north is defined by the orientation of the dipole). On a  $\beta$ -plane, the strength of the dipole is maintained through Rossby wave radiation and in this experiment, without  $\beta$ -effect, the predominant effect is axisymetrisation.

## 5.2 Analytical approach

In this subsection, we now investigate the propagation of a structure defined by  $h = h_o + h_1$  where  $h_o$  is the Gaussian defined by  $h_o^* \exp^{-\frac{r^2}{2L^2}}$  and  $h_1$  the dipole defined by  $h_1 = C(y - x) \exp^{-\frac{r^2}{2L^2}}$  (45° tilt). The total potential vorticity  $q$  is defined as

$$q = \frac{\xi_1 + \xi_o + f_o + \beta y}{H + h_o + h_1}$$

If we consider  $h_1 \ll h_o \ll H$ , then the potential vorticity can be expressed as  $q_o + q_1$  where

$$q_o = \frac{\xi_o + f_o}{H} - \frac{\xi_o + f_o}{H^2} h_o$$

$$q_1 = \frac{\xi_1 + \beta y}{H} - \frac{\xi_o + f_o}{H^2} h_1.$$

If we assume the structure to propagate at a constant speed  $\underline{c}$ , then the potential vorticity equation can be written as

$$\underline{c} \cdot \nabla q_o = \underline{u}_o \cdot \nabla q_1 + \underline{u}_1 \cdot \nabla q_o. \quad (18)$$

We can perform an expansion around the center which leads to

$$q_{o,c} = ax, \quad q_{o,y} = by$$

$$q_1 = a'x + b'y.$$

The geostrophic velocities at the center for  $\underline{u}_o$  are

$$u_o = \frac{h_o^* g'}{f_o L^2} y, \quad v_o = -\frac{h_o^* g'}{f_o L^2} x$$

and the drift speeds can be expressed from (18) as

$$c_x = u_1(0) - A \frac{b'}{a} \quad (19)$$

$$c_y = v_1(0) + A \frac{a'}{b} \quad (20)$$

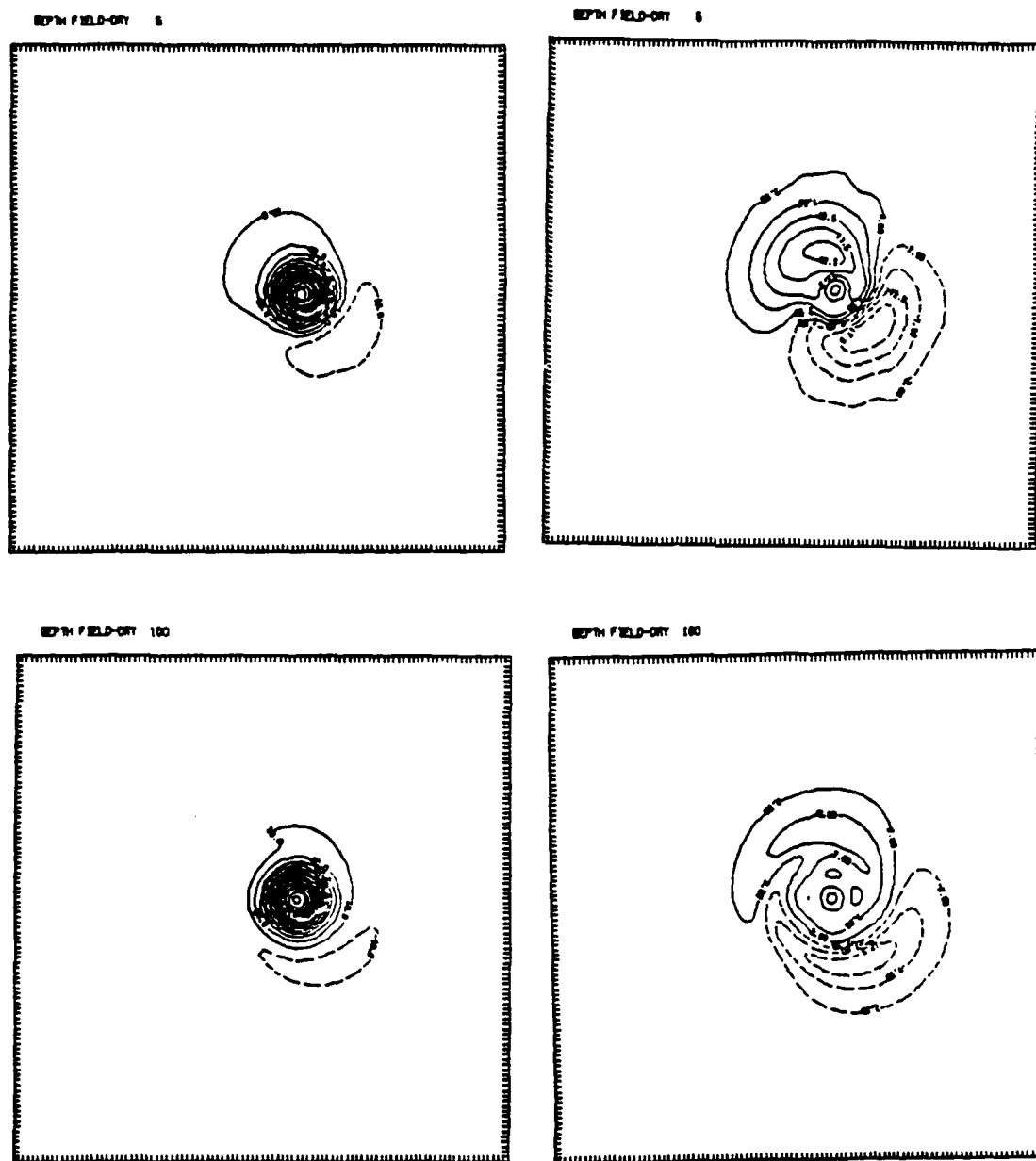


Figure 11: Interface displacement field of experiment D4 and perturbation field at day 5 and 100



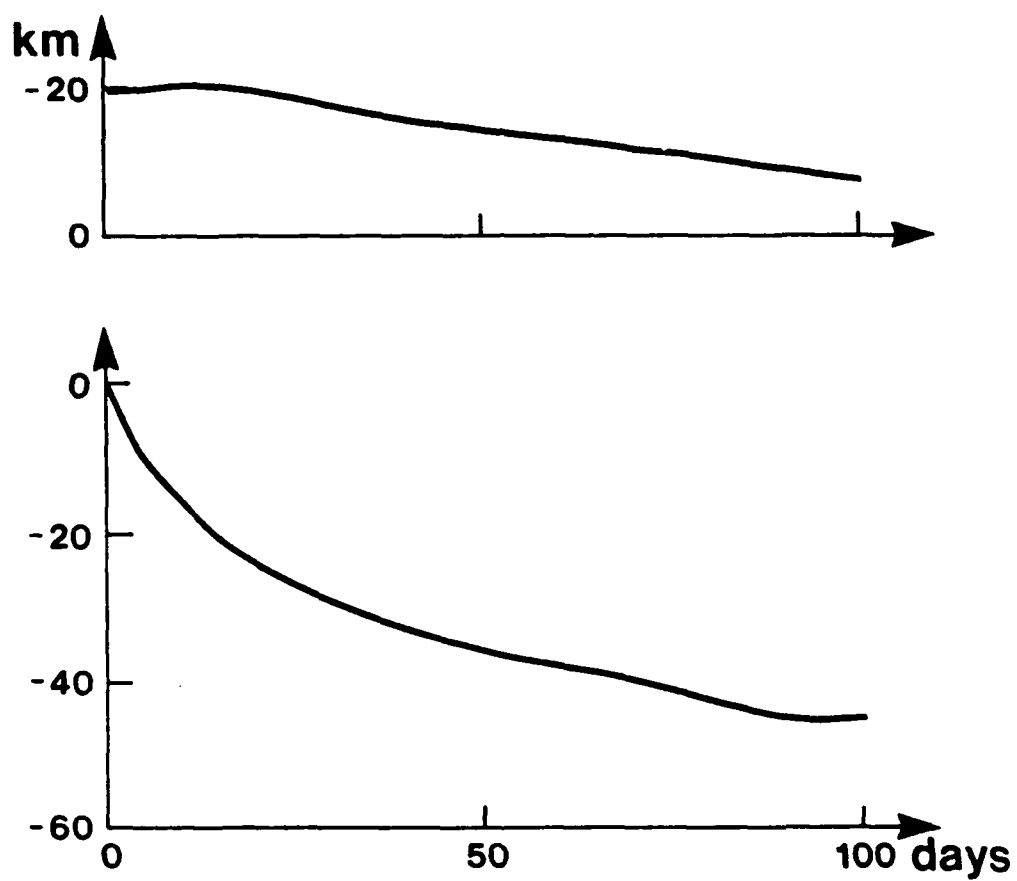


Figure 12: Trajectories of the center of experiment D4 (a) meridionally and (b) zonally.

where  $A = \frac{h_o^* g'}{f_o L^2}$ . We can now compute  $a', b', a$  and  $b$  and find that

$$a = b = \frac{4A}{HL^2} - \frac{4Ah_o^*}{H^2 L^2} + \frac{(-2A + f_o)h_o^*}{H^2 L^2}, \quad (21)$$

$$a' = \frac{4B}{H} + \frac{(-2A + f_o)}{H^2} \quad (22)$$

$$b' = -\frac{4B}{H} - \frac{(-2A + f_o)}{H^2} + \frac{\beta}{H} \quad (23)$$

where  $B = \frac{g'C}{f_o L^2}$ . The geostrophic velocities at the center for the dipole are

$$u_1(0) = v_1(0) = -\frac{g'C}{f_o}.$$

This leads to expressions for the drift speeds

$$c_x = -\frac{g'C}{f_o} + \frac{4BL^2 + (-2A + f_o)\frac{CL^2}{H} - \beta L^2}{4 + \gamma^2 L^2 - 6\frac{h_o^*}{H}} \quad (24)$$

$$c_y = -\frac{g'C}{f_o} + \frac{4BL^2 + (-2A + f_o)\frac{CL^2}{H}}{4 + \gamma^2 L^2 - 6\frac{h_o^*}{H}} \quad (25)$$

where  $\gamma = \frac{1}{Rd} = \frac{f_o}{\sqrt{g'H}}$ .

In the quasi-geostrophic case, in the expression of  $q_o$  and  $q_1$ , we neglect  $\xi_o$  in the terms in  $h_o$  and  $h_1$ . This gives a simpler expression for  $c_x$  and  $c_y$ ,

$$c_x = -\beta \frac{L^2}{4 + L^2 \gamma^2} + 4 \frac{g'C}{f_o} \frac{L^2 - L_o^2}{L_o^2 (4 + \gamma^2 L^2)} \quad (26)$$

$$c_y = 4 \frac{g'C}{f_o} \frac{L^2 - L_o^2}{L_o^2 (4 + \gamma^2 L^2)}. \quad (27)$$

Application to the present case with  $h_o^* = 375 \text{ m}$ ,  $L = 70 \text{ km}$ ,  $C = 1.7 \cdot 10^{-4}$  and  $L_o = 170 \text{ km}$  provides  $c_x = 4.1 \text{ cm s}^{-1}$  and  $c_y = 1.7 \text{ cm s}^{-1}$ . These values are smaller for  $c_x$  that observed while  $c_y$  on the contrary is too large. On the other hand, this calculation was performed for  $h_o \ll H$  which is not the case for the numerical experiment.

## 6 CONCLUSIONS

The meridional motion of isolated eddies was investigated in detail in several numerical experiments. One has to differentiate between eddy center (defined from either the interface displacement or potential vorticity field) and the center of mass. The center of mass was found to propagate only westward while the eddy center moved

significantly meridionally (except in the lens case). When the propagating eddy is decomposed into the sum of an axisymmetric vortex and a perturbation field, the latter has the shape of a dipole. It was shown that the presence of such a dipole in the perturbation field can induce a meridional displacement. Future work will include an exact derivation of the perturbation field in the same spirit as Flierl (1984) and the study of its impact on the eddy motion.

**ACKNOWLEDGEMENTS:** I express my appreciation to Glenn Flierl for initiating this study and for his numerous suggestions. Discussions with Benoit Cushman-Roisin, Melvin Stern and Bill Young proved timely and valuable. I would like also to thank Patty Forrestel for the drafting of the figures and all the GFD group for a stimulating summer.

## REFERENCES

- Bleck, R. and D.B. Boudra (1986): Wind-driven spin up in eddy-resolving ocean models formulated in isopycnic and isobaric coordinates. *J. Geophys. Res.*, **91**, 7611-7621.
- Chassignet E.P., D. Nof and B. Cushman-Roisin (1989): The propagation of isolated nonlinear eddies in a two-layer ocean. To be submitted to *J. Phys. Oceanogr.*
- Cushman-Roisin, B., E.P. Chassignet and Benyang Tang (1989): On the westward motion of isolated eddies. Submitted to *J. Phys. Oceanogr.*
- Davey, M. K. and P. D. Killworth (1984): Isolated waves and eddies in a shallow water model. *J. Phys. Oceanogr.*, **14**, 1047-1064.
- Flierl, G. (1977): The application of linear quasi-geostrophic dynamics to Gulf Stream rings. *J. Phys. Oceanogr.*, **7**, 365-379.
- Flierl, G. (1984): Rossby wave radiation from a strongly nonlinear warm eddy. *J. Phys. Oceanogr.*, **14**, 47-58.
- McWilliams, J. and G. Flierl (1979): On the evolution of isolated, nonlinear vortices, with application to Gulf Stream rings. *J. Phys. Oceanogr.*, **9**, 1155-1192.
- McWilliams, J., P. Gent and N. Norton (1986): The evolution of balanced, low-mode vortices on the  $\beta$ -plane. *J. Phys. Oceanogr.*, **16**, 838-855.

- Mied, R.P. and G.J. Lindemann 1979: The propagation and evolution of cyclonic Gulf Stream rings. *J. Phys. Oceanogr.*, **9**, 1193-1206.
- Nof, D. (1981): On the  $\beta$ -induced movement of isolated baroclinic eddies. *J. Phys. Oceanogr.*, **11**, 1662-1672.
- Nof, D. (1983): On the migration of isolated eddies with application to Gulf Stream rings. *J. Mar. Res.*, **41**, 399-425.
- Olson, D.B. (1980): The physical oceanography of two rings observed by the cyclonic ring experiment. II. Dynamics. *J. Phys. Oceanogr.*, **10**, 514-528.

## FINITE AMPLITUDES LONG WAVE BAROCLINIC INSTABILITY

Liang Gui Chen

## ABSTRACT

A finite amplitude long wave equation of motion on a two-layer  $f$ -plane is derived for piecewise potential vorticity structure using contour dynamics and an asymptotic expansion on two small parameters. A proper scaling between these two parameters  $\epsilon = \delta^{\frac{1}{2}}$  where  $\bar{\epsilon}^1$  is proportional to the wave length scale and  $\delta$  is the depth ratio of the two layers ( $\delta = H_1/H_2$ ) reduce the vorticity front evolution equation to a set of two linear equations. These equations predict that the instability of a sinusoidal long wave disturbance can grow from infinitesimal amplitude to finite amplitude without harmonic distortion, until the disturbance amplitude is comparable to its wave length. This prediction is verified by a numerical calculation.

## 1 INTRODUCTION

The Gulf Stream meander is one of the major features of the oceanic circulation. This strongly baroclinic current has variability over a very large scale. It retains its integrity over a long distance compared to its width or the Rossby deformation radius. The time scale of such meandering motion is also very long. Previous researchers have used different approaches to study this problem. One of them is the use of the linear instability in either barotropic or baroclinic or both to calculate the properties of waves upon the current, (Flierl, 1975; Talley, 1982). Another is the derivation of equations for changes in the direction of current by using the cross-stream integrated vorticity balance. Flierl *et al.* (1984), in the second approach, developed a 'thin jet' theory for the time evolution of Gulf Stream meandering under the basic assumption that the down-stream scale is much longer than the jet width. They also obtained a dispersion relation for long waves on a baroclinic jet and proved that the small amplitude limit of the thin jet model gives the same dispersion relationship as instability theory in the long wave limit. The method of 'contour dynamics' method is another approach. Pratt and Stern

(1986) used this method to develop a theory describing the nonlinear evolution of the meander. Their model is a quasi-geostrophic  $1\frac{1}{2}$  layer, with piecewise uniform potential vorticity. They obtained a path equation for the large amplitude, small curvature meandering motion. Pratt (1988) used this path equation to study the nonlinear meandering and the "pinch off" process of the Gulf Stream.

The purpose of this work is to look at the baroclinic instability problem of a finite amplitude disturbance on the two layer quasi-geostrophic region. The simplest possible model is used (*e.g.* no  $\beta$  effect ) in order to gain physical insight. One of the main assumptions is that the two-layer depth ratio  $\delta = H_1/H_2$  is a small parameter. In this case, all the unstable wave length are much longer than the Rossby deformation radius so that the wavenumber  $\epsilon$  is small also. We shall also restrict ourselves to a periodic wave-form in the x-direction. The two small parameters  $\epsilon$  and  $\delta$  will be linked together by proper scaling and asymptotic approximation. We also choose a piecewise uniform potential vorticity on each layer and contour dynamics is used to set up the evolution equations for the vorticity front. One of the reasons for choosing such a piecewise uniform structure is because at the center of the Gulf Stream the local potential vorticity gradient is much stronger than that of the planetary potential vorticity gradient. Also, this assumption greatly simplifies the problem by reducing the number of the dimension so that the result will be easy to understand and perhaps can be used to understand more difficulty problem. We will further simplify these equations by letting  $\delta \rightarrow 0$ . A proper scaling to these simplified equations shows that  $\delta \sim \epsilon^3$  and the slow time evolution scale is proportional to  $\delta^{-1}$ . It then turns out, somewhat surprisingly, is that the equations for the time evolution of the finite amplitude vorticity fronts are linear. A numerical calculation is then used to test our equations and the result agrees well with the theoretical result.

This report is divided into four sections. In the first section, we give a brief review of the linear instability theory for the problem. Although solving such a linear problem is a simple and standard process, it does give us a very good guideline in the scaling of the more complicated finite amplitude nonlinear problem. It also help us in understanding the long wave instability mechanism on such two-layer system. Section 2 is my main work on this problem. Section 3 is the numerical calculations.

Section 4 is the conclusion and some discussion of future work.

## 1 LINEAR THEORY

Figure-1 shows a jet flow in the two layer f-plane quasi-geostrophic system. The upper layer has depth  $H_1$  and density  $\rho$  and the lower layer has depth  $H_2$  and density  $\rho + \Delta\rho$ . The interface between the two layers has such a structure that the potential vorticity produced by the interface are piecewise uniform in each layer. A discontinuity occurs at the center of the jet,  $y=0$ , so there is a potential vorticity jump there. In the upper layer the northern region uniform potential vorticity is zero while the southern region is  $-2\Delta q$ . In the lower layer the northern part is zero and the southern part is  $2\delta\Delta q$ .

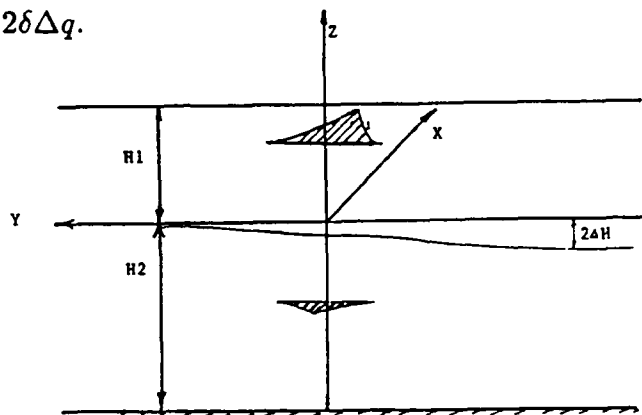


Fig.1. Geometry sketch of the two-layer, quasi geostrophic model with piecewise uniform potential vorticity on each layer. All the variables are dimensional.

The quasi-geostrophic potential vorticity equation governing such flows is:

$$\nabla^2 \psi_1 + \frac{f^2}{g^* H_1} (\psi_2 - \psi_1) = \begin{cases} 0 & y > 0 \\ -\frac{2\Delta H f}{H_1} & y < 0 \end{cases} \quad (1)$$

$$\nabla^2 \psi_2 + \frac{f^2}{g^* H_2} (\psi_1 - \psi_2) = \begin{cases} 0 & y > 0 \\ -\frac{2\Delta H f}{H_2} & y < 0 \end{cases} \quad (2)$$

where  $\psi_1$  and  $\psi_2$  are the streamfunctions of the upper layer and the lower layer respectively.  $g^*$  is the reduced gravity and  $f$  is the Coriolis parameter. The horizontal velocities are given by:

$$u_1 = -\partial\psi_1/\partial y \quad v_1 = \partial\psi_1/\partial x \quad (3)$$

$$u_2 = -\partial\psi_2/\partial y \quad v_2 = \partial\psi_2/\partial x \quad (4)$$

We now nondimensionalize equations (1) to (4). The nondimensionalized parameters are chosen as: potential vorticity  $q^*$ , horizontal length as the Rossby deformation radius  $L^*$ , velocity  $U^*$ , time  $T^*$ :

$$q^* = \sqrt{\frac{H_1 + H_2}{H_2}}$$

$$L^* = \sqrt{\frac{g^* H_1}{f_2}}$$

$$U^* = \sqrt{\frac{g^* H_2}{H_1(H_1 + H_2)}} \Delta H$$

$$T^* = \frac{H_1}{\Delta H f} \sqrt{\frac{H_1 + H_2}{H_2}}$$

The nondimensionalized parameter of the horizontal velocity is chosen in such a way that the maximal velocity at the upper layer jet equals to one. The nondimensionalized form of equation (1) and (2) become:

$$\nabla^2 \psi_1 + (\psi_2 - \psi_1) = \begin{cases} 0 & y > 0 \\ -2 & y < 0 \end{cases} \quad (5)$$

$$\nabla^2 \psi_2 + \delta(\psi_1 - \psi_2) = \begin{cases} 0 & y > 0 \\ 2\delta & y < 0 \end{cases} \quad (6)$$

For convenience, we use the same notations for the nondimensionalized forms so equations (3) and (4) remain the same forms.

The basic state time independent solution of (5) and (6) are

$$\bar{\psi}_1 = \begin{cases} \frac{1}{\sqrt{1+\delta}} e^{-y\sqrt{1+\delta}} & y > 0 \\ \frac{2}{1+\delta} - \frac{1}{\sqrt{1+\delta}} e^{y\sqrt{1+\delta}} & y < 0 \end{cases} \quad (7)$$

$$\bar{\psi}_2 = \begin{cases} \frac{-\delta}{\sqrt{1+\delta}} e^{-y\sqrt{1+\delta}} & y > 0 \\ \frac{-2\delta}{1+\delta} + \frac{\delta}{\sqrt{1+\delta}} e^{y\sqrt{1+\delta}} & y < 0 \end{cases} \quad (8)$$

For the time-dependent problem, the total streamfunction can be described as the sum of the basic state streamfunction plus the time dependent streamfunction

$$\psi_i = \bar{\psi}_i(y) + \psi'_i(x, y, t) \quad i = 1, 2 \quad (9)$$



The equations governing  $\psi_1$  and  $\psi_2$  are

$$\nabla^2 \psi'_1 + (\psi'_2 - \psi'_1) = 0 \quad (10)$$

$$\nabla^2 \psi'_2 + \delta(\psi'_1 - \psi'_2) = 0 \quad (11)$$

Assume  $\psi_1, \psi_2$  have such wave forms:

$$\psi'_i = \psi'_i(y)e^{ik(x-ct)} \quad i = 1, 2 \quad (12)$$

then the solution of (10) and (11) give :

$$\psi'_1(y) = \begin{cases} \frac{1}{1+\delta}(Ae^{-ky} - e^{-\lambda y}) & y > 0 \\ \frac{1}{1+\delta}(Ae^{ky} - e^{\lambda y}) & y < 0 \end{cases} \quad (13)$$

$$\psi'_2(y) = \begin{cases} \frac{1}{1+\delta}(Ae^{-ky} + \delta e^{-\lambda y}) & y > 0 \\ \frac{1}{1+\delta}(Ae^{ky} + \delta e^{\lambda y}) & y < 0 \end{cases} \quad (14)$$

$$\lambda^2 = 1 + \delta + k^2$$

where  $\lambda^2 = 1 + \delta + k^2$ , A is a constant which will be determined later. We must match the pressure across  $y = 0$  which gives:

$$(\bar{u}_i - c) \frac{\partial \psi'_i}{\partial x} - \psi'_i \frac{\partial \bar{u}_i}{\partial y} = \text{constant} \quad i = 1, 2. \quad (15)$$

By (7) and (8), the associated undisturbed velocities are :

$$\bar{u}_1 = \begin{cases} e^{-y\sqrt{1+\delta}} & y > 0 \\ e^{y\sqrt{1+\delta}} & y < 0 \end{cases} \quad (16)$$

$$\bar{u}_2 = \begin{cases} -\delta e^{-y\sqrt{1+\delta}} & y > 0 \\ -\delta e^{y\sqrt{1+\delta}} & y < 0 \end{cases} \quad (17)$$

Substituting (13),(14),(16) and (17) into (15) yields:

$$(\delta + c)(Ak + \delta\lambda) = \delta\sqrt{1+\delta}(A + \delta) \quad (18)$$

$$(1 - c)(Ak - \lambda) = \sqrt{1+\delta}(A - 1) \quad (19)$$

Equation (18) and (19) leads to the quadratic equation of phase speed c:

$$-\lambda k(1+\delta)c^2 + k(1-\nabla^2)(\lambda - \sqrt{1+\delta})c + \delta(\lambda - \sqrt{1+\delta})(k - \sqrt{1+\delta})(1-\delta) = 0 \quad (20)$$

Now, assume both  $\delta$  and wavenumber  $k$  are small:

$$\delta \ll 1 \quad k \ll 1$$

this means that the lower layer is much deeper than the upper layer and the disturbance waves are long waves compared to the radius of deformation. so (20) becomes:

$$2c^2 - k^2c + \delta k = 0 \quad (21)$$

A proper scaling is needed to assure that the three terms have the same order and balance each other. This leads to the requirement that

$$k = \delta^{1/3}K, \quad c = \delta^{2/3}C_0 \quad (22)$$

where both  $K$  and  $C_0$  are of order  $O(1)$  now. Equation (21) becomes :

$$2C_0^2 - C_0K^2 + K = 0 \quad (23)$$

which leads to the solution of  $C_0$  :

$$C_0 = \frac{K^2 \pm \sqrt{K(K^3 - 2^3)}}{4}$$

or

$$c = \delta^{2/3} \left[ \frac{K^2}{4} \pm \frac{1}{4} \sqrt{K(K^3 - 2^3)} \right] \quad (24)$$

This is the dispersion relation for the linear problem. It shows that for a very deep second layer the most unstable wave length is the the long wave of which the wavenumber  $k$  is associated to the  $k \sim \delta^{1/3}$ . The growth rate, or the order of  $kc$ , is associated to the  $\delta$  also, This scaling, connecting the time growth rate, wavenumber and depth ratio, is the basic guideline in the scaling of the finite amplitude problem in section two.

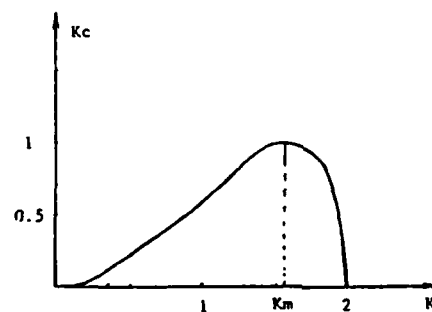


Fig.2. The instability growth rate  $Kc$ , versus wavenumber  $K$ . The most unstable wavenumber is  $K_m$ . Short wave with wavenumbers  $K \geq 2$  are stable

Figure-2 is the unstable growth rate  $Kc_i$  versus wavenumber  $K$ ,

This curve shows that the unstable occurs at  $K$  between 0 to 2 and the maximal growth rate, or the most unstable wavenumber, happens at  $K = 4^{\frac{1}{3}} = 1.587$ . As the  $K$  gets smaller, the unstable growth rate becomes small. At the limit of  $K \rightarrow 0$ , the growth rate approaches zero also. This means that a very long wave is almost stable. So although at the initial stage, the infinitesimal disturbance might consist of a broad range of wavenumbers  $K$ , the dispersion relation (24) shows that after some time, the disturbance will be dominated by the wavenumbers around  $K = 1.587$ , or  $k = 1.587\delta^{\frac{1}{3}}$ .

Knowing  $c$  enables us to look at the motion of the two vorticity fronts  $L_1$  and  $L_2$ , (figure-3), which are given by:

$$\frac{\partial \psi'_i}{\partial x} = v_i = \frac{dL_i}{dt} = \frac{\partial L_i}{\partial t} + \bar{u}_i \frac{\partial L_i}{\partial x} \quad i = 1, 2. \quad (25)$$

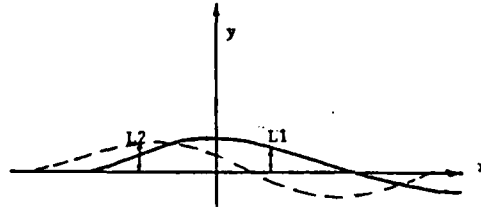


Fig-3. Plan view of the two vorticity fronts  $L_1$  and  $L_2$ .

The assumption that they have the wave forms  $L_i = l_i e^{ik(x-ct)}$  leads to

$$L_i = \frac{\psi'_i}{\bar{u}_i - c}, \quad i = 1, 2 \quad (26)$$

The undetermined constant  $A$  can also be solved by (19) :

$$A = \delta^{2/3} \frac{C_0}{1 - C_0 K} \quad (27)$$

Equations (12), (16), (17), (26), (27) together give the ratio of the two vorticity fronts as:

$$\frac{L_1}{L_2} = (1 - KC_0) \quad (28)$$

The magnitude of the ratio is

$$\left| \frac{L_1}{L_2} \right| = \sqrt{(1 - Kc_r)^2 + (Kc_i)^2} \quad (29)$$

where

$$c_r = \text{Re}(C_0) = K^2/4 \quad c_i = \text{Im}(C_0) = \sqrt{K(2^3 - K^3)}$$

The phase different between  $L_1$  and  $L_2$  is

$$\theta = \arctan\left(\frac{Kc_i}{1 - Kc_r}\right) \quad (30)$$

When the wave is stable, say  $K > 2$ ,  $c_i = 0$  so the phase shift is zero. For the most unstable wavenumber  $K = 4^{1/3}$ , the amplitude ratio of the two fronts is one while the phase shift is about  $90^\circ$ . Actually, the amplitude ratio is independent of  $K$ , it is always one in this asymptotic approximation.

## 2 FINITE AMPLITUDE ASYMPTOTIC THEORY

As shown in the linear theory a long wave with wavenumber  $k \sim \delta^{1/3}$  is unstable. It will grow from infinitesimal amplitude to finite amplitude consequently the linear theory become invalid. Our interest now is taking the linear theory as a guide for the finite amplitude disturbance problem, we will pay particular attention to the scaling of the depth ratio  $\delta$  to the wavenumber  $k$  and the time evolution scale.

The model is very much the same as in the linear model except that the amplitude of the disturbance now is finite. Also, we assume that it is periodic in  $x$ -direction. The reason we chose such a periodic distribution structure in  $x$ -direction comes from the consideration of the barotropic component effect from the far field. With the use of a periodic structure, we do not need to consider the far field effect which will cause some kind of difficult and uncertain discussion on the far field structure. I worked on this nonperiodic structure also but have not reached any conclusion yet.

The governing equations for the streamfunctions and the basic flow are (5) (6) and (16) and (17). We rewrite here:

$$\nabla^2 \psi_1 + (\psi_2 - \psi_1) = \begin{cases} 0 & y > 0 \\ -2 & y < 0 \end{cases} \quad (31)$$

$$\nabla^2 \psi_2 + \delta(\psi_1 - \psi_2) = \begin{cases} 0 & y > 0 \\ 2\delta & y < 0 \end{cases} \quad (32)$$

$$\bar{u}_1 = \begin{cases} e^{-y\sqrt{1+\delta}} & y > 0 \\ e^{y\sqrt{1+\delta}} & y < 0 \end{cases} \quad (33)$$

$$\bar{u}_2 = \begin{cases} -\delta e^{-y\sqrt{1+\delta}} & y > 0 \\ -\delta e^{y\sqrt{1+\delta}} & y < 0 \end{cases} \quad (34)$$

Again, assume that the total streamfunction is the sum of the basic state streamfunction and the time dependent streamfunction

$$\psi_i = \bar{\psi}_i(y) + \psi'_i(x, y, t) \quad i = 1, 2 \quad (35)$$

Now the time dependent streamfunction is no longer a small term. The governing equations of these time dependent streamfunction, after dropping the prime for convenience:

$$\nabla^2 \psi_1 + (\psi_2 - \psi_1) = M_1 = \begin{cases} -2 & 0 < y < L_1 \\ 2 & L_1 < y < 0 \\ 0 & \text{elsewhere} \end{cases} \quad (36)$$

$$\nabla^2 \psi_2 + \delta(\psi_1 - \psi_2) = M_2 = \begin{cases} 2\delta & 0 < y < L_1 \\ -2\delta & L_1 < y < 0 \\ 0 & \text{elsewhere} \end{cases} \quad (37)$$

Here,  $M_1$  and  $M_2$  on the right hand side can be referred to as the vorticity anomaly to the basic state. Equations (36) and (37) can be rewritten into a Laplace equation and a Helmholtz equation:

$$\nabla^2 (\delta\psi_1 + \psi_2) = \delta M_1 + M_2 \quad (38)$$

$$\nabla^2 (\psi_2 - \psi_1) - (1 + \delta)(\psi_2 - \psi_1) = M_2 - M_1 \quad (39)$$

The solution of equation (38) corresponds to the barotropic component and (39) corresponds to the baroclinic component. In contour dynamic method, solutions of equation (38) and (39) can be constructed by using the Green's function kernels  $G_1$  and  $G_2$ .  $G_1$  is for the Laplace operator  $\nabla^2$  and  $G_2$  is for the Helmholtz operator  $\nabla^2 - \gamma^2$ .  $G_1$  and  $G_2$  are:

$$G_1(x, \xi, y, \eta) = \ln(\cosh \frac{(y - \eta)2\pi}{a} - \cos \frac{(x - \xi)2\pi}{a}) \quad (40)$$

$$G_2(x, \xi, y, \eta) = K_0(\gamma((x - \xi)^2 + (y - \eta)^2)^{1/2}) \quad (41)$$

$$\gamma^2 = 1 + \delta$$

where constant  $a$  is the wave length of the periodic disturbance,  $\gamma^2 = 1 + \delta$ ,  $\xi$  and  $\eta$ , represent the  $x$  and  $y$  coordinates of a point source of potential vorticity anomaly.  $K_0$  is the zeroth order modified Bessel function.

The solution of the streamfunction caused by a single point potential vorticity source at  $(\xi, \eta)$  are given by:

$$\psi_1 = AG_1(x, \xi, y, \eta) + BG_2(x, \xi, y, \eta) \quad (42)$$

$$\psi_2 = AG_1(x, \xi, y, \eta) - \delta BG_2(x, \xi, y, \eta) \quad (43)$$

In which

$$A = \frac{\delta M_1 + M_2}{4\pi(1 + \delta)} \quad (44)$$

$$B = \frac{M_2 - M_1}{2\pi(1 + \delta)} \quad (45)$$

The total contribution of all the potential vorticity anomaly points can be computed by integrating (42) and (43) over those region of  $(\xi, \eta)$  where there is a potential vorticity anomaly in either upper layer or lower layer or both.

$$\psi_1 = \iint^{(1)} AG_1(x, \xi, y, \eta) d\xi d\eta + \iint^{(2)} \delta BG_2(x, \xi, y, \eta) d\xi d\eta \quad (46)$$

$$\psi_2 = \iint^{(1)} AG_1(x, \xi, y, \eta) d\xi d\eta - \iint^{(2)} \delta BG_2(x, \xi, y, \eta) d\xi d\eta \quad (47)$$

Now we must look carefully at the integral of  $\iint^{(1)}$  and  $\iint^{(2)}$ . First, the  $\xi$  direction integral in  $G_1$  and  $G_2$  have different regions. The integral of  $G_1$  is from  $\xi = 0$  to  $\xi = a$  while  $G_2$  is from  $-\infty$  to  $+\infty$ .

$$\iint^{(1)} = \int_0^a d\xi \int (A) d\eta \quad (48)$$

$$\iint^{(2)} = \int_{-\infty}^{\infty} d\xi \int (B) d\eta \quad (49)$$

The integral in  $\eta$  direction depends on  $L_1$  and  $L_2$ , as do the coefficients of  $A(M_1, M_2)$  and  $B(M_1, M_2)$ . Six different combinations of  $L_1$  and  $L_2$  (see figure-4), along with  $A(M_1, M_2)$  and  $B(M_1, M_2)$  are given as:

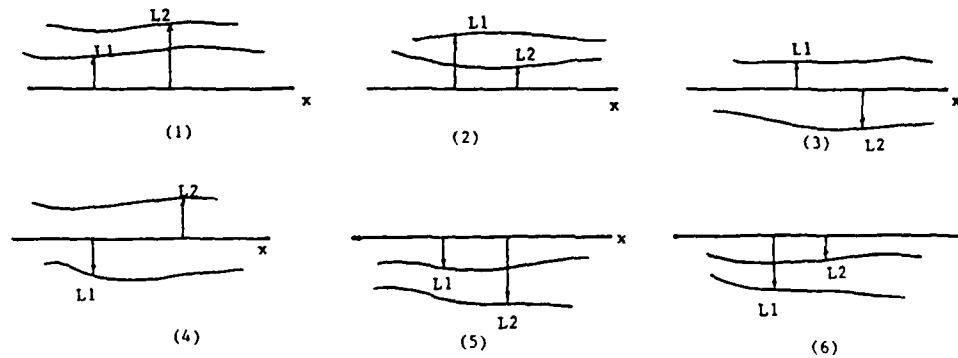


Fig-4. Six different combinations of  $L_1$  and  $L_2$ . The integral region and the coefficients  $M_1$  and  $M_2$  dependent on them.

1)  $L_2 > L_1 > 0$ , the integral region is divided into  $(0, L_1)$  with  $M_1 = -2, M_2 = 2\delta$ ,  $(L_1, L_2)$  with  $M_1 = 0, M_2 = 2\delta$ .

2)  $L_1 > L_2 > 0$ , the integral region is divided into  $(0, L_2)$  with  $M_1 = -2, M_2 = 2\delta$ ,  $(L_2, L_1)$  with  $M_1 = -2, M_2 = 0$ .

3)  $L_2 < 0, L_1 > 0$ , the integral region is divided into  $(L_2, 0)$  with  $M_1 = 0, M_2 = -2\delta$ ,  $(0, L_1)$  with  $M_1 = -2, M_2 = 0$ .

4)  $L_1 < 0, L_2 > 0$ , the integral region is divided into  $(L_1, 0)$  with  $M_1 = 2, M_2 = 0$ ,  $(0, L_2)$  with  $M_1 = 0, M_2 = 2\delta$ .

5)  $L_2 < L_1 < 0$ , the integral region is divided into  $(L_2, L_1)$  with  $M_1 = 0, M_2 = -2\delta$ ,  $(L_1, 0)$  with  $M_1 = 2, M_2 = -2\delta$ .

6)  $L_1 < L_2 < 0$ , the integral region is divided into  $(L_1, L_2)$  with  $M_1 = 2, M_2 = 0$ ,  $(L_2, 0)$  with  $M_1 = 2, M_2 = -2\delta$ . careful manipulating of these six cases can lead to a general integral form in  $\eta$  direction:

$$\int d\eta = \int_0^{L_1} + \int_{L_1}^{L_2} d\eta \quad (50)$$

In which the first integral has:  $M_1 = -2, M_2 = 2\delta$ . and the second integral has  $M_1 = 0, M_2 = 2\delta$ . Now

$$\iint^{(1)} = \int_0^a d\xi \int_{L_1}^{L_2} L_1 A d\eta \quad (51)$$

$$\iint^{(2)} = \int_{-\infty}^{\infty} d\xi \left[ \int_0^{L_1} B_1 d\eta + \int_{L_1}^{L_2} B_2 d\eta \right] \quad (52)$$

where

$$A = \frac{\delta}{2\pi\lambda^2}, \quad B_1 = \frac{1}{\pi}, \quad B_2 = \frac{\delta}{\pi\lambda^2} \quad (53)$$

Now  $\psi_1$  and  $\psi_2$  can be rewritten as :

$$\psi_1 = \int_0^a d\xi \int_{L_1}^{L_2} A G_1(x, \xi, y, \eta) d\eta + \int_{-\infty}^{\infty} d\xi \left[ \int_0^{L_1} B_1 + \int_{L_1}^{L_2} B_2 \right] G_2(x, \xi, y, \eta) d\eta \quad (54)$$

$$\psi_2 = \int_0^a d\xi \int_{L_1}^{L_2} A G_1(x, \xi, y, \eta) d\eta + \int_{-\infty}^{\infty} d\xi \left[ \int_0^{L_1} B_1 + \int_{L_1}^{L_2} B_2 \right] G_2(x, \xi, y, \eta) d\eta \quad (55)$$

The time dependent horizontal velocities can be calculated from the streamfunction

$$u_1 = -\partial\psi_1/\partial y$$

$$v_1 = \partial\psi_1/\partial x$$

$$u_2 = -\partial\psi_2/\partial y$$

$$v_2 = \partial\psi_2/\partial x$$

where

$$\frac{\partial\psi_1}{\partial y} = \quad (56)$$

$$A \int_0^{-a} [G_1(0, \xi, y, L_2(x - \xi)) - G_1(0, \xi, y, L_1(x - \xi))] d\xi \\ - \int_{-\infty}^{\infty} [B G_2(0, \xi, y, L_1(x - \xi)) + B_1 G_2(0, \xi, y, L_2(x - \xi)) + B_2 G_2(0, \xi, y, 0)] d\xi$$

$$\frac{\partial\psi_2}{\partial y} = \quad (57)$$

$$A \int_0^{-a} [G_1(0, \xi, y, L_2(x - \xi)) - G_2(0, \xi, y, L_1(x - \xi))] d\xi \\ \delta \int_{-\infty}^{\infty} [B G_2(0, \xi, y, L_1(x - \xi)) + B_1 G_2(0, \xi, y, L_2(x - \xi)) - B_2 G_2(0, \xi, y, 0)] d\xi$$



$$\frac{\partial \psi_1}{\partial x} = \quad (58)$$

$$A \int_0^{-a} \left[ \frac{\partial L_1(x-\xi)}{\partial x} G_1(0, \xi, y, L_2(x-\xi)) - \frac{\partial L_2(x-\xi)}{\partial x} G_1(0, 0, y, L_1(x-\xi)) \right] d\xi$$

$$+ \int_{-\infty}^{\infty} \left[ B \frac{\partial L_1(x-\xi)}{\partial x} G_2(0, \xi, y, L_1(x-\xi)) - B_1 \frac{\partial L_2(x-\xi)}{\partial x} G_2(0, \xi, y, L_2(x-\xi)) \right] d\xi$$

$$\frac{\partial \psi_2}{\partial x} = \quad (59)$$

$$A \int_0^{-a} \left[ \frac{\partial L_1(x-\xi)}{\partial x} G_1(0, \xi, y, L_2(x-\xi)) - \frac{\partial L_2(x-\xi)}{\partial x} G_1(0, 0, y, L_1(x-\xi)) \right] d\xi$$

$$- \delta \int_{-\infty}^{\infty} \left[ B \frac{\partial L_1(x-\xi)}{\partial x} G_2(0, \xi, y, L_1(x-\xi)) - B_1 \frac{\partial L_2(x-\xi)}{\partial x} G_2(0, \xi, y, L_2(x-\xi)) \right] d\xi$$

The assumption that the disturbance is periodic has been used to derive equations (58) and (59).

Once we know the solutions of the horizontal velocity caused by the vorticity anomaly, we will focus on the evolution of the vorticity fronts  $L_1$  and  $L_2$ . The governing equations for  $L_1$  and  $L_2$  are

$$v_i = \frac{dL_i}{dt} = \frac{\partial L_i}{\partial t} + (\bar{u}_i + u_i) \frac{\partial L_i}{\partial x} \quad \text{at } y = L_i, i = 1, 2.$$

or

$$\frac{\partial L_i}{\partial t} = \frac{\partial \psi_i}{\partial x} - (\bar{u}_i - \frac{\partial \psi_i}{\partial y}) \frac{\partial L_i}{\partial x} \quad \text{at } y = L_i, i = 1, 2. \quad (60)$$

Substitute (56), (57), (58), (59) into (60) yield:

$$\frac{\partial L_1}{\partial t} = \left( \frac{\partial \psi_1}{\partial x} + \frac{\partial \psi_1}{\partial y} \frac{\partial L_1}{\partial x} \right) - e^{-|L_1|\lambda} \frac{\partial L_1}{\partial x} \quad (61)$$

$$= A \int_0^{-a} \left( \frac{\partial L_1(x-\xi)}{\partial x} - \frac{\partial L_1(x)}{\partial x} \right) G_1(0, \xi, L_1(x), L_1(x-\xi)) d\xi$$

$$- A \int_0^{-a} \left( \frac{\partial L_2(x-\xi)}{\partial x} - \frac{\partial L_1(x)}{\partial x} \right) G_1(0, \xi, L_1(x), L_2(x-\xi)) d\xi$$

$$+ B \int_{-\infty}^{\infty} \left( \frac{\partial L_1(x-\xi)}{\partial x} - \frac{\partial L_1(x)}{\partial x} \right) G_2(0, \xi, L_1(x), L_1(x-\xi)) d\xi$$

$$+ B_1 \int_{-\infty}^{\infty} \left( \frac{\partial L_2(x-\xi)}{\partial x} - \frac{\partial L_1(x)}{\partial x} \right) G_2(0, \xi, L_1(x), L_2(x-\xi)) d\xi$$

$$\begin{aligned}
& + (B_2 \int_{-\infty}^{\infty} G_2(0, \xi, L_1(x), 0) d\xi - e^{-|L_1|\lambda}) \frac{\partial L_1(x)}{\partial x} \\
\frac{\partial L_2}{\partial t} & = \left( \frac{\partial \psi_2}{\partial x} + \frac{\partial \psi_2}{\partial y} \frac{\partial L_2}{\partial x} \right) + \delta e^{-|L_2|\lambda} \frac{\partial L_2}{\partial x} \\
& = A \int_0^{-a} \left( \frac{\partial L_1(x-\xi)}{\partial x} - \frac{\partial L_2(x)}{\partial x} \right) G_1(0, \xi, L_2(x), L_1(x-\xi)) d\xi \\
& - A \int_0^{-a} \left( \frac{\partial L_2(x-\xi)}{\partial x} - \frac{\partial L_2(x)}{\partial x} \right) G_1(0, \xi, L_2(x), L_2(x-\xi)) d\xi \\
& - \delta B \int_{-\infty}^{\infty} \left( \frac{\partial L_1(x-\xi)}{\partial x} - \frac{\partial L_2(x)}{\partial x} \right) G_2(0, \xi, L_2(x), L_1(x-\xi)) d\xi \\
& - \delta B_1 \int_{-\infty}^{\infty} \left( \frac{\partial L_2(x-\xi)}{\partial x} - \frac{\partial L_2(x)}{\partial x} \right) G_2(0, \xi, L_2(x), L_2(x-\xi)) d\xi \\
& + \delta [-B_2 \int_{-\infty}^{\infty} G_2(0, \xi, L_2(x), 0) d\xi + e^{-|L_2|\lambda}] \frac{\partial L_2(x)}{\partial x}
\end{aligned} \tag{62}$$

(61) and (62) are the principle equations for the evolution of the vorticity fronts of  $L_1$  and  $L_2$ . They are quite complicated nonlinear equations and can be solved by numerically work or by further simplification. But before we carry the work further, let's have a look at each term in (61) and (62) and try to understand its physical meaning. This will help us to make a proper scaling and asymptotic approximation to the equations.

First, recall the Green's kernel solution in (40) and (41), terms involved Green's function  $G_1$  represents the contribution from the barotropic component, terms involving the Green's function  $G_2$  represent the contribution from the baroclinic component. Terms with  $\frac{\partial L_1(x-\xi)}{\partial x}$  comes from the  $v_i$  terms which represent the induced motion in the  $y$ -direction caused by the potential vorticity anomaly. Terms with  $\frac{\partial L_1(x)}{\partial x}$  come from the  $u_i$  term and represent the advection in  $x$ -direction caused by the potential vorticity anomaly and the basic flow, see figure-5 In Green's function

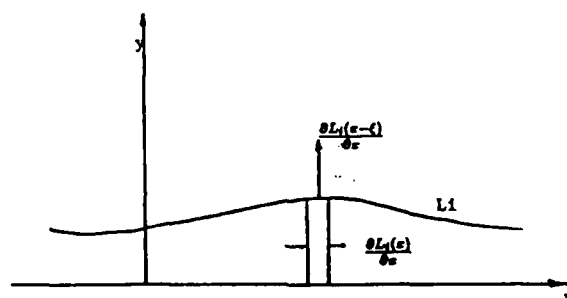


Fig-5. Sketch of the effect of induced velocities caused by the vorticity anomaly on the vorticity fronts  $L_i$ .  $\frac{\partial L_1(x-\xi)}{\partial x}$  represents the induced motion in  $y$ -direction,  $\frac{\partial L_1(x)}{\partial x}$  represents the advection in  $x$ -direction.

$G_i(x, y, L_i(x), L_j(x - \xi))$ , the  $L_i$  and  $L_j$  mean that the vorticity front  $L_i$  at the point  $x$  is effected by the vorticity front  $L_j$  at  $(x - \xi)$  as shown in figure-6,  $i = j$  means that the effect come from the same front and  $i \neq j$  means that the effect comes from another front.

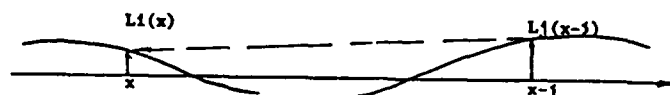


Fig-6. Sketch of the interaction between vorticity fronts  $L_i(x)$  and  $L_j(x - \xi)$ .

To solve the equation analytically, further assumption and simplification are needed to deal with this complicated nonlinear structure of the integrands. Using the linear theory as a guide, we look at the time evolution of the vorticity fronts with finite amplitude, long wave length and slow time variation. This leads to:

$$X = \epsilon x \quad (63)$$

$$\zeta = \epsilon \xi \quad (64)$$

$$K = \frac{2\pi}{\epsilon a} \quad (65)$$

$$\tau = \epsilon^p t \quad (66)$$

$$L_i(x - \xi, t) = l_i(X - \zeta, \tau) \quad (67)$$

In which  $X, \zeta, K, \tau$  and  $l_i$  are all order  $O(1)$ , and  $\epsilon$  is a small parameter,  $\epsilon \ll 1$ . This small parameter will be linked to the depth ratio  $\delta$  after we give a proper asymptotic expansion and scaling.  $p$  is an undetermined number here and will be decided after the scaling.

By (63) and (67), we have :

$$\frac{\partial L_i(x - \xi, t)}{\partial x} = \epsilon \frac{\partial l_i(X - \zeta, \tau)}{\partial X} \sim O(\epsilon)$$

in which we assume the derivative of the new variable is order  $O(1)$ , this means

$$\frac{\partial l_i(X - \zeta, \tau)}{\partial X} \sim O(1) \quad (68)$$

together with (65):

$$\int_0^{-a} \frac{\partial L_i(x - \xi, t)}{\partial x} d\xi \Rightarrow \int_0^{-2\pi/K} \frac{\partial l_i(X - \zeta, \tau)}{\partial X} d\zeta \quad (69)$$

Asymptotic expansion is carried to each term in the principle equations (61) and (62). First, look at the Green's function  $G_1$ :

$$\begin{aligned} G_1(0, \xi, L_i(x), L_j(x - \xi)) &= \ln(\cosh(L_i(x) - L_j(x - \xi)) * \frac{2\pi}{a} - \cos \frac{\xi 2\pi}{a}) \\ &= \ln(\cosh \epsilon K(l_i(X) - l_j(x - \zeta)) - \cos \zeta K) \\ &= \ln(1 - \cos K\zeta + \frac{1}{2}\epsilon^2 K^2(l_i(X) - l_j(X - \zeta))^2) \\ &\approx \ln(1 - \cos K\zeta) + \frac{1}{2} \frac{\epsilon^2 K^2(l_i(X) - l_j(X - \zeta))^2}{1 - \cos K\zeta} \\ &\approx \ln(1 - \cos K\zeta) + O(\epsilon^2) \end{aligned} \quad (70)$$

This shows that the leading order of the Green's function  $G_i$  is independent of the values of the front  $L_i$ , so the first two terms in equations (61) can be rewritten as:

$$\begin{aligned} A \int_0^{-2\pi/K} [(\frac{\partial l_1(X - \xi)}{\partial X} - \frac{\partial l_1(X)}{\partial X}) - (\frac{\partial l_2(X - \xi)}{\partial X} - \frac{\partial l_1(X)}{\partial X})] \ln(1 - \cos K\xi) d\xi \\ = \frac{\delta}{2\pi\gamma^2} \int_0^{-2\pi/K} (\frac{\partial l_1(X - \xi)}{\partial X} - \frac{\partial l_2(X - \xi)}{\partial X}) \ln(1 - \cos K\xi) d\xi \end{aligned} \quad (71)$$

This form clearly shows that the nonlinear effect of the vorticity front  $L_i$  only enters at second order  $O(\epsilon^2)$ .

A similar calculation on the first two terms of (62) gives the same formula as (71). This means that the contribution from the barotropic component to the evolution of the upper layer vorticity front  $L_1$  and the lower layer vorticity front  $L_2$  are equal.

The baroclinic component of the Green's function  $G_2$  is

$$\begin{aligned} G_2(0, \xi, L_i(x), L_j(x - \xi)) \\ = K_0[\gamma(\xi^2 + (L_i(x) - L_j(x))^2 + 2\epsilon\xi L_{jX}(L_i(x) - L_j(x))) \\ + \epsilon^2(\xi^2 L_{jX}^2 - \frac{\xi^2}{2} L_{jXX}(L_i(x) - L_j(x)))^{1/2}] \end{aligned} \quad (72)$$

in which Taylor series expansion in powers of  $\xi$  is used.

For  $i = j$ , (self induction), equation (72) becomes:

$$G_2(0, \xi, L_i(x), L_i(x - \xi)) = K_0[\gamma(|\xi| + \frac{\xi^2}{2}\epsilon^2 L_{iX}^2)] + O(\epsilon^3) \quad (73)$$

For  $i \neq j$

$$G_2(0, \xi, L_i(x), L_j(x - \xi)) = K_0[\gamma\sqrt{\xi^2 + (L_i(x) - L_j(x))^2}] + O(\epsilon) \quad (74)$$

Equation (73) can be further simplified by introducing the modified Bessel function definition:

$$K_n(z) = \int_0^\infty d\theta \cosh(n\theta) e^{-z \cosh(\theta)} \quad (75)$$

so now (73) becomes:

$$\begin{aligned} & K_0(\gamma(|\xi| + \frac{\xi^2}{2}\epsilon^2 L_{iX}^2)) \\ &= \int_0^\infty d\theta e^{-\gamma(|\xi| + \frac{\xi^2}{2}\epsilon^2 L_{iX}^2) \cosh(\theta)} \\ &= \int_0^\infty d\theta e^{-\gamma|\xi| \cosh \theta} [1 - \frac{\xi^2}{2}\epsilon^2 L_{iX}^2 \cosh \theta] \\ &= K_0(\gamma|\xi|) - \frac{\xi^2}{2}\epsilon^2 L_{iX}^2 K_1(\gamma|\xi|) \end{aligned} \quad (76)$$

Substituting (76) into the third term in (61) yields:

$$\begin{aligned}
& B \int_{-\infty}^{\infty} \epsilon [-\epsilon \xi l_{1XX} + \frac{\epsilon^2 \xi^2}{2} l_{1XXX}] [K_0(\gamma | \xi |) - \frac{\epsilon^2}{2} | \xi | l_{1X}^2 K_1(\gamma | \xi |)] d\xi \\
&= \frac{\epsilon^3 B}{2} l_{1XXX} \int_{-\infty}^{\infty} \xi^2 K_0(\gamma | \xi |) d\xi + O(\epsilon^4) \\
&= \frac{\epsilon^3 B l_{1XXX}}{\gamma^3} \int_0^{\infty} \xi^2 K_0(\xi) d\xi + O(\epsilon^4) \\
&= \frac{\epsilon^3 l_{1XXX}}{2\gamma^5} + O(\epsilon^4) \tag{77}
\end{aligned}$$

Again a Taylor series expansion is used. The integral involves terms like  $\xi l_{1XX}$  vanishes identically because the integral is odd. The final step of the evaluation comes from the formula, (see Pratt and Stern, 1986):

$$\int_0^{\infty} \xi^2 K_0(\xi) d\xi = \pi/2 \tag{78}$$

The fourth term in (61) can be evaluated by inserting (74):

$$\begin{aligned}
& B_1 \int_{-\infty}^{\infty} \left( \frac{\partial L_2(x-\xi)}{\partial x} - \frac{\partial L_1(x)}{\partial x} \right) G_2(0, \xi, L_1(x), L_2(x-\xi)) d\xi \\
&= \frac{\delta \epsilon}{\pi \gamma^2} \int_{-\infty}^{\infty} \left( \frac{\partial l_2(x-\xi)}{\partial X} - \frac{\partial l_1(x)}{\partial X} \right) K_0(\gamma \sqrt{\xi^2 + (L_1(x) - L_2(x))^2}) d\xi \tag{79}
\end{aligned}$$

We are not going to evaluate this whole integral any further but just keep in mind that this term is order of  $O(\delta \epsilon)$  or smaller if we use the result of (78) to estimate this integral.

The last term in equation (61) is:

$$\begin{aligned}
& (B_2 \int_{-\infty}^{\infty} G_2(0, \xi, L_1, 0) d\xi - e^{|L_1| \gamma} \frac{\partial L_1}{\partial x}) \\
&= \left( \frac{1}{\pi} \int_{-\infty}^{\infty} K_0(\gamma \sqrt{\xi^2 + (L_1(x) - L_2(x))^2}) d\xi - e^{-|L_1| \sqrt{1+\delta}} \right) \frac{\partial L_1}{\partial x} \\
&= -\epsilon e^{-|L_1| \gamma} \left( \frac{1}{\gamma} - 1 \right) \frac{\partial l_1}{\partial X} \\
&= -\frac{\delta \epsilon}{2} e^{-|L_1| \gamma} \frac{\partial l_1}{\partial X} + (\delta \epsilon^2) \tag{80}
\end{aligned}$$

The evaluated of this integral comes from the formula:

$$\int_{-\infty}^{\infty} K_0[\sqrt{(a-z)^2 + b^2}] dz = \pi e^{-|b|} \quad (S1)$$

Again, this integral is order  $O(\delta\epsilon)$ .

It is easy to perform the similar process to evaluate each integral in equation (62). The major difference of equation (62) is that many of its coefficients are a factor  $\delta$  smaller than those in (61) so the order of these integrals are:

order of the first two terms are  $\delta$

order of the third term is  $\delta\epsilon$

order of the fourth term is  $\delta^2\epsilon^3$

order of the fifth term is  $\delta^2\epsilon$  The righthand sides of the equations (61) and (62) are

$$\frac{\partial L_i}{\partial t} = \epsilon^p \frac{\partial l_i}{\partial \tau} \quad i = 1, 2 \quad (S2)$$

Now, we have evaluated all the integrals in the principle equations. It is time to assemble them together and scale them. We write down the order of each integral term as

For equation (61):

$$\epsilon^p = \delta + \epsilon^3 + \delta\epsilon + \delta\epsilon \quad (S3)$$

For equation (62):

$$\epsilon^p = \delta + \delta^2\epsilon + \delta^2\epsilon^3 + \delta^2\epsilon \quad (S4)$$

Since the basic assumption is that both  $\delta$  and  $\epsilon$  are small, the dominant terms in (83) are the first three terms and the dominant terms in equation (84) are the first two terms, so that:

$$\epsilon^p \sim \delta \sim \epsilon^3 \quad (S5)$$

So we have  $p=3$  and  $\epsilon^3 = \delta$ . The time evolution scale and the vorticity front length scale are now related to the depth ratio  $\delta$  as we anticipated. It is interesting to note that the relationship are exactly the same as we obtained in the linear theory .

Another interesting thing from this scaling is that the time evolution scale is proportional to the wavenumber as the cubic relation  $\frac{t}{\tau} = \epsilon^3$  in both linear theory and finite amplitude theory. This relationship also was found in Pratt and Stern (1986) 's theory when they obtained their path equation. Although their model is a  $1\frac{1}{2}$  layer model and the amplitude of the disturbance is large compared to the radius of deformation. The common feature of these three models is that they all deal with long waves whose wave length is much larger than the radius of deformation and the only length scale parameter involved is the wave length. It seems that the amplitude of the disturbance, whether it is infinitesimal or finite or large, does not really matter here. It is the wave length scale that decides the time evolution scale. Is this scaling relation only true for these models or does it implies some kinds of more general relationship in the long wave theory?

The final simplified equations after dropping out the higher order terms are:

$$\frac{\partial l_1}{\partial \tau} = \frac{1}{2\pi} \int_0^{-2\pi/K} \left[ \left( \frac{\partial l_1(X-\zeta)}{\partial X} - \frac{\partial l_2(X-\zeta)}{\partial X} \right) \ln(1 - \cos K\zeta) d\zeta + \frac{l_{1XXX}}{2} \right] \quad (86)$$

$$\frac{\partial l_2}{\partial \tau} = \frac{1}{2\pi} \int_0^{-2\pi/K} \left[ \left( \frac{\partial l_1(X-\zeta)}{\partial X} - \frac{\partial l_2(X-\zeta)}{\partial X} \right) \ln(1 - \cos K\zeta) d\zeta \right] \quad (87)$$

or

$$\frac{\partial l_1}{\partial \tau} = \frac{\partial l_2}{\partial \tau} + \frac{l_{1XXX}}{2} \quad (88)$$

Equations (87) and (88) are my major result on this work. They are the governing equations for the time evolution of the vorticity fronts  $L_1$  and  $L_2$ . The first impression is that the equations are linear although they describe the finite amplitude wave motion. To understand these equations, let's have one more look at each term in these equations. The term on the righthand side of (87) is the contribution of the barotropic component. Compared to the first two terms in (62), the  $\frac{\partial l_i(x-\zeta)}{\partial x}$  terms remain but the  $\frac{\partial l_i(x)}{\partial x}$  terms vanish. This means that the contribution to the evolution of the vorticity fronts mainly comes from the y-direction induction velocity  $v_i$  while the effect on the x-direction advection cancel each other so the total effect is of smaller order. If we remember our long wave, finite amplitude assumptions, it will be more easy to understand this by looking at the figure-5.



The elimination of the last terms in (61) and (62) means that the potential vorticity anomaly produce a horizontal x-direction velocity that just cancels the affect of the basic flow  $\bar{u}_i$ .

The second term in (88) is  $\frac{l_{xxx}}{2}$ . Its physical interpretation is unclear now, but at least we know that this term comes from the contribution of the baroclinic component. It should also be pointed out that it is this term in the scaling equation (83) that decides the proper order between the  $\delta$  and  $\epsilon$  and the time scale  $\epsilon^p$ . So we can say that it is the baroclinic motion links the scaling between the wave length scale and the time evolution scale and it is the barotropic motion that links the depth ratio  $\delta$  to the wave length scale, or wavenumber  $\epsilon$ .

Now let's look at a simple solution of equations (87) and (88). Assume that the initial vorticity fronts have finite amplitudes and sinusoidal forms, that can be written as:

$$l_i = l_{i0} e^{ik(X-c\tau)} \quad i = 1, 2 \quad (89)$$

Substituting (89) into the right hand side of (87) yield:

$$\begin{aligned} & \frac{1}{2\pi} \int_0^{-2\pi/K} iK(l_{10} - l_{20}) e^{iK(X-c\tau)} e^{-iK\zeta} \ln(1 - \cos K\zeta) d\zeta \\ &= \frac{i}{2\pi} (l_{10} - l_{20}) e^{iK(X-c\tau)} \int_0^{-2\pi} e^{-i\zeta} \ln(1 - \cos \zeta) d\zeta \\ &= i(l_{10} - l_{20}) e^{iK(X-c\tau)} \end{aligned} \quad (90)$$

The evaluation of this integral involves several variable transformation. Now (87) and (88) become:

$$l_{10} + (Kc - 1)l_{20} = 0 \quad (91)$$

$$l_{10}(1 + Kc - \frac{K^3}{2}) - l_{20} = 0 \quad (92)$$

So the dispersion relation of  $c$  is

$$2c^2 - K^2c + K = 0 \quad (93)$$

One can recognize immediately that (93) is the same dispersion relation obtained in the linear theory (23), so the most unstable wavenumber remains the same, and most of the discussion in the last part of section one is valid here also. The identical of the scaling and the dispersion relation of both infinitesimal amplitude and finite amplitude theories gives us a simple, continuous picture of baroclinic time evolution from the infinitesimal disturbance to the finite amplitude vorticity fronts, see figure-7.

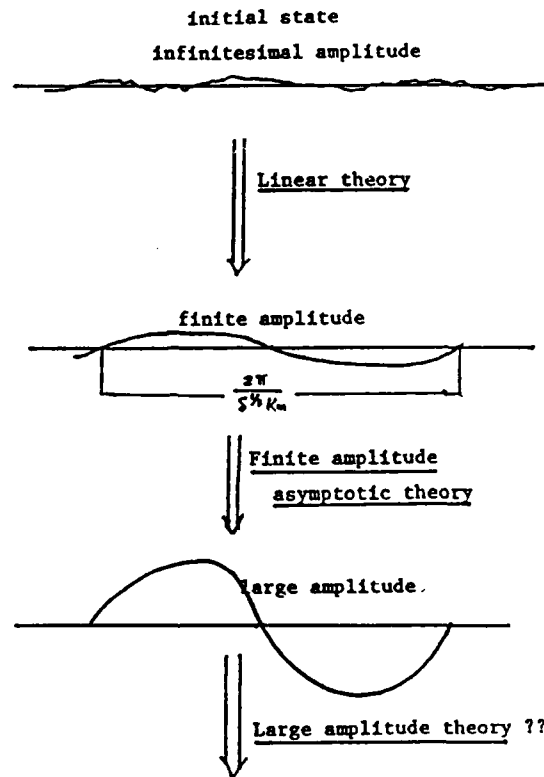


Fig-7. Three stages of the time evolution of the disturbance. The first stage is the infinitesimal amplitude described by the linear theory. The second stage is the finite amplitude described by the finite amplitude asymptotic theory. The third stage is the large amplitude which needs some new theory to describe it.

At the initial state, assume there is an infinitesimal disturbance with a broad range of wavenumbers. According to the dispersion relation (23), those waves with wavenumber  $k$  of order  $\delta^{1/3}$  are unstable and begin to grow. Shorter waves are stable and very long waves grow very slowly. As time goes by, the most unstable wave with wavenumber  $k_m = K_m \delta^{1/3}$  dominates. When the disturbance amplitude is no

longer infinitesimal that the linear theory is no longer formally valid, then our finite amplitude asymptotic theory comes in. At this stage, The new theory provides such an instability mechanism that the wave with wavenumber around  $k_m$  still keep the fastest growing. Because the equations describing this time evolution have linear forms, a sinusoidal front can preserve its sinusoidal form during this growing without any harmonic distortion. This finite amplitude front can keep growing untill the amplitude is comparable to the wave length scale that the basic assumption of small slope (68) can not hold any more and then a new large amplitude theory is needed for this stage of evolution.

In the Gulf Stream system, with the consideration of above discussion, the most possible Gulf Stream meandering length scale should be in the range related to the depth ratio  $\delta^{\frac{1}{3}}$ . If we choose the typical  $\delta$  value in the Gulf Stream system as  $\delta = 1/5$  and the Rossby deformation radius as  $L^* = 50 \text{ km}$ . then from the instability growing curve in figure-2, the possible meandering scale should be about  $300 \sim 1000 \text{ km}$  which is not so far away from the reality.

The stability of the very long wave, which means  $k \ll \delta^{\frac{1}{3}}$ , is worth one more look. Note that in figure-2 when  $K \rightarrow 0$ , the growth rate approach zero also. This means that a very long wave actually is stable. Recalling the order equation (65), this means when  $\epsilon \ll \delta^{\frac{1}{3}}$  the third term with  $\epsilon^3$  is no longer the dominant term and the remaining two terms lead to:

$$\begin{aligned} \frac{\partial l_1}{\partial \tau} &= \frac{\partial l_2}{\partial \tau} \\ &= \frac{1}{2\pi} \int_0^{-2\pi/K} \left[ \left( \frac{\partial l_1(X-\zeta)}{\partial X} - \frac{\partial l_2(X-\zeta)}{\partial X} \right) \ln(1 - \cos K\zeta) \right] d\zeta \end{aligned} \quad (94)$$

Equation (94) shows that two vorticity fronts have exactly time evolution behavior and the dominant motion is totally barotropic. Because the baroclinic component disappears along with the baroclinic instability mechanism so that the very long wave motion actually is stable.

### 3 NUMERICAL CALCULATION

We ran a numerical calculation to test the finite amplitude asymptotic theory in section 2. The numerical model we used was run by Stephen. P. Meacham of M.I.T.

His model also has a periodic disturbance but the depth ratio  $\delta$  is not restricted to small values. The parameter set we used was:

$$\delta = 1/125, \quad \epsilon = 1/5, \quad K = 1.26$$

The initial disturbance is given as a sine wave, with amplitude  $L_i = 0.8, i = 1, 2$ . The wave length is 24.9. Note that although the amplitude divided by the wave length is very small, it should be emphasized that the amplitude is not small compared to the width of the basic flow structure as shown in figure-8a,b.

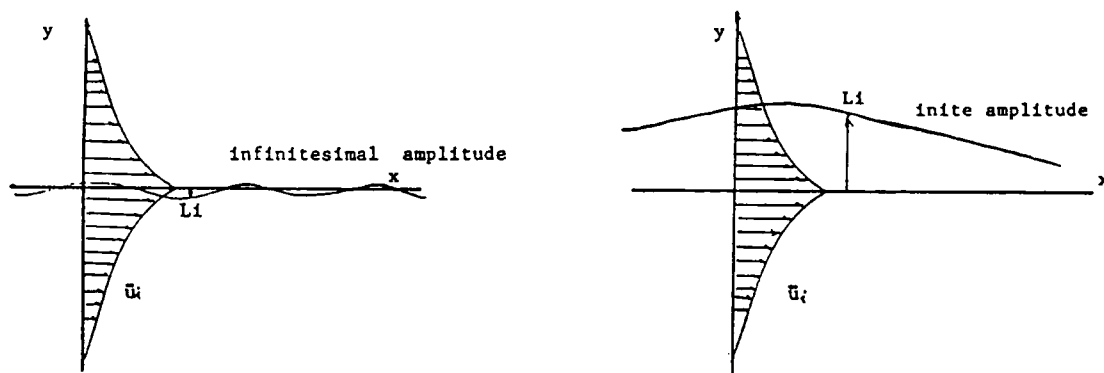


Fig-8a,b. The comparison of the infinitesimal disturbance and the finite amplitude disturbance to the basic flow structure.

Figure-8a is the infinitesimal amplitude approximation for linear theory and figure 8b is our finite amplitude case. We can see clearly that in fig-8b the vorticity front displacement is far from the center of the basic flow jet and this is the measurement of nonlinearity.

The depth ratio  $\delta$  is a small number too which is a little far from the the real ocean, but it is still closer to the real ocean than the  $1\frac{1}{2}$  layer model which has depth ratio 0.

Numerical (Meacham's) results for the time evolution of the two vorticity fronts are shown in figure-9:

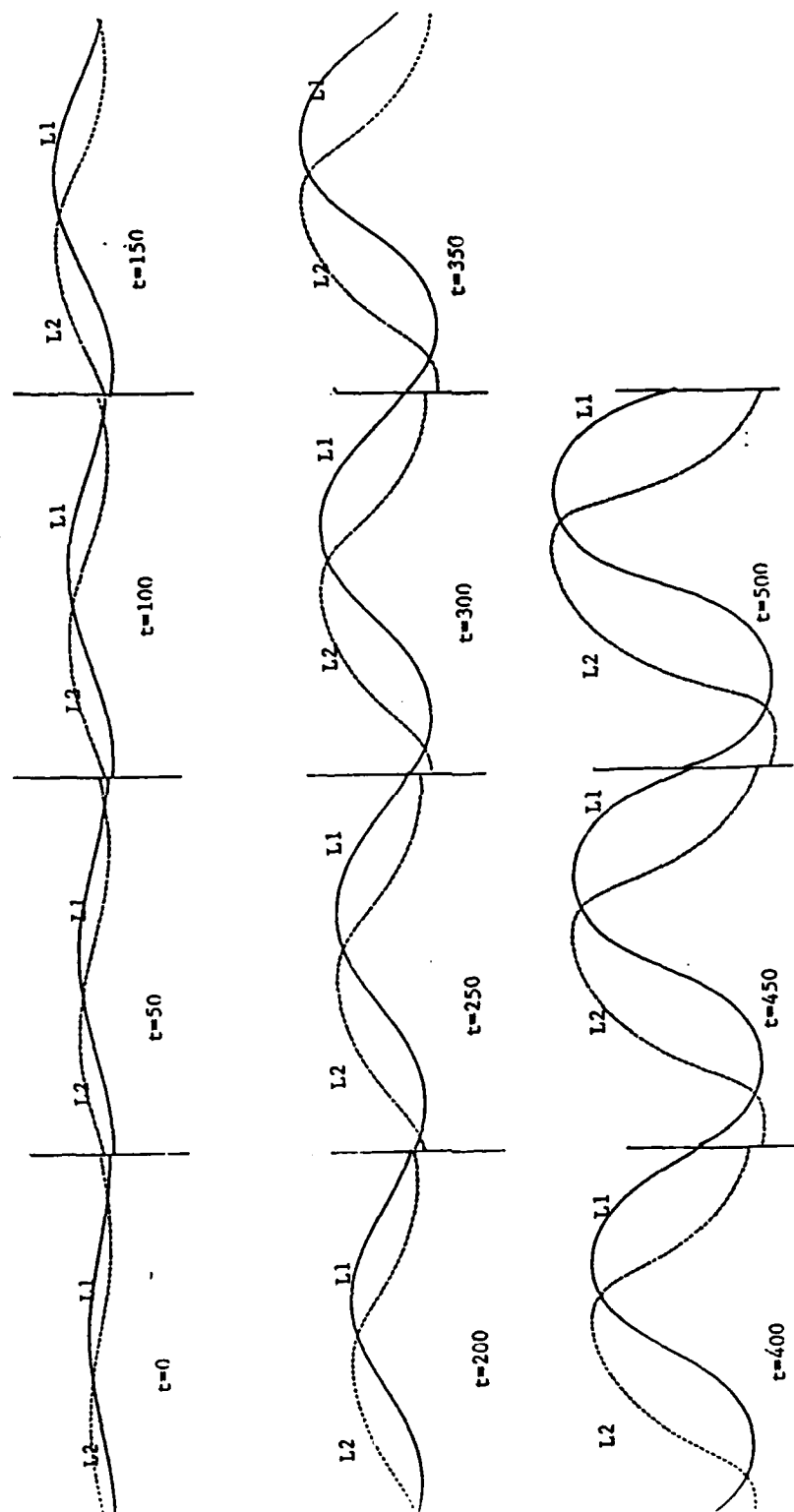


Fig-9. The numerical results of the time evolution of the two vorticity fronts. Up to time  $t = 300$ , the fronts keep growing without much harmonic distortion. This is just what the finite amplitude asymptotic theory predicts.

The solid line is the upper layer front and the dashed line is the lower layer front. The numbers below the curve are the nondimensional time  $t$ , which is related to our slow time unit  $\tau = t/125$ .

This result shows that both vorticity fronts grow with time and the sinusoidal wave forms are preserved up until time ( $t = 300$ ) in which the amplitudes grow without much harmonic distortion from 0.8 to 4. This behavior is just what the finite amplitude asymptotic theory predicts and explains.

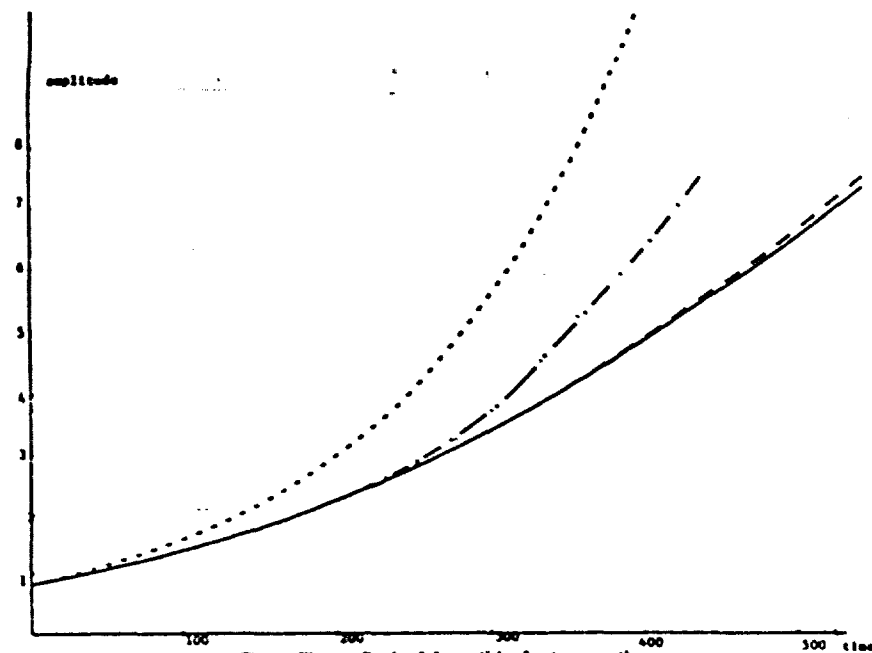


Fig. 10. The amplitude of the vorticity fronts versus the time curves. The numerical results agree well with the theoretical prediction up to time  $t = 300$ .

Figure-10 shows the maximal amplitudes versus time  $t$  curve. Again, the solid line is the upper layer front and the dashed line is the lower layer front. The asymptotic theory predicts that the two vorticity fronts grow with the same rate that  $|\frac{L_1}{L_2}| = 1$ . This is shown by the near identical  $L_1$  and  $L_2$  curves up to time  $300 \sim 400$ . After this, they begin to separating.

The dashed-dotted line shown in figure-10 is the growth rate curve obtained from the exact dispersion relationship (20). The dotted line is from the dispersion

relationship (21), which is the asymptotic form of (20) in the limit of small  $\delta$ . As we can see, up to time  $t = 300$ , the numerical result and the exact dispersion relation prediction is very close.

So up to time 300, the overall numerical result agrees very well with that of the theoretical prediction and hence verifies the theory.

The reason why the numerical result differs from the theoretical result after  $t = 300$  is due to breakdown of our basic assumption. As at the beginning, the maximal slope, or the maximal value of the  $\frac{\partial L_i}{\partial x}$  is about 0.2, but at  $t = 300$ , this increases to  $0.8 \sim 1$  and our basic assumption that it should be small is obviously being violated. At this stage, the higher order nonlinear terms must be taken into account as they are no longer small.

One will note that the two theoretical curves (dashed-dotted line and the dotted line) give quite different growth rate estimates, the reason being due to the asymptotic expansion. On the limit of the very small  $\delta$ , they are supposed to be identical. So for the finite amplitude asymptotic theory, when  $\delta$  is not very small, it probably will not be able to give a good quantitative growth rate estimate. However it does give a good qualitative explanation of why the finite amplitude front can continuously grow without much harmonic distortion and why the exact linear dispersion relation fits so well with the numerical calculation.

#### 4 CONCLUSION

We have developed an asymptotic equation for the finite amplitude, baroclinic wave motion subject to the following assumption

- 1: the depth ratio  $\delta$  is small
- 2: the disturbance amplitude is of the same order of deformation radius
- 3: the disturbance is periodic in the  $x$ -direction

At this level of amplitude, there are no nonlinear terms so that the sinusoidal disturbance can grow without any distortion. The numerical calculation verifies this up to a certain time until the amplitude versus wave length is no longer small. Now some questions arise:

**What determines the large amplitude disturbance?**

**What determines the final stage of the amplitude equilibrium?**

**Is there no equilibration?**

If we look back to the complicated nonlinear principal equations (61) and (62) and the simplified asymptotic equations of (87) and (88), we can see that the simple form of (87) and (88) suggest that it is quite possible to go one more step to develop a relatively simple nonlinear theory for the next stage of evolution in which the amplitudes of the disturbance become comparable to the wave length. This stage is quite similar to that of the theory of Pratt and Stern (1986) in their  $1\frac{1}{2}$  layer 'path equation' model which has large amplitude and small radius of curvature. Although our problem is two-layer with two vorticity fronts interacting, the small parameter  $\delta$  will enable us to use the asymptotic expansion to simplify the equations. In addition, they don't have a mechanism to generate the large amplitude disturbance in their model but assume there is a such initial disturbance. In our work here, we have an instability mechanism to generate from the infinitesimal amplitude to finite values. So it is quite worthwhile to go to this next stage to understand the whole instability evolution process, and that will form the basis of our future work.

#### ACKNOWLEDGEMENTS

I would like to express my sincere gratitude to Dr. M.E. Stern who suggested this problem and provided his constant discussion and valuable advice. He told me 'take the ball and run!' and then guided me all through the summer to this end. I thank Dr. G. R. Flierl for his many interesting and useful discussions on this topic and help in many computational aspect of the problem. I also thank Dr. S. Meacham for providing his numerical model and results and Dr. L.J. Pratt for discussions on this topic. Finally, I should like to thank all the faculty and fellows who made this an enjoyable and stimulating summer.

#### REFERENCES

- Flierl, G.R., 1975: Gulf Stream meandering, ring formation and ring propagation. Ph.D. thesis, Harvard University.
- Flierl, G. R. and A. R. Robinson, 1984: On the time dependent meandering of a thin jet. *J.Phys.Oceanogr.*, 14,412-443
- Pratt, L.J., and M. E. Stern, 1986: Dynamics of potential vorticity fronts and



eddy detachment. *J. Phys. Oceanogr.*, 16, 1101-1120.

Pratt, L. J., 1988: Meandering and eddy detachment according to a simple (looking) path equation. *J. Phys. Oceanogr.*, 18, 1627-1640.

Talley, L. D., 1982: Instabilities and radiation of thin jets, Ph.D. thesis, M.I.T.-W.H.O.I. Joint program, 233pp.

# Barotropic Boundary Layer Separation Regimes

R. Vance Condie

## 1. Introduction

In this report we use a regional numerical model to investigate boundary layer separation regimes for a steady, barotropic, quasi-geostrophic fluid. The steady potential vorticity equation is written as:

$$J(\psi, q) = \kappa \nabla^2 q \quad \text{where } q = \nabla^2 \psi + \beta y. \quad (1.1)$$

As general circulation models incorporate more complete sets of physics, several features in the outflow region of the western boundary current become dominant for both steady and time-dependent simulations. The figure below shows the time-averaged circulation in a one layer quasi-geostrophic model.

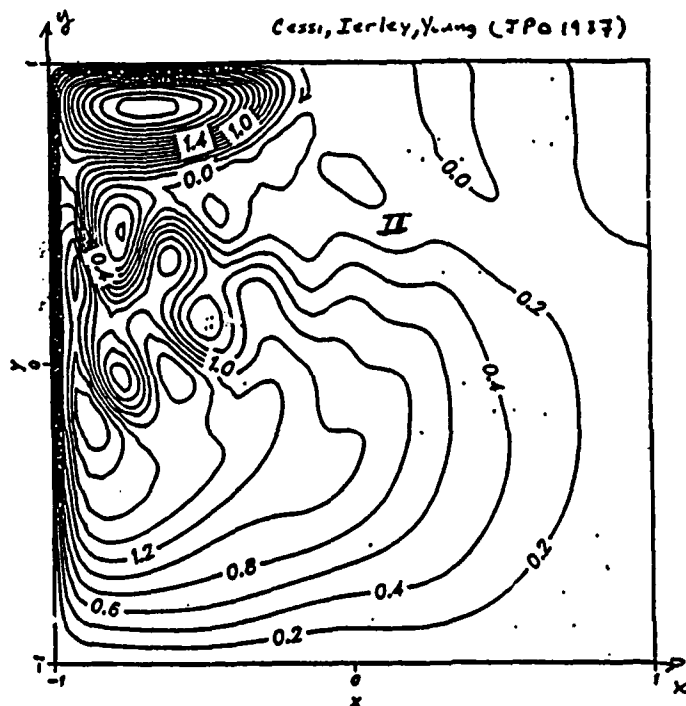


Figure 1.1

The dominant feature in the figure above is the recirculation cell in the north-west corner of the basin where the boundary current separates from the coast. There

is also a region, marked II, which is reminiscent of Moore's (Moore 1963) theory of vorticity dissipation by a series of stationary, damped Rossby waves. These features are not unique to the one-layer model and are observed in time dependent numerical simulations with multiple layers for both slip and no-slip boundary conditions (personal observation of five and two layer QG simulations done by W.R. Young; and in a barotropic QG model, Panteleev(1984) respectively). A review of numerical experiments as well as ocean observations relevant to recirculation may be found in Cessi et al, (1987).

The steady, one-layer, quasi-geostrophic model has the advantage of being analytically tractable, and we consider the inertial boundary layer for different upstream (outer) conditions in sections 2 and 3. In section 4 we use scaling arguments to determine the structure of a viscous sublayer imbedded within the inertial solution. At the end of section 4 we derive an analytical solution for the boundary layer in the limit where the viscous and inertial layers merge. In section 5 we investigate the effect of a northern slippery wall ( $\nabla^2\psi = 0$ ) on the separation as well as an outflow condition well below the northern wall. Preliminary results seem to indicate that dynamics of the separation region for the two cases are different. In the case of the boundary layer reaching the northern wall, anomalously low values of potential vorticity are dissipated in a well homogenized recirculation gyre. For runs with the outflow condition well below the northern boundary we find that the fluid dissipates the excess potential vorticity anomaly by setting up a damped series of standing Rossby waves.

## 2. Inertial Boundary Layer

In this section we determine the form of a steady, inertial western boundary layer for a prescribed upstream velocity profile. The steady, inviscid, quasigeostrophic potential vorticity equation is

$$J(\psi, q) = 0, \quad (2.1)$$

with boundary conditions

$$\psi(0, y) = 0, \quad \psi(\text{upstream}) = \psi^*(y). \quad (2.2)$$

In particular, we consider the case in which

$$\psi^*(y) = \phi_0 \left( \frac{y}{y^*} \right)^p, \quad \text{for } y \geq 0 \quad (2.3)$$

$$u = -\psi_y = \frac{-p\phi_0}{y^*} \left( \frac{y}{y^*} \right)^{p-1}.$$

In the boundary layer  $u \ll v$  and  $\partial/\partial x \gg \partial/\partial y$ , so that the relative vorticity is approximately

$$\frac{\partial v}{\partial x} - \frac{\partial u}{\partial y} \approx \frac{\partial v}{\partial x} = \psi_{xx}.$$

Equation (2.1) in the boundary-layer then reduces to  $J(\psi, \psi_{xx} + \beta y) \approx 0$  or

$$q \approx \psi_{xx} + \beta y = F(\psi), \quad (2.4)$$

where  $F$  is an arbitrary function of  $\psi$  to be determined by the boundary conditions on the flow. Specifically, for large  $x$ ,  $\psi_{xx} \rightarrow 0$  and we have

$$\beta y = F(\psi). \quad (2.5)$$

Inverting (2.3) for  $y = y(\psi)$  we see that

$$\beta \left( \frac{\psi^*}{\phi_0} \right)^{\frac{1}{p}} y^* = F(\psi) \quad \text{yielding} \quad \psi_{xx} + \beta y = \beta y^* \left( \frac{\psi}{\phi_0} \right)^{\frac{1}{p}}. \quad (2.6)$$

The case  $p = 1$  corresponds to Fofonoff's (1954) solution for a uniform westward flow in the interior. It is useful to repeat that solution here to outline the method

of solution for all  $p$ , and the free streamline solution in the next section. If we let  $n \equiv 1/p$ , and  $\alpha \equiv \beta y^*/\phi_o^n$  then (2.6) becomes

$$\psi_{xx} + \beta y = \alpha \psi^n, \quad \psi(0) = 0, \quad \psi(x \rightarrow \infty, y) = \left(\frac{\beta y}{\alpha}\right)^{\frac{1}{n}}. \quad (2.7)$$

Consider a solution of the form  $\psi = (y/y^*)^{\frac{1}{n}} \phi(\eta)$  where  $\eta = x/(y/y^*)^s$ , then (2.7) is

$$\left(\frac{y}{y^*}\right)^{\frac{1}{n}} \left(\frac{y^*}{y}\right)^{2s} \phi'' + \beta y = \alpha \left(\frac{y}{y^*}\right) \phi^n(\eta). \quad (2.8)$$

Choosing  $s = (1-n)/2n$  and  $\eta = x(y^*/y)^{(1-n)/2n}$  (2.8) becomes

$$\phi'' + \beta y - \alpha \phi^n = 0, \quad \phi(0) = 0, \quad \phi(\eta \rightarrow \infty) = \phi_o. \quad (2.9)$$

We integrate (2.9) resulting in

$$\frac{1}{2} \phi'^2 + \beta y^* \phi - \frac{\alpha}{n+1} \phi^{n+1} = C_n \quad (2.10)$$

where  $C_n$  is determined from the interior condition, using the previous definition  $\alpha \equiv \beta y^*/\phi_o^n$ , as

$$\frac{\alpha n}{n+1} \phi_o^{n+1} = C_n. \quad (2.11)$$

At this point the solution of (2.10) is reduced to quadrature:

$$\pm \left(\frac{2\alpha}{n+1}\right)^{\frac{1}{2}} x \left(\frac{y^*}{y}\right)^{\frac{1-n}{2n}} = \int_0^\phi \frac{d\phi}{(\phi^{n+1} - (n+1)\phi_o^n \phi + n\phi_o^{n+1})^{\frac{1}{2}}} \quad (2.12)$$

and for the case  $n = p = 1$ , (2.12) reduces to

$$\pm(\alpha)^{\frac{1}{2}} x = \int_0^\phi \frac{d\phi}{(\phi - \phi_o)} \quad (2.13)$$

$$\text{or} \quad \psi = \left(\frac{y}{y^*}\right) \phi_o \left(1 - e^{-x/\delta_I}\right) \quad \text{where} \quad \delta_I \equiv \left(\frac{\phi_o}{\beta y^*}\right)^{\frac{1}{2}}. \quad (2.14)$$

It is necessary to only keep the decaying solution in  $x$  to satisfy the interior boundary condition for large  $x$ . Pedlosky (1987) derives this same result for the case  $p = 1$  where  $\delta_I$  is the inertial layer thickness.

It is also tractable to solve the case for large  $n$ , in which case the behavior of the solution is quite different. If we consider the limit as  $n \rightarrow \infty$ , then  $\alpha\phi^n$  tends to zero and (2.9) simplifies to:

$$\phi'' + \beta y^* = 0, \quad \phi(0) = 0, \quad \phi(\eta \rightarrow \infty) = \phi_o, \quad \phi_\eta(\eta \rightarrow \infty) = 0. \quad (2.15)$$

The solution is immediately obtained by integrating (2.15) twice

$$\phi(\eta) = -1/2\beta y^* \eta^2 + C_1 \eta + C_2. \quad (2.16)$$

No normal flow at the western boundary,  $\eta = 0$  gives  $C_2 = 0$ , and  $\psi(x, y)$  with the remaining constant  $C_1$  may be rewritten as:

$$\psi(x, y) = -1/2\beta y^* x^2 \left( \frac{y}{y^*} \right) + C_1 x \left( \frac{y}{y^*} \right)^{\frac{1}{2}}. \quad (2.17)$$

The remaining boundary conditions are satisfied on a free streamline,  $x = \ell(y)$ , such that

$$\psi(\ell(y), y) = \phi_o, \text{ and } \nabla\psi(\ell(y), y) = 0.$$

This solution is shown schematically below:

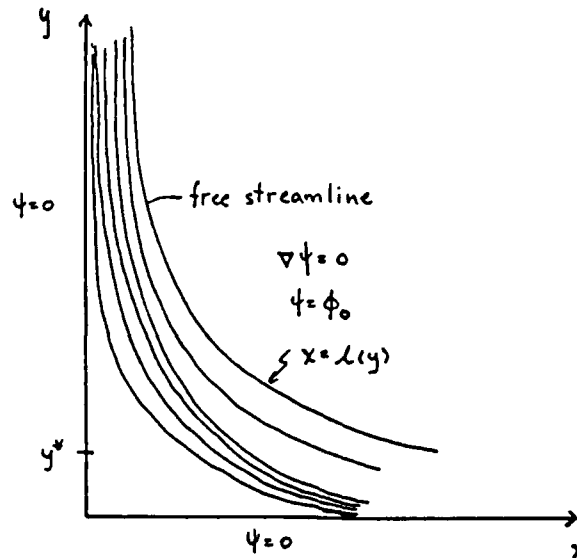


Figure 2.1

To determine  $\ell(y)$  and  $C_1$ , we solve simultaneously:

$$\psi(\ell(y), y) = -1/2\beta y^* \ell^2 \left( \frac{y}{y^*} \right) + C_1 \ell \left( \frac{y}{y^*} \right)^{\frac{1}{2}} = \phi_o \quad (2.18)$$

$$\psi_x(\ell(y), y) = -\beta y^* \ell \left( \frac{y}{y^*} \right) + C_1 \left( \frac{y}{y^*} \right)^{\frac{1}{2}} = 0 \quad (2.19)$$

The result is:

$$\begin{aligned} \psi(x, y) &= \phi_o \left( 1 - \left( \frac{x}{\ell(y)} - 1 \right)^2 \right) & \text{if } x \leq \ell(y) \\ \psi(x, y) &= \phi_o & \text{if } x \geq \ell(y) \end{aligned} \quad (2.20)$$

where

$$\ell(y) = \left( \frac{2\phi_o}{\beta y} \right)^{1/2}. \quad (2.21)$$

Interesting characteristics of this solution are that the free streamline is contracting towards the western wall as  $y^{-1/2}$ , and consequently to conserve mass the velocity is increasing as  $y^{1/2}$ . The  $n \rightarrow \infty$  limit corresponds to  $p \rightarrow 0$  in (2.3). For  $p \leq 0$  the transport along  $y = 0$  becomes infinite and the solution breaks down in the sense that there is no longer an inertial boundary-current along the western wall. This analysis suggests another class of solutions in which the incoming westward velocities decrease faster than algebraically as  $y \rightarrow \infty$  and have finite transports.

### 3. The Free Streamline

The methods of the last section can be used to solve a slightly more complicated version involving a specified upstream velocity profile which is limited in its  $y$  extent. We pose the problem as shown below with given inflow profile  $\psi^*$  and undetermined free streamline boundary  $y = \ell(x)$ .

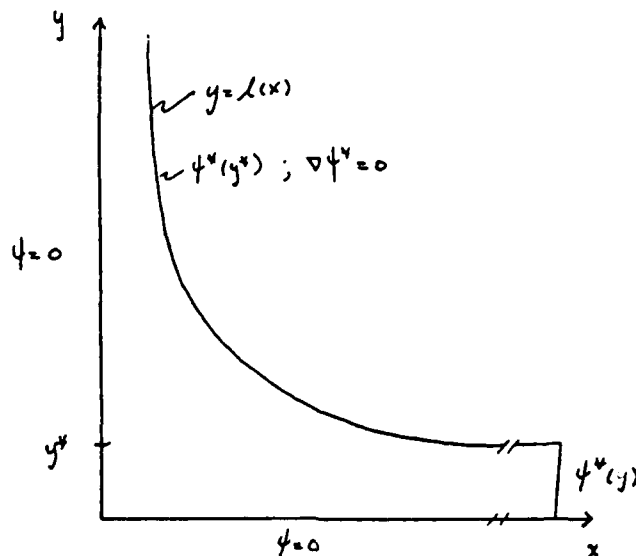


Figure 3.1

$$J(\psi, \nabla^2 \psi + \beta y) = 0. \quad (3.1)$$

with boundary conditions

$$\psi(x \rightarrow \infty, y) = \psi^*(y), \quad \psi(x, \ell(x)) = \psi^*(y^*), \quad \psi(x, 0) = \psi(0, y) = 0.$$

It is necessary to apply a second condition along the free streamline to determine the equation of the free streamline itself. It was pointed out during the GFD lectures that the following treatment in solving for the free streamline is only valid in the region of large  $y/y^*$ . That is, we assume that any small velocity discontinuity in the inflow profile will become subdominant in the boundary layer analysis for large values of  $y/y^*$ . We solve this system for uniform inflow conditions:

$$\psi^*(y) = \phi_o \left( \frac{y}{y^*} \right), \quad 0 \leq y \leq y^* \quad (3.2)$$

$$u = -\psi_y = -\frac{\phi_o}{y^*}, \quad 0 \leq y \leq y^*. \quad (3.3)$$

In the boundary layer,  $x < \ell^{-1}(y)$ , the relative vorticity is again dominated by  $v_x$ , and we write (3.1) as :

$$J(\psi, \psi_{xx} + \beta y) = 0 \quad (3.4)$$

Using the property that the potential vorticity is conserved along streamlines we have

$$\psi_{xx} + \beta y = F(\psi) = \frac{\beta y^*}{\phi_o} \psi. \quad (3.5)$$

Equation (3.2) has been inverted for  $y = y(\psi)$  in the inflow region where  $\psi_x(x) = 0$ . Defining  $\mu^2 = \beta y^*/\phi_o$  (3.5) is written as:

$$\psi_{xx} + \beta y - \mu^2 \psi = 0. \quad (3.6)$$

We now proceed analogously to the previous section, but allow a  $y$  dependence in the function  $\phi$ . That is we try a solution of the form  $\psi = (y/y^*) \phi(x, y)$ . After making this substitution we have the system

$$\phi'' + \beta - \mu^2 \phi = 0 \quad (3.7)$$

$$\phi(0, y) = 0, \quad \phi(x, \ell(x)) = \frac{\phi_o}{y}, \quad \phi_x(x, \ell(x)) = 0.$$



We try a linear combination of particular and homogeneous solutions with  $y$  dependent coefficients as

$$\phi = \frac{\phi_0 y}{y^*} (1 + B(y) \cosh \mu x + A(y) \sinh \mu x). \quad (3.8)$$

The condition  $\phi(0, y) = 0$  sets  $B(y) = -1$  and application of the two conditions on the free streamline are sufficient to determine both  $A(y)$  and the equation of the free streamline,  $y = \ell(x)$ :

$$\frac{y^*}{y} = 1 - \cosh \mu \ell^{-1}(y) + A(y) \sinh \mu \ell^{-1}(y) \quad (3.9)$$

$$0 = \sinh \mu \ell^{-1}(y) + A(y) \cosh \mu \ell^{-1}(y) \quad (3.10)$$

The algebra is a little messy but we find

$$A^2(y) = 2 \left( \frac{y^*}{y} \right) - \left( \frac{y^*}{y} \right)^2, \text{ and } \ell(x) = y^* \frac{\cosh \mu x}{\cosh \mu x - 1}. \quad (3.11)$$

The solution including (3.11) is

$$\psi(x, y) = \frac{y \phi_0}{y^*} (1 - \cosh \mu x + \left( 2 \frac{y^*}{y} - \left( \frac{y^*}{y} \right)^2 \right)^{\frac{1}{2}} \sinh \mu x). \quad (3.12)$$

One feature to stress in the solution above is the presence of an inertial boundary current beyond the point of westward zonal interior velocity. In fact, as long as there remains no interior velocity the stream continues up the western boundary. In limit of large  $y$  and  $x \ll \mu^{-1} = (\phi_0 / \beta y^*)^{1/2}$  we expand  $\ell(x)$  as

$$y = \ell(x) \approx \frac{2y^*}{\mu^2 x^2}, \quad (3.13)$$

which shows that the inertial layer continually contracts, i.e.

$$x = \left( \frac{2\phi_0}{\beta y} \right)^{1/2}. \quad (3.14)$$

By continuity and since  $u \ll v$  in the inertial layer, we see that  $v(0, y)$  goes as  $y^{1/2}$  and is accelerating up the western boundary. This property will be considered

in the next section where we append a viscous sub-layer to the solution. Presently however it is shown that for any inflow velocity profile  $\psi^*(y)$ , with the condition that the zonal velocity vanishes at  $y = y^*$  and having finite transport, in the asymptotic limit of large  $y$  the free stream shrinks like  $y^{-1/2}$ .

Consider the schematic diagram of the problem below:

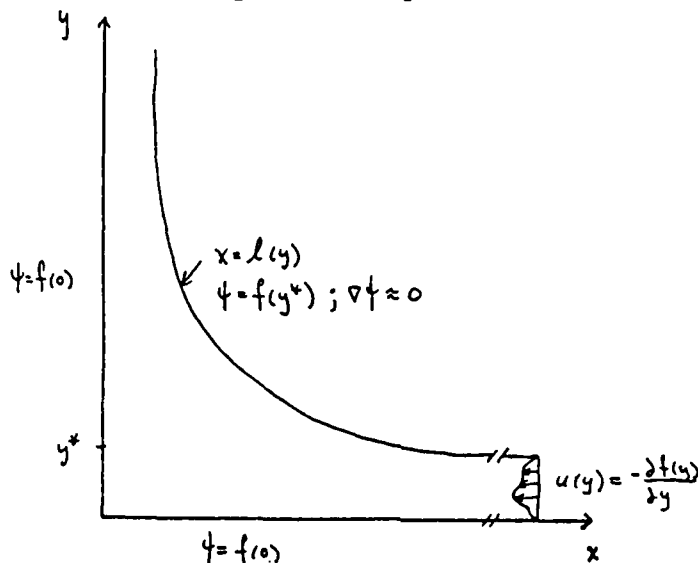


Figure 3.2

Prescribing the upstream velocity  $u = -\partial f / \partial y$  on  $y \in (0, y^*)$  we determine the boundary layer properties of the following system.

$$J(\psi, \nabla^2 \psi + \beta y) = 0 \quad (3.15)$$

$$\psi(0, y) = \psi(x, 0) = f(0), \quad \psi(l(y), y) = f(y^*)$$

For regions in the western boundary in which the relative vorticity is dominated by  $v_x$ , (3.15) reduces to

$$\psi_{xx} + \beta y \approx F(\psi) \quad (3.16)$$

since potential vorticity is conserved along streamlines. We determine the form of  $F(\psi)$  from the upstream condition as:

$$F(\psi) = \beta f^{-1}(\psi) \quad \text{and} \quad y = f^{-1}(\psi),$$

$$\text{and (3.16) becomes} \quad \psi_{xx} + \beta y = \beta f^{-1}(\psi). \quad (3.17)$$

If we now let  $\psi = f(0)\phi$  then

$$f(0)\phi_{xx} + \beta y = \beta f^{-1}(f(0)\phi) \quad (3.18)$$

$$\phi(0, y) = \phi(x, 0) = 1, \quad \phi(\ell(y), y) = \frac{f(y^*)}{f(0)}.$$

We now consider the properties of the system in the limit of large  $y \gg y^*$ . Because  $\beta f^{-1}(\psi)$  is bounded by  $(0, y^*)$ , the term on the rhs of (3.18) must become subdominant, thus the solution will behave as

$$\phi = -\frac{1}{2} \frac{\beta}{f(0)} y x^2 + C_1 x + 1 \quad (3.19)$$

using  $\phi(0, y) = 1$ . The equation  $x = \ell(y)$  and constant  $C_1$  may be determined as in the previous section by simultaneously satisfying the conditions

$$\phi(\ell(y), y) = f(y^*), \text{ and } \phi_x(\ell(y), y) = 0$$

and we write the solution, with  $\phi_o \equiv f(y^*) - f(0)$ :

$$\psi(x, y) = -\frac{1}{2} \beta y x^2 + (2\beta y \phi_o)^{\frac{1}{2}} x + 1 \quad (3.20)$$

$$\text{where } \ell(y) = \left( \frac{2\phi_o}{\beta y} \right)^{\frac{1}{2}} \quad (3.21)$$

We have shown that in the limit of large  $y \gg y^*$ , the inertial boundary layer shrinks as  $y^{-1/2}$ , and by differentiating (3.20) with respect to  $x$  that the velocity along the wall increases as  $y^{1/2}$ . The next step in the study of the western boundary layer properties is to append to these solutions a frictional sub-layer, this is done in the following section.

#### 4. Frictional Layers

In this section we pursue the effects of viscosity on the purely inertial flow. Treating the viscous term in the steady barotropic potential vorticity equation as a small perturbation to the free stream solution we consider a balance between the northward advection and diffusion of relative vorticity along a western no-slip boundary. The relative vorticity is again dominated by  $v_x$  so we consider the boundary-layer approximation

$$J(\psi, \psi_{xx}) + \beta \psi_x = \kappa \psi_{xxxx}. \quad (4.1)$$

Integrating this equation once we have:

$$J(\psi, \psi_x) + \beta \psi = \kappa \psi_{xxx} - \beta \phi_o \quad (4.2)$$

where  $\phi_o$  is the stream function evaluated on the free streamline. In the viscous sublayer we have the balance

$$J(\psi, \psi_x) \approx \kappa \psi_{xxx} \quad (4.3)$$

and in the limit of large  $y$  (4.2) reduces to a member of the family of similarity solutions given by Falkner and Skan (Batchelor Ch. 5.9). In the previous general case  $\psi_x(0, y) = (2\beta\phi_o)^{1/2}y^{1/2}$ , and we are able to obtain a similarity solution in the viscous sub-layer of the form

$$\psi = (2\kappa^2\beta\phi_o)^{1/4}y^{3/4}f(\eta), \quad \eta = \left(\frac{2\beta\phi_o}{\kappa^2y}\right)^{1/4}x. \quad (4.4)$$

We use the form of the similarity variable  $\eta$  to suggest that the viscous sublayer is growing proportional to  $y^{1/4}$  for our general inertial layer in the limit of large  $y$ . This suggests the possibility of the inertial and viscous layers merging.

Two questions immediately arise in the analysis of allowing viscosity in the presence of the purely inertial boundary-layer. 1. How does the viscous sub-layer grow for intermediate values of  $y$ ? 2. At what point does the sub-layer intersect the inertial layer, and what might be the form of solution there.?

To study the viscous layer scaling in the region  $y > y^*$ , we return to equation (4.3). Let  $\psi^I$  be the inertial layer stream function. The advection of relative vorticity at the outer edge of the sub-layer then scales as

$$J(\psi, \psi_x) \approx \frac{\psi_x^{I^2}(0, y)}{y}, \quad (4.4)$$

and the diffusion of relative vorticity at the outer edge of the sub-layer scales as :

$$\kappa \psi_{xxx} \approx \kappa \frac{\psi_x^I(0, y)}{\delta_v^2}. \quad (4.5)$$

Equating these two scales determines the sub-layer scaling:

$$\delta_v^2 \approx \frac{\kappa y}{\psi_x^I(0, y)} = \frac{y^2}{R_e} \quad \text{where} \quad R_e = \frac{\psi_x^I(0, y)y}{\kappa}. \quad (4.6)$$

Using our analytic solution (3.12) we find

$$\delta_v \approx \left( \frac{\kappa}{\mu \phi_0} \right)^{1/2} \frac{y^{1/2}}{\left( 2 \frac{y}{y^*} - 1 \right)^{1/4}}. \quad (4.7)$$

The limit for large  $y$  is as expected, and  $\delta_v$  grows as  $y^{1/4}$ , but in the intermediate limit  $y > y^*$  we see that the viscous sub-layer grows faster, as  $y^{1/2}$ . We visualize these relationships in the figure below, and answer the second question, at what point,  $\lambda$ , do the viscous sub-layer and inertial layer merge.

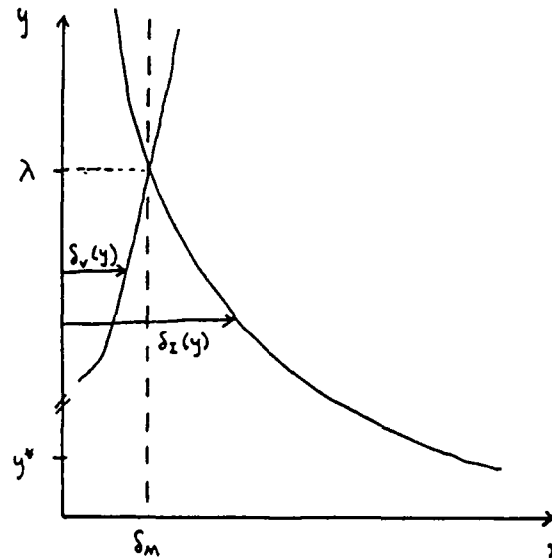


Figure 4.1

In the limit of  $y \gg y^*$  (4.7) may be approximated by

$$\delta_v(y) \approx \left( \frac{\kappa^2}{2\phi_0\beta} \right)^{1/4} y^{1/4}. \quad (4.8)$$

Equating this expression with equations (3.21), the asymptotic limit of the inertial-layer pinching, at  $y = \lambda$  we have  $\lambda = (8\phi_o/\beta\kappa^2)^{1/3}$  ( $\phi_o \equiv f(y^*) - f(0)$ ) and interestingly find that the boundary layers merge at

$$\delta_v(\lambda) = \delta_I(\lambda) = \delta_M = \left(\frac{\kappa}{\beta}\right)^{1/3}. \quad (4.10)$$

where  $\delta_M$  is the Munk viscous-layer thickness.

We now seek a solution to (4.2) in the regime where all terms may be important for  $y > \lambda$ . Choosing a solution independent of  $y$  the Jacobian term vanishes and we write the solution as a linear combination of the particular and homogeneous solutions, the result is

$$\psi(x) = \phi_o \left( 1 - e^{-x/2\delta_M} \left( \frac{1}{\sqrt{3}} \sin \frac{\sqrt{3}x}{2\delta_M} + \cos \frac{\sqrt{3}x}{2\delta_M} \right) \right). \quad (4.10)$$

We now combine sections 3. and 4. to formulate a scenerio for the evolution of the western boundary layer as it turns and flows northward. Initially, close to some latitude  $y^*$ , the inertial flow bends and accelerates northward due to the presence of the western wall, advecting with it anomalously low values of planetary vorticity. Due to viscosity in the system, high values of relative vorticity are generated at the wall in a viscous sub-layer which subsequently expands out into the inertial layer. As the stream accelerates further up the boundary we found that the growth rate of the viscous-layer became proportional to  $y^{1/4}$ . At some latitude,  $\lambda$ , the dissipation of relatively high values of potential vorticity through the sub-layer are able to completely balance the advection of planetary vorticity by the stream, and a non-accelerating Munk layer solution was found (4.10). This layer, independent of  $y$ , then continued up the western boundary. In the steady numerical model to follow it is seen that unless the stream comes into contact with a northern wall or the constant value  $\phi_o$  of the interior fluid is changed by prescribing an outflow condition, the stream will not separate from the western boundary. We thus conclude that there is no internal mechanism in a steady, barotropic, quasi-geostrophic boundary layer without bottom topography that will allow the western boundary layer to leave the wall.

## 5. The Regional Model

It has been demonstrated that a barotropic model is able to simulate the essential features of the recirculation transport in eddy-resolving general circulation models (Boning, 1986). In this section we simplify the problem a step further by numerically simulating the separation region of a western boundary current. The numerical model uses Newton's method to solve the steady, one-layer quasi-geostrophic potential vorticity equation, (1.1), with dissipation modeled by lateral diffusion.

We choose the region outlined in figure 5.1 below as representative of both the boundary layer region studied in sections 2-4, and the outflow region. The meridional extent of the region was chosen as 1500km and the longitudinal extent as 750km. With these choices we are able to resolve structure  $\geq O(10km)$  in the boundary layer. Figure 5.1b also shows the boundary conditions for the model. The boundary layer jet is described by an analytical expression for the stream function together with  $\psi_{yy} = 0$ . The western boundary satisfies the no normal flow and no-slip conditions. The northern boundary is treated as the southern extent of a cyclonic gyre, zero wind-stress curl line, hence  $\psi_{yy} = \psi = 0$ . It was pointed out in the GFD talk that a true, no-slip, northern wall may be an interesting future consideration. Two conditions are considered for the outflow region along the eastern boundary, and we outline these expressions as well as the analytical expressions used for the boundary layer jet below.

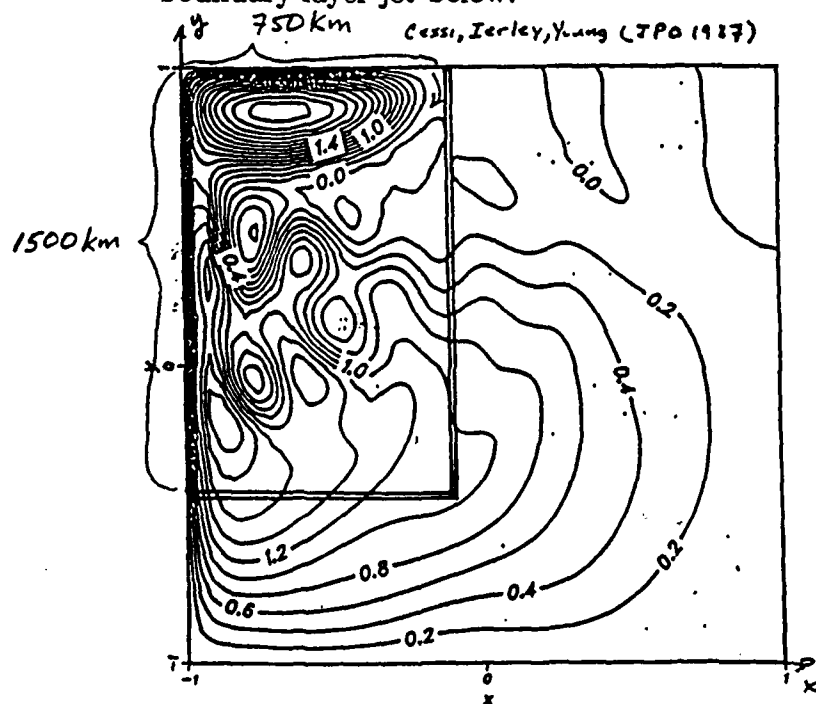


Figure 5.1a

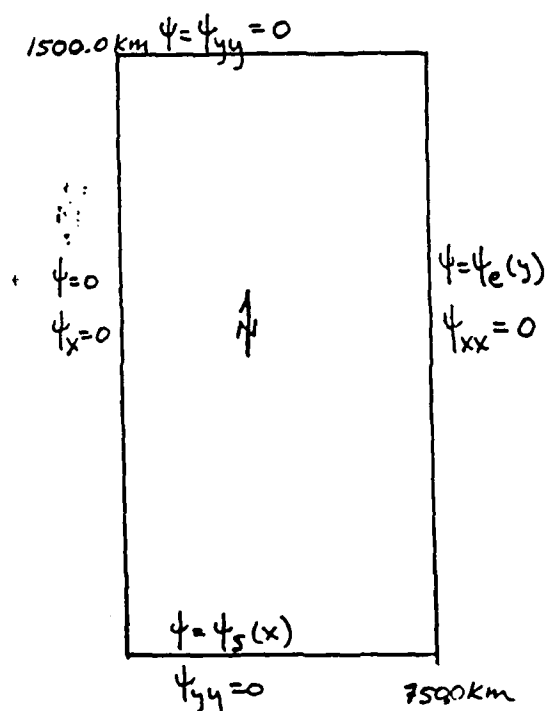


Figure 5.1b

### The Inflow Region

The boundary layer inflow jet is prescribed initially, at  $y = 0$ , with separation between the inertial and viscous sub-layer boundary widths. This condition is chosen in order to study the adjustment region as the two layers merge. The profile is given by:

$$v(x, 0) = \frac{\phi_o}{\delta_I} \left( e^{-x/\delta_I} - e^{-x/\delta_v} \right) \quad (5.1)$$

$$\psi_o(x) = \phi_o \left( 1 - \frac{\delta_v}{\delta_I} + \frac{\delta_v}{\delta_I} e^{-x/\delta_v} - e^{-x/\delta_I} \right), \quad (5.2)$$

where, for runs performed this summer, the following parameters were used.

$$\phi_o = 24.3 * 10^3 m^2/s \quad \delta_I = 74. * 10^3 m \quad \delta_v = 35. * 10^3 m.$$

The transport in the jet corresponds to 18 Sv for a 1500 m deep layer, and for  $\kappa < 1000 m^2/s$ , we expect  $\lambda > 0$ , that is, some separation between the inertial and viscous sub-layers. The profile of the jet is summarized in figure 5.2 below.

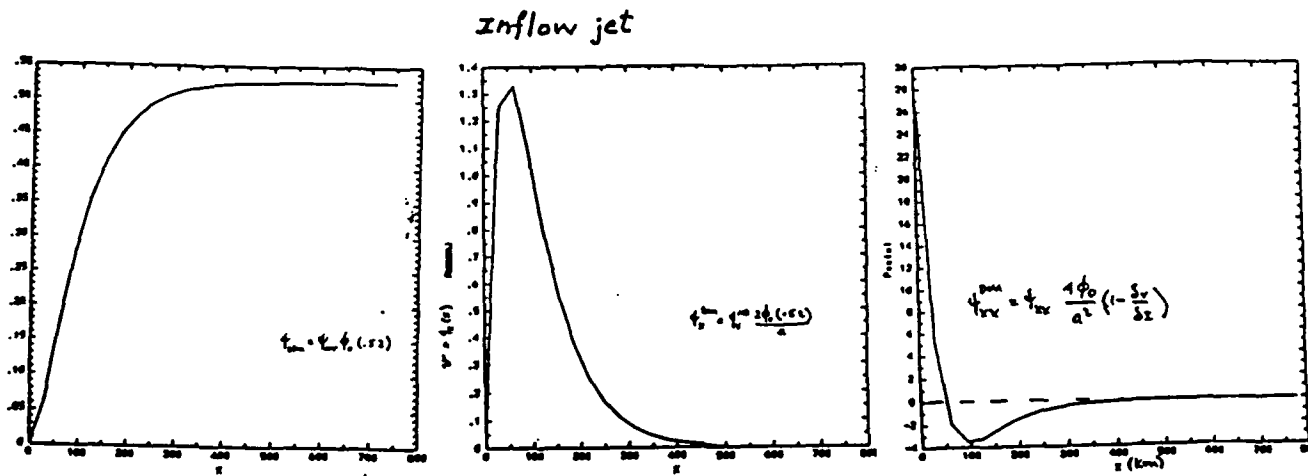


Figure 5.2

### The Outflow Region

Two experiments were run with different outflow conditions. In experiment 1. we chose an exponential profile of the form:

$$\psi_e(y) = \psi_o(a) \left( 1 + e^{-b/y_c} \left( 1 - e^{-y/\delta_v} \right) \right). \quad (5.3)$$



In experiment 2. we removed the fluid well below the southern wall by imposing :

$$\psi_e(y) = \frac{\psi_e(a)}{2} \left( 1 - \tanh \frac{y - y_c}{\alpha/2} \right) \quad (5.4)$$

These profiles can be seen in the form of the stream function in figures 5.3 and 5.5 respectively.

### *Model Results*

A description of the results will be divided into two parts: the exponential profile, Experiment 1, and the  $\text{sech}^2$  profile, Experiment 2.

**Experiment 1:** Figure 5.3 shows two runs for the exponential outflow profile. The upper two panels, from right to left, show the stream function and potential vorticity contours for an eddy-viscosity,  $\kappa = 1000 \text{ m}^2/\text{s}$ . The values on the contours are non-dimensional and may be dimensionalized using the constants in Fig. 5.2. The lower two panels are again the stream function and potential vorticity, but in this run the eddy viscosity is reduced by a factor of almost 3 ( $\kappa = 350 \text{ m}^2/\text{s}$ ). The most striking difference is the recirculation gyre which develops as the viscosity is reduced. This is consistent with the idea that the onset of recirculation is sensitive to the ratio: (Ierley, 1987)

$$r = \frac{\delta_I}{\delta_M} \approx \frac{\left( \frac{2\phi_e}{\beta y^*} \right)^{1/2}}{\left( \frac{\kappa}{\beta} \right)^{1/3}}$$

That is, as we reduce  $\kappa$ ,  $r$  becomes larger and for some critical value  $\kappa$  ( $\approx 500 \text{ m}^2/\text{s}$ ) we see that the boundary layer is non-compliant and the boundary layer significantly effects the interior flow.

Our expression for  $\lambda$  derived in section 4. is only approximate, and as can be seen in Fig. 5.4, the relative vorticity  $\psi_{xx}$  along the western boundary quickly adjusts to the Munk solution within a distance  $y \approx 400 \text{ km}$  from the southern wall. A lack of resolution prevented further decrease in  $\kappa$ , but from other runs it is clear that the recirculation continues to intensify. The value of homogenized  $q$  also decreases for decreasing values of eddy-viscosity. These decreasing values of  $q$  are due to lower potential vorticity anomalies being advected in the boundary current as the flow becomes more inertial. (See Ierley and Young (1988) for a more detailed analysis of how the value of homogenized  $q$  scales with varying eddy-viscosity).

**Experiment 2:** Fig. 5.5 shows two runs for  $\kappa = 1000 \text{ m}^2/\text{s}$  and  $\kappa = 250 \text{ m}^2/\text{s}$  for outflow parameters  $y_c = 800 \text{ km}$ ,  $\alpha = 400 \text{ km}$ . In this case the region of boundary current separation is very different from Experiment 1. Rather than develop a recirculation gyre to dissipate anomalously low values of potential vorticity, the flow sets up a series of damped stationary Rossby waves. Although not shown here, the transition of the steady solution from the  $\kappa = 1000 \text{ m}^2/\text{s}$  case to  $\kappa = 250 \text{ m}^2/\text{s}$  is continuous in the sense that the amplitude of the standing wave grows smoothly as the eddy-viscosity is reduced.

Figure 5.6 is a comparison between the model relative vorticity,  $\psi_{xx}$ , and the analytical Munk expression (eq. 4.10). For  $\kappa = 1000 \text{ m}^2/\text{s}$  we see in Fig. 5.6a that the flow in the boundary layer adjusts to the Munk type solution over a short distance,  $y \approx 200 \text{ km}$ . In contrast, for the run  $\kappa = 250 \text{ m}^2/\text{s}$  we can see in Fig. 5.6b that the relative vorticity of the model boundary layer never reaches that predicted by our Munk solution. We also see in Figs. 5.5 that the overshoot of the boundary layer, as it leaves the western wall, is increasing as the amplitude of the standing waves increase.

## 6. Conclusion

A simple one-layer, quasi-geostrophic model for two regimes of western boundary current separation has been studied. Bringing together ideas on the analytical structure of the boundary layer and numerical results, we have shown that the western boundary current separates in the region of a northern wall or a non-homogeneous interior outflow condition. The nonlinear Munk solution derived in section 4 is partially verified by considering the value of relative vorticity at the western wall.

The most relevant conclusion to be drawn from this project is the persistence of the damped Rossby wave solution in experiment 2 for lower values of eddy-viscosity. Papers by Ierley and Ruehr(1986) and Ierley(1987) suggest that boundary layer solutions are unstable for the ratio  $\delta_I/\delta_v > r_c$ , which excludes the possibility of a Moore type solution. For this reason we remain skeptical of the stability of the stationary Rossby wave solution found in experiment 2.

In all runs this summer, the boundary layer contracted towards the Munk solution over a short meridional distance, and we were not able to model the possible effects of free boundary layer streamlines which do not pass through a viscous layer. Further analysis on these topics will further the understanding of western boundary layer separation regimes. In particular, one question remains which deserves im-

mediate attention: How does the northern wall effect the high amplitude Rossby waves?. Higher resolution experiments would allow for a more inertial flow and hence higher amplitude waves. Higher resolution runs would also allow insight into the role of  $\lambda$ , the merger point of the viscous and inertial boundary layers.

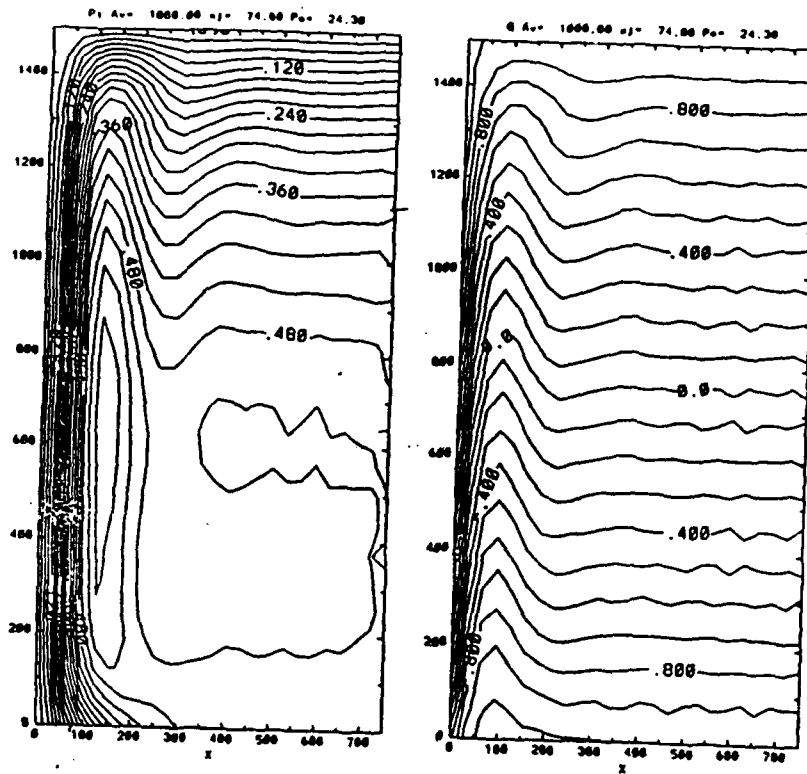
### Acknowledgements

This Fellow wishes to express his most sincere appreciation to the fellowship committee for the opportunity to participate in this summers GFD program. This project was conceived and developed under the guidance of Bill Young and Paola Cessi, and I would like to thank them both for their continued interest and patience throughout the summer.

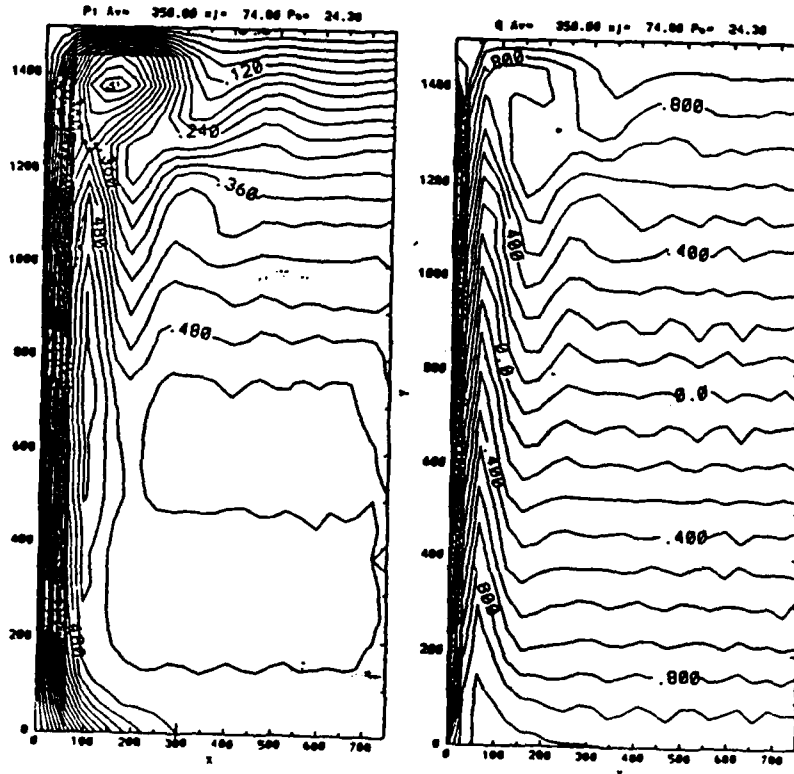
### REFERENCES:

- 1 Batchelor, G.K., 1970: *An Introduction to Fluid Mechanics*, Cambridge University Press, xviii +615 pp.
- 2 Boning, C.W., 1986: On the influence of frictional parameterization on wind-driven ocean circulation models. *Dyn. Atmos. Oceans*, 10, 63-92.
- 3 Cessi, P., G.R. Ierley and W.R. Young, 1987: A model of the inertial recirculation driven by potential vorticity anomalies., *J. Phys. Oceanogr.*, 17, 1640-1652.
- 4 Fofonoff, N.P., 1954: Steady flow in a frictionless homogeneous ocean. *J. Mar. Res.*, 13, 254-262.
- 5 Ierley, G.R., 1987: On the onset of inertial recirculation in barotropic recirculation models. *J. Phys. Oceanogr.*, 17, 2366-2374.
- 6 Ierley, G.R., W.R. Young, 1987: Inertial recirculation in a  $\beta$ -plane corner., *J. Phys. Oceanogr.*, 18, 683-689.
- 7 Ierley, G.R., O.G. Ruehr, 1986: Analytic and numerical solutions of a nonlinear boundary layer problem. *Stud. Appl. Math.*, 75, 1-36.
- 8 Moore, D.W., 1963: Rossby waves in ocean circulation. *Deep-Sea Res.*, 10, 735-747.
- 8 Pantelev, M.C., (1985): The Influence of friction on the character of the barotropic wind driven circulation. (in Russian) *Izvestia POLYMODE* 15, 34-38.
- 9 Pedlosky, N.P., 1979: *Geophysical Fluid Dynamics*, Springer-Verlag, 624 pp.

$K=1000 \text{ m}^2/\text{s}$



$K=350 \text{ m}^2/\text{s}$



Experiment 1.

Figure 5.3

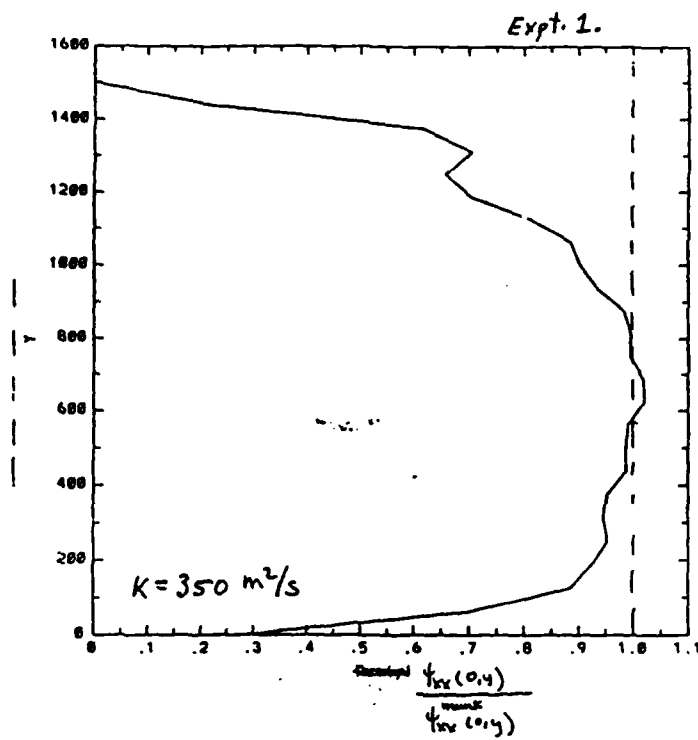
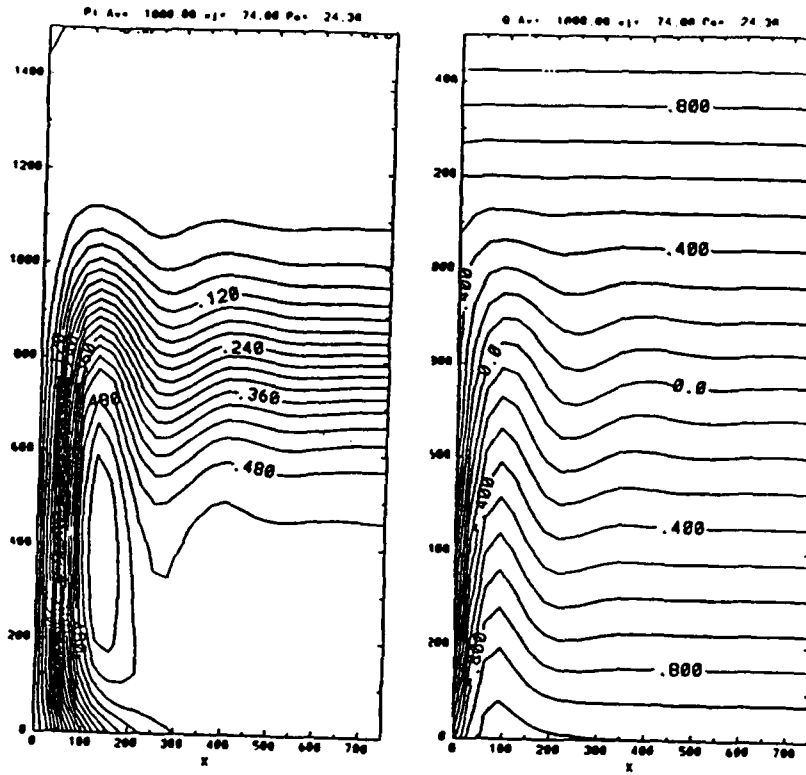
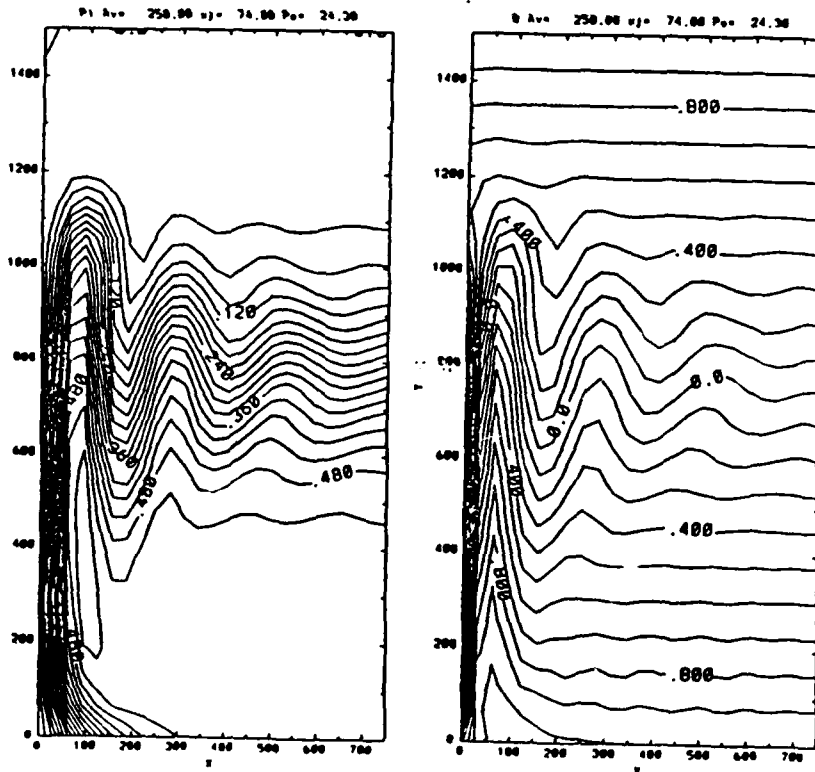


Figure S.4

$K = 1000 \text{ m}^2/\text{s}$



$K = 250 \text{ m}^2/\text{s}$



Experiment 2.

Figure 5.5

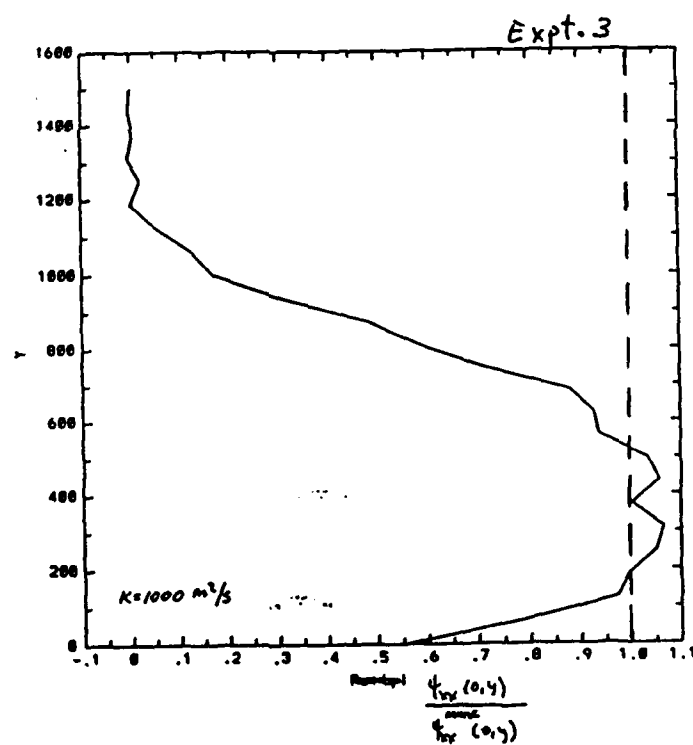
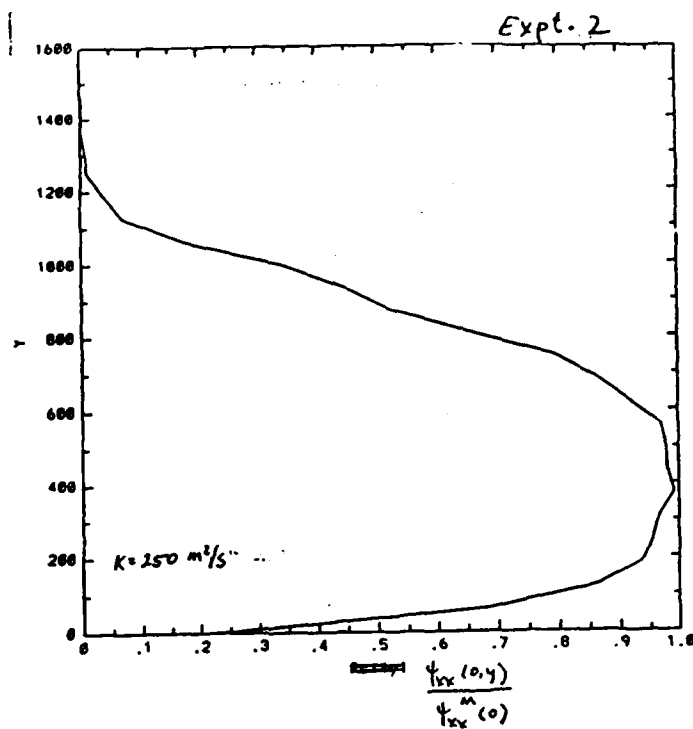


Figure 5.6

# CONVECTION WITH HEAT SOURCES

Sandip Ghosal

## ABSTRACT

The stability of a fluid layer to convection is studied when the medium has a volume distribution of heat sources proportional to the mass and linearly dependent on temperature. It is shown steady convection can occur for a class of boundary conditions even when the background static temperature gradient is subadiabatic. The convection then occurs on very large horizontal scales.

## 1 INTRODUCTION

The condition of hydrostatic equilibrium in a star is

$$\frac{dp}{dr} = -\rho g \dots\dots\dots (1-1)$$

where  $p, \rho, g$  are pressure, density and local acceleration due to gravity at radius  $r$ . If  $M$  and  $R$  are the mass and radius of a star,

$$\frac{dp}{dr} \sim \frac{P}{R}, \quad \rho \sim \frac{M}{R^3}, \quad g \sim \frac{GM}{R^2} \dots\dots (1-2)$$

With

$$\begin{aligned} M &= M_{\odot} = 2 \times 10^{30} \text{ kg} \\ R &= R_{\odot} = 7 \times 10^8 \text{ m} \\ C^2 &= \frac{P}{\rho} \cong \frac{GM}{R} \cong 2 \times 10^{11} (\text{m/s})^2 \end{aligned}$$



$c$ =speed of acoustic waves in the medium.

Therefore any departures from equilibrium conditions in a star is neutralized in a typical time of  $t = R/c \sim 1500 \text{ sec.} \sim 1 \text{ hour}$ . Since stars are observed to remain constant on much longer time scales, we draw the very important conclusion that stars are in a state of hydrostatic equilibrium.

The main balance in this equilibrium is gas pressure balancing gravity. Using the ideal gas law

$$P = \frac{\rho k T}{\mu}$$

( $k$ =Boltzmann's constant,  $\mu$  = atomic weight =  $10^{-27}$ kg for hydrogen) we have  $c^2 = P/\rho = kT/\mu$  which gives  $T \approx 10^7 K$  as a typical temperature inside stars. This temperature is sufficient to maintain nuclear reactions in the core which is the source of the star's energy. This energy can be carried to the surface by three possible mechanisms : conduction, convection and radiation. Conduction can be shown to be almost entirely negligible in stars. Radiative transport is always present and convective transport can occur under certain conditions. *Schwarzschild's criterion* is used to decide whether or not convection can occur in a given layer of the star. The condition is, a layer is convectively unstable if

$$-\frac{dT}{dr} > \frac{g}{C_p}$$

where  $C_p$  = specific heat per unit mass at constant pressure.[12]

In the derivation of Schwarzschild's criterion the effects of viscosity and heat sources are left out. The motivation for this work is to try to gain some insight into how the presence of temperature dependent heat sources affect Schwarzschild's criterion. (We are trying to model the situation where heat is being generated in the medium itself, due to nuclear fusion- a strongly temperature dependent process.)

The question of convective stability is very important for stars. Firstly, it decides whether or not mixing is going on at the core bringing in fresh fuel thereby keeping the reactions going. Another reason is, if a region inside the star proves to be convectively unstable, usually the convection is so vigorous that we may take the temperature gradient in such regions as the critical gradient for onset of convection. This situation is called "convective equilibrium" The Schwarzschild's criterion therefore decides

- (a) which regions are unstable and
- (b) what temperature gradient should be used in the unstable region.

Thus, any modification of the Schwarzschild's criterion would have profound implications in terms of integration of the stellar structure equations.

In this study we will be looking only at thin layers of fluids. This may be relevant either if

- (a) we are looking at high radial modes, or
- (b) we are looking at a star where the fuel in the core is exhausted and nuclear burning is going on in a thin layer around the core.

## 2 THE BOUSSINESQ EQUATIONS

The basic equations expressing the conservation of mass, momentum and energy in a fluid are

$$\frac{d\rho}{dt} = 0 \quad \dots \dots \dots (2-1)$$

$$\rho \frac{d\bar{u}}{dt} = -\nabla p - g \hat{z} \rho + \mu \nabla^2 \bar{u} \dots (2-2)$$

$$\dot{T} \frac{ds}{dt} = Q \quad \dots \dots \dots (2-3)$$

Here  $\rho$  is the density,  $\bar{u}$  is the velocity,  $p$  the pressure,  $T$  the temperature and  $S$  the entropy per unit mass at point  $(x,y,z)$  at time  $t$ .  $Q$  is the heat gained per unit mass of the fluid at  $(x,y,z)$  per unit time and it is specified by the physical situation.  $\mu$  is the molecular viscosity coefficient and the  $z$ -axis is chosen vertically upwards.

For liquids we also have the following equation of state

$$\rho = \rho_0 [1 - \alpha (T - T_0)] \quad \dots (2-4)$$

where  $\alpha$  is the coefficient of expansion. For a liquid it is reasonable to assume the density is constant except on the right hand side of equation (2-2) where it drives the buoyancy effects. This is the Boussinesq approximation [1]. Using

$$T ds = \rho_0 C_v dT \quad \dots (2-5)$$

$$Q = \nabla \cdot (k \nabla T) + \mathcal{E}(T) \quad \dots (2-6)$$

$$\nu = \mu / \rho_0 \quad \dots (2-7)$$

where  $C_v$  is the specific heat per unit mass at constant volume  $k(T)$  is the conductivity and  $\mathcal{E}(T)$  represents heat generation within the body of the fluid, (Note: viscous heating can be shown to be negligible in such problems.)

$$\nabla \cdot \bar{u} = 0 \quad \dots (2-8)$$

$$\frac{\partial \bar{u}}{\partial t} + (\bar{u} \cdot \nabla) \bar{u} = - \frac{\nabla p}{\rho_0} - g \hat{z} [1 - \alpha (T - T_0)] + \nu \nabla^2 \bar{u} \quad \dots (2-9)$$

$$\frac{\partial T}{\partial t} + (\bar{u} \cdot \nabla) T = \nabla \cdot (k \nabla T) + \mathcal{E}(T) \quad \dots (2-10)$$

$\kappa = k/\rho_0 C_v$  is called the thermometric conductivity and  $\mathcal{E}(\tau) = \mathcal{E}(\tau)/\rho_0 C_v$ . Equations (2-8) to (2-10) are the Boussinesq equations for a liquid with heat sources. We will study the situation of an infinite plane parallel region of fluid. (See Fig 1) If we write down the boundary conditions of continuity of temperature and heat flux at a boundary and use the exact solution of the heat conduction equation inside the solid then it is shown the boundary conditions at  $z=0$  or  $d$  within the liquid can be written as

$$\frac{dT}{dz} + B T = \text{constant} \quad \dots (2-11)$$

where  $B \propto$  conductivity of solid/conductivity of fluid.[2] When the solid is a perfect conductor this reduces to

$$T(\text{boundary}) = \text{constant} \quad \dots (2-12)$$

and when the boundary is perfectly insulating

$$\frac{dT}{dz}(\text{boundary}) = \text{constant} \quad \dots (2-13)$$

For boundary conditions on the velocity, we have, the vertical velocity must vanish at the boundary

$$w(\text{boundary}) = 0 \quad \dots (2-14)$$

Further we have  
either

$$u = v = 0 \quad \dots \dots \dots (2-15)$$

or

$$\frac{\partial u}{\partial z} = \frac{\partial v}{\partial z} = 0 \quad \dots \dots \dots (2-16)$$

depending on whether the fluid is in contact with a rigid surface or is free. Using equation (2-15), (2-16) and (2-8) we also have  
(free)

$$\frac{\partial w}{\partial z} = 0 \quad \dots \dots \dots (2-17)$$

(rigid)

$$\frac{\partial^2 w}{\partial z^2} = 0 \quad \dots \dots \dots (2-18)$$

Here  $\bar{u} = (u, v, w)$

### 3 LINEAR THEORY

Let  $\kappa(T) = \kappa_0 C(T)$   
and  $\epsilon(T) = \epsilon_0 S(T)$

where  $C(T)$  and  $S(T) \sim 1$  In steady state,  $\bar{u} = 0$  &  $\frac{\partial}{\partial t} = 0$  and equation (2-8) to (2-10) gives

$$-\frac{\nabla p_s}{\rho_0} - g \hat{z} [1 - \alpha (T_s - T_0)] = 0 \quad \dots\dots (3-1)$$

$$\nabla \cdot (C(T_s) \nabla T_s) + \frac{\varepsilon_0}{k_0} S(T_s) = 0 \quad \dots\dots (3-2)$$

We will assume the steady states to be independent of  $x$  and  $y$ ,

$$T_s = T_s(z) \quad \dots\dots\dots (3-3)$$

$$p_s = p_s(z) \quad \dots\dots\dots (3-4)$$

When  $S(T) = 0$  and  $C(T) = 1$  equation (3-2) gives

$$T_s(z) = T_0 - \beta z$$

where  $\beta = -dT_s/dz$  is determined from boundary conditions. In the general case we will define  $\beta$  such that

$$\frac{dT_s}{dz} \sim \beta$$

If we perturb equations (2-8) to (2-10) about the steady state,

$$\left. \begin{aligned} T(x, y, z, t) &= T_s(z) + \theta(x, y, z, t) \\ p(x, y, z, t) &= p_s(z) + \pi(x, y, z, t) \end{aligned} \right\} \dots (3-5)$$

then to first order in the small quantities  $\theta$ ,  $\pi$  and  $u$

$$\frac{\partial \bar{u}}{\partial t} = - \frac{\nabla \pi}{\rho_0} + g \alpha \theta \hat{z} + \nu \nabla^2 \bar{u} \dots (3-6)$$

$$\begin{aligned} \frac{\partial \theta}{\partial t} + w \frac{dT_s}{dz} &= \kappa_0 \nabla \cdot (C(T_s) \nabla \theta + C'(T_s) \nabla T_s \theta) \\ &+ E_0 S'(T_s) \theta \dots (3-7) \end{aligned}$$

$$\nabla \cdot \bar{u} = 0 \dots (3-8)$$

If we scale all lengths by  $d$ , all times by  $d^2/\nu$  (the diffusion time for momentum) all temperatures by  $\beta d$  ( $\sim$  temperature difference between top and bottom) the pressure by  $\rho_0 g d$  and the velocities by  $\kappa_0/d$  then equations (3-6) to (3-8) become

$$\frac{\partial \bar{u}}{\partial t} = - \frac{g d^3}{\kappa_0 \nu} \nabla \pi + R \theta \hat{z} + \nabla^2 \bar{u} \dots (3-9)$$

$$\begin{aligned} \sigma \frac{\partial \theta}{\partial t} + w \frac{dT_s}{dz} &= \frac{d}{dz} \left( C'(T_s) \theta \frac{dT_s}{dz} \right) + \nabla \cdot (C(T_s) \nabla \theta) \\ &+ \Omega^2 S'(T_s) \theta = 0 \dots (3-10) \end{aligned}$$

$$\nabla \cdot \bar{u} = 0$$

where

$$R = \frac{g \alpha \beta d^4}{\kappa_0 \nu}$$

$$\sigma = \nu / \kappa_0$$

$$\Omega^2 = \frac{\epsilon_0 d^2}{\nu}$$

are dimensional numbers.  $R$  is called the Rayleigh number,  $\sigma$  is the Prandtl number and  $\Omega^2$  will be called the Ed number. One can eliminate  $u, v$  and  $\pi$  from the seven equations (3-9) and (3-10). Taking the curl of the curl of (3-9) and writing it's  $z$ -component,

$$\frac{\partial}{\partial t} \nabla^2 \omega = R \nabla_H^2 \theta + \nabla^4 \omega \quad \dots (3-11)$$

where

$$\nabla_H^2 = \frac{\partial^2}{\partial x^2} + \frac{\partial^2}{\partial y^2}$$

#### 4 REVIEW OF KNOWN RESULTS

For the moment let us take the conductivity to be constant and heat sources to



be zero.

$$C(\tau) = 1$$

$$S(\tau) = 0$$

Then equation (3-10) and (3-11) become

$$\sigma \frac{\partial \theta}{\partial t} + w \frac{dT_s}{dz} = \nabla^2 \theta \quad \dots \dots (4-1)$$

$$\frac{\partial}{\partial t} \nabla^2 w = R \nabla_H^2 \theta + \nabla^4 w \quad \dots \dots (4-2)$$

In this section we deal only with the constant temperature and constant flux cases. Therefore (in dimensional units)

$$T_s(z) = T_s(0) - \beta z \quad \dots \dots (4-3)$$

where  $k\beta$  = specified heat flux (in fixed flux case)  
and  $\beta = \Delta T/d$  (in the fixed temperature case.  $\Delta T$  = the temperature difference between top and bottom.)

Therefore

$$\frac{dT_s}{dz} = -\beta$$

In non-dimensional units

$$\frac{dT_s}{dz} = -1$$

If we assume solutions of the form

$$\begin{pmatrix} \theta \\ w \end{pmatrix} = e^{i(k_x x + k_y y) + \beta t} \begin{pmatrix} \phi(z) \\ W(z) \end{pmatrix}$$

then (4-1) and (4-2) gives

$$\sigma \beta \phi = W + (D^2 - k^2) \phi \quad \dots \dots (4-4)$$

$$\beta (D^2 - k^2) W = -k^2 R \phi + (D^2 - k^2)^2 W \quad \dots (4-5)$$

where  $D = d/dz$  and  $k = \sqrt{k_x^2 + k_y^2}$ . For fixed  $R, \sigma, \beta$  and  $k$  equations (4-4) and (4-5) together with the appropriate boundary conditions form an eigenvalue problem for  $p$ . It may be shown, the eigenvalues of equation (4-4) and (4-5) are always real. (See Chap2 of [4] also Appendix A) This is often called "The principle of exchange of stabilities". For  $R=0$  one can show all the eigenvalues are negative for all  $k$ . Therefore the system is stable. As  $R$  is increased keeping  $k$  fixed, a critical value is reached when the largest eigenvalue becomes zero. This is the marginal

state. If one plots  $R$  at marginality as a function of  $k^2$  then for  $R$  above this curve the system is unstable and below it it is stable. At  $R = R(\text{marginal})$  we have steady convection. The case of fixed temperatures at the boundary was first studied by Rayleigh [5]. (also see [4] for a detailed discussion of the linear theory) and this problem has been studied extensively since by various authors. (See table 1 of [6]) The  $R$  vs.  $k^2$  curve is shown in Fig 2. The value of  $R_c$  depends on the velocity boundary conditions (see Table 1)

The case of fixed flux was first studied by Jeffreys [7] and subsequently by Sparrow, Goldstein and Jonsson [8] and Hurle, Jakeman and Pike [16]. The striking feature is the critical horizontal wave number at the onset of convection,  $k_c=0$ . The values of  $R_c$  in the various cases are shown in Table 2

## 5 COMPRESSIBLE MEDIUM

If the medium is compressible the Boussinesq equations (2-8) to (2-10) are not strictly valid. However, Spiegel and Veronis have shown [3] for an ideal gas if

(a) the depth of the fluid layer is much less than any of the scale heights of the variables in the problem and

(b) if the motion induced fluctuations in the pressure and density do not exceed in order of magnitude the total static variations of these quantities

the equations of compressible convection reduce to the Boussinesq equations with  $C_v$  replaced by  $C_p$  (=specific heat at constant pressure per unit mass) and  $T_s'(\tau)$  in equation (3-7) replaced by  $T_s'(\tau) + g/C_p$  (dimensional units). When  $T_s' = -\beta$  (a constant) we get after rescaling  $\Theta$ , equations (4-4) and (4-5) with the minor modifications -

$\sigma = \nu/\kappa_0$  where  $\kappa_0 = k/\rho_0 C_p$  ( $C_p$  in place of  $C_v$ )

and

$$R = \frac{g d^4}{\kappa \nu} \left( \beta - \frac{g}{C_p} \right)$$

Because of this result we can immediately take over any results found for liquids to the compressible case. Note however, the Rayleigh number defined in this generalized sense can be either positive or negative. For an isentropic atmosphere it can be shown that the temperature gradient is  $g/C_p$ . Therefore when the imposed temperature gradient  $\beta > g/C_p$  or  $R > 0$  we say that the static state is superadiabatic and when  $R < 0$  we say it is subadiabatic.

## 6 STEADY SOLUTIONS

Let us look for steady state solutions of equation (3-2) with fixed fluxes at both boundaries—

$$\left(\frac{dT}{dz}\right)_{z=0} = -\beta_0 \quad \dots\dots\dots (6-1)$$

$$\left(\frac{dT}{dz}\right)_{z=1} = -\beta_1 \quad \dots\dots\dots (6-2)$$

Assume  $C(T)=1$  and  $S(T)=1+s^2T$  where  $s^2$  is a positive number. Then,

$$\frac{d^2T}{dz^2} + \frac{\epsilon_0}{\kappa_0} (1 + s^2T) = 0 \quad \dots\dots\dots (6-3)$$

Integrating both sides with respect to  $z$  from  $z=0$  to  $z=1$  and using equations (6-1) and (6-2) we get the constraint

$$1 + s^2 \int_0^1 T dz = \frac{\kappa_0}{\epsilon_0} (\beta_1 - \beta_0) \quad \dots\dots\dots (6-4)$$

which simply means nett heat leaving the system = heat produced by the internal sources.

The exact solution of equations (6-1) to (6-3) is

$$T_s(z) = -\frac{1}{\lambda^2} + \left( \frac{\beta_1 \cos \chi z - \beta_0 \cos \chi (z-d)}{\chi \sin \chi d} \right) \dots (6-5)$$

where

$$\chi = \lambda \sqrt{\frac{\epsilon_0}{\kappa_0}}$$

In the limit  $\chi \approx 0$  (weak source or arbitrary source with weak temperature dependence.)

$$T_s(z) = \frac{1}{\lambda^2} \left[ \frac{\kappa_0}{\epsilon_0} \cdot \frac{\beta_1 - \beta_0}{d} - 1 \right] + \frac{1}{2} \beta_0 d - \beta_0 z - \frac{1}{2} \left( \frac{\beta_1 - \beta_0}{d} \right) z^2 \dots (6-6)$$

Then

$$\frac{dT_s}{dz} = -\beta_0 - \left( \frac{\beta_1 - \beta_0}{d} \right) z \dots (6-7)$$

To avoid complications due to nonconstant coefficients, in our future work we will

assume  $\beta_1 \approx \beta_0$  so that

$$\frac{dT_s}{dz} \cong -\beta_0 \dots \dots \dots (6-8)$$

In nondimensional units

$$\frac{dT_s}{dz} \cong -1 \dots \dots \dots (6-9)$$

## 7 ASYMPTOTIC EXPANSIONS FOR CRITICAL R

As in section 6 we take  $C(T)=1$ ,  $S(T)=1+s^2T$  and  $T'_s(z)=-1$  in equations (3-10) and (3-11). Also assume

$$\begin{pmatrix} w \\ \theta \end{pmatrix} = e^{i(k_x x + k_y y) + \frac{1}{2}t} \begin{pmatrix} W \\ \Theta \end{pmatrix}$$

and  
Then

$$k = \sqrt{k_x^2 + k_y^2}$$

$$\frac{1}{2}(\partial^2 - k^2)W = -k^2 R \Theta + (\partial^2 - k^2)^2 W \dots \dots (7-1)$$

$$\sigma \frac{1}{2} \Theta - W = (\partial^2 - k^2) \Theta + \Omega^2 s^2 \Theta \dots \dots (7-2)$$

As long as  $R \geq 0$  the principle of exchange of stabilities holds, that is,  $\text{Im}(p) = 0$ .  
(For proof see Appendix A)

Let us look for the marginal states  $p=0$ . Putting  $p=0$  in equations (7-1) and (7-2)

$$(\mathcal{D}^2 - k^2)^2 W = k^2 R \Theta \quad \dots\dots\dots (7-3)$$

$$(\mathcal{D}^2 - k^2) \Theta + \Omega^2 S^2 \Theta = -W \quad \dots\dots\dots (7-4)$$

Equations (7-3) and (7-4) together with the boundary conditions, for fixed  $k$  define an eigenvalue problem for  $R$ . The smallest of the eigenvalues give the marginal  $R$ . We may expect on physical grounds that  $W$  and  $\Theta$  are finite at  $k=0$ . The result we are going to derive now is valid even when  $T'_s(z)$  and  $\epsilon'(T_s)$  are not constant. Let us therefore generalize equations (7-3) and (7-4) to

$$(\mathcal{D}^2 - k^2)^2 W = k^2 R \Theta \quad \dots\dots\dots (7-5)$$

$$(\mathcal{D}^2 - k^2) \Theta + g(z) \Theta = W f(z) \quad \dots\dots\dots (7-6)$$

*Theorem:* If  $W$  is finite at  $k=0$  and the boundary conditions are those of fixed flux then  $R$  must be singular at  $k=0$  except for special choices of  $g$  (discussed later).

*Proof:* Combining equations (7-5) and (7-6),

$$(\mathcal{D}^2 - k^2)^3 W + g(z) (\mathcal{D}^2 - k^2)^2 W = k^2 R f(z) W \quad \dots\dots (7-7)$$

Let us assume if possible  $R \rightarrow R_0$  (as  $k \rightarrow 0$ ) and  $W = k^m \phi$  where  $\phi \rightarrow \phi_0$ . Here  $m \geq 0$  and  $R_0, \phi_0$  are finite. Then taking the limit  $k \rightarrow 0$  in equation (7-7)

$$\mathcal{D}^6 \phi_0 + g(z) \mathcal{D}^4 \phi_0 = 0 \quad \dots\dots\dots (7-8)$$

Let  $G = \mathcal{D}^4 \phi_0$ . Then from equation (7-5) the condition of fixed flux at the boundaries is

$$\mathcal{D} (\mathcal{D}^2 - k^2)^2 W = 0 \quad (z = 0, 1)$$

and going to the limit  $k \rightarrow 0$

$$\mathcal{D}^5 \phi_0 = 0 \quad (z = 0, 1) \quad \dots\dots\dots (7-9)$$

Equations (7-8) and (7-9) may be written as

$$\mathcal{D}^2 G + g(z) G = 0 \quad \dots\dots\dots (7-10)$$

$$\left. \begin{aligned} \mathcal{D} G(0) &= 0 \\ \mathcal{D} G(1) &= 0 \end{aligned} \right\} \quad \dots\dots\dots (7-11)$$



We assume  $g(z)$  is sufficiently well behaved so that the conditions of existence and uniqueness of solutions of equations of type (7-10) are satisfied.

Let  $G=G_1$  be the solution of equation (7-10) for

$$\left. \begin{aligned} G_1(0) &= 1 \\ DG_1(0) &= 0 \end{aligned} \right\} \dots \dots \dots (7-12)$$

If  $G_2$  is any other solution which satisfies  $DG_2(0)=0$  then  $G_2=CG_1$  for some constant  $C$ . Indeed, assume that this is not true. Let  $G_3=G_2/G_1(0)$ . ( $G_2(0) \neq 0$  since that would imply  $G_2 = CG_1$  with  $C=0$ ). Then  $G_3(0)=1$  and  $DG_3(0)=0$ . The uniqueness theorem then gives  $G_3 \equiv G_1$  or  $G_2(z)=G_2(0)G_1=(\text{constant})G_1$  contradicting our hypothesis.

Therefore all solutions of (7-10) satisfying  $DG(0)=0$  are given by  $G(z)=CG_1(z)$  for some constant  $C$ . (See Fig 4). For nontrivial solutions for  $G$  (which is essential for nontrivial  $W$ )  $C \neq 0$ . Then the second b. c. of (7-11) gives

$$DG_1(1) = 0 \quad \dots \dots \dots (7-13)$$

Equation (7-13) is in general not true for arbitrary functions  $g$ . Using (7-10), (7-13) can be put in the form

$$\int_0^1 g(z) G_1(z) dz = 0 \quad \dots \dots (7-14)$$

(Q.E.D.)

If  $g \equiv 0$  equation (7-14) is satisfied which explains the finite critical Rayleigh number in the fixed flux case at  $k=0$  (without heat sources) discussed in section 6. If  $g(z)=\omega^2$  (where  $\omega = \Omega s$ ) as in the present case  $G_1(z)=\cos \omega z \Rightarrow$

$$\begin{aligned}\int_0^1 g(z) G_1(z) dz &= \omega^2 \int_0^1 \cos \omega z dz \\ &= \omega \sin \omega\end{aligned}$$

Therefore

$$\int_0^1 g(z) G_1(z) dz = 0$$

if and only if  $\omega = n\pi$  ( $n=0, 1, 2, \dots$ )

Therefore when there are heat sources  $R(\text{marginal})$  at  $k=0$  can be finite only for discrete values of the Ed number.

This is true for a more general  $g$ . There exists only discrete values of the heating parameter(s) for which  $R(\text{marginal})$  at  $k=0$  is allowed to be finite. In the generic case  $R$  is singular at  $k=0$ .

At this stage we could stop and turn over the solution of the eigenvalue problem (7-3), (7-4) to the computer. However we will pursue the analytical investigation for a while and see what else we can learn about the general behaviour of the solution. *The distinguished limit:* When  $\omega=0$ ,  $k_c=0$ . But when  $\omega \neq 0$  from the above discussion we may expect that the  $R$  vs.  $k^2$  curve has a corner (See Fig 5) which gradually gets smoothed as  $\omega$  is increased.  $R$  as a function of  $k^2$  and  $\omega$  may be expected to look something like Fig 6. Clearly there is a discontinuity at the origin. If we approach the origin along some curve in the  $k^2$ - $\omega$  plane,  $R$  reaches some limit which in general depends on the path chosen. If we study these limits we may glean some information regarding the behaviour of  $R$  near the origin. This procedure is called "the distinguished limit".

Let the parametric representation of the curve be

$$k^2 = k_0^2 \varepsilon^2 \dots \dots \dots (7-15)$$

$$\omega^2 = \varepsilon^2 (\alpha_0 + \alpha_1 \varepsilon^2 + \alpha_2 \varepsilon^4 + \dots) \dots (7-16)$$

We further expand  $R, \Theta$  and  $W$  in the small parameter  $\epsilon^2$

$$R = R_0 + \epsilon^2 R_1 + \epsilon^4 R_2 + \dots \quad (7-17)$$

$$\Theta = \Theta_0 + \epsilon^2 \Theta_1 + \epsilon^4 \Theta_2 + \dots \quad (7-18)$$

$$W = \epsilon^2 (W_0 + \epsilon^2 W_1 + \dots) \quad (7-19)$$

Substituting (7-15) to (7-19) in (7-3) and (7-4) and equating coefficients of like powers of  $\epsilon$  we have

$$D^2 \Theta_0 = 0 \quad (7-20)$$

$$D^4 W_0 = \kappa_0^2 R_0 \Theta_0 \quad (7-21)$$

for the lowest order. Equation (7-20) together with the b. c.  $D\Theta_0=0$  at  $z=0,1 \Rightarrow \Theta_0=1$ . (Linear theory does not determine the absolute amplitudes so we are free to choose the normalizations.) Substituting this in (7-21)

$$W_0 = \kappa_0^2 R_0 P(z) \quad (7-22)$$

where  $P(z)$  satisfies

$$D^4 P = 1 \quad \dots \dots (7-23)$$

and the constants of integration are determined from the velocity boundary conditions.  $P(z)$  is evidently a fourth order polynomial. We will not write down the explicit form for  $P(z)$  in various cases but will refer the reader to [9] or [2].

To next order equation (7-4) gives

$$D^2 \Theta_1 - \kappa_0^2 \Theta_0 + \alpha_0 \Theta_0 = -W_0 \quad \dots (7-24)$$

Substituting the values for  $\Theta_0$  and  $W_0$ ,

$$D^2 \Theta_1 = \kappa_0^2 - \alpha_0 - \kappa_0^2 R_0 P(z) \quad \dots (7-25)$$

Integrating equation (7-25) from  $z=0$  to 1 and using the b. c.  $D\Theta_1=0$  at  $z=0$  and 1 we have the following consistency condition

$$\kappa_0^2 - \alpha_0 - \kappa_0^2 R_0 \int_0^1 P(z) dz = 0$$

or

$$R_0 = \left(1 - \frac{\alpha_0}{\kappa_0^2}\right) / \int_0^1 P(z) dz \quad \dots (7-26)$$

(Note:  $\int_0^1 p(z) dz \neq 0$ ) By suitably choosing  $\alpha_0 / k_0^2$  we see from (7-26) we can reach negative values of  $R_0$ , even  $-\infty$ . This suggests our guess as to the behaviour of  $R$  vs.  $k^2$  at small  $k$  and  $\omega$  shown in Fig 5 is quite incorrect. Instead the curves should look more like Fig 7. This is such a remarkable result we will verify it by an independent method. But first we need a variational principle.

## 8 VARIATIONAL METHOD

Let us generalize the  $\Theta$  boundary conditions to

$$\mathcal{D} \Theta = 0, \quad z = 0 \quad \dots \quad (8-1)$$

$$(\cos \gamma) \mathcal{D} \Theta + (\sin \gamma) \Theta = 0, \quad z = 1 \quad \dots \quad (8-2)$$

where  $\gamma$  is a parameter. By varying  $\gamma$  from 0 to  $\pi/2$  one can see the entire spectrum of b. c. from the fixed flux to the fixed temperature extremes. Also,

$$\left. \begin{aligned} W &= \mathcal{D} W = 0 \quad \text{at } z = 0, 1 \\ \text{or } W &= \mathcal{D}^2 W = 0 \quad \text{at } z = 0, 1 \end{aligned} \right\} \quad (8-3)$$

Multiplying (7-3) by  $W$  and (7-4) by  $\Theta$  and integrating from  $z=0$  to 1

$$\int_0^1 dz W (\mathcal{D}^2 - k^2) W = k^2 R \int_0^1 dz \Theta W \quad \dots \quad (8-4)$$

$$\int_0^1 dz \Theta (\mathcal{D}^2 - k^2) \Theta + \int_0^1 \omega^2 \Theta^2 dz = - \int_0^1 dz \Theta W \quad \dots \quad (8-5)$$

Eliminating  $\int_0^1 dz \Theta W$  from (8-4) and (8-5)

$$\int (D^2 W)^2 + 2k^2 (DW)^2 + k^4 W^2 + \{ \Theta (D^2 - k^2) \Theta + \omega^2 \Theta^2 \} k^2 R \dots (8-6)$$

(The boundary terms drop out by virtue of (8-3))

$$\begin{aligned} \int \Theta D^2 \Theta &= \int D(\Theta D \Theta) - (D\Theta)^2 \\ &= \Theta D\Theta \Big|_0^1 - \int (D\Theta)^2 \end{aligned}$$

Putting all that back in (8-6) we have

$$\frac{1}{k^2 R} = \frac{\int_0^1 [(D\Theta)^2 + (k^2 - \omega^2) \Theta^2] dz - [\Theta D\Theta]_0^1}{\int_0^1 [(D^2 W)^2 + 2k^2 (DW)^2 + k^4 W^2]} \dots (8-7)$$

In equation (8-7)  $\Theta$  and  $W$  are eigenfunctions of the eigenvalue problem for  $R$ . Define a functional

$$\Lambda = \frac{\int_0^1 [(D\Theta)^2 + (k^2 - \omega^2) \Theta^2] dz - [\Theta D\Theta]_0^1}{\int_0^1 [(D^2 W)^2 + 2k^2 (DW)^2 + k^4 W^2]} \dots (8-8)$$

where the only restriction on  $W$  and  $\Theta$  is that they satisfy the b. c. (8-1) to (8-3) and they are 'well behaved' functions.

It is proved in Appendix B if  $W$  and  $\Theta$  are eigenfunctions of the problem then

$$\delta \Lambda = 0 \dots (8-9)$$

Note however in the case  $\omega \neq 0$  (8-9) does not in general represent a global maximum or minimum. To see this let us restrict ourselves to the fixed flux b. c. If we take  $\Theta$  in the form of a sine wave then as  $\lambda \rightarrow 0$ ,  $\int (\nabla \Theta)^2 \rightarrow \infty$  while  $\int \Theta^2$  remains bounded (See Fig 8). Therefore  $\Lambda$  has no upper bound. Now take  $\Theta = C$ . Then for  $k < \omega$ ,  $\Lambda \rightarrow -\infty$  as  $C \rightarrow \pm \infty$  so that  $\Lambda$  has no lower bound.

We can still use this variational principle however since (8-9) says if we guess an eigenfunction which is close to the correct one our error in  $\Lambda$  will only be in the second or higher orders.

For the rest of this section we use the free b. c. Let us take as our trial function the exact solution for the fixed temperature problem with no heat sources.

$$W = \sin \pi z \quad \dots \dots \dots (8-10)$$

(See [4]) Substitute this in (6-4)

$$\nabla^2 \Theta + (\omega^2 - k^2) \Theta = - \sin \pi z \quad \dots (8-11)$$

and solve (8-11) to get the trial function for  $\Theta$ .

For  $\omega > k$  we have

$$\Theta = A \cos \alpha z + B \sin \alpha z + \frac{\sin \pi z}{\pi^2 - \alpha^2} \quad \dots (8-12)$$

where

$$\alpha = \sqrt{\omega^2 - k^2}$$

For  $\omega < k$  we have

$$\Theta = A e^{\beta z} + B e^{-\beta z} + \frac{\sin \pi z}{\pi^2 + \beta^2} \quad \dots \dots (8-13)$$

where  $\beta = \sqrt{k^2 - \omega^2}$

Here A and B are determined by the b. c. (8-1) and (8-2). If we substitute these trial functions in (8-8) and evaluate the necessary integrals, we have

*Solution 1: ( $k > \omega$ )*

$$\frac{1}{R} = \frac{k^2}{(\pi^2 + k^2)^2 (\pi^2 + \beta^2)} \left[ 1 + \frac{2\pi^2}{(\pi^2 + \beta^2) Q} \left\{ (1 + \cosh \beta) 2 \cos \gamma + \sin \gamma \frac{\sinh \beta}{\beta} \right\} \right]$$

where

$$\beta = \sqrt{k^2 - \omega^2}$$

$$Q = \sin \gamma \cosh \beta + \beta \cos \gamma \sinh \beta$$

*Solution 2: ( $k < \omega$ )*

$$\frac{1}{R} = \frac{k^2}{(k^2 + \pi^2)^2 (\pi^2 - \alpha^2)} \left[ 1 + \frac{2\pi^2}{(\pi^2 - \alpha^2) Q} \left\{ \cos \gamma (1 + \cos \alpha)^2 + \frac{\sin \alpha}{\alpha} \sin \gamma \right\} \right]$$



where

$$\alpha = \sqrt{\omega^2 - k^2}$$

$$Q = \sin^2 \cos \alpha - \alpha \cos^2 \sin \alpha$$

### LIMITING FORMS:

Case(i)

If we set  $\omega=0$  and  $\gamma=\pi/2$  (See (8-2)) solution 1 gives the following limiting forms for  $k \rightarrow 0$  and  $k \rightarrow \infty$ .

$$\frac{1}{R} \sim \frac{3k^2}{\pi^6} \quad (k \rightarrow 0) \quad \dots\dots\dots (8-14)$$

$$R \sim k^4 \quad (k \rightarrow \infty) \quad \dots\dots\dots (8-15)$$

Chandrasekhar gives the following exact solution for the case of fixed temperature at both boundaries and free b. c. for the velocity [4].

$$R = \frac{(\pi^2 + k^2)^3}{k^2} \quad \dots\dots\dots (8-16)$$

Therefore

$$\frac{1}{R} \sim \frac{k^2}{\pi^6} \quad (k \rightarrow 0) \quad \dots\dots\dots (8-17)$$

$$R \sim k^4 \quad (k \rightarrow \infty) \quad \dots\dots\dots (8-18)$$

Therefore we see the effect of keeping the flux fixed at the lower boundary instead of the temperature introduces a factor 3 on the right hand side of (8-17). Otherwise the two solutions have the same general behaviour. (Note: Our solution differs from Chandrasekhar's because we have kept the fixed flux b. c. at the lower boundary.)

*Case(ii)* If we set  $\omega=0$  and  $\gamma=0$  (fixed flux case with no heating) solution 1 gives in the limit  $k \rightarrow 0$ ,

$$\lim_{k \rightarrow 0} R = \frac{\pi^6}{8} \cong 120.1$$

We see the variational method not only captures the unique feature of the Rayleigh number becoming finite at  $k=0$  in the fixed flux case (see section 4) but gives an excellent approximation for  $R_0 = \lim_{k \rightarrow 0} R$ . The exact value is 120.

*Case(iii)* For the general b. c. (8-2) we have using solution 2

$$\frac{1}{Rk^2} \underset{k \rightarrow 0}{\cong} \frac{1}{\pi^4 (\pi^2 - \omega^2)} \left[ 1 + \frac{2\pi^2}{(\pi^2 - \omega^2) Q_0} \left\{ \cos \gamma (1 + \cos \omega)^2 + \frac{\sin \omega}{\omega} \sin \gamma \right\} \right]$$

$$Q_0 = \sin \gamma \cos \omega - \omega \cos \gamma \sin \omega$$

Therefore

$$R \sim \frac{\text{constant}(\omega)}{k^2} \quad (k \rightarrow 0)$$

... (8-19)

If we put  $k=\omega$  directly in (8-11) and proceed with the analysis, we get the same answer. Also note (8-20) gives  $R=0$  for the fixed flux case.

Using all this information we put together Fig 9. If we consider only small  $\omega$  then there is no qualitative change in the  $R$  vs.  $k^2$  curve for the fixed temperature case. As we shift the b. c. towards the fixed flux case, there is some value

$$\gamma = \gamma_c$$

at which  $\text{constant}(\omega)$  in (8-19) becomes 0 and  $R$  is finite at  $k=0$ . Below  $\gamma_c$  ( $\gamma < \gamma_c$ ),  $R \rightarrow -\infty$  as  $k \rightarrow 0$ . When  $\omega=0$ ,  $\gamma_c=0$ . For small but finite  $\omega$ ,  $\gamma_c > 0$ .

It should also be noted that for  $R < 0$  the principle of exchange of stabilities proved in Appendix A is no longer valid, as a result overstability is possible. That is, if  $R$  is above the marginality curve in Fig 7, the system is definitely unstable. However if  $R$  is below the marginality curve *and*  $R$  is negative then the system may still go unstable through growing oscillations or overstability.

This phenomenon of the marginal Rayleigh number going to minus infinity can be very roughly understood as follows. When there are no heat sources, the stability criterion can be understood from the following picture. Imagine a fluid element at the bottom is given a small upward velocity. The time scale of its motion is  $t \sim d^2/\nu$ . If the conductivity is large enough so it can get rid of its extra heat and come into thermal equilibrium with the surrounding cooler fluid within this time then the system is stable otherwise it is unstable [10]. When the fluid has internal heat sources however, a different kind of instability can occur. This depends on the answer to the following question: is the heat produced per unit time by the sources in a given parcel greater or less than that conducted away per unit time? If it is greater the parcel will keep getting hotter and start rising irrespective of what the viscous time scale is. I think we are seeing two distinct mechanisms in Fig 9. When the b. c. are close to the fixed temperature case conductive losses are relatively high and the onset of instability is controlled by viscosity just as in the case with no heat sources. As we approach the fixed flux case the isotherms diffuse into the

constant( $\omega$ ) can be positive, negative or zero depending on  $\omega$  and  $\gamma$ . In the fixed flux case ( $\gamma=0$ )

$$\frac{1}{R k^2} \underset{k \rightarrow 0}{\approx} \frac{1}{\pi^4 (\pi^2 - \omega^2)} \left[ 1 - \frac{2 \pi^2}{(\pi^2 - \omega^2) \omega \sin \omega} (1 + \cos \omega)^2 \right]$$

$$\rightarrow - \frac{8}{\pi^6} \frac{1}{\omega^2} \quad (as \ \omega \rightarrow 0)$$

In the case where the upper boundary is fixed temp. (lower boundary is always at fixed flux) we have ( $\gamma=\pi/2$ )

$$\frac{1}{R k^2} \underset{k \rightarrow 0}{\approx} \frac{1}{\pi^4 (\pi^2 - \omega^2)} \left[ 1 + \frac{2 \pi^2}{(\pi^2 - \omega^2) \cos \omega} (1 + \cos \omega)^2 \right]$$

The right hand expression is positive for  $\omega < \pi/2$ .

Note in the general case solutions 1 and 2 match at  $k=\omega$  and the common value is

$$\frac{1}{R} = \frac{\omega^2}{\pi^2 (\pi^2 + \omega^2)^2} (3 + 8 \cot^2 \gamma) \dots (8-20)$$

boundaries lowering the temperature gradients and therefore conductive losses till a "pinch off" is reached and the second kind of instability takes over. This kind of instability is insensitive to viscosity therefore it sends the marginality curve to minus infinity. To isolate this second kind of instability "in pure form", in the next section we do the linear theory in the absence of viscosity.

## 9 CONVECTIVE GROWTH RATES WITH NO VISCOSITY

We write (3-6) to (3-8) setting

$$\nu = 0$$

$$C(T_s) = 1, \quad C'(T_s) = 0$$

$$S'(T_s) = \lambda^2, \quad \frac{dT_s}{dz} = -\beta$$

$$\left\{ \begin{array}{l} \frac{\partial \bar{u}}{\partial t} = - \frac{\nabla \pi}{\rho_0} + g \alpha \theta \hat{z} \quad \dots (9-1) \\ \frac{\partial \theta}{\partial t} = \beta \omega + \kappa_0 \nabla^2 \theta + \epsilon_0 \lambda^2 \theta \quad \dots (9-2) \end{array} \right.$$

We adopt the scaling

$$\begin{aligned} x, y, z &\sim d, & t &\sim d^2 / \kappa_0 \\ u, v, w &\sim \kappa_0 / d, & T_s, \theta &\sim \beta d \\ \pi &\sim \rho_0 g d \end{aligned}$$

and take the z-component of the curl of curl of (9-1)

$$\frac{\partial}{\partial t} \nabla^2 \omega = \sigma R \bar{V}_H^2 \theta \quad \dots\dots (9-3)$$

$$\frac{\partial \theta}{\partial t} = \omega + \nabla^2 \theta + \omega^2 \theta \quad \dots (9-4)$$

where

$$\sigma R = \frac{g \alpha \beta d^4}{\kappa_0^2}$$

$$\omega^2 = \frac{\epsilon_0 d^2 s^2}{\kappa_0}$$

We look for solutions of (9-3) and (9-4) in the form

$$\begin{pmatrix} \omega \\ \theta \end{pmatrix} = e^{i(k_x x + k_y y) + p t} \begin{pmatrix} W \\ \Theta \end{pmatrix}$$

Then

$$p (D^2 - k^2) W = - \sigma k^2 R \quad (4) \quad \dots (9-5)$$

$$p (4) = W + (D^2 - k^2 + \omega^2) (4) \quad \dots (9-6)$$

with the b. c.

$$D(4) = 0, \quad (z = -1, +1) \quad \dots (9-7)$$

$$W = 0, \quad (z = -1, +1) \quad \dots (9-8)$$

(Note: We have less b. c. because (9-5) is of second order instead of fourth order.) It can readily be proved (the method is shown in Appendix A) that for  $\sigma R > 0$ ,  $p$  in the eigenvalue problem (9-5) to (9-8) is real. Eliminating  $\Theta$  between (9-5) and (9-6)

$$p (D^2 - k^2) (D^2 - k^2 + \omega^2 - p) W = \sigma k^2 R W \quad \dots (9-9)$$

We look for solutions of (9-9) in the form  $W \sim e^{\mu z}$ . Then,

$$p (\mu^2 - k^2) (\mu^2 - k^2 + \omega^2 - p) - \sigma R k^2 = 0 \quad \dots (9-10)$$

which has the four roots  $\mu = +m, -m, +n, -n$  where,

$$m = \left[ k^2 + \frac{1}{2} (p - \omega^2) + \sqrt{\left( \frac{\omega^2 - p}{2} \right)^2 + \frac{\sigma R k^2}{p}} \right]^{1/2}$$

$$n = \left[ k^2 + \frac{1}{2} (p - \omega^2) - \sqrt{\left( \frac{\omega^2 - p}{2} \right)^2 + \frac{\sigma R k^2}{p}} \right]^{1/2}$$

(If the quantity under the squareroot sign is negative we understand the solution with the positive imaginary part)

Since the system (9-5) to (9-8) have parity ( $z \rightarrow -z$ ) invariance there exists a basis consisting of even and odd solutions. Therefore the solutions of (9-5) and (9-6) are

$$(\text{Odd}) \quad \psi = A \sinh(mz) + B \sinh(nz) \dots (9-11-a)$$

$$(\text{Even}) \quad \psi = A \cosh(mz) + B \cosh(nz) \dots (9-11-b)$$

(Note: in this section  $z$  goes from  $-1$  to  $+1$ ) Let us first take the even solution.



(9-7) can be written as

$$D (D^2 - k^2) W = 0 \quad \dots \dots (9-12)$$

Substituting (9-11-b) in (9-8) and (9-12) we have

$$A \cosh m + B \cosh n = 0 \quad \dots \dots (9-13)$$

$$A m (m^2 - k^2) \sinh m + B n (n^2 - k^2) \sinh n = 0$$

$$\dots \dots (9-14)$$

which gives the solvability condition

$$n (n^2 - k^2) \sinh n \cosh m$$

$$- m (m^2 - k^2) \cosh n \sinh m = 0$$

$$\dots \dots (9-15)$$

with  $m$  and  $n$  expressed in terms of  $p$ , (9-15) determines the permissible values of  $p$ .

With the odd solution we get

$$n (n^2 - k^2) \sinh m \cosh n$$

$$- m (m^2 - k^2) \sinh n \cosh m = 0$$

$$\dots \dots (9-16)$$

*Limiting form (even):*

Let us put  $\omega=0$  and look for solutions in the form

$$\left. \begin{aligned} k &= k_0 \epsilon \\ p &= p_0 \epsilon^2 \end{aligned} \right\} \dots\dots\dots (9-17)$$

where  $\epsilon$  is a small parameter. Substituting in the expressions for  $m$  and  $n$  and keeping only lowest order terms in  $\epsilon$  we have

$$m = \left( \frac{k_0^2 R_0}{p_0} \right)^{1/4} \dots\dots\dots (9-18)$$

$$n = i \left( \frac{k_0^2 R_0}{p_0} \right)^{1/4} = i m \dots\dots (9-19)$$

Let us assume  $R/p_0$  to be positive. Substituting  $k=k_0\epsilon$  and (9-18), (9-19) in (9-15) and retaining only lowest order terms

$$m \left\{ \sin m \cosh m - \cos m \sinh m \right\} = 0$$

$\dots\dots (9-20)$

which has solutions

$$m = 0 \quad \dots \dots \dots (9-21)$$

&  $\tan m = \tanh m \quad \dots \dots \dots (9-22)$

(9-21) is incompatible with b. c. and the solutions of the transcendental equation (9-22) are  $m=m_l$ , ( $l=1, 2, \dots$ ) (see Fig 10)

Therefore

$$p_0 = \frac{\sigma R k_0^2}{m_l^4}$$

$$\Rightarrow \quad p \underset{k \rightarrow 0}{\approx} \frac{\sigma R}{m_l^4} k^2 \quad \dots \dots \dots (9-23)$$

The fastest growing mode is

$$p = \frac{\sigma R}{m_1^4} k^2$$

$$\approx \left(\frac{2}{3\pi}\right)^4 \sigma R k^2$$

$$\approx \frac{\sigma R}{5\pi^4} k^2$$

(if we approximate  $m_1$  by  $3\pi/2$ ) So we have a set of unstable solutions for  $R > 0$  and a set of stable modes for  $R < 0$ . Let us see how these results are changed when we put back the heat source.

With  $\omega$  finite let us do the expansion as follows

$$\left. \begin{aligned} k &= k_0 \varepsilon + \dots \\ p &= p_0 + \dots \end{aligned} \right\} \dots\dots\dots (9-25)$$

We then have, for  $p_0 > \omega^2$

$$m = (p_0 - \omega^2)^{1/2}, \quad n = 0$$

and for  $p_0 < \omega^2$

$$m = 0, \quad n = i(\omega^2 - p_0)^{1/2}$$

In the first case (9-15) gives

$$(p_0 - \omega^2)^{3/2} \sinh (p_0 - \omega^2)^{1/2} = 0$$

\dots\dots\dots (9-26)

$$\Rightarrow p_0 = \omega^2$$

In the latter case (9-15) gives

$$(\omega^2 - p_0)^{3/2} \sin(\omega^2 - p_0)^{1/2} = 0 \quad \dots\dots (9-28)$$

$$\Rightarrow (\omega^2 - p_0)^{1/2} = l\pi, \quad (l = 0, 1, 2, \dots)$$

$\dots\dots (9-29)$

Therefore the general solution is

$$p_0 = \omega^2 - l^2 \pi^2$$

(where  $l=0,1,2,\dots$ ) For  $\omega$  small only one mode is unstable viz.

$$p_0 = \omega^2$$

irrespective of what the Rayleigh number is. The situation is shown in Fig 11.

*Limiting form (odd):*

If  $\omega=0$  the only difference with the previous case is in (9-22) which now becomes

$$\tan m = - \tanh m$$

With the heat sources we do not get solutions for  $p$  that remain finite as  $k \rightarrow 0$ . We do not investigate this any further.

## 10 CALCULATION OF GAMMA (CRITICAL)

We write equations (7-3), (7-4) and b. c. (8-1), (8-2) in the following way

$$(\mathcal{D}^2 - k^2)^2 W = k^2 R \Theta \dots\dots\dots (10-1)$$

$$(\mathcal{D}^2 - k^2) \Theta + \omega^2 \Theta = -W \dots\dots (10-2)$$

$$\mathcal{D} \Theta (z=0) = 0 \dots\dots (10-3)$$

$$\left[ \mathcal{D} \Theta + \alpha \Theta \right]_{z=1} = 0 \dots\dots (10-4)$$

We want to find the critical value of  $\alpha$ ,  $\alpha = \alpha_c$  for which the Rayleigh number becomes finite at  $k=0$ .

Let  $k = \kappa \epsilon$  and let us expand  $R, \alpha, \Theta, W$  in asymptotic series in  $\epsilon$  ( $\omega$  is kept constant)

$$R = R_0 + \epsilon^2 R_1 + \epsilon^4 R_2 + \dots$$

$$\alpha = \alpha_0 + \epsilon^2 \alpha_1 + \epsilon^4 \alpha_2 + \dots$$

$$\Theta = \Theta_0 + \epsilon^2 \Theta_1 + \epsilon^4 \Theta_2 + \dots$$

$$W = \epsilon^2 (W_0 + \epsilon^2 W_1 + \dots)$$

Substituting in (10-1) and (10-2) we have to lowest order in  $\epsilon$ ,

$$D^4 W_0 = \kappa^2 R_0 \psi_0 \dots \dots (10-5)$$

$$D^2 \psi_0 + \omega^2 \psi_0 = 0 \dots \dots (10-6)$$

Equation (10-6)  $\Rightarrow$

$$\psi_0 = A \cos \omega z + B \sin \omega z$$

Equation (10-3) then gives  $B=0 \Rightarrow$

$$\psi_0 = A \cos \omega z \dots (10-7)$$

Equation (10-4) gives to the lowest order

$$\left[ D \psi_0 + \alpha_0 \psi_0 \right]_{z=1} = 0 \dots (10-8)$$

Using (10-7) and (10-8)

$$A (-\omega \sin \omega + \alpha_0 \cos \omega) = 0 \dots (10-9)$$

To obtain nontrivial solutions for  $\Theta_0$  we must have

$$\alpha_0 = \omega \tan \omega \dots\dots (10-10)$$

Let us go back to the variational calculation of  $R$  in section 8. Equation (8-19) gives

$$R \sim \frac{\text{constant}(\omega)}{k^2} \quad (k \rightarrow 0)$$

where

$$(\text{constant}(\omega))^{-1} = \frac{1}{\pi^4 (\pi^2 - \omega^2)} \left[ \frac{Q_0 + 2\pi^2 \left\{ \cos \gamma (1 + \cos \omega)^2 + \frac{\sin \omega}{\omega} \sin \gamma \right\}}{Q_0} \right]$$

Therefore  $\gamma_c$  corresponds to



$$Q_0 = 0$$

$$\text{or } \sin \gamma_c \cos \omega - \omega \cos \gamma_c \sin \omega = 0$$

$$\text{or } \tan \gamma_c = \omega \tan \omega \dots (10-11)$$

This is the same as (10-10) if one remembers, by definition  $\alpha = \tan \gamma$ .

Let us continue further to calculate  $R_0$ . Substituting  $\Theta_0 = \cos \omega z$  (we normalize to  $A=1$ ) in (10-5),

$$D^4 W_0 = K^2 R_0 \cos(\omega z)$$

Therefore

$$W_0 = K^2 R_0 \left[ \frac{\cos \omega z}{\omega^4} + A z^3 + B z^2 + C z + D \right]$$

$$W_0(0) = 0 \quad \Rightarrow \quad D = 0$$

The other three b. c. determines A, B and C. Note A, B and C depend only on  $\omega$

$$W_0 = K^2 R_0 \left[ \frac{\cos \omega z}{\omega^4} + A z^3 + B z^2 + C z \right] \quad \dots (10-13)$$

Equations (10-1) and (10-2) give to the next order

$$D^4 W_1 - 2 K^2 D^2 W_0 = K^2 (R_0 \psi_1 + R_1 \psi_0) \quad \dots (10-14)$$

$$D^2 \psi_1 - 2 K^2 \psi_0 + \omega^2 \psi_1 = - W_0 \quad \dots (10-15)$$

Using (10-7) and (10-13) in (10-15)

$$\begin{aligned} D^2 \psi_1 + \omega^2 \psi_1 &= K^2 \left\{ 2 \cos \omega z - R_0 \left( \frac{\cos \omega z}{\omega^4} + P(z) \right) \right\} \\ &= K^2 \left\{ \left( 2 - \frac{R_0}{\omega^4} \right) \cos \omega z - R_0 P(z) \right\} \\ &\quad \dots (10-16) \end{aligned}$$

where

$$P(z) = A z^3 + B z^2 + C z \quad \dots (10-17)$$

Let  $\Theta_1 = \kappa^2 f(z)$  be a particular solution of (10-16) where  $f$  depends on  $R$  and  $\omega$  but not  $\kappa$ . Then the general solution of (10-16) is

$$\Theta_1 = \kappa^2 (F \cos \omega z + G \sin \omega z + f(z)) \dots (10-18)$$

The b. c. (10-3) and (10-4) give

$$D \Theta_1 (z=0) = 0 \dots (10-19)$$

$$\left[ D \Theta_1 + \alpha_0 \Theta_1 + \alpha_1 \Theta_0 \right]_{z=1} = 0 \dots (10-20)$$

Equations (10-18) and (10-19)  $\Rightarrow$

$$G = - \frac{f'(0)}{\omega} \dots (10-21)$$

Equation (10-18), (10-7) and (10-20) gives

$$\begin{aligned} & \kappa^2 F (\alpha_0 \cos \omega - \omega \sin \omega) \\ & + G \kappa^2 (\alpha_0 \sin \omega + \omega \cos \omega) \\ & + \kappa^2 (\alpha_0 f(1) + f'(1)) + \alpha_1 \cos \omega = 0 \end{aligned}$$

Using (10-10) and (10-21)

$$-\frac{f'(0) \kappa^2}{\cos \omega} + \kappa^2 (\alpha_0 f(1) + f'(1)) + \alpha_1 \cos \omega = 0$$

This is a relation between  $R_0, \omega, \alpha_1$  and  $\kappa$ . (Note:  $f$  contains  $\omega$  and  $R_0$  as parameters.) We know  $R_0$  depends only on  $\omega$  and is independent of  $\alpha_1$  and  $\kappa$ . If we set  $\alpha_1=0$  in the above equation, both  $\alpha_1$  and  $\kappa$  drop out and we are left with an equation for determining  $R_0$ .

$$\omega \tan \omega f(1) + f'(1) = \frac{f'(0)}{\cos \omega} \quad \dots (10-22)$$

$f(z)$  is a solution of a forced oscillation problem with an anharmonic driving force. It can be expressed as a Fourier series with  $\omega$  as the fundamental frequency.

## 11 CONCLUSION

We have found, the presence of heat sources in the medium can give rise to an instability that may bring into question the validity of using the Schwarzschild's criterion as a test of convective stability. The model studied here is certainly oversimplified. In real stars the internal heat sources depend on temperature according to power laws with very large exponents. Also since we are finding instabilities with very large horizontal scale§ the infinite plane parallel model is no longer a valid one – we will have to take into account the spherical shape of the star in any serious model of the phenomenon. This work is nothing more than a preliminary investigation whose main conclusion is that the more realistic version of this problem is

worth investigating.

## ACKNOWLEDGEMENTS

The author would like to thank Edward Spiegel for his guidance and the 'summer student fellowship program in GFD' of the WHOI for making available a fellowship. Thanks are also due to Wilhelm Malkus, Claes Rooth and Paul Mathews for useful discussions.

## REFERENCES

- [1] J. Boussinesq, *Theorie Analytique de la Chaleur*, 2:172, Gauthier- Villars, Paris 1903
- [2] E.A. Spiegel, Convection on very large horizontal scales, GFD proceedings, 1981
- [3] E.A. Spiegel and G. Veronis, On the Boussinesq approximation for a compressible fluid, 1960, *Ap.J.*, 131:442
- [4] S. Chandrasekhar, *Hydrodynamic and hydromagnetic stability*, Ox. Univ. press., 1961
- [5] Lord Rayleigh, 1916, On convective currents in a horizontal layer of fluid when the higher temperature is on the underside., *Phil. Mag.*, 32(6) :529-546
- [6] Henry Som<sup>t</sup>mel, 1947, Theory of convection cells, *Annals N.Y. academy of sciences*, 48:715
- [7] H. Jeffreys, 1926, The stability of a layer heated from below, *Phil. Mag.*, 2:833-844
- [8] Sparrow E.M., Goldstein, R.J., and Jonsson, V.H., 1964, Thermal instability in a horizontal fluid layer: effect of boundary conditions and nonlinear temperature profile, *JFM*, 18:513-528
- [9] Chapman C.J., Proctor M.R.E., 1980, *JFM*, 101:759-782
- [10] Levadowsky, M., Childress, S., Spiegel, E.A. and Hutner, S.H., 1975, A mathematical model for pattern formation in swimming microorganisms, *J. Protozool.*, 22:296-306
- [11] Ledoux P., *Stellar stability*, *Handbuch der Physik*, 51:605
- [12] Schwarzschild M., *Structure and evolution of the stars*, Dover 1965
- [13] Eddington A.S., *The Internal Constitution of the Stars*
- [14] Defouw, R.J., 1970a., *Ap.J.*, 160:659

[15] Roberts, P.H., 1967c., JFM, 30:33 [16] Hurle, D.T.J., Jakeman, E., Pike, E.R., 1967, On the solution of the Benard problem with boundaries of finite conductivity., Proc.Roy.Soc.A, 296:469-475

## APPENDIX A

We will prove the eigenvalues  $p$  of the following equations subject to certain b.c. are always real.

$$(D^2 - k^2)(D^2 - k^2 - p)W = k^2 R \quad (4) \quad \dots (A-1)$$

$$(D^2 - k^2 + \omega^2 - \sigma p) \quad (4) = -W \quad \dots (A-2)$$

Let  $G = (D^2 - k^2)W$  &  $F = (D^2 - k^2 - p)G$

Then  $F = k^2 R \quad \dots (A-3)$

and we have the b.c.

$$\left. \begin{array}{l} F = 0 \quad (\text{fixed temp.}) \\ \text{or } DF = 0 \quad (\text{fixed flux}) \end{array} \right\} \quad \dots (A-4)$$

For the velocity b.c.

$$W = 0 \quad \dots (A-5)$$

$$\left. \begin{array}{l} DW = 0 \quad (\text{rigid}) \\ \text{or } D^2 W = 0 \quad (\text{free}) \end{array} \right\} \quad \dots (A-6)$$

Using (A-3) in (A-2)

$$(D^2 - k^2 + \omega^2 - \sigma p)F = -k^2 R W \quad \dots (A-7)$$

$$\Rightarrow \int F^* (D^2 - k^2 + \omega^2 - \sigma p) F = -k^2 R \int W F^* \quad \dots (A-8)$$

$$\int W F^* = \int W (D^2 - k^2 - p^*) G^*$$

$$\int W D^2 G^* = \int D^2 W G^* \quad (\text{integrating by parts})$$

$$\begin{aligned} \therefore \int W F^* &= \int G^* (D^2 - k^2 - p^*) W \\ &= \int G^* G - p^* \int W G^* \end{aligned}$$

$$\begin{aligned} \int W G^* &= \int W (D^2 - k^2) W^* \\ &= - \int |DW|^2 + k^2 |W|^2 \quad (\text{integrating by parts}) \end{aligned}$$

$$\therefore \int W F^* = \int |G|^2 + p^* |DW|^2 + p^* k^2 |W|^2 \quad \dots (A-9)$$

$$\int F^* D^2 F = - \int |DF|^2 \quad \dots \dots \dots (A-10)$$

Substituting (A-9) & (A-10) in (A-8)

$$\begin{aligned} &\int \{ |DF|^2 + (k^2 + \sigma p - \omega^2) |F|^2 \} \\ &= k^2 R \int \{ |G|^2 + p^* |DW|^2 + p^* k^2 |W|^2 \} \\ &\quad \dots (A-11) \end{aligned}$$

Taking imaginary part of (A-11)

$$(\text{Imp}) \left\{ \int \sigma |F|^2 + k^2 R |DW|^2 + k^4 R |W|^2 \right\} = 0$$

For  $R \geq 0$  and  $W, \textcircled{4} \neq 0$  we must have  $\text{Im } p = 0$ .

## APPENDIX B

$$(D^2 - k^2)^2 W = k^2 R \Theta \quad \dots \dots \dots (B-1)$$

$$(D^2 - k^2) \Theta + \chi^2 \Theta = -W \quad \dots \dots \dots (B-2)$$

B. c.

$$D \Theta + \alpha_0 \Theta = 0, \quad (z=0) \quad \dots \dots \dots (B-3)$$

$$D \Theta + \alpha_1 \Theta = 0, \quad (z=1) \quad \dots \dots \dots (B-4)$$

$$W = 0, \quad (z=0,1) \quad \dots \dots \dots (B-5)$$

$$\left. \begin{array}{l} \text{either } DW = 0 \\ \text{or } D^2 W = 0 \end{array} \right\} (z=0,1) \quad \dots \dots \dots (B-6)$$

$$\Lambda \equiv \frac{\int_0^1 [(D\Theta)^2 + (k^2 - \chi^2) \Theta^2] - [\Theta D\Theta]_0^1}{\int_0^1 [(D^2 W)^2 + 2k^2 (DW)^2 + k^4 W^2]}$$

Let

$$W \rightarrow W + \delta W$$

$$\Theta \rightarrow \Theta + \delta \Theta$$

$$\text{If } \Lambda = I_1 / I_2,$$

$$\delta \Lambda = \frac{\delta I_1}{I_2} - \frac{I_1}{I_2^2} \delta I_2$$

After integration by parts

$$\delta I_1 = [D\Theta \delta \Theta - \Theta D \delta \Theta]_0^1 - 2 \int \{D^2 \Theta + (\chi^2 - k^2) \Theta\} \delta \Theta$$



At any boundary

$$\begin{aligned} D\psi \delta\psi - \psi D\delta\psi &= -\alpha_i \psi \delta\psi - \psi \delta(-\alpha_i \psi) \\ &= 0 \quad (\alpha_i = \alpha_0 \text{ or } \alpha_1) \end{aligned}$$

$$\therefore \delta I_1 = -2 \int \{ D^2 \psi + (\chi^2 - k^2) \psi \} \delta\psi$$

$$\delta I_2 = 2 \int (D^2 - k^2)^2 \psi \delta\psi$$

(after repeated integration by parts)

$$= 2 k^2 R \int \psi \delta\psi = 2 \frac{I_2}{I_1} \int \psi \delta\psi$$

$$\therefore \delta \Lambda = \frac{\delta I_1}{I_2} - \frac{I_1}{I_2^2} \delta I_2$$

$$= -\frac{2}{I_2} \left[ \int \{ D^2 \psi + (\chi^2 - k^2) \psi \} \delta\psi + \int \psi \delta\psi \right]$$

... (B-7)

From (B-2)

$$\int \psi \delta\psi = [D\psi \delta\psi - \psi D\delta\psi]_0^1 - \int \{ D^2 \psi + (\chi^2 - k^2) \psi \} \delta\psi$$

Boundary term has been shown = 0

$\therefore$  substituting in (B-7) gives

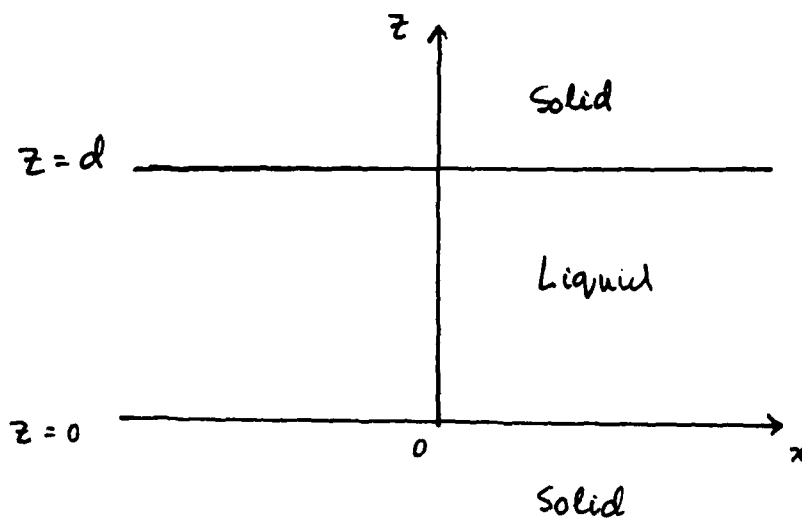
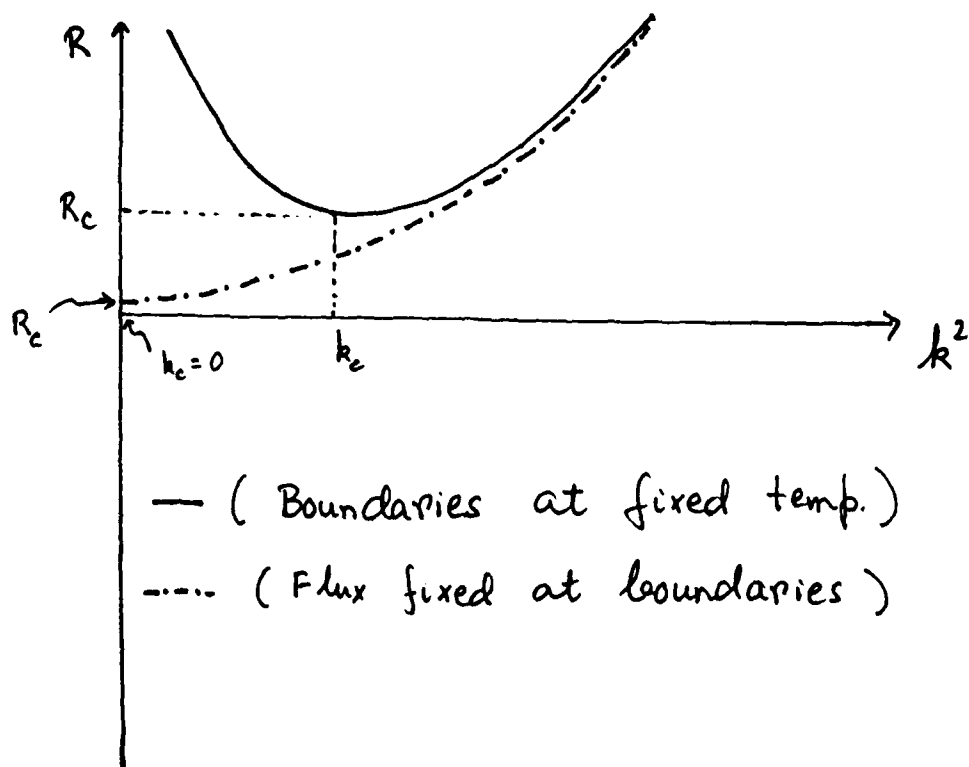
$$\delta \Lambda = 0.$$

TABLE 1 (FIXED TEMPERATURE)

Boundary condition	$R_c$
Free - Free	657.5
Free - Rigid	1107.7
Rigid - Rigid	1707.8

TABLE 2 (FIXED FLUX)

Boundary condition	$R_c$
Free - Free	120
Free - Rigid	320
Rigid - Rigid	720

FIG 1FIG 2 & 3

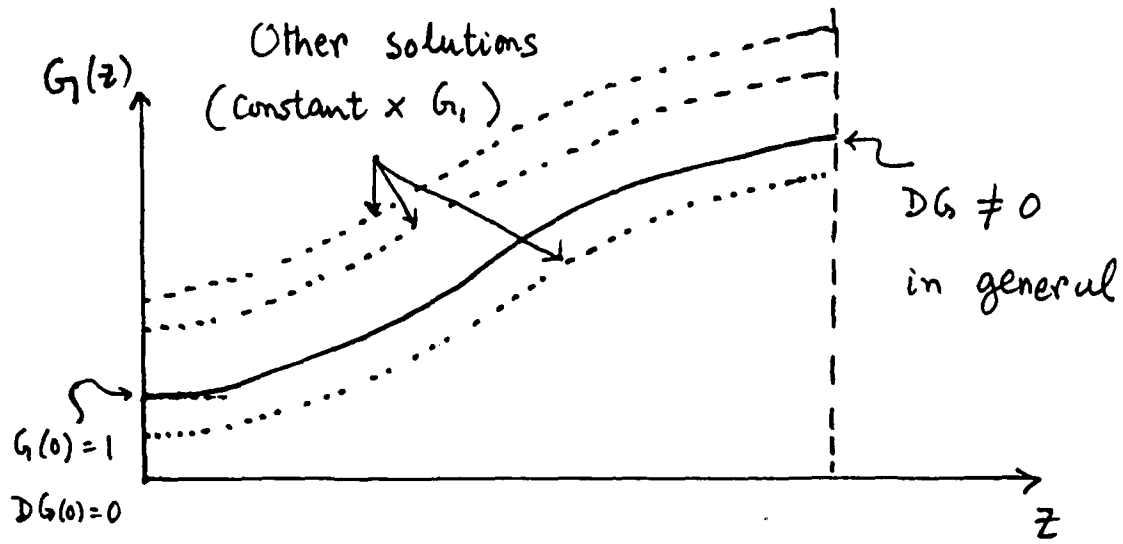


FIG 4

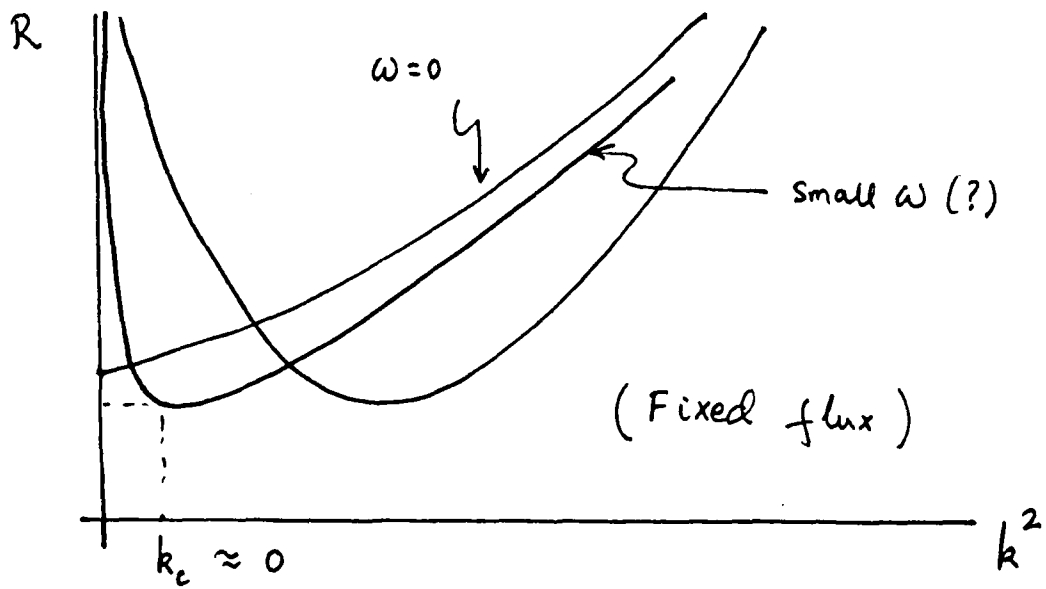


FIG 5

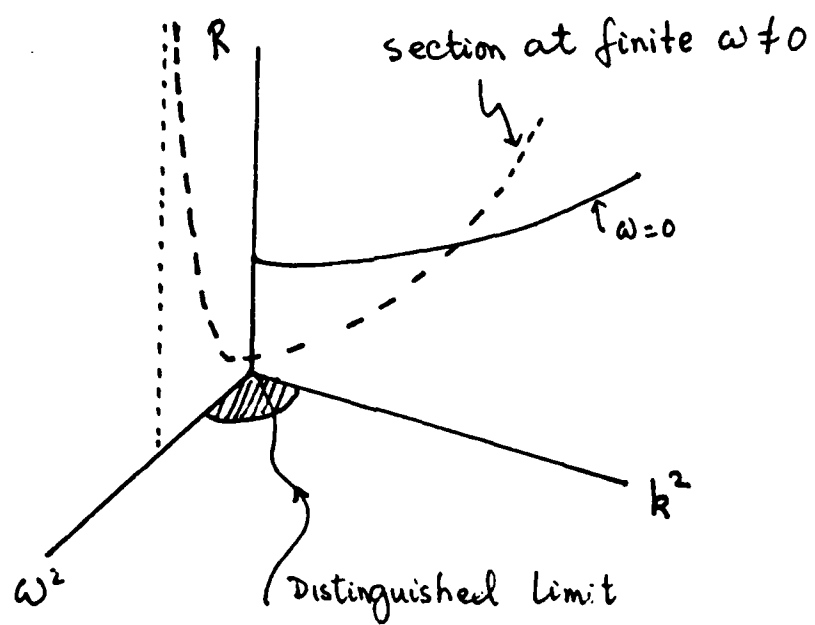


FIG 6

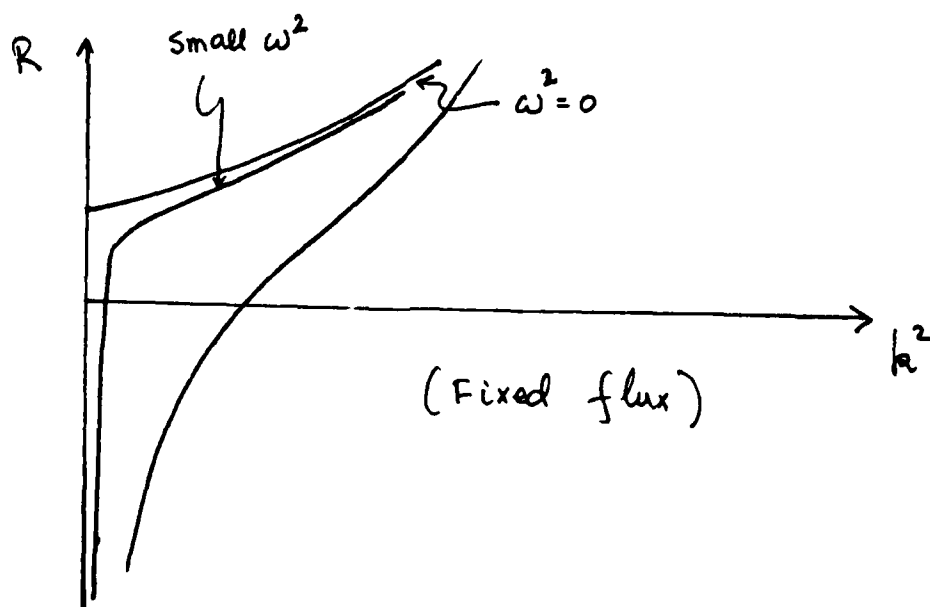


FIG 7

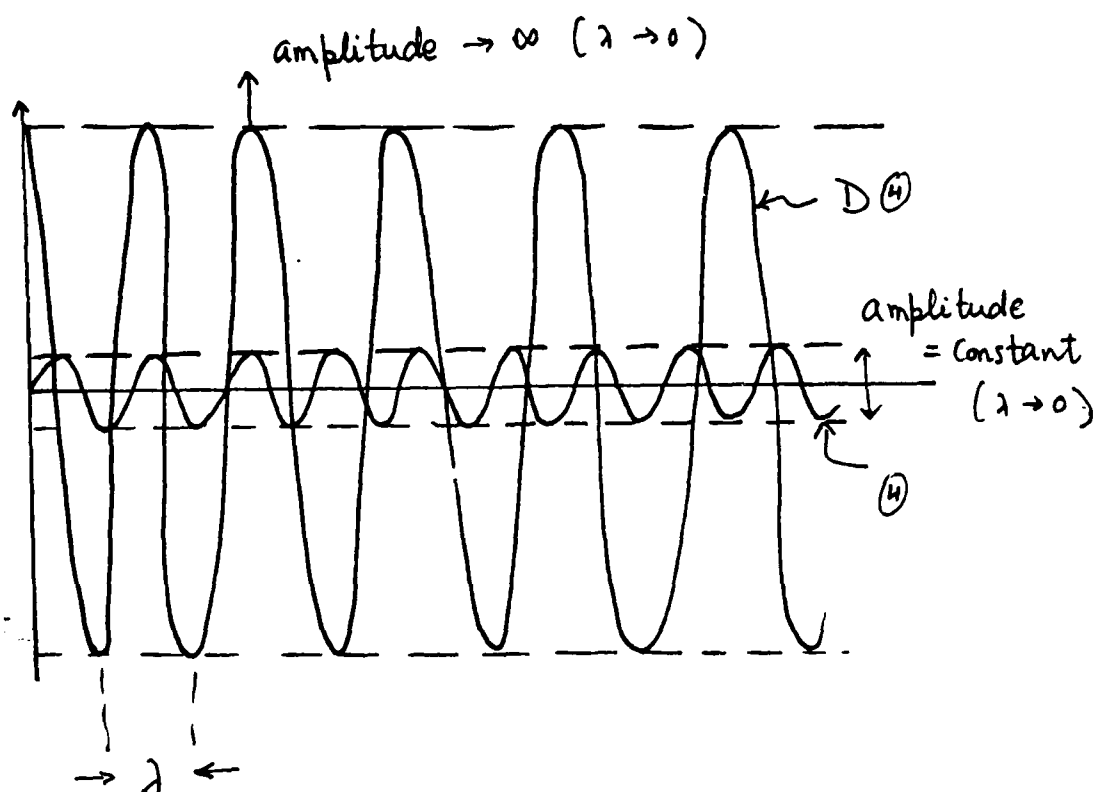


Fig 8

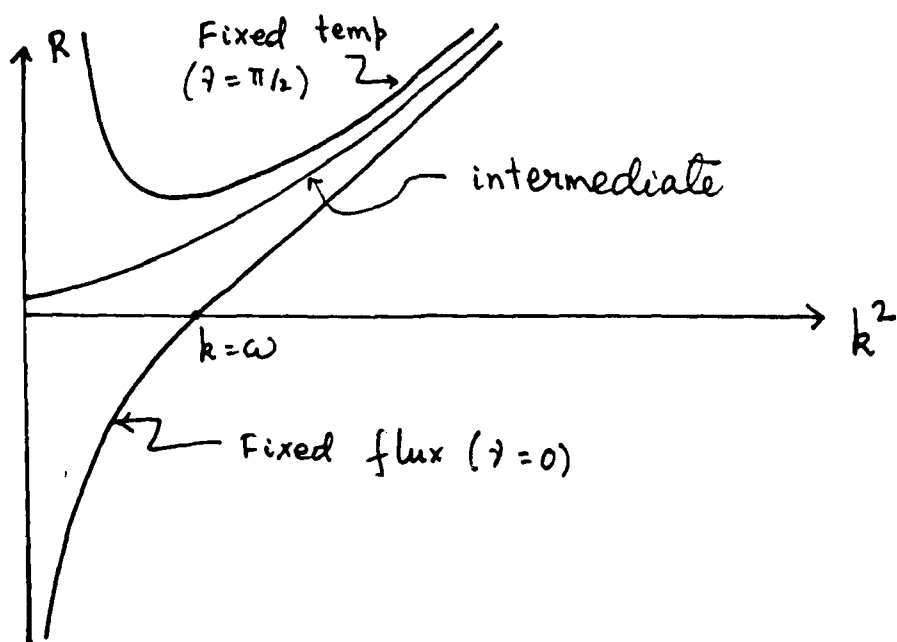


Fig 9

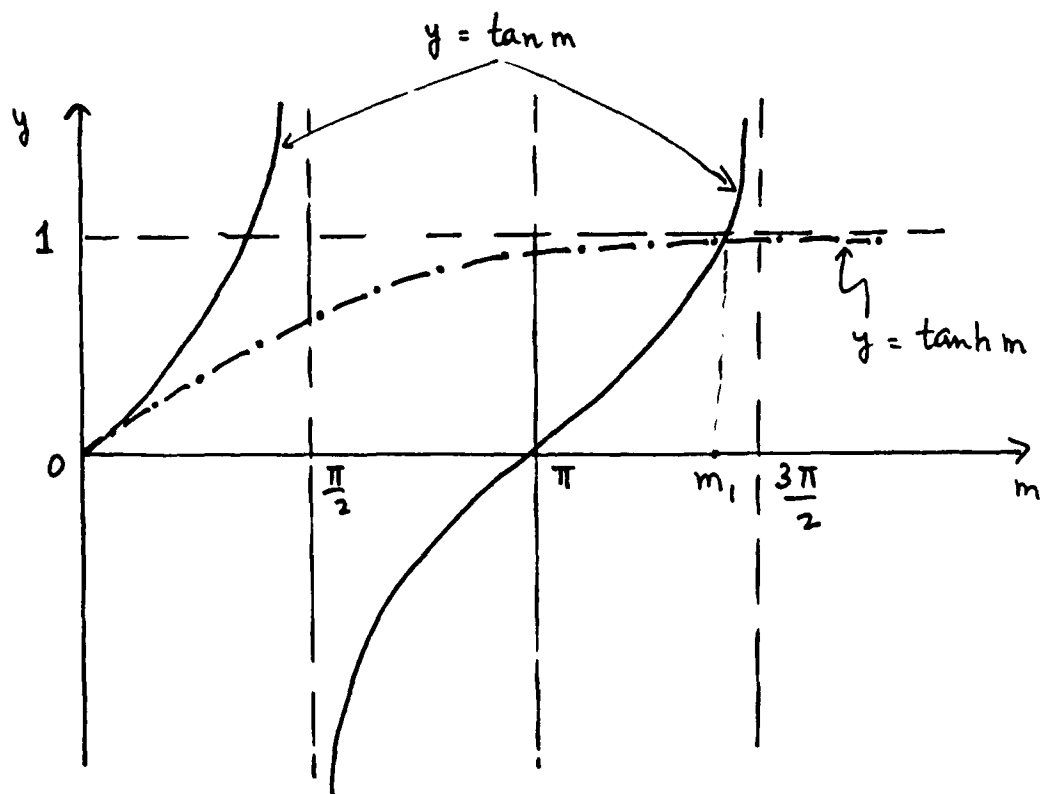


FIG 10

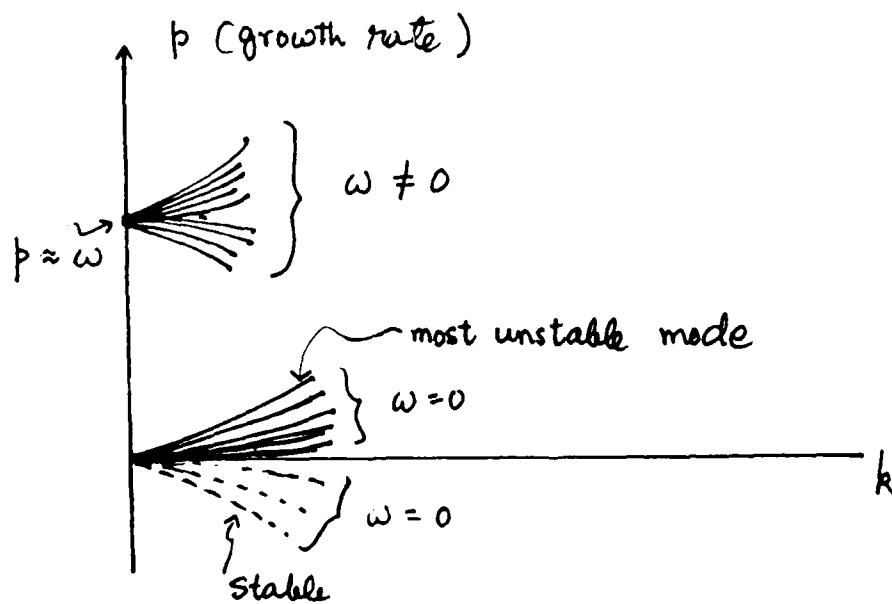


FIG 11

## A Two-Layer Wind-Driven Ocean With Recirculation

Richard A. Jarvis

In a two-layer, rectangular ocean model where the lower layer does not become exposed through outcropping, the lower layer is usually assumed to be motionless. Young & Rhines (1982) showed that conservation of potential vorticity can lead to regions being cut off from control by eastern boundary conditions and therefore able to allow motion in the lower layer. The quasi-geostrophic model of Young & Rhines (1982) is extended to the shallow-water case, thereby allowing for the possibility of surfacing of the lower layer, with the western boundary considered fundamental in the determination of flow in the interior, as shown by Ierley & Young (1983). We formulate the problem for the interior and the western boundary in terms of the two layer depths and, by treating the solution as a perturbation to the  $1\frac{1}{2}$ -layer solution, we reduce the problem to a set of quadratures of known functions and arbitrary functions of latitude  $y$ , which can be solved much more simply than the full partial differential equations.

### 1. Introduction

The separation of the Gulf Stream has long been of interest to oceanographers, with two different theoretical approaches being taken. The first school of thought treats the separation mechanism as being essentially barotropic, but this is not the approach taken here; we are taking the view of Parsons (1969), and later Veronis (1973), that separation is associated with the surfacing of the thermocline, with cold deep water outcropping to the north-west and thereby diverting the Gulf Stream. This is consistent with the observation of cold water north of the warm, separated Gulf Stream.

The simplest model that one can employ to investigate this mechanism is two-layer, and the Parsons-Veronis model treats the lower layer as being quiescent, even when exposed. This is partially based on the idea that the lower layer is not directly driven by wind stresses prior to outcropping. Kamenkovich & Reznick (1972) studied the effects of wind driving upon the lower layer once outcropping has occurred, finding the original Parsons-Veronis model to be robust to the inclusion of direct wind forcing. Rhines & Young (1982) suggested a mechanism whereby motion in the lower layer can occur in the absence of direct wind forcing and developed a quasi-geostrophic model to describe it. The dynamical balance proposed was between the interfacial driving of the lower layer by the upper layer motion and some dissipation mechanism in the lower layer, such as bottom friction. This can occur only in regions 'cut off' from the influence of the eastern boundary. Any fluid



column that may be moved to the eastern boundary in such a manner as to conserve its potential vorticity must have originated from a region of no flow. Young & Rhines (1982), and later Ierley & Young (1983), extended the quasi-geostrophic model to wind forcings for which a western boundary layer exists. It is our intention to extend the Rhines-Young model to a situation in which outcropping may occur by using the shallow-water equations. The ultimate aim is to apply the model presented here to the case of a separated boundary layer.

In the following note, we shall begin in §2 by formulating the equations which govern the system. The ocean is modelled as rectangular and two-layered, with an anticyclonic cosine zonal wind stress. There is an interfacial drag between the layers and ultimately the dissipation mechanism is bottom friction. In §3, we determine the conditions under which a region of the lower layer may become isolated from the eastern boundary conditions and in §4 discuss the nature of any possible lower layer recirculation within that cut off region. Taking the main result of Ierley & Young (1983) as a guide, namely that the western boundary layer is instrumental in determining the lower layer flow, we develop western boundary layer equations in terms of the two layer depths in §5. These equations are nonlinear, partial differential equations which in general require a numerical solution. In §6, we describe how by perturbing the solution about the  $1\frac{1}{2}$ -layer model of Parsons (1969), we can linearise the system and solve for the perturbation layer depths in terms of known integrals and arbitrary functions of latitude  $y$ .

## 2. Shallow-water equations

The work presented here is based on a two-layer, shallow-water model. We are considering a steady ocean, driven by an anticyclonic zonal wind stress

$$\tau^x = -W \cos\left(\frac{\pi y}{L}\right), \quad (2.1)$$

with dissipation through interfacial and bottom friction.  $L$  is the latitudinal extent of the basin and so  $\text{curl } \tau = 0$  at the northern and southern boundaries of the basin. Ekman layers at the surface, at the interface between the layers, and at the bottom are incorporated into one or other of the upper and lower layers, as suitable; since the properties of each layer are independent of depth, we integrate over the layer depths to obtain the depth-averaged shallow-water equations

$$-fv_1 = -gh_x + \frac{\tau^x}{h_1} - \frac{\rho_2}{\rho_1} \frac{R}{h_1} (u_1 - u_2) \quad (2.2a)$$

$$fu_1 = -gh_y - \frac{\rho_2}{\rho_1} \frac{R}{h_1} (v_1 - v_2) \quad (2.2b)$$

$$-fv_2 = -g \frac{\rho_1}{\rho_2} h_x - g \frac{\Delta \rho}{\rho_2} h_{1x} - \frac{R}{h_2} (u_2 - u_1) - \frac{K}{h_2} u_2 \quad (2.3a)$$

$$fu_2 = -g \frac{\rho_1}{\rho_2} h_y - g \frac{\Delta \rho}{\rho_2} h_{2y} - \frac{R}{h_2} (v_2 - v_1) - \frac{K}{h_2} v_2. \quad (2.3b)$$

$\mathbf{v}_1 = (u_1, v_1)$  and  $\mathbf{v}_2 = (u_2, v_2)$  are the velocities of the upper layer, which has depth  $h_1$ , and the lower layer, which has depth  $h_2$ , respectively. The total depth  $h$  is given by

$$h = h_1 + h_2. \quad (2.4)$$

Interfacial and bottom friction are linearly related to the velocity difference and the lower layer velocity, with coefficients  $R$  and  $K$  respectively ( $R/fh, K/fh \ll 1$ ). The upper layer has density  $\rho_1$  and the lower layer density  $\rho_2$ , the difference being  $\Delta \rho = \rho_2 - \rho_1 > 0$ . The Coriolis parameter is  $f = f_0 + \beta y$ , where  $\beta$  is a constant and  $y$  the meridional distance north from the southern boundary of the basin. Typically a basin corresponding to the North Atlantic subtropical gyre extends from  $15^\circ \text{N}$  to  $45^\circ \text{S}$ , and so the north-south extent  $L$  of the basin is about 3200 km. The east-west extent is taken to be 5000 km.

In conjunction with the shallow-water equations, we have incompressibility

$$\nabla \cdot (h_1 \mathbf{v}_1) = 0 \quad (2.5a)$$

$$\nabla \cdot (h_2 \mathbf{v}_2) = 0, \quad (2.5b)$$

and application of this in the lower layer, combined with (2.3a,b), gives us

$$h_2 \mathbf{v}_2 \cdot \nabla \left( \frac{f}{h_2} \right) = -R \hat{\mathbf{k}} \cdot \left( \text{curl} \left( \frac{\mathbf{v}_2}{h_2} \right) - \text{curl} \left( \frac{\mathbf{v}_1}{h_2} \right) \right) - K \hat{\mathbf{k}} \cdot \text{curl} \left( \frac{\mathbf{v}_2}{h_2} \right). \quad (2.6)$$

The frictional terms are very small in the interior of the basin, dissipation becoming important only in regions of strong flow, such as the western boundary layer, and so, defining a lower layer potential vorticity

$$q_2 = \frac{f}{h_2}, \quad (2.7)$$

with relative vorticity being neglected, we obtain for the interior

$$h_2 \mathbf{v}_2 \cdot \nabla q_2 = 0. \quad (2.8)$$

If we further define a lower layer transport streamfunction  $\psi_2$  by  $h_2 \mathbf{v}_2 = \text{curl } \hat{\mathbf{k}} \psi_2$ , we can rewrite (2.8) as

$$J(\psi_2, q_2) = 0, \quad (2.9)$$

which implies that  $\psi_2$  and  $q_2$  are functionally related in the interior. This is an important consideration when discussing the existence and character of recirculation in the lower layer, as we shall see in §3.

In passing, it is worth noting that the usual Sverdrup balance applies in the interior for this shallow water system. Taking the divergence of (2.2a) minus (2.2b), we obtain

$$\beta \left( h_1 v_1 + \frac{\rho_2}{\rho_1} h_2 v_2 \right) = \hat{\mathbf{k}} \cdot \text{curl } \tau - \frac{\rho_2}{\rho_1} K \hat{\mathbf{k}} \cdot \text{curl } \mathbf{v}_2, \quad (2.10)$$

which in the interior reduces to

$$\beta V = \hat{\mathbf{k}} \cdot \text{curl } \tau, \quad (2.11)$$

where  $V = h_1 v_1 + \frac{\rho_2}{\rho_1} h_2 v_2$  is the total north-south transport.

We shall now consider the implications of the functional relationship for the  $1\frac{1}{2}$ -layer model as described by Parsons (1969), and how we can allow the possibility of lower layer motion (without requiring the lower layer to surface and therefore be directly driven by the wind stress, as studied by Kamenkovich & Reznick 1972).

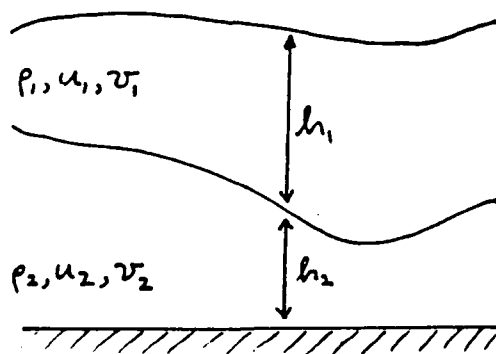


Figure 1. A vertical section showing the two-layer structure of the model.

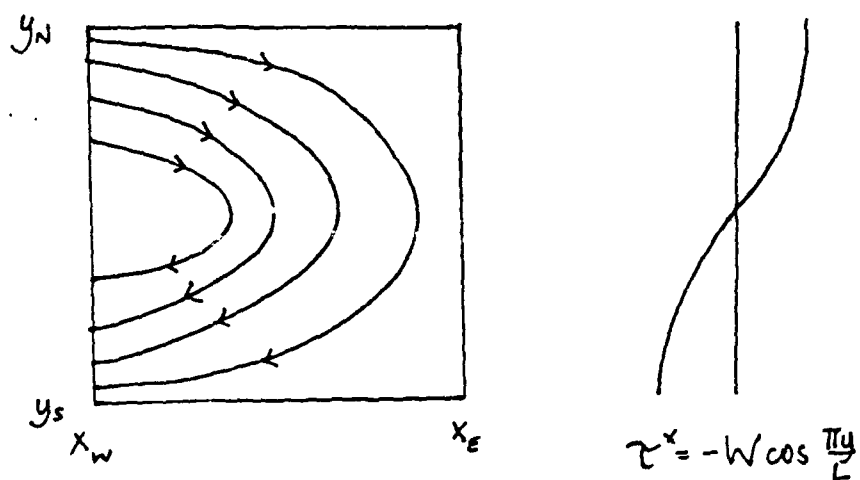


Figure 2. The Sverdrup transport induced by the anticyclonic zonal wind stress  $\tau^x = -W \cos(\pi y/L)$ .

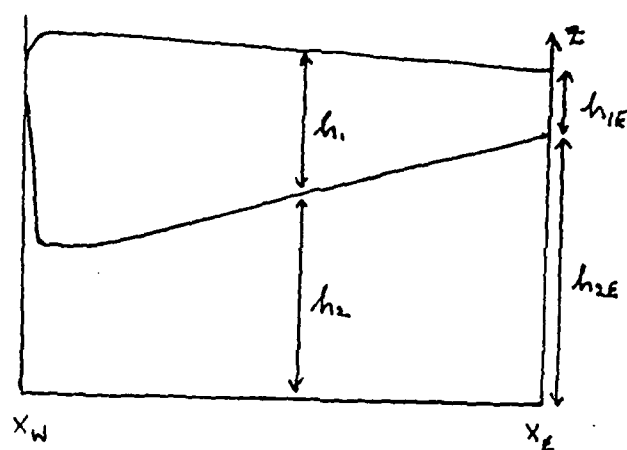


Figure 3. A vertical section of the reduced gravity solution of Parsons (1969) for  $Q < 0$ , showing the large layer depth gradients close to the western boundary.

### 3. The unblocked region

Parsons (1969), in his simple, yet effective, model of the separation of the Gulf Stream, treated a two-layer ocean with the lower layer motionless. This can be justified as follows: since the streamfunction  $\psi_2$  and the potential vorticity  $q_2$  are functionally related, contours of  $q_2$  are contours of  $\psi_2$ . However, on the eastern boundary,  $\psi_2 = 0$  and so if a particular contour of  $q_2$  meets the eastern boundary,  $\psi_2 = 0$  all along that contour. The contours of constant  $q_2$  can be viewed as characteristics, propagating the information that there is no lower layer flow from the eastern boundary. This is known as 'blocking'. The possibility exists, however, that there is a region of the basin isolated from the eastern boundary in the sense that it is inaccessible to characteristics originating at the eastern boundary. This isolated region is therefore 'unblocked'. Within the unblocked region, the possibility of lower layer flow exists, which is physically related to transients providing a continual mechanism for the transfer of horizontal momentum from the wind-stress driving to the lower layer through the propagation of Rossby waves. This can be modelled as a steady state in which interfacial frictional driving of the lower layer by the upper layer is balanced by dissipation through bottom drag, as suggested by Young & Rhines (1982) in their development of the equivalent quasi-geostrophic model.

To determine the existence and extent of the unblocked region, let us first consider there to be no motion in the lower layer implying that, in the interior, the reduced gravity model applies. The upper layer depth  $h_1$  is given by

$$h_1^2 = h_{1E}^2 - \frac{\rho_2}{\Delta\rho} \frac{2}{g} \left( \tau^x + \frac{f}{\beta} \hat{\mathbf{k}} \cdot \text{curl } \tau \right) (x_E - x), \quad (3.1)$$

where  $h_{1E}$  is the upper layer depth at the eastern boundary.  $h_{1E}$  is independent of  $y$  to satisfy the condition of no normal flux at the eastern boundary. Let us define the function  $Q$  to be

$$Q(y) = \tau^x + \frac{f}{\beta} \hat{\mathbf{k}} \cdot \text{curl } \tau, \quad (3.2)$$

which is proportional to  $\hat{\mathbf{k}} \cdot \text{curl } (\tau/f)$  and is negative except for a small region in the north of the basin. If we further define  $y^*$  to be the latitude at which  $Q(y) = 0$  then, for  $y < y^*$ , (3.1) implies a shallowing of the lower layer away from the eastern boundary, as the hydrostatic pressure balance in the lower layer relates the two layer depths through

$$h_2 - h_{2E} = -\frac{\rho_1}{\rho_2} (h_1 - h_{1E}). \quad (3.3)$$

Since  $q_2 = f/h_2$ , a column of fluid displaced westwards must also be displaced southwards if it is to conserve its potential vorticity as  $h_2$  decreases. This implies that the characteristics, or contours of  $q_2$ , must run from the south-west to the north-east of the basin. Similarly, for  $y > y^*$ , a column of fluid displaced westward must also be displaced *northwards*. This suggests a region on the western side of the basin, around the  $Q = 0$  line, which is not accessible to characteristics originating from the eastern boundary. This is the region in which lower layer motion will occur and it is bounded by the characteristic corresponding to the potential vorticity  $q_2 = f^*/h_{2E}$ , where  $f^*$  is the planetary vorticity at  $y = y^*$  and  $h_{2E}$  the upper layer depth at the eastern boundary. If two possible values of  $y^*$  exist, the correct choice is the one at which  $Q'(y^*) > 0$ .

Figure 5 shows the position and extent of the unblocked region for differing values of  $h_{1E}$ ,  $h_{2E}$  and  $W$ , the wind strength. In both cases, the density difference  $\Delta\rho$  between the layers is  $10^{-3} \text{ g cm}^{-3}$  and the calculations are for the basin described in §2. Figure 5(b) suggests that there is a minimum value  $W = W_{\text{crit}}$  of the wind stress amplitude for which recirculation can occur. This is straightforward to determine: if we combine (3.1) and (3.3), we obtain an expression for the characteristic corresponding to potential vorticity  $q_2^* = f^*/h_{2E}$ ,

$$x = X(y; q_2^*) = x_E + g \frac{\Delta\rho}{\rho_1} \frac{h_{2E}}{2Q(y)} \left(1 - \frac{f}{f^*}\right) \left(2h_{1E} + \frac{\rho_2}{\rho_1} h_{2E} \left(1 - \frac{f}{f^*}\right)\right). \quad (3.4)$$

Taking the limit  $y \rightarrow y^*$ , the unblocked region penetrates eastward to

$$X(y^*; q_2^*) = x_E - g \frac{\Delta\rho}{\rho_1} \frac{\beta h_{1E} h_{2E}}{f^* Q'(y^*)} \quad (3.5)$$

and so, for  $X(y^*, q_2^*) > x_W$ , the longitude of the western boundary, and for our choice of wind stress (2.1), we require the amplitude  $W$  of the wind stress to be

$$W > W_{\text{crit}} = -g \frac{\Delta\rho}{\rho_1} \frac{\beta^2 L^2 h_{1E} h_{2E}}{\pi^2 f^{*2} (x_E - x_W) \cos \pi y^*/L}. \quad (3.6)$$

Note that the unblocked region never reaches the eastern boundary  $x = x_E$ . Surfacing, where the upper layer depth vanishes and the lower layer outcrops, first occurs at the north-west corner of the basin for a wind stress  $W_{\text{surf}}$  obtained from (3.1), viz.

$$W_{\text{surf}} = g \frac{\Delta\rho}{\rho_2} \frac{h_{1E}^2}{2(x_E - x_W)} \quad (3.7)$$

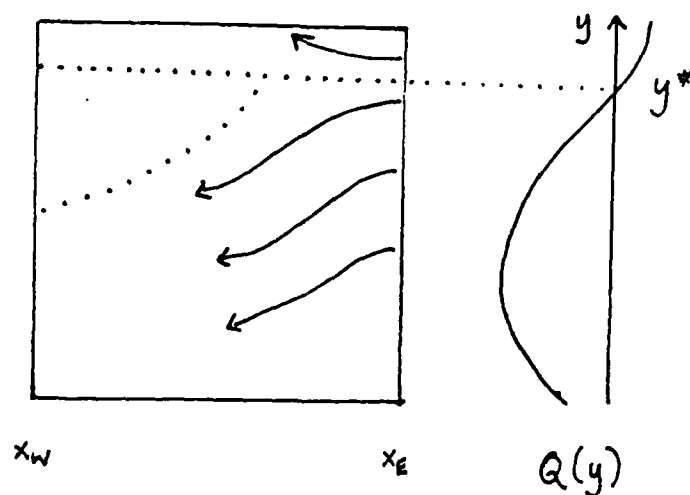


Figure 4. Schematic showing the possibility of the existence of a region isolated from the influence of the eastern boundary. For  $Q < 0$ , characteristics are directed south-west from the eastern boundary, while for  $Q > 0$  they are directed north-west.

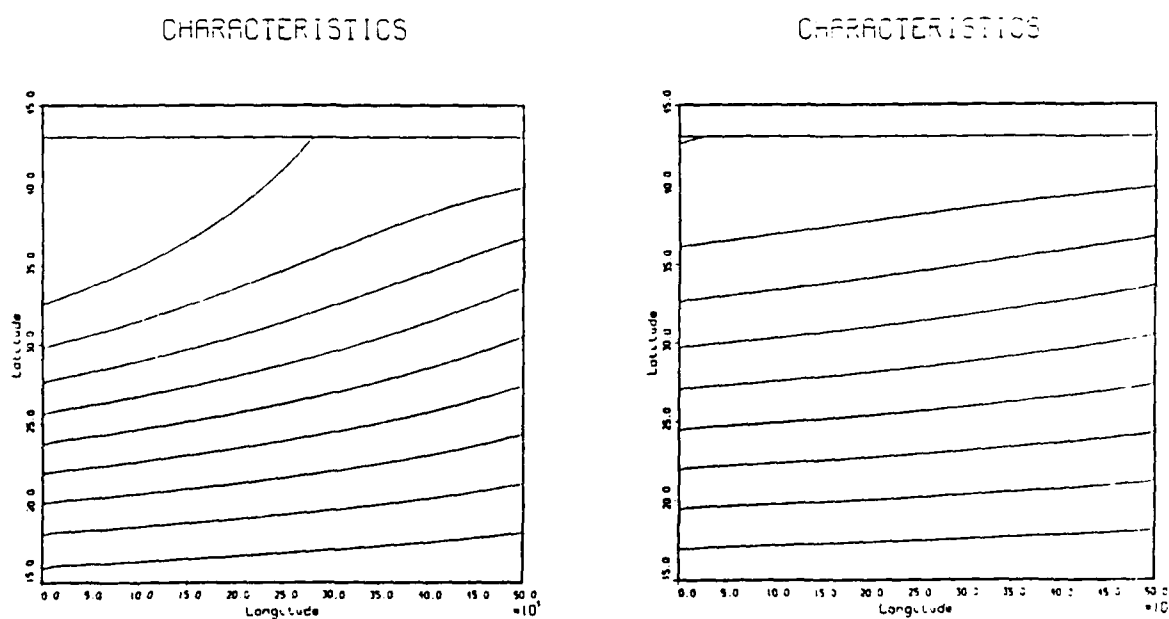


Figure 5. Calculated contours of lower layer potential vorticity  $q_2 = f/h_2$  for (a)  $h_{1E} = 600$  m,  $h_{2E} = 3400$  m,  $W = 5 \times 10^{-4} \text{ kg m}^{-1} \text{ s}^{-2}$ , and (b)  $h_{1E} = 400$  m,  $h_{2E} = 3600$  m,  $W = 1.3 \times 10^{-4} \text{ kg m}^{-1} \text{ s}^{-2}$ . Note that the unblocked region is very small in the second case.

and so, for recirculation to occur before surfacing, and therefore affect surfacing, it is necessary that  $W_{\text{crit}} < W_{\text{surf}}$ , which implies that we require

$$\frac{h_{2E}}{h_{1E}} < -\frac{\pi^2 \rho_1}{2 \rho_2} \left( \frac{f^*}{\beta L} \right)^2 \cos \frac{\pi y^*}{L}. \quad (3.8)$$

For the basin considered here, this is approximately equal to 11.4 and so we are justified in pursuing the study of recirculation in the lower layer of a two-layer ocean prior to outcropping. If the critical ratio (3.8) had been of the order of 1 rather than 10, we would have had to study the surfacing problem first. In a sense, however, this is immaterial as we intend including surfacing in our model at a later stage, although we are now in a position to consider the effects of lower layer recirculation upon the surfacing condition.

#### 4. Recirculation in the lower layer

Once the possibility of flow in the lower layer exists, we are no longer able to use the reduced gravity model solution, although as we shall see in §6 it is still valuable as a zeroth order approximation. The reduced gravity solution gives us the position of the unblocked region, but is inapplicable to further analysis of lower layer flow. Returning therefore to the full shallow water equations (2.2), (2.3) and the Sverdrup relation (2.11), we obtain a relation between the layer depths in the interior, i.e. neglecting dissipative terms,

$$h^2 + \frac{\Delta \rho}{\rho_1} h_2^2 = \frac{2Q}{g}(x - x_E) + h_E^2 + \frac{\Delta \rho}{\rho_1} h_{2E}^2. \quad (4.1)$$

Doing the same for the upper layer alone,

$$\frac{fg}{\beta} J(h_1, h) + gh_1 h_x = Q \quad (4.2)$$

and so, eliminating derivatives of  $h_1$  between the two and recalling that  $q_2 = f/h_2$ , we arrive at the nonlinear characteristic equation for  $q_2$

$$\left[ -\frac{\beta g}{f} \frac{\Delta \rho}{\rho_1} h_1 h_2 + Q_y(x_E - x) \right] q_{2x} + Q q_{2y} = 0. \quad (4.3)$$

This is similar to the expression obtained by Veronis (1988) for the sum of the upper two layer depths in his three-layer model of ocean circulation driven by winds and surface cooling.



In the western boundary layer, the interfacial stresses will be large and so we expect the lower layer flow to be northward in the western boundary layer, implying southward flow in the interior. Since  $Q < 0$ , this is consistent with our choice of sign for (4.3), since information will be advected along characteristics with the flow. The two terms multiplying  $q_{2x}$  correspond respectively to the westward propagation of information by a nondispersive Rossby wave and the eastward motion induced by the wind, as we are considering the wind stress to be such that the unblocked region is confined to the northern half basin.

In general, the characteristic equation (4.3) can be solved, in conjunction with (4.1), so long as  $q_2$  is known at some point on each characteristic. Unfortunately, the only externally imposed boundary conditions are the layer depths at the eastern boundary from which the unblocked region is, by definition, cut off. Young & Rhines (1982) attacked the problem by utilising the functional relationship (2.9) between lower layer streamfunction and potential vorticity and imposing a first order balance between interfacial forcing and bottom friction in the lower layer. They integrated around an unknown closed streamline of the lower layer flow to determine an integral balance. In their quasi-geostrophic case, it is in fact possible to determine the functional relationship between  $\psi_2$  and  $\hat{q}_2$ , a modified (and known) potential vorticity, thereby solving the problem completely without needing to know the particular details of the flow. We can construct a similar integral equation for the shallow water model, but are unable to solve for the functional relationship in the same manner. This is of no account, however, as the argument of Young & Rhines (1982) applies only away from regions, such as western boundary layers, where dissipation becomes a zero-order effect.

Ierley & Young (1983) clarified this point, analysing the western boundary layer dynamics correctly. They showed that the western boundary layer is instrumental (for their quasi-geostrophic model) in determining the nature of the interior flow in the unblocked lower layer region. There is no reason to suppose that the shallow-water model will be any different in this fundamental qualitative respect. We shall therefore direct our attention to the western boundary layer. To solve for the interior flow, it will be necessary to determine the outflow conditions from the western boundary layer, which itself will be solved by matching to the interior solution. This suggests an iterative approach to the problem in which the interior and western boundary layer solutions are each determined assuming knowledge of the other.

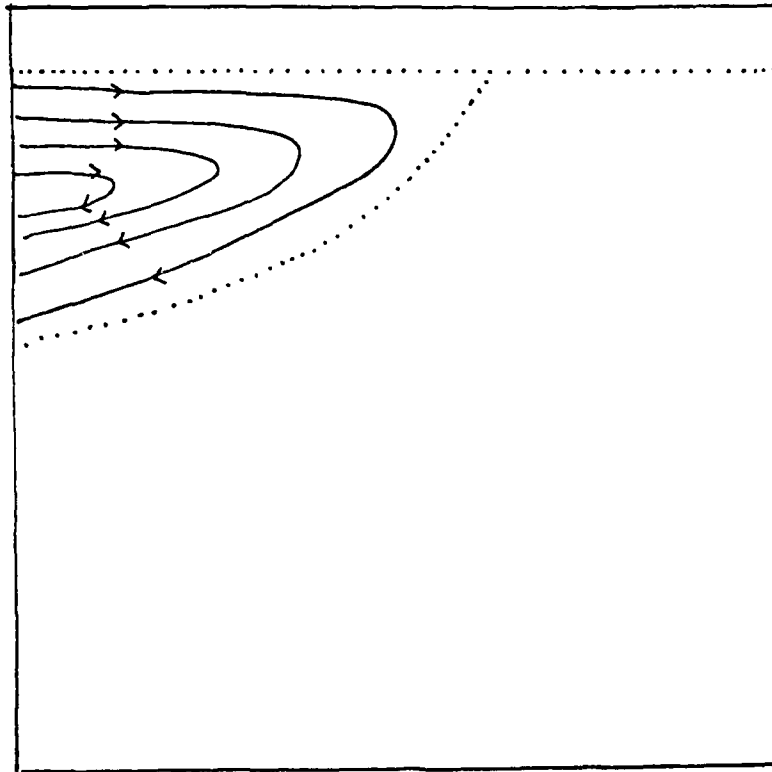


Figure 6. Schematic of the lower layer flow expected as a result of the existence of an unblocked region.

### 5. Western boundary layer dynamics

As in Ierley & Young (1983) for the quasi-geostrophic case, we expect the western boundary layer to play a fundamental role in determining the solution in the unblocked region. In the western boundary layer, the north-south velocities are sufficiently large for interfacial and bottom drag to become important and also correspond to high east-west gradients in the layer depths. The wind-stress effects and east-west velocities are much weaker, and can be neglected in the zonal momentum equations, and so the shallow water equations (2.2) (2.3) reduce to

$$-fv_1 = -gh_x \quad (5.1a)$$

$$fu_1 = -gh_y - \frac{\rho_2}{\rho_1} \frac{R}{h_1} (v_1 - v_2) \quad (5.1b)$$

$$-fv_2 = -g \frac{\rho_1}{\rho_2} h_x - g \frac{\Delta\rho}{\rho_2} h_{2x} \quad (5.2a)$$

$$fu_2 = -g \frac{\rho_1}{\rho_2} h_y - g \frac{\Delta\rho}{\rho_2} h_{2y} - \frac{R}{h_2} (v_2 - v_1) - \frac{K}{h_2} v_2 \quad (5.2b)$$

In the lower layer,  $\nabla \cdot (h_2 \mathbf{v}_2) = 0$  and so

$$-f \frac{\mathbf{v}_2 \cdot \nabla h_2}{h_2} + \beta v_2 = -R \left[ \left( \frac{v_2}{h_2} \right)_x - \left( \frac{v_1}{h_2} \right)_x \right] - K \left( \frac{v_2}{h_2} \right)_x \quad (5.3)$$

Substituting for  $\mathbf{v}_1, \mathbf{v}_2$  we obtain, after some manipulation,

$$-fJ(h_1, h) + \beta h_2 \left( h_x + \frac{\Delta\rho}{\rho_1} h_{2x} \right) = R \frac{\Delta\rho}{\rho_1} h_{1xx} - K \left( h_{xx} + \frac{\Delta\rho}{\rho_1} h_{2xx} \right), \quad (5.4)$$

which suggests the rescaling  $x = \frac{KH}{\beta} \xi$ , where  $H$  is a characteristic upper layer depth, e.g.  $h_{1E}$ .

A second equation can be derived from the full Sverdrup balance (2.10), again neglecting the wind-stress term and variations in  $u$ . The balance in the western boundary layer is

$$\beta \left( h_1 v_1 + \frac{\rho_2}{\rho_1} h_2 v_2 \right) = -K \frac{\rho_2}{\rho_1} v_{2x} \quad (5.5)$$

which upon substitution for  $v_1, v_2$  gives us

$$\beta \left( hh_x + \frac{\Delta\rho}{\rho_1} h_2 h_{2x} \right) = -K \left( h_{xx} + \frac{\Delta\rho}{\rho_1} h_{2xx} \right), \quad (5.6)$$

suggesting the same boundary layer scaling. Therefore let us rescale the layer depths  $h_1$ ,  $h_2$  by  $H$  and stretch the  $x$ -coordinate through  $x = \frac{K}{\beta H} \xi$ . As  $K \ll \beta H$ , we can consider the boundary layer to range from  $\xi = 0$  to  $\xi = \infty$  and the edge of the western boundary layer to be at  $x = x_W$ . Simplifying (5.4) by combination with (5.6), we eventually derive the western boundary layer equations in relatively simple form, viz.

$$h_1 h_\xi + \hat{f} J(h_1, h) = -\alpha \frac{\Delta \rho}{\rho_1} h_{1\xi\xi} \quad (5.7a)$$

$$h h_\xi + \frac{\Delta \rho}{\rho_1} h_2 h_{2\xi} = -\left( h_{\xi\xi} + \frac{\Delta \rho}{\rho_1} h_{2\xi\xi} \right) \quad (5.7b)$$

where  $\hat{f} = f/\beta$  and  $\alpha = R/K$ . This reduction, which is similar to the approach of Welander (1966), who considered only the blocked case, simplifies the model greatly. Suitable boundary conditions can be derived from mass transport considerations. There is no normal flow in the upper layer at the western wall, i.e.  $u_1 = 0$  at  $\xi = 0$  and so, from the simplified shallow water equations (5.1), (5.2) we have

$$\hat{f} h_1 h_y \Big|_{\xi=0} = -\alpha \frac{\Delta \rho}{\rho_1} h_{1\xi} \Big|_{\xi=0} \quad (5.8)$$

and  $\rho_1 h_1 u_1 + \rho_2 h_2 u_2 = 0$  at  $\xi = 0$  implies that

$$\hat{f} \left( h h_y + \frac{\Delta \rho}{\rho_1} h_2 h_{2y} \right) \Big|_{\xi=0} = -\left( h_{\xi\xi} + \frac{\Delta \rho}{\rho_1} h_{2\xi\xi} \right) \Big|_{\xi=0}. \quad (5.9)$$

As  $\xi \rightarrow \infty$ , we must match  $h_1$ ,  $h_2$  to their values in the interior of the basin. If we are to solve this system in an iterative manner, posing successive interior values for  $h_1$ ,  $h_2$  and then solving for the western boundary to obtain new values for the layer depths, it is better to match to only one, or a linear combination, of the layer depths and derive a new matching condition based on the north-south mass transport. Southwards transport in the interior must be returned in the western boundary layer, i.e. for the upper layer,

$$\int_{x_W}^{x_E} h_1 v_1 dx = 0, \quad (5.10)$$

which becomes

$$\int_0^\infty h_1 h_\xi d\xi + \int_{x_W}^{x_E} h_1 h_x dx = \frac{\tau}{g} (x_E - x_W). \quad (5.11)$$

The western boundary layer equations contain derivatives in both  $\xi$  and  $y$ , requiring us to set boundary conditions at the northern and southern walls. Simply applying  $v_1 = v_2 = 0$  at the southern wall gives us  $h_{1\xi} = h_{2\xi} = 0$  at  $y = y_S$ , which can be satisfied only if there is no net southwards geostrophic transport in the interior, i.e. only if  $\text{curl } \tau = 0$  at  $y = y_S$ . Welander (1966) managed to apply  $v_1 = v_2 = 0$  at a northern  $\text{curl } \tau = 0$  boundary also, by considering the linearised case of zero Jacobian  $J(h_1, h)$  between the layer depths, but matching at a given northern boundary is not guaranteed by the boundary layer equations (5.7) as they contain only a single  $y$ -derivative. In general a two-dimensional nonlinear system such as described here requires a fully numerical solution, or an *Ansatz*, as employed by Ierley & Young (1983) for the quasi-geostrophic case. We can avoid much of this by considering the effects of the postulated flow in the unblocked region of the lower layer upon the dynamics of the system to be small, allowing us to perturb about the reduced gravity solution (Parsons, 1969), which arises when no lower layer flow is allowed. This is likely to be so when the lower layer is relatively deep and so we shall formally expand to first order in  $h_1/h_2$ , the ratio of the layer depths. However, it should be noted that for a two-layer ocean of finite depth, with driving at the surface and dissipation by interfacial and bottom friction, some flow must occur in the lower layer to effect the dissipation mechanism (Welander 1966). It can easily be shown with a linear quasi-geostrophic model that this flow is restricted to a thin region of thickness  $h_1/h_2$  times the thickness of the western boundary layer itself, in the absence of any interior lower layer flow.

## 6. Deepish lower layer approximation

To continue further, we shall consider the solution to the nonlinear boundary layer and interior equations to be not significantly different from the reduced gravity model, for which there is no flow in an infinitely deep lower layer. As we shall see, this enables us to decouple the boundary layer equations and reduce the solution to a set of arbitrary functions in  $y$  and various integrals of the known reduced gravity approximate solution.

In the ensuing discussion, we shall write superscript  $^0$  for the reduced gravity solution and superscript  $'$  for the perturbation, i.e.

$$h_1 = h_1^0 + h_1' \quad (6.1)$$

with corresponding expressions for  $h_2$  and  $h = h_1 + h_2$ . The reduced gravity solution, as described by Parsons (1969), is as follows. In the interior, the upper layer depth is given by

$$h_1^{02} = h_{1E}^2 + 2 \frac{\rho_2}{\Delta \rho} \frac{Q(y)}{gH^2} (x - x_E), \quad (6.2)$$

which is the same as (3.1), and in the boundary layer by

$$h_1^0 = h_{1I} \left[ \frac{1 - Ae^{-\lambda\xi}}{1 + Ae^{-\lambda\xi}} \right] \quad (6.3)$$

where

$$h_{1I}^2 = h_{1E}^2 - 2 \frac{\rho_2}{\Delta\rho} \frac{Q(y)}{gH^2} x_E \quad (6.4a)$$

$$h_{1W}^2 = h_{1E}^2 - 2 \frac{\rho_2}{\Delta\rho} \frac{\tau(y)}{gH^2} x_E \quad (6.4b)$$

$$A = \frac{h_{1I} - h_{1W}}{h_{1I} + h_{1W}} \quad (6.4c)$$

$$\lambda = \frac{h_{1I}\rho_1}{\alpha\rho_2}. \quad (6.4d)$$

$h_{1I}$  is the upper layer depth just outside the western boundary layer and  $h_{1W}$  the upper layer depth at the western wall. All layer depths are now non-dimensional, having been scaled by a typical depth scale  $H$ . Everywhere,  $h_2^0$  is related to  $h_1^0$  by the simple form

$$h_2^0 - h_{2E} = -\frac{\rho_1}{\rho_2}(h_1^0 - h_{1E}). \quad (6.5)$$

### 6.1 Western boundary layer

The second boundary layer equation (5.7b) can be regrouped as follows:

$$h_1 h_\xi + h_2 \left( h_\xi + \frac{\Delta\rho}{\rho_1} h_{2\xi} \right) + h_{\xi\xi} + \frac{\Delta\rho}{\rho_1} h_{2\xi\xi} = 0 \quad (6.6)$$

and since  $\nabla(h^0 + \frac{\Delta\rho}{\rho_1} h_2^0) = 0$ , (6.6) is satisfied to zeroth order in  $h_1^0/h_2^0$  by the reduced gravity solution. To next order, we have

$$h_2^0 \left( h'_\xi + \frac{\Delta\rho}{\rho_1} h'_{2\xi} \right) + h'_{\xi\xi} + \frac{\Delta\rho}{\rho_1} h'_{2\xi\xi} = -h_1^0 h'_\xi \quad \text{at } \xi = 0. \quad (6.7)$$

Writing

$$\mathcal{H} = h' + \frac{\Delta\rho}{\rho_1} h'_2, \quad (6.8)$$

(6.7) becomes

$$h_2^0 \mathcal{H}_\xi + \mathcal{H}_{\xi\xi} = -h_1^0 h_\xi^0, \quad (6.9)$$

which can be integrated twice, yielding

$$\mathcal{H}(\xi, y) = -I_1(\xi, y) + C_1(y)I_2(\xi, y) + C_2(y) \quad (6.10)$$

where

$$I_1(\xi, y) = \int_0^\xi \int_0^{\xi'} h_1^0 h_{\xi''}^0 e^{-\int_{\xi''}^{\xi'} h_2^0 d\xi'''} d\xi'' d\xi' \quad (6.11a)$$

$$I_2(\xi, y) = \int_0^\xi e^{-\int_0^{\xi'} h_2^0 d\xi''} d\xi'. \quad (6.11b)$$

$I_1$  and  $I_2$  are known functions, requiring only a quadrature. We do need, however, to determine the arbitrary functions  $C_1(y)$  and  $C_2(y)$ . To zeroth order the boundary condition (5.9) applied at  $\xi = 0$  is satisfied by the reduced gravity solution, and to first order in  $h_1^0/h_2^0$  it becomes

$$\hat{f} h_2^0 \mathcal{H}_y + \mathcal{H}_\xi = -\hat{f} h_1^0 h_y^0 \quad \text{at } \xi = 0 \quad (6.12)$$

which is an expression in  $\mathcal{H}$  alone. As  $\xi \rightarrow \infty$  we can simply match  $\mathcal{H}$  to its value in the interior and so, noting that  $\mathcal{H} = C_2$  and  $\mathcal{H}_\xi = C_1$  at  $\xi = 0$ , we have

$$\hat{f} h_2^0 \left| \frac{dC_2}{dy} + C_1 = -\hat{f} h_1^0 h_y^0 \right|_{\xi=0} \quad (6.13a)$$

$$-I_1^\infty + C_1 I_2^\infty + C_2 = \mathcal{H}^{\text{int}}. \quad (6.13b)$$

Superscript  $\infty$  refers to integrals evaluated in the limit  $\xi \rightarrow \infty$  and  $\mathcal{H}^{\text{int}}$  is the value of  $\mathcal{H}$  at the outer edge of the western boundary layer and is zero for the blocked region as reduced gravity describes the solution exactly there. The relations (6.13a,b) reduce to a first order ordinary differential equation in  $y$  for  $C_2$ , which we can close by applying  $\mathcal{H} = \mathcal{H}^{\text{int}} \forall \xi$  along the southern boundary  $y = y_S$ , as  $h_1$  and  $h_2$  are both constant for  $v_1 = v_2 = 0$ . This corresponds to setting  $C_2(y_S) = \mathcal{H}^{\text{int}}$  and  $C_1(y_S) = 0$  (note that  $I_1^\infty = 0$  at  $y = y_S$ ).

Having solved for  $\mathcal{H}$ , which is a linear combination of the perturbation layer depths, we return to the first boundary layer equation (5.7a) to obtain an equation for  $h_1'$ , the perturbation upper layer depth. Equation (5.7a) is in fact satisfied exactly by the reduced gravity solution, as are the two remaining boundary conditions (5.8) and (5.11). The perturbed first boundary layer equation is

$$h_1' h_\xi^0 + h_1^0 h_\xi' + \hat{f} [J(h_1', h^0) + J(h_1^0, h')] = -\alpha \frac{\Delta \rho}{\rho_1} h_{1\xi\xi}' \quad (6.14)$$

which, after some manipulation, reduces to

$$\alpha \frac{\rho_2}{\rho_1} h'_{1\xi\xi} + (h'_1 h^0_1)_\xi = \frac{\Delta\rho}{\rho_1} [\hat{f}J(\mathcal{H}, h^0_1) - h^0_1 \mathcal{H}_\xi] \quad (6.15)$$

The importance of being able to decouple the boundary layer equations is now apparent. We have obtained an equation for  $h'_1$ , which allows us to write  $h'_1$  also in terms of arbitrary functions of  $y$  and known integrals, using the completed calculation for  $\mathcal{H}$ . The solution for  $h'_1$  can now be written

$$h'_1 = K_1(\xi, y) + C_3(y)K_2(\xi, y) + C_4(y)K_3(\xi, y) \quad (6.16)$$

where

$$K_1(\xi, y) = \frac{\rho_1}{\alpha\rho_2} \frac{\Delta\rho}{\rho_1} \int_0^\xi e^{-\int_{\xi'}^\xi \frac{h^0_{\rho_1}}{\alpha\rho_2} d\xi''} \int_0^{\xi'} [\hat{f}J(\mathcal{H}, h^0_1) - h^0_1 \mathcal{H}_{\xi''}] d\xi'' d\xi' \quad (6.17a)$$

$$K_2(\xi, y) = \frac{\rho_1}{\alpha\rho_2} \int_0^\xi e^{-\int_{\xi'}^\xi \frac{h^0_{\rho_1}}{\alpha\rho_2} d\xi''} d\xi' \quad (6.17b)$$

$$K_3(\xi, y) = \frac{\rho_1}{\alpha\rho_2} e^{-\int_0^\xi \frac{h^0_{\rho_1}}{\alpha\rho_2} d\xi''} d\xi' \quad (6.17c)$$

Note that  $K_1$  is a function of  $\mathcal{H}$  and is therefore dependent on the values of the arbitrary functions  $C_1, C_2$ . To be useful,  $K_1$  should be decomposed so that it is a sum of known integrals multiplied by  $C_1, C_2$  and their derivatives. We shall address this later, but first let us consider the remaining boundary conditions. Upon perturbation, (5.8) becomes

$$\hat{f}(h'_1 h^0_y + h^0_1 h'_y) = -\alpha \frac{\Delta\rho}{\rho_1} h'_{1\xi}. \quad (6.18)$$

Employing  $h' = \frac{\rho_1}{\rho_2} \mathcal{H} + \frac{\Delta\rho}{\rho_2} h'_1$  and  $h^0_y = \frac{\Delta\rho}{\rho_2} h^0_{1y}$ , this can be written

$$\frac{\Delta\rho}{\rho_2} \hat{f}(h^0_1 h'_1)_y + \frac{\rho_1}{\rho_2} \hat{f} \mathcal{H}_y = -\alpha \frac{\Delta\rho}{\rho_1} h'_{1\xi} \quad \text{at } \xi = 0. \quad (6.19)$$

The final boundary condition (5.11), which matches the northward return flow in the western boundary layer to the total southward flow in the interior, yields

$$\int_0^\infty h'_1 h^0_\xi + h^0_1 h'_\xi d\xi = - \int_{x_w}^{x_E} h'_1 h^0_x + h^0_1 h'_x dx, \quad (6.20)$$



which can be simplified by integration by parts and applying a limited matching of perturbation quantities at the edge of the western boundary layer to

$$\frac{\Delta\rho}{\rho_1} h_1^0 h_1' \Big|_{\xi=0} = - \int_{x_w}^{x_E} \mathcal{H} h_{1x}^0 dx + \int_0^\infty h_1^0 \mathcal{H}_\xi d\xi - h_1^0 \mathcal{H} \Big|_{\xi=\infty} \quad (6.21)$$

Now,

$$\int_0^\xi h_1^0 \mathcal{H}_{\xi'} d\xi' = \int_0^\xi h_1^0 \left[ C_1 e^{-\int_0^{\xi'} h_2^0 d\xi''} - \int_0^{\xi'} h_1^0 h_{\xi''}^0 e^{-\int_{\xi''}^{\xi'} h_2^0 d\xi'''} d\xi'' \right] d\xi' \quad (6.22)$$

and so define

$$\int_0^\xi h_1^0 \mathcal{H}_{\xi'} d\xi' = C_1 M_2(\xi, y) - M_1(\xi, y) \quad (6.23)$$

where

$$\text{Integrand}(M_1) = h_1^0(\xi') \times \text{Integrand}(I_1) \quad (6.24a)$$

$$\text{Integrand}(M_2) = h_1^0(\xi') \times \text{Integrand}(I_2) \quad (6.24b)$$

We are finally able to write down the boundary conditions in manageable form, viz.

$$\frac{\rho_1}{\alpha\rho_2} \frac{\Delta\rho}{\rho_1} \hat{f} \frac{d}{dy} (h_{1w} C_4) + \hat{f} \frac{dC_2}{dy} + \frac{\Delta\rho}{\rho_1} \left( C_3 - \frac{\rho_1}{\alpha\rho_2} h_{1w} C_4 \right) = 0 \quad (6.25a)$$

$$-\frac{\rho_1}{\alpha\rho_2} \frac{\Delta\rho}{\rho_1} h_{1w} C_4 - \int_{x_w}^{x_E} \mathcal{H} h_{1x}^0 dx - h_{1I} \mathcal{H}^{\text{int}} - M_1^\infty + C_1 M_2^\infty = 0 \quad (6.25b)$$

leaving us only to determine the integral of  $\mathcal{H} h_{1x}^0$  across the interior. We shall discuss this in §6.2 below, but for solving the western boundary layer equations consider all interior quantities to be known. Again imposing  $v_1 = v_2 = 0$  at  $y = y_S$ , where there is blocking, we obtain the boundary condition  $C_3 = C_4 = 0$  at  $y = y_S$ .

We are therefore able to solve for  $\mathcal{H}$  and  $h_1'$  in the western boundary layer of the blocked region up to  $y = y_C$ , the southern boundary of the cut off unblocked region at the western boundary. Since reduced gravity holds in the interior of the blocked region, the perturbation quantities  $\mathcal{H}$  and  $h_1'$  are zero there and so the solution is immediately found for the western boundary layer south of  $y = y_C$ . The values of  $C_1, C_2, C_3$  and  $C_4$  found at  $y = y_C$  can then be used as boundary conditions for the solution of the unblocked region  $y_C < y < y^*$ . Having solved for the unblocked western boundary layer, we now have a new guess for  $h_1'$  at the edge of the western boundary layer. This is given by

$$h_1' = K_1^\infty + C_3 K_2^\infty + C_4 K_3^\infty. \quad (6.26)$$

This again involves known integrals and can be greatly simplified. These and other simplifications will be discussed in the Appendix.

We now need to solve for the interior given the western boundary layer outflow as well as develop a simple expression for the integral of  $\mathcal{H}h_{1x}^0$  across the interior of the unblocked region.

### 6.2 Interior characteristic equation

Within the interior, the relation (4.1) between the layer depths applies. Upon perturbation and recasting in terms of  $\mathcal{H}$  and  $h_1'$  this becomes

$$\mathcal{H} = \frac{\Delta\rho}{\rho_1} \frac{h_1^0}{h_1^0} h_1', \quad (6.27)$$

which implies that  $\mathcal{H} \ll h_1'$  and so, ignoring higher order terms, the perturbation layer depths are related by

$$h_2' = -\frac{\rho_1}{\rho_2} h_1'. \quad (6.28)$$

Hence, if we know  $h_2'$ , we immediately have  $h_1'$  and  $\mathcal{H}$  and are therefore in a position to calculate the integral of  $\mathcal{H}h_{1x}^0$ . The characteristic equation (4.3) becomes, upon perturbation

$$\left[ -\frac{\beta g}{f} \frac{\Delta\rho}{\rho_1} h_1^0 h_2^0 + Q_v(x_E - x) \right] h_{2x}' + Q h_{2v}' = \frac{Q\beta}{f} \frac{\rho_2 h_2^0}{\rho_1 h_1^0} h_2' \quad (6.29)$$

which can be rewritten

$$x_\sigma = -\frac{\beta g}{f} \frac{\Delta\rho}{\rho_1} h_1^0 h_2^0 + Q_v(x_E - x) \quad (6.30a)$$

$$y_\sigma = Q \quad (6.30b)$$

$$h_{2\sigma}' = \frac{Q\beta}{f} \frac{\rho_2 h_2^0}{\rho_1 h_1^0} h_2'. \quad (6.30c)$$

The characteristic paths are therefore known, being given by (6.30a,b), with (6.30c) implying that

$$h_2' = h_2'(\text{outflow}) \exp \left( \int_0^\sigma \frac{Q\beta}{f} \frac{\rho_2 h_2^0}{\rho_1 h_1^0} d\sigma' \right). \quad (6.31)$$

$\sigma$  is the distance along the characteristic from the western boundary layer outflow.

The interior solution is now found by integrating (6.30a,b) back to the western boundary and hence determining the relevant outflow point for each point in the interior. From

the western boundary layer calculation, we have  $h'_2$ (outflow) and therefore  $h'_2$  at the original interior point from (6.31).  $\mathcal{H}$  is then determined from (6.27) and (6.28), giving us new guesses for  $\mathcal{H}^{\text{int}}$  and the  $x$ -integral of  $\mathcal{H}h_{1x}^0$ . Note that the perturbed characteristic system is equivalent to mapping the outflow values of  $h'_2$  along the edge of the western boundary layer onto values of  $\mathcal{H}h_{1x}^0$  along lines of latitude in the interior. Therefore, if we are to find the integral of  $\mathcal{H}h_{1x}^0$  by some quadrature based on  $n$  points, we can write, for  $y = y_j$ ,

$$\int_{x_E}^{x_W} \mathcal{H}h_{1x}^0 dx = \sum_{i=1}^n g_{ij} h'_2(x_W, y^{\text{out}}(x_{ij})), \quad (6.32)$$

where  $x_{ij}$  is the  $i$ th quadrature point for  $y = y_j$ ,  $y^{\text{out}}$  is the mapping from the interior to the edge of the western boundary layer and  $g_{ij}$  is the product of  $h_{1x}^0$ , the exponential part of (6.31) and constants dependent upon the particular quadrature scheme selected.

We have therefore, by this perturbation approach, reduced a nonlinear partial differential system to a small set of quadratures, which can be evaluated prior to the iteration stage of solution, and the solution of a small set of ordinary differential equations.

### 6.3 Lower layer streamfunction

Having solved iteratively for the layer depths in the entire basin, blocked and unblocked, it remains to determine the strength of the lower layer flow. This is obtained by disturbing the interior shallow-water equations (2.3a,b) to give

$$-f\psi_{2x} = -g \frac{\rho_1}{\rho_2} h_2^0 \mathcal{H}_x \quad (6.33a)$$

$$-f\psi_{2y} = -g \frac{\rho_1}{\rho_2} h_2^0 \mathcal{H}_y \quad (6.33b)$$

which are not immediately integrable analytically, but either expression can be used to determine  $\psi_2$  from  $\mathcal{H}$  numerically.

To recapitulate, the proposed solution procedure is as follows:

- (i) solve for the blocked western boundary layer,
- (ii) pose an initial guess for  $h'_2$  at the edge of the western boundary layer,
- (iii) solve for the unblocked interior using the perturbed characteristic equation,
- (iv) solve for the unblocked western boundary layer, iterating from (iii) until convergence, and
- (v) evaluate the lower layer transport streamfunction.

## 7. Discussion

We have developed a two-layer model of a wind-driven ocean which allows the possibility of lower layer motion without requiring surfacing. After identifying the western boundary layer as being critical to the behaviour of the model, we proceeded to treat the western boundary layer. Considering the full solution to be a small perturbation to the reduced gravity model of Parsons (1969) enabled us to simplify greatly the nonlinear, partial differential system to a set of quadratures and ordinary differential equations.

The proposed solution procedure has not yet been fully implemented, but preliminary results are encouraging. We feel that the model presented here has much promise and we intend continuing with this work, first extending to the situation in which outcropping of the lower layer occurs and then including a northern, subpolar gyre.

**Acknowledgments.** This work is the result of a close collaboration with George Veronis, who has been a constant source of advice and encouragement, and with whom I have greatly enjoyed working. I would like to thank all the GFD staff and fellows for their contributions to a most enjoyable summer. Finally, I would like to express my gratitude to the GFD Fellowship Committee and to St. John's College, Cambridge for their provision of an airline ticket.

## References

- Ierley, G.R. & Young, W.R. 1983. Can the western boundary layer affect the potential vorticity distribution in the Sverdrup interior of a wind gyre? *J. Phys. Oceanogr.* **39**, 1753-1763.
- Kamenkovich, V.M. & Reznick, G.M. 1972. A contribution to the theory of stationary wind-driven currents in a two-layer liquid. *Izv. Atm. Ocean Phys.* **8**, 238-245.
- Parsons, A.T. 1969. A two-layer model of Gulf Stream separation. *J. Fluid Mech.* **39**, 511-528.
- Rhines, P.B. & Young, W.R. 1982. A theory of wind-driven circulation I. Mid-ocean gyres. *J. Mar. Res.* **40**(supp.), 559-596.
- Veronis, G. 1973. Model of world ocean circulation I. Wind-driven, two-layer. *J. Mar. Res.* **31**(3), 228-288.
- Veronis, G. 1988. Circulation driven by winds and surface cooling. *J. Phys. Oceanogr.* **18**, 1920-1932.
- Welander, P. 1966. A two-layer frictional model of wind-driven motion in a rectangular ocean basin. *Tellus* **18**, 54-62.

Young, W.R. & Rhines, P.B. 1982. A theory of wind-driven circulation II. Gyres with western boundary layer. *J. Mar. Res* 40(3), 849-872.

### Appendix

The integrals in §6 can be calculated from the reduced gravity solution (6.3), (6.4) and we shall outline here the extent to which the integrals  $I_1^\infty$ ,  $I_2^\infty$ ,  $M_1^\infty$ ,  $M_2^\infty$ ,  $K_1^\infty$ ,  $K_2^\infty$  and  $K_3^\infty$  can be simplified. The lower layer depth in the reduced gravity approximation is related to the upper layer depth through the expression (6.5), allowing us to obtain

$$e^{-\int_0^{\xi'} \Lambda_2^0 d\xi''} = e^{-\mu\xi'} \left[ \frac{1 + Ae^{-\lambda\xi'}}{1 + A} \right]^{2\alpha}, \quad (A1)$$

where

$$\mu = h_{2E} + \frac{\rho_1}{\rho_2}(h_{1E} - h_{1I}). \quad (A2)$$

This reduces (6.11a), or  $I_1$ , to a double integral and (6.11b), or  $I_2$ , to a single integral. Similarly reduced are (6.24a) for  $M_1$  and (6.25b) for  $M_2$ . The real savings to be made are in the expressions for  $K_1^\infty$ ,  $K_2^\infty$  and  $K_3^\infty$ . Now,

$$e^{-\int_0^{\xi'} \frac{\Lambda_2^0 \rho_1}{\alpha \rho_2} d\xi''} = \left[ \frac{1 + A}{1 + Ae^{-\lambda\xi'}} \right]^2 e^{-\lambda\xi'}, \quad (A3)$$

which with a little thought reduces (6.17b) for  $K_2$  and (6.17c) for  $K_3$  to

$$K_2^\infty = \frac{1}{h_{1I}} \quad (A4a)$$

$$K_3^\infty = 0. \quad (A4b)$$

Substituting (A3) into (6.17a) for  $K_1$  and integrating once by parts in  $\xi'$ ,  $K_1$  is given by

$$K_1 = \frac{\rho_1}{\alpha \rho_2} \frac{\Delta \rho}{\rho_1} \frac{1}{\lambda} \frac{e^{-\lambda\xi}}{(1 + Ae^{-\lambda\xi})^2} \int_0^\xi \left( e^{\lambda\xi} - A^2 e^{-\lambda\xi} + 2A\lambda(\xi - \xi') - e^{\lambda\xi'} + A^2 e^{-\lambda\xi'} \right) \\ \times \left( \hat{f}J(\mathcal{H}, h_1^0) - h_1^0 \mathcal{H}_{\xi'} \right) d\xi', \quad (A5)$$

which as  $\xi \rightarrow \infty$ , noting that  $\xi$ -derivatives of  $\mathcal{H}$  and  $h_1^0$  also disappear rapidly as  $\xi \rightarrow \infty$ , reduces further to

$$K_1^\infty = \frac{1}{h_{1I}} \frac{\Delta \rho}{\rho_1} \int_0^\infty \hat{f}J(\mathcal{H}, h_1^0) - h_1^0 \mathcal{H}_{\xi'} d\xi'. \quad (A5)$$

The integral of  $h_1^0 \mathcal{H}_{\xi'}$  is given by  $M_1^\infty$  and  $M_2^\infty$ , with which we have already dealt, and the integral of  $J(\mathcal{H}, h_1^0)$  can be rewritten

$$\int_0^\infty J(\mathcal{H}, h_1^0) d\xi' = \frac{d}{dy} \int_0^\infty h_1^0 \mathcal{H}_{\xi'} d\xi' - [\mathcal{H}_y h_1^0]_0^\infty \quad (\text{A6})$$

after integrating by parts with respect to  $y$ . Much work can therefore be saved by making an approximation for the  $y$ -derivatives in (A6) as the integral of  $h_1^0 \mathcal{H}_{\xi'}$  and  $\mathcal{H}$  are both simply related to arbitrary functions of  $y$  and known integrals of the reduced gravity quantities. Therefore only four integrals need to be calculated in advance by quadrature, viz.  $I_1^\infty$ ,  $I_2^\infty$ ,  $M_1^\infty$  and  $M_2^\infty$ , as well as the functions  $g_{ij}$  and the mapping  $y^{\text{out}}$  for the interior region defined by (6.32).

# Multiple Resonant Topographic Waves in a Barotropic Flow

Scott W. Jones

Barotropic quasi-geostrophic flow on a  $\beta$ -plane is examined for the case in which the flow is resonant with two topographic modes. The linear problem is solved exactly and this solution is used to prescribe the form of the bottom topography. A weakly nonlinear analysis is performed to derive the amplitude equations for the time evolution of topographically generated Rossby waves. It is found that up to nine stationary equilibrium states can be found. Analysis treating the two-mode problem as a perturbation of the one-wave problem shows small changes in the shape and position of the domain in parameter space in which multiple equilibria are found. Numerical calculations suggest that when the amplitude of the second mode is large the boundary becomes more complicated.

## 1. Introduction

It is well-established that model solutions of large-scale topographically-forced flows can possess multiple stationary equilibria for fixed external parameters (Charney & DeVore 1978, Hart 1979, Pedlosky 1981, Samelson & Allen 1987, Hart 1989). This observation, apparently first made by Charney & DeVore (1978), was proposed as an explanation of the bimodal behavior observed in atmospheric flows. In their study the basic zonal flow is destabilized by the topography and a field of Rossby waves is generated. The resulting flow can be of two types: a strong zonal flow with small wave amplitude, or a weak zonal flow with large wave amplitude. The latter condition is qualitatively similar to so-called "blocked" states found in the atmosphere. Although the analysis of Charney & DeVore relies on a severely truncated spectral decomposition of the fields subsequent studies by Hart (1979) and Pedlosky (1981) have verified the essential features of their result. Each of these model problems have been solved for steady flow over simple (one mode) topography.

Time-periodic flows have been investigated by Samelson & Allen (1987) and Hart (1989). Again multiple equilibria are observed. In addition several new features are found. For example zero-mean temporal forcing can generate a non-zero zonal mean current. This rectified flow is demonstrated in both studies. Samel-

son & Allen also find that for ranges of their parameters all steady solutions are unstable. Instead numerical simulations suggest that limit cycles, period doubling sequences and chaotic trajectories govern the evolution of the modal amplitudes of the Eulerian flow. Finally, the introduction of time-dependence permits chaotic Lagrangian trajectories in simple Eulerian flows.

At this time the connection between the bimodality of atmospheric flows and multiple stationary equilibria is no more than a plausible assertion based on simple models. A limitation of the previously cited papers is the restriction to idealized topography. The motivation for this study is to investigate the consequences of more complicated forms of topography and time-dependence on the flow. If it is found that more realistic topography contracts the parameter domain of multiple equilibria, the dynamical arguments for this connection are weakened. Unfortunately the converse situation, an expansion of this domain, is not proof of the above assertion and many further questions must be answered. Perhaps the most crucial issue is the identification of the triggering mechanism responsible for the flipping between the stable modes.

In the following pages we wish to determine the effect of a multiplicity of resonant modes on the size and position of the region in parameter space where multiple equilibria exist. As will be shown there are several ways in which two (or more) modes can be simultaneously resonant. Here we will only treat the most simple case. The organization of the paper is as follows: In §2 the flow geometry and basic equations are presented. The linear problem is solved exactly in §3. A weakly non-linear analysis of the near-resonant expansion is performed in §4. In §5 these results are used to examine the domain of multiple equilibria. Finally the conclusions and suggestions for future research are discussed in §6.

## 2. The model

We consider barotropic flow in a zonally periodic channel. The geometry and the rectilinear coordinate system are shown in figure 1. The width of the channel is  $L$  and its mean depth is  $D$ . At this time we do not explicitly state the form of



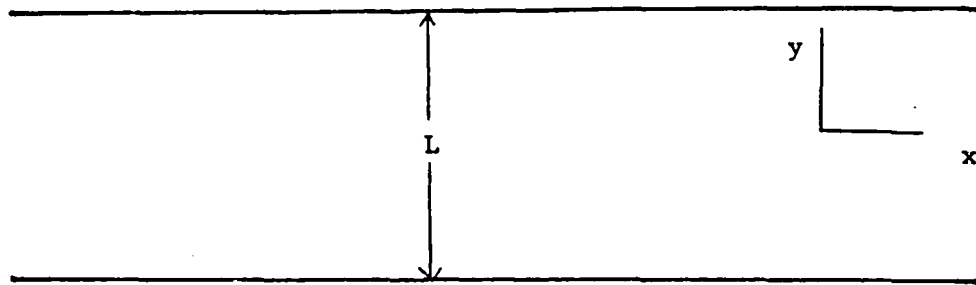


Figure 1. The zonal channel and the rectilinear coordinate system used in this paper.

the bottom topography, however, the general form is

$$h(x, y) = \sin \pi y \sum_{n=1}^N a_n e^{ik_n x}. \quad (1)$$

The basic flow is oscillatory and is given by

$$\mathbf{u}_0 = (\delta\omega \sin \omega t, 0). \quad (2)$$

To simulate the latitudinal dependence of the Coriolis parameter we let  $f = f_0 + \beta_0 y$ . Consequently the Rossby number can be defined as  $\epsilon = \omega/f_0$ . The problem is governed by the non-dimensional quasi-geostrophic vorticity equation

$$\zeta_t + \eta \mathbf{u} \cdot \nabla \zeta + \beta v = -r\zeta + s\mathbf{u} \cdot \nabla h \quad (3)$$

and the boundary condition prohibiting normal flow at the channel walls. Here and throughout the paper subscripts will be used to denote differentiation with respect to the subscripted variable. In (3) the velocity has been nondimensionalized by  $\delta\omega$ , horizontal lengths by  $L$ , time by  $1/\omega$ , the vorticity by  $\omega$  and the bottom topography by  $\epsilon D\Gamma$ . The terms on the right-hand side of (3) represent damping by the bottom Ekman layer and stretching or compression of the vertical fluid columns respectively. The coefficients of these terms are

$$r = \frac{\sqrt{\nu f_0}}{\omega D}, \quad s = \eta \Gamma \quad (4)$$

where  $\nu$  is an eddy diffusivity. Finally the parameters  $\eta$  and  $\beta$  are

$$\eta = \frac{\delta}{L}, \quad \beta = \frac{\beta_0 \delta}{\omega}. \quad (5)$$

We let the velocity field be written as the sum of the basic flow,  $u_0$ , and the disturbance velocity,  $u^R$

$$u = u_0 + u^R \quad (6)$$

where  $u_0$  is given by (2). Now (3) can be written as

$$\mathcal{L}(\psi) = -r \nabla^2 \psi - s \sin t h_x - J(\psi, \nabla^2 \psi + \Gamma h) \quad (7)$$

where

$$\begin{aligned} \mathcal{L} &= \nabla^2 \partial_t + \eta \sin t \nabla^2 \partial_x + \beta \partial_x \\ \nabla^2 \psi &= \zeta \\ (u, v) &= (-\psi_y, \psi_x) \\ J(a, b) &= a_x b_y - b_x a_y. \end{aligned}$$

Equation (7) defines the model problem considered throughout the remainder of the paper.

### 3. Linear solution

To simplify the subsequent analysis we separate the streamfunction in a manner analogous to (6)

$$\psi = -y \sin t + \phi(x, y, t) \quad (8)$$

and determine the form of the disturbance streamfunction  $\phi$ . We first consider the linear forced and damped problem

$$\mathcal{L}(\phi) = -r \nabla^2 \phi - s \sin t h_x. \quad (9)$$

The solution is obtained by making the ansatz

$$\phi = A(t) \sin \pi y e^{ikx} \quad (10)$$

and letting  $A(t)$  have the form

$$A(t) = G(t) e^{i\eta \cos t + i\beta t - rt} \quad (11)$$

where  $\hat{\eta} = k\eta$ ,  $\hat{\beta} = k\beta/\alpha^2$  and  $\alpha^2 = \pi^2 + k^2$ . The result of these substitutions is an integral expression for  $G$

$$G(t) = i\hat{s} \int_0^t e^{-i\hat{\eta} \cos t' + \gamma t'} \sin t' dt' \quad (12)$$

where  $\hat{s} = ks/\alpha^2$  and  $\gamma = r - i\hat{\beta}$ . This integral is easily solved by integration by parts and application of the generating function for the modified Bessel function  $I_\nu$

$$e^{z \cos t} = I_0(z) + 2 \sum_{j=1}^{\infty} I_j(z) \cos jt. \quad (13)$$

The final expression for  $A$  is

$$A(t) = \frac{2\gamma\hat{s}}{\hat{\eta}} e^{i\hat{\eta} \cos t} \sum_{j=1}^{\infty} e^{-i\frac{\pi}{2}j} J_j(\hat{\eta}) \left( \frac{\gamma \cos jt + j \sin jt}{j^2 + \gamma^2} \right). \quad (14)$$

It is easy to show, by integrating over a cycle of the forcing, that the flow has a non-zero mean zonal current. The denominator inside the sum can be expanded to give

$$j^2 + \gamma^2 = j^2 - \hat{\beta}^2 + r^2 - 2ir\hat{\beta} \quad (15)$$

so, in the absence of damping, we have the resonance condition

$$j = \frac{\beta k}{\pi^2 + k^2}. \quad (16)$$

The dispersion relation (16) is shown in figure 2. Because  $j$  is restricted to integer values there are no resonant modes for  $\beta < 2\pi$ . However, for  $\beta > 2\pi$  two modes are simultaneously resonant with  $j = 1$ . For  $\beta > 4\pi$  we add the two modes that are resonant with  $j = 2$ , and so on for larger values of  $\beta$ .

We now choose the topography to consist of the two resonant modes that satisfy (16) for  $j = 1$ . Thus the topography is given by

$$h(x, y) = \sin \pi y (a_1 \cos k_1 x + a_2 \cos k_2 x). \quad (17)$$

In the introduction we claimed that this study would extend the previous work by incorporating more realistic topography. However the addition of a second mode would appear to be a modest step. We argue that because the linear solution is

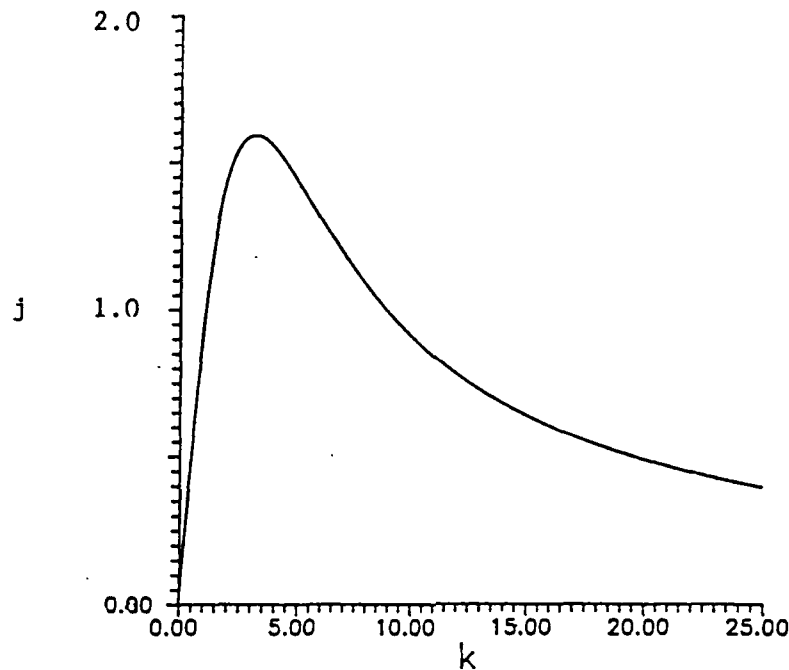


Figure 2. The dispersion relation (16).

dominated by the resonant modes, and for  $2\pi < \beta < 4\pi$  there are only two resonant modes, that in this range of  $\beta$  the two-mode problem is a good approximation to general topography. For steady flow the resonance condition is  $\alpha^2 = \beta/u_0$  where  $u_0$  is the steady zonal flow speed (cf. Pedlosky 1981). Consequently for steady flow there can only be one resonant mode. By the preceding argument, the work of the previous authors is probably a reasonable description of steady flow over general topography.

#### 4. Finite-amplitude analysis

The analysis of this section parallels that of Pedlosky (1981) who emphasized that the finite amplitude analysis of topographic waves is considerably simplified by restricting attention to the near resonant state. To do this we introduce the detuning parameter  $\Delta$  such that

$$\hat{\beta} = j + \sigma^2 \Delta \quad (18)$$

and expand the streamfunction  $\phi$  in the asymptotic series

$$\phi = \sigma \phi^{(1)} + \sigma^2 \phi^{(2)} + \dots \quad (19)$$

If we renormalize the external parameters by  $r = \sigma^2 \tilde{r}$ ,  $s = \sigma^3 \tilde{s}$ ,  $\Gamma = \sigma^3 \tilde{\Gamma}$  and separate time into a fast time,  $t$  ( $\mathcal{O}(1)$ ), and a slow time,  $\tau$  ( $\mathcal{O}(\sigma^2)$ ), then (7) becomes

$$\mathcal{L}(\phi) + \sigma^2 = -\sigma^2 \tilde{r} \nabla^2 \phi - \sigma^3 \tilde{s} \sin t h_x - \eta J(\phi, \nabla^2 \phi + \sigma^3 \tilde{\Gamma} h) \quad (20)$$

Inserting (19) in (20) yields a relatively simple hierarchy of equations for  $\phi$ .

To solve (20) we also need to consider the time and zonal average of (20)

$$\sigma^2 \overline{\phi_{yy\tau}}^{x,t} + \eta \overline{(\phi_x \nabla^2 \phi_y)}_y^{x,t} + \sigma^3 \tilde{s} \overline{(\phi_x h)}_y^{x,t} + \sigma^2 \tilde{r} \overline{\phi_{yy}}^{x,t} = 0 \quad (21)$$

to determine the slow time mean flow correction. The averages are defined by

$$\begin{aligned} \overline{(\bullet)}^x &= \lim_{L \rightarrow \infty} \frac{1}{2L} \int_{-L}^L (\bullet) dx \\ \overline{(\bullet)}^t &= \frac{1}{2\pi} \int_0^{2\pi} (\bullet) dt \end{aligned}$$

and for future reference

$$\overline{(\bullet)}^y = \int_0^1 (\bullet) dy. \quad (22)$$

The  $\mathcal{O}(\sigma)$  problem is

$$\mathcal{L}(\phi^{(1)}) = 0. \quad (23)$$

The solution of (23) is

$$\phi^{(1)} = A(\tau) \sin \pi y e^{i(k_1 \eta \cos t + t)} + B(\tau) \sin \pi y e^{i(k_2 \eta \cos t + t)}. \quad (24)$$

The goal of the subsequent analysis is to obtain an expression for the slow-time evolution of the complex amplitudes  $A$  and  $B$ .

At  $\mathcal{O}(\sigma^2)$  the problem becomes

$$\mathcal{L}(\phi^{(2)}) = -\eta J(\phi^{(1)}, \nabla^2 \phi^{(1)}). \quad (25)$$

Unlike the single topographic mode case, the Jacobian in (25) does not vanish. Instead wave-wave interactions produce sidebands whose wavenumbers are the sum

and difference of the two topographic modes. Also at this order there will be a slow-time correction to  $\phi^{(2)}$ . We represent  $\phi^{(2)}$  by

$$\phi^{(2)}(x, y, t, \tau) = \phi_s^{(2)}(x, y, t) + \Phi^{(2)}(y, \tau) \quad (26)$$

where

$$\phi_s^{(2)}(x, y, t) = \sin 2\pi y \{G_+ A B e^{ik_+ x} e^{i(k_+ \eta \cos t + 2t)} + G_- A B^* e^{ik_- x} e^{i(k_- \eta \cos t)}\} \quad (27)$$

and \* denotes the complex conjugate. Here the coefficients  $G_+$  and  $G_-$  are

$$G_+ = -\frac{\pi \eta k_+ k_-^2}{2\alpha_+^2(2 - \beta k_+/\alpha_+^2)}$$

$$G_- = \frac{\pi \eta k_+^2}{2\beta}$$

where  $k_{\pm} = k_1 \pm k_2$  and  $\alpha_{\pm}^2 = \pi^2 + k_{\pm}^2$ . From (21) it is clear that the mean zonal flow  $\Phi^{(2)}$  cannot be determined at this order. That calculation must be deferred to  $O(\sigma^4)$ .

At  $O(\sigma^3)$  the equation determining  $\phi^{(3)}$  is

$$\begin{aligned} \mathcal{L}(\phi^{(3)}) + \nabla^2 \phi_{\tau}^{(1)} &= -\bar{r} \nabla^2 \phi^{(1)} - \bar{s} \sin t h_x - \frac{\alpha_{\pm}^2 \Delta}{k_{\pm}} \phi_x^{(1)} \\ &\quad - \eta (J(\phi^{(1)}, \nabla^2 \phi^{(2)}) + J(\phi^{(2)}, \nabla^2 \phi^{(1)})). \end{aligned} \quad (28)$$

The solvability conditions for the amplitudes  $A$  and  $B$  are obtained by requiring that the terms on the right-hand side of (28) do not project onto the homogeneous solutions. The secular resonances are removed by multiplying (28) by  $\phi^{(1)*}$  and averaging over the spatial domain and one cycle of the forcing. Because

$$\overline{\phi^{(1)*} \mathcal{L}(\phi^{(3)})^{x,y,t}} = \overline{\phi^{(3)} \mathcal{L}(\phi^{(1)*})^{x,y,t}} \quad (29)$$

we have, after averaging

$$\begin{aligned} A_{\tau} + rA - i \left( \Delta + \frac{\eta}{\alpha_1^2} K_1 |B|^2 \right) A + i \frac{2\pi k_1 A}{\alpha_1^2} \times \\ \int_0^1 \sin 2\pi y (\Phi_{yy\tau}^{(2)} + \alpha_1^2 \Phi^{(2)}) dy &= \frac{\Gamma a_1}{\alpha_1^2} J_1(k_1 \eta) \\ B_{\tau} + rB - i \left( \Delta + \frac{\eta}{\alpha_2^2} K_2 |A|^2 \right) B + i \frac{2\pi k_2 B}{\alpha_2^2} \times \\ \int_0^1 \sin 2\pi y (\Phi_{yy\tau}^{(2)} + \alpha_2^2 \Phi^{(2)}) dy &= \frac{\Gamma a_2}{\alpha_2^2} J_1(k_2 \eta). \end{aligned} \quad (30)$$

The coefficients  $K_1 = K_{11} + K_{12}$  and  $K_2 = K_{21} + K_{22}$  are found from

$$\begin{aligned} K_{11} &= \pi(\alpha_-^2 G_-(k_2 + \frac{1}{2}k_-) - \alpha_+^2 G_+(k_2 - \frac{1}{2}k_+)) \\ K_{12} &= \pi k_2^2(k_2(G_+ - G_-) - \frac{1}{2}(k_+G_+ + k_-G_-)) \\ K_{21} &= \pi(\alpha_-^2 G_-(k_1 - \frac{1}{2}k_-) - \alpha_+^2 G_+(k_1 - \frac{1}{2}k_+)) \\ K_{22} &= \pi k_1^2(k_1(G_+ - G_-) - \frac{1}{2}(k_+G_+ - k_-G_-)). \end{aligned}$$

To close the problem (31) we need an expression relating  $\Phi^{(2)}$  and the amplitudes. To do this it is necessary to consider (21) at  $\mathcal{O}(\sigma^4)$

$$\Phi_{yy\tau}^{(2)} + \bar{\tau}\Phi_{yy}^{(2)} = -\eta(\overline{\phi_x^{(1)}\nabla^2\phi^{(3)} + \phi_x^{(3)}\nabla^2\phi^{(1)}})^{x,t}. \quad (31)$$

As noted by Pedlosky (1981) it is not necessary to solve for  $\phi^{(3)}$  explicitly. Instead multiply (28) by  $\nabla^2\phi^{(1)}$  and (23) by  $\nabla^2\phi^{(3)}$ . Adding these two equations and averaging over  $x$  and  $t$  yields

$$\overline{\phi_x^{(1)}\nabla^2\phi^{(3)} + \phi_x^{(3)}\nabla^2\phi^{(1)}}^{x,t} = -\frac{1}{2\beta}((\nabla^2\phi^{(1)})_\tau^2)^{x,t} + 2\bar{\tau}(\nabla^2\phi^{(1)})^2)^{x,t}. \quad (32)$$

Using the result

$$(\nabla^2\phi^{(1)})^2)^{x,t} = 2\alpha_1^4|A|^2\sin^2\pi y + 2\alpha_2^4|B|^2\sin^2\pi y \quad (33)$$

and combining (31) and (32) we find

$$\Phi_{yy\tau}^{(2)} + \bar{\tau}\Phi_{yy}^{(2)} = \frac{\pi\eta}{\beta}\sin 2\pi y\{\alpha_1^4(|A|^2 + 2\bar{\tau}|A|^2) + \alpha_2^4(|B|^2 + 2\bar{\tau}|B|^2)\}. \quad (34)$$

Combining the product of  $A^*$  and (31) with  $A$  times the complex conjugate of (31) we obtain

$$|A|_\tau^2 + 2\bar{\tau}|A|^2 = \frac{2\tilde{\Gamma}a_1}{\alpha_1^2}J_1(k_1\eta)A_r \quad (35)$$

where  $A = A_r + iA_i$ . A similar expression is obtained for  $B$ . Now using (35) in (34) we have

$$\Phi_{yy\tau}^{(2)} + \bar{\tau}\Phi_{yy}^{(2)} = \frac{2\pi\tilde{s}}{\beta}\sin 2\pi y\{a_1\alpha_1^2J_1(k_1\eta)A_r(\tau) + a_2\alpha_2^2J_1(k_2\eta)B_r(\tau)\}. \quad (36)$$

From (36) it is apparent that  $\Phi^{(2)}(y, \tau)$  can be separated. Let

$$\Phi^{(2)}(y, \tau) = \frac{1}{4\pi}(\sin 2\pi y - 2\pi y)U(\tau). \quad (37)$$

Using (37) to evaluate the integrals in (31) and to obtain an evolution equation for  $U$  in (34) we derive the following set of five amplitude equations

$$\begin{aligned} \dot{A}_r + \bar{r}A_r + (\Delta + \eta \frac{K_1}{\alpha_1^2}|B|^2 + (\frac{k_1}{4} - \frac{\pi^2 k_1}{\alpha_1^2})U)A_i &= \frac{\bar{\Gamma}a_1}{\alpha_1^2}J_1(k_1\eta) \\ \dot{A}_i + \bar{r}A_i + (\Delta + \eta \frac{K_1}{\alpha_1^2}|B|^2 + (\frac{k_1}{4} - \frac{\pi^2 k_1}{\alpha_1^2})U)A_i &= 0 \\ \dot{B}_r + \bar{r}B_r + (\Delta + \eta \frac{K_2}{\alpha_2^2}|A|^2 + (\frac{k_2}{4} - \frac{\pi^2 k_2}{\alpha_2^2})U)B_i &= \frac{\bar{\Gamma}a_2}{\alpha_2^2}J_1(k_2\eta) \\ \dot{B}_i + \bar{r}B_i + (\Delta + \eta \frac{K_2}{\alpha_2^2}|A|^2 + (\frac{k_2}{4} - \frac{\pi^2 k_2}{\alpha_2^2})U)B_r &= 0 \\ \dot{U} + \bar{r}U &= \frac{2\bar{s}}{\beta}(a_1\alpha_1^2J_1(k_1\eta)A_r + a_2\alpha_2^2J_1(k_2\eta)B_r). \end{aligned} \quad (38)$$

We can simplify (39) by rescaling the variables. Introducing the new variables

$$\begin{aligned} A &= \frac{\bar{\Gamma}a_1}{\alpha_1^2}J_1(k_1\eta)\tilde{A} \\ B &= \frac{\bar{\Gamma}a_2}{\alpha_2^2}J_1(k_2\eta)\tilde{B} \\ U &= -\frac{2\bar{s}\bar{\Gamma}}{\beta}a_1^2J_1^2(k_1\eta)\tilde{U} \\ \kappa_{1,2} &= \frac{\eta\bar{\Gamma}^2K_{1,2}a_{2,1}^2}{\alpha_{1,2}^2\alpha_{2,1}^4}J_1(k_{2,1}\eta) \\ P_{1,2} &= \frac{2\bar{s}\bar{\Gamma}a_{1,2}}{\beta}\left(\frac{k_{1,2}}{4} - \frac{\pi^2 k_{1,2}}{\alpha_{1,2}^2}\right)J_1^2(k_{1,2}\eta) \\ \chi &= \frac{a_2^2J_1^2(k_2\eta)}{a_1^2J_1^2(k_1\eta)} \end{aligned}$$

gives

$$\begin{aligned} \dot{\tilde{A}}_r + \bar{r}\tilde{A}_r + (\Delta + \kappa_1|\tilde{B}|^2 - P_1\tilde{U})\tilde{A}_i &= 1 \\ \dot{\tilde{A}}_i + \bar{r}\tilde{A}_i + (\Delta + \kappa_1|\tilde{B}|^2 - P_1\tilde{U})\tilde{A}_r &= 0 \end{aligned}$$



$$\begin{aligned}
\dot{\tilde{B}}_r + \tilde{r}\tilde{B}_r + (\Delta + \kappa_2|\tilde{A}|^2 - P_2\tilde{U})\tilde{B}_i &= 1 \\
\dot{\tilde{B}}_i + \tilde{r}\tilde{B}_i + (\Delta + \kappa_2|\tilde{A}|^2 - P_2\tilde{U})\tilde{B}_r &= 0 \\
\dot{\tilde{U}} + \tilde{r}\tilde{U} - \tilde{A}_r - \chi\tilde{B}_r &= 0
\end{aligned} \tag{39}$$

Analysis of the structure of (39) will constitute the remainder of the paper.

### 5. Multiple equilibria

We are interested in finding the stationary solutions of (39). Therefore we set all time derivatives equal to zero. We now wish to write (39) (suppressing the tildes) as a single equation. Combining the  $A_r$  and  $A_i$  equations we get the two relations

$$r|A|^2 = A_r \tag{40}$$

$$r^2|A|^2\left(r + \frac{1}{r}(\Delta + \kappa_1|B|^2 - P_1U)^2\right) = 1. \tag{41}$$

Similarly

$$r|B|^2 = B_r \tag{42}$$

$$r^2|B|^2\left(r + \frac{1}{r}(\Delta + \kappa_2|A|^2 - P_2U)^2\right) = 1. \tag{43}$$

Using (40) and (42) to rewrite the expression for  $U$  and substituting in (41) and (43) we find

$$|A|^2(r^2 + (\Delta - \lambda_1|A|^2 - \lambda_2|B|^2)^2) = 1 \tag{44}$$

$$|B|^2(r^2 + (\Delta - \lambda_3|A|^2 - \lambda_4|B|^2)^2) = 1 \tag{45}$$

where  $\lambda_1 = P_1$ ,  $\lambda_2 = \chi - \kappa_1$ ,  $\lambda_3 = P_2 - \kappa_2$ ,  $\lambda_4 = P_2\chi$ . We can eliminate  $\lambda_1$  by the rescaling

$$H = \lambda_1^{2/3}|A|^2$$

$$I = \lambda_1^{2/3}|B|^2$$

$$\hat{r}^2 = \lambda_1^{-2/3}r^2$$

$$\hat{\Delta} = \lambda_1^{-1/3}\Delta$$

so now

$$\begin{aligned}
H(\hat{r}^2 + (\hat{\Delta} - H - c_1I)^2) &= 1 \\
I(\hat{r}^2 + (\hat{\Delta} - c_2H - c_3I)^2) &= 1
\end{aligned} \tag{46}$$

where  $c_1 = \lambda_2/\lambda_1$ ,  $c_2 = \lambda_3/\lambda_1$ ,  $c_3 = \lambda_4/\lambda_1$ .

First we examine the case in which the amplitude of the second topographic mode becomes small. In this case  $c_1$  and  $c_3$  go to zero like  $(a_2/a_1)^2$  and we recover the one-mode equation of Pedlosky (1981)

$$H(\hat{r} + (\hat{\Delta} - H)^2) = 1. \quad (47)$$

We now calculate the domain in  $(\hat{\Delta}, \hat{r})$  space in which multiple stationary equilibria are found. Rewriting (47) as

$$F(H) = \frac{1}{\hat{r} + (\hat{\Delta} - H)^2} = H \quad (48)$$

we can calculate the transition from one to three solutions by requiring that

$$\begin{aligned} F'(H) &= 1 \\ F(H) &= H. \end{aligned}$$

From these constraints we derive a set of parametric equations that defines the border between the one and three solutions states

$$\hat{r}^2 = \frac{1}{H} - \frac{1}{4H^2} \quad (49)$$

$$\hat{\Delta} = H + \frac{1}{2H^2}. \quad (50)$$

The restriction that  $\hat{r}^2$  be positive restricts  $H \geq (1/4)^{1/3}$ . At  $H = (1/4)^{1/3}$   $\hat{\Delta}$  is  $\approx 1.8899$ . For large  $H$ ,  $\hat{\Delta} \approx H$  so  $\hat{r}^2 \approx 1/\hat{\Delta}$ . Furthermore  $\hat{r}_{\max}^2 = 3/4$  and  $\hat{\Delta}_{\min} = 3/2$ . These two values occur for the same value of  $H$  ( $H = 1$ ). This implies that the point  $(\hat{\Delta}, \hat{r}^2)$  is a cusp. The curve given by (49) and (50) is shown in figure 3. From this curve it is apparent that at large values of the detuning multiple equilibria will be found only if  $\hat{r}^2$  is quite small.

A general solution of (46) can, in principle, be found in a similar way. This solution can possess up to nine real roots. As before

$$\hat{r}^2 = \frac{1}{H} - \frac{1}{4H^2} \quad (51)$$

but now we must solve

$$\hat{\Delta}^3 - (F + 2c_2H)\hat{\Delta}^2 + (\hat{r}^2 + c_2H^2 + 2c_2F)\hat{\Delta} - F(\hat{r}^2 + c_2H) - c_1 = 0. \quad (52)$$

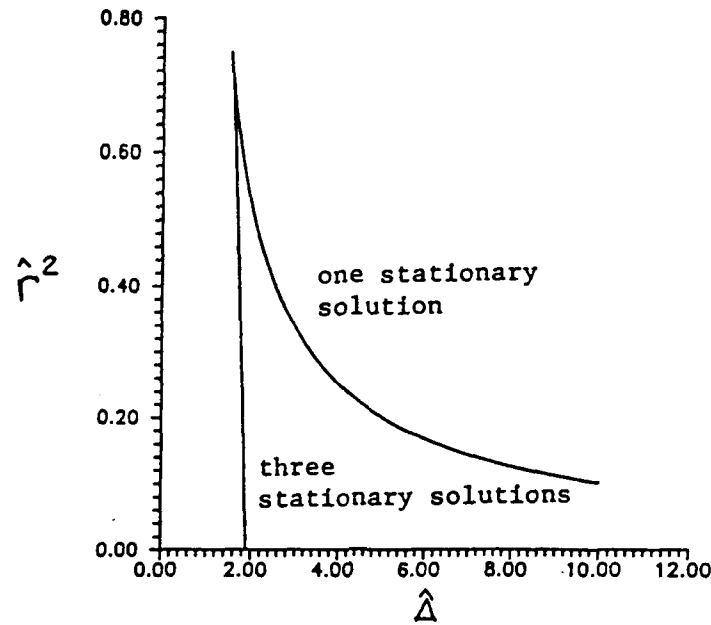


Figure 3. The domain of multiple equilibria for the one-wave case.

Rather than solve this cubic we look at the behavior in some limiting cases. For the sake of illustration consider the situation  $c_1 > 0$ ,  $c_2, c_3 \rightarrow 0$ . Equations (49) and (50) become

$$\begin{aligned}\hat{r}^2 &= \frac{1}{H} - \frac{1}{4H^4} \\ \tilde{\Delta} &= \hat{\Delta} - \frac{c_1}{\hat{\Delta}^2 + \hat{r}^2} = H + \frac{1}{2H^2}.\end{aligned}\quad (53)$$

The relationship for  $\tilde{\Delta}$  is identical to (50). It is possible to estimate the stretching of the multiple equilibria domain by evaluating

$$\tilde{\Delta} = \hat{\Delta} - \frac{c_1}{\hat{\Delta}^2 + \hat{r}^2} \quad (54)$$

For large values of  $\hat{\Delta}$ ,  $\hat{\Delta} \approx \tilde{\Delta}$ , so the effect of multiple resonances is small. However, at small values of  $\hat{\Delta}$  there will be a stretching and shifting of the boundary. For  $c_1 > 0$  the shift is towards larger values of  $\hat{\Delta}$ . Equation (53) has been calculated numerically. The results are shown in figure 4. We note that for  $c_2$  and  $c_3$  small requires that  $c_1$  be small as well. Consequently the effect of multiple resonances in this flow is quite small. However we note that for other multiple resonances (e.g. multiple cross-stream modes) this may not be the case.

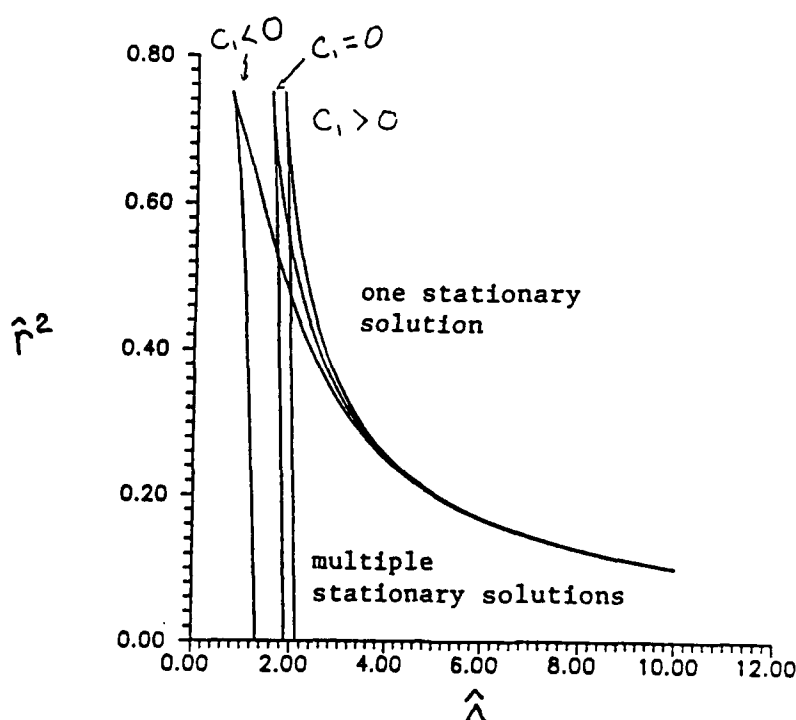


Figure 4. The effect of two resonant modes on the parameter domain of multiple equilibria in the limit  $c_2 = 0$  and  $c_3 \ll 1$ .

Although multiple resonant modes do not modify the domain of multiple equilibria substantially there is increased structure inside this domain. This is because there are up to nine stationary states inside the domain as opposed to just three for the single wave case. This internal structure is shown in figure 5 where the number of roots has been determined numerically. Note that in figure 5b the boundary has become more complicated by the addition of a second spike.

Finally we consider a special case to illustrate how the nine roots arise. Consider (46) in the limit  $c_1, c_3$  small and  $c_2$  large. In this case we have

$$H \left( \hat{r}^2 + \left( \hat{\Delta} - H - c_1 \left( \frac{1}{\hat{r}^2 + (\hat{\Delta} - c_2 H)^2} \right) \right)^2 \right) = 1. \quad (55)$$

For  $c_1 = 0$  there are three roots of  $H$  but for  $c_1$  nonzero there must be nine roots. The effect of this additional term, when  $c_1$  is small, is to "split" the three basic roots into three triples of roots.



## 6. Discussion

In this paper we have derived a general set of equations that determine the structure of flows with two resonant modes. Here we have investigated a case in which one meridional and two zonal modes contribute to the resonance. However it is possible for two meridional modes and one zonal mode to satisfy (16). The zonal wave number must be

$$k^2 = \frac{(j_1 m_1^2 - j_2 m_2^2) \pi^2}{j_2 - j_1} \quad (56)$$

where the  $m$ 's are the meridional wave numbers and the  $j$ 's are integers.

Elucidation of the multiple equilibria boundary, as determined by (46), for realistic parameter values probably requires detailed numerical investigation. In addition a determination of the stability of the solutions is necessary to understand the mathematical equations (46) as a model for a physical system. One or more steady solutions appear to exist for all parameter values. If this steady solution is stable the Eulerian flow will be regular. However if there is a regime for which the steady solution is unstable the Eulerian flow may be chaotic.

As mentioned in the introduction the behavior of Lagrangian trajectories may be chaotic even if the Eulerian flow is simple. Figure 6 contrasts the structure of the two stable solutions of the one-wave amplitude equations that are found for fixed parameter values as determined by stroboscopic portraits of Lagrangian particles. In both panels there is a mixture of regular and chaotic orbits, however, it is clear that figure 6a is more regular than figure 6b. It is of fundamental interest in fluid mechanics (and a critical issue in oceanography) to determine if Lagrangian particles are sensitive to transitions in the Eulerian flow. For example can drifter trajectories be used to signal changes in the amplitude equations from steady solutions to limit cycles to chaos?

**Acknowledgements.** This work is the product of a collaborative effort with John Hart. I thank John for the time and effort spent with me to make these results possible. Jack Whitehead and Bob Frazel provided laboratory space and technical assistance for experiments not presented here. Finally I would like to express my appreciation to the GFD staff and, especially, to the other fellows for their substantial contributions to an enjoyable and productive summer.

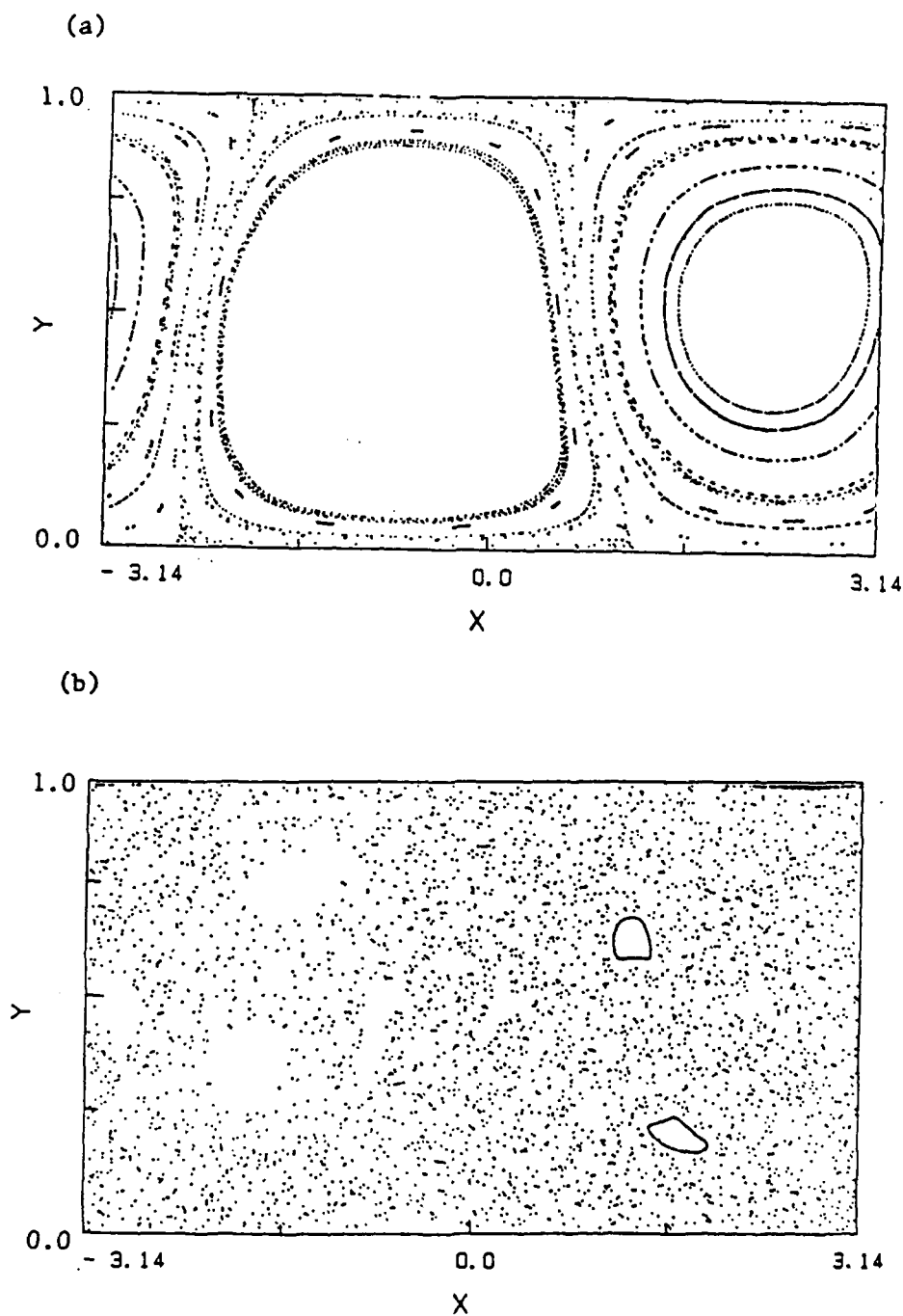


Figure 6. Poincaré sections for the two stable steady solutions with  $\hat{r}^* = 0.1, \hat{\Delta} = 1.0$ . (a) corresponds to the "blocked" state.

## References

- Charney, J. G. & DeVore, J. G. 1979 Multiple flow equilibria in the atmosphere and blocking. *J. Atmos. Sci.* **36**, 1205-1216.
- Hart, J. E. 1979 Barotropic quasi-geostrophic flow over anisotropic mountains. *J. Atmos. Sci.* **36**, 1736-1746.
- Hart, J. E. 1989 On oscillatory flow over topography in a rotating fluid. Submitted *J. Fluid Mech.*
- Pedlosky, J. 1981 Resonant topographic waves in barotropic and baroclinic flows. *J. Atmos. Sci.* **38**, 2626-2641.
- Samelson, R. M. & Allen, J. S. 1987 Quasi-geostrophic topographically generated mean flow over the continental margin. *J. Phys. Oceanogr.* **17**, 2043-2064.



# The Parametric Model of Western Boundary Outflow

Roland Mallier

An infinite system of coupled ordinary differential equations governing the visco-inertial western-boundary layer in a two-dimensional one-layer model of the large-scale ocean circulation is presented and truncations of this system at first and second order are discussed. It is found that the second order truncation has pole-like structures present for an ocean basin with infinite aspect ratio. Numerical calculations for the non-infinite aspect ratio suggest that there is a possibility that the infinite aspect ratio may be a singular limit.

## 1. Introduction

Perhaps one of the best known features of the large-scale circulation in an ocean is "westward intensification", the boundary-layer that arises near the western boundary of an ocean, with the Gulf Stream being probably the most famous manifestation of this; the separation of the Gulf Stream is a particularly fascinating phenomenon. Various simple models of the ocean circulation, such as those due to Stommel (1948) and Munk (1950), which display this westward intensification have been constructed and it is these simple models with which we shall work and to which we shall seek to apply boundary-layer techniques, of the kind first used by Goldstein (1930), which are more usually found in areas such as mechanical engineering with the hope that we will be able to shed some light on the phenomenon of separation and the onset of recirculation. The report is set out as follows: in §2 we shall derive the basic equations and review the first order analysis, which we shall attempt to extend to higher orders in §3. In §4 we present a simple model which displays some of the behavior that arises from the boundary-layer analysis. A brief appendix summarizes our numerical techniques.

## 2. The First Order Analysis

In this section we will examine the visco-inertial boundary-layer which arises at the western boundary in a two-dimensional one-layer model of the large-scale circulation in an ocean [for a review of such models, the reader is referred to the principal lecture in this volume by M.C.Hendershott]. We will concentrate on two

such models: the Stommel or "bottom drag" model (Stommel, 1948) in which the frictional forces are represented by an effective bottom drag  $-r\nabla^2\psi$  so that we can write the time independent potential vorticity equation as

$$J(\psi, q) = W - r\nabla^2\psi \quad (1)$$

which we will examine from a largely analytical standpoint; and the Munk or lateral friction model (Munk, 1950) in which the viscous terms are represented by lateral friction  $\frac{1}{Re}\nabla^4\psi$  so that the time independent potential vorticity equation becomes

$$J(\psi, q) = W + \frac{1}{Re}\nabla^4\psi \quad (2)$$

which we will examine from a largely numerical standpoint. Here of course  $q = \nabla^2\psi + \beta y$  is the potential vorticity,  $J(a, b) = \partial_x a \partial_y b - \partial_y a \partial_x b$  is the Jacobian and  $W = \beta \text{curl} r$  is the curl of the wind stress. We can write  $J(\psi, q)$  as

$$J(\psi, q) = J(\psi, \nabla^2\psi) + \beta\psi_x \quad (3)$$

where  $\beta\psi_x$  is the Coriolis acceleration.

To make the problem considerably more tractable we will restrict our attention to a zonally uniform interior (Welander, 1976) with the flow in the interior given by

$$\psi = 2 \cos\left(\frac{\pi y}{2L_y}\right) \quad (4)$$

and the curl of the wind stress by

$$W = r\nabla^2\psi = -W_s \cos\left(\frac{\pi y}{2L_y}\right) \quad (5)$$

for the Stommel case and

$$W = -\frac{1}{Re}\nabla^4\psi = -W_m \cos\left(\frac{\pi y}{2L_y}\right) \quad (6)$$

for the Munk case where

$$W_s = \frac{r\pi^2}{2L_y^2} \quad \text{and} \quad W_m = \frac{\pi^4}{8ReL_y^4} \quad (7)$$

We will suppose that the western boundary of our ocean lies at  $x = -1$ . As  $\psi|_{x=-1} \neq \text{const}$ , clearly to satisfy the boundary condition a boundary-layer is required at  $x = -1$  in which  $x$  derivatives are assumed to be substantially greater than  $y$  derivatives

$$\frac{\partial}{\partial x} \gg \frac{\partial}{\partial y}. \quad (8)$$

In this layer we will seek to balance the viscous term  $\frac{1}{Re} \nabla^4 \psi$  or  $-r \nabla^2 \psi$  and the Coriolis acceleration  $\beta \psi_x$ . We will introduce stretched boundary-layer coordinates  $\xi$  and  $\eta$  about the wall ( $x = -1$ ) and  $y = -L_y$  where the curl of the wind stress vanishes. The position  $y = -L_y$  is chosen because

$$\left[ \frac{\partial^{2n}}{\partial y^{2n}} \cos \left( \frac{\pi y}{2L_y} \right) \right] |_{y=-L_y} = 0 \quad (9)$$

for  $n$  an integer so that a Taylor series in  $y$  about that point has a particularly simple form. We will set

$$\xi = \frac{x+1}{\delta} \quad \text{and} \quad \eta = \frac{y+L_y}{L_y} \quad (10)$$

and denoting

$$\lambda = \frac{\pi}{\beta L_y \delta^2} \quad \text{and} \quad \varepsilon = \left( \frac{\delta}{L_y} \right)^2 \quad (11)$$

the balance of terms tells us that

$$\delta_S = \frac{r}{\beta} \quad \text{and} \quad \delta_M = (\beta Re)^{-\frac{1}{3}} \quad (12)$$

[for those readers more familiar with the scalings used in Pedlosky (1979),  $\lambda$  is equivalent to  $\pi \left( \frac{\delta_I}{\delta_M} \right)^2$ , where  $\delta_I$  is the inertial boundary layer thickness, and may be thought of as a measure of the nonlinearity of the equations] so that we recover

$$\psi_\xi + \frac{\lambda}{\pi} J(\psi, \nabla_{BL}^2 \psi) = -\frac{\pi^2 \varepsilon}{2} \sin \left( \frac{\pi \eta}{2} \right) - \nabla_{BL}^2 \psi \quad (13)$$

for the Stommel case and

$$\psi_\xi + \frac{\lambda}{\pi} J(\psi, \nabla_{BL}^2 \psi) = -\frac{\pi^4 \varepsilon^2}{8} \sin \left( \frac{\pi \eta}{2} \right) + \nabla_{BL}^4 \psi \quad (14)$$

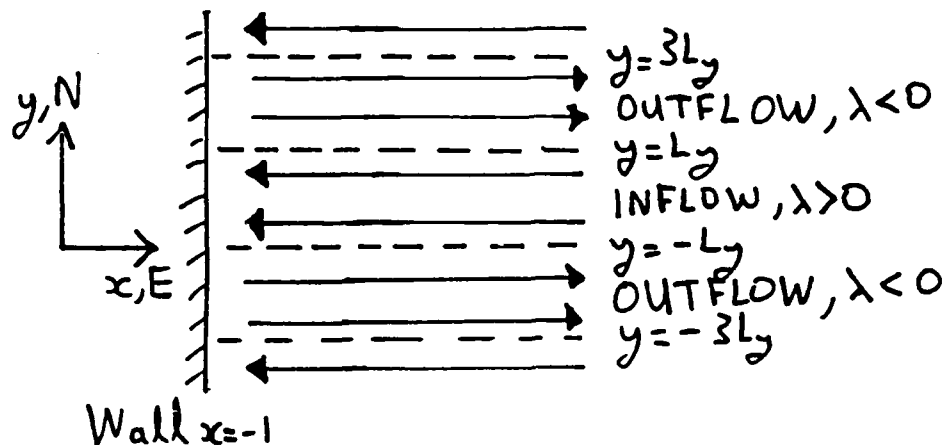


Figure 1: The geometry of our problem in unstretched coordinates.

for the Munk case where

$$\nabla_{BL}^2 \psi = (\partial_{\xi\xi}^2 + \varepsilon \partial_{\eta\eta}^2) \psi \quad (15)$$

with boundary conditions that  $\psi \rightarrow \psi_\infty = 2 \sin\left(\frac{\pi\eta}{2}\right)$  as  $\xi \rightarrow \infty$ ,  $\psi_\xi \rightarrow 0$  as  $\xi \rightarrow \infty$  and  $\psi|_{\xi=0} = 0$  with an additional condition for the Munk case that either  $\partial_\xi \psi|_{\xi=0} = 0$  for no-slip boundaries or  $\partial_{\xi\xi}^2 \psi|_{\xi=0} = 0$  for slip boundaries. [We require an additional boundary condition for the lateral friction case because the presence of  $\nabla_{BL}^4 \psi$  as opposed to  $-\nabla_{BL}^2 \psi$  in the bottom drag case means that the governing equation is fourth order as opposed to third order in  $\xi$ .]

The observant reader will note that physically  $\lambda$  is always a positive quantity. However, we could equally well have taken  $\eta = \frac{y-L_y}{L_y}$  which corresponds to an outflow region as opposed to the region of inflow which we have chosen to consider above and this would effectively change the sign of  $\lambda$  and hence we can think of  $\lambda > 0$  as corresponding to an inflow and of  $\lambda < 0$  as corresponding to an outflow. As we shall see at a later stage, the sign of  $\lambda$  does make a significant difference to the problem. The geometry of the problem is shown schematically in figure 1.

As  $\eta \rightarrow 0$ ,  $\psi_\infty \sim \pi\eta$  and we will suppose initially following Ierley & Ruehr (1986) [to which we shall refer hereafter as I&R] that this leading order term determines

the flow in the boundary-layer and set  $\psi = \pi\eta\phi_0(\xi)$ . Take  $\varepsilon = 0$ . This gives us

$$\phi_0' + \lambda(\phi_0'\phi_0'' - \phi_0\phi_0''') = -\phi_0'' \quad (16)$$

for the Stommel case where  $\phi_0' \equiv \partial_\xi \phi_0$  and

$$\phi_0' + \lambda(\phi_0'\phi_0'' - \phi_0\phi_0''') = \phi_0''' \quad (17)$$

for the Munk case with boundary conditions that  $\phi_0(0) = 0$ ,  $\phi_0(\xi) \rightarrow 1$  as  $\xi \rightarrow \infty$  and  $\phi_0'(\xi) \rightarrow 0$  as  $\xi \rightarrow \infty$  and for the Munk case in addition that either  $\phi_0'(0) = 0$  (no-slip) or  $\phi_0''(0) = 0$  (slip). Integrating these equations once from  $\xi$  to  $\infty$  with respect to  $\xi$  using the extra condition that  $\phi_0''(\infty) = \phi_0'''(\infty) = 0$  yields

$$\phi_0 - 1 + \lambda(\phi_0'^2 - \phi_0\phi_0'') = -\phi_0' \quad (18)$$

for the Stommel case and

$$\phi_0 - 1 + \lambda(\phi_0'^2 - \phi_0\phi_0'') = \phi_0''' \quad (19)$$

for the Munk case. The latter equation is the parametric model studied by I&R and also Il'in & Kamenkovich (1964).

The bottom drag case has an exact solution

$$\phi_0 = 1 - e^{-\mu\xi} \quad (20)$$

where  $\lambda\mu^2 + \mu - 1 = 0$  or

$$\mu = \frac{-1 \pm \sqrt{1 + 4\lambda}}{2\lambda}, \quad (21)$$

so for a solution to exist we need  $1 + 4\lambda \geq 0$ , i.e.

$$\lambda \geq \lambda_c = -\frac{1}{4} \quad (22)$$

and we can also note that for  $-\frac{1}{4} < \lambda < 0$  there are two solutions arising from the  $\pm$  in the above formula for  $\mu$ .

In the Munk case,  $\lambda = 0$  corresponds to the linear Munk problem with solutions

$$\phi_0(\xi) = 1 - e^{-\frac{1}{2}\xi} \left[ \cos\left(\frac{\sqrt{3}}{2}\xi\right) + \frac{1}{\sqrt{3}} \sin\left(\frac{\sqrt{3}}{2}\xi\right) \right] \quad (23)$$

for no-slip boundaries and

$$\phi_0(\xi) = 1 - e^{-\frac{1}{2}\xi} \left[ \cos\left(\frac{\sqrt{3}}{2}\xi\right) - \frac{1}{\sqrt{3}} \sin\left(\frac{\sqrt{3}}{2}\xi\right) \right] \quad (24)$$

for slip boundaries. The Munk case has been extensively studied numerically by Il'in & Kamenkovich (1964) and I&R with the latter work containing substantial analytical work in addition to the computations. It was demonstrated that just as in the bottom drag case there was a critical value of  $\lambda$ ,  $\lambda_c$  below which no solutions existed; I&R give values for  $\lambda_c$  of  $-0.79130$  for the no-slip case and  $-0.29657$  for the slip case. It was also shown that for both boundary conditions there are two solutions for  $\lambda_c < \lambda < 0$  and that for the slip case there are also two solutions for  $\lambda > 0$ . In the course of this project we have found a possible second solution for  $\lambda > 0$  for the no-slip case but further tests must yet be performed to verify that this is a solution of the parametric equation involved and not merely a solution of the numerical discretization used. In either case it must be emphasized that when more than one solution exists only one of these solutions is stable and physical; any other solutions that might exist are unstable and unphysical. The results of I&R are shown in figures 2(a) and (b) for no-slip and slip boundaries respectively where they plot a parameter they christen  $\beta$  as a function of  $\lambda$ ;  $\beta$  here is the lowest derivative of  $\phi_0$  which has not been specified at  $\xi = 0$ ; for the no-slip case both  $\phi_0(0)$  and  $\phi'_0(0)$  are specified so that  $\beta = \phi''_0(0)$  and similarly for the slip case  $\beta = \phi'_0(0)$ . In deference to the oceanographers present (and under intense pressure from Bill Young) I will rechristen this parameter  $\beta$  as  $S$ .

Our attempts to reproduce figures 2(a) and (b) are shown in figures 3(a) and (b) respectively; our possible new branch is evident in figure 3(a) and it can be seen that for small negative  $\lambda$  our code is producing some peculiar results for the no-slip case. Our code differed from that used in I&R in that we solved the fourth order equation directly rather than using the third order equation which we obtained from integrating once with respect to  $\xi$  as was done there; we did this to ensure that our results from this section were strictly comparable with other parts of this project and, because of the nature of the solutions [they contain exponential oscillations as  $\xi \rightarrow \infty$ ], as far as accuracy of the results is concerned the fewer derivatives one takes the better. It can also be observed that the slip case appears to behave in a more

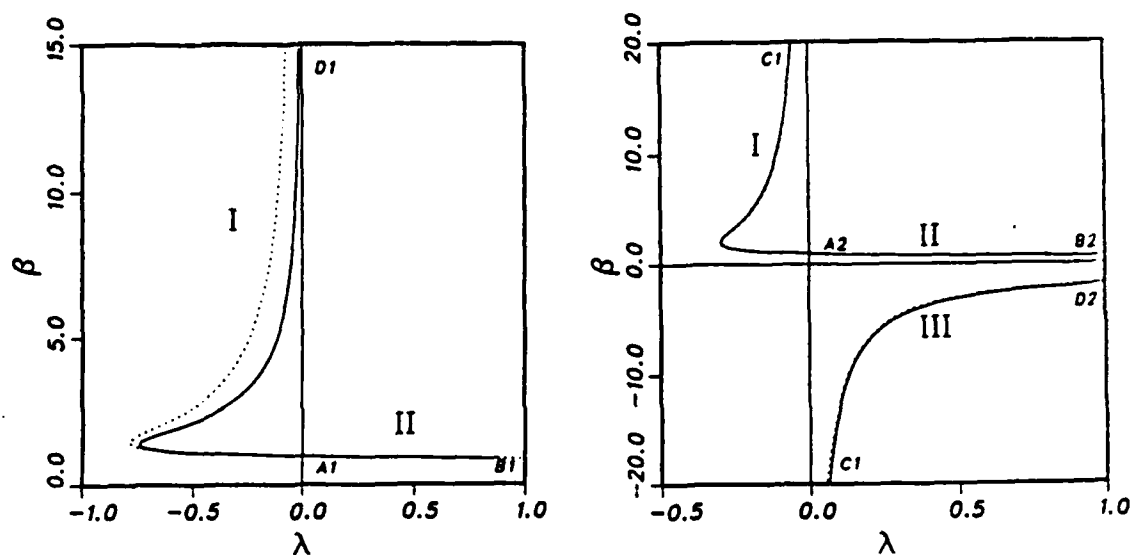


Figure 2: (a) no-slip boundaries,  $\phi_0''(0) = \beta(\lambda)[= S(\lambda)]$ . (b) slip boundaries,  $\phi_0'(0) = \beta(\lambda)[= S(\lambda)]$ . In both cases, actual  $\beta$  shown as a solid line, theoretical prediction from a continued fraction shown as a dotted line. [From I&R.]

orderly fashion than the no-slip case and this appears to be true to a certain extent of this project as a whole. [Details of the numerical techniques used are contained in the appendix.]

These solutions can also be plotted in physical space and again we will show the results obtained by I&R where they plot  $\phi_0(\xi)$  as a function of  $\xi$ . These results are shown in figures 4 to 6 with our possible new branch shown in figure 7. The parametric description of the solutions is split into the upper (singular) branch which is labelled I in figures 2(a) and (b), the lower branch (II) and the bottom branch (III). In both cases it is branch II that is stable. Several differences between the two boundary conditions are apparent, one being that for the upper branches both peak height and location depend upon the value of  $\lambda$  in the no-slip case whereas in the slip case only the peak height depends upon  $\lambda$ . Figures 6 and 7, the lower branches (III) for  $\lambda > 0$ , would appear to correspond to a southward flow immediately adjacent to the wall in the boundary-layer. This arises because in our formulation, as can be seen from figure 1, both a northward and a southward flow from regions of inflow to regions of outflow are possible. It should be recalled, however, that this particular branch (III) is both unstable and unphysical.

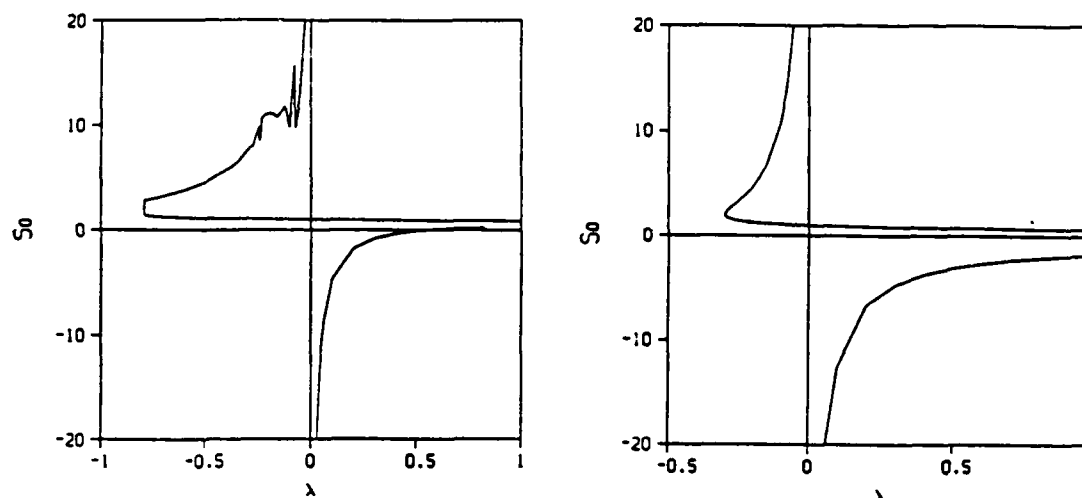


Figure 3: Our attempt to reproduce figures 2(a) and (b) respectively.

### 3. Higher Order Analysis

We have seen that for both the Stommel and Munk cases there is a critical value of  $\lambda$ ,  $\lambda_c$ , such that for  $\lambda < \lambda_c$  these parametric models have no solutions. In a series of numerical experiments with a lateral friction regional model Ierley (1987) found that for a sufficiently large ratio of basin scale to viscous boundary-layer scale, that is for sufficiently small  $\epsilon$ , there is very good agreement between the failure of the boundary-layer model, that is  $\lambda < \lambda_c$ , and the onset of recirculation in the solution of the partial differential equations. However, for less extreme basin ratios, that is for larger  $\epsilon$ , the onset of recirculation was deferred; this would seem to suggest that  $\lambda_c$  depends upon the ratio  $\epsilon = \left(\frac{\delta_M}{L_v}\right)^2$ . In figures 8(a) and (b) we show some of the results from Ierley (1987) for a slip boundary and  $\lambda = -0.7$  [recall that  $\lambda_c = -0.29657$  for  $\epsilon = 0$ ]. It is clear that even for these extremely small values of  $\epsilon$  there has been a substantial increase in the range of outflow values and Ierley (1987) makes a very crude estimate of  $\lambda_c(\epsilon) \sim \lambda_c|_{\epsilon=0} - 70\epsilon^{\frac{1}{2}}$ .

We will try to predict this dependence upon  $\epsilon$  by keeping  $y$  derivatives in the equation. We will take a Taylor series about  $\eta = 0$  of the streamfunction that we match onto as  $\xi \rightarrow \infty$ ,  $\psi_\infty = 2 \sin\left(\frac{\pi\eta}{2}\right)$

$$\psi_\infty \sim \pi\eta \sum_{n=0}^{\infty} \eta^{2n} \left(\frac{\pi}{2}\right)^{2n} \frac{(-1)^n}{(2n+1)!}. \quad (25)$$



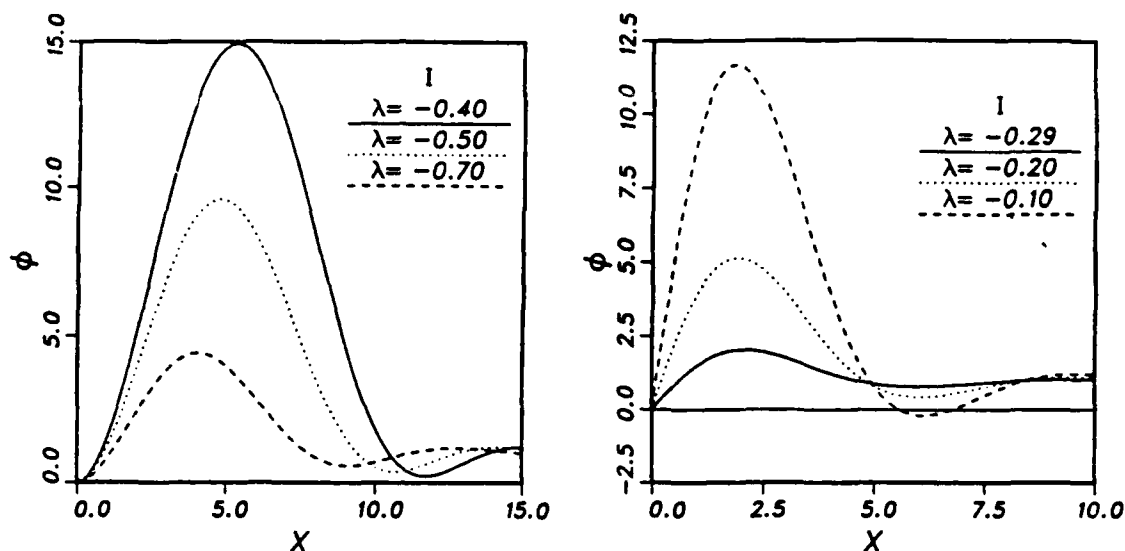


Figure 4: Upper-branch solutions at three values of  $\lambda$ . (a) no-slip: both peak height and location depend upon  $\lambda$ . (b) slip: peak height but not location depends upon  $\lambda$ . [From I&R.]

This suggests that we might follow the procedure suggested by Goldstein (1930) and seek a solution in the boundary-layer of the form

$$\psi \sim \pi \eta \sum_{n=0}^{\infty} \eta^{2n} \phi_n(\xi). \quad (26)$$

Then at  $\mathcal{O}(\eta^{2n+1})$  we obtain, again denoting  $\phi'_n \equiv \partial_\xi \phi_n$ ,

$$\begin{aligned} \phi'_n &+ \lambda \sum_{m=0}^n \left[ (2m+1) \phi'_{n-m} \phi''_m - (2n-2m+1) \phi_{n-m} \phi'''_m \right] \\ &+ \varepsilon \lambda \sum_{m=0}^n (2m+2)(2m+3)(2m+1) \phi'_{n-m} \phi_{m+1} \\ &- \varepsilon \lambda \sum_{m=0}^n (2m+2)(2m+3)(2n-2m+1) \phi_{n-m} \phi'_{m+1} \\ &= - \left( \frac{\pi}{2} \right)^{2n+2} \frac{\varepsilon (-1)^n}{(2n+1)!} - \phi''_n - \varepsilon (2n+2)(2n+3) \phi_{n+1} \end{aligned} \quad (27)$$

for the bottom drag case and

$$\phi'_n + \lambda \sum_{m=0}^n \left[ (2m+1) \phi'_{n-m} \phi''_m - (2n-2m+1) \phi_{n-m} \phi'''_m \right]$$

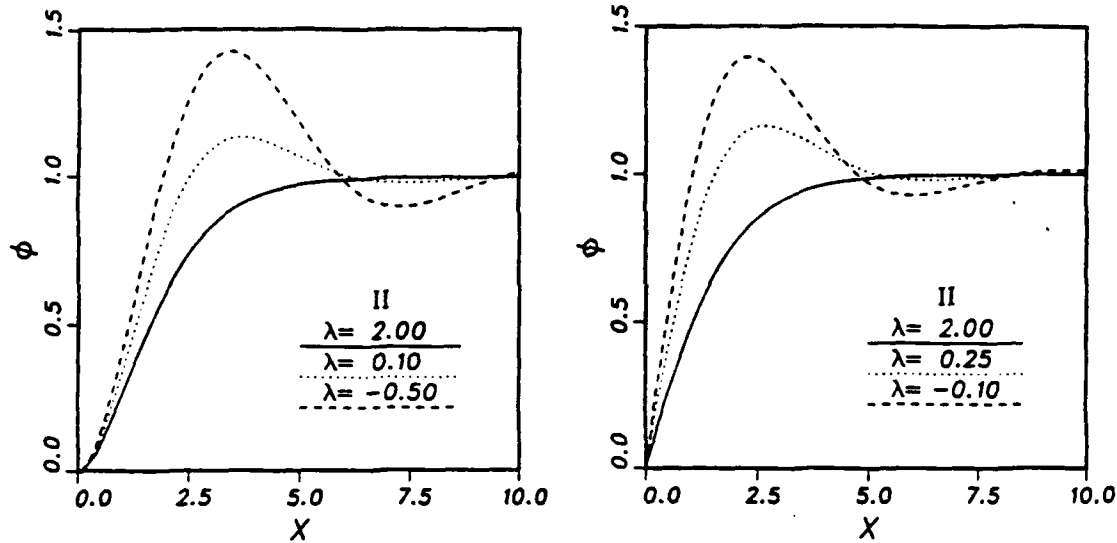


Figure 5: Middle-branch solutions. (a) no-slip boundaries for  $\lambda$  near the "nose" (dashed line), near zero (dotted line), and moderately large and positive (solid line). (b) slip boundaries for  $\lambda$  small and negative (dashed line), small and positive (dotted line), and moderately large (solid line). [From I&R.]

$$\begin{aligned}
 & + \epsilon \lambda \sum_{m=0}^n (2m+2)(2m+3)(2m+1) \phi'_{n-m} \phi_{m+1} \\
 & - \epsilon \lambda \sum_{m=0}^n (2m+2)(2m+3)(2n-2m+1) \phi_{n-m} \phi'_{m+1} \\
 = & - \left(\frac{\pi}{2}\right)^{2n+4} \frac{\epsilon^2 (-1)^n}{(2n+1)!} + \phi_n''' + 2\epsilon(2n+2)(2n+3) \phi_{n+1}'' \\
 & + \epsilon^2 (2n+2)(2n+3)(2n+4)(2n+5) \phi_{n+2}
 \end{aligned} \tag{28}$$

for the Munk case, with boundary conditions that

$$\phi_n(0) = 0 \tag{29}$$

$$\phi_n(\xi) \rightarrow \left(\frac{\pi}{2}\right)^{2n} \frac{(-1)^n}{(2n+1)!} \text{ as } \xi \rightarrow \infty \tag{30}$$

$$\phi_n'(\xi) \rightarrow 0 \text{ as } \xi \rightarrow \infty \tag{31}$$

with the additional condition in the Munk case that either  $\phi_n'(0) = 0$  for no-slip boundaries or  $\phi_n''(0) = 0$  for slip. We will restrict our attention to the two

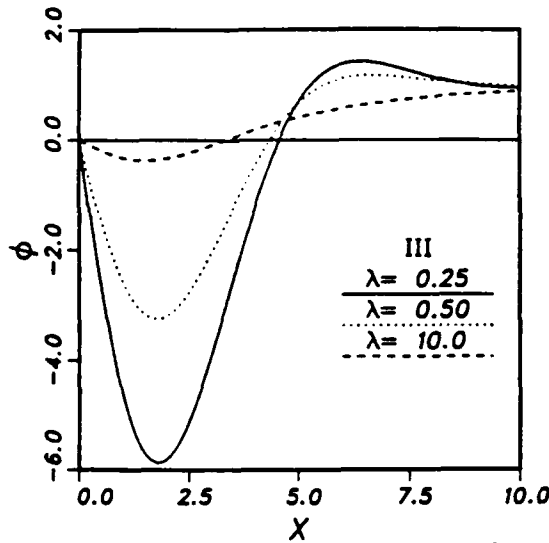


Figure 6: Lower-branch solutions for slip boundaries at three values of  $\lambda$ . For moderately large  $\lambda$  the peak height becomes independent of  $\lambda$ , while the peak-height dependence scales as in figure 4(b). [From I&R.]

component case so that  $\phi_2 \equiv \phi_3 \equiv \phi_4 \equiv \dots \equiv 0$  and we get a coupled pair of ordinary differential equations

$$\phi_0' + \lambda(\phi_0'\phi_0'' - \phi_0\phi_0''') + 6\epsilon\lambda(\phi_0'\phi_1 - \phi_0\phi_1') = -\frac{\pi^2}{4}\epsilon - \phi_0'' - 6\epsilon\phi_1 \quad (32)$$

$$\phi_1' + \lambda(\phi_0''\phi_1' - 3\phi_0'''\phi_1 + 3\phi_0'\phi_1'' - \phi_0\phi_1''') - 12\epsilon\lambda\phi_1\phi_1' = -\phi_1'' \quad (33)$$

for the Stommel case and

$$\phi_0' + \lambda(\phi_0'\phi_0'' - \phi_0\phi_0''') + 6\epsilon\lambda(\phi_0'\phi_1 - \phi_0\phi_1') = \phi_0''' + 12\epsilon\phi_1'' \quad (34)$$

$$\phi_1' + \lambda(\phi_0''\phi_1' - 3\phi_0'''\phi_1 + 3\phi_0'\phi_1'' - \phi_0\phi_1''') - 12\epsilon\lambda\phi_1\phi_1' = \phi_1''' \quad (35)$$

for the Munk case. In both cases the second equation can be integrated once from  $\xi$  to  $\infty$  yielding

$$\phi_1 + \frac{\pi^2}{24} + \lambda(4\phi_0'\phi_1' - \phi_0\phi_1'' - 3\phi_0''\phi_1) - 6\epsilon\lambda\phi_1^2 = -\phi_1' \quad (36)$$

for the Stommel case and

$$\phi_1 + \frac{\pi^2}{24} + \lambda(4\phi_0'\phi_1' - \phi_0\phi_1'' - 3\phi_0''\phi_1) - 6\epsilon\lambda\phi_1^2 = \phi_1''' \quad (37)$$

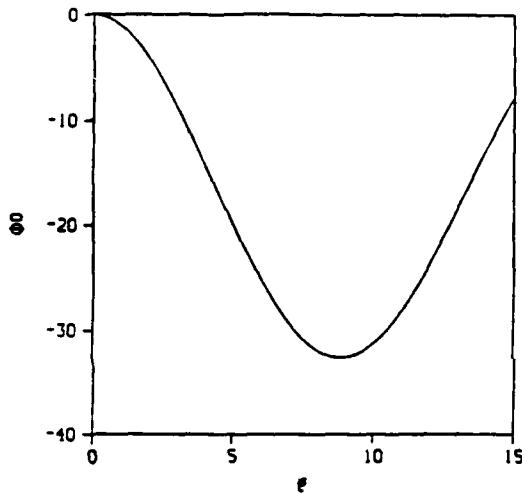


Figure 7: Our possible lower-branch solution for no-slip boundaries at  $\lambda = 0.5$ .

for the Munk case. It should be noted that there is a term due to the wind stress,  $-\frac{\pi^2}{4}\varepsilon$  in the first equation for bottom drag but not for lateral friction. The corresponding term in the lateral friction case will only come in if we keep  $\phi_2(\xi)$ .

### 3.1. The case $\varepsilon = 0$

For an infinite aspect ratio these are partially decoupled (the coupling parameter  $\varepsilon = 0$ ) and we can again integrate the first equation in both cases to once from  $\xi$  to  $\infty$  with respect to  $\xi$  to obtain

$$\phi_0 - 1 + \lambda (\phi_0'^2 - \phi_0 \phi_0'') = -\phi_0' \quad (38)$$

$$\phi_1 + \frac{\pi^2}{24} + \lambda (4\phi_0' \phi_1^{prime} - \phi_0 \phi_1'' - 3\phi_0'' \phi_1) = -\phi_1' \quad (39)$$

for the Stommel case and

$$\phi_0 - 1 + \lambda (\phi_0'^2 - \phi_0 \phi_0'') = \phi_0''' \quad (40)$$

$$\phi_1 + \frac{\pi^2}{24} + \lambda (4\phi_0' \phi_1' - \phi_0 \phi_1'' - 3\phi_0'' \phi_1) = \phi_1''' \quad (41)$$

for the Munk case.

In both cases the first equation is of course simply that obtained earlier when we considered only the one component case and it should be pointed out that the

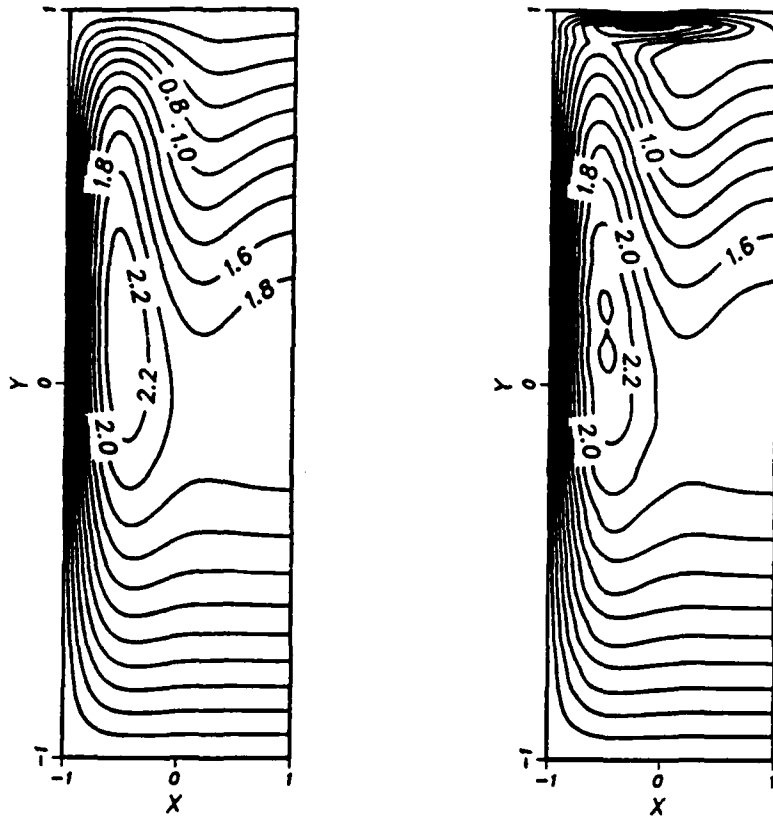


Figure 8: (a) solution of the regional model for  $\psi$  for  $\epsilon = 1.6 \times 10^{-3}$  and  $\lambda = -0.7$  for a slip boundary. Although  $\lambda < \lambda_c$  a parametric solution persists. (b) as in (a) except that  $\epsilon = 2.5 \times 10^{-5}$ . There is a region of strong variation extending southward from the northern wall to form a closed recirculation cell and a boundary-layer solution does not exist for the outflow region. [From Ierley (1987).]

second equation in both cases is linear in  $\phi_1(\xi)$ . The system is completely decoupled for  $\lambda = 0$  when  $\phi_1$  is simply a linear multiple of  $\phi_0$ ,  $\phi_1 = -\frac{\pi^2}{24}\phi_0$ . For general  $\lambda$ , once again the bottom drag equation has a solution

$$\phi_0 = 1 - e^{-\mu\xi} \quad (42)$$

$$\phi_1 = -\frac{\pi^2}{24} \left( 1 + Ce^{-\mu\xi} + D\xi e^{-\mu\xi} + Ee^{-2\mu\xi} + Fe^{-3\mu\xi} \right) \quad (43)$$

where

$$D = \frac{3\mu^3\lambda}{\mu - 2}, \quad E = \frac{2\mu D\lambda}{3 - 2\mu}, \quad F = \frac{-\mu^2 E\lambda}{2(4 - 3\mu)}, \quad \text{and} \quad C = -1 - E - F \quad (44)$$

and  $\mu$  is given once again by  $\lambda\mu^2 + \mu - 1 = 0$ . It can be clearly seen that, when thought of as a function of  $\mu$ ,  $\phi_1(\xi)$  has a series of poles or resonances at  $\mu = 2$  corresponding to  $\lambda = \lambda_c = -\frac{1}{4}$  which is the nose for  $\phi_0$ , at  $\mu = -\frac{3}{2}$  which corresponds to  $\lambda = -\frac{2}{9}$  and at  $\mu = \frac{4}{3}$  which is  $\lambda = -\frac{3}{16}$ . Thus it can be seen that we have a series of poles at locations tending towards  $\mu = 1$  from above and  $\lambda = 0$  from below and it seems probable that for the  $\varepsilon = 0$  case that if we kept one more equation, i.e. if we no longer set  $\phi_2(\xi) \equiv 0$ , we would get additional resonances that continue this series. If we evaluate the second of the bottom drag equations at  $\xi = 0$ , using  $\phi_0 = 1 - e^{-\mu\xi}$  and  $\phi_1(0) = 0$ , we recover

$$\phi_1'(0)(1 + 4\lambda\mu) = \phi_1(\infty) \quad (45)$$

where we require  $\phi_1(\infty) = -\frac{\pi^2}{24}$ . Clearly we cannot satisfy the boundary condition on  $\phi_1$  as  $\xi \rightarrow \infty$  when  $1 + 4\lambda\mu = 0$ . This was the resonance we obtained at  $\mu = \frac{4}{3}$  and  $\lambda = -\frac{3}{16}$ . However, we can find  $\phi_1(\xi)$  such that  $\phi_1(0) = \phi_1(\infty) = 0$  and  $\phi_1'(\infty) = 0$  which is a free homogeneous solution. Similarly, evaluating the derivative with respect to  $\xi$  of the second bottom drag equation at  $\xi = 0$  gives

$$\mu\phi_1'(0) = -\phi_1''(0)(1 + 3\mu\lambda) \quad (46)$$

since  $1 - \mu^2\lambda = \mu$ . This says that we require  $\phi_1'(0) = 0$  when  $1 + 3\mu\lambda = 0$  which corresponds to  $\mu = \frac{3}{2}$  and  $\lambda = -\frac{2}{9}$ . Hence we lose one shooting parameter and we will be unable to satisfy the boundary conditions on both  $\phi_1(\xi)$  and  $\phi_1'(\xi)$  as  $\xi \rightarrow \infty$  because since we have a linear equation for  $\phi_1(\xi)$  we can normalise it to anything we desire. One further point of interest is that these two relations between  $\phi_1(\infty)$ ,  $\phi_1'(0)$  and  $\phi_1''(0)$  turn what we viewed originally as a boundary value problem into an initial value problem except at the points where these resonances occur.

These resonances seem to be a fairly ubiquitous feature of the second term in a boundary layer expansion; they crop up in the field of magnetohydrodynamics (Buckmaster, 1971) amongst other places and also in the Munk case as we can see from figures 9(a) and (b), where we see that the no-slip case has numerous such poles but the slip case appears only to have one. Glenn Ierley (private communication) has tried to fit the structure that we obtained numerically for the poles in the Munk case with several trial analytic functions but without success.

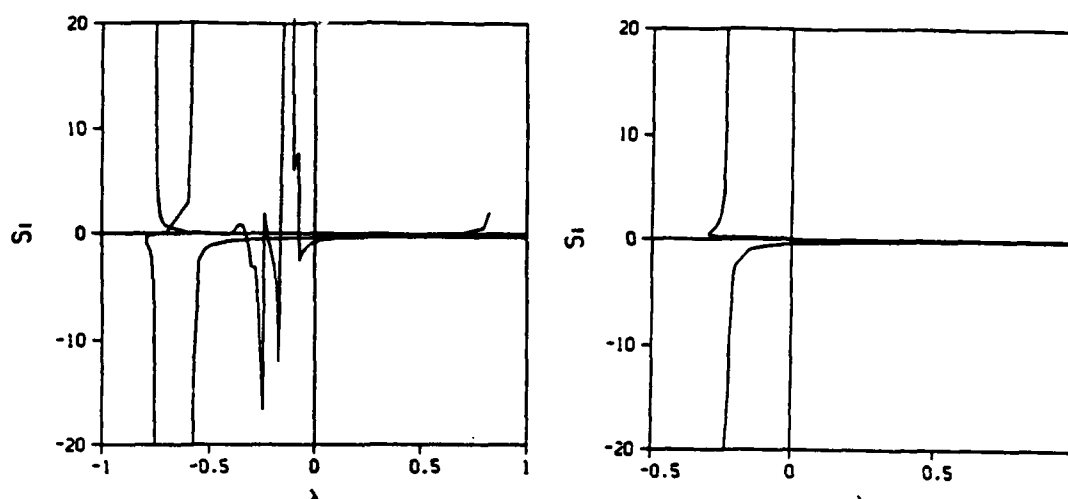


Figure 9: (a)  $S_1 = \phi_1''(0)$  for the no-slip case. (b)  $S_1 = \phi_1'(0)$  for the slip case.

The spatial behavior of  $\phi_1(0)$  either side of one of these resonances, that on the upper branch of the slip case, is shown in figures 10(a) and (b) and it can be seen that the function appears to have changed sign at the poles in the sense that  $\phi_1(\xi; \lambda = -0.225)$  is remarkably similar to  $-\phi_1(\xi; \lambda = -0.229)$  [both functions supposedly asymptote to  $-\frac{\pi^2}{24}$  as  $\xi \rightarrow \infty$  which seems to indicate that they are still highly oscillatory at values of  $\xi$  as large as 15].

### 3.2. The case $\varepsilon \neq 0$

The case  $\varepsilon \neq 0$  is much more complicated. To date an analytical solution for the bottom drag has eluded us except at  $\lambda = 0$  where the governing equations are

$$\phi_0' = -\frac{\pi^2}{4}\varepsilon - \phi_0'' - 6\varepsilon\phi_1 \quad (47)$$

$$\phi_1 = -\phi_1' \quad (48)$$

which has the simple solution

$$\phi_0 = 1 - e^{-\xi} - \frac{\pi^2}{4}\varepsilon\xi e^{-\xi} \quad (49)$$

$$\phi_1 = -\frac{\pi^2}{24}(1 - e^{-\xi}). \quad (50)$$

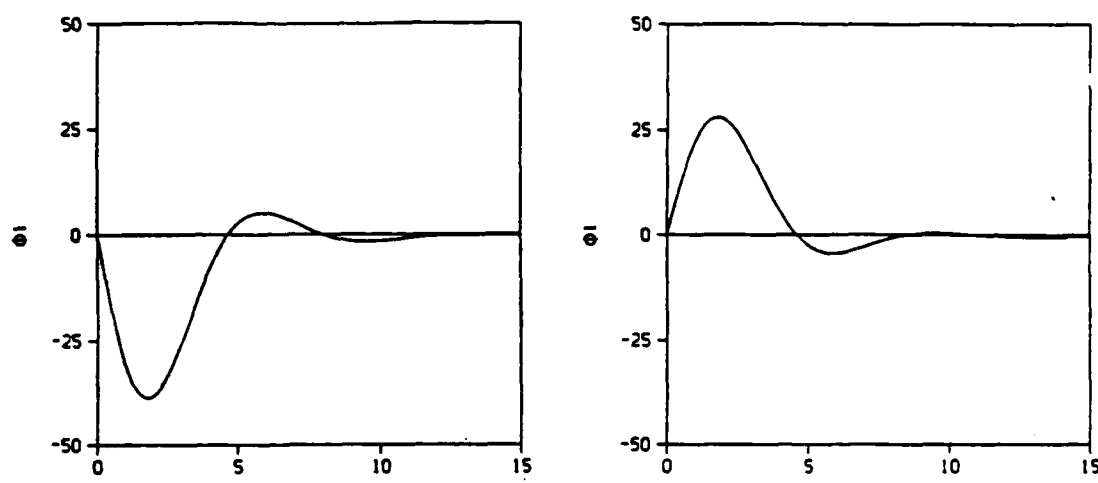


Figure 10: (a) the function  $\phi_1$  on the upper branch for slip boundaries for  $\lambda = -0.225$ , which is very close to a resonance. (b) as for (a) but for  $\lambda = -0.229$  which lies on the other side of the resonance.

The Munk case can also be solved for  $\lambda = 0$ , the equations being

$$\phi_0 - 1 = \phi_0''' + 12\varepsilon\phi_1' \quad (51)$$

$$\phi_1 = \phi_1''' \quad (52)$$

which has a solution

$$\begin{aligned} \phi_0 = 1 & - e^{-\frac{\xi}{2}} \left[ 1 - \frac{\pi^2 \varepsilon}{6} \xi \right] \cos \left( \frac{\sqrt{3}}{2} \xi \right) \\ & - e^{-\frac{\xi}{2}} \left[ \frac{1}{\sqrt{3}} + \frac{\pi^2 \varepsilon}{3\sqrt{3}} + \frac{\pi^2 \varepsilon}{6\sqrt{3}} \xi \right] \sin \left( \frac{\sqrt{3}}{2} \xi \right) \end{aligned} \quad (53)$$

$$\phi_1 = -\frac{\pi^2}{24} \left[ 1 - e^{-\frac{\xi}{2}} \left[ \cos \left( \frac{\sqrt{3}}{2} \xi \right) + \frac{1}{\sqrt{3}} \sin \left( \frac{\sqrt{3}}{2} \xi \right) \right] \right] \quad (54)$$

for no-slip boundaries and

$$\begin{aligned} \phi_0 = 1 & - e^{-\frac{\xi}{2}} \cos \left( \frac{\sqrt{3}}{2} \xi \right) \\ & + e^{-\frac{\xi}{2}} \left[ \frac{1}{\sqrt{3}} - \frac{2\pi^2 \varepsilon}{3\sqrt{3}} - \frac{\pi^2 \varepsilon}{3\sqrt{3}} \xi \right] \sin \left( \frac{\sqrt{3}}{2} \xi \right) \end{aligned} \quad (55)$$



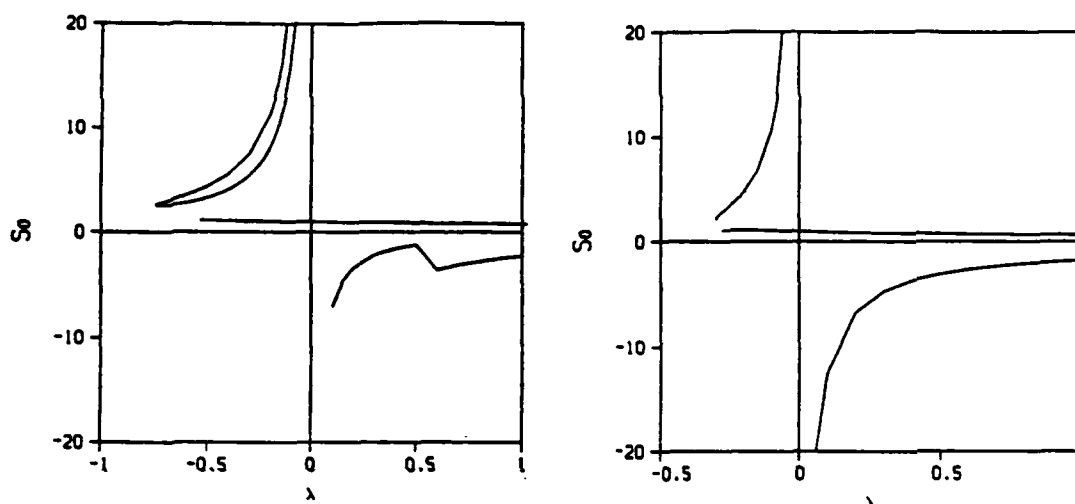


Figure 11:  $S_0(\lambda)$  for  $\varepsilon = 0.01$ . (a) no-slip boundaries; observe the apparent splitting of the upper branch. (b) slip boundaries.

$$\phi_1 = -\frac{\pi^2}{24} \left[ 1 - e^{-\frac{1}{2}\xi} \left[ \cos\left(\frac{\sqrt{3}}{2}\xi\right) - \frac{1}{\sqrt{3}} \sin\left(\frac{\sqrt{3}}{2}\xi\right) \right] \right] \quad (56)$$

for slip boundaries.

Numerically, we encountered several difficulties trying to analyze the lateral friction case, most notably that we were unable to reach the “nose” for  $\varepsilon \neq 0$  and instead hit a numerical wall that we were unable to push past as we tried to locate a nose; this made our original objective of finding how  $\lambda_c$  depended on  $\varepsilon$  impossible. The curves that we were able to construct are shown in figures 11(a) and (b) for no-slip and slip respectively. The slip case looks as though a nose should be there and it should be merely a question of edging very slowly out along the curves to locate it; however, the plot of  $S_1$  for the slip case (figure 12(b)) shows the two branches of  $S_1$  diverging as we decrease  $\lambda$  indicating that there may well be no nose. This may simply be because of simple numerical failure [details of the numerical methods employed are contained in the appendix] caused by the fact that we map the semi-infinite region  $(0, \infty)$  onto  $(-1, 1)$  and because the solutions oscillate exponentially as  $\xi \rightarrow \infty$  when we make this transformation we concertina these oscillations and hence, as pointed out in I&R, there is very little spectral decay [our spectrum decayed in places by as little as  $10^{-3}$  which tends to make one

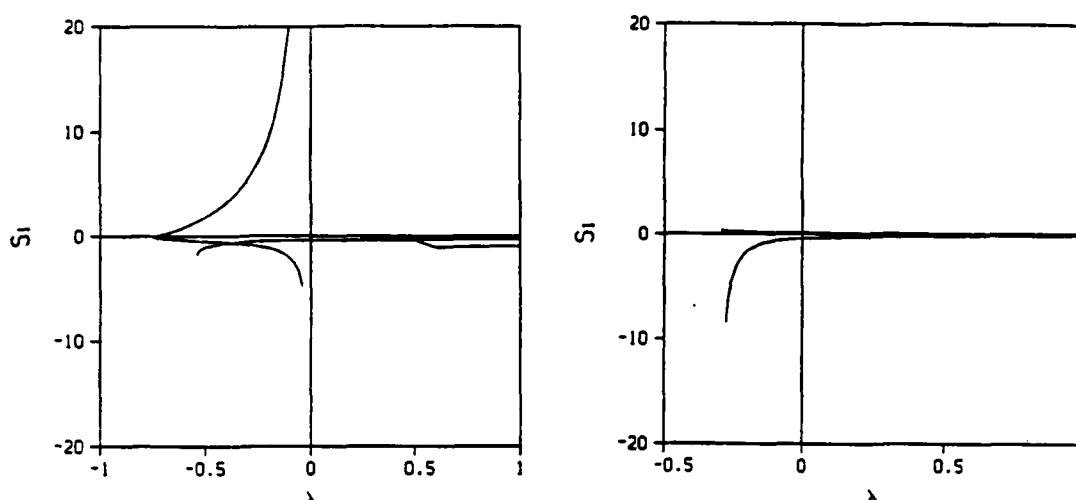


Figure 12:  $S_1(\lambda)$  for  $\varepsilon = 0.01$ . (a) no-slip boundaries. (b) slip boundaries.

treat the results warily; we were unable to use a larger number of spectral basis elements to get better spectral decay because the time per iteration appears to be proportional to the cube of the number of polynomials used and it was already taking just over thirty minutes of cpu time on a Microvax to converge  $\phi_0$  and  $\phi_1$  for each value of  $\lambda$ ; researchers attempting to tackle similar problems in the future might be well advised to employ some sort of basis set on the semi-infinite interval itself to avoid compressing these oscillations].

It is also possible that there is a physical mechanism at work. We see in figure 11(a) that the upper branch of  $S_0$  for the no-slip case appears to have undergone some sort of splitting mechanism; we have tried to find a similar splitting for the lower branch but to date without success. In figures 13(a) and 13(b) we show  $\phi_0$  for points above and below this apparent splitting and we can see that they are very similar with figure 13(a) having a slightly higher peak than figure 13(b), which leaves unanswered the tantalizing question as to whether this is a genuine splitting or merely a numerical failure in which case the two lines are merely one and the same. There are indications from the bottom drag case that some sort of splitting may be afoot: when we substitute  $\phi_0 = 1 - A_0 e^{-\mu \varepsilon}$  and  $\phi_1 = -\frac{\pi^2}{24} (1 + A_1 e^{-\mu \varepsilon})$  into the governing equations and neglect boundary conditions and consider only terms  $\mathcal{O}(e^{-\mu \varepsilon})$  we obtain a quartic equation for  $\mu$  with four roots instead of the two roots

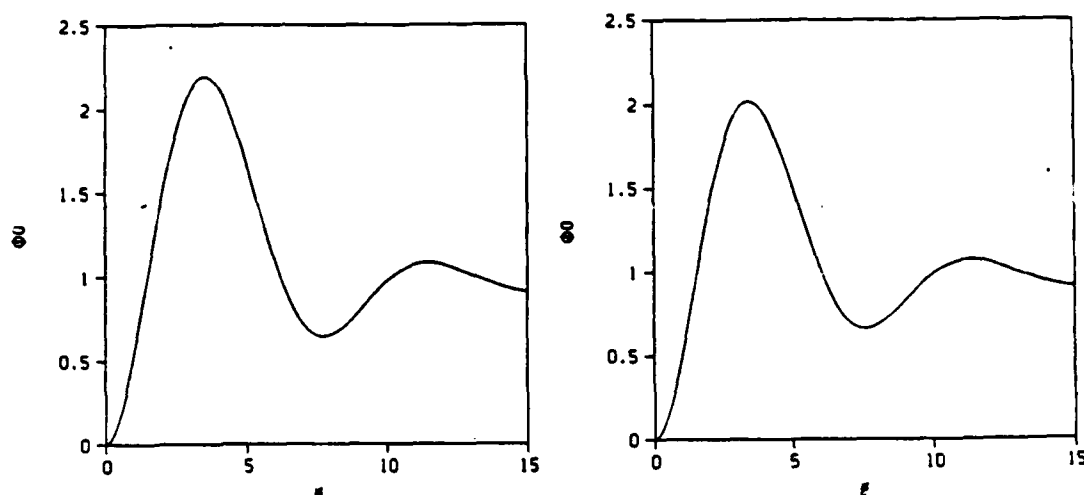


Figure 13:  $\phi_0(\xi)$  for  $\lambda = -0.73$  either side of the apparent splitting in figure 11(a): (a) above and (b) below.

of  $1 - \lambda\mu^2 - \mu$  we had when we took  $\varepsilon = 0$ . For  $\lambda < 0$  numerically we find that for moderately small negative  $\lambda$  this quartic equation has two pairs of roots with the elements of each pair being extremely close together.

In figures 12(a) and (b) much of the pole-like structure that was evident in figures 9(a) and (b) is no longer present which suggests that  $\varepsilon = 0$  may have been a singular limit; however as we have a relatively complete set of data for only one non-zero value of  $\varepsilon$  more work is needed on this aspect of the problem.

In figures 14 to 17 we show the function  $\phi_0(\xi)$  for various values of  $\lambda$  and with one exception the curves all appear to be very similar to their  $\varepsilon = 0$  counterparts. The no-slip solution shown for the upper branch (figure 14(a)) however has a peak that is significantly reduced in size compared to figure 4(a). As it was this branch that appeared to undergo the splitting in figure 11(a) this only heightens the intrigue.

#### 4. A (Seemingly) Simple Model

As the behavior of the functions we have considered in earlier sections has been at times fairly complex, in true Walsh Cottage tradition we have constructed a simple model that exhibits much of the same structure. If we consider the time independent potential vorticity equation for the bottom drag case in the boundary-

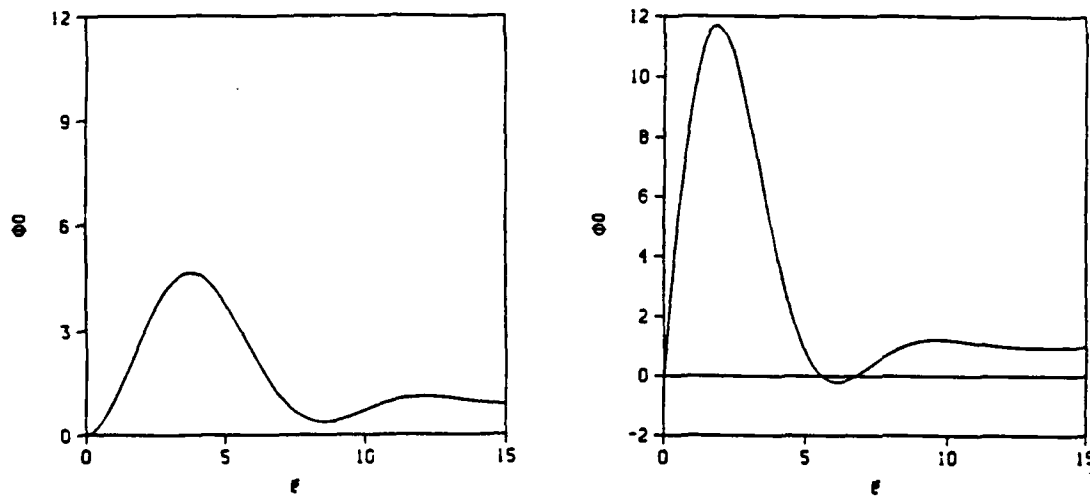


Figure 14:  $\phi_0(\xi)$  for  $\varepsilon = 0.01$ , upper branch. (a) no-slip  $\lambda = -0.5$ . (b) slip  $\lambda = -0.1$ .

layer and we make the boundary-layer approximation that  $\psi_{yy} = 0$  so that  $\zeta = \psi_{xx}$  then we can write this equation in the form

$$J(\psi, \zeta) + \beta\psi_x = -r\zeta, \quad (57)$$

where  $\zeta$  is the vorticity with the boundary conditions that  $u \rightarrow 0$  and  $\psi \rightarrow \psi_\infty$  as  $x \rightarrow \infty$ . If we integrate this equation from  $x$  to  $\infty$  we obtain

$$J(\psi, \psi_x) + \beta(\psi - \psi_\infty) = -r\psi_x. \quad (58)$$

If we evaluate these two equations at  $x = 0$  we obtain a closed set of equations for the velocity and vorticity at the wall

$$vv_y - \beta\psi_\infty = -rv \quad (59)$$

$$v\zeta_y + \beta v = -r\zeta. \quad (60)$$

We will consider only the first of these two equations and pose an expansion of the form

$$\beta\psi_\infty \sim a_0y + a_1y^3 + a_2y^5 + \dots \quad (61)$$

$$v \sim v_0y + v_1y^3 + v_2y^5 + \dots \quad (62)$$

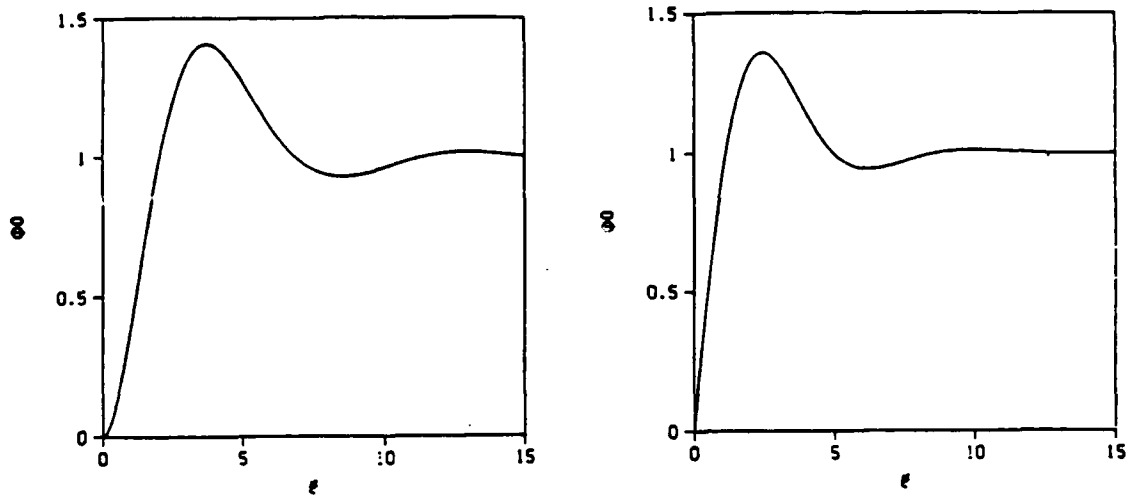


Figure 15:  $\phi_0(\xi)$  for  $\epsilon = 0.01$ , middle branch. (a) no-slip  $\lambda = -0.5$ . (b) slip  $\lambda = -0.1$ .

$$v_y \sim v_0 + 3v_1y^2 + 5v_2y^4 + \dots \quad (63)$$

and equate powers of  $y$  then we will obtain a series of equations for these coefficients  $v_n$  given the  $a_n$ . The first of these is at  $\mathcal{O}(y)$

$$v_0^2 + rv_0 = a_0 \quad (64)$$

hence

$$v_0 = \frac{-r \pm \sqrt{r^2 + 4a_0}}{2} \quad (65)$$

and we need  $a_0 \geq -\frac{r^2}{4}$  for a solution to exist. This is equivalent to the condition of  $\lambda \geq -\frac{1}{4}$  that we obtained for the bottom-drag case using boundary layer techniques. At the next order  $\mathcal{O}(y^3)$  we obtain

$$v_1(4v_0 + r) = a_1 \quad (66)$$

and if we pick  $v_0 = -\frac{r}{4}$ , which corresponds to  $a_0 = -\frac{3r^2}{16}$  we see that in this case we require  $a_1 = 0$  and that  $v_1$  is arbitrary. At  $\mathcal{O}(y^5)$  we find that

$$v_2(6v_0 + r) + 3v_1^2 = a_2 \quad (67)$$

thus

$$v_2 = \frac{6v_1^2}{r} - \frac{2a_2}{r} \quad (68)$$

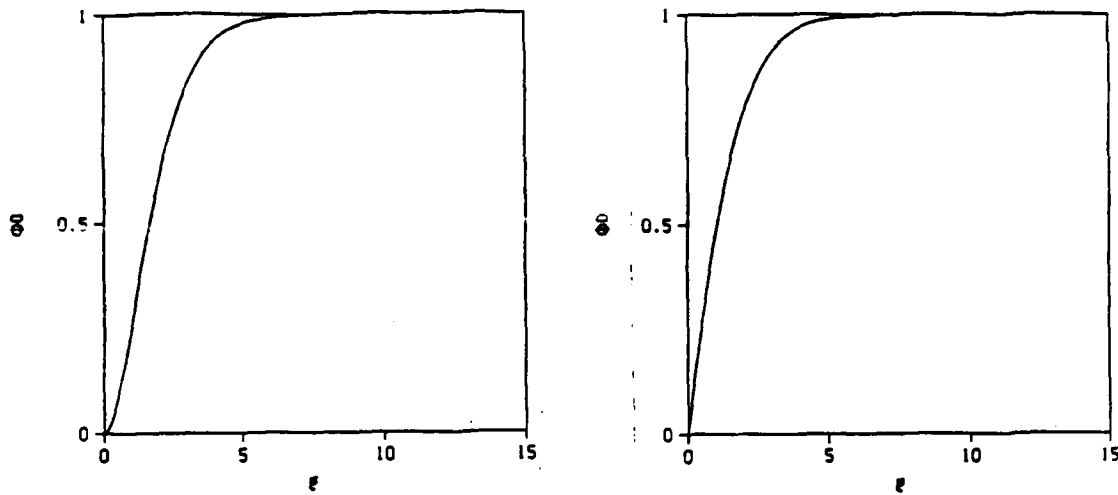


Figure 16:  $\phi_0(\xi)$  for  $\varepsilon = 0.01$ ,  $\lambda = 2.0$ , middle branch. (a) no-slip boundaries. (b) slip boundaries.

and at  $\mathcal{O}(y^7)$  the corresponding equation is

$$v_3(8v_0 + r) + 8v_1v_2 = a_3 \quad (69)$$

with solution

$$v_3 = \frac{48v_1^3}{r^2} - \frac{16a_2v_1}{r^2} - \frac{a_3}{r}. \quad (70)$$

It can be seen that this is clearly not a unique solution as  $v_1$  is arbitrary and this is comparable to the free homogeneous solution that we found in the boundary-layer equations for the bottom drag case.

It is also the case that this is not the only resonance present and this system appears to have a countably infinite number of poles or resonances as  $v_0$  approaches  $r \rightarrow 0$  from below. This is apparent from merely writing the solution down at successive orders

$$v_1 = \frac{a_1}{4v_0 + r} \quad (71)$$

which corresponds to a resonance at  $v_0 = -\frac{r}{4}$

$$v_2 = \frac{a_2 - 3v_1^2}{6v_0 + r} \quad (72)$$

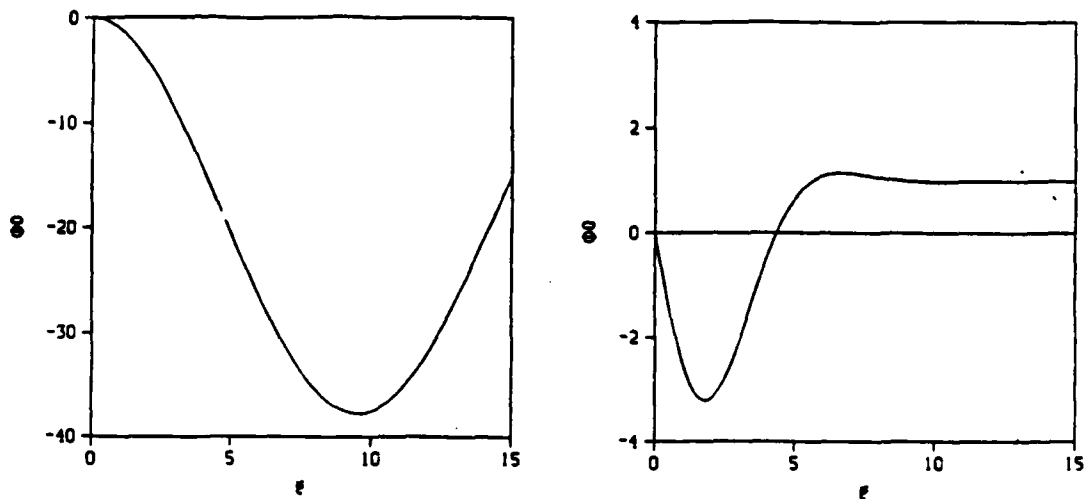


Figure 17:  $\phi_0(\xi)$  for  $\varepsilon = 0.01$ ,  $\lambda = 0.5$ , bottom branch. (a) our possible solution for no-slip boundaries. (b) slip boundaries.

which corresponds to a resonance at  $v_0 = -\frac{r}{6}$

$$v_3 = \frac{a_3 - 8v_1v_2}{8v_0 + r} \quad (73)$$

which corresponds to a resonance at  $v_0 = -\frac{r}{8}$  and

$$v_4 = \frac{a_4 - 10v_1v_3 - 5v_2^2}{10v_0 + r} \quad (74)$$

which corresponds to a resonance at  $v_0 = -\frac{r}{10}$ . The general case is

$$v_n = \frac{a_n - \sum_{m=1}^{n-1} (2m+1)v_{n-m}v_m}{2(n+1)v_0 + r} \quad (75)$$

which corresponds to a resonance at  $v_0 = -\frac{r}{2(n+1)}$ . It would appear that these resonances each have a non-uniqueness associated with the solution at that value of  $v_0$ . What this appears to be telling us is that we require an expansion of a different form for  $v_0 < 0$ . Just exactly what that expansion should be remains a mystery.

**Acknowledgements.** The work is the product of a collaborative effort with Glenn Ierley and Bill Young, and I would like to express my gratitude to both of them and also to Andy Woods who was extremely helpful, to Paola Cessi who amongst

numerous other things taught me how to use MATLAB, to John Hart who pointed out analogous work in other fields, notably that in magnetohydrodynamics (Buckmaster, 1971), and to Vance Condie my co-fellow with whom I had many useful discussions. The extensive numerical calculations which constituted part of this project were performed on an IBM 3090 and a Microvax at Brown University and I would like to thank the Division of Applied Mathematics there for making those facilities available to me. The codes used were written by Glenn Ierley. Finally I would like to express my appreciation to those people who made my stay at Woods Hole this summer both possible and enjoyable; I hope that this turns out to be merely the first of many visits here.

#### Appendix : Numerical Methods

The semi-infinite interval  $(0, \infty)$  was mapped onto the finite interval  $(-1, 1)$  using the algebraic transformation

$$z = \frac{\alpha\xi - 1}{\alpha\xi + 1} \quad (76)$$

where  $\alpha$  is a stretching parameter. This transformation maps  $(0, \frac{1}{\alpha})$  onto  $(-1, 0)$  and  $(\frac{1}{\alpha}, \infty)$  onto  $(0, 1)$ . The parameter  $\alpha$  was generally taken to be 0.1.

A spectral relaxation scheme was used for the calculations in the lateral friction case; the scheme used was a modification of that used in I&R. [For an introduction to relaxation methods the reader is referred to Fox (1957).] The solution was represented as a series of Chebyshev polynomials (Clenshaw, 1957)

$$\phi_0(\xi) = \sum_{n=0}^N C_n^{(0)} T_n(z) \quad (77)$$

$$\phi_1(\xi) = \sum_{n=0}^N C_n^{(1)} T_n(z) \quad (78)$$

with nonlinear terms calculated using the relation

$$T_n(z) T_m(z) = \frac{1}{2} [T_{m+n}(z) + T_{|m-n|}(z)] \quad (79)$$

Generally  $N = 69$  polynomials were used for both  $\phi_0$  and  $\phi_1$ . Derivatives were explicitly evaluated in recurrence form as outlined by Orszag & Gottlieb (1977).



Boundary conditions were imposed by linear algebraic constraints on the unknown coefficients which determine the last four terms in the expansion.

To converge the solution Newton's method was used by successively varying each of the  $C_n$  and seeking a zero of the least square residues. This method was quite robust but rather time consuming requiring slightly more than half an hour of cpu time on a Microvax for each value of  $\lambda$  and  $\epsilon$ .

As we noted in the main body of this report, there are regions of the parameter range where the solutions have very little spectral decay since the solutions there oscillate exponentially as  $\xi \rightarrow \infty$  and we convert these oscillations onto a finite interval. Further work might be better conducted using basis functions which are orthogonal on  $(0, \infty)$  itself in order to avoid compressing these oscillations [and thus better resolve the behavior of the functions  $\phi_n$  as  $\xi \rightarrow \infty$ ] instead of transforming this interval onto a finite interval as has been done here.

#### References

- Buckmaster, J. 1971 Boundary-layer structure at a magnetohydrodynamic rear stagnation point. *Quart. Journ. Mech. and Applied Math.* **24**, 373-386.
- Clenshaw, C. W. 1957 The numerical solution of linear differential equations in Chebyshev series. *Proc. Camb. Phil. Soc.* **53**, 134-149.
- Fox, L. 1957 *The Numerical Solution of Two-Point Boundary Value Problems in Ordinary Differential Equations*, Oxford.
- Goldstein, S. 1930 On laminar boundary-layer flow near a position of separation. *Proc. Camb. Phil. Soc.* **26**, 1-18.
- Ierley, G. R. 1987 On the onset of inertial recirculation in barotropic general circulation models. *J. Phys. Oceanogr.* **17**, 2366-2374.
- Ierley, G. R., and O. G. Ruehr 1986 Analytic and numerical solutions of a nonlinear boundary-layer problem. *Stud. Appl. Math.* **75**, 1-36.
- Il'in, A. M., and V. M. Kamenkovich 1964 The structure of the boundary-layer in the two-dimensional theory of ocean currents. (in Russian) *Okeanologiya* **4**(5), 756-769.
- Munk, W. H. 1950 On the wind-driven ocean circulation. *J. Meteorol.* **7**, 79-93.
- Orszag, S. A., and D. Gottlieb 1977 *Numerical Analysis of Spectral Methods: Theory and Application*, SIAM, Philadelphia.

- Pedlosky, J. 1979 *Geophysical Fluid Dynamics*, Springer, 624pp.
- Stommel, H. 1948 The westward intensification of wind-driven ocean currents. *Trans. Amer. Geophys. Union* 99, 202-206.
- Welander, P. 1976 A zonally uniform regime in the oceanic circulation. *J. Phys. Oceanogr.* 6, 121-124.

## A COUPLED THERMOCLINE-ABYSSAL GENERAL GEOSTROPHIC MODEL

G.G. Sutyrin  
P.P. Shirshov' Institute of oceanology, Moscow

### ABSTRACT

The filtered two-layer model allowing order-one variation of the upper layer depth is proposed. Various dynamical regimes are considered. The conservation of total energy and potential enstrophy is analysed. The energy integral expression of energy that contains only quadratic terms in the general geostrophic regime is obtained. Coupling of upper and lower layers motion is discussed.

### 1 INTRODUCTION

It was recognized many years ago that eliminating the occurrence of high-frequency oscillation modes is an important problem in numerical predictions of large scale atmospheric and oceanic phenomena. Replacing the realistic primitive-equations model, which permits undesirable inertial gravity waves, by a simpler quasigeostrophic model has been extensively used owing to the simplicity and conservation of analogues of both energy and enstrophy as in the primitive equations (Pedlosky, 1979). But the traditional quasigeostrophic equations apply only to slight departures of the density stratification from its average distribution. A great deal of effort was directed to develop some intermediate models, which filter out the relatively fast inertial gravity waves and still retain some degree of physical simplicity compared to the primitive equations (McWilliams and Gent, 1980).

Higher accuracy in respect to the Rossby number is achieved in the so-called balance equations (Gent and McWilliams, 1983: b). These are obtained by the decomposition of the velocity into solenoidal and potential parts and seem to be rather complicated for practical use. Another approach to develop the general filtered model is allowing order-one variation of the stratification while using the lagrangian vertical coordinate (Sutyrin, 1985). In this way for a three-dimensional flow all variables are expressed by the geopotential as in the quasigeostrophic model.

In recent years a reduced gravity model has been used to consider a number of geostrophic regimes for large-scale flows beyond the radius of deformation: the intermediate geostrophic (IG) regime (Charney and Flierl, 1981; Yamagata, 1982), the planetary geostrophic (PG) regime (Williams and Yamagata, 1984), the frontal geostrophic (FG) regime (Cushman-Roisin, 1986). A unification and generalization of these studies lead to the general geostrophic (GG) model (Williams, 1985; Sutyrin and Yushina, 1986a, b; Cushman-Roisin and Tang, 1989).

In the general geostrophic equation all variables are expressed only by variation of the thickness of the layer like in the quasigeostrophic one but the GG equation may not rightly describe all conservation laws possessed by the primitive equations. The addition of small, negligible but carefully chosen terms might lead to either energy or enstrophy conservation but not both simultaneously (Hukuda and Yamagata, 1988). To guarantee that energy together with

enstrophy be conserved for the general geostrophic case, at least two variables should be considered [e.g, components of ageostrophic velocity on the basis of Hamilton's principle (Salmon, 1985) or the Bernoulli function and vorticity (Sutyrin, 1986)].

Unlike the QG regime the IG and GG numerical simulations display the essential differences in the formation, evolution and interaction of cyclones and anticyclones (Matsuura and Yamagata, 1982; Williams and Yamagata, 1984; Sutyrin and Yushina, 1986a, b, 1989). An important role of frontal effects in maintenance of elliptical shape of an isolated cyclone has been demonstrated by Hukuda and Yamagata (1988). The saturation of the energy cascade on the IG scale and predominance of anticyclones has been obtained in modeling of geostrophic turbulence (Cushman-Roisin and Tang, 1989). In all these simulations only a single baroclinic mode was considered without interaction with others.

The coupling of motions in the thermocline and in the abyss may be essential in the ocean. It is of considerable interest to analyse various geostrophic regimes to incorporate vertical modal coupling. In particular, a two-layer version of a general geostrophic model is considered in this paper.

## 2. THE PRIMARY EQUATIONS AND PARAMETERS

The equations governing the upper and lower layers motion are written as

$$\mathbf{V}_{1t} + (f + \text{rot}_z \mathbf{V}_1)(\mathbf{k} \times \mathbf{V}_1) + \nabla P_1 = 0 \quad (2.1)$$

$$H_{1t} + \nabla \cdot (H_1 \mathbf{V}_1) = 0, \quad i = 1, 2 \quad (2.2)$$

$$g'Z = P_1 - P_2 - V_1^2/2 + V_2^2/2 \quad (2.3)$$

Here  $\mathbf{V}_1$  is the depth-averaged velocity for the thermocline ( $i = 1$ ) and the abyss ( $i = 2$ ),  $f$  is the Coriolis parameter,  $\mathbf{k}$  is the unit vertical vector,  $P_1 = p'_1/\rho_0 + V_1^2/2$ ,  $p'_1$  is the disturbance of pressure,  $g' = g(\rho_2 - \rho_1)/\rho_2$  is the reduced gravity,  $H_1$  is the layer thickness,  $D_1$  is the mean thickness of each layer,  $Z = H_1 - D_1 = D_2 - H_2$  is the perturbation of the depth of thermocline.

If the reference latitude is  $\theta$  on a planet of radius  $R$  and rotating with angular speed  $\Omega$ , the beta-plane approximation yields

$$f = f_0 + f_y y \quad (2.4)$$

where  $f_0 = 2\Omega \sin \theta$  and  $f_y = 2\Omega \cos \theta / R$ .

We make a dimensionless set of basic equations by using the scaling  $(U_1, L, T)$  for velocities of each layer, horizontal length and time scale. The scale for  $P_1$  is taken to be  $f_0 W_1$  from the geostrophic relation. From the hydrostatic relation (2.3) the nondimensional displacement  $\eta = g'Z/f_0 W_1$  is introduced. Thus a dimensionless set corresponding to (2.1)-(2.3) becomes

$$\tau \mathbf{v}_{1t} + \omega_1 \mathbf{k} \times \mathbf{v}_1 + \nabla p_1 = 0, \quad \omega_1 = 1 + \beta y + \varepsilon_1 \operatorname{rot}_z \mathbf{v}_1 \quad (2.5)$$

$$\tau \eta_t + \nabla \cdot [(s_1 + \varepsilon_1 \eta) \mathbf{v}_1] = 0 \quad (2.6)$$

$$-\tau \eta_t + \nabla \cdot [(s_2 \varepsilon_2 / \varepsilon_1 - \varepsilon_2 \eta) \mathbf{v}_2] = 0 \quad (2.7)$$

$$\varepsilon_1 \eta = \varepsilon_1 p_1 - \varepsilon_2 p_2 - \varepsilon_1^2 K_1 + \varepsilon_2^2 K_2, \quad K_1 = \mathbf{v}_1^2 / 2 \quad (2.8)$$

$$\varepsilon_1 = U_1 / L f_0, \quad s_1 = g' D_1 / L^2 f_0^2, \quad \beta = L f_y / f_0, \quad \tau = 1 / T f_0$$

Here the nondimensional parameters  $\varepsilon_1$  and  $s_1$  characterize the Rossby and Froude numbers for each layer. The beta-effect yields  $\beta$ . The value of  $\tau$ , defining the time scale  $T$  relative to the inertial period, and  $\mu = \varepsilon_2 / \varepsilon_1$  should be determined by the dynamics.

To obtain the law of energy conservation we multiply (2.6) by  $p_1$  and  $\mu p_2$  while taking into account (2.5) and (2.7)

$$\tau p_1 (p_{1t} - \mu p_{2t} - \varepsilon K_{1t} + \varepsilon \mu^2 K_{2t}) + \nabla \cdot [(s_1 + \varepsilon \eta) p_1 \mathbf{v}_1] =$$

$$(s_1 + \varepsilon \eta) \mathbf{v}_1 \nabla p_1 = -\tau (s_1 + \varepsilon p_1 - \mu \varepsilon p_2 - \varepsilon^2 K_1 + \varepsilon^2 \mu^2 K_2) K_{1t}$$

$$\mu \tau p_2 (\mu p_{2t} - p_{1t} + \varepsilon K_{1t} - \varepsilon \mu^2 K_{2t}) + \mu^2 \nabla \cdot [(s_2 - \varepsilon \eta) p_2 \mathbf{v}_2] =$$

$$\mu^2 (s_2 - \varepsilon \eta) \mathbf{v}_2 \nabla p_2 = -\tau (s_2 - \varepsilon p_1 + \mu \varepsilon p_2 + \varepsilon^2 K_1 - \varepsilon^2 \mu^2 K_2) \mu^2 K_{2t}$$

Here  $\varepsilon$  denotes  $\varepsilon_1$  for the simplicity. Adding these equations and integrating we obtain  $\iint E dx dy = \text{const}$ , where

$$\begin{aligned} E &= \eta^2/2 + (s_1 + \varepsilon\eta)K_1 + (s_2 - \varepsilon\eta)\mu^2 K_2 = \\ &= (p_1 - \mu p_2)^2/2 + s_1 K_1 + s_2 \mu^2 K_2 - \varepsilon^2 (K_1 - \mu^2 K_2)^2/2 \end{aligned} \quad (2.9)$$

It should be noted that to order  $\varepsilon^2$  the last expression for energy contains only quadratic terms while using  $p_1 - \mu p_2$  instead of  $\eta$ . The conservation of potential vorticity for fluid columns in each layer can be rewritten in terms of the potential thickness anomaly  $q_1$  as follows

$$\tau q_{1t} + \varepsilon_1 \nabla_1 \nabla q_1 = 0 \quad (2.10)$$

$$q_1 = s_1/\varepsilon - (s_1/\varepsilon + \eta)/\omega_1 = (s_1 \beta y/\varepsilon + s_1 \text{rot}_z \mathbf{v}_1 - \eta)/\omega_1$$

$$q_2 = s_2/\varepsilon - (s_2/\varepsilon - \eta)/\omega_2 = (s_2 \beta y/\varepsilon + \mu s_2 \text{rot}_z \mathbf{v}_2 + \eta)/\omega_2$$

Our purpose is to derive a set of equations for slowly varying flows ( $\tau \ll 1$ ) considering various relations between  $\beta$ ,  $\varepsilon$ ,  $\mu$ ,  $s_1$  and  $s_2$ .

### 3. GENERAL FILTERED MODEL

At mid latitudes and for the open-ocean mesoscale range, typical scales are:  $f_0 = 7 \cdot 10^{-5} \text{ s}^{-1}$ ,  $f_y = 2 \cdot 10^{-11} \text{ m}^{-1} \text{ s}^{-1}$ ,



$L = 70 \text{ km}$ ,  $U_1 = 0.5 \text{ ms}^{-1}$ ,  $U_2 = 0.1 \text{ ms}^{-1}$ ,  $g' = 2 \cdot 10^{-2} \text{ ms}^{-2}$ ,  
 $D_1 = 0.4 \text{ km}$ ,  $D_2 = 4 \text{ km}$ , yielding

$$\beta = 0.02, \quad \varepsilon = 0.1, \quad \mu = 0.2, \quad s_1 = 0.3, \quad s_2 = 3$$

Thus the typical relation between parameters are

$$10^{-2} \leq \beta \leq \varepsilon \leq \mu \leq s_1 \leq 1 \leq s_2 \quad (3.1)$$

From (2.11) we see that  $\tau \leq \varepsilon$ , thus the nearly geostrophic flow ( $\varepsilon \ll 1$ ) can be considered to be slowly varying ( $\tau \ll 1$ ) and from (2.5) the geostrophic velocity is correct to lowest order in  $\varepsilon$

$$\mathbf{v}_1 \approx \mathbf{k} \times \nabla p_1 \quad (3.2)$$

Substituting (3.2) into equations (2.8) and (2.10) while dropping small terms of order or less than the order  $s_1 \varepsilon^2$  gives

$$\begin{aligned} \tau q_{1t} &\approx J[(s_1 + \varepsilon p_1)(\beta y + \varepsilon \nabla^2 p_1) + \varepsilon^2 (\nabla p_1)^2 / 2 + \varepsilon \mu p_2, p_1] \\ \tau q_{2t} &\approx J[\beta \mu s_2 y + \varepsilon \mu^2 s_2 \nabla^2 p_2 + \varepsilon \mu p_1, p_2] \end{aligned} \quad (3.3)$$

Taking into account (3.1) and following Cushman-Roisin and Tang (1989) the time scale can now be determined as the biggest term in the right parts of (3.3). In this way we have

$$\tau \approx \varepsilon \max[s_1, \mu] \approx \mu s_2 \max[\beta, \varepsilon \mu] \quad (3.4)$$

The abyssal motion is considered to be generated mainly by the variation of the thermocline thickness, i.e., to be stretching dominated. Since  $\mu \leq s_1$  is taken in (3.1), to consider the self-consistent regimes in the two-layer system we suppose

$$\tau = \varepsilon s_1 = \beta, \quad \mu s_2 = 1 \quad (3.5)$$

Another relations between parameters was analyzed by Chassignet and Cushman-Roisin (1989). Dividing the equations (3.3) by  $\tau$  we obtain

$$q_{1t} = J[(1 + \alpha p_1)(sy + \nabla^2 p_1) + \alpha(\nabla p_1)^2/2 + \delta p_2, p_1] \quad (3.6)$$

$$q_{2t} = J[y + \delta \nabla^2 p_2 + \delta p_1, p_2] \quad (3.7)$$

$$\alpha = \varepsilon/s_1 = \beta/s_1^2 = (L/L_1)^5, \quad L_1 = (g'^2 D_1^2 / f_0^3 f_y)^{1/5}$$

$$\delta = 1/s_1 s_2 = (L/L_b)^4, \quad L_b = (g'^2 D_1 D_2)^{1/4} / f_0$$

Here  $s$  replaces  $s_1$  and  $\alpha$  characterizes the amplitude of relative variation of the thermocline thickness. With (3.5) one can see that the finite amplitude is reached if  $L \approx L_1 \approx 100$  km. Coupling between the thermocline and abyss is

characterized by  $\delta$ ;  $L_b$  is the scale of fastest growth of baroclinically unstable waves (Pedlosky, 1979).

By fixing two relations (3.5) between five parameters (3.1) we have now three parameters  $s$ ,  $\alpha$ ,  $\delta$  in the equations (3.6)-(3.7). Depending on the choice of the approximate form of their left sides we can obtain enstrophy or energy conserving variants of the general filtered two-layer model as Hukuda and Yanagata (1988) did for the reduced gravity unified geostrophic equations. If

$$q_1 \approx s[(1 + \alpha p_1)(sy + \nabla^2 p_1) + \alpha(\nabla p_1)^2/2 + \delta p_2] - p_1 \quad (3.8)$$

$$q_2 \approx y\delta^{-1} + \nabla^2 p_2 + p_1 - s\delta p_2 \quad (3.9)$$

then the equations (3.6)-(3.7) take the scaled form of (2.10)

$$q_{1t} + J[p_1, q_1] = 0, \quad q_{2t} + J[\delta p_2, q_2] = 0 \quad (3.10)$$

Here for each layer an arbitrary function of  $q_1$  is a lagrangian invariant and the enstrophy  $\iint q_1^2 dx dy$  is globally conserved. Dropping the  $\alpha$ -terms in (3.8) which are of the order  $\varepsilon = \alpha s$  in the left side of (3.6) we obtain the two-layer filtered model governed by the equations (3.6)-(3.9) with the energy conservation of the quadratic form

$$E = (p_1 - \delta s p_2)^2/2 + s(\nabla p_1)^2/2 + \delta s(\nabla p_2)^2/2 \quad (3.11)$$

In this case multiplying (3.6) by  $x$  and  $y$  and integrating over the whole beta-plane we obtain the momentum balance

$$\iint x(p_1 - \delta s p_2)_t + s \iint (p_1 + \alpha p_1^2/2) = \delta \iint p_2 p_{1y} \quad (3.12)$$

$$\iint y(p_1 - \delta s p_2)_t = -\delta \iint p_2 p_{1x} \quad (3.13)$$

Similar relations were obtained by Flierl (1974) for a lens-like eddy. Expressions (3.12)-(3.13) show that his analysis of the Rossby wave field and vortex motion can be extended to the more general case.

#### 4. COUPLED GEOSTROPHIC REGIMES

Using the reduced gravity model, being obtained from (3.6) and (3.8) for  $\delta = 0$ , seem to be quite problematic for the mesoscale oceanic eddies with the scale  $L \sim L_b$  ( $\delta \sim 1$ ). In this case a feedback between thermocline and abyssal motions should be taken into account.

The difference with the traditional quasigeostrophic model is described by the frontal effects connected with  $\alpha$ -terms in the equation (3.6) for the upper layer (Cushman-Roisin, 1986). Dropping these terms ( $\alpha = 0$ ) leads to commonly used two-layer quasigeostrophic equations.

Two kinds of coupling can be deduced from (3.6). The first is described by  $s\delta p_{2t}$ ; it is responsible for energy exchange between layers. The second is described by  $\delta J(p_2, p_1)$ ; it

does not change the energy and might be termed advective. In the quasigeostrophic regime when  $s \sim \delta \sim 1$  they both are essential and lead to the potential energy decay and barotropization in geostrophic turbulence (Rhines, 1979).

The most interesting (new) regime when  $\alpha \sim \delta \sim 1$  can be characterized as a coupled frontal geostrophic one. In this case  $s \sim \beta^{1/2} \ll 1$  and in the leading order approximation we drop terms connected with  $s$  to obtain from (3.6)-(3.9)

$$p_{1t} = J[p_1, F + p_2], \quad F = (1 + p_1)\nabla^2 p_1 + (\nabla p_1)^2/2 \quad (4.1)$$

$$\nabla^2 p_{2t} = J[y + \nabla^2 p_2, p_2] + J[F, p_1] \quad (4.2)$$

Here the available potential energy is conserved on the synoptic time scale  $T_s \sim L/f_y$ :  $\iint p^2 dx dy = \text{const.}$

The dispersive abyssal motions are excited by  $J[F, p_1]$  in (4.2) and cause only advection in the upper layer. Thus only advective type of coupling is considered in this regime. Any circular or rectilinear thermocline flows while being compensated, i.e. without motion in the abyss ( $p_2 = 0$ ), are steady solutions of (4.1)-(4.2). Such compensated solutions, if baroclinically stable, could be considered as attractors when the viscosity is small.

It should be noted that in the coupled frontal geostrophic regime the Froude number in the upper layer is small ( $s \ll 1$ ) while the one in the lower layer is large ( $s_2 \sim s^{-1} \gg 1$ ).

The two-layer model with small Froude numbers in the both layers has been recently analyzed by Kamenkovich (1989). In this case strong baroclinically instability of an arbitrary flow should be expected because of  $L \gg L_b$  ( $\delta \gg 1$ ) (Colin de Verdiere, 1986).

*Acknowledgments.* In preparing of this work during the GFD Summer Program conversations with Benoit Cushman-Roisin, Glenn Flierl, Melvin Stern and George Veronis were very helpful.

#### REFERENCES

- Charney, J.C. and G.R. Flierl (1981): Oceanic analogues of large scale atmospheric motions. In: B.A. Warren and C. Wunsch (Eds), Evolution of Physical Oceanography. The MIT Press, pp. 504-548.
- Colin de Verdiere, A (1986): On the mean flow instabilities within the planetary geostrophic equations. J. Phys. Ocean., 16, 1981-1984.
- Chassignet, E. and B. Cushman-Roisin (1989): On the Influence of the Lower Layer on an Upper Layer Isolated Ocean Ring in a Two-layer System.
- Cushman-Roisin, B. (1986): Frontal geostrophic dynamics. J. Phys. Oceanogr., 16, 132-143.
- Cushman-Roisin, B. and B. Tang (1989): Geostrophic regimes and geostrophic turbulence beyond the radius of deformation. In: J.C.J. Nihoul and B.M. Jamart (Eds), Mesoscale/Synoptic Coherence Structures in Geophysical Turbulence.

- Elsevier Science Publishers B.V. Amsterdam, pp. 51-74.
- Flierl, G.R. (1984): Rossby wave radiation and motion of strong warm core eddy. *J. Phys. Oceanog.*, 14,
- Flierl, G.R. (1987): Isolated eddy models in geophysics. *Ann. Rev. Fluid Mech.* 19, 493-530.
- Gent, P.R. and J.C. McWilliams (1983a): Consistent balanced models in bounded and periodic domain. *Dyn. Atmos. Oceans*, 7, 67-93.
- Gent, P.R. and J.C. McWilliams (1983b): Regimes of validity for balanced models. *Dyn. Atmos. Oceans*, 7, 167-183.
- Hukuda, H. and T. Yamagata (1988): A unified geostrophic equation with application to a cold core ring. *Tellus*, 45, 638-650.
- Kamenkovich, V.M. (1989): On the theory of quasigeostrophic motions in the two-layer ocean with the scale larger than the Rossby scale. *Okeanologia*, 29, 181-188.
- Matsuura, T. and T. Yamagata (1982): On the evolution of nonlinear planetary eddies larger than the radius of deformation. *J. Phys. Oceanogr.*, 12, 440-456.
- McWilliams, J.C. and P.R. Gent (1980) Intermediate models of planetary circulations in the atmosphere and ocean. *J. Atmos. Sci.*, 37, 1657-1678.
- Pedlosky, J. (1979): *Geophysical Fluid Dynamics*. Springer-Verlag, New-York, 624 p.
- Rhines, P.B. (1979): Geostrophic turbulence. *Ann. Rev. Fluid Mech.* 11, 401-441.

- Salmon, R. (1985): New equations for nearly geostrophic flow. *J. Fluid Mech.*, 153, 461-477.
- Sutyrin, G.G. (1985): On the calculation of vertical motions in the ocean. *Morskoy Hydrofiz. Zhurnal*, N 4, 25-33.
- Sutyrin, G.G. (1986): Synoptic motions of finite amplitude. *Dokl. Acad. Sci. USSR*, 280, 1101-1105.
- Sutyrin, G.G. and I.G. Yushina (1986a) On the evolution of isolated eddies in a rotating fluid. *Izv. Acad. Sci. USSR, Mekh. Zhidk. Gaza*, N 4, 52-59.
- Sutyrin, G.G. and I.G. Yushina (1986b): Interaction of synoptic eddies with finite amplitudes. *Dokl. Acad. Sci. USSR*, 288, 585-589.
- Sutyrin, G.G. and I.G. Yushina (1989): Numerical modelling of the formation, evolution, interaction and decay of isolated vortices. In: J.C. J. Nihoul and B.M. Jamart (Eds), *Mesoscale/Synoptic Coherence Structures in Geophysical Turbulence*. Elsevier Science Publishers B.V. Amsterdam, pp. 721-736.
- Williams, G.P. (1985): Geostrophic regimes on a sphere and a beta-plane. *J. Atm. Sci.*, 42, 1237-1243.
- Williams, G.P. and T. Yamagata (1984): Geostrophic regimes, intermediate solitary vortices and Jovian eddies. *J. Atmos. Sci.*, 41, 453-478.
- Yamagata, T. (1982): On nonlinear planetary waves: a class of solutions missed by the quasigeostrophic approximation. *J. Oceanogr. Soc. Japan*, 38, 236-244.



## Can Potential Vorticity Homogenize in Closed Gyres?

LuAnne Thompson

### Abstract

A process model of the Gulf Stream recirculation is modified to show that the solution that results from taking the inviscid limit of the quasi-geostrophic equations is not necessarily a free inertial mode. The model is forced by anomalous potential vorticity on the northern and western boundaries of a rectangular domain. When the boundary is rotated by a positive angle with respect to the lines of constant planetary potential vorticity, the solutions always become frictionally dominated as the viscosity is reduced. The frictionally dominated solution on the northern boundary asymptotes to a simple analytic form, analogous to the Munk balance, as the viscosity is reduced.

### 1 Introduction

Certain features of the general circulation of the ocean are dominated by inertial rather than frictional effects, and both the planetary and the relative vorticity are important. Dramatic examples of this regime are western boundary currents that appear in both ocean observations and in numerical models of large scale wind driven ocean circulation. In the Atlantic ocean, there is recirculation of water in two gyres north and south of the Gulf Stream. These gyres have limited meridional extent and their circulation results in enhanced Gulf Stream transport. The wind driven portion of the North Atlantic circulation is believed to have a transport of about  $30 \times 10^6 \text{ m}^3/\text{s}$ , while the maximum transport of the Gulf Stream is almost  $150 \times 10^6 \text{ m}^3/\text{s}$  (Richardson, 1985). This recirculation can appear where there is no local wind forcing. Cessi et al. (1987) (hereafter CIY) demonstrated this by forcing a homogeneous ocean with a wind stress curl that is zero above a certain latitude. The solution shows a recirculation gyre in the northwest corner of the box where the wind stress curl is zero. In the solution, the potential vorticity is uniform within the recirculation gyre. Within this gyre the relative vorticity is important, and inertial effects dominate. Oceanographers are not yet able to measure the relative sizes of relative and planetary vorticity within the Gulf Stream recirculation, but it is clear

that both could be important there.

Several analytic models have been used to explore the dynamics of the recirculation. In order to make analytical progress, friction is assumed to be unimportant in the dynamics of this feature (CIY, Marshall and Nurser, 1986). The assumption behind the neglect of friction is that the solution will be a free inertial mode of the system when the viscosity is reduced. We will show that this assumption does not hold when the geometry of the recirculation model of CIY is varied by a small amount. The work that follows suggests that one cannot easily extend inviscid solutions of two-dimensional problems to more general geometries and forcings.

The model of the recirculation that is considered is the one described in CIY and Ierley and Young (1988) (hereafter IY). In this model, the quasi-geostrophic potential vorticity equation is driven by anomalous potential vorticity applied at the boundary. The steady quasi-geostrophic potential vorticity equation is then solved numerically in the presence of lateral diffusivity. The dynamics of the recirculation are isolated from the wind driven part of the circulation in this process model. No wind stress curl is applied for the results given below. The anomalously low values of potential vorticity that are applied in the northwest corner model the effect of northward advection of low values of potential vorticity of southern origin by the Gulf Stream, or alternatively the generation of low values of potential vorticity locally by buoyancy effects. The relationship between the potential vorticity forcing and the dynamics of the gyre as a whole will not be discussed here, but the relative simplicity of the model allows a thorough exploration of the behavior of the system as the diffusivity is reduced. The advantages of this model are its time independence and confined spatial extent, which make many realizations of the solution affordable; unlike time dependent models of the ocean circulation that exhibit qualitatively similar behavior.

As motivated by observations and numerical experiments, the recirculation gyre is assumed to be dominated by inertial effects in its interior. Both CIY and Marshall and Nurser(1986) suggest that this gyre is a free inertial mode of the basin. As the diffusivity is reduced, the local Reynold's number for both of these solutions will go to infinity. In particular the CIY solution is one with uniform potential vorticity. Constant potential vorticity occurs within closed streamlines which never

pass through frictional boundary layers (Rhines and Young, 1982). This result holds as the viscosity,  $\kappa$ , is reduced, and is motivated by an application of the Prandtl-Bachelor theorem that tracers in two-dimensional flow will become constant within closed streamlines. In contrast, when every closed streamline passes through a frictional boundary layer, friction will be dominant everywhere. In fact, as  $\kappa$  is reduced this frictional regime can be realized instead of a free inertial mode.

In IY, anomalous potential vorticity is applied in the northwest corner of a box in order to model the confined longitudinal extent of the Gulf Stream recirculation. The resulting gyre is of nearly constant potential vorticity, but the strength of the circulation diminishes as dissipation is decreased. The Reynolds number does tend to infinity as  $\kappa$  is reduced, and a free inertial mode results. In this paper, the geometry of IY is slightly altered by rotating the boundary with respect to the lines of constant planetary potential vorticity by an angle  $\theta$ , but the forcing is kept at the IY value. The problem now has two free parameters,  $\theta$ , the angle of the tilt, and  $\kappa$ , the dimensional viscosity, as in IY. This study will show that when  $\theta > 0^\circ$ , the free inertial mode is no longer realized as the inviscid limit of the equations, but instead, a frictionally dominated solution results.

## 2 The Model

The quasi-geostrophic formulation for a one layer ocean is used. The governing equations are

$$J(\psi, q) = \kappa \nabla^2 q \quad (1)$$

where

$$(-\psi_y, \psi_x) = (u, v)$$

and

$$q = \zeta + \beta y \cos \theta + \beta x \sin \theta .$$

Here  $\zeta = \nabla^2 \psi$ . The boundary conditions are

$$\zeta = \zeta_b(s),$$

where  $s$  is the arclength around a rectangular box. Also,  $\psi = 0$  there.

The parameterization of friction on the scale of interest as Laplacian friction is motivated by Rhines and Young (1982) and has been used extensively in oceanography. This form of friction also allows analogies with more general two-dimensional fluid mechanics problems.

The angle  $\theta$  measures the tilt of the planetary vorticity contours relative to the boundary of the domain where the forcing is applied. This simple change in the recirculation model of IY mimics the Gulf Stream exiting the coast with a trajectory not aligned with a planetary potential vorticity contour. This situation can be realized in a more general wind driven time dependent numerical model by tilting the zero wind stress curl line with respect to a latitude circle (P. B. Rhines; personal communication). When  $\theta$  is positive, the northern boundary is rotated counter-clockwise by an angle  $\theta$ . Therefore, some planetary potential vorticity contours originating at the eastern boundary and terminate at the northern boundary. On the other hand, when  $\theta$  is negative, some planetary potential vorticity contours originating at the northern boundary and terminate at the western boundary (Figure 1).

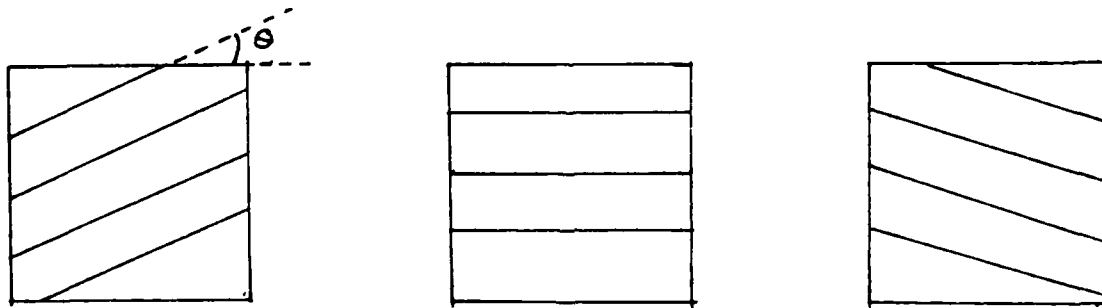


Figure 1: Schematic of planetary potential vorticity lines with respect to the boundaries of the domain. The angles of rotation from left to right are  $\theta < 0^\circ$ ,  $\theta = 0^\circ$ , and  $\theta > 0^\circ$ .

We consider steady solutions to this problem in a rectangular domain  $-L < y < L$  and  $-L/\alpha < x < L/\alpha$  where  $\alpha$  is the horizontal aspect ratio of the basin. On the sides of the basin, the boundary conditions are  $\psi = 0$  and a prescribed relative

vorticity distribution, independent of  $\theta$  given by:

$$\begin{aligned} y = L \quad \zeta &= \beta L [\tanh(10\alpha/L) - 1] / 2 \\ x = -L\alpha \quad \zeta &= \beta L [\tanh\{(y + L)/L\} / \tanh 2] - \beta L - y \\ \text{otherwise} \quad \zeta &= 0. \end{aligned}$$

This problem is solved numerically by Newton's iteration in a program developed by Glenn Ierley. In IY  $\alpha = 0.3$ , and  $\theta = 0^\circ$ . The structure of the boundary condition on  $\zeta$  is shown in Figure 2.

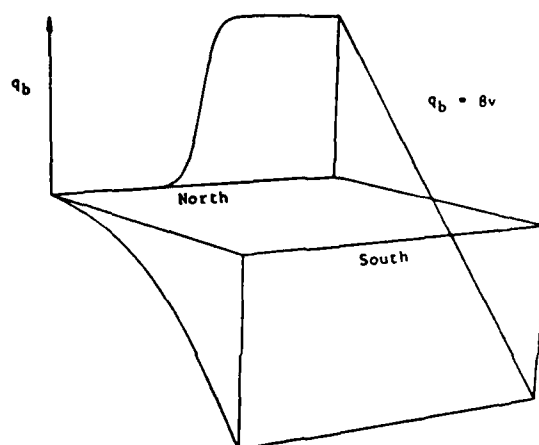


Figure 2: A perspective view of  $\zeta_b + \beta y \cos \theta + \beta x \sin \theta$  for  $\theta = 0^\circ$ . Except in the northwest corner, the potential vorticity is the planetary potential vorticity, and  $\zeta_b$  is constant on the first half of the northern boundary, and then falls to zero for the second half. (Figure taken from IY).

The introduction of anomalous relative vorticity ( $\zeta = -u_v < 0$ ) at the northern boundary drives a current towards the east there. This vorticity is advected eastward and diffused southward into the interior. At some point after the forcing goes to zero, the current turns into the interior in order to return all of the fluid to the western boundary, closing the gyre. To consider the relative sizes of advection and

diffusion, a local Reynolds number is defined as

$$R = \frac{U/\Delta}{\kappa/w^2},$$

where  $U$  is the eastward velocity scale of the gyre, and  $\Delta$  and  $w$  are the length scales of the gyre in the  $x$  and  $y$  directions respectively.

IY show that when  $\theta = 0^\circ$ ,  $w \propto \kappa^{1/6}$ ,  $\delta \propto \kappa^{1/3}$  and  $\psi \propto \kappa^{1/2}$ , where  $\delta$  is the frictional boundary layer scale. Here, they assume that  $\Delta$  is independent of  $\kappa$ . Therefore  $R \propto \kappa^{-1/3}$ . It is clear that  $\Delta$  depends on  $\kappa$  (IY, their Figure 3), but a consistent scaling for its dependence has yet to be found. To review their scaling, the size of the terms in (1) are examined. In the interior, potential vorticity is uniform and  $\partial_x \ll \partial_y$ , so that  $u_y$  must balance  $\beta y$ , or  $U = \beta w^2$ . In the frictional sub-layer near the northern boundary,  $-u_y = \zeta_b$  or  $U = \zeta_b \delta$  must hold. Since  $x$  variations are negligible, in the boundary layer diffusion of  $\psi_{yy}$  in the  $y$  direction is balanced by advection in the  $x$  direction, so  $\zeta_b \alpha / L \beta = \kappa / \beta \delta^3$ , since the length of the forcing region is  $L/\alpha$ . Thus  $\delta = (\kappa L / \alpha \zeta_b)^{1/3}$ . Since the velocity must be continuous from the boundary layer to the interior, then the scale for  $w$  is given by  $w = (\kappa L / \alpha \zeta_b)^{1/6} (\zeta_b / \beta)^{1/2}$ .

### 3 The Numerical Solutions

In order to infer something about the dynamics of the ocean using the results of IY, it is necessary to show that changes in the boundary conditions or the geometry do not greatly effect these results. IY show that forcing the gyre from the center of the northern boundary produces a similar gyre as described above. Here, a small change in geometry is shown to drastically effect the inviscid limit of this problem.

A series of numerical solution to (1) for  $\theta = 0^\circ$ ,  $5^\circ$ ,  $10^\circ$ , and  $45^\circ$  are calculated (see Figures 3-7 for the following discussion). Since these experiments have an aspect ratio  $\alpha = 1$ , a detailed comparison to IY cannot be made. For all of the solutions there is a closed recirculating gyre in the northwest corner. As  $\kappa$  decreases, or as  $\theta$  increases the gyre becomes narrower in the  $y$  direction, and the transport decreases. For the solutions found, for  $\theta = 0^\circ$ ,  $5^\circ$ , and  $10^\circ$ , the gyre elongates in the  $x$  direction as  $\kappa$  decreases. For  $\theta = 45^\circ$ , the gyre remains the same length. Only for  $\theta = 0^\circ$  does the solution become more nonlinear as  $\kappa$  is reduced, for the other angles, as  $\kappa$  is reduced, the solution actually becomes viscously dominated.

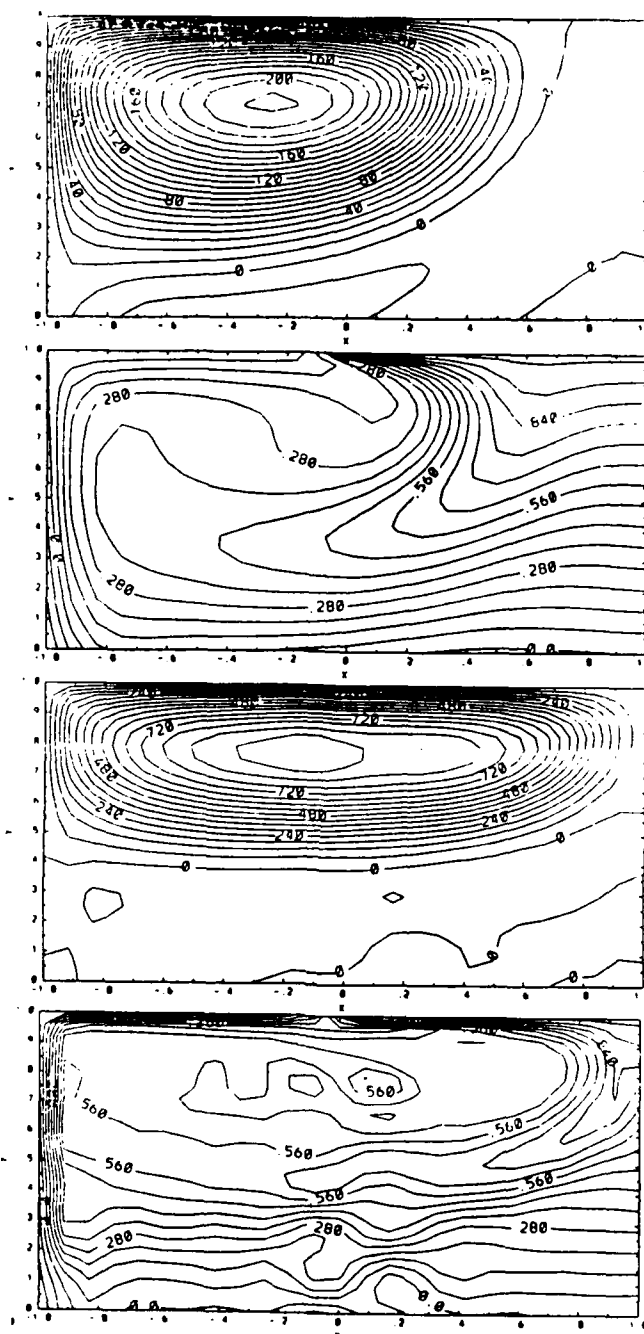


Figure 3: Contours of stream function in units of  $\beta L^3$  and potential vorticity in units of  $\beta L$  for the upper half of the box for  $\theta = 0^\circ$ . The fluid in the rest of the box is essentially at rest. From top to bottom is  $\psi$  for  $\kappa = 0.001$ ,  $q$  for  $\kappa = 0.001$ ,  $\psi$  for  $\kappa = 0.0001$ , and  $q$  for  $\kappa = 0.0001$ .

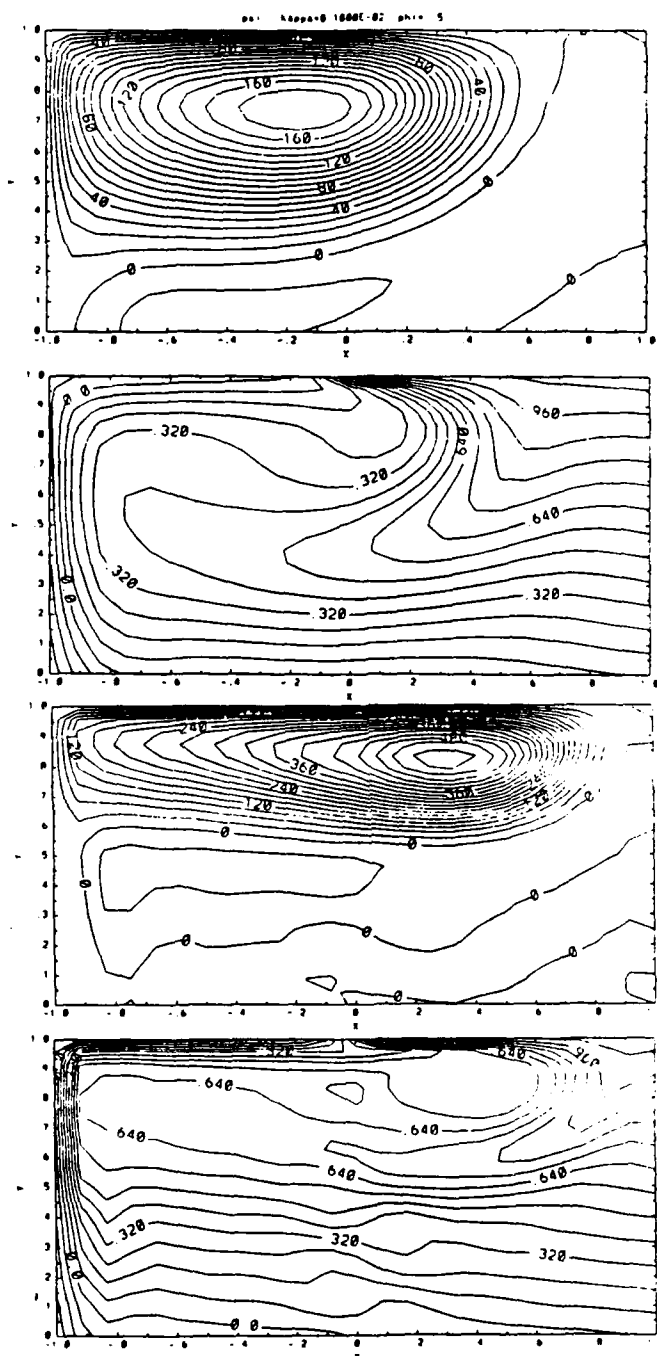


Figure 4: As for Figure 3 except  $\theta = 5^\circ$ .



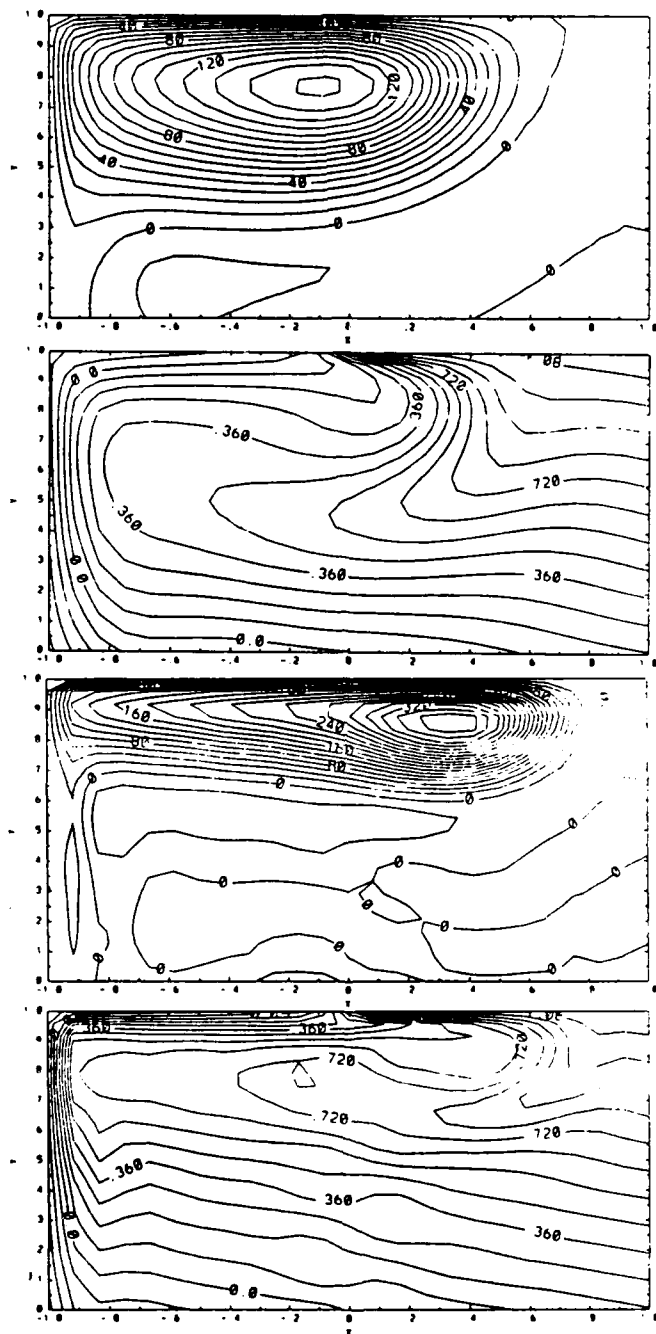


Figure 5: As for Figure 3 except  $\theta = 10^\circ$ .

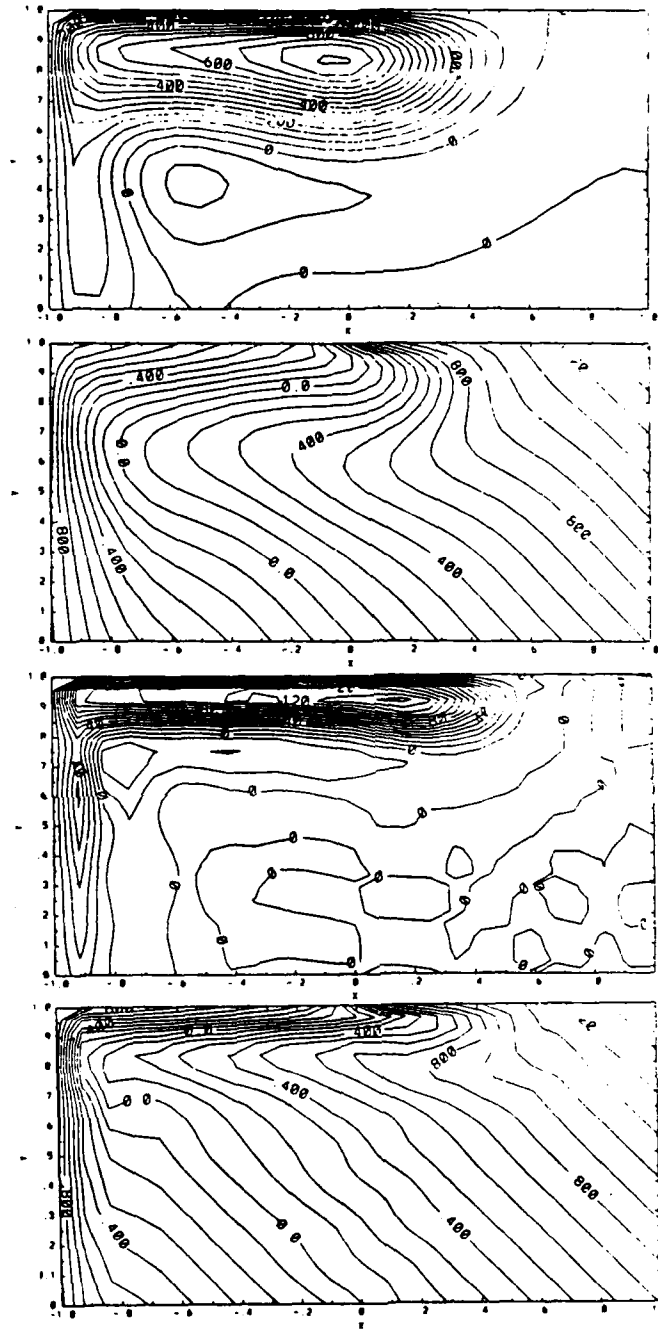


Figure 6: As for Figure 3 except  $\theta = 45^\circ$ .

The high viscosity solutions for all of the angles are qualitatively similar to the  $\theta = 0^\circ$  runs. However, as  $\kappa$  is decreased, with  $\theta > 0^\circ$  the gyre becomes more asymmetric. For  $\theta = 5^\circ$  and  $10^\circ$ , the point where the stream function is maximum moves further to the east, whereas for  $\theta = 45^\circ$ , the point where the stream function is maximum remains close to the end of the forcing region and the gyre turns just after the forcing stops. All these solutions are in contrast to the  $\theta = 0^\circ$  solutions where the gyre becomes symmetric about  $x = 0$ . The slope of the outermost streamline is negative initially for the larger values of viscosity and  $\theta > 0^\circ$ . However, as the viscosity is decreased, the streamlines become parallel to the northern boundary. The gyre becomes independent of  $x$  between the western boundary and the end of the forcing region, particularly for the solutions found for  $\theta = 45^\circ$ . For the most inviscid solutions for  $\theta = 10^\circ$ , and  $45^\circ$  (Figure 7), the streamlines and the lines of constant potential vorticity cross throughout the gyre, an indication that diffusion is important throughout the gyre.

#### 4 Boundary Layer Dynamics and the Breakdown of the Inviscid Solution

The above behavior can be explained in terms of changes in the boundary layer dynamics when  $\theta > 0^\circ$ . In fact, the boundary layer scaling suggests that, in the inviscid limit of the frictional problem posed above, if  $\theta$  is a small fixed angle, and the viscosity is reduced, the solutions will approach a viscously dominated solution instead of a free inertial mode of the inviscid equations.

When  $\theta > 0^\circ$ , some of the potential vorticity contours which originate at the eastern boundary terminate at the northern boundary. The northern boundary becomes an effective extension of the western boundary, along which the planetary potential vorticity is increasing. On the northern boundary, a jet is set up as in IY, however now fluid parcels traveling along the boundary must cross lines of constant planetary potential vorticity. If the fluid is to conserve its potential vorticity, then the relative vorticity must decrease as the fluid moves along the boundary. This change results in an increased shear ( $\zeta = -u_y$ ). There are two possible adjustments. First, the velocity can increase both in the interior and in the frictional boundary layer, increasing the shear in the interior while keeping the width of the gyre fixed.

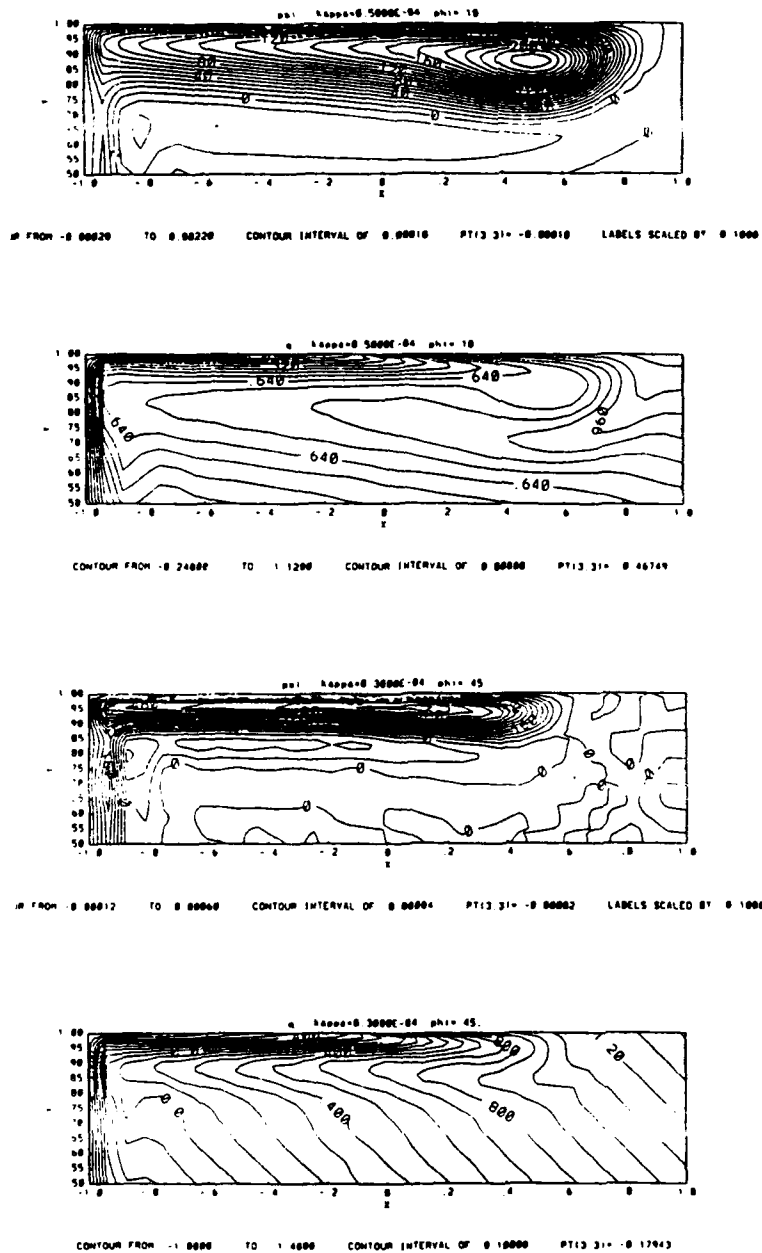


Figure 7: Contours of stream function in units of  $\beta L^3$  and potential vorticity in units of  $\beta L$ . Only the upper quarter of the box is presented because the fluid in the rest of the box is essentially at rest. From top to bottom is  $\psi$ ,  $q$  for  $\kappa/\beta L^3 = 5 \times 10^{-5}$  and  $\theta = 10^\circ$ ,  $\psi$ ,  $q$  for  $\kappa/\beta L^3 = 3 \times 10^{-5}$  and  $\theta = 45^\circ$

In this case the frictional boundary layer scale has to increase to keep the shear at the boundary equal to the boundary value, resulting in less of a scale separation between the interior and the boundary layer. Alternatively, the width of the gyre can decrease, increasing the shear in the interior, once again resulting in an increased influence of friction.

The balance of terms in (1) gives an indication of how a solution of homogeneous potential vorticity breaks down as viscosity is decreased for a fixed angle of rotation. At the northern wall, as for IY,  $U = \zeta_b \delta$  where  $\delta$  is the frictional boundary layer width and  $\delta \propto \kappa^{1/3}$ . If the interior has constant potential vorticity, then the relative vorticity must balance gradients in planetary vorticity either along or across the gyre. That is

$$U/w = \max(\beta \sin \theta \text{ or } \beta \cos \theta w). \quad (2)$$

where  $U/w$  is the scale for  $\zeta$  in the interior of the homogenized gyre. Since the velocity must be continuous from the boundary layer to the interior of the gyre, the width scale of the gyre will be given by (2) and will be the smaller of

$$\left( \frac{\zeta_b \delta}{\beta \cos \theta} \right)^{1/2} \quad (3)$$

and

$$\frac{\zeta_b \delta}{\Delta \beta \sin \theta}. \quad (4)$$

In general  $\delta \propto \kappa^{1/3}$  (as will be discussed in Section 5), so that for fixed angle as  $\kappa$  is decreased, (4) becomes the width of the gyre instead of the IY result which is given by (3). This balance holds no matter how small the fixed angle  $\theta$  is. When the angle is small (for example  $5^\circ$ ), (4) suggests that the width of the gyre is much larger than the frictional boundary layer, which implies that the gyre may be inertially dominated. To see if the inviscid solution is an inertial mode, the Reynolds number must be considered. At fixed angle, if the limit as  $\kappa$  goes to zero is taken, and an inviscid solution is reached, and  $R$  is infinite. In this case we find that

$$R = \left( \frac{\zeta_b}{\Delta \beta} \right)^3 \frac{\delta^3}{\kappa \beta^3 \sin^3 \theta}.$$

Now,  $\Delta$  must be at least as big as  $L/\alpha$ , the length of the forcing region, so that at most,  $R$  is independent of  $\kappa$ , and does not go to infinity as the inviscid limit is

taken. Therefore, an inviscid solution will not be reached at fixed angle as the limit as  $\kappa$  goes to zero is taken. Since the forcing is independent of  $x$  for a region long compared with the boundary layer scale, we can find an analytic solution for  $\psi$  as  $\kappa$  is reduced at fixed  $\theta$ .

## 5 The Frictionally Dominated Solution

The inviscid limit of this problem when the angle of rotation  $\theta > 0^\circ$  is a viscously dominated solution. In order to see what the solution might look like, we consider the balance of terms in the viscous boundary layer, and decide which terms are important. In the boundary layer the dominant terms in the vorticity equation (1) are

$$J(\psi, \psi_{yy}) + \beta \cos \theta \psi_x - \beta \sin \theta \psi_y = \kappa \psi_{yyyy} . \quad (5)$$

The length scale in the  $y$  direction is given by  $\delta$ , the frictional boundary layer thickness, the length scale in the  $x$  direction is  $L/\alpha$ , the length of the forcing, and  $\psi$  scales as  $\psi \delta^2$  as required by the boundary conditions on the relative vorticity. The size of the each term in (4) is given by

$$\frac{J(\psi, \psi_{yy})}{\frac{\delta^2 \delta \alpha}{L}} + \frac{\beta \cos \theta \psi_x}{\frac{\beta \cos \theta \delta_b \delta^2 \alpha}{L}} - \frac{\beta \sin \theta \psi_y}{\beta \sin \theta \delta_b \delta} = \frac{\kappa \psi_{yyyy}}{\frac{\kappa \delta_b}{\delta^2}} . \quad (6)$$

We now scale everything by the size of the viscous term to get

$$\frac{\delta^3 \beta}{\kappa} \left[ \alpha \quad \frac{\delta \alpha \cos \theta}{L} \quad \sin \theta \right] = 1$$

where  $\delta_b = \beta L$ . The viscous term is expected to be important everywhere in the viscous boundary layer near the northern wall. The second term,  $\beta v$  the advection of planetary vorticity in the north-south direction, is always subdominant as the viscosity is reduced. If this term balances the friction, this would correspond to a linear Munk balance at the northern wall of the box. It is important to note that all of this discussion concerns flow that is far from the linear regime, because the size of the forcing is  $\beta L$ , which is larger even than changes in the planetary vorticity across the gyre. Therefore the first and the third terms balance the frictional term in the boundary layer when  $\theta > 0^\circ$ . Particularly when the the angle is large, the character of the gyre is  $x$  independent south of the forced region, and the first term

vanishes identically, so the third term balances the friction by itself. This balance results in a simple solution which satisfies the non-linear balance throughout the interior of the gyre south of the forcing region. This solution is analogous to the Munk western boundary layer solution, where linear dynamics apply, however, here the solution satisfies the nonlinear equation (5). The boundary conditions for the solution here are  $\psi_{yy} = \zeta_b$  and  $\psi = 0$  at  $y = L$ . Thus

$$\psi = -\zeta_b \delta^2 \frac{2}{\sqrt{3}} e^{(y-L)/2\delta} \sin\{(y-L)\sqrt{3}/2\delta\} \quad (7)$$

where

$$\delta = \left( \frac{\kappa}{\sin \theta \beta} \right)^{1/3}.$$

This solution is valid because  $\zeta_b$  is independent of  $x$  in a large region. If the forcing function varied in  $x$  then the first and the third terms would combine to balance friction when  $\theta > 0^\circ$ . This boundary layer balance reduces smoothly to the boundary layer balance of IY as  $\theta$  goes to zero. For the forcing chosen here, even for small angles, the solutions become quite independent of  $x$  when  $\kappa$  is small enough south of the forcing region (Figure 7). This suggests that for this choice of forcing, the solution will always approach (7) as long as  $\theta > 0^\circ$ . Quantitatively (7) agrees quite well with the numerical solution for  $\psi$  when compared with a cut across the gyre south of the forcing (Figure 8). The correspondence improves as  $\theta$  increases, or as  $\kappa$  is decreased.

As a summary of the numerical solutions used in this study, the maximum streamfunction versus  $\kappa$  on a log log scale is of interest (Figure 9). The slope of the line gives  $a$  where  $\psi_{max} \propto \kappa^a$ . Also shown is the maximum streamfunction for (7) on the same scale for each angle of rotation used. Although the transition to the solution given by (7) occurs at much lower viscosity for smaller angles, all the solutions approach it in a quantitative comparison. This behavior confirms that even for small angles of rotation, the entire solution is dominated by friction. In fact, as  $\kappa$  is reduced, the agreement between the numerical and analytic solutions improves, so that the solutions become more viscously dominated as  $\kappa$  is reduced.

If the set of experiments were redone for a forcing function that depended on  $x$ , the comparison to (7) would no longer hold, but the maximum streamfunction

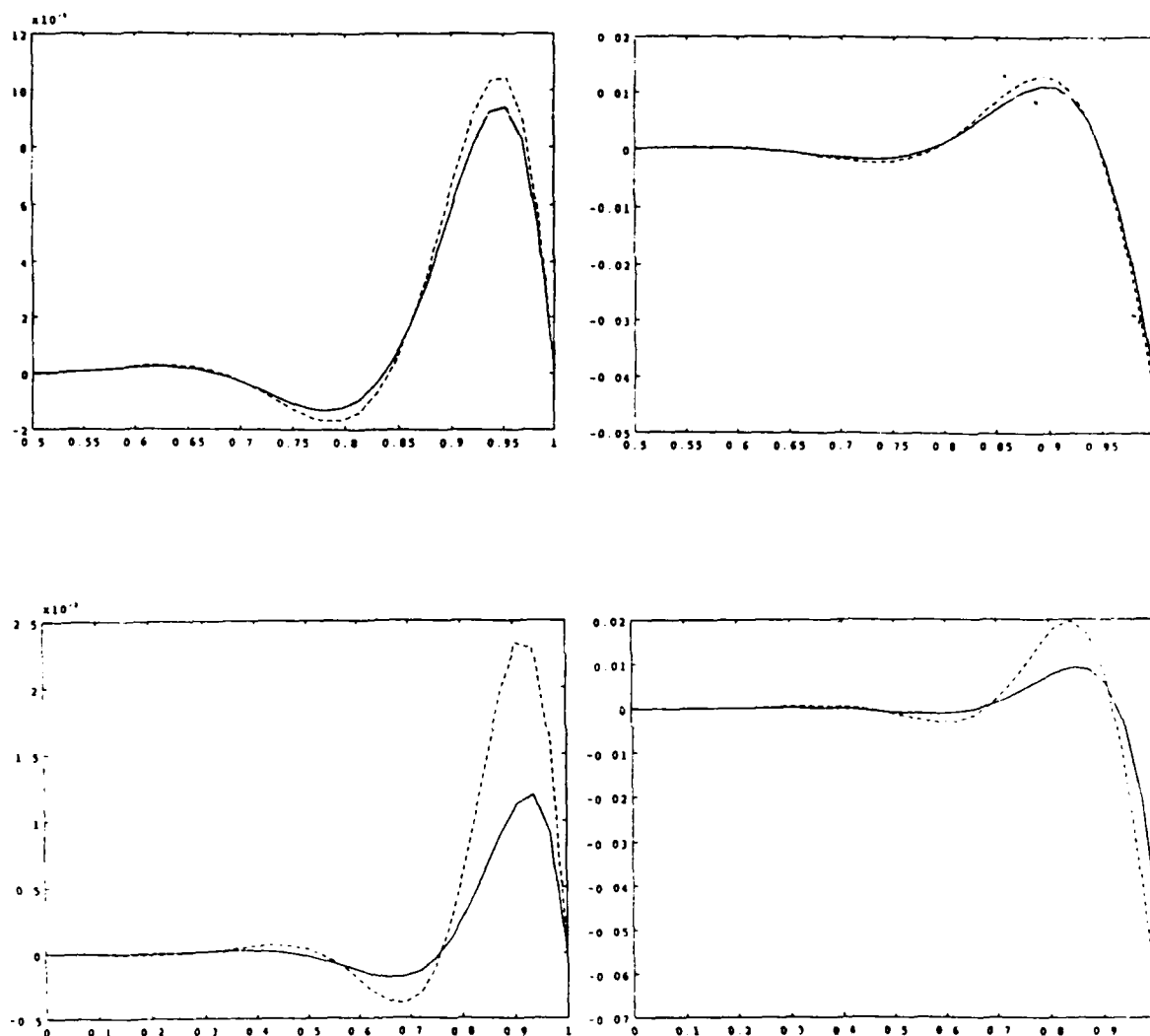


Figure 8: A comparison of  $\psi/\beta L^3$  and  $\psi_y/\beta L^2$  for the numerical solution (solid line) and (7) the Munk solution (dashed line). The top graphs are for  $\theta = 45^\circ$ ,  $x = -0.2/L$ ,  $\kappa = 5 \times 10^{-5}$ , and the bottom graphs are for  $\theta = 10^\circ$ ,  $x = -0.5/L$ ,  $\kappa = 6 \times 10^{-5}$ .



northern boundary is independent of  $x$ , then the solution approaches the simple solution given by (7) and is dominated by friction everywhere. The change in behavior results when the planetary potential vorticity lines are tilted with respect to the boundary where the forcing is applied. The northern boundary becomes an extended western boundary, and variations in planetary potential vorticity along the boundary dominate the dynamics of the recirculation gyre. The fact that the potential vorticity forcing is applied along a meridian is an important aspect of the  $\theta = 0^\circ$  case which is vital to the conclusions of IY.

The boundary layer scalings suggested above, and the predicted size of the transport in the gyre, no longer hold when the gyre reaches the eastern boundary. The turning region has not been discussed, but the gyre turns when it has diffused enough relative vorticity to allow the velocity to approach a stagnation point. However, when the gyre reaches the eastern boundary, it can support a pressure gradient which allows the gyre to turn back to the west with less of the vorticity diffused into the interior and more carried back into the interior, breaking the frictional domination in the interior and allowing a free inertial mode to set up in at least part of the gyre. The lowest viscosity solution found for  $\theta = 10^\circ$  confirms this assertion. In this solution, the gyre has reached the eastern boundary (Figure 10) and the maximum streamfunction is only slightly smaller than the one found with larger  $\kappa$ , where the gyre has not felt the influence of the eastern boundary (Figure 7). The potential vorticity distribution suggests that if the viscosity were reduced even further, the gyre in the northeast corner would develop constant potential vorticity. This result is consistent with CIY where the gyre is forced on the western, northern and eastern boundaries, the strength of the gyre is influenced only by the strength of the forcing, and the resulting solution is independent of the value of the viscosity.

If on the other hand the gyre is rotated in the opposite direction, the northern boundary now becomes an extension of the eastern boundary. By the argument given above, the northern boundary is able to support a pressure gradient and the potential vorticity will be uniform at an even larger  $\kappa$  than for  $\theta = 0^\circ$ . Since fluid parcels along the boundary are moving to lower values of potential vorticity, the shear decreases. Reversing the argument given above, the separation between the

would still scale as  $\kappa^{2/3}$  and the slope of the lines in (Figure 9) would again approach  $2/3$ , instead of the IY result of  $1/2$  (IY their Figure 7). Because the forcing function here is simple, a quantitative comparison between the known frictionally dominated solution and the numerical results is possible.

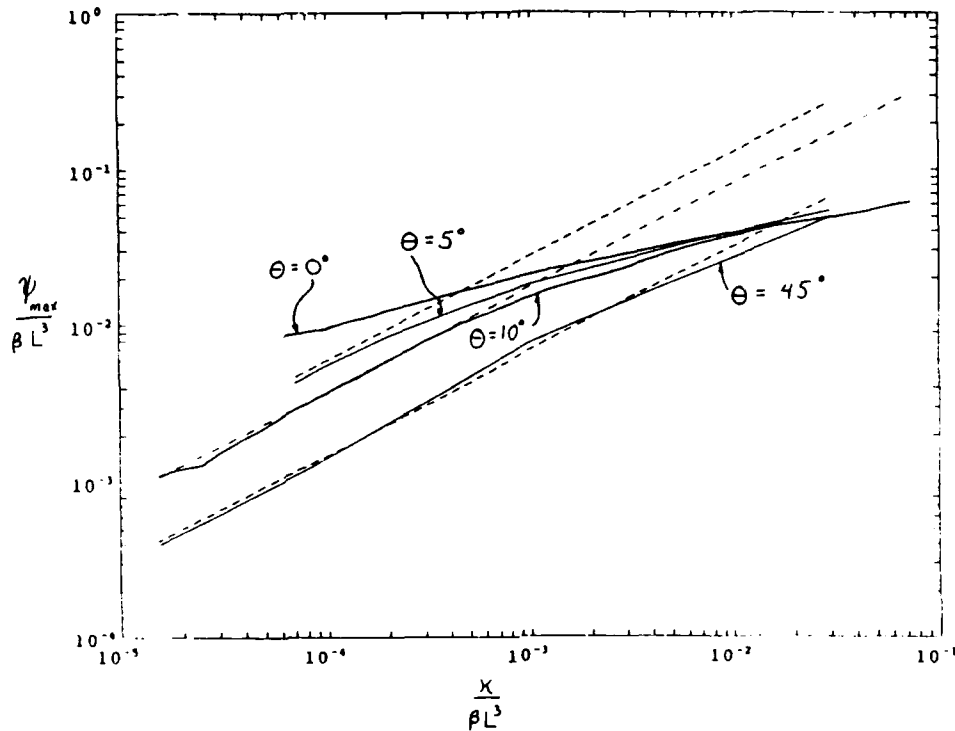


Figure 9: Maximum stream function ( $\psi_{max}/\beta L^3$ ) versus  $\kappa/\beta L^3$  for  $\theta = 0^\circ, 5^\circ, 10^\circ$ , and  $45^\circ$ . The solid lines are the numerical solutions, and the dashed lines are the solution given by (7). Notice that for  $\theta > 0^\circ$ ,  $\psi_{max}$  approaches that given by (7). The gyre feels the influence of the eastern boundary at the last points for  $\theta = 0^\circ$  and  $10^\circ$ , which is why the slope of the numerical solutions changed there. There the scalings no longer hold and the maximum stream function becomes independent of  $\kappa$ .

## 6 Summary and Discussion

An oceanographic problem has been explored where when one parameter, the angle of rotation  $\theta$ , is changed, even by a small amount, the inviscid limit of solution is no longer an inviscid solution of the equations. In fact, if the forcing on the

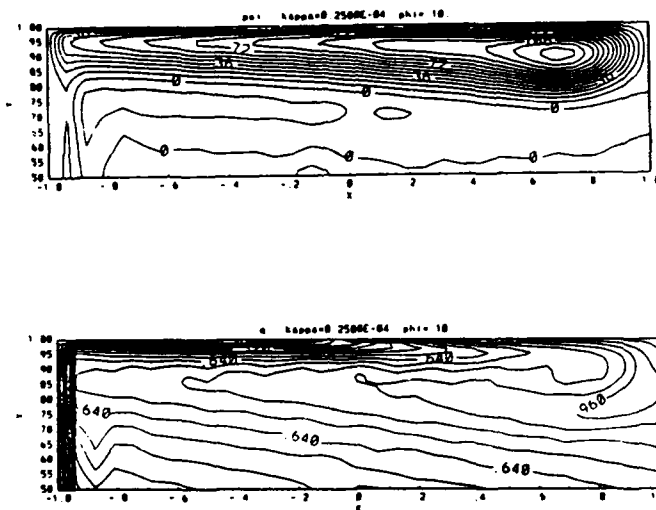


Figure 10: Stream function and potential vorticity contoured for  $y = 0.5$  to  $y = 1$ ,  $\kappa = 2.5 \times 10^{-5}$  and  $\theta = 10^\circ$  for only the top quarter of the domain. The gyre has reached the eastern boundary.

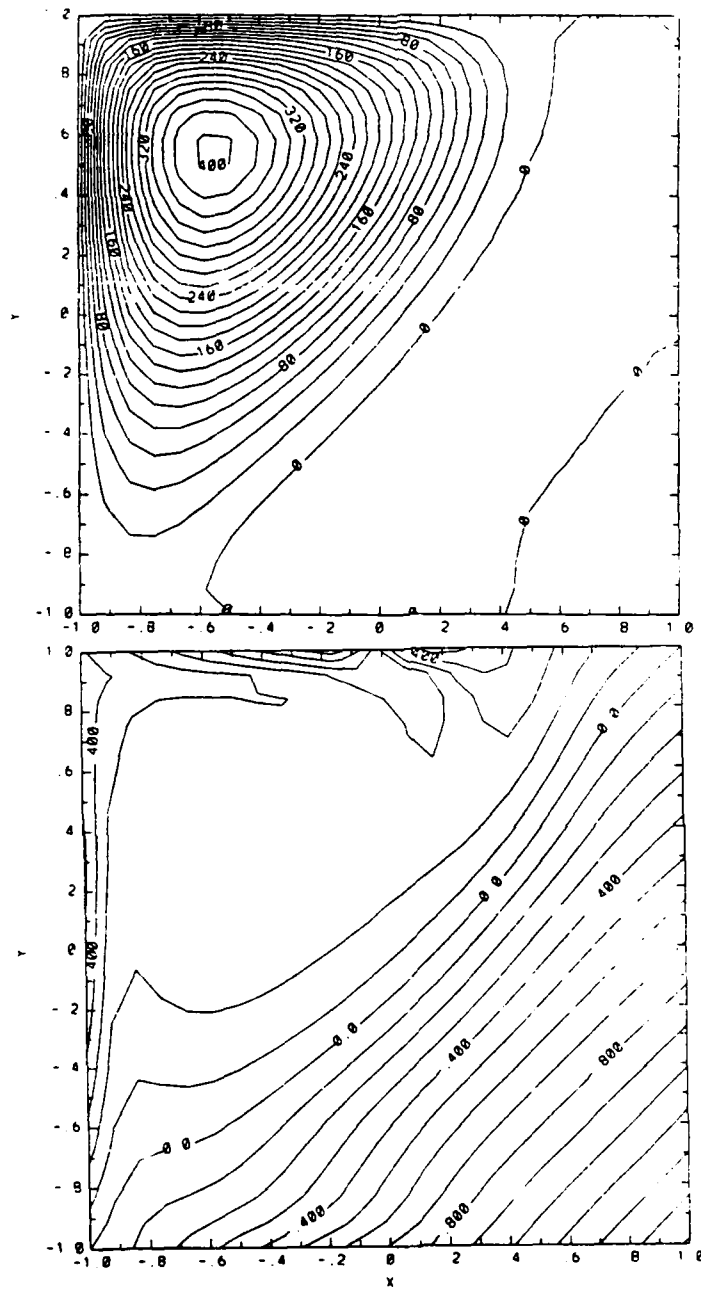


Figure 11: Stream function and potential vorticity contoured for the entire box for  $\kappa = .001$  and  $\theta = -45^\circ$ .

boundary layer scale and the interior scale is increased. A solution was found that shows an extreme example of this for a moderate values of  $\kappa$  and the solution has potential vorticity that is nearly constant in a very large region (Figure 11).

As with any model of this sort, the connection with oceanographic observations is tenuous, however, the results of this study suggest that since the Gulf Stream exits the coast at a positive angle with respect to meridians, the southern recirculation gyre would be weaker than what one would expect from a symmetric wind driven model. In turn, the northern recirculation gyre would be expected to be stronger. The results of this study also suggest that a strong recirculation depends crucially on the fact that the Gulf Stream separates from the coast and begin to travel approximately along lines of constant planetary potential vorticity. In the extreme case of  $\theta = 90^\circ$ , the forcing would be applied on the western boundary, the frictional regime would dominate, and a very weak recirculating gyre would result. The literature is fairly limited in this regard, so time will tell if this conclusion is consistent with observations.

### Acknowledgments

I would like to thank the GFD selection committee for giving me this opportunity to work so extensively with those in Walsh cottage. Paola Cessi provided invaluable advice and enthusiasm for this project. The computer code that solved this problem was written by Glenn Ierley who generously performed some of the lowest viscosity runs at Michigan Technical University. Glenn Flierl allowed the use of his computer at MIT for the rest of the computations. I also had several useful conversations with Bill Young, Joe Pedlosky, and Mike McCartney.

### References

- Cessi, P., G. R. Ierley, W. R. Young (1987): A model of the inertial recirculation driven by potential vorticity anomalies. *J. Phys. Oceanogr.*, , **17**, 1640-1626.
- Ierley, G. R., W. R. Young (1988): Inertial recirculation in a beta-plane corner. *J. Phys. Oceanogr.*, **18**, 683-689.
- Marshall, J., Nuser, G. (1986): Steady, free circulation in a stratified quasi-geostrophic ocean. *J. Phys. Oceanogr.*, **16**, 1799-1813.

Rhines, P. B., W. R. Young (1982): Homogenization of potential vorticity in planetary gyres. *J. Fluid Mech.*, **122**, 347-367.

Richardson, P. L. (1985): Average velocity and transport of the Gulf Stream near 55W. *J. Marine Res.*, **43**, 83-111.

## EVOLUTION OF THE NEAR-WALL JET.

by Irene G. Yushina.

Institute of oceanology , Acad. Sci.USSR, 23 Krasikova  
Street, 117218, Moscow, USSR

## ABSTRACT

The behavior of the inflow near the wall is studied in the framework of a two-dimensional model with the resolution of the boundary layer near a slippery and no-slip wall. It is shown that the evolution of the inflow is due to the presence of the region of negative vorticity (boundary layer) near the wall.

## I. Introduction

An important phase of turbulence production in the flow past a wall occurs with the intermittent inflexional instability of the streamwise current. Although fully developed turbulent flows must be regarded as stable in the mean, the classical theory of laminar instability captures a key process which occurs intermittently in space-time. In the flow of a homogeneous fluid past a wall patches of inflexionally unstable flow associated with large Reynolds stress develop as a result of local spanwise circulations. It appears that the ever-present large-amplitude disturbances in fully developed laboratory or geophysical flow evolve into locally unstable patches in which one or more eddies develop, and this process is addressed herein. (M.E.Stern, 1989)

A barotropic jet emerging from a point source in a rotating fluid is deflected to the right (northern hemisphere) and starts to accumulate in an anticyclonic vortex. This vortex gives rise to a cyclonic neighbor, and the dipole (modon) then propagates away from the source in a circular path (Flierl et al, 1983). It is suggested that the modon model captures certain essential features of geophysical eddies. This is based on a

theorem, that any slowly varying and isolated disturbance on the beta plane must have zero net relative angular momentum, so that the dipole is the simplest dynamically consistent representation of such a disturbance.

When a laminar jet flows into a resting fluid of the same density the vorticity front form. M.E.Stern and L.J.Pratt studied this process and its consequences in an inviscid two-dimensional model by the method of contour dynamics. They showed that for large amplitudes wave-breaking and engulfment of irrotational fluid occurs, and for smaller amplitudes a lee-wave develops behind the leading edge of the shear intrusion, and each wavelet tends to equilibrate in amplitude and preserve its form (Stern and Pratt, 1985).

M.E.Stern considered the temporal evolution of a slow downstream decrease in the velocity of a coastal current contained in the light upper layer of the ocean in the framework of quasi-geostrophic model and showed that the formation of plume near the nose of the vorticity front is responsible for some of cold water plumes which extend to large distances from the coast of California (M.E.Stern, 1986).

In the laboratory experiments J.A.Whitehead studied the behavior of the isolated eddies and showed that the eddy pair can be made from a barotropic current, vertical streaked eddies can be made by density currents over a sloping bottom (J.A.Whitehead, 1989).

The behavior of vortex pair and the conditions of its formation in the laboratory experiment was studied by G.J.F.Van Heijst and J.B.Flor (1989), J.M.Nguyen Duc and J.Sommeria (1988), S.I.Voropaev (1989). All these studies are connected with a free jet and with formation of vortex pairs and with the interaction between two symmetric couples.

The results of numerical simulations presented here refer to behavior of the jet near the wall with the resolution of the boundary layer. It appears that the existence of the region of the negative vorticity near the wall cause the formation of the big vortex in the nose of the jet and the propagation of the jet along the wall ceases.



## II. Formulation of the problem.

Consider a two-dimensional model of inflow into the rectangular domain  $A < a < B$ ,  $0 < b < Y$ . Let the half width of inflow be  $\tilde{L}$  and let the characteristic flow velocity be  $\tilde{V}$ .

Let us introduce the dimensionless variables

$$x = a/\tilde{L}, \quad y = b/\tilde{L}, \quad t = \tau \tilde{V}/\tilde{L}, \quad (1)$$

where  $a, b, \tau$  are coordinates and time,  $x, y, t$  are nondimensional coordinates and time. The constants with tildes are dimensional and the constants  $A, B, Y, L, V$  are non-dimensional. In the experiments with a jet near the wall  $A = -10$ ,  $B = s$ ,  $Y = 10$ ,  $L = 1$ ,  $V = 1$ .  $s$  is thickness of boundary layer. In the experiments with a free jet  $A = -5$ ,  $B = 5$ ,  $Y = 10$ ,  $L = 1$ ,  $V = \pi$  in experiment 3 and  $V = 1$  in experiment 4. In the experiments with a steady motion  $A = -10$ ,  $B = 0$ ,  $Y = 10$ . The evolution equation has the form

$$\frac{\partial \psi}{\partial t} + J(\psi, \omega) = \varepsilon \Delta \omega \quad (2a)$$

$$\omega = \Delta \psi \quad (2b)$$

where  $\omega$  is the nondimensional vorticity,  $\psi$  is the stream function,  $\varepsilon$  is the viscosity.  $\Delta$  is the horizontal Laplacian operator  $\Delta = \partial^2/\partial x^2 + \partial^2/\partial y^2$ ,

$$J(\alpha, \beta) = \frac{\partial \alpha}{\partial x} \frac{\partial \beta}{\partial y} - \frac{\partial \alpha}{\partial y} \frac{\partial \beta}{\partial x}$$

Although several different initial and boundary conditions were used, in most of the numerical experiments presented here the Neumann boundary condition was used on the outflow boundaries:

$$\frac{\partial \psi}{\partial n} = 0; \quad \frac{\partial \omega}{\partial n} = 0 \quad (3)$$

at  $x = A$ , ( $0 < y < Y$ ) and at  $y = Y$ , ( $A < x < B$ ), slip or no-slip boundary conditions at  $x = B$ , ( $0 < y < Y$ ) and

at  $y = 0$ , ( $A \leq x \leq B$ ) except at the region of the inflow.

In most experiments the conditions  $\psi = 0$  and  $\partial^2 \psi / \partial n^2 = 0$  were used for the slip boundary and the conditions  $\psi = \text{const}$  and  $\partial \psi / \partial n = 0$  for the no-slip boundary, except at the region of inflow, where  $\omega$  and  $\psi$  remained constant in time at each point of inflow. In one experiment the no-slip condition was enforced at the boundary  $x = A$ , ( $0 \leq y \leq Y$ ), but the result of that calculation was similar to the experiments with the Neumann boundary condition. This similarity is because the duration of the calculation was less than the time for boundary effects to be significant.

For the initial condition the vorticity is zero throughout the domain and the stream function, as determined by the equation  $\omega = \Delta \psi$  describes the potential flow in the interior (Fig.1).

The vorticity at the region of inflow was specified to be

$$\begin{aligned} \omega &= -6(x+L/2)^2 + 1.5L^2, & -L \leq x \leq 0 \\ \omega &= -2x/S^2, & 0 \leq x \leq S \end{aligned} \quad (4)$$

This form of the vorticity gives the velocity profile

$$\begin{aligned} v &= -2(x+L/2)^3 + 1.5(x+L/2)L^2 + 0.5L^3, & -L \leq x \leq 0 \\ v &= (S^2 - x^2)/S^2, & 0 \leq x \leq S \end{aligned} \quad (5)$$

with its maximum value usually equal to one at  $x = 0$ , as shown in Fig.2. Note that if  $S^2$  is  $1/3$  there is a smooth profile of vorticity because :

$$\frac{\partial \omega}{\partial x} \Big|_{x \rightarrow +0} = \frac{\partial \omega}{\partial x} \Big|_{x \rightarrow -0}, \text{ when } S^2 = 1/3 \quad (6)$$

Equation (2b) was solved by the iteration method of overrelaxation. The relaxation parameter at the first time step was 1.97 and about 300 iterations were necessary to achieve an accuracy of  $5 \times 10^{-5}$  in the stream function. Subsequently the relaxation parameter diminished to 1.3

and the number of iterations essentially decreased and remained in the range from 7 to 20 slowly increasing in time. The calculations were made for a region of 50 x 50 gridpoints, the grid resolution was  $dx = dy = 0.2$  or  $dx = dy = 0.1$ . The finite-difference representation of (2a) was a centered second-order formula in both space and time. In particular, the nonlinear Jacobian operations were calculated by the spatially conservative formula of Arakawa (Arakawa, 1966). The nondimensional viscosity coefficient was  $\mathcal{E} = 0.01$  or  $\mathcal{E} = 0.005$ .

We performed two experiments for the verification of the numerical calculations, one with numerical dissipation only ( $\mathcal{E} = 0$ ) and the second with explicit viscosity ( $\mathcal{E} = 0.005$ ).

For the case of line vortices, originally analysed by Lamb (Lamb, 1932), the recirculation cell of the vortex takes the shape of an oval that encloses both vortices; the resulting motion is steady.

In theoretically describing the structure of the vortex for verification of the numerical calculations, it is possible to assume two distributions of vorticity concentrated in two line vortices symmetrically located about the centerline of the vortex pair. It is possible to retain the conditions for steady motion of the vortex pair in the case when the vorticity is distributed throughout the recirculation cell assuming that the relation

$$\omega = -k^2 \psi$$

is valid throughout the domain of non-zero vorticity (Batchelor, 1967). The governing equation in terms of the stream function and the constant  $k$  takes the form

$$\frac{\partial^2 \psi}{\partial r^2} + \frac{1}{r} \frac{\partial \psi}{\partial r} + \frac{1}{r^2} \frac{\partial^2 \psi}{\partial \theta^2} = -k^2 \psi \quad (7)$$

For this form of  $\psi$  the solution is a Bessel function of the first order:

$$\psi = C J_1(kr) \sin \theta \quad (8)$$

In this solution the circle  $r = R$  bounds the recirculation cell (Homa et al., 1988). If we take

$$\begin{aligned}\omega &= J_1(kr) \sin \theta, \quad r \leq R \\ \omega &= 0, \quad r > R\end{aligned}\quad (9)$$

as the initial condition for the numerical experiment we can expect that the vortex pair motion will be steady and the decrease of the amplitude of vortices will depend on the viscosity only. The estimation of the time of the decrease of the amplitude of the vortex pair in e folding times is  $T = L / (2\varepsilon)$ . In the case when  $L$  is equal to 1 and  $\varepsilon = 0.005$  the estimation of the time is  $T = 100$ . The initial field of vorticity given by (9) for the numerical experiment 1 with periodic boundary conditions at  $y = 0$ , ( $A \leq x \leq B$ ) and at  $y = Y$ , ( $A \leq x \leq B$ ), and slip boundary at  $x = B$ , ( $0 \leq y \leq Y$ ) and the centerline of vortex pair is at that boundary is shown in Fig.3, the profile of the initial vorticity is shown in Fig.4. The decrease of the initial amplitude of the vortex by a factor of  $e$  occurs at  $T=65.6$ . The location of the center of vortex changes from  $y = 2.6$  to  $y = 9$ , that corresponds to the speed of vortex of about 0.09 (note that the amplitude of the vortex is 0.58). Since the boundary conditions correspond to the unbounded fluid at rest at infinity, the following integrals are conserved in the absence of viscosity:

$$\Gamma = \iint \omega dA, \quad E = \iint (\nabla \psi)^2 dA, \quad P = \iint \omega^2 dA$$

When  $\Gamma = 0$  as in our numerical experiment,  $E$  and  $P$  are equal respectively to the energy and enstrophy of the flow. (In the numerical experiment which is described above we must remember that there is an image outside the domain with the vortex with the opposite sign of the vorticity and these two vortices are a vortex pair.)

All these integrals are conserved when  $\varepsilon = 0$  and the decrease of the integrals is only due to the implicit

viscosity. In Fig.6 the behavior of these integrals is shown for the experiment 1 with implicit viscosity only. The profiles of energy and enstrophy coincide with the line  $y = 1$  and the profile of the maximum of the amplitude is changed chaotically from 0.98 to 1.03. This behavior is due to the grid-representation of the vorticity field. So, for the times of the simulation of about 100 the influence of the implicit viscosity is negligible for such a scheme. In any case it is much smaller than the explicit viscosity in our experiments. Each gridpoint in the numerical experiment 2 is shown in Fig.5 using its stream function  $\psi$  and vorticity  $\omega$  as coordinates. The points collapse approximately on a curve with two branches one of which is on the  $\psi$ -axis and corresponds to the irrotational flow outside the couple.

This behavior corresponds to that expected for the steady solution of the Euler equations. This result is thus a direct proof that we have a stationary state and the structure function  $\omega = \phi(\psi)$  is linear as in Lamb's vortex pair (Lamb, 1932).

### III. Free jet.

The numerical experiments of a free jet with different  $\mathcal{E}$  (0.01 and 0.005) and the different initial vorticity profiles are shown in Fig.7-11. The initial vorticity profile in experiment 3 with  $\mathcal{E} = 0.01$  is a cosine function in the region of inflow. The profiles of  $U$ ,  $\psi$  and  $\omega$  are shown in Fig.7 for this case. In this experiment the maximum velocity of the flow equals  $\pi$  so the nose of the jet is going faster than in the experiments with the maximum velocity equal to 1, and travels a distance of about 6L during the time  $T = 5$  (Fig.8). The result of numerical experiment 4 of the inflow with the linear initial vorticity profile as in Fig.7 is shown in Fig.9. Here the maximum velocity is equal to 1, so the nose of the jet propagates only to the distance of 5L during the time  $T = 8$ . In Fig.10 the isolines of the vorticity and of the stream function for experiment 4 are shown at  $T=24$  and Fig.11 exhibits the

trajectories of the particles which were at the region of inflow at the time  $T = 0$ . All these particles were initially at the nose of the jet and their trajectories are analogues to the trajectories of the particles in the laboratory experiment by Flierl et al., 1983.

#### IV. Inflow near a no-slip wall.

The numerical experiments 5-7 were made with the outflow boundary conditions at  $x = A$ , ( $0 \leq y \leq Y$ ) and  $y = Y$ , ( $A \leq x \leq B$ ). The boundary condition at  $x = B$ , ( $0 \leq y \leq Y$ ) was no-slip; i.e. at this boundary  $\psi = \text{const}$ , say 0 and  $\partial\psi/\partial n = 0$ . The profile of the vorticity in the region of inflow was as in Fig.2 with  $s = 1.0.6$  and  $0.4$  respectively. In Fig.12-14 the isolines of vorticity are shown for the experiments 5,6 and 7 at times  $T=24,32$  and  $40$ . One can see that there is no qualitative difference between the developments of the nose of the leading edge of the modons in these experiments; the difference in time is due to the thickness of the region of negative vorticity near the wall. It seems that when  $s$  becomes smaller, the speed of advection is smaller too; that's why the propagation of the nose of negative vorticity is similar in Fig.12-14 for different times. In Fig.15-17 the isolines of the stream function for the experiments 5-7 are shown for the times  $T = 24,32$  and  $40$  respectively. The differences are small in these figures. So we can conclude that in this range of  $s$  there is no qualitative difference in the evolution of the jet near the no-slip wall. It propagates a distance of about  $5L$  and separates. The nose of the jet appears to follow isolines of the stream function, i.e. it propagates in accordance with the potential flow. In Fig. 18 - 20 the trajectories of the particles, initially located in the region of inflow are shown with the isolines of the initial stream function (isolines of potential flow). Note that the decrease of the coefficient of the viscosity from  $0.01$  to  $0.005$  doesn't influence the behavior of the jet. That's why all experiments which follow were made with  $\mathcal{E} = 0.005$ .

So, in these numerical experiments with a two-

dimensional model when there is a region of negative vorticity near the wall we could not make a jet to go along the wall.

#### V. Inflow near a slippery wall.

In the numerical experiments 8 and 9 the fluid was allowed to slip along the boundary at  $x = B$ , ( $0 \leq y \leq Y$ ) i.e.  $\psi = 0$  and  $\partial^2 \psi / \partial n^2 = 0$ . The profile of vorticity in the region of inflow is shown in Fig.21 and it is defined by

$$\omega = -6(x + L/2)^2 + 1.5L^2, \quad -L \leq x \leq 0$$

$$\omega = 6(x - S/2)^2 - 1.5S^2, \quad 0 < x \leq S$$

and the velocity profile is

$$v = -2(x + L/2)^3 + 1.5(x + L/2)L^2 + 0.5L^3, \quad -L \leq x \leq 0$$

$$v = 2(x - S/2)^3 - 1.5(x - S/2)S^2 + 0.5S^3, \quad 0 < x \leq S$$

s equals to 1 in these experiments.

The only difference between experiments 8 and 9 is that the boundary condition at  $x = A$ , ( $0 \leq y \leq Y$ ) is outflow (Neumann condition) in the experiment 8 and no-slip boundary in the experiment 9. The potential flow at  $T = 0$  for the experiment 9 is shown in Fig.22. The numerical simulations showed that there is no influence of the boundary  $x = A$ , ( $0 \leq y \leq Y$ ) on the behavior of jet before the time when non-zero vorticity achieved this boundary; that means that in our experiments we can use any boundary condition at  $x = A$ , ( $0 \leq y \leq Y$ ) because we never make the calculations for such times. The isolines of the vorticity and the stream function for  $T = 32$  are shown in Fig.23-26. It appears that the jet as in the previous experiments doesn't propagate along the wall, but separates at the same distance as in the previous experiments.

Thus, in all probability the process of the separation in these numerical calculations depends only on the

existence of the region of negative vorticity near the wall.

For the confirmation of this conclusion we carried out experiment 10 with the region of the negative vorticity near the wall as narrow as our computer resources allow ( $s = 0.2$  in this experiment). The grid resolution was  $dx = dy = 0.1$  and the domain was  $100 \times 100$  gridpoints.

The result of this experiment is shown in Fig.27 which contains the isolines of vorticity for the time  $T = 32$ . One can see that in accordance with the results of previous experiments the jet separates at the same distance from the point of inflow.

In the last experiment 11 the initial condition was changed. At the time  $T = 0$  the profile of the vorticity described by the equation 4 was prolonged to 10 gridpoints. (10 gridpoints corresponds to the distance equal to  $2L$ .) The initial fields of the vorticity and the stream function and the field of the vorticity at  $T = 24$  are shown in Fig.28-30. For comparison with the result of experiment with no-slip boundary at  $x = B$ , ( $0 < y < Y$ ) and  $s = 1$  Fig.31 shows isolines of the vorticity for the time  $T = 24$  for the experiment 8. If we compare Fig.30 and Fig.31 we can see that the jet separates at the same distance from the point of the beginning of the simulation. So we can conclude that if there is a region of negative vorticity near the wall the jet separates at the distance of about  $5L$  ( $L$  is half-width of inflow) and we could not make it to go along the wall in the framework of a two-dimensional numerical model.

#### R E F E R E N C E S.

1. A.Arakawa 1966 Computational design for long-term numerical integration of the equations of fluid motion. J.Comput.Phys.,1: 119-143.
2. A.Arakawa and V.R.Lamb 1981 A Potential Enstrophy and Energy Conserving Scheme for Shallow Water Equations. Mon.Wea.Rev.,109: 13-36
3. G.K.Batchelor 1967 An Introduction to Fluid Dynamics. Cambridge Univ.Press, London, 615pp.



4. G.R.Flierl, M.E.Stern and J.A.Whitehead 1983 The Physical Significance of Modons: Laboratory Experiments and General Integral Constraints. *Dyn. Atmos.Oceans*, 7: 233-263.
5. B.J.Homa, M.Lucas and D.Rockwell 1988 Interaction of Impulsively Generated Vortex Pairs with Bodies. *J. Fluid Mech.*, 197: 571-594
6. H.Lamb 1932 *Hydrodynamics*. 6th ed., Cambridge Univ. Press, 223pp.
7. J.-M.Nguyen Duc and J.Sommeria 1988 Experimental Characterization of Steady Two-Dimensional Vortex Couples. *J.Fluid Mech.*, 192: 175-192
8. M.E.Stern 1984 Formation of Vorticity Fronts in Shear Flow. *Phys. Fluids*, 27: 848-855.
9. M.E.Stern 1986 On the Amplification of Convergences in Coastal Currents and the Formation of "Squirts". *J.Mar.Res.*, 44: 403-421
10. M.E.Stern 1989 Vorticity Frontogenesis. In: J.C.J.Nihoul and B.M.Jamart (Eds), *Mesoscale / Synoptic Coherence Structures in Geophysical Turbulence*. Elsevier Science Publishers B.V. (Amsterdam, The Netherlands): 95-101
11. M.E.Stern and L.J.Pratt 1985 Dynamics of Vorticity Fronts. *J.Fluid Mech.*, 161: 513-532.
12. G.J.F.Van Heijst and J.B.Flor 1989 Laboratory Experiments on Dipole Structures in a Stratified Fluid. In: J.C.J.Nihoul and B.M.Jamart (Eds), *Mesoscale/Synoptic Coherence Structures in Geophysical Turbulence*. Elsevier Science Publishers B.V. (Amsterdam, The Netherlands): 591-608
13. S.I.Voropaev 1989 Flat Vortex Structures in a Stratified Fluid. In: J.C.J.Nihoul and B.M. Jamart (Eds), *Mesoscale/Synoptic Coherence Structures in Geophysical Turbulence*. Elsevier Science Publishes B.V. (Amsterdam, The Netherlands): 671-689
14. J.A.Whitehead 1989 Laboratory Studies of Isolated Eddies in a Rotating Fluid. In: J.C.J.Nihoul and B.M.Jamart (Eds), *Mesoscale/Synoptic Coherence Structures in Geophysical Turbulence*. Elsevier Science Publishes B.V. (Amsterdam, The Netherlands): 627-637

### ACKNOWLEDGEMENTS

The present work was performed under the guidance of Melvin E. Stern. I am very grateful to M.E. Stern for his help. I express my gratitude to George Veronis and George Sutyryn for the very useful discussions. I would also like to thank the rest of the GFD staff and fellows for a very enjoyable and stimulating summer.

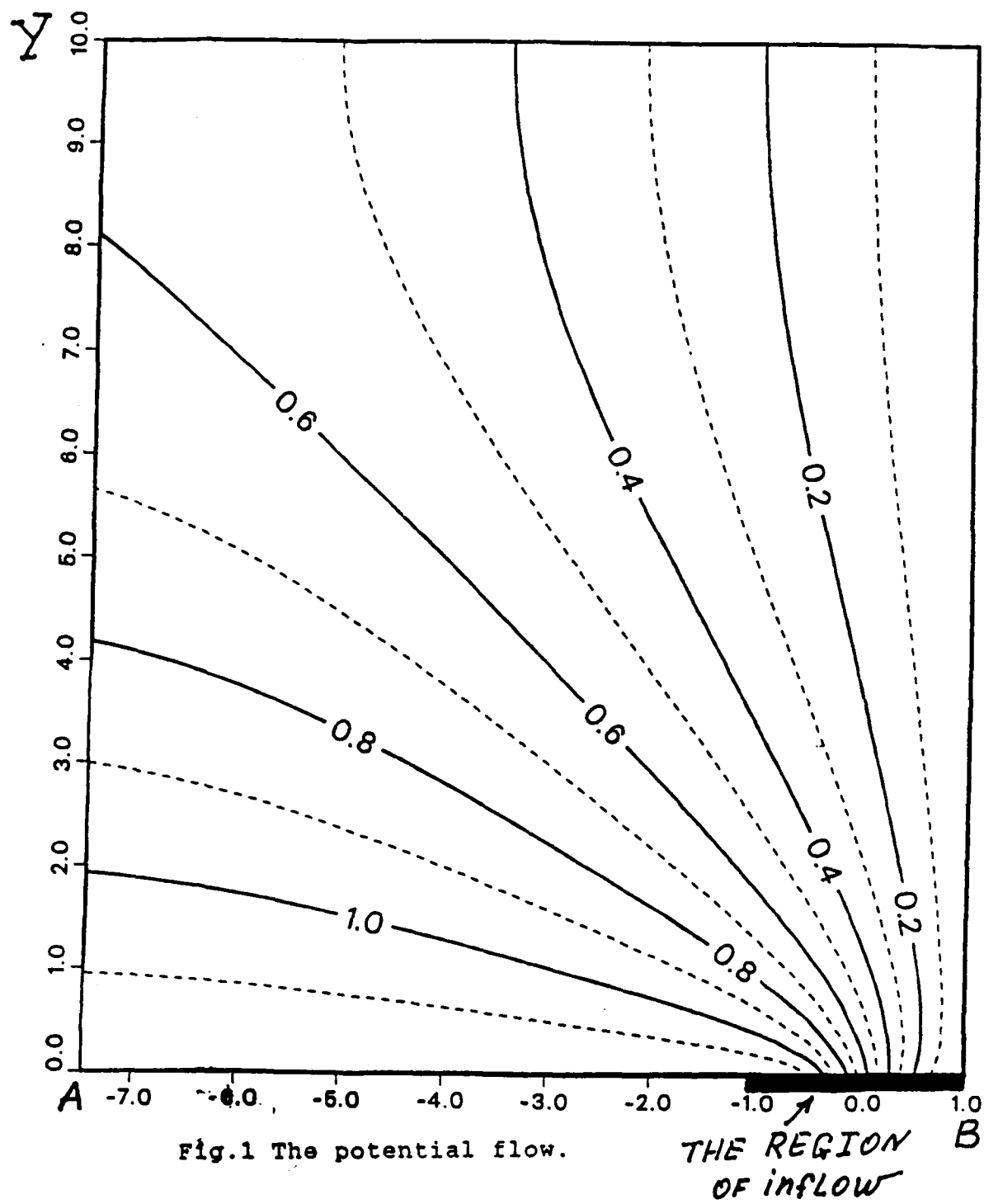


Fig.1 The potential flow.

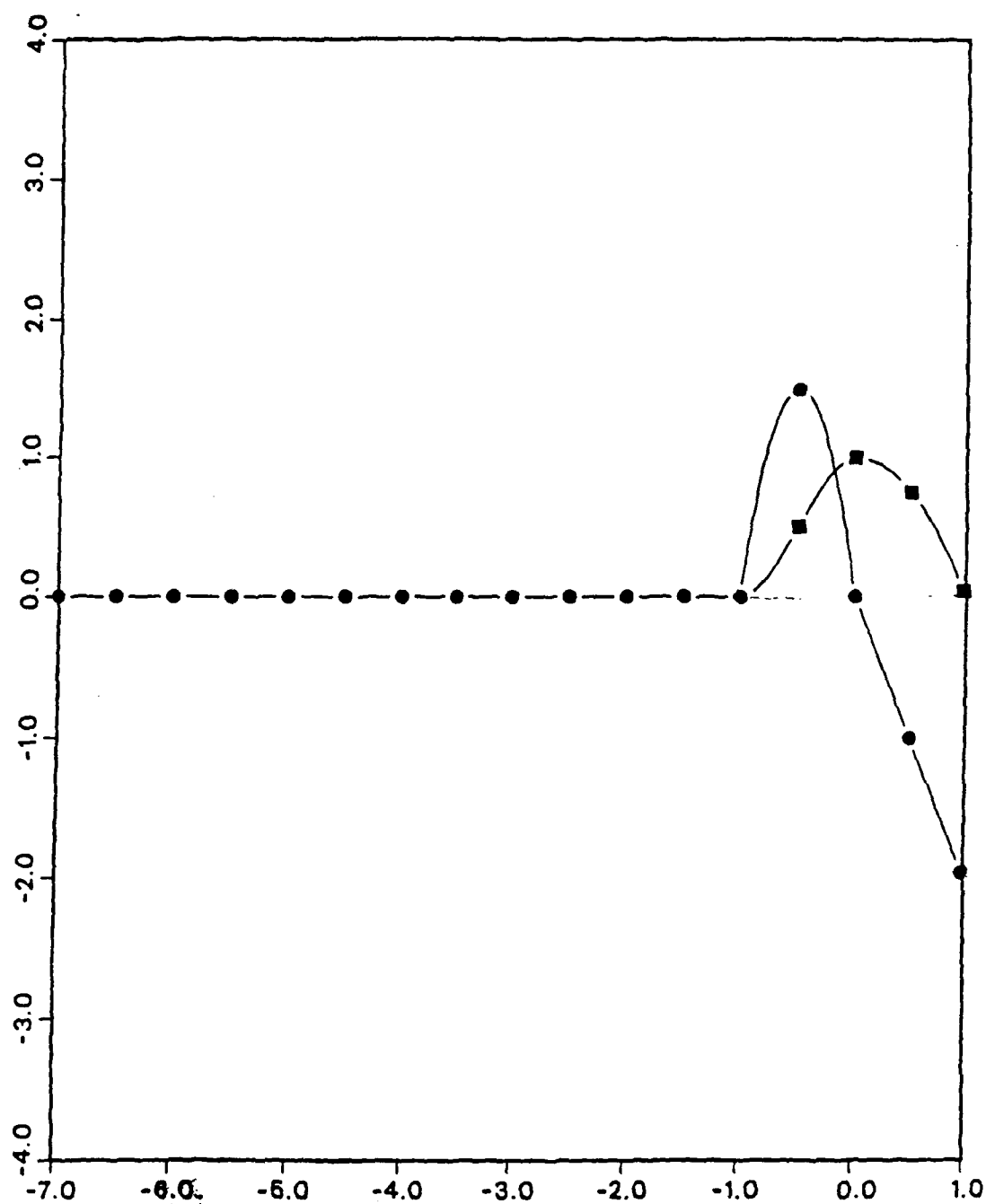


Fig.2 The profiles of the vorticity (●) and of the velocity (■) in the region of inflow.

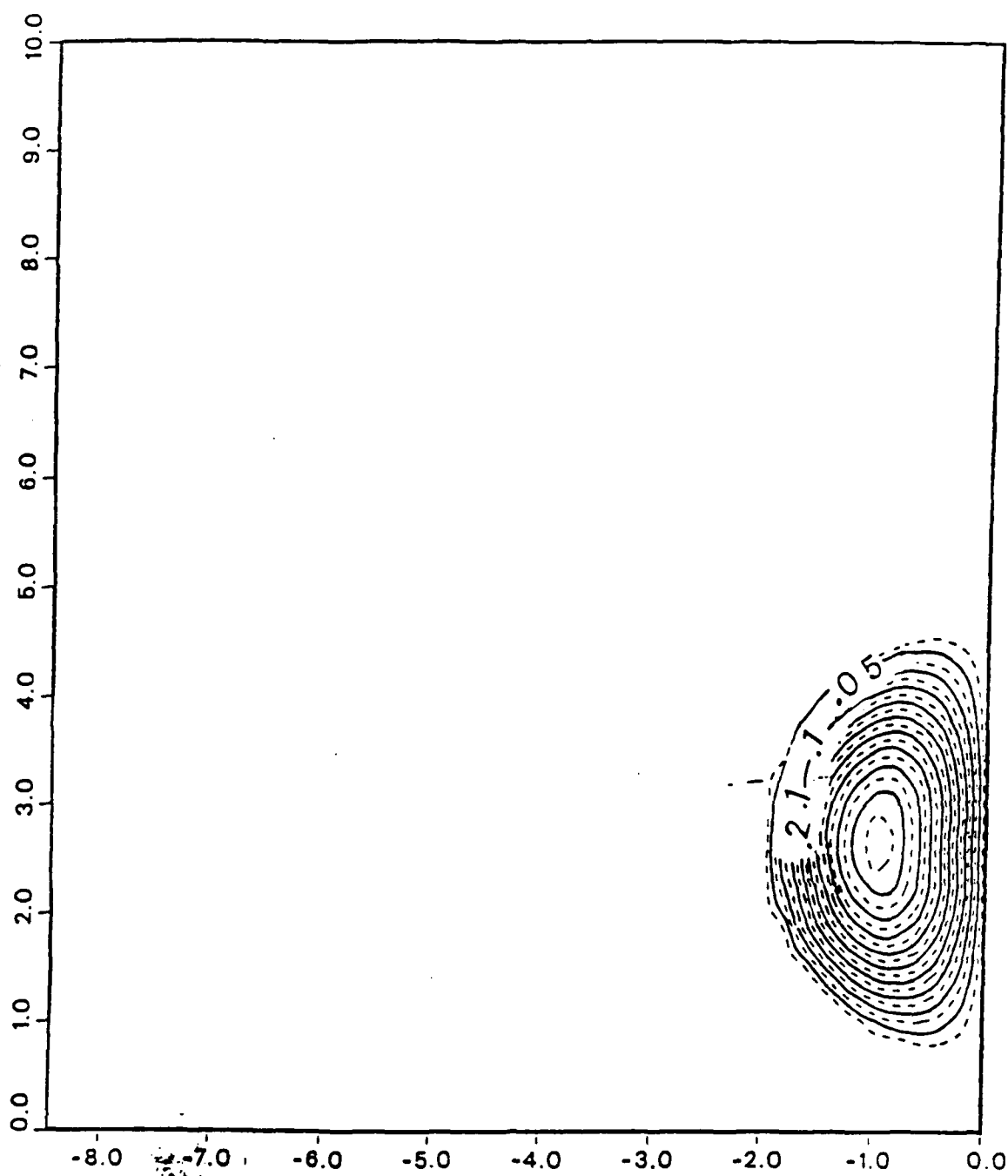


Fig.3 The initial field of the vorticity for the steady modon.

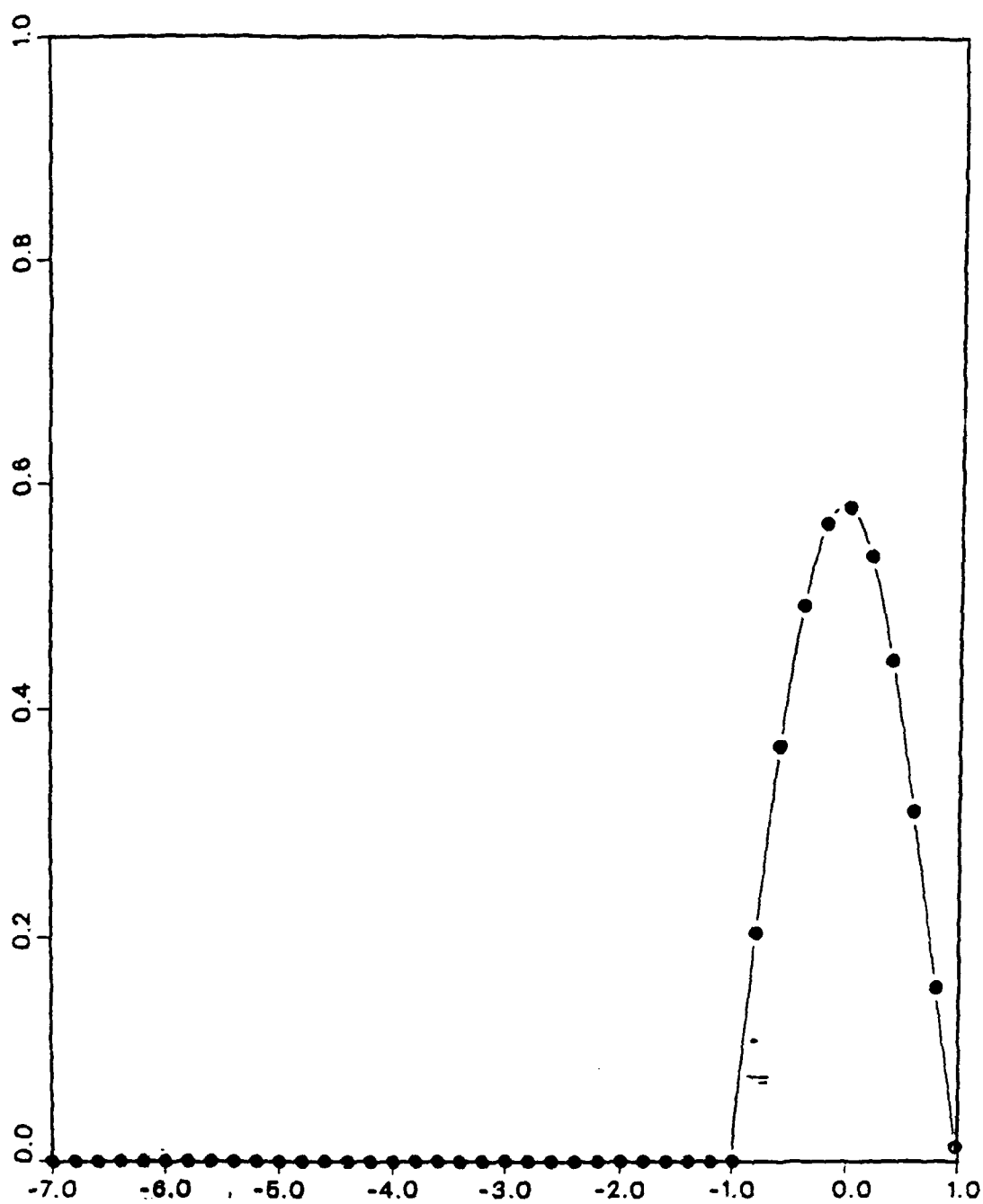


Fig.4 The profile of the initial vorticity in the direction parallel to x-axis for the steady modon.

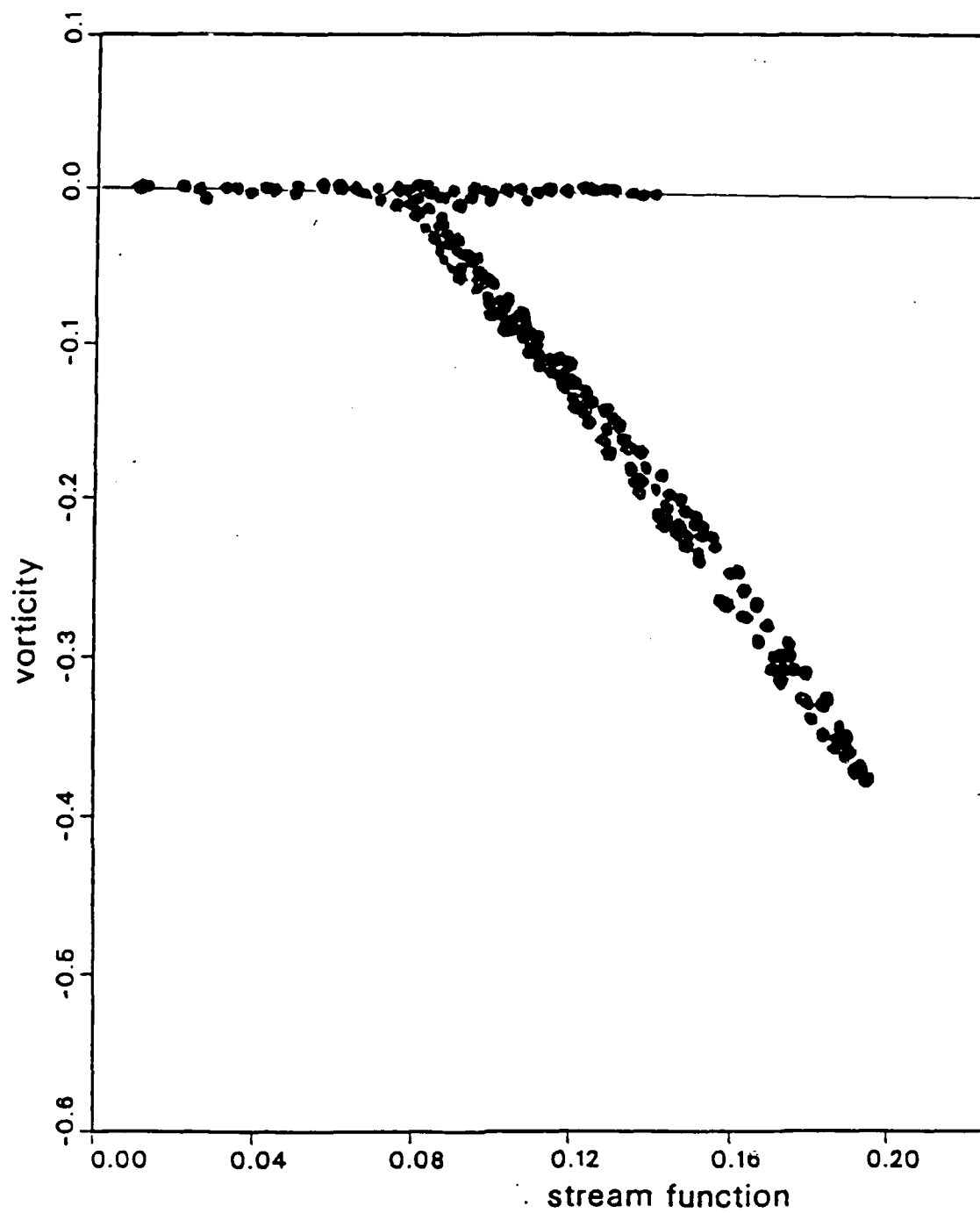


Fig. 5 The relation  $\omega, \psi$  for the steady modon at  $T = 20$ .

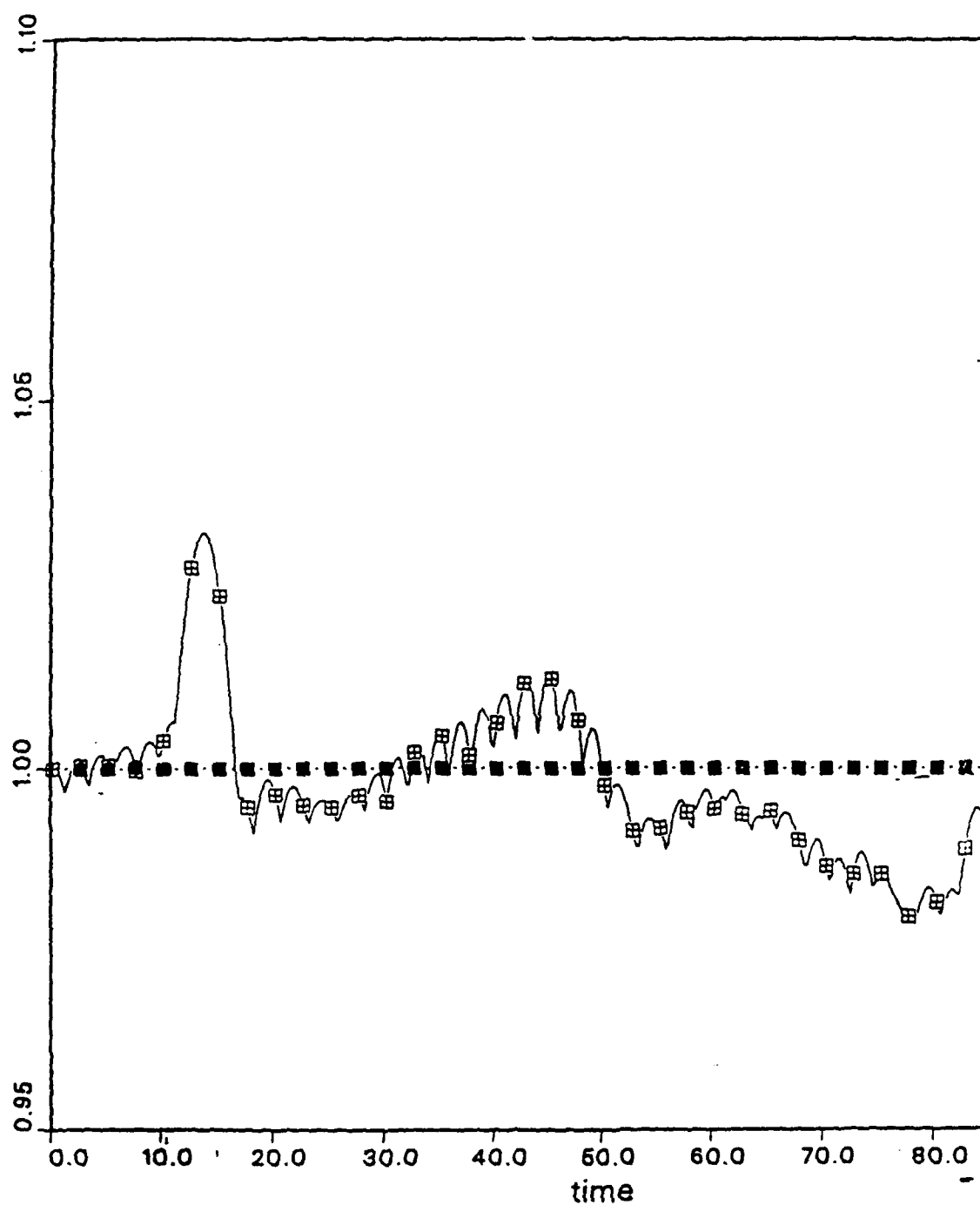


Fig.6 The evolution of the energy (■), the enstrophy (●) and of the maximum vorticity (■) in time.



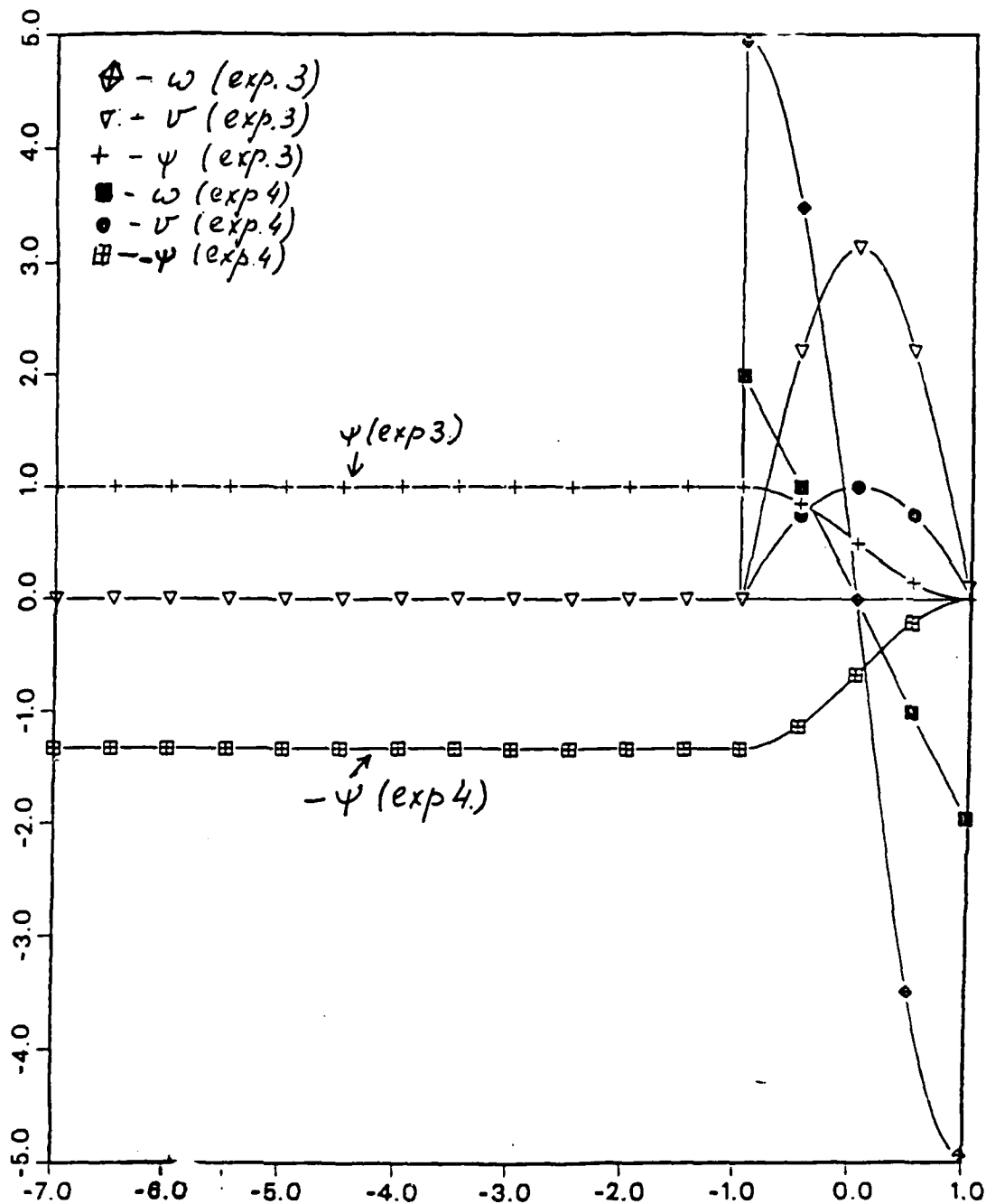


Fig.7 The profiles of vorticity, velocity and stream function in the region of inflow for the experiments 3 and 4.

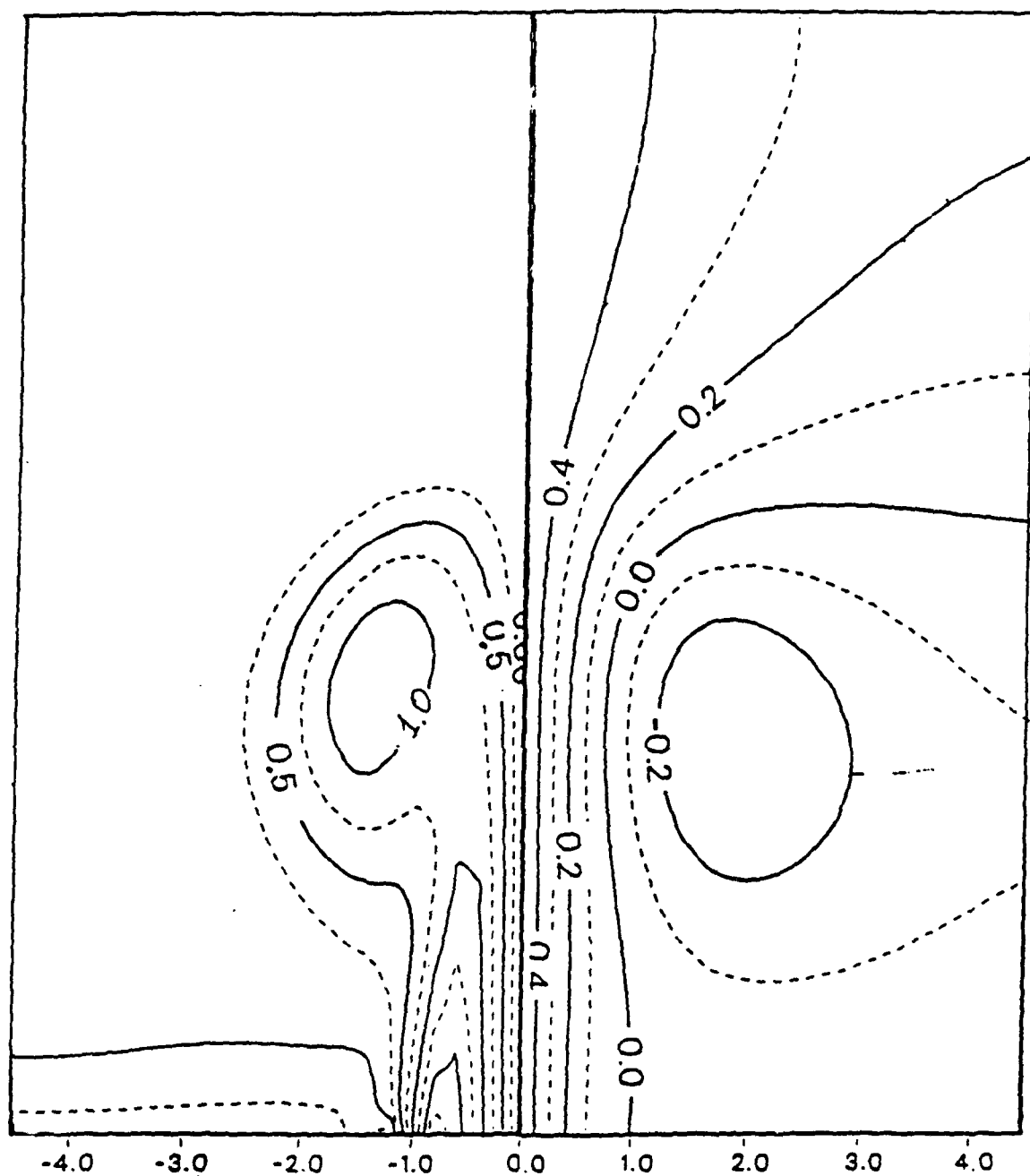


Fig. 8 The isolines of the vorticity (left) and the stream function (right) for the experiment 3,  $T = 5$ .

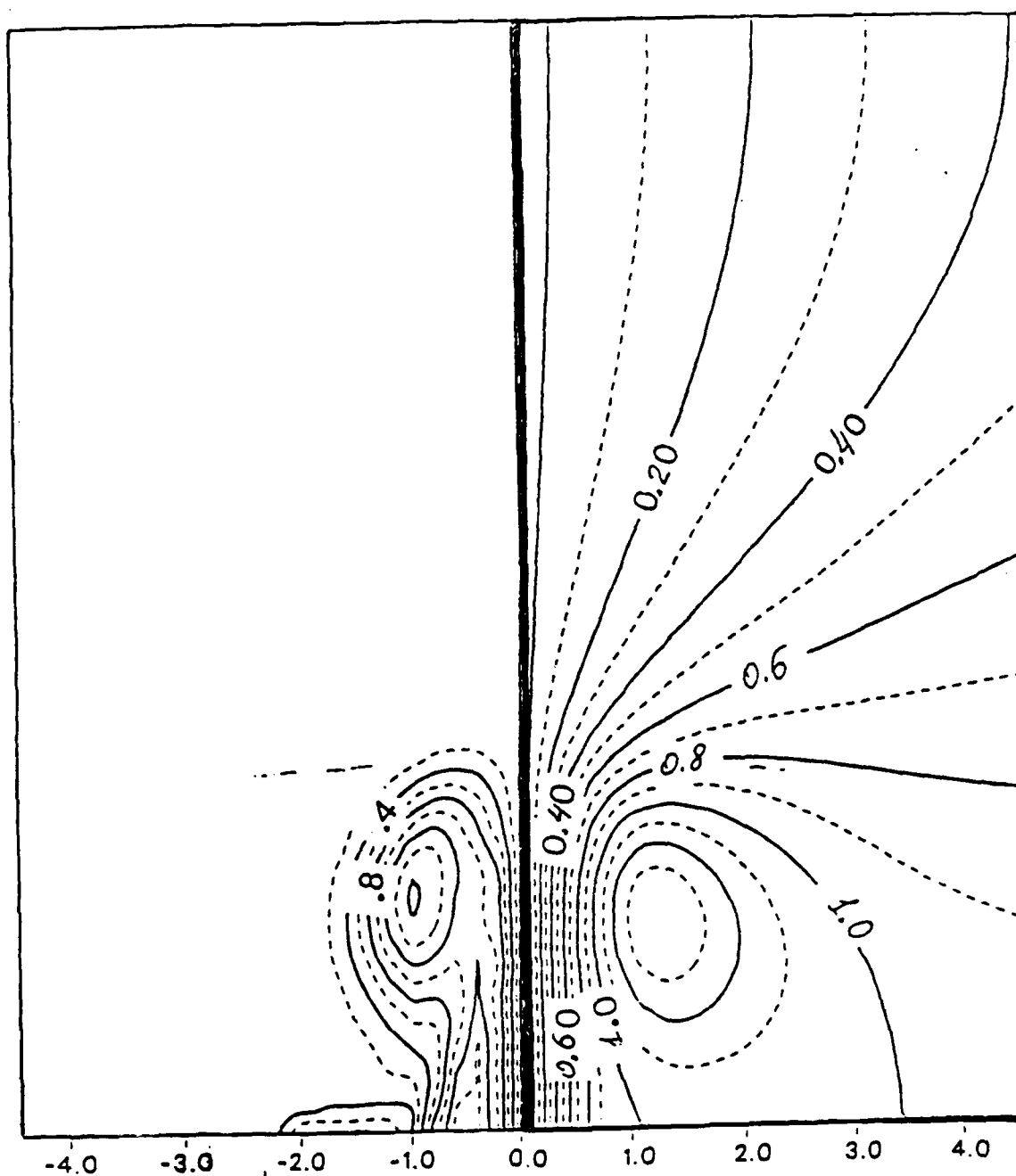


Fig.9 The isolines of the vorticity (left) and the stream function (right) for the experiment 4,  $T = 3$ .

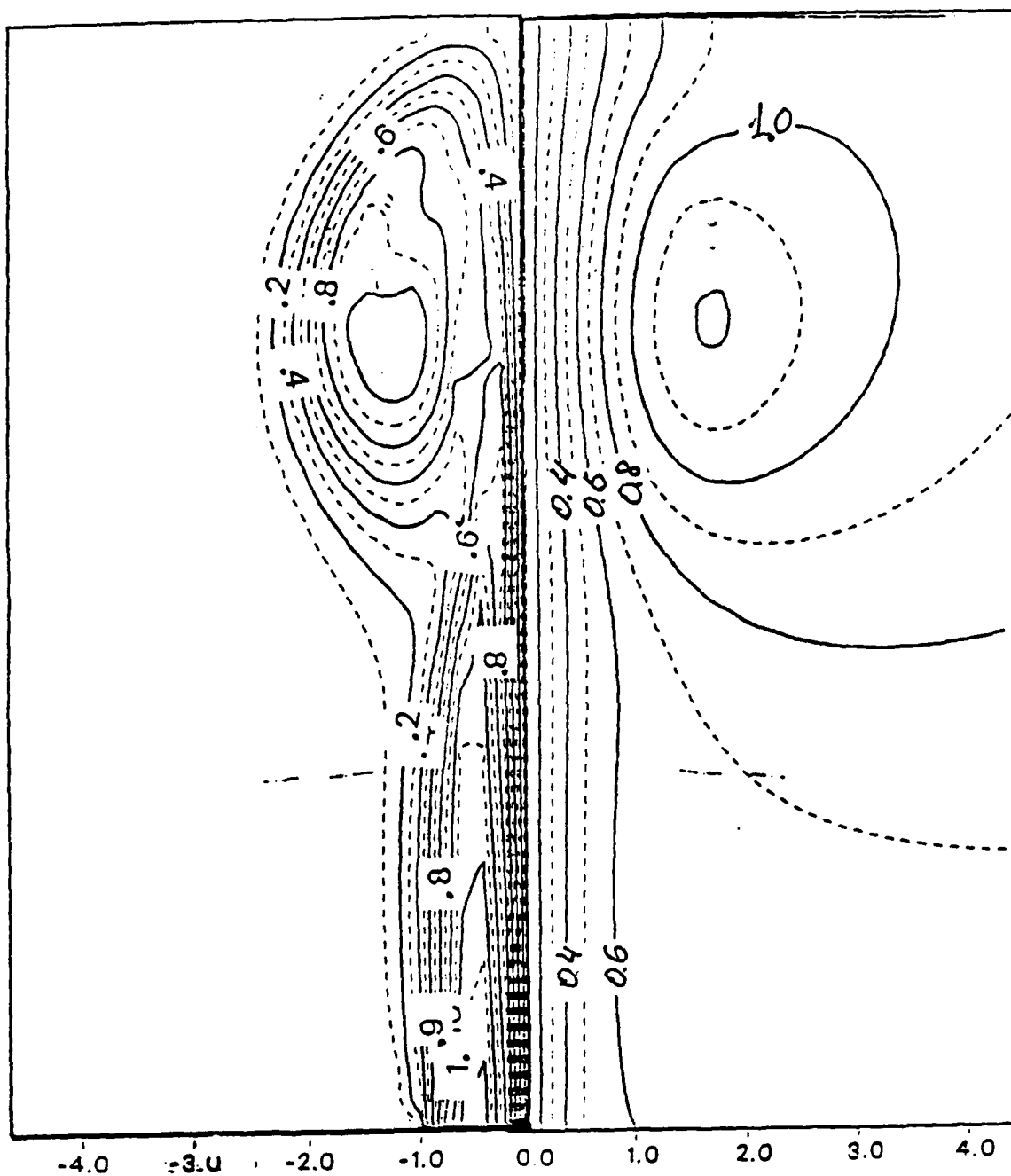


Fig.10 The isolines of the vorticity (left) and the stream function (right) for the experiment 4,  $T = 24$ .

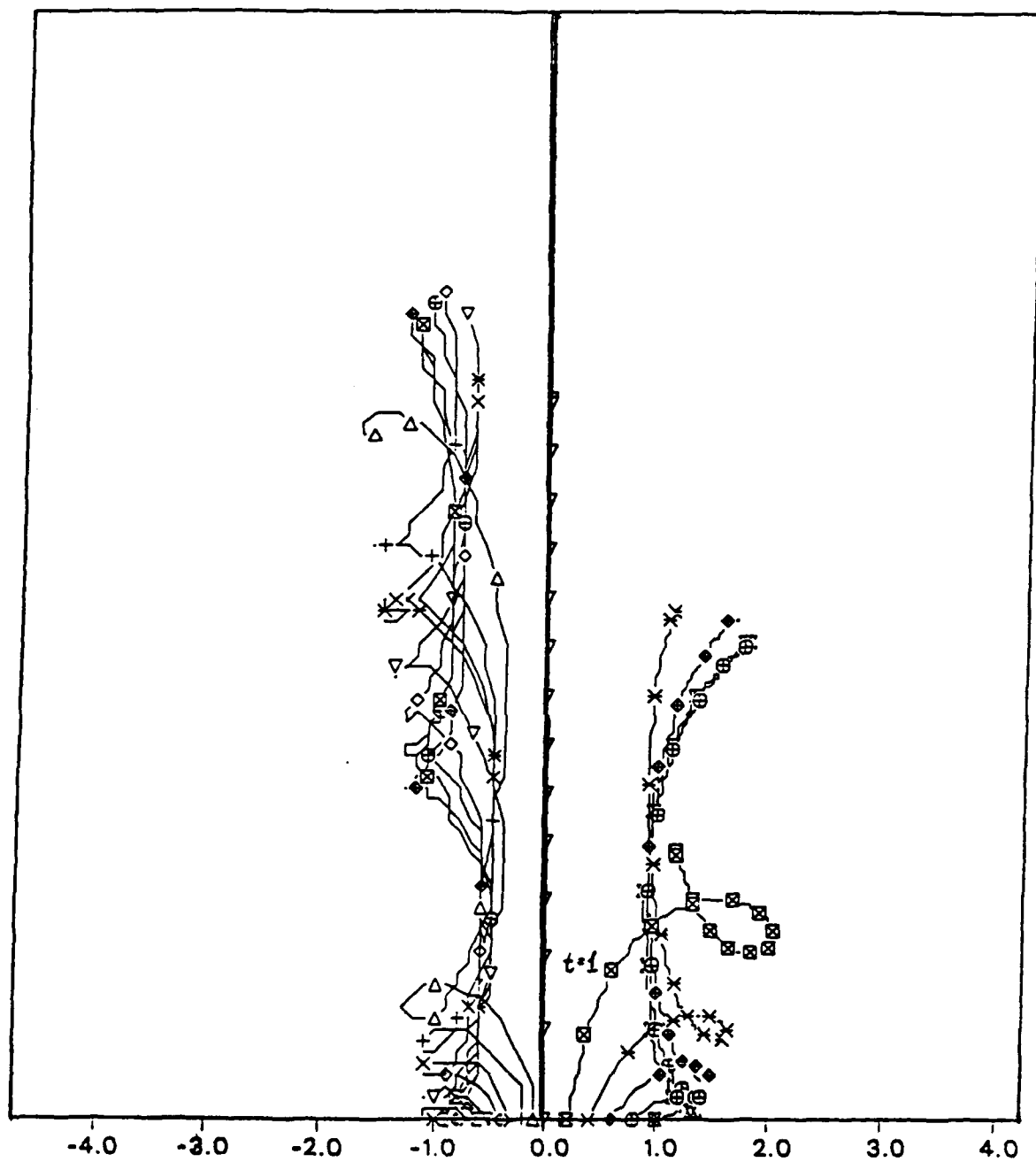


Fig.11 The trajectories of the particles which were at the region of inflow at  $T = 0$ . (For the experiment 3-right, for the experiment 4-left)

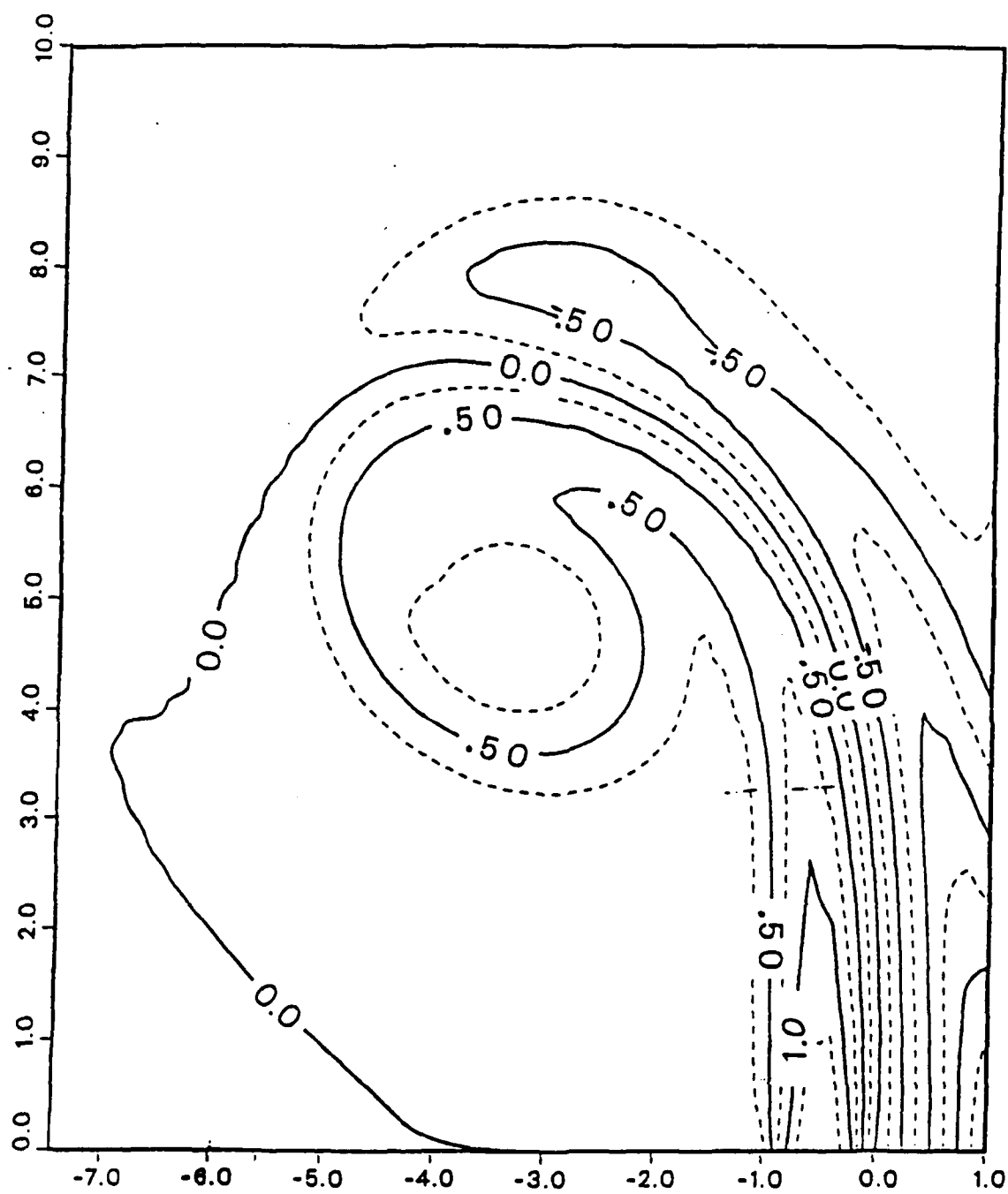


Fig.12 The isolines of the vorticity. Experiment 5,  $T = 24$ .

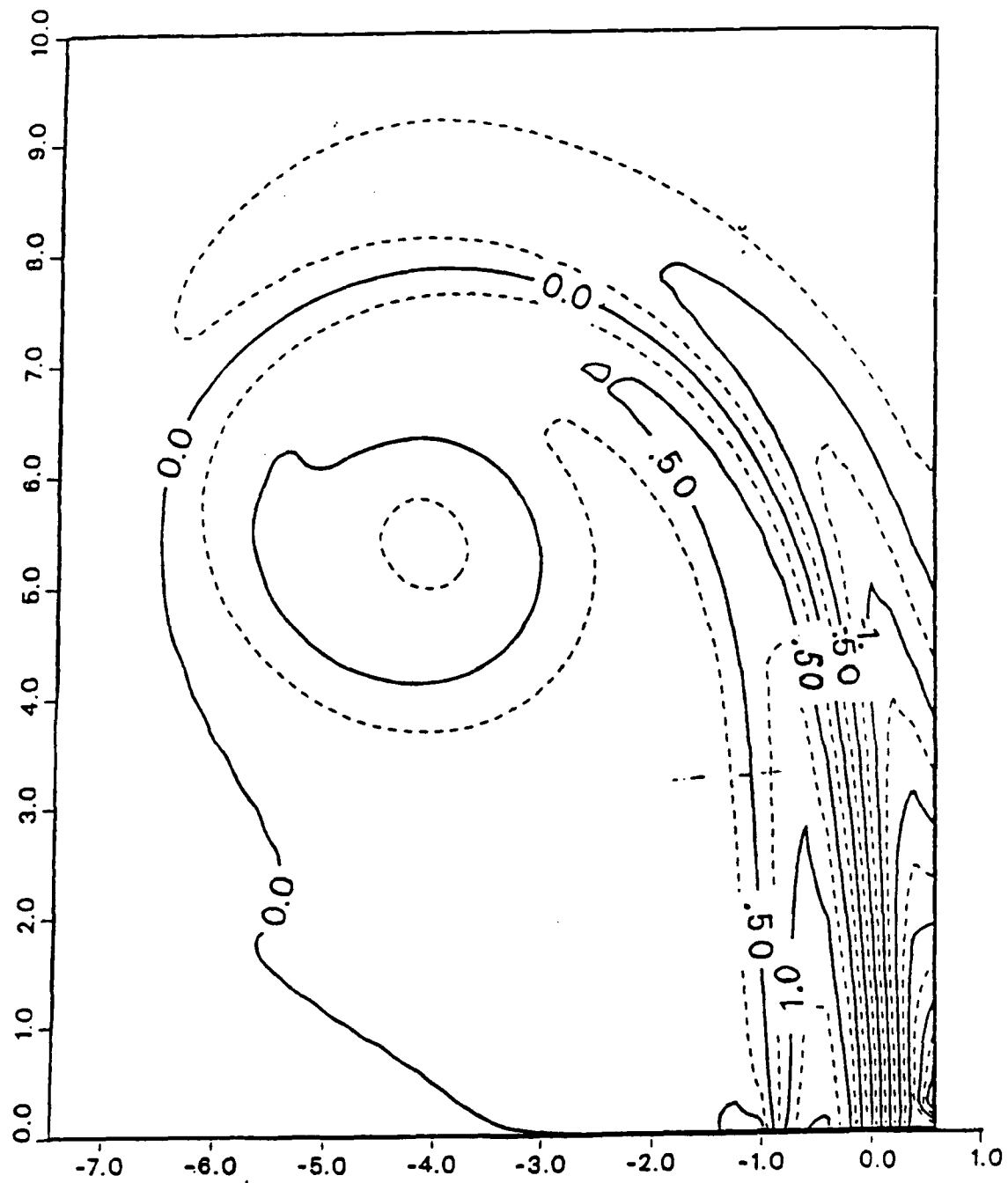


Fig.13 The isolines of the vorticity. Experiment 6,  $T = 32$ .

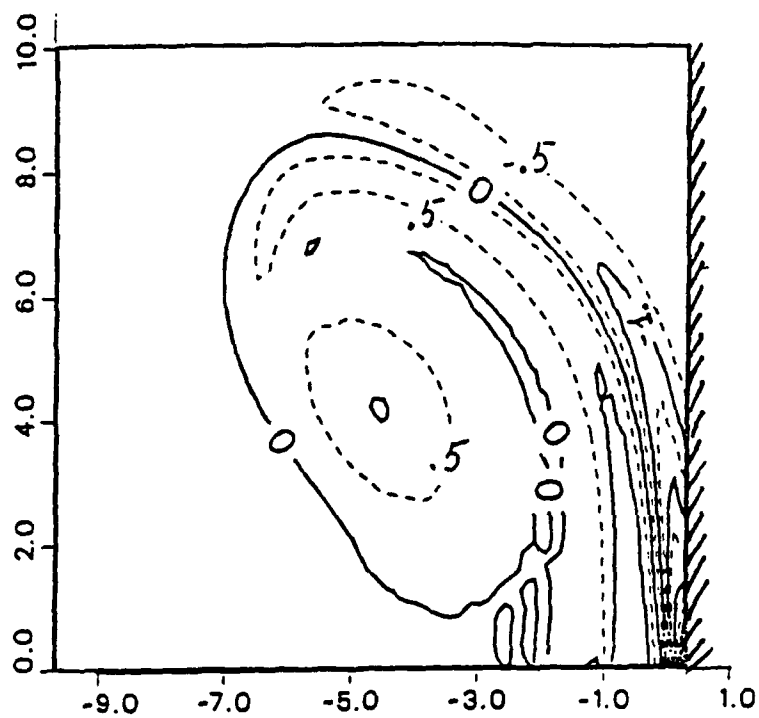


Fig.14 The isolines of the vorticity. Experiment 7,  $T = 40$ .



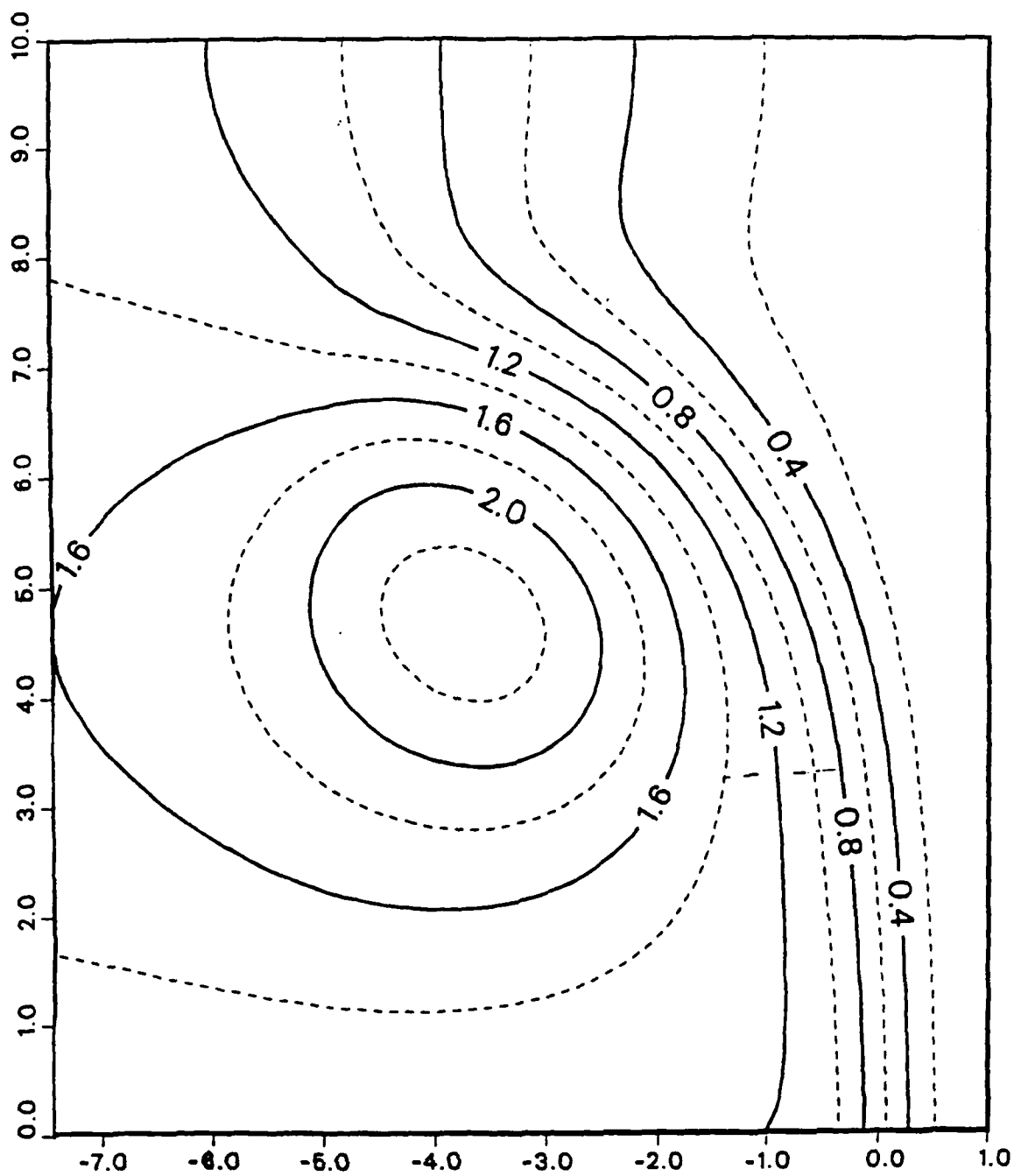


Fig.15 The isolines of the stream function. Experiment 5,  
 $T = 24$ .

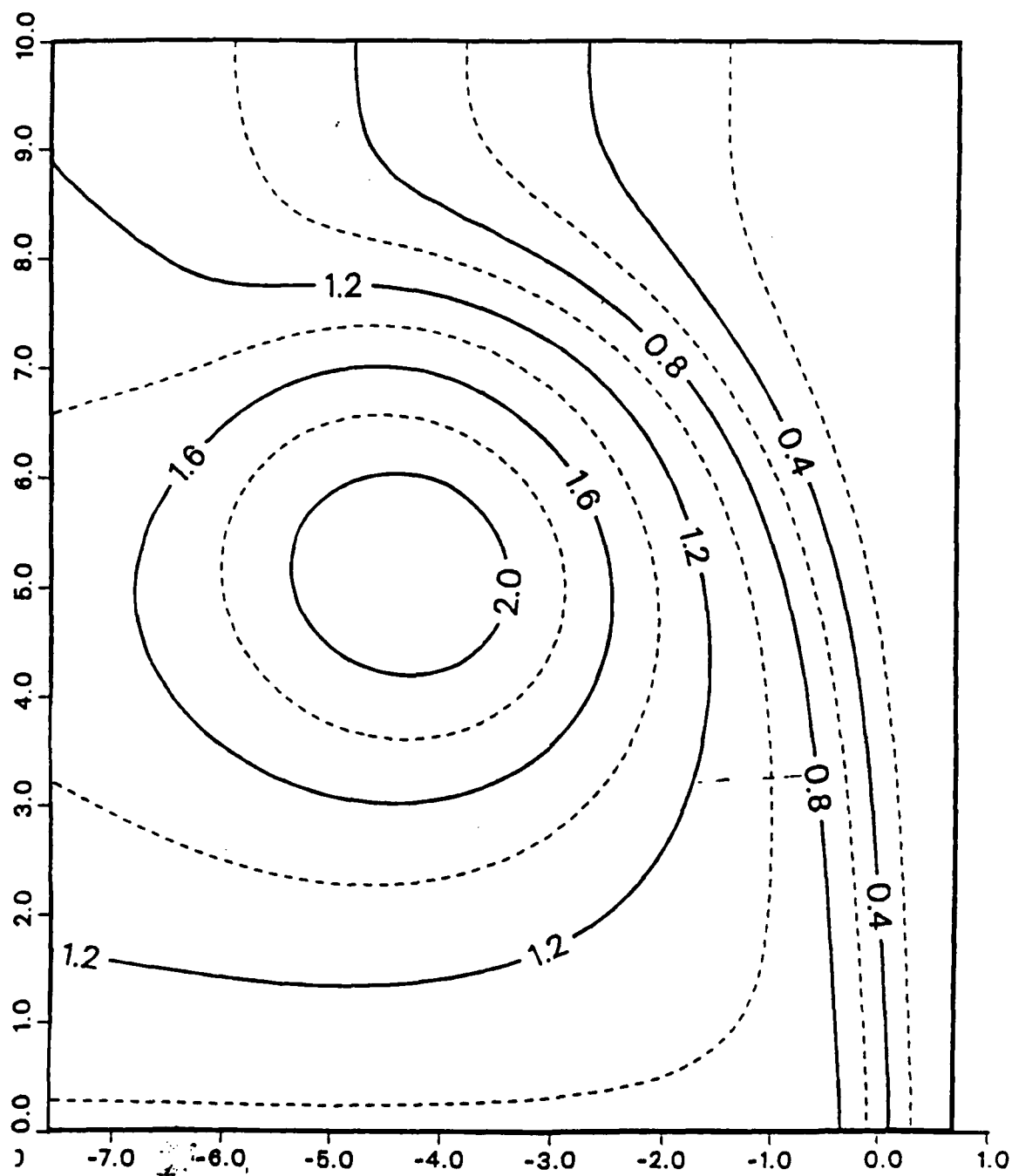


Fig.16 The isolines of the stream function. Experiment 6,  
 $T = 32$ .

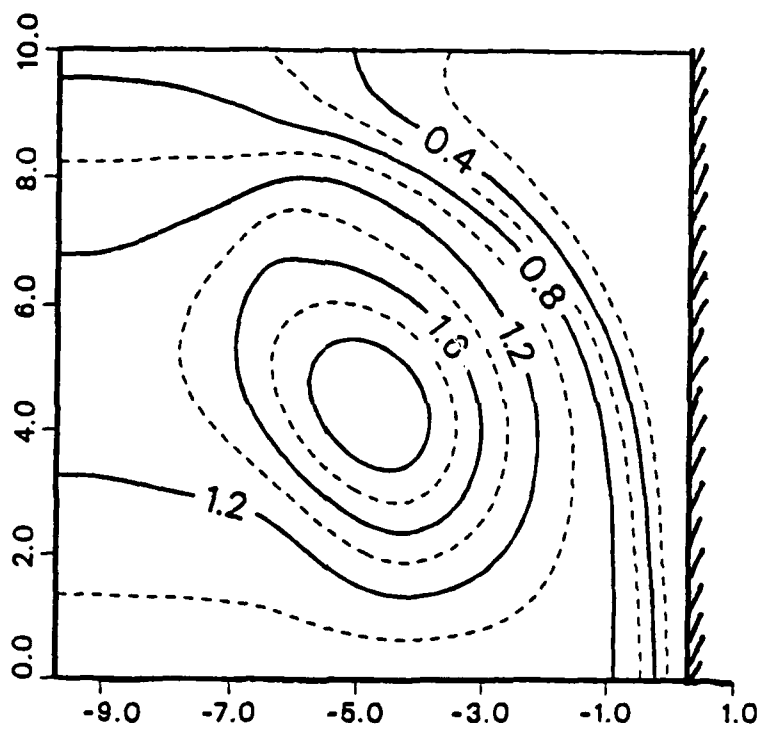


Fig.17 The isolines of the stream function. Experiment 7,  
 $T = 40$ .

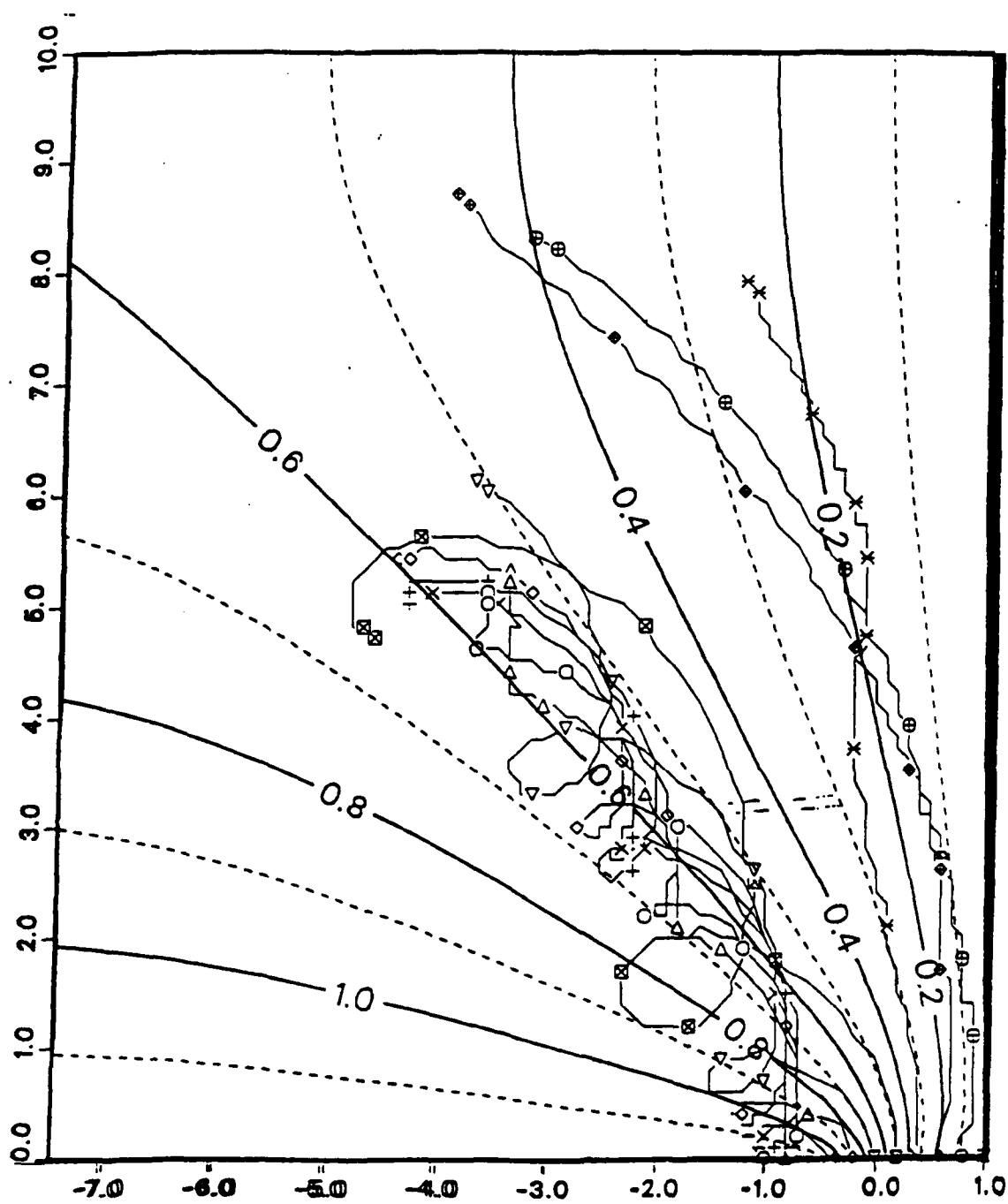


Fig.18 The trajectories of the particles with the initial stream function. Experiment 5.

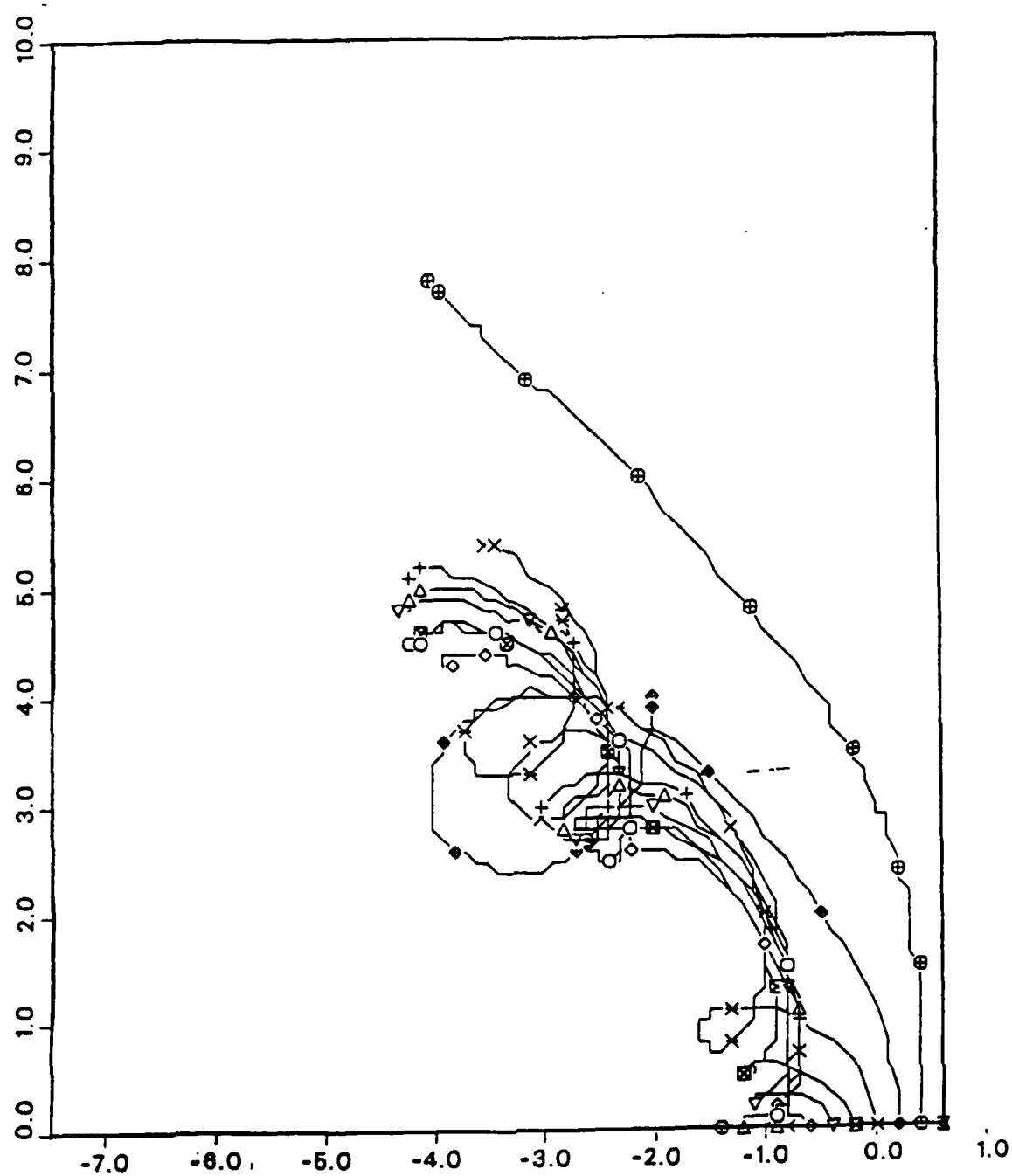


Fig.19 The trajectories of the particles. Experiment 6.

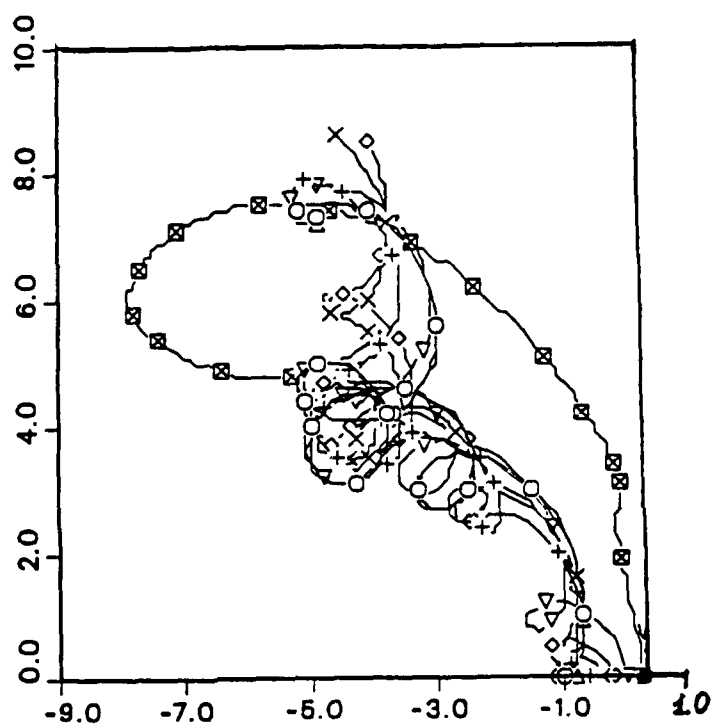


Fig.20 The trajectories of the particles. Experiment 7.

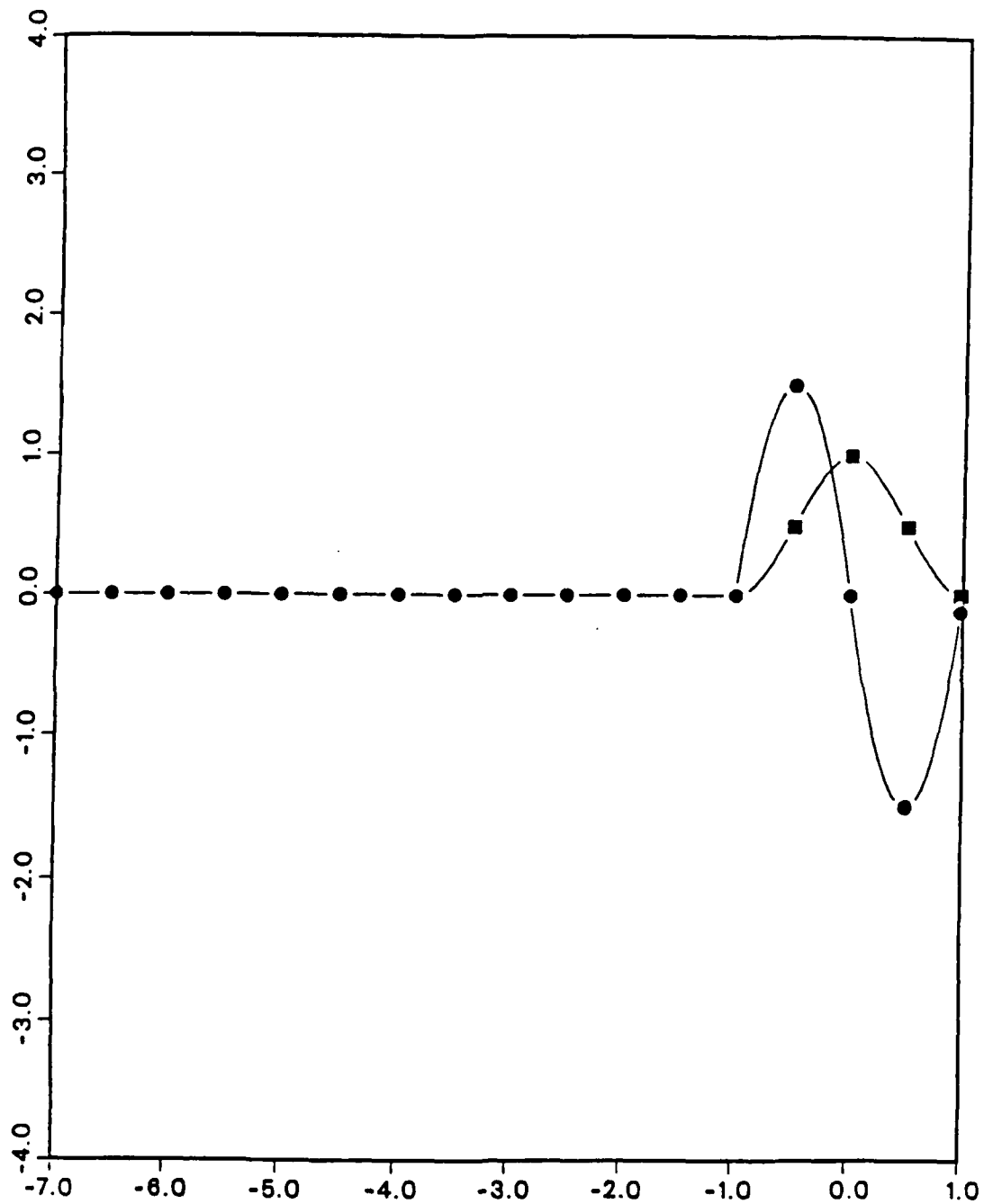


Fig.21 The profile of the vorticity (●) and the velocity (■) for the experiments 8 and 9 with a slippery wall.

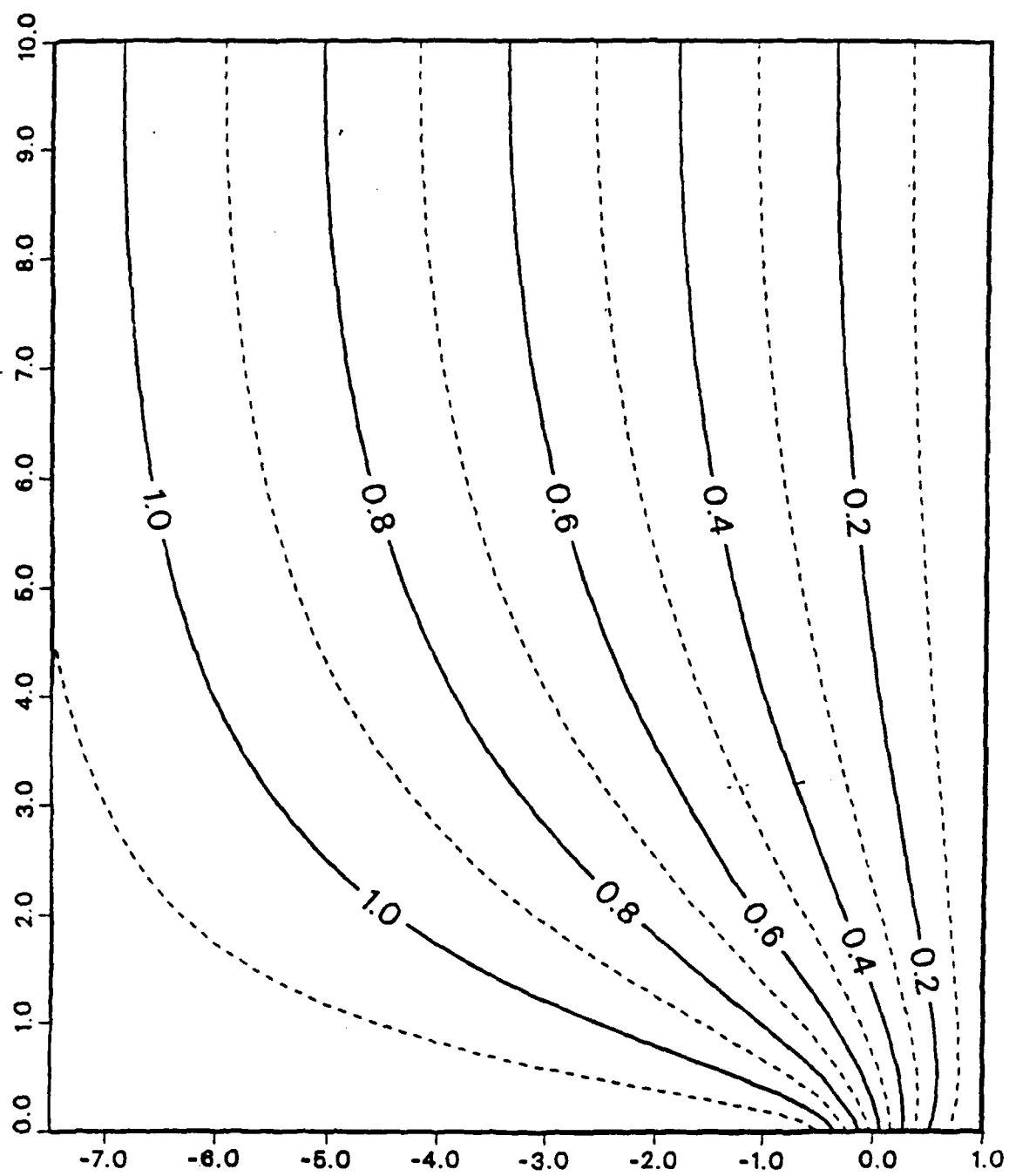


Fig.22 The potential flow for the experiment 9.



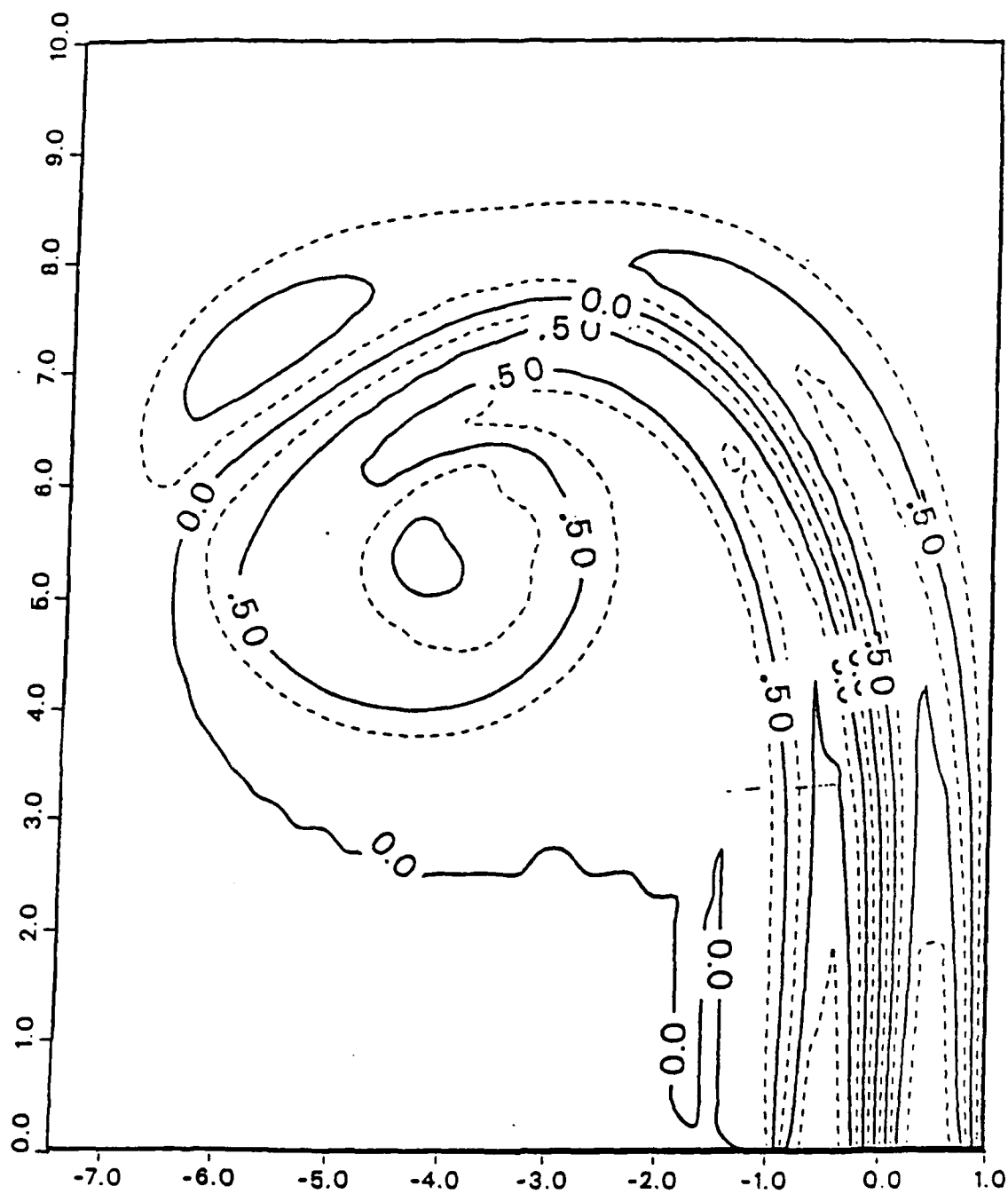


Fig.23 The isolines of the vorticity. Experiment 3,  $T = 32$ .

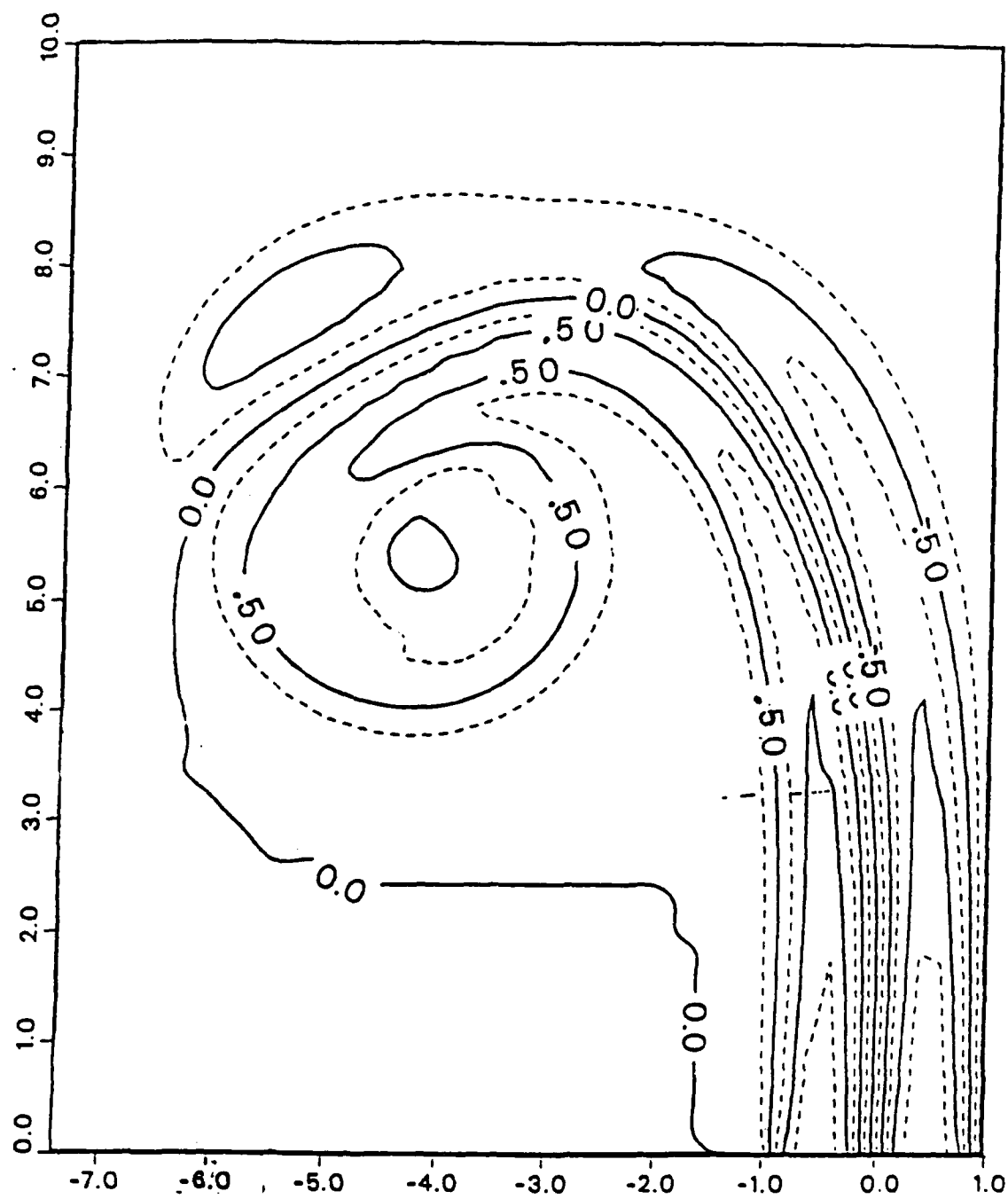


Fig.24 The isolines of the vorticity. Experiment 9,  $T = 32$ .

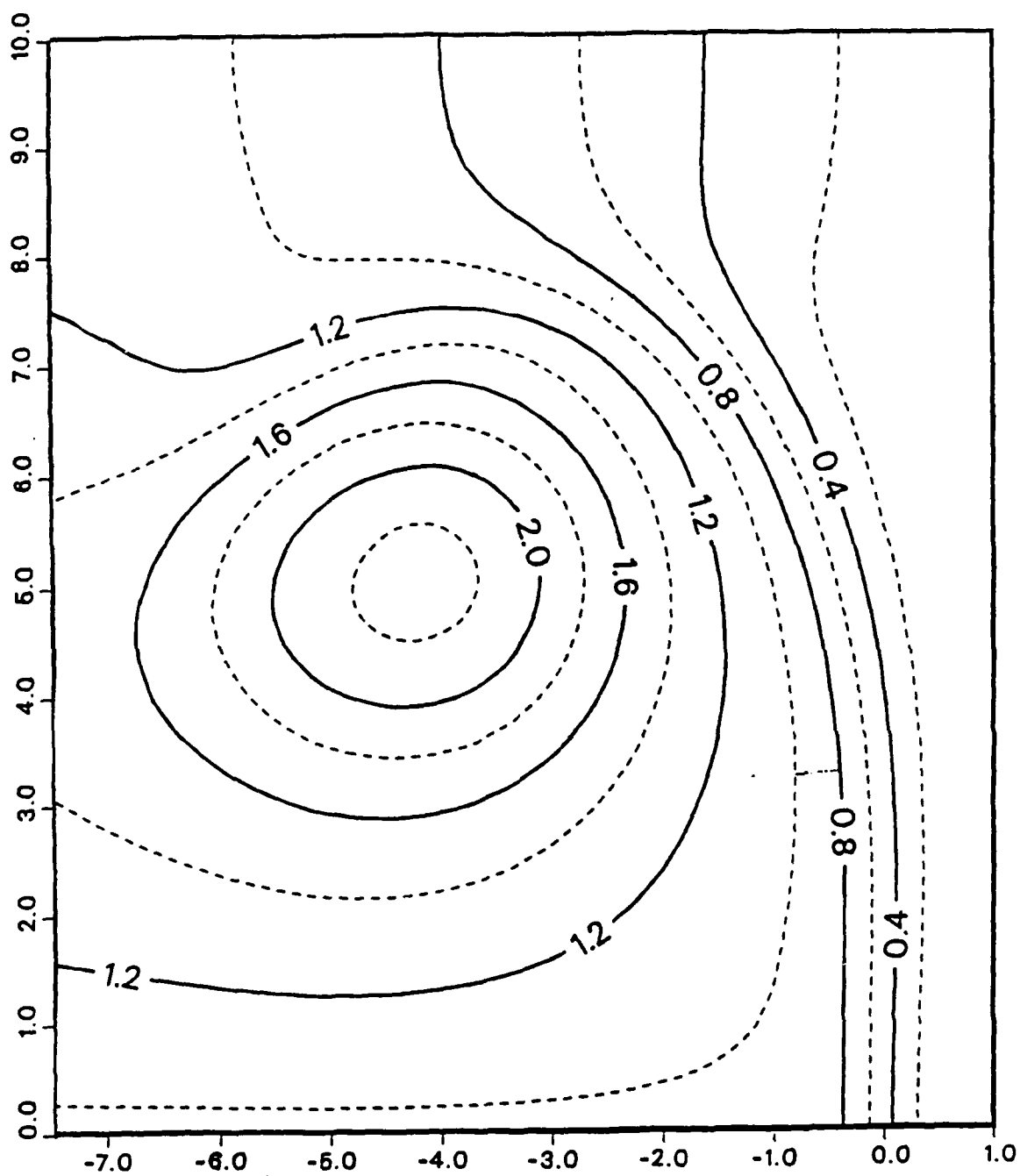


Fig.25 The isolines of the stream function. Experiment 8,  
 $T = 32$ .

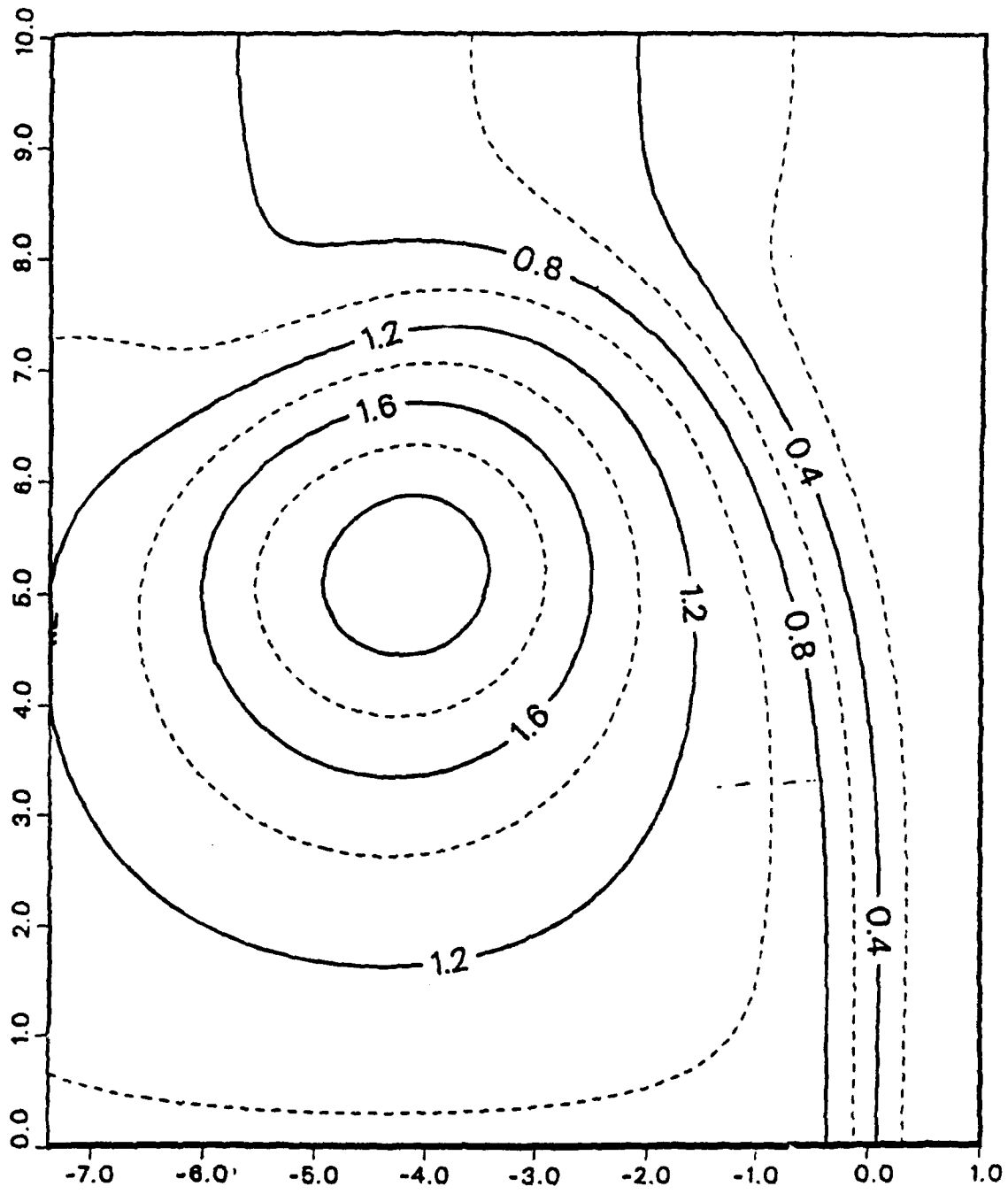


Fig.26 The isolines of the stream function. Experiment 9,  
 $T = 32$

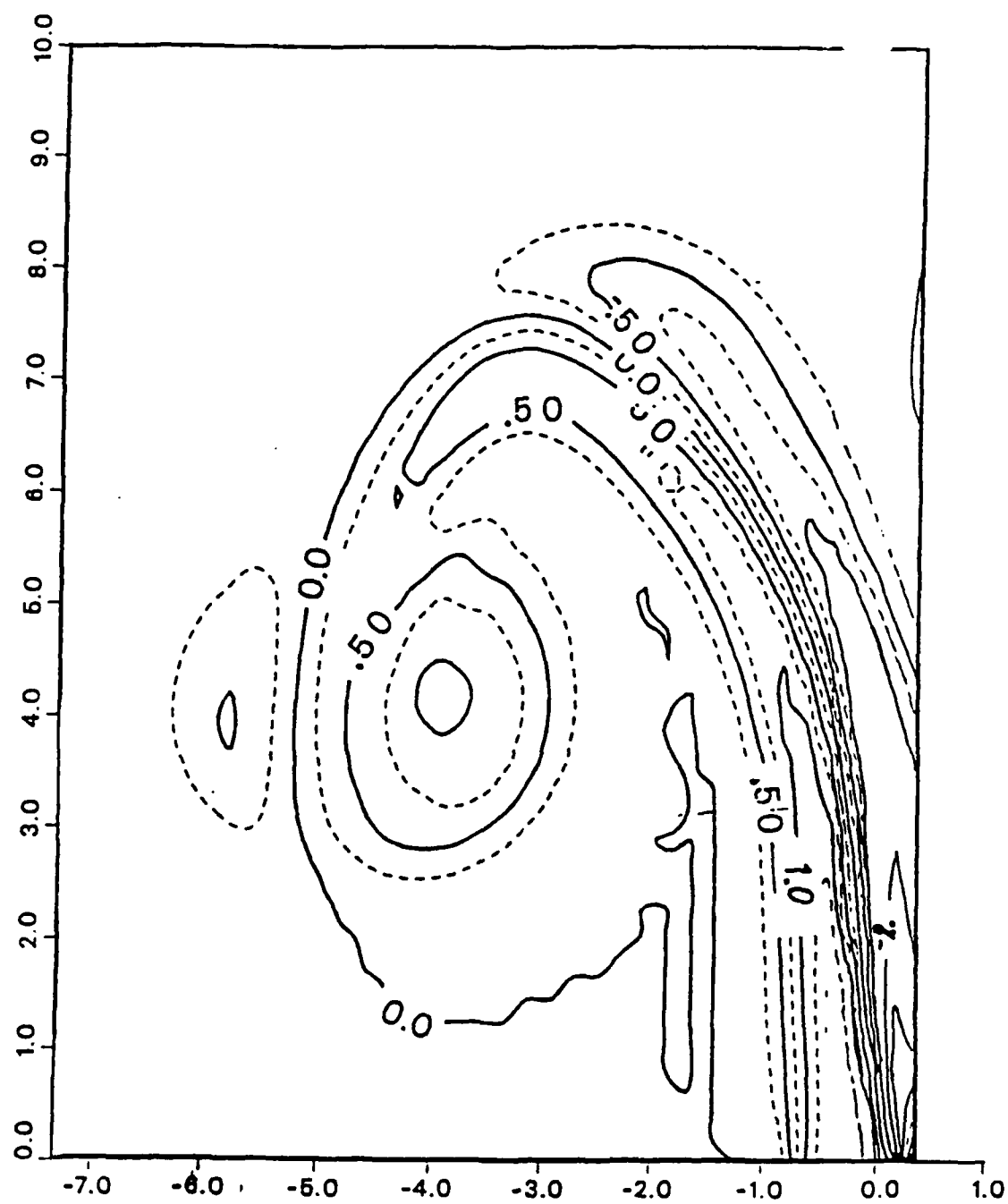


Fig.27 The isolines of the vorticity. Experiment 10,  $T = 32$ .

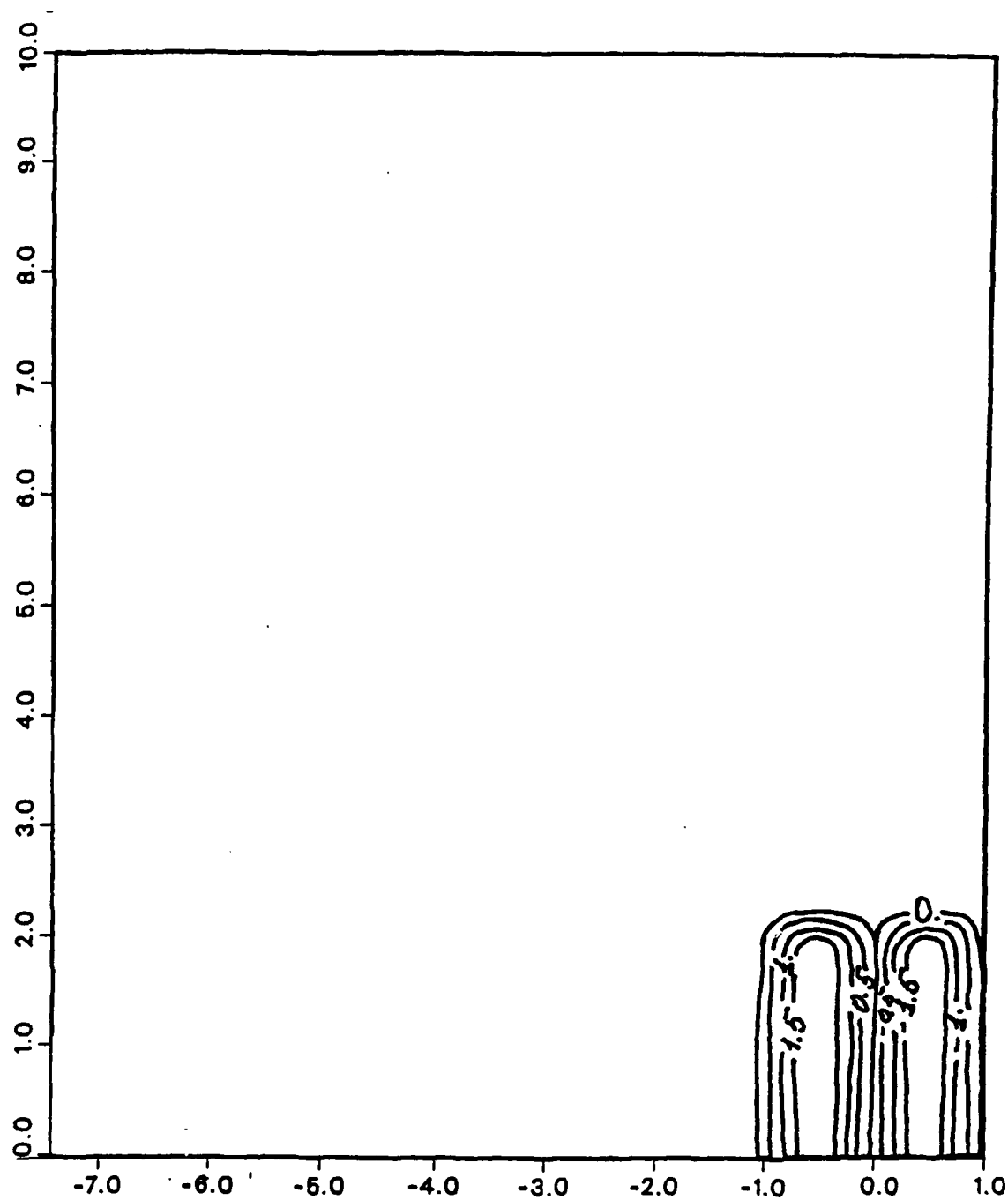


Fig.28 The initial field of the vorticity. Experiment 11.

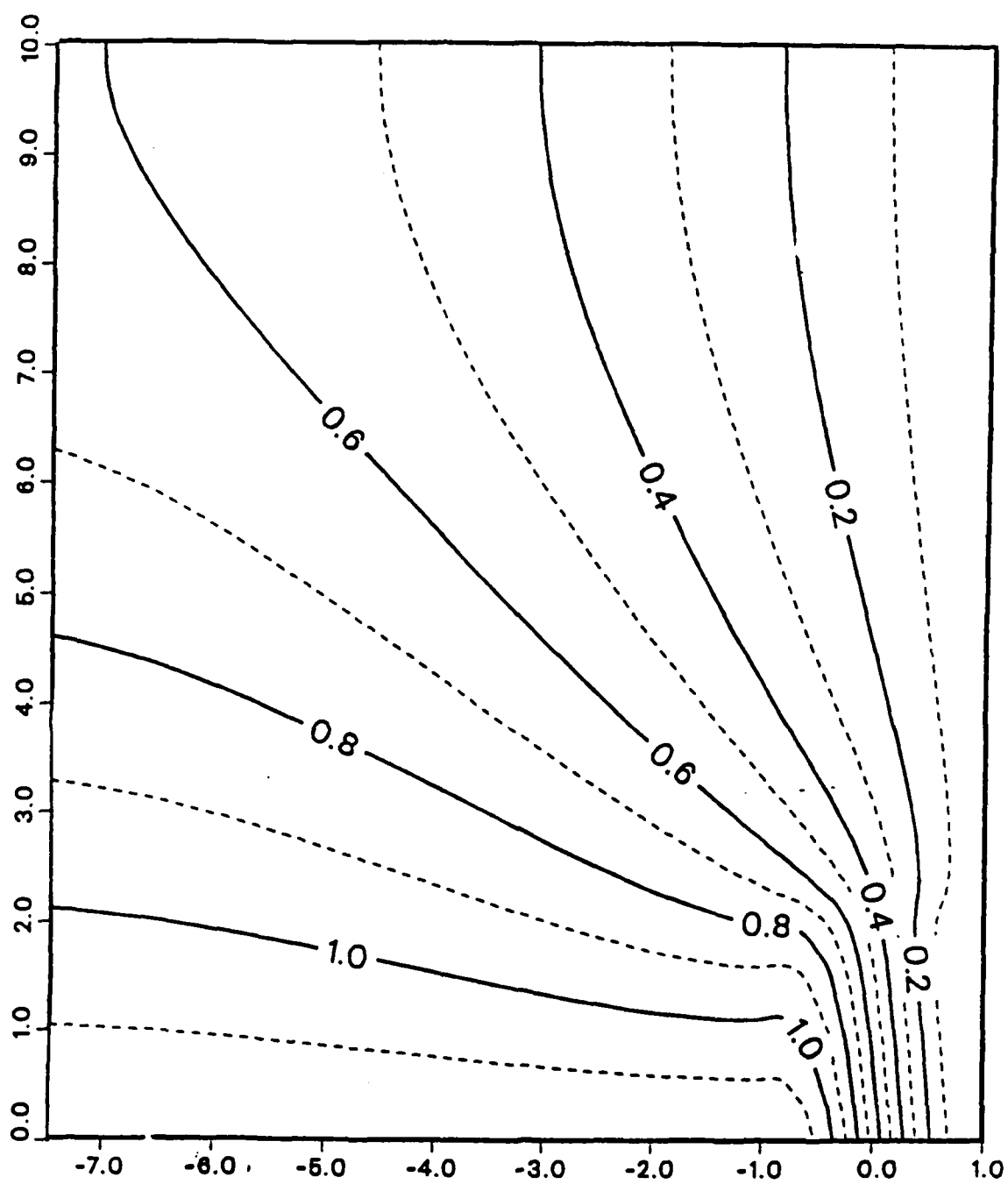


Fig.29 The initial stream function. Experiment 11.

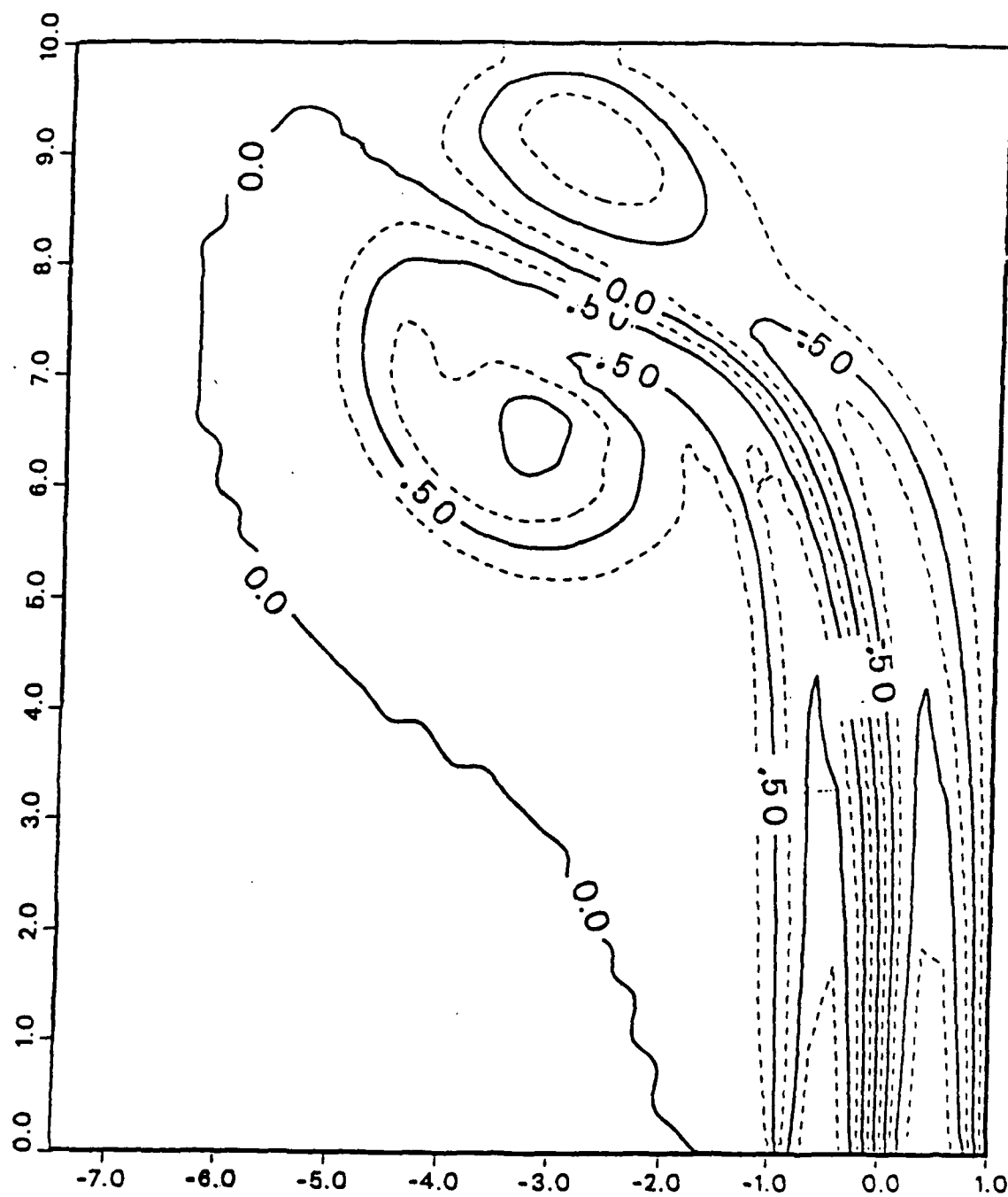


Fig.30 The isolines of the vorticity. Experiment 11,  $T = 24$ .



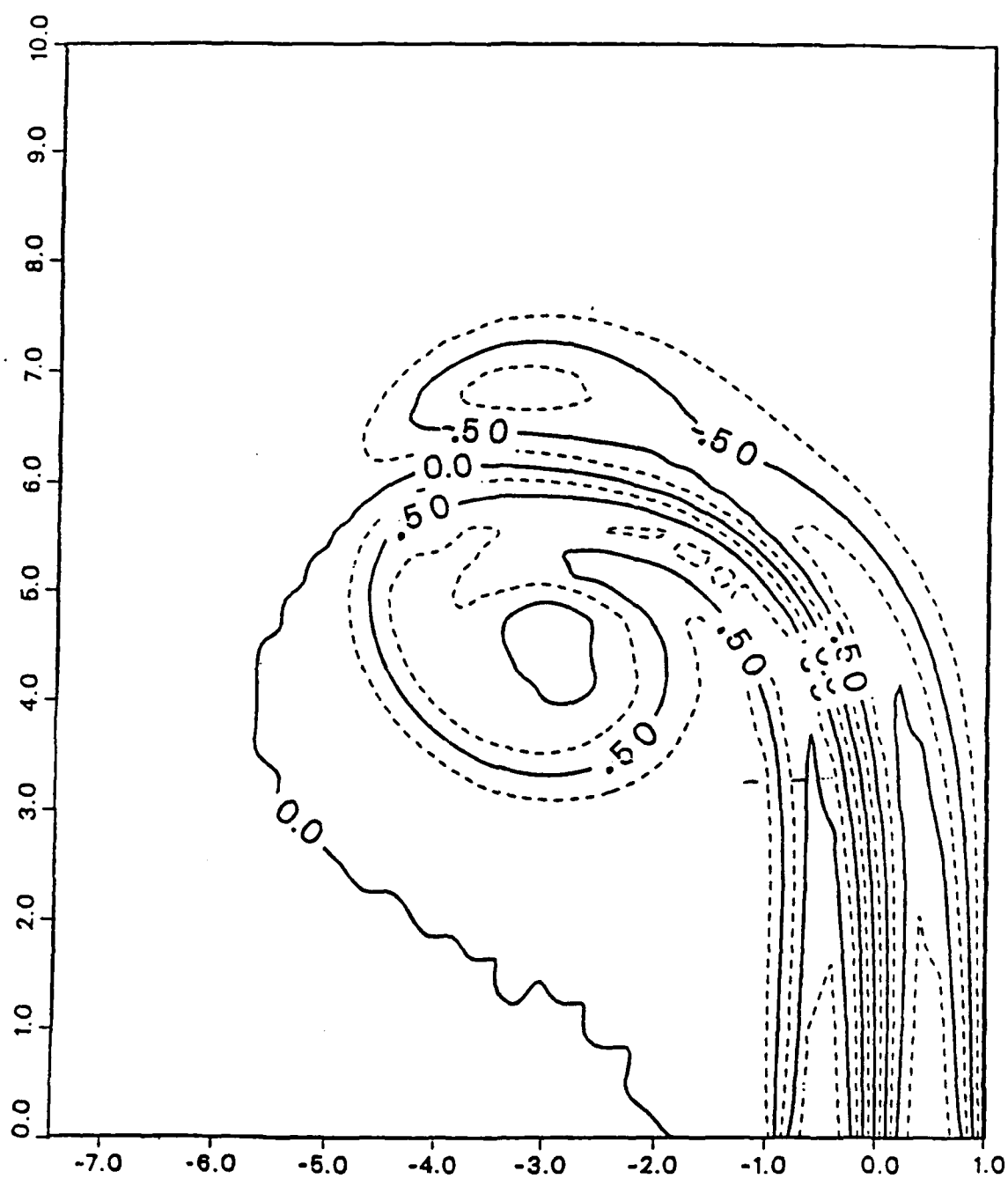


Fig.31 The isolines of the vorticity. Experiment 8,  $T = 24$ .

## DOCUMENT LIBRARY

July 5, 1989

### *Distribution List for Technical Report Exchange*

Attn: Stella Sanchez-Wade  
Documents Section  
Scripps Institution of Oceanography  
Library, Mail Code C-075C  
La Jolla, CA 92093

Hancock Library of Biology &  
Oceanography  
Alan Hancock Laboratory  
University of Southern California  
University Park  
Los Angeles, CA 90089-0371

Gifts & Exchanges  
Library  
Bedford Institute of Oceanography  
P.O. Box 1006  
Dartmouth, NS, B2Y 4A2, CANADA

Office of the International  
Ice Patrol  
c/o Coast Guard R & D Center  
Avery Point  
Groton, CT 06340

Library  
Physical Oceanographic Laboratory  
Nova University  
8000 N. Ocean Drive  
Dania, FL 33304

NOAA/EDIS Miami Library Center  
4301 Rickenbacker Causeway  
Miami, FL 33149

Library  
Skidaway Institute of Oceanography  
P.O. Box 13687  
Savannah, GA 31416

Institute of Geophysics  
University of Hawaii  
Library Room 252  
2525 Correa Road  
Honolulu, HI 96822

Library  
Chesapeake Bay Institute  
4800 Atwell Road  
Shady Side, MD 20876

MIT Libraries  
Serial Journal Room 14E-210  
Cambridge, MA 02139

Director, Ralph M. Parsons Laboratory  
Room 48-311  
MIT  
Cambridge, MA 02139

Marine Resources Information Center  
Building E38-320  
MIT  
Cambridge, MA 02139

Library  
Lamont-Doherty Geological  
Observatory  
Columbia University  
Palisades, NY 10964

Library  
Serials Department  
Oregon State University  
Corvallis, OR 97331

Pell Marine Science Library  
University of Rhode Island  
Narragansett Bay Campus  
Narragansett, RI 02882

Working Collection  
Texas A&M University  
Dept. of Oceanography  
College Station, TX 77843

Library  
Virginia Institute of Marine Science  
Gloucester Point, VA 23062

Fisheries-Oceanography Library  
151 Oceanography Teaching Bldg.  
University of Washington  
Seattle, WA 98195

Library  
R.S.M.A.S.  
University of Miami  
4600 Rickenbacker Causeway  
Miami, FL 33149

Maury Oceanographic Library  
Naval Oceanographic Office  
Bay St. Louis  
NSTL, MS 39522-5001

Marine Sciences Collection  
Mayaguez Campus Library  
University of Puerto Rico  
Mayaguez, Puerto Rico 00708

<b>REPORT DOCUMENTATION PAGE</b>	<b>1. REPORT NO.</b> WHOI-89-54	<b>2.</b>	<b>3. Recipient's Accession No.</b>
<b>4. Title and Subtitle</b> 1989 Summer Study Program in Geophysical Fluid Dynamics General Circulation of the Oceans			<b>5. Report Date</b> November, 1989
<b>7. Author(s)</b> Steering Committee edited by Barbara Ewing-DeRemer			<b>8. Performing Organization Rept. No.</b> WHOI-89-54
<b>9. Performing Organization Name and Address</b>  The Woods Hole Oceanographic Institution Woods Hole, Massachusetts 02543			<b>10. Project/Task/Work Unit No.</b>
			<b>11. Contract(C) or Grant(G) No.</b> (C) (G) OCE 89-01012
<b>12. Sponsoring Organization Name and Address</b>  Funding was provided by the National Science Foundation			<b>13. Type of Report &amp; Period Covered</b>  Technical Report
			<b>14.</b>
<b>15. Supplementary Notes</b> This report should be cited as: Woods Hole Oceanog. Inst. Tech. Rept., WHOI-89-54			
<b>16. Abstract (Limit: 200 words)</b>  The success of this summer's Geophysical Fluid Dynamics Program owes much to Myrl Hendershott's excellent and engaging survey of the Oceans' General Circulation, including recent developments in the Theory of Recirculation Gyres and Thermocline Ventilation. Hendershott's lecture notes are included in the first part of this volume.  The diverse fluid dynamical subjects discussed in this summer's program are summarized in the abstracts of lectures by the staff and visitors. But the main thrust of this summer is, as always, revealed in the reports of the individual research by the Fellows.  This document should be treated as an unpublished manuscript. The fellows' reports may become part of doctoral work or publications. Permission of the author should be obtained if you wish to reference work in this document.			
<b>17. Document Analysis a. Descriptors</b>  1. geophysical fluid dynamics 2. general circulation 3. ocean  <b>b. Identifiers/Open-Ended Terms</b>     <b>c. COSATI Field/Group</b>			
<b>18. Availability Statement</b> Approved for publication; distribution unlimited.		<b>19. Security Class (This Report)</b> UNCLASSIFIED	<b>21. No. of Pages</b> 512
		<b>20. Security Class (This Page)</b>	<b>22. Price</b>